Nanostructure Science and Technology
Series Editor: David J. Lockwood

Harekrushna Sahoo
Jitendra Kumar Sahoo *Editors*

Iron Oxide-Based Nanocomposites and Nanoenzymes

Fundamentals and Applications

Springer

Nanostructure Science and Technology

Nanostructure science and technology now forms a common thread that runs through all physical and materials sciences and is emerging in industrial applications as nanotechnology. The breadth of the subject material is demonstrated by the fact that it covers and intertwines many of the traditional areas of physics, chemistry, biology, and medicine. Within each main topic in this field there can be many subfields. For example, the electrical properties of nanostructured materials is a topic that can cover electron transport in semiconductor quantum dots, self-assembled molecular nanostructures, carbon nanotubes, chemically tailored hybrid magnetic-semiconductor nanostructures, colloidal quantum dots, nanostructured superconductors, nanocrystalline electronic junctions, etc. Obviously, no one book can cope with such a diversity of subject matter. The nanostructured material system is, however, of increasing significance in our technology-dominated economy and this suggests the need for a series of books to cover recent developments.

The scope of the series is designed to cover as much of the subject matter as possible – from physics and chemistry to biology and medicine, and from basic science to applications. At present, the most significant subject areas are concentrated in basic science and mainly within physics and chemistry, but as time goes by more importance will inevitably be given to subjects in applied science and will also include biology and medicine. The series will naturally accommodate this flow of developments in the sciences and technology of nanostructures and maintain its topicality by virtue of its broad emphasis. It is important that emerging areas in the biological and medical sciences, for example, not be ignored as, despite their diversity, developments in this field are often interlinked. The series will maintain the required cohesiveness from a judicious mix of edited volumes and monographs that while covering subfields in depth will also contain more general and interdisciplinary texts.

Thus the series is planned to cover in a coherent fashion the developments in basic research from the distinct viewpoints of physics, chemistry, biology, and materials science and also the engineering technologies emerging from this research. Each volume will also reflect this flow from science to technology. As time goes by, the earlier series volumes will then serve as reference texts to subsequent volumes.

Harekrushna Sahoo · Jitendra Kumar Sahoo
Editors

Iron Oxide-Based Nanocomposites and Nanoenzymes

Fundamentals and Applications

Springer

Editors
Harekrushna Sahoo
Department of Chemistry
National Institute of Technology Rourkela
Rourkela, Odisha, India

Jitendra Kumar Sahoo
Department of Chemistry
School of Sciences
GIET University
Gunupur, Odisha, India

ISSN 1571-5744 ISSN 2197-7976 (electronic)
Nanostructure Science and Technology
ISBN 978-3-031-44598-9 ISBN 978-3-031-44599-6 (eBook)
https://doi.org/10.1007/978-3-031-44599-6

This Springer imprint is published by the registered company Springer Nature Switzerland AG
The registered company address is: Gewerbestrasse 11, 6330 Cham, Switzerland

Paper in this product is recyclable.

Dedicated
to
"All Researchers around the world"

Foreword

Nanomaterials have revolutionized numerous areas of science and technology. Because of their diversity, nanomaterials have a wide range of applications. In particular, iron oxide-based nanotechnology is a rapidly evolving field that promises unique advantages for the development of a broad array of bioactive molecules and electronic compounds. The book edited by Harekrushna Sahoo and Jitendra Kumar Sahoo is a collection of a variety of chapters that cover the most important topics in the field, starting from the synthesis and characterization of magnetic iron oxide nanoparticles to applications like photocatalysis and biomedicines. The book provides the reader with an overview of the diversity of magnetic iron oxide nanoparticles, from basic design concepts to their application in various contexts. At last, one can get a general idea of the utility of magnetic nanoparticles. Recognized experts in materials science explain how such nanoparticles exhibit their usefulness in biotechnology and environmental studies. Electronics specialists working on integrated circuits have participated in the miniaturization race, moving from micro- to submicrodimensions, while getting closer and closer to application in supercapacitors. The presented compilation affects not only electronics, biotechnology, and environmental sciences, but also other disciplines such as biomedicine and water treatment. As might be expected, all these technological applications come with some concerns, mainly because of their potentially large impact on humanity and society. We therefore need to be aware of the current challenges and the associated risks. I would like to invite the reader to join the editors on their journey to put together an important and meaningful book aimed at a wide audience around the world. With the help of this book, let us discover the new world of magnetic iron oxide nanoparticles focusing on the main perspectives of their applications.

Aleksander Czogalla
Professor in Biotechnology
University of Wrocław
Wrocław, Poland

Preface

Nanotechnology, as a complement to physical chemistry, forms a means of knowledge and mastery of the core materials or interface with antimatter. Nanotechnology provides many benefits in many areas of life. We are really happy to represent this book, keeping in mind the requirements of research in the fields of industries, aeronautics, biotechnology, electronics, medicines, chemistry, physics, environment, and ecology. Each chapter gives a broad perspective on the iron oxide-based nanomaterials used in various fields such as environmental, medical, supercapacitor, and photovoltaic applications. Chapter 1 includes various routes for the synthesis of iron oxide nanoparticles and details modifications of iron oxide nanoparticles. Chapter 2 of the book illustrates the action of magnetic iron oxide-based nanocomposite towards the removal of various organic dyes from wastewater. This chapter sums up the synthesis and characterization of the nanocomposites and discusses various parameters studied about organic dye removal and its mechanism. Chapter 3 presents the applications of iron oxide nanozymes in human health, such as cancer and tumours, wound healing, and cardiac diseases. Chapter 4 discusses the removal of organic pollutants from aqueous media using iron oxide-based photocatalysts. This chapter particularly focused on the evolution of composites and heterostructures of iron oxide-based photocatalysts and their photocatalytic applications towards the removal of organic pollutants. Chapter 5 of this book represents a brief study about functionalized iron oxide in order to increase the electrochemical performance of supercapacitors. Chapter 6 interprets the medicinal use of iron oxide nanozymes (IONzymes). This chapter is a collective study of the synthesis, properties, and application of IONzymes. Chapter 7 explains the synthesis of nanoscale zero-valent iron (nZVIO) and its composites for the removal of toxic heavy metals from wastewater. Chapter 8 represents the synthesis and application of bismuth ferrite (BFO) and its photovoltaic applications. Chapter 9 discusses the reusability of various magnetic adsorbents and the removal of organic pollutants using them. In this chapter, various adsorption parameters are also studied. Chapter 10 of the book presents the morphological study of iron oxide-based nanoarchitectures. This chapter contains the environmental applications of iron oxide-based nanostructures, such as the removal of heavy meals and organic contaminants. Chapter 11 explains the remediation of the environment using

magnetic nanomaterials. This study includes information about the uses of magnetic nanomaterials in the field of wastewater treatment, like the removal of toxic metal ions, pesticides, and antibiotics. Chapter 12 discusses wastewater treatment using iron oxide-based nanomaterials. This chapter briefly explains various parameters for the removal of pesticides, organic dyes, and other pollutants. Chapter 13 explains that iron and iron oxide-based catalysts or supports have been extensively tested due to their intrinsic activity or promotional activity as supports, high natural abundance, low cost, and no toxicity. Chapter 14 suggests the synthesis and application of non-spherical iron oxide particles. This chapter also includes the interfacial behaviour of non-spherical iron oxide particles. Chapter 15 represents the application of different magnetic nanomaterials in the biotechnology field. This study states that magnetic nanoparticles provide significant future potential for efficient cancer treatment. This book was developed from a course taught by the author that is targeted towards master's and research students of science and engineering.

Rourkela, India — Harekrushna Sahoo
Gunupur, India — Jitendra Kumar Sahoo

Acknowledgements Writing a book is harder than I thought and more rewarding than I could ever imagine. None of this would have been possible without my research friends, who contributed chapters to this book. Thanks to everyone on the Scribe team who helped me so much. I convey my special thanks to Juhi, Himanshu, Preeti, Jyoti, Debasish, Jayshree, and Biswajit for providing us with careful and thoughtful feedback. I want to convey my sincere gratitude to my alma mater, NIT Rourkela, and GIET University, Gunupur, who encouraged and assisted me in every possible way to make this impossible possible. Thanks to everyone on my publishing team.

Contents

Editors and Contributors

About the Editors

Dr. Harekrushna Sahoo is a faculty of Chemistry at NIT Rourkela (a premier academic institute in India) since 2012. Before joining at NIT Rourkela, Dr. Sahoo had the postdoctoral experiences at multiple universities (UMASS Amherst [USA], TUD Dresden [Germany], and MBC Dresden [Germany]). Dr. Sahoo finished his Ph.D. in 2007 at Jacobs University Bremen (Germany) in a group advised by Prof. Werner M. Nau in the field of peptide chemistry. Thereafter, Dr. Sahoo experienced in the field of protein and membrane fields using advanced optical spectroscopic techniques. Currently, Dr. Sahoo is working in different research fields such as protein dynamics, extracellular matrix, nanocomposites, and environmental chemistry. To make his research work wider and more visible, he is collaborating with national and international faculties.

Dr. Jitendra Kumar Sahoo completed his Ph.D. from NIT Rourkela in the field of nano- and environmental Chemistry. In 2019, he joined as Assistant Professor in Chemistry at GIET University, Gunupur, Rayagada, Odisha, India. He has established a Nano and Environmental Laboratory in GIET University. Dr. Sahoo received B.Sc., M.Sc., and Ph.D. degrees in chemistry. His Ph.D. thesis was on the "Iron Oxide Based Magnetic Nanocomposites: Removal of Inorganic and Organic Water Contaminants and Antimicrobial Properties". He has expertise in the fields of wastewater treatment, graphene-based materials, nanomaterials, photocatalysis, adsorption of inorganic and organic contaminates synthesis of novel magnetic nanomaterials, and antibacterial activity. He has got many collaborative works with eminent professor from IIT, NIT, and CSIR Laboratory of India and foreign professors as well. He taught various courses to undergraduate and postgraduate students. Dr. Sahoo is a frequent speaker at national and international conferences. Dr. Sahoo is Editorial Board member in Environmental Protection Research Journal. He has authored many book chapters with Cambridge Press, Stadium Press, Springer, and Elsevier. He has a good number of publications to his credit in many peer-reviewed, high-impact journals of international repute. He has received the Young Scientist Award in 2021 for his contribution and honourable achievements in innovative research. He has received the Incredible Young Researchers of India award in 2022 from Record Owner.

Contributors

Diptikanta Acharya Department of Biotechnology, GIET University, Gunupur, Rayagada, Odisha, India

S. Anaina Department of Chemistry, Indian Institute of Technology Palakkad, Kozhipara, Palakkad, Kerala, India

T. G. Anjali Polymer Engineering and Colloid Science (PECS) Laboratory, Department of Chemical Engineering, Indian Institute of Technology Madras, Chennai, India

Madivala G. Basavaraj Polymer Engineering and Colloid Science (PECS) Laboratory, Department of Chemical Engineering, Indian Institute of Technology Madras, Chennai, India

Tapan Kumar Bastia Environmental Science Laboratory, School of Applied Sciences, Kalinga Institute of Industrial Technology, Deemed to be University, Bhubaneswar, India

D. Krishna Bhat Department of Chemistry, National Institute of Technology Karnataka, Surathkal, Mangalore, India

Adarshi Bhattacharya Environmental Science Laboratory, School of Applied Sciences, Kalinga Institute of Industrial Technology, Deemed to be University, Bhubaneswar, India

Yagna Prakash Bhoi Hefei National Laboratory for Physical Sciences at Microscale, Department of Chemical Physics, University of Science and Technology of China, Hefei, P.R. China

Manisha Dash Environmental Science Laboratory, School of Applied Sciences, Kalinga Institute of Industrial Technology, Deemed to be University, Bhubaneswar, India

Jyotirmayee Giri Environmental Science Laboratory, School of Applied Sciences, Kalinga Institute of Industrial Technology, Deemed to be University, Bhubaneswar, India

Nishesh Kumar Gupta Department of Environmental Research, University of Science and Technology (UST), Daejeon, Korea;
Department of Environmental Research, Korea Institute of Civil Engineering and Building Technology (KICT), Goyang, Korea

Weixin Huang Hefei National Laboratory for Physical Sciences at Microscale, Department of Chemical Physics, University of Science and Technology of China, Hefei, P.R. China

D. Jagadeesan Department of Chemistry, Indian Institute of Technology Palakkad, Kozhipara, Palakkad, Kerala, India;
Environmental Sciences and Sustainable Engineering Centre (ESSENCE), Indian Institute of Technology Palakkad, Kozhipara, Palakkad, Kerala, India

Sudarshan Khudwakar Department of Civil and Environmental Engineering, California State University, Fullerton, CA, USA

Amit Kumar Department of Human and Molecular Genetics, Virginia Commonwealth University, School of Medicine, Richmond, VA, USA

Hemant Kumar Polymer Engineering and Colloid Science (PECS) Laboratory, Department of Chemical Engineering, Indian Institute of Technology Madras, Chennai, India

Carolina Leyva Instituto Politécnico Nacional, Centro de Investigación en Ciencia Aplicada y Tecnología Avanzada, Mexico City, Mexico

Biswajit Mohanty Department of Chemistry, GIET University, Gunupur, Odisha, India

Hari Sankar Mohanty Department of Physics, GIET University, Gunupur, Odisha, India

Shibani Mohapatra Environmental Science Laboratory, School of Applied Sciences, Kalinga Institute of Industrial Technology, Deemed to be University, Bhubaneswar, India

Alok Kumar Panda Environmental Science Laboratory, School of Applied Sciences, Kalinga Institute of Industrial Technology, Deemed to be University, Bhubaneswar, India

Gagan Kumar Panigrahi School of Applied Sciences, Centurion University of Technology and Management, Bhubaneswar, Odisha, India

Priyanka Patel School of Applied Sciences, Centurion University of Technology and Management, Bhubaneswar, Odisha, India

Raj Kishore Patel Department of Chemistry, National Institute of Technology, Rourkela, India

Dillip Pattanayak Department of Physics, GIET University, Gunupur, Rayagada, Odisha, India

Samita Pattanayak Department of Physics, Odisha University of Technology and Research, Bhubaneswar, Odisha, India

Sourav Prusty Department of Chemistry, GIET University, Gunupur, Rayagada, Odisha, India

Shengyan Pu State Key Laboratory of Geohazard Prevention and Geoenvironment Protection, Chengdu University of Technology, Chengdu, Sichuan, People's Republic of China

Mohammad Qureshi Department of Chemistry, IIT Guwahati, Guwahati, Assam, India

Jyoti Prakash Rath Department of Chemistry, GIET University, Gunupur, Odisha, India

Prasanta Rath Environmental Science Laboratory, School of Applied Sciences, Kalinga Institute of Industrial Technology, Deemed to be University, Bhubaneswar, India

M. Roshni Department of Chemistry, Indian Institute of Technology Palakkad, Kozhipara, Palakkad, Kerala, India

Chinmaya Rout Department of Physics, GIET University, Gunupur, Rayagada, Odisha, India

Anupama Sahoo School of Applied Sciences, Centurion University of Technology and Management, Bhubaneswar, Odisha, India

Dipti Mayee Sahoo School of Applied Sciences, Centurion University of Technology and Management, Bhubaneswar, Odisha, India

Harekrushna Sahoo Department of Chemistry, National Institute of Technology, Rourkela, India

Jitendra Kumar Sahoo Department of Chemistry, GIET University, Gunupur, Rayagada, Odisha, India

Shraban Kumar Sahoo School of Applied Sciences, Centurion University of Technology and Management, Bhubaneswar, Odisha, India

Manoj Kumar Sahu Department of Chemistry, GIET University, Gunupur, Odisha, India

Sushil Kumar Sahu Department of Zoology, Siksha-Bhavana, Visva-Bharati University, Santiniketan, West Bengal, India

Tushar Kanta Sahu Department of Chemistry, IIT Guwahati, Guwahati, Assam, India

Uttam Kumar Sahu State Key Laboratory of Geohazard Prevention and Geoenvironment Protection, Chengdu University of Technology, Chengdu, Sichuan, People's Republic of China;
Department of BSH, GIET University, Gunupur, Odisha, India

Sagarika Satapathy Department of Biotechnology, GIET University, Gunupur, Rayagada, Odisha, India

Soumyaranjan Senapati Environmental Science Laboratory, School of Applied Sciences, Kalinga Institute of Industrial Technology, Deemed to be University, Bhubaneswar, India

Meenaketan Sethi Department of Chemistry, National Institute of Technology Karnataka, Surathkal, Mangalore, India

Himanshu Shekhar Department of Chemistry, National Institute of Technology, Rourkela, India

U. Sandhya Shenoy Department of Materials Science and Engineering, Institute of Engineering and Technology, Srinivas University, Mukka, Mangalore, India

Silpa Subhalaxmi School of Applied Sciences, Centurion University of Technology and Management, Bhubaneswar, Odisha, India

Pooja Upadhyaya Department of Chemistry, GIET University, Gunupur, Rayagada, Odisha, India

Herlys Viltres School of Engineering Practice and Technology, McMaster University, Hamilton, ON, Canada

Melaku Masresha Woldeamanuel Environmental Science Laboratory, School of Applied Sciences, Kalinga Institute of Industrial Technology, Deemed to be University, Bhubaneswar, India

Chapter 1
Introduction

Jitendra Kumar Sahoo and Sourav Prusty

1.1 Introduction

Nanomaterials comprise the study of chemical materials or substances within the nanoscale, i.e. in the range of 1–100 nm. At this nanoscale, materials show inimitable properties based on their quantum phenomena (electron tunnelling, near field-optical methods, electron confinement ballistic transport, and quantum entanglement) or on the basis of subdomains (superparamagnetism and overlapping of double layers in the fluids) [1, 2]. In the present era, nanomaterials are regarded as the emerging advanced research domain in chemistry, physics, material engineering, and bioscience. In comparison with conventional materials, nanomaterials permit distinctive and unique physical, electrical, chemical, mechanical, and optical properties [3, 4]. Nanomaterials have a wide range of applications for various commercial purposes, for instance in semiconductors, cosmetics, catalysts, adsorbents, photocatalysts as carriers of drugs, fillers, antifriction coatings, storage, microelectronics, energy storage, etc. In addition, nanomaterials also have a broad range of applications in wastewater treatment, the production of energy, and sensing. In the preceding period, most of the research was focused on experimental and theoretical advancements in characterisation, novel synthesis, and an assortment of applications using a variety of nanostructures such as ceramics, nanocomposite materials, and metal oxides [5–10]. Among the widely available inorganic materials, metal oxide nanomaterials have gained significant attention, particularly in the fields of engineering and science. Metal oxide possesses exceptional physical and chemical properties due to its diminutive size and high density. Metal oxides also have large-scale applications in the treatment of wastewater, like degradation, catalysis, sensors, and adsorption [11, 12].

J. K. Sahoo (✉) · S. Prusty
Department of Chemistry, GIET University, Gunupur, Rayagada, Odisha 765022, India
e-mail: jksahoo@giet.edu

H. Sahoo and J. K. Sahoo (eds.), *Iron Oxide-Based Nanocomposites and Nanoenzymes*,
Nanostructure Science and Technology, https://doi.org/10.1007/978-3-031-44599-6_1

As the metals formed various types of oxide compounds, they showed several structural geometries through different electronic structures with semiconductor, metallic, and insulator characteristics. Metal oxides exhibit various properties such as magnetic, optical, photoelectrochemical, mechanical, optoelectronic, thermal, and catalytic [13, 14]. Metal oxides are small-scale-based nanomaterials that can augment the surface area-to-volume ratio and enhance their properties in comparison to vast materials. Additionally, metal oxide nanoparticles have been widely applied for the treatment of wastewater [11, 15]. For the treatment of wastewater and other functions, various metal oxides such as copper oxide (CuO), cerium oxide (CeO_2), magnesium oxide (MgO), manganese oxide (MnO_2), titanium oxide (TiO_2), iron oxide (Fe_2O_3, Fe_3O_4), and zirconium oxide (ZrO_2) have been extensively employed.

The past few years have drawn the attention of a variety of materials, such as metal–organic frameworks, molecularly imprinted materials, ionic liquids, and carbonaceous materials, in a wide range of techniques in order to diminish the amount of chemicals needed for sample preparation during extraction methods [12–14, 16]. In the middle of all this, magnetic nanomaterials have been found to gain special consideration as they possess special properties like being superparamagnetic due to the pressure of the thermal energy on a nanoparticle with ferromagnetic characteristics [7–10]. Apart from this, magnetic nanomaterials have a special characteristic in that they can separate themselves from the sample with the help of an external magnetic field and effortlessly coalesce with other materials, which shows their diverse functionality. The magnetic nanoparticles are mainly dependent on their surface effects and finite size. For magnetic nanoparticles, the configuration of spherical walls provides a state of high energy as a result of which particles combine together in the form of clumps or clusters. In order to avoid cluster formation, the magnetic nanoparticles are layered with different shells of polymer, carbon, metal oxide, and silica. Moreover, the magnetic nanoparticles have a large surface area, which enhances their catalytic activities [11, 13, 15, 17].

In the present circumstances, researchers are more aligned towards iron oxide-based nanoparticles as they show exceptional magnetic behaviour, a large surface area-to-volume ratio, exist in different oxidation states, can be separated easily from aqueous solutions, are cheap in comparison with other metal oxides, are small in size, have little toxicity, and are environmentally friendly in nature [18–20]. Iron oxide is found to exist in the form of hydroxides, oxides, and oxy-hydroxides. The majority of them include: Fe_3O_4, Fe_4O_3, FeO, Fe_4O_5, and polymorphic forms of Fe_2O_3 (γ-Fe_2O_3 and α-Fe_2O_3, FeOOH, and $Fe(OH)_3$). Amid the various available forms of iron oxide, basically three important phases can be categorised, such as magnetite (Fe_3O_4), hematite (α-Fe_2O_3), and maghemite (γ-Fe_2O_3), which are areas of greater interest due to their magnetic and opto-electrical properties [21]. These phases of iron oxide have practical applications in colour imaging, optical devices, drinking water, gas sensing, magnetocaloric refrigerant, ferrofluid technology, and as magnetic strong media. In the environmental condition, hematite (α-Fe_2O_3) was found to possess a stable form of iron oxide, but it is anti-ferromagnetic in nature as it demonstrates the weak magnetic property as well as being an n-type semiconductor with a band gap of 2.3 eV. Hematite shows a rhombohedral structure, which can be

designated as its most common form, and it shows application in the photocatalyst driven by light in the visible range of 600 nm [17, 22–24]. Maghemite (γ-Fe_2O_3) shows a cubic structure with a band gap of 2.0 eV and possesses magnetic properties in every condition. Maghemite exemplifies a vast range of applications in the field of the fabrication of biocompatible magnetic fluids, in electronic devices, magnetic recorder media, and in MRI. Maghemite consists of 211/3 numbers of Fe^{3+} ions and 32 numbers of O^{2-} ions, and vacancy sites are 21/3, whereas the magnetite shows a cubic spinel-type structure and is found mainly in two oxidation states, such as Fe^{2+} and Fe^{3+}, whose stoichiometric ratio is found to be 1/2. Magnetite that is Fe_3O_4 can be operated as both an n-type and p-type semiconductor with a band gap of 0.1 eV [25, 26]. Magnetite proved to be an effective metal oxide for wastewater treatment due to its fast production rate, rapid uptake, high adsorption capacity, and easy separation. After adsorption, magnetite can be easily separated from an aqueous solution by using an external magnetic field [9, 27]. This iron oxide nanocomposite shows extraordinary efficiency towards wastewater treatment and the removal of dyes as well as toxic heavy metals with carcinogenic effects on aquatic biota.

1.2 Various Routes of Synthesis of Iron Oxide Nanoparticles

Nanoparticles of iron oxide can be synthesised using various physical, biological, and chemical methods. Among all these methods, the chemical method is widely preferred because, in the chemical method, the appearance of bulk material takes place with desirable morphology, tuneable sizes, and shapes possessing all the scientific properties [28, 29]. Iron oxide can be synthesised using various chemical synthetic methods such as coagulation, flocculation, co-precipitation, the sol–gel method, microwave irradiation, microemulsion, hydrothermal, and thermal decomposition techniques [13, 20].

1.2.1 Coagulation

Nanotechnology refers to the ability to produce and design nanoparticles by manipulating atoms as well as molecules at the nanoscale. Wastewater treatment is the most favourable environmental application of this technology. In the present era, iron oxide nanoparticles are studied by researchers as compared to other materials because of their wide utilisation, magnetic properties, low cost, very high adsorption capacity, and high surface area. In coagulation, iron oxide is used as a coagulant. Coagulation is the chemical process by which the electrostatic repulsive force among the particles changes in water. The main role of iron oxide NPs in this technology is due to their magnetic properties. The key term Fe_3O_4 nanoparticles shows innovative

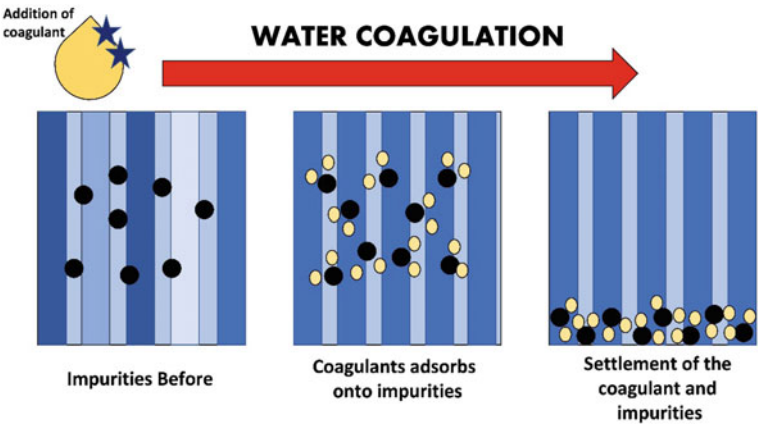

Fig. 1.1 Methods of coagulation

research objects and a database for adsorption mechanisms. The colloidal α-Fe_2O_3 particles have a well-defined coagulation rate at constant temperature. The range of W values is from 1 to 10^4, and pH values vary from 3 to 12. The results of iron oxides are specific for coagulation mechanisms. For anions, the stabilisation concentration of critical coagulation shows a range from 10^{-7} to 10^{-4} molar. With the help of the diffusion layer model, generally, the information regarding potential as well as charges of coagulation species can be known. Ferric sulphate, ferrous sulphate, and ferric chloride are the different forms of iron coagulants. Usually, ferric sulphate is treated as a coagulant in conjugation when it reacts with chlorine, and it refers to the hydrated form that is $FeSO_4 \cdot 7H_2O$. During this period, polymeric ferric sulphates are also available, in which 12.5% w/w of iron is present [12, 30, 31]. Figure 1.1 shows the method of coagulation.

1.2.2 Flocculation

In mineral processing, flocculation is the most adequate technique for the separation of solids, which form larger flocs when removed from water. It is a very spontaneous process, with the help of chemical reagents. In the recent communication, an investigation is being conducted on the kinetics study of flocculation of Fe_3O_4 due to the variation in polyacrylamide's weight. This process was completely studied by taking PAM with the same pH, molecular weight, and ionic strength as the medium. It was observed that the percentage rate of flocculation is directly proportional to the molecular weight of the polymer. Polymers with a higher molecular mass have a higher adsorption capacity to adsorb a higher number of particles. According to the researcher, flocculation also depends on the electrostatic force of attraction. It was observed that the flocculation process is indirectly proportional to the percentage

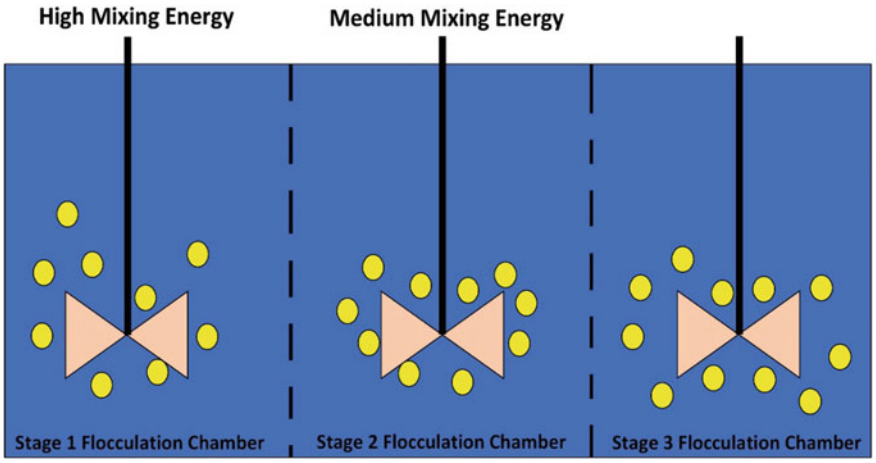

Fig. 1.2 Methods of flocculation

of pH. So, the pH differs from 1.5 to 8.5 range. Using the PAM, the test of flocculation technique is carried out by mixing kaolin and Fe_3O_4 at a ratio of 1:1. H_2O_2, which is an oxidising reagent, can also be used for the preparation of modified iron coagulant, in which it was observed that its density is 1.43 g/mL and 9.47% iron is present [8, 16, 32]. Figure 1.2 shows the method of flocculation.

1.2.3 Co-precipitation

The co-precipitation method refers to the dissolution of materials in a solvent initially and then, after addition of a precipitating reagent, forming a homogeneous inorganic solid. The iron oxide nanoparticles show wide applications in catalysis, biomedicine, and wastewater treatment. Co-precipitation is an extremely ubiquitous method for the formation of Fe_3O_4 NPs, where the pH of the ferric and ferrous solutions depends upon the base added. In this technique, the pH range transits very slowly, i.e. in the range of 2–8. Whenever the divalent iron oxide reacts with the ammonia for the preparation of nanoparticles, by using the co-precipitation method, we get greater magnetisation properties. The co-precipitation method is eco-friendly, the most common, and a simple procedure for the preparation of iron oxide nanoparticles. According to this method, it holds cations very close to each other in the medium and decomposes at a lower temperature. The most common example of this method is the synthesis of metal oxide, i.e. $FeCr_2O_4$. At first, the Fe (III) ion dissolves, and the chromate ion, which is present in water, gets converted to Fe^{3+} and CrO_4^- ions. Then it gets precipitated by the NH_4^+ solution to form a new complex. At last, the precipitate is decomposed at a higher temperature into $FeCr_2O_4$ [6, 17, 22]. Figure 1.3 shows the method of co-precipitation.

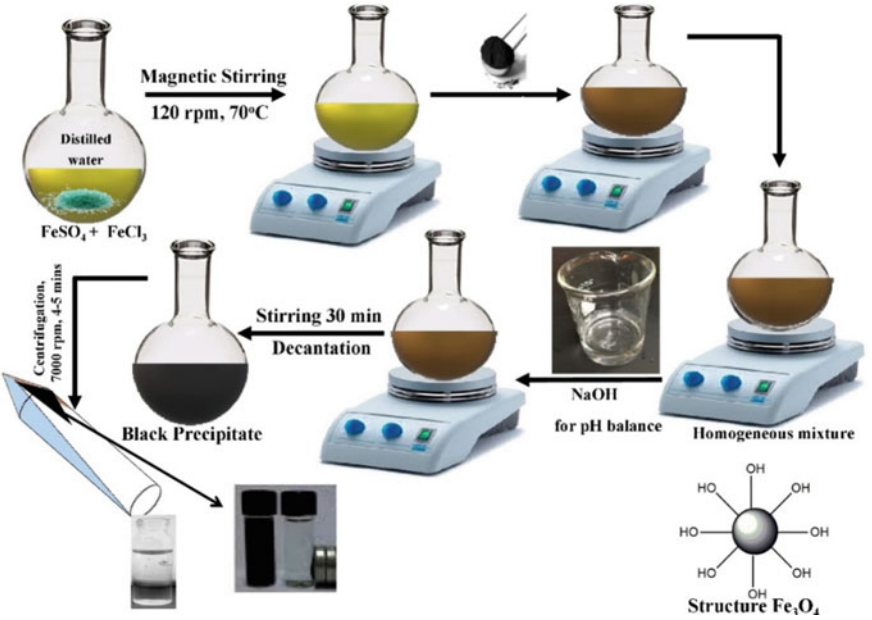

Fig. 1.3 Methods of co-precipitation

1.2.4 Sol–Gel Method

The most common chemical method for the synthesis of metal oxide nanoparticles is the sol–gel method. By stirring as well as heating, the dissolved molecules get converted into gel. This method follows parameters like nature, kinetics, pH, concentration, temperature, etc. Iron oxide nanocomposites can also be prepared by the sol–gel method. Commercially, Fe (III) is dissolved in aqueous medium and converted into gel format by heating for the generation of the final product. The formation of nanoparticles depends upon the reactivity, which is directly related to the surface area of iron oxide NPs. The synthesis of iron oxide NPs is also formed from ferric hydroxide gel, which is again subjected to this technique for 8 days at 100 °C to get the magnetite. Hematite, magnetite, and goethite are different forms of iron oxide NPs [33]. Figure 1.4 shows the method of sol–gel.

1.2.5 Microwave Irradiation

The microwave irradiation technique shows great potential as compared to other methods due to its high scaling rate of nanoparticles of iron oxide with a high specific absorption rate. The use of microwave irradiation has overcome a critical and

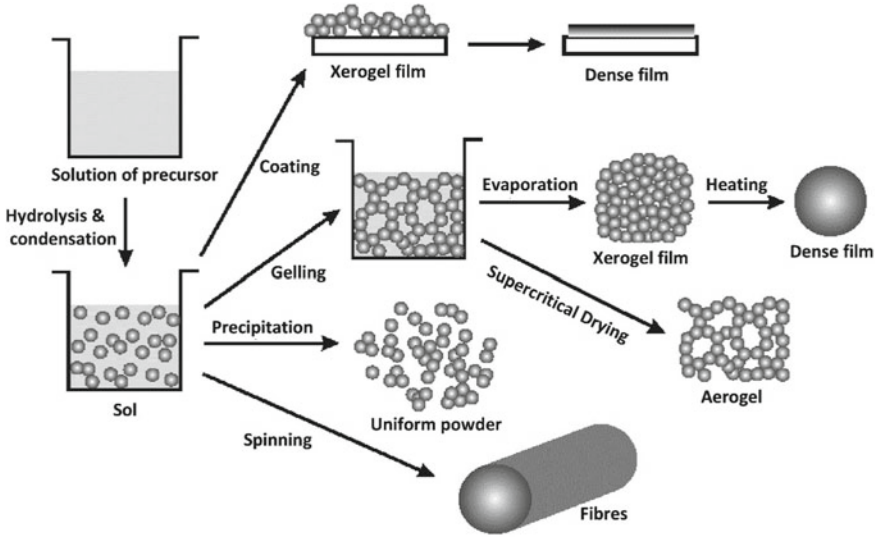

Fig. 1.4 Methods involved in sol–gel technique

perplexing issue during the preparation of iron oxide nanoparticles. Microwave radiation provides heating at a controlled rate with selective heating capability. Generally, in solution, the surface of the nanoparticles absorbs more radiation as compared to the core, which results in a change in their reactivity and surface energy. This feature attributes to the controllable exchange between the undesired adsorbed species and additional moieties such as coating agents. The best coating agent for this purpose is citric acid due to its biocompatibility. A mixture solution containing polyethylene glycol (PEG), urea, and $FeCl_3 \cdot 6H_2O$ was subjected to microwave irradiation for 10 min at 650 W. After cooling, the precipitate is subjected to centrifugation and air-dried by washing with distilled water. Then the product obtained is characterised using different characterisation techniques. Microwave radiation shows the greater advantage of a lower reaction temperature and a shorter reaction time [34, 35]. Figure 1.5 shows the method of microwave irradiation.

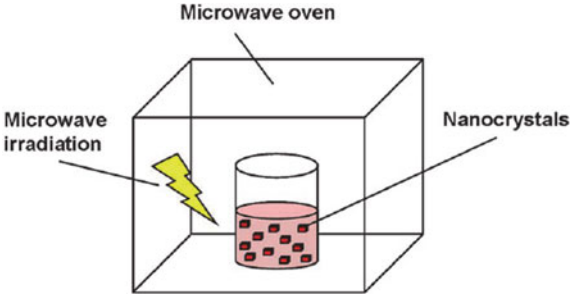

Fig. 1.5 Schematic diagram representing microwave irradiation technique

1.2.6 Microemulsion

In order to prepare iron oxide nanoparticles of ultrafine dimension, microemulsions are predominantly one of the striking reactive mediums. In microemulsions, it contains water droplets of nanosized that are continuously dispersed in the oil medium, and surfactants are used as stabilising agents that accumulate at the oil or water periphery. Microemulsions show less polydispersity, that is, droplet sizes are uniform in nature. Ionic reactants are subjected to the interior of an aqueous medium, as a result of which they can be precipitated initially to the droplet's dimension. This method is followed by the transport of precipitate from one droplet to another. During this process, large particles are formed, which can be termed as secondary growth. The reaction generally occurs in precipitating particles, which are of large size as compared to droplets in the aqueous core. A significant factor during the synthesis of microemulsion is the water-to-surfactant molar ratio, which is Wo and responsible for controlling the diameter of droplets of water. In a W/O microemulsion of oil and water, when particles of cadmium sulphide are synthesised, it is found that with Wo, the particle size goes on increasing. Particle size is independent of cadmium ion concentration. These consequences were construed in terms of an improved nucleation process and lesser secondary growth at an advanced concentration of metal salt. Fabrication of colloidal particles such as Pt, Pd, Rh, and Ir in a water–oil microemulsion resulted in particle sizes of 2–5 nm. An isooctane/water-based microemulsion system can be efficiently employed for the precipitation of ferrous oxalate, which is ultrafine in shape. Further, the ignition of ferrous oxalate in the presence of moist air at a temperature of 225–300 °C conferred a mixture of α-Fe_2O_3 and γ-Fe_2O_3. The γ-Fe_2O_3 synthesised during the microemulsion technique shows a higher yield as compared to the aqueous medium. The yield resulted from γ-Fe_2O_3 is mainly dependent upon the droplet size, due to which the precursor material can be precipitated [19, 36]. Figure 1.6 shows the method of microemulsion.

1.2.7 Hydrothermal

Hydrothermal serves as a brisk and incessant crystallisation novel method for the synthesis of fine particles of metal oxide, for example: NiO, Co_3O_4, ZrO_2, α-Fe_2O_3, etc. The aqueous solution of metal salt is taken, which is quickly heated in hydrothermal conditions, in which hydrolysis occurs followed by dehydration. With the growing resident time and feed concentration, the resulting particle size of α-Fe_2O_3 and Co_3O_4 goes on increasing. In the subcritical state, the reaction temperature will not show any momentous influences when a continuous flow reaction is performed. In this method, α-Fe_2O_3 can be synthesised by using activated carbon at 500 °C, as a result of which well-formed crystalline particles are formed. In this method, the dielectric constant of an aqueous solution plays a pivotal role in the properties of the solvent. With an increase in the hydrothermal temperature,

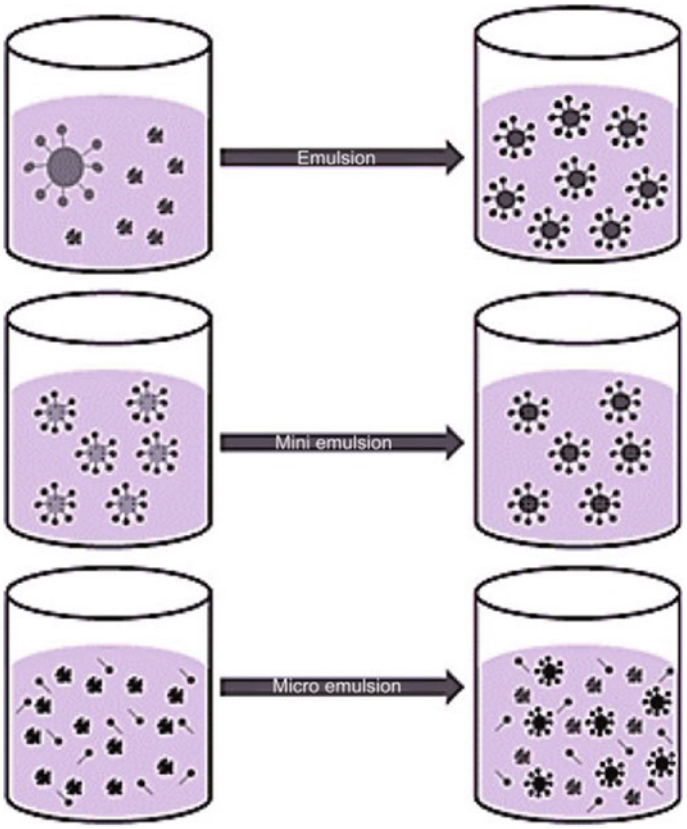

Fig. 1.6 Representation of microemulsion technique

the dielectric constant goes on decreasing. Declination takes place quickly as the temperature goes beyond the critical temperature, which leads to a considerable decrease in the solvent capability of water. When AlOOH is synthesised by the hydrothermal method at 350 °C, generally larger particles are obtained in comparison with synthesis at 400 °C. In the supercritical water when the reaction pressure increases, this results in the increase of particle size of AlOOH. But when the alcohol is added during the hydrothermal process, this largely exaggerates the crystallisation process. In hydrothermal method, iron oxide of superparamagnetic nature can be synthesised. Generally during synthesis process, anhydrous $FeCl_3$ was used as the precursor source of iron and ethylene glycol was used as solvent [37, 38]. Figure 1.7 shows hydrothermal method.

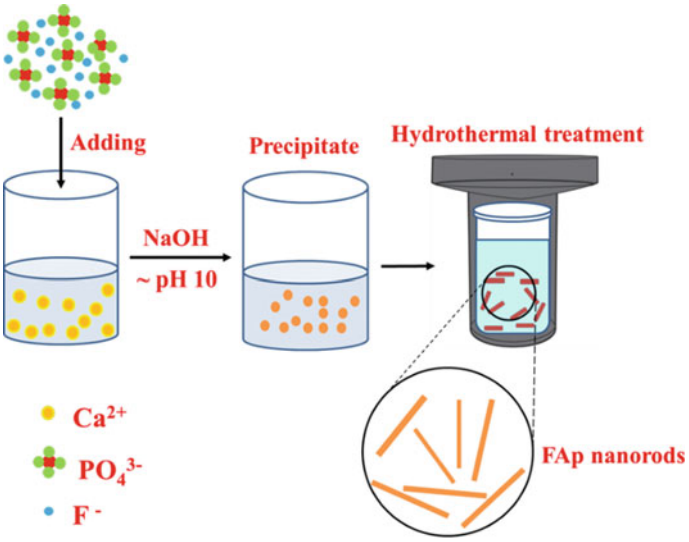

Fig. 1.7 Different steps involved in hydrothermal technique

1.2.8 Thermal Decomposition

Presently, various synthesis routes are available for the synthesis of nanoparticles of iron oxide. By using a salt solution of Fe (II) and Fe (III) with alkali-based metal hydroxide, particles can be synthesised by the co-precipitation method. But particles with a larger size and a narrower distribution can only be best prepared through the thermal decomposition method. Conventionally, certain batch methods are employed for the synthesis of magnetic-based nanoparticles. But these batch methods have various limitations, such as being limited to a smaller scale as it is difficult to maintain thermal control during the reaction. The heating rate, absolute temperature, and annealing time play a crucial role in the distribution of particle size at the nanoscale. When the batch is outsized, it is very complicated to maintain the temperature, as a result of which the particles are not compacted. To overcome all these problems, thermal decomposition proved to be a crucial method for the synthesis of magnetic-based nanoparticles. By decomposition of three precursors that are different from each other, iron oxide nanoparticles can be synthesised in the thermal decomposition method. Iron (III) oleate is used as an important reaction intermediate during this synthesis. By the adjustment of different parameters such as thermal rate, composition, and concentration of precursor particles, particle sizes of 2–30 nm were obtained. Initially, the iron particles were treated with oleic acid to form a complex of iron (III) oleate. Owing to the significance of the iron oleate composite, it is subjected to different thermal characterisations. Particle breakdown of iron oleate occurs at or above 250 °C. When the iron oleate complex is treated with 1-octadecene, it yields a larger particle size of up to 10 nm. But if the iron

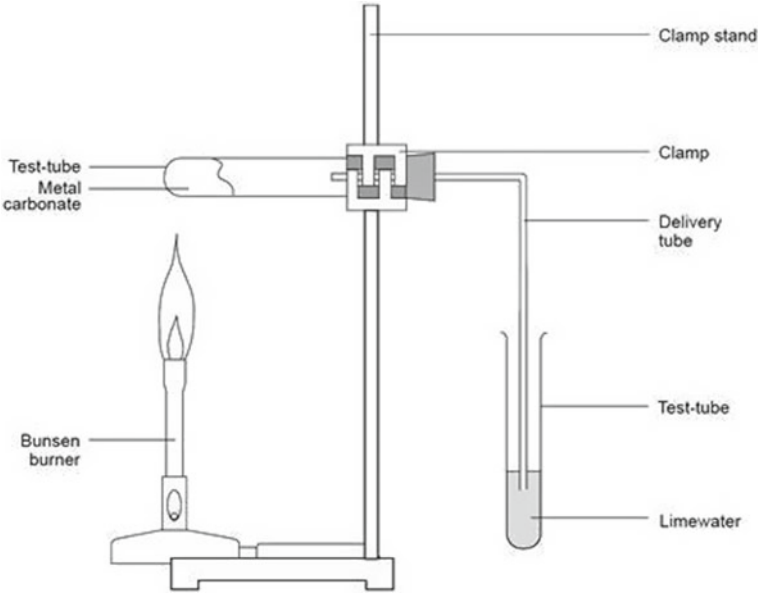

Fig. 1.8 Technical set-up of thermal decomposition process

oleate complex undergoes dilution with a sufficient amount of oleic acid, the process of nucleation as well as the growth rate is slowed. By increasing the ratio of iron oleate from 5:1 to around 20:1, it results in a particle size of around 25 nm [25, 39]. Figure 1.8 shows thermal decomposition method.

1.3 Various Modification Techniques

Generally, iron oxide nanoparticles endure certain foremost issues, such as oxidation into the physiological atmosphere due to chemical reactivity, higher surface area, large surface energy, which results in magnetism loss, and rapid agglomeration. Therefore, to overcome these issues, surface modification of iron oxide is done to make it biocompatible. Modification of iron oxide nanoparticles not only thwarts agglomeration and oxidation but also provides a further route for functionalisation. The main advantages of surface modifications are: (1) to enhance the surface action of magnetic nanoparticles; (2) to improve or modify the diffusion of magnetic nanoparticles; (3) to augment the mechanical and physiological properties; and (4) to enhance the biocompatibility of magnetic nanoparticles. Here, iron oxide modification studies were done using metal oxide, bioadsorbents, polymers, and graphene [40, 41].

1.3.1 Metal Oxide

Iron oxide-based magnetic nanoparticles have superior magnetic properties, as a result of which iron oxide-based nanoparticles can be functionalised as well as modified with the help of different techniques. The progression of technology enabled the researchers to come up with the modification and functionalisation by incorporating various supporting materials that can be used as stabilising or capping agents, for example dopamine, cystein, trimethoxysilane, carboxylic acid, phosphonic acid, and amine. Basically, iron oxide-based magnetic nanomaterials are generally coated with layers possessing inorganic elements (gold, cobalt oxide, platinum, aluminium oxide, silica, and activated carbon) and with some organic layers (glycol, dextran, and polyethylene) in order to make them stable against different properties like oxidation, corrosion, and aggregation and to increase the efficiency of their adsorption capacity. For example, iron coated with sand can be eliminated between 1.34 and 1.10 mg/g Se (IV) and in the range of 1.10 and 1.026 mg/g Se (VI), which is more effective than iron oxide nanoparticles that are uncoated. Furthermore, the modifications of the surface of iron oxide, hydroxide nanoparticles, and oxyhydroxide facilitate colloidal activity and biocompatibility in the intricate environment when the modifications are carried out. The adaptation of these nanoparticles shows the removal of various potent pollutants such as Ni (II), Cd (II), Cr (III), Co (II), Cu (II), As (III), and Pb (II) from the wastewater [42, 43].

1.3.2 Bioadsorbent

For the past few years, the amalgamation of biochar has been extensively utilised for the adsorption of dyes such as cationic and anionic dyes, which are abundantly found in wastewater. It has been seen by various researchers throughout the world that the preparation technique involved for biochar is generally exorbitant. So for the deportation of basic as well as acidic dyes, low-cost and budget-friendly bioadsorbents, which contain numerous agricultural products and various by-products, are being put into practice in a sustainable manner. Numerous adsorbents of non-conventional nature, such as bagasse fly ash [44], modified rice husk, de-oiled soy, distinct peel neem sawdust, and rice straw-based iron humate sugarcane bases, are used for the removal of carcinogenic dyes. In conjunction with the bioadsorbents, scientists throughout the world have made significant considerations towards modifying the bioadsorbents with metal oxide-based nanoparticles. The adsorption process using metal oxide is being highly implemented due to its plentiful advantages, such as its small size and persuasiveness towards functionality as well as the adsorption process. So in this condition, iron oxide is being utilised as a considerable adsorption agent for decontaminating the deteriorated dye water [45–48].

1.3.3 Polymer

Among all the polymers that are naturally available, chitosan is found in profusion in seawater. It is non-antigenic, non-toxic, hydrophilic, biocompatible, and biodegradable. It contains the residue of hexosaminidase, which consists of two hydroxyl groups and one amino group. These functional groups that are present on the chitosan are responsible for the formation of complexes with the surface of iron oxide, making iron oxide nanoparticles stable, biocompatible, and hydrophilic. This has a wide range of applications in therapeutic gene delivery. Naturally available chitosan polymer is also responsible for providing better disparity in magnetic resonance imaging. When chitosan is coated with iron oxide nanoparticles, they form a complex in which the amine group is bonded to the desired particle and the hydroxyl group remains non-bonded. As a result of which the synthesised particle carries some positive charge. There is some repulsion in the form of Coulomb forces that remain in the colloidal state when no surfactant or organic solvent is used. The diameter of the synthesised particle was found to be 67 nm.

Polyethylene glycol is a water-soluble polymer that is extensively used for enhancing the water solubility of drugs. PEG coating diminishes the uptake and is responsible for increasing the efficiency of circulation timing. When iron oxide nanoparticles are coated with polyethylene glycol, they operate as an efficient adsorbent for attachment to various biomolecules. If antibodies and proteins are attached to iron oxide nanoparticles, the addition will be more target-specific in the area of interest. One problem associated with the PEG is that coating may result in the mixing of particles as a result of which particles are exposed to the cells. This problem can be overcome by mixing iron oxide with poly(ethylene glycol)-co-fumarate (PEGF). The role of fumaric acid is highly important as it is a macromer that is highly unsaturated. The hydrogel property of PEGF makes the iron oxide nanoparticles more stable, which makes them more efficient for absorption of water. Moreover, when the iron oxide nanoparticles are covered with crosslinked PEG starch, it is responsible for accelerating tumour imaging because it is a non-toxic coated material.

Dextran, which is a polysaccharide, has been successfully and extensively used for an assortment of applications. Iron oxide nanoparticles coated with dextran are commercially available and well-conventional methods for MRI and also in cancer treatment. The coating can be improved by the introduction of carboxymethyl groups, which improve functionality as well as stability. Epichlorohydrin is crosslinked with dextran to form crosslinked iron oxide nanoparticles.

Polyvinyl alcohol has a wide variety of applications in drug delivery, tendon repair, contact lenses, ophthalmic materials, and the biomedical field. Polyvinyl alcohol shows a high compatibility rate, and it serves as a water-soluble material and exceptional biocompatible agent when coated with iron oxide nanoparticles. When carboxylate groups are modified with PVA structures, they are strongly attached to metal oxide. The coated iron oxide nanoparticles are insoluble in water and are used as a phase transfer catalyst that replaces oleic acid and oleylamine acid. Moreover, when iron oxide nanoparticles are modified with PVA, they serve as an anti-cancer

agent for drug delivery. Through hydrogen bonding, the polar functional group of PVA can adsorb successfully onto the oxide surface.

Poly(vinyl pyrrolidine) is extensively used in the field of biomedicine as it has a wide variety of applications due to its neutral charge, biocompatibility, and aqueous solubility. Iron oxide nanoparticles are generally coated with PVP, which increases their efficiency for MRI. Through the thermal decomposition method, the nanoparticle is successfully synthesised and is also soluble in buffer solution in addition to its water solubility capacity. Also, the coated nanoparticle possesses a high magnetic moment, which shows high relaxivity. In addition to that, when binding takes place through surface-initiated radical polymerisation, the nanoparticles are found to be superparamagnetic and possess the stability and dispersibility capacity of water for a long time [49–51].

1.3.4 Graphene

In the current scenario, hybrid materials can be synthesised by coating the iron oxide with graphene materials like nanosheets of graphene, reduced graphene oxide, and carbon nanotubes. Graphene shows a variety of applications in the fields of drugs, biomolecules, cells, metals, and other functional groups. Graphene oxide also attracted many researchers due to its unique combination of sp^3 and sp^2 carbons as well as various functional groups such as epoxy and hydroxyl and carboxyl groups. Graphene also possesses strong electrical conductivity, which is useful for the installation of electrochemical devices. When Fe_2O_3 is modified with graphene oxide, it shows a dominant magnetic property, which is used to prevent the stacking of graphene oxide and can also be used as a drug delivery agent for targeting a specific area.

When the iron salts are modified with reduced graphene oxide, the synthesised hybrid materials are used to improve the grafting efficiency and also increase the efficiency of the polymer matrix. When gelatin is mixed with graphene oxide, it improves the dispersion stability of the synthesised particle as well as prevents the oxidation of Fe_3O_4. Coating of iron oxide with a graphene layer contains oxygen-based functional groups used in the nanofluid application. The synthesised nanoparticle is used to enhance the thermal conductivity. When graphene aerogel is successfully modified with iron oxide nanoparticles, it is used for the electro-Fenton system. The nanoparticle is prepared by using a natural drying method that has electrocatalytical and electrochemical performance with reusability and corrosion resistance properties for the treatment of wastewater containing organic pollutants.

When the iron oxide is coated with 3D foam-based graphene, the synthesised nanoparticle has a spherical shape with a particle size of 320 nm. These nanocrystals have a higher surface area, which shows exceptional electrochemical properties such as rate of capability, specific capacitance, and capacitance retention of around 89.8%. When the chemical reduction of iron oxide nanoparticles is done with graphene oxide, it shows a wide variety of applications in electrode applications, such as the

installation of supercapacitors, due to its good cycling capacity. Iron oxide is also modified with multi-walled carbon nanotubes through microwave-assisted Fenton's procedure via the green route. The synthesised nanoparticles improve the efficiency of the final material with high energy density and high capacitance in supercapacitors [52–54].

References

1. Taghipour F (2004) Ultraviolet and ionizing radiation for microorganism inactivation. Water Res 38(18):3940–3948. https://doi.org/10.1016/j.watres.2004.06.016
2. Amodu OS, Ojumu TV, Ntwampe SK, Ayanda OS (2015) Rapid adsorption of crystal violet onto magnetic zeolite synthesized from fly ash and magnetite nanoparticles. J Encaps Adsorp Sci 05(04):191–203. https://doi.org/10.4236/jeas.2015.54016
3. Wu R, Liu JH, Zhao L, Zhang X, Xie J, Yu B, Ma X, Yang S-T, Wang H, Liu Y (2014) Hydrothermal preparation of magnetic Fe_3O_4@C nanoparticles for dye adsorption. J Environ Chem Eng 2(2):907–913. https://doi.org/10.1016/j.jece.2014.02.005
4. Stoia M, Pəcurariu C, Istratie R, Nižňanský D (2015) Solvothermal synthesis of magnetic Fe_xO_y/C nanocomposites used as adsorbents for the removal of methylene blue from wastewater. J Therm Anal Calorim 121(3):989–1001. https://doi.org/10.1007/s10973-015-4641-x
5. Fayazi M, Ghanei-Motlagh M, Taher MA (2015) The adsorption of basic dye (Alizarin red S) from aqueous solution onto activated carbon/γ-Fe_2O_3 nano-composite: kinetic and equilibrium studies. Mater Sci Semicond Process 40:35–43. https://doi.org/10.1016/j.mssp.2015.06.044
6. Madrakian T, Afkhami A, Ahmadi M, Bagheri H (2011) Removal of some cationic dyes from aqueous solutions using magnetic-modified multi-walled carbon nanotubes. J Hazard Mater 196:109–114. https://doi.org/10.1016/j.jhazmat.2011.08.078
7. Ranjithkumar V, Sangeetha S, Vairam S (2014) Synthesis of magnetic activated carbon/α-Fe_2O_3 nanocomposite and its application in the removal of acid yellow 17 dye from water. J Hazard Mater 273:127–135. https://doi.org/10.1016/j.jhazmat.2014.03.034
8. Liu F, Jin Y, Liao H, Cai L, Tong M, Hou Y (2013) Facile self-assembly synthesis of titanate/Fe_3O_4 nanocomposites for the efficient removal of Pb^{2+} from aqueous systems. J Mater Chem A 1(3):805–813. https://doi.org/10.1039/c2ta00099g
9. Anbia M, Khoshbooei S (2015) Functionalized magnetic MCM-48 nanoporous silica by cyanuric chloride for removal of chlorophenol and bromophenol from aqueous media. J Nanostruct Chem 5(1):139–146. https://doi.org/10.1007/s40097-014-0145-7
10. Zhang LH, Sun Q, Liu DH, Lu AH (2013) Magnetic hollow carbon nanospheres for removal of chromium ions. J Mater Chem A 1(33):9477–9483. https://doi.org/10.1039/c3ta10430c
11. Zhang X, Wang Y, Chang X, Wang P, Pan B (2017) Iron oxide nanoparticles confined in mesoporous silicates for arsenic sequestration: effect of the host pore structure. Environ Sci Nano 4(3):679–688. https://doi.org/10.1039/c6en00514d
12. Gwak GH, Kim MK, Oh JM (2016) Nanocomposites of magnetite and layered double hydroxide for recyclable chromate removal. J Nanomater 2016(V). https://doi.org/10.1155/2016/8032615
13. Jafari Kang A, Baghdadi M, Pardakhti A (2016) Removal of cadmium and lead from aqueous solutions by magnetic acid-treated activated carbon nanocomposite. Desalin Water Treat 57(40):18782–18798. https://doi.org/10.1080/19443994.2015.1095123
14. Wu Z, Li W, Webley PA, Zhao D (2012) General and controllable synthesis of novel mesoporous magnetic iron oxide@carbon encapsulates for efficient arsenic removal. Adv Mater 24(4):485–491. https://doi.org/10.1002/adma.201103789
15. Bayazit ŞS (2014) Magnetic multi-wall carbon nanotubes for methyl orange removal from aqueous solutions: equilibrium, kinetic and thermodynamic studies. Sep Sci Technol (Philadelphia) 49(9):1389–1400. https://doi.org/10.1080/01496395.2013.879595

16. Egodawatte S, Datt A, Burns EA, Larsen SC (2015) Chemical insight into the adsorption of chromium(III) on iron oxide/mesoporous silica nanocomposites. Langmuir 31(27):7553–7562. https://doi.org/10.1021/acs.langmuir.5b01483
17. Dwivedi MK, Agrawal R, Sharma P (2016) Adsorptive removal of methylene blue from wastewater using zeolite-iron oxide magnetic nanocomposite. Int J Adv Res Sci Eng 5(2):515–522
18. Deligeer W, Gao YW, Asuha S (2011) Adsorption of methyl orange on mesoporous γ-Fe_2O_3/SiO_2 nanocomposites. Appl Surf Sci 257(8):3524–3528. https://doi.org/10.1016/j.apsusc.2010.11.067
19. Jain N, Dwivedi MK, Agarwal R, Sharma P (2015) Removal of malachite green from aqueous solution by zeolite-iron oxide magnetic nanocomposite. IOSR J Environ Sci Ver I 9(6):2319–2399. https://doi.org/10.9790/2402-09614250
20. Yao S, Sun S, Wang S, Shi Z (2016) Adsorptive removal of lead ion from aqueous solution by activated carbon/iron oxide magnetic composite. Indian J Chem Technol 23(2):146–152
21. Sahoo JK, Paikra SK, Baliarsingh A, Panda D, Rath S, Mishra M, Sahoo H (2020) Surface functionalization of graphene oxide using amino silane magnetic nanocomposite for chromium (VI) removal and bacterial treatment. Nano Express 1(1):010062. https://doi.org/10.1088/2632-959x/ab9e3f
22. Kloster GA, Mosiewicki MA, Marcovich NE (2019) Chitosan/iron oxide nanocomposite films: effect of the composition and preparation methods on the adsorption of Congo red. Carbohydr Polym 221:186–194. https://doi.org/10.1016/j.carbpol.2019.05.089
23. Chu JH, Kang JK, Park SJ, Lee CG (2020) Application of magnetic biochar derived from food waste in heterogeneous sono-Fenton-like process for removal of organic dyes from aqueous solution. J Water Process Eng 37:101455. https://doi.org/10.1016/j.jwpe.2020.101455
24. Amer R, Hadi H (2021) Application of CTAB-coated magnetic nanoparticles for solid-phase extraction of thiamine hydrochloride from pharmaceutical formulations and urine samples. Arab J Sci Eng 0123456789. https://doi.org/10.1007/s13369-021-05671-y
25. Zhang J, Liu M, Yang T, Yang K, Wang H (2016) A novel magnetic biochar from sewage sludge: synthesis and its application for the removal of malachite green from wastewater. Water Sci Technol 74(8):1971–1979. https://doi.org/10.2166/wst.2016.386
26. Schneider M, Ballweg T, Groß L, Gellermann C, Sanchez-Sanchez A, Fierro V, Celzard A, Mandel K (2019) Magnetic carbon composite particles for dye adsorption from water and their electrochemical regeneration. Part Part Syst Charact 36(6):1–11. https://doi.org/10.1002/ppsc.201800537
27. Borth KW, Galdino CW, Teixeira VDC, Anaissi FJ (2021) Iron oxide nanoparticles obtained from steel waste recycling as a green alternative for Congo red dye fast adsorption. Appl Surf Sci 546. https://doi.org/10.1016/j.apsusc.2021.149126
28. Jia Z, Liu J, Wang Q, Li S, Qi Q, Zhu R (2015) Synthesis of 3D hierarchical porous iron oxides for adsorption of Congo red from dye wastewater. J Alloy Compd 622:587–595. https://doi.org/10.1016/j.jallcom.2014.10.125
29. Abdullah NH, Shameli K, Abdullah EC, Abdullah LC (2019) Solid matrices for fabrication of magnetic iron oxide nanocomposites: synthesis, properties, and application for the adsorption of heavy metal ions and dyes. Compos B Eng 162:538–568. https://doi.org/10.1016/j.compositesb.2018.12.075
30. Othman NH, Alias NH, Shahruddin MZ, Abu Bakar NF, Nik Him NR, Lau WJ (2018) Adsorption kinetics of methylene blue dyes onto magnetic graphene oxide. J Environ Chem Eng 6(2):2803–2811. https://doi.org/10.1016/j.jece.2018.04.024
31. Tan KB, Vakili M, Horri BA, Poh PE, Abdullah AZ, Salamatinia B (2015) Adsorption of dyes by nanomaterials: recent developments and adsorption mechanisms. Sep Purif Technol 150:229–242. https://doi.org/10.1016/j.seppur.2015.07.009
32. Lilhare S, Mathew SB, Singh AK, Carabineiro SAC (2021) Calcium alginate beads with entrapped iron oxide magnetic nanoparticles functionalized with methionine—a versatile adsorbent for arsenic removal. Nanomaterials 11(5). https://doi.org/10.3390/nano11051345

33. Dai H (2019) Green and facile fabrication of pineapple peel cellulose/magnetic diatomite hydrogels in ionic liquid for methylene blue adsorption. Cellulose 6(381). https://doi.org/10.1007/s10570-019-02283-6
34. Wang H, Zhao W, Chen Y, Li Y (2020) Nickel aluminum layered double oxides modified magnetic biochar from waste corncob for efficient removal of acridine orange. Bioresour Technol 315:123834. https://doi.org/10.1016/j.biortech.2020.123834
35. Ehsan A, Bhatti HN, Iqbal M, Noreen S (2017) Native, acidic pre-treated and composite clay efficiency for the adsorption of dicationic dye in aqueous medium. Water Sci Technol 75(4):753–764. https://doi.org/10.2166/wst.2016.435
36. Rajabi M, Mahanpoor K, Moradi O (2019) Preparation of PMMA/GO and PMMA/GO-Fe_3O_4 nanocomposites for malachite green dye adsorption: kinetic and thermodynamic studies. Compos B Eng 167:544–555. https://doi.org/10.1016/j.compositesb.2019.03.030
37. Zhang P, O'Connor D, Wang Y, Jiang L, Xia T, Wang L, Tsang DCW, Ok YS, Hou D (2020) A green biochar/iron oxide composite for methylene blue removal. J Hazard Mater 384:121286. https://doi.org/10.1016/j.jhazmat.2019.121286
38. Kanwal A, Bhatti HN, Iqbal M, Noreen S (2017) Basic dye adsorption onto clay/$MnFe_2O_4$ composite: a mechanistic study. Water Environ Res 89(4):301–311. https://doi.org/10.2175/106143017x14839994522984
39. Sehlleier YH, Hardt S, Schulz C, Wiggers H (2016) A novel magnetically-separable porous iron-oxide nanocomposite as an adsorbent for methylene blue (MB) dye. J Environ Chem Eng 4(4):3779–3787. https://doi.org/10.1016/j.jece.2016.08.018
40. Pramanik N, Ranganathan S, Rao S, Suneet K, Jain S, Rangarajan A, Jhunjhunwala S (2019) A composite of hyaluronic acid-modified graphene oxide and iron oxide nanoparticles for targeted drug delivery and magnetothermal therapy. ACS Omega 4(5):9284–9293. https://doi.org/10.1021/acsomega.9b00870
41. Rebuttini V, Fazio E, Santangelo S, Neri F, Caputo G, Martin C, Brousse T, Favier F, Pinna N (2015) Chemical modification of graphene oxide through diazonium chemistry and its influence on the structure-property relationships of graphene oxide-iron oxide nanocomposites. Chem Eur J 21(35):12465–12474. https://doi.org/10.1002/chem.201500836
42. Eren E, Cubuk O, Ciftci H, Eren B, Caglar B (2010) Adsorption of basic dye from aqueous solutions by modified sepiolite: equilibrium, kinetics and thermodynamics study. Desalination 252(1–3):88–96. https://doi.org/10.1016/j.desal.2009.10.020
43. El Qada EN, Allen SJ, Walker GM (2008) Adsorption of basic dyes from aqueous solution onto activated carbons. Chem Eng J 135(3):174–184. https://doi.org/10.1016/j.cej.2007.02.023
44. Mall ID, Srivastava VC, Agarwal NK, Mishra IM (2005) Adsorptive removal of malachite green dye from aqueous solution by bagasse fly ash and activated carbon-kinetic study and equilibrium isotherm analyses. Colloids Surf A Physicochem Eng Asp 264(1–3):17–28. https://doi.org/10.1016/j.colsurfa.2005.03.027
45. Shen D, Fan J, Zhou W, Gao B, Yue Q, Kang Q (2009) Adsorption kinetics and isotherm of anionic dyes onto organo-bentonite from single and multisolute systems. J Hazard Mater 172(1):99–107. https://doi.org/10.1016/j.jhazmat.2009.06.139
46. Nageeb M (2013) Adsorption technique for the removal of organic pollutants from water and wastewater. In: Organic pollutants—monitoring, risk and treatment. https://doi.org/10.5772/54048
47. Bhatti HN, Jabeen A, Iqbal M, Noreen S, Naseem Z (2017) Adsorptive behavior of rice bran-based composites for malachite green dye: isotherm, kinetic and thermodynamic studies. J Mol Liq 237:322–333. https://doi.org/10.1016/j.molliq.2017.04.033
48. Demirbas A (2009) Agricultural based activated carbons for the removal of dyes from aqueous solutions: a review. J Hazard Mater 167(1–3):1–9. https://doi.org/10.1016/j.jhazmat.2008.12.114
49. Santhosh C, Daneshvar E, Tripathi KM, Baltrėnas P, Kim TY, Baltrėnaitė E, Bhatnagar A (2020) Synthesis and characterization of magnetic biochar adsorbents for the removal of Cr(VI) and Acid orange 7 dye from aqueous solution. Environ Sci Pollut Res 27(26):32874–32887. https://doi.org/10.1007/s11356-020-09275-1

50. Wang L, Hu G, Lyu F, Yue T, Tang H, Han H, Yang Y, Liu R, Sun W (2019) Application of red mud in wastewater treatment. Minerals 9(5). https://doi.org/10.3390/min9050281
51. Samrot AV, Ali HH, Selvarani J, Faradjeva E, Raji P, Prakash P, Kumar SS (2021) Adsorption efficiency of chemically synthesized superparamagnetic iron oxide nanoparticles (SPIONs) on crystal violet dye. Curr Res Green Sustain Chem 4:100066. https://doi.org/10.1016/j.crgsc.2021.100066
52. McCoy TM, Brown P, Eastoe J, Tabor RF (2015) Noncovalent magnetic control and reversible recovery of graphene oxide using iron oxide and magnetic surfactants. ACS Appl Mater Interfaces 7(3):2124–2133. https://doi.org/10.1021/am508565d
53. Yang X, Chen C, Li J, Zhao G, Ren X, Wang X (2012) Graphene oxide-iron oxide and reduced graphene oxide-iron oxide hybrid materials for the removal of organic and inorganic pollutants. RSC Adv 2(23):8821–8826. https://doi.org/10.1039/c2ra20885g
54. Pham XH, Hahm E, Kim HM, Son BS, Jo A, An J, Thi TAT, Nguyen DQ, Jun BH (2020) Silica-coated magnetic iron oxide nanoparticles grafted onto graphene oxide for protein isolation. Nanomaterials 10(1):1–14. https://doi.org/10.3390/nano10010117

Chapter 2
Magnetic Iron Oxide-Based Nanocomposites: Synthesis, Characterization, and Its Application Towards Organic Dye Removal

Jitendra Kumar Sahoo, Himanshu Shekhar, Jyoti Prakash Rath, Biswajit Mohanty, and Harekrushna Sahoo

Abstract A significant release of toxic substances, particularly coloring agents and dye particles, into ecological regions such as water bodies has turned into a major environmental issue. An immense release of toxic dye pollutants from various anthropogenic exercises might represent a tremendous challenge to the living organism and its adverse effect to the biological system. This chapter includes adsorption of organic dyes such as cationic and anionic dyes using various magnetic iron oxide-based nanocomposites that were reported by different researchers. Compare the impact of different parameters like pH, contact time, kinetics, and isotherm on dye removal which were discussed. The adsorption mechanism of cationic and anionic dyes on magnetic iron oxide-based nanocomposites was critically analyzed.

Keywords Iron oxide · Nanocomposites · Wastewater · Dye · Adsorption

2.1 Introduction

In the current scenario wastewater treatment is a major environmental issue. Around the world a number of researchers are working on wastewater treatment. Different researchers are synthesizing various materials such as activated carbon [1], aerogels [2], industrial solid waste [3], bio-adsorbent [4], nanoparticles [5], and nanocomposite [5] for wastewater treatment. Wastewater contains lots of contaminants such as metals [6], pesticides [7], industrial effluents [8], fluorides [9], organic dyes [10], and pharmaceuticals waste [11]. Among various contaminates organic dyes are highly

J. K. Sahoo · J. P. Rath · B. Mohanty
Department of Chemistry, GIET University, Gunupur, Odisha 765022, India

H. Shekhar · H. Sahoo (✉)
Department of Chemistry, National Institute of Technology, Rourkela 769008, India
e-mail: sahooh@nitrkl.ac.in

H. Sahoo and J. K. Sahoo (eds.), *Iron Oxide-Based Nanocomposites and Nanoenzymes*, Nanostructure Science and Technology, https://doi.org/10.1007/978-3-031-44599-6_2

carcinogenic toward aquatic life [12]. Industrialized activities such as paper, textile, cosmetics, tanning, dyeing, and printing manufacturing industries discharge industrial effluents containing organic dyes. The organic dyes affect the human bodies and create multiple diseases such as gastrointestinal, weakness, respiratory toxicity, reduce fertility, cancer, teratogenesis, various skin problems, and blindness [13]. The classification of textile dyes is illustrated in Fig. 2.1. Furthermore, organic dyes were separated in to two parts (cationic and anionic) based on charge on their particle [14]. Due to carcinogenic nature of organic dyes, it is required to remove before discharging into water bodies. From literature study we know that there are several techniques available such as bio-degradation [15], precipitation [16], ion exchange [17], reverse osmosis [18], coagulation [19], ozonation [20], filtration [21], membrane separation [17], adsorption [22], electrodialysis [23], solvent extraction [24], flocculation [19], and distillation [25]. Magnetic nanocomposite was an efficient material for different environmental and biomedical applications. Among all removal techniques, adsorption technique is suitable for its cost-effective, ease to operate, time saving, simple, and no toxic waste produce [22].

The adsorbent having proper active functional groups and large surface area and pore volume plays a key role for any adsorption process [26]. Compared with general adsorbents, nanoparticles and nanocomposites have higher adsorption efficiency because of high surface area-to-volume ratio than bulk materials [27]. Due to the unique properties nanoparticles are used in various biomedical [28], drug analysis [29], sensor [30], solar panel [31], fuel additives [32], and environmental applications. The researches have greater interest on metal oxide nanoparticles and magnetic metal oxide-based nanocomposites as an effective adsorbent for organic dyes removal.

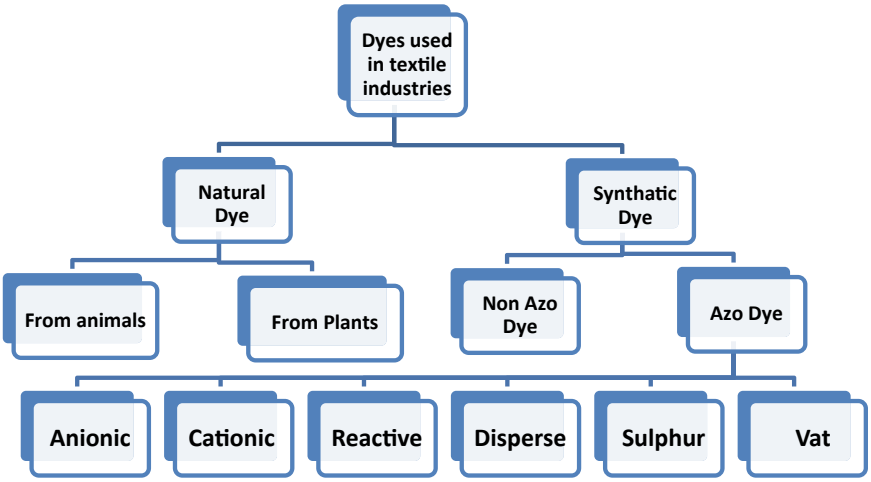

Fig. 2.1 Classification of textile dyes

2.1.1 Metal Oxide Nanoparticles

Metal oxides show metallic, insulating, and semiconductor character based on their structural geometries and electronic structures [33]. Metal oxides demonstrate magnetism, optics, thermal, optoelectronic, electrochemical, and catalytic nature based on their preparation and composition [34]. As compared to other bulk materials, metal oxide nanoparticles have higher surface area and novel properties that increase its adsorption efficacy toward various cationic and anionic dyes, making it one of the best options to use in wastewater treatment [35]. Various metal oxide nanoparticles such as copper oxide [36], cerium oxide [35], manganese oxide [37], zirconium oxide [38], titanium oxide [39], and iron oxide [40] have been commonly used in cationic and anionic dyes removal. Researchers were greater interest on magnetic iron oxide nanoparticles because of easy separation from aqueous solution using external magnetic fields.

2.1.2 Magnetic Iron Oxide Nanoparticles

Magnetic nanostructures have the capacity to eliminate the fine particles, natural contaminations, and colloids that turn out to be too dangerous to be isolated by regular strategies [41]. Among different attractive nanoparticles, magnetic iron oxide was found to be good for the adsorption of organic dyes due to its small size and ferromagnetic nature [42, 43]. They have the ability to adsorb many organic dyes, such as cationic and anionic. In current times, the application of magnetic nano-adsorbents for the decontamination process has become very efficient and has received considerable demand and attention due to their easy separation ability from aqueous solution [44]. The iron oxide has several phases, such as Fe_4O_5, FeO, Fe_3O_4, $Fe(OH)_3$, FeOOH, Fe_4O_3, and polymorphs of Fe_2O_3 (–Fe_2O_3, and –Fe_2O_3). Among these, maghemite (–Fe_2O_3), hematite (–Fe_2O_3), and magnetite (Fe_3O_4) are of superior interest for their electrical and magnetic properties [45–48]. This compound has a lot of influence and impact on the remediation of water, such as fast and easy preparation, high adsorption capacity, rapid uptake, high surface area, and easy separation [49]. Therefore, researchers are interested in magnetic iron oxide nanoparticles for removal of cationic and anionic dyes [50]. Then few researchers modified other materials with iron oxide nanoparticles to enhance the removal efficiency [51–85].

2.1.3 Magnetic Iron Oxide-Based Nanocomposites

Magnetic iron oxide-based nanocomposites have many applications in various fields such as adsorbent for removal of cationic and anionic dyes [51, 55, 72, 83, 85–87], magnetic-optical materials [88], sensors [30], and biomedical [88] due to its unique

physiochemical properties. Compared to simple magnetic iron oxide nanoparticles, magnetic iron oxide-based nanocomposite was potentially more efficient toward removal of cationic and anionic dyes from wastewater [89]. Bare magnetic iron oxide nanoparticles have some limitations like low adsorption capacity, leaching problem in low pH, and more time required. In current times many researches were reported on modification of cost-effective, nontoxic, and environmental-friendly material on the surface of magnetic iron oxide nanoparticles and to make potential adsorbent [90]. This modifications enhance the active binding sites of adsorbent, and the active binding sites play an important role in cationic and anionic dye adsorption.

2.2 Characterization of Magnetic Iron Oxide

The FT-IR spectrum of iron oxide (Fe_3O_4) nanoparticles shows the peak at 441 cm^{-1} which is attributed to the shifting of Fe–O (the frequency υ_2 band of bulk iron oxide phase), two strong peaks at 583 and 628 cm^{-1} corresponding to the presence of Fe–O, and two peaks at 3431 and 1622 cm^{-1} attribute to the stretching and bending frequency of water molecules [91]. The XRD patterns of Fe_3O_4 showed six intense peaks at $2\theta = 220$ (30.3°), 311 (35.7°), 400 (43.5°), 422 (53.9°), 511 (57.5°), and 440 (63.0°), which have been attributed to the structure of Fe_3O_4 nanoparticles according to JCPDS no. 65-3107 [91]. As the XRD patterns of maghemite and magnetite are very similar to each other, Mossbauer spectroscopy has been performed to determine the oxidation states of iron as Fe^{+2} and Fe^{+3} oxidation states. The data of Mossbauer spectra are well fitted to two sextet patterns attributing to the tetrahedral and octahedral sites of iron (Fe^{+2} and Fe^{+3}), respectively, which corroborates the presence of magnetite [92].

2.3 Removal of Cationic Dyes Using Magnetic Iron Oxide-Based Nanocomposites

This section describes various reported magnetic iron oxide-based nanocomposites for the adsorption of cationic dyes. Furthermore, compare the adsorption parameters such as optimum pH and contact time of various reported adsorbents. Some important observations such as maximum uptake capacity (q_{max}), isotherm model, and kinetic models of different adsorption are illustrated in Table 2.1. The mechanism of various dyes was also discussed.

Pietrzyk et al. [78] prepared superparamagnetic nanoparticles and green nanocomposites based on biomass adsorbents through the wet co-precipitation technique. In this experiment iron oxide nanoparticles were encrusted on the cores based on cellulose, red volcanic algae waste, and coffee. Authors prepared adsorbents like Coffee@ Fe_3O_4, Cellulose@ Fe_3O_4, and Algae@ Fe_3O_4 that were used against methylene blue

Table 2.1 Different parameters like contact time, pH, as well as maximum adsorption capacity, and isotherm and kinetic models of cationic dye removal using various adsorbents were illustrated

Adsorbent	Dye adsorbed	Isotherm model	q_{max} (mg/g)	Kinetic model	Optimum pH/time	References
Magnetic Fe_3O_4/polypyrrole/carbon black nanocomposite	Methylene blue	Langmuir	90.9	Pseudo-second-order	8/240 min	[79]
Coffee@ Fe_3O_4	Methylene blue	Redlich–Peterson	38.2	Pseudo-second-order	8/180 min	[78]
Cellulose@ Fe_3O_4	Methylene blue	Langmuir	41.6	Pseudo-second-order	8/180 min	[78]
Algae@ Fe_3O_4	Methylene blue	Redlich–Peterson	48.1	Pseudo-second-order	7/180 min	[78]
AWB-based Fe_3O_4	Crystal violet	Langmuir	269.7	Pseudo-second-order	7/–	[72]
Fe_3O_4@inulin nanocomposite	Crystal violet	Langmuir	223.57	Pseudo-second-order	7/180 min	[75]
MNP/CTAB-EC	Crystal violet	Freundlich	448	Pseudo-second-order	8/120 min	[76]
MOP	Crystal violet	Langmuir	556.6	Pseudo-second-order	8/70 min	[77]
Z-Fe_3O_4	Methyl violet	Langmuir	153.85	Pseudo-second-order	7/150 min	[83]
ACOW600/ZnO/Fe_3O_4	Methyl violet	Freundlich	48.59	Pseudo-second-order	9/60 min	[85]
Clay/starch/Fe_3O_4 nanocomposite	Methyl violet	Freundlich	29.67	Pseudo-second-order	9/150 min	[84]
HNT-Fe_3O_4 magnetic adsorbent	Malachite green	Freundlich	44.25	Pseudo-second-order	5.5/240 min	[69]
nZVI/BC composite	Malachite green	Langmuir	515.77	Pseudo-second-order	6/10 min	[68]
α-Fe_2O_3	Malachite green	Freundlich	973	Pseudo-second-order	–/120 min	[65]
PACT@γ-Fe_2O_3	Malachite green	Langmuir	86.28	Pseudo-second-order	6/170 min	[66]

dye. Authors observed that Algae@ Fe_3O_4 shows the highest adsorption capacity of 48.1 mg/g at a pH 7 and contact time of 180 min. Coffee@ Fe_3O_4 and Cellulose@ Fe_3O_4 show adsorption capacity of 38.2 mg/g and 41.6 mg/g, respectively, for pH and contact time of 8 and 180 min. From the above three adsorbents coffee- and algae-based nanocomposites undergo Redlich–Peterson isotherm model, while cellulose-based nanocomposites undergo Langmuir isotherm. From kinetic model study all of them show pseudo-second-order kinetics. Ali and Ismail [79] investigated the removal of methylene blue using magnetic Fe_3O_4/polypyrrole/carbon black nanocomposite. This study revealed that maximum adsorption capacity of the adsorbent was found to be 90.9 mg/g under optimum pH of 8 and contact time of 240 min. The mechanism of methylene blue dye on magnetic Fe_3O_4/polypyrrole/carbon black nanocomposite was shown in Fig. 2.2. Four interactions were reported between adsorbent and adsorbate such as hydrogen bonding, π–π interaction, electrostatic interaction, and surface complexation. Experimental data were well sweated with Langmuir isotherm R^2 value and adsorption capacity of 0.995 and 90.9 mg/g, respectively. Kinetic model studies show that the adsorption process follows the pseudo-second-order kinetics. From the above literature studies we concluded that the highest adsorption capacity for methylene blue dye was seen in case of Algae@ Fe_3O_4 nanocomposite adsorbent.

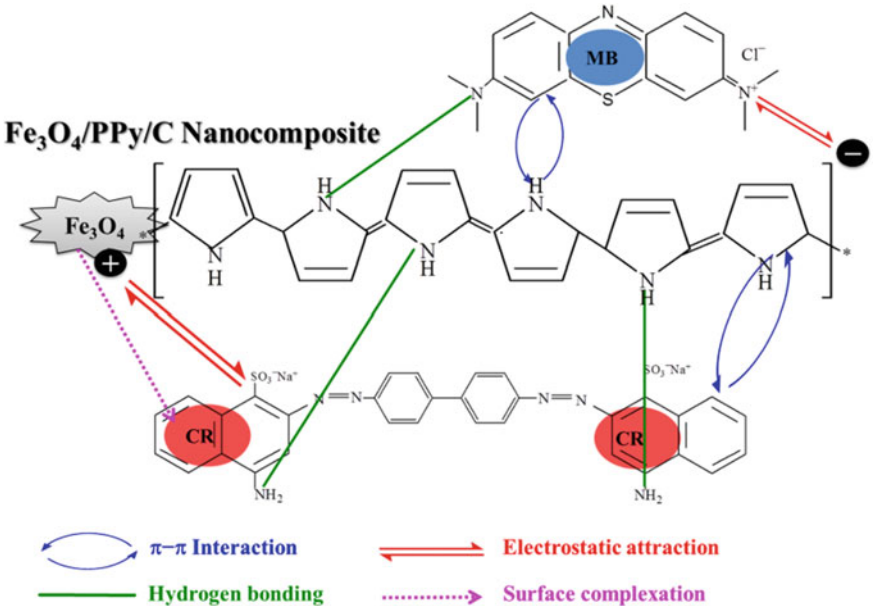

Fig. 2.2 Adsorption mechanism of methylene blue dye removal using magnetic Fe_3O_4/polypyrrole/carbon black nanocomposite [79]

In 2022 Valizadeh et al. [75] synthesized a nano-bio-adsorbent called Fe_3O_4@inulin nanocomposite using in-situ co-precipitation procedure while considering crystal violet dye removal. From different experimental data it was seen that Fe_3O_4@inulin nanocomposite has a maximum adsorption capacity of 223.57 mg/g in optimum conditions mentioned in Table 2.1. The mechanism of crystal violet dye adsorption on Fe_3O_4@inulin nanocomposite was shown in Fig. 2.3. Three types of interactions such as electrostatic attraction, dipole–dipole attraction, and hydrogen bonding were observed in adsorption mechanism of crystal violet. Langmuir adsorption isotherm was by far best suited for this adsorption process, which followed pseudo-second-order kinetics. Again Abu Sharib et al. [72] used weathered basalt-activated nanocomposites (AWB-based Fe_3O_4) as adsorbents for effective removal of crystal violet from wastewater. This nanocomposite was prepared using thermal activation at 950 °C for 3 h. In his experiments he found that AWB-based Fe_3O_4 has a maximum adsorption capacity of 269.7 mg/g under a neutral pH. According to R^2 value, the Langmuir model was well fitted for crystal violet dye adsorption data as compared to the Freundlich model. The number of adsorbed crystal violet molecules per adsorption site suggested that it follows multi-interactions mechanism where the density of iron oxide active sites was governing the removal process.

In the year 2020 Barakat et al. [76] published an article about modifying magnetic Fe_3O_4 nanoparticles (MNP) with surfactant-modified exfoliated Fayum clay (CTAB-EC) to obtain final nanocomposite (MNP/CTAB-EC) by mixing CTAB-EC with magnetic Fe_3O_4 at 50 °C for 2 h. This composite was then tested against a model cationic dye, crystal violet, to estimate its adsorptive capability. The optimum pH

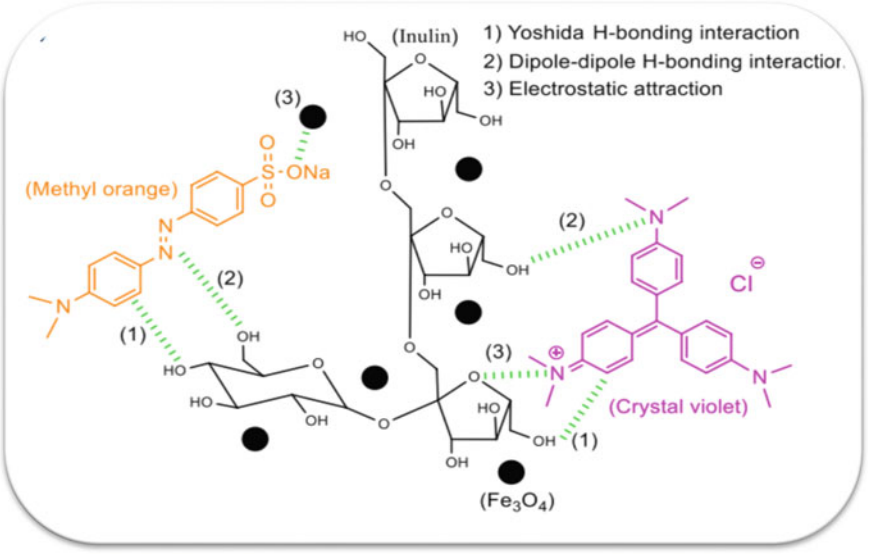

Fig. 2.3 Adsorption mechanism of crystal violet dye removal using Fe_3O_4@inulin nanocomposite [75]

was obtained as 8. The q_{max} value was found out to be 448 mg/g. They varied at some temperatures (25, 40, and 55 °C), and the pseudo-second order for the kinetics and Freundlich model for adsorption isotherm well suited the crystal violet removal experimental data. In the same year Ahmed et al. [77] published an article on magnetized orange peel as adsorbent for crystal violet dye which has a high adsorption efficacy of 556.6 mg/g at optimal pH of 8. Adsorption equilibrium data of magnetized orange peel were well fitted with Langmuir isotherm model. The pseudo-second-order model was confirmed by the kinetic data, and the mechanism indicating crystal violet adsorption was more probable to be chemisorption.

Ansari Mojarad et al. [84] reported a clay/starch/iron oxide composite to eliminate the methyl violet dye from aqueous media. Chemical precipitation method was employed to prepare clay/starch/Fe_3O_4 nanocomposite. Then, the effect of various parameters on the adsorption of methyl violet dye was examined. The outcomes demonstrated that maximum percentage of dye removal was obtained at pH of 9 and contact time of 150 min. The maximum uptake capacity of methyl violet dye was 29.67 mg/g. The Freundlich isotherm model was in good agreement with Langmuir or Temkin isotherm models. The adsorption followed pseudo-second-order kinetic model.

To remove methyl violet, activated carbon made from oak wood (ACOW600) and modified activated carbon made from ZnO and Fe_3O_4 nanoparticles (ACOW600/ZnO/Fe_3O_4) were used by a researcher via Foroutan et al. [85]. The maximum adsorption capacity of methyl violet using ACOW600/ZnO/Fe_3O_4 was determined 48.59 mg/g indicating that alteration of ACOW600 directed to increase its performance in eliminating methyl violet. Optimum pH recorded for elimination of methyl violet dye was 9. The isotherm study revealed that the methyl violet uptake by the ACOW600/ZnO/Fe_3O_4 magnetic nanocomposite followed Freundlich model.

Altintig et al. [83] studied removal of methyl violet using Fe_3O_4-loaded clinoptilolite (a natural zeolite) nanocomposite (Z-Fe_3O_4). The adsorption study of methyl violet was in good agreement with pseudo-second-order kinetic model. The maximum adsorption capacity was found to be 153.85 mg/g. The optimal pH was 7 and contact time of 150 min. Langmuir isotherm model embodied the adsorption isotherm data of Z-Fe_3O_4 most appropriately. For clinoptilolite and clinoptilolite loaded with Fe_3O_4, the computed ΔH^0 values are 11.65 and 11.96 kJ/mol, respectively, showing that the adsorption process was endothermic and spontaneous.

De Marco et al. [69] prepared HNT-Fe_3O_4 magnetic adsorbent using chemical precipitation method from consuming a solution of halloysite clay and iron salts. At an optimal pH of 5.5, the maximum adsorption value was found to be 44.25 mg/g, and the adsorption kinetics well fitted with pseudo-second-order model. The equilibrium data were well fitted for the Freundlich isotherm model. Similarly, in the year 2020 Hasan et al. [66] prepared polyacrylamide-g-chitosan γ-Fe_2O_3 nanocomposite (PACT@γ-Fe_2O_3) as an adsorbent for malachite green removal. According to the reactions dynamic factors, molecules are absorbed by PACT@-Fe_2O_3 through the formation of coordination bonds between the solute and the surrounding material. The optimized values obtained by researchers were found to be 170 min as contact time, pH 6,

and uptake capacity of 86.28 mg/g. The experimental data well fitted with Langmuir isotherm model and pseudo-second-order model.

Eltaweil et al. [68] published an article in the year 2020, regarding the application of nZVI/BC composite as suitable adsorbent for malachite green removal. He reduced nZVI magnetic composite on the surface of corn straw-derived biochar to prepare this nZVI/BC composite. The maximum adsorption capacity was found to be 515.77 mg/g at pH of 6. From observations he saw that this extraction mechanism fits well with pseudo-second-order kinetics and Langmuir isotherm model. Dehbi et al. [65] reported the hematite iron oxide nanoparticles (α-Fe_2O_3) and found the maximum adsorption capacity of 973 mg/g for malachite green extraction in only 120 min. Precipitation method was implemented to prepare this adsorbent which is one of the most green methods. The equilibrium and kinetics data were well fitted for the Freundlich isotherm model and pseudo-second-order kinetic model, respectively.

2.4 Removal of Anionic Dyes Using Magnetic Iron Oxide-Based Nanocomposites

This section describes various reported magnetic iron oxide-based nanocomposites for the adsorption of anionic dyes. Furthermore, compare the adsorption parameters such as optimum pH and contact time of various reported adsorbents. Some important observations such as maximum uptake capacity (q_{max}), isotherm model, and kinetic models of different adsorption are illustrated in Table 2.2. The mechanism of various anionic dyes was also discussed.

Ali and Ismail [79] adsorbed Congo red dye using magnetic Fe_3O_4/polypyrrole/carbon black nanocomposite. The q_{max} was observed to be 500 mg/g. Kinetic study was well allied with pseudo-second-order kinetics which indicates that it is a chemisorptions mechanism. The mechanism for Congo red dye chemisorptions was illustrated in Fig. 2.2 which shows π−π interactions as well as hydrogen bonding. For the maximum adsorption of Congo red, the optimum pH was 4 at a contact time of 180 min.

Sahoo et al. [91] prepared Fe_3O_4-TSPED-Tryptophan using the given procedure in Fig. 2.4. In this preparation process Fe_3O_4 and TSPED were first processed with methanol in argon atmosphere, then Tryptophan was added in presence of $SOCl_2$/DMF. Prepared nanocomposites followed Langmuir model of adsorption isotherm and pseudo-second-order kinetics for Congo red dye. The maximum adsorption capacity (q_{max}) for Congo red dye on the prepared Fe_3O_4-TSPED-Tryptophan nanocomposite was calculated to be 183.15 mg/g with an optimal pH of 3 and contact time of 10 min.

Mahmud and Benamor [93] published an article on preparation and application of magnetic Fe_3O_4-Kaolinite composite. Researcher prepared this nanocomposite using simplistic co-precipitation method for the effective removal of Congo red dye.

Table 2.2 Different parameters like contact time, pH, as well as maximum adsorption capacity, and isotherm and kinetic models of anionic dye removal using various adsorbents were illustrated

Adsorbent	Dye adsorbed	Isotherm model	q_{max} (mg/g)	Kinetic model	Optimum pH/time (min)	References
Magnetic Fe_3O_4/polypyrrole/carbon black nanocomposite	Congo red	Langmuir	500	Pseudo-second order	4/180	[79]
Fe_3O_4-TSPED-Tryptophan	Congo red	Langmuir	183.15	Pseudo-second order	3/10	[91]
Magnetic Fe_3O_4-Kaolinite composite	Congo red	Langmuir	45.59	Pseudo-second order	5.5/40	[93]
Fe_3O_4/NiO magnetic nanocomposites	Congo red	Langmuir	210.78	Pseudo-second order	5/90	[94]
Fe_2O_3–MgO	Congo red	Langmuir	200	Pseudo-second order	4/60	[95]
Fe_3O_4@MUS composite	Methyl orange	Langmuir	149.25	Pseudo-first order	3/60	[96]
$MnFe_2O_4$@CPB	Methyl orange	Langmuir–Freundlich	134.9	Pseudo-second order	3/240	[97]
Asparagus plant-capped Fe_3O_4 NPs	Methyl orange	Langmuir	167.7	Pseudo-second order	7/20	[74]
Ricinus communis-capped Fe_3O_4 NPs	Methyl orange	Langmuir	30.5	Pseudo-second order	3/60	[63]
CF-MF-NC	Eriochrome black T	Langmuir	416.66	Pseudo-second order	2/15	[98]
Polypeptidylated Hb/iron oxide (1:1)	Eriochrome black T	Langmuir	217	Pseudo-second order	7/120	[99]
GO-Fe_3O_4	Eriochrome black T	Langmuir–Freundlich	160.08	Pseudo-second order	2/120	[100]
PMNs	Acid red	Langmuir	888.68	Pseudo-second order	3/100	[101]
PMNs	Remazol Red	Langmuir	808.43	Pseudo-second order	4/100	[101]

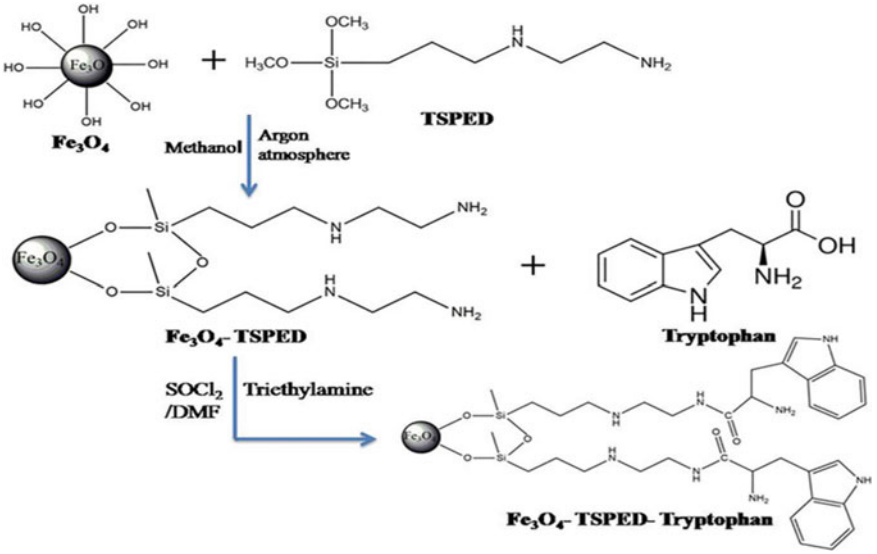

Fig. 2.4 Illustration of the synthetic procedure for Fe_3O_4-TSPED-Tryptophan nanocomposite preparation [91]. Copyright 2019. Reproduced with permission from Elsevier

The maximum adsorption capacity 45.59 mg/g was observed at pH of 5.5 and contact time of 40 min. Langmuir isotherm model and pseudo-second-order kinetics were found to be the most suitable for Congo red dye adsorption.

Koohi et al. [94] synthesized Fe_3O_4/NiO nanocomposite via precipitation process as an adsorbent to eliminate the Congo red from wastewater. Among the Langmuir, Freundlich, Halsey, Jovanovic, and Temkin isotherm model studies, it follows Langmuir isotherm with q_{max} value 210.78 mg/g at 293 K. Maximum adsorption efficiency of congo red dye was observed at pH 5 and contact time 90 min. It followed the pseudo-second-order kinetic model.

Sahoo et al. [95] used ferric nitrate, magnesium nitrate, and polyethylene glycol and carried out one-step hydrothermal method to produce Fe_2O_3–MgO nanorods. The process of Congo red adsorption on the nanorod surface is mostly due to pH where adsorbate molecules are linked to the adsorbent through electrostatic interaction as shown in Fig. 2.5. As Congo red adsorption mainly depended on the pH, maximum adsorption capacity (q_{max} = 200 mg/g) arises at pH of 4 with a contact time of 60 min. Congo red adsorption on Fe_2O_3–MgO nanocomposites followed pseudo-second-order kinetic and Langmuir isotherm models.

Barakat et al. [96] reported removal of methyl orange dye using Fe_3O_4@MUS composite. In the preparation process, layered silicate muscovite (MUS) was decorated with magnetic Fe_3O_4 used. Maximum adsorption capacity of Fe_3O_4@MUS composite toward methyl orange adsorption was about 149.25 mg/g at pH of 3. Figure 2.6 gives an idea on the adsorption of methyl orange on Fe_3O_4@MUS composite. In this image hydrogen bonding and electrostatic attraction were shown

Fig. 2.5 Mechanism of CR extractions on Fe_2O_3–MgO surface by electrostatic interaction [95]. Copyright 2020. Reproduced with permission from Elsevier

as the driving force behind adsorption of methyl orange on the prepared composite. Pseudo-first-order kinetics model and Langmuir isotherm model were well suited for this removal mechanism.

Through a mild chemical co-precipitation method, Wang et al. [97] successfully developed a novel composite for methyl orange removal using chitosan-modified biochar (CPB) and $MnFe_2O_4$ ($MnFe_2O_4$@CPB). Due to π–π interactions between MO and $MnFe_2O_4$@CPB and the presence hydrogen bonding forces, the maximum

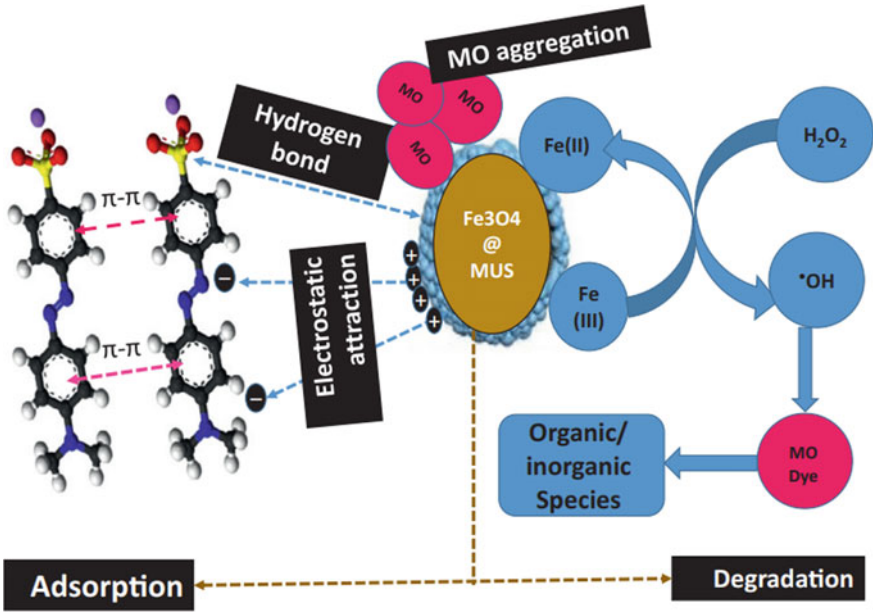

Fig. 2.6 Adsorption and degradation mechanisms of MO adsorption using Fe_3O_4@MUS composite [96]. Copyright 2020. Reproduced with permission from Elsevier

adsorption capacity of prepared composite was 160 mg/g at a pH of 3 after 240 min. Langmuir–Freundlich model was used for the isotherm data and pseudo-second-order model for kinetics data obtained from observing the mechanism.

Geramizadegan [74] removed methyl orange dye from wastewater using asparagus plant-capped Fe_3O_4 NPs. The isotherm and kinetics data well fitted with Langmuir monolayer isotherm model and pseudo-second-order kinetics, respectively. The maximum adsorption capacity was found to be 167.7 mg/g. The percentage removal of methyl orange dye was obtained at pH of 7 and contact time of 20 min.

Niknam and Davoudi [63] studied the application of *Ricinus communis* functionalized with iron oxide nanoparticles toward methyl orange dye removal. The optimum values for adsorption of methyl orange dye onto *R. communis* coated Fe_3O_4 NPs were pH of 5.0 and contact time of 60 min. The maximum adsorption was found to be 30.5 mg/g for methyl orange dye. The adsorption process follows Langmuir adsorption isotherm model and pseudo-second-order kinetics.

Bhowmik et al. [98] published an article about efficiency of magnetic nano-scale adsorbent CF-MF-NC for the Eriochrome black T dye adsorption from wastewater. The mechanism of EBT dye adsorption on the surface of magnetic calcium ferrite and manganese ferrite nanocomposite was discussed in Fig. 2.7. The electrostatic interactions between the anionic part of EBT dye and the protonated surfaces of adsorbent were reported. The maximum adsorption of EBT dye was 416.667 mg/g. The maximum percentage of removal of EBT dye was achieved at pH of 2 with 15 min contact time. Pseudo-second-order kinetic model and Langmuir adsorption isotherm were best fitted with observed isotherm and kinetic data.

Essandoh et al. [99] prepared iron oxide-coated polypeptidylated hemoglobin as an effective adsorbent for Eriochrome black T dye adsorption. Polypeptidylated Hb/iron oxide (1:1) has q_{max} value of 217 mg/g which was calculated using Langmuir adsorption isotherm at a pH of 7. Electrostatic attraction, hydrogen bonding, and charge–charge interaction were the factors at work for the adsorption of EBT dye on polypeptidylated Hb/iron oxide adsorbent. EBT adsorption on prepared nanocomposites followed pseudo-second-order kinetic and Langmuir isotherm models (Fig. 2.8).

Raghu et al. [100] prepared GO-Fe_3O_4 adsorbent through the formation of amide bond between graphene oxide and amine containing Fe_3O_4. Researcher employed this adsorbent for the effective removal of Eriochrome black T dye. This GO-Fe_3O_4 nanocomposite had an adsorption capacity of 147.25 mg/g at pH of 2. At contact time of 120 min maximum percentage of removal was obtained. The adsorption process follows pseudo-second-order kinetic and both Langmuir and Freundlich isotherm models.

El-Desouky et al. [101] prepared magnetite with pores as high-performance adsorbent in order to remove anionic dyes like Remazol Red and acid red 57 from an aqueous solution. This adsorption process followed pseudo-second-order kinetics and Langmuir isotherm models for both the dyes. Maximum adsorption capacity for Remazol Red and acid red 57 dyes was 808.43 and 888.68 mg/g, respectively.

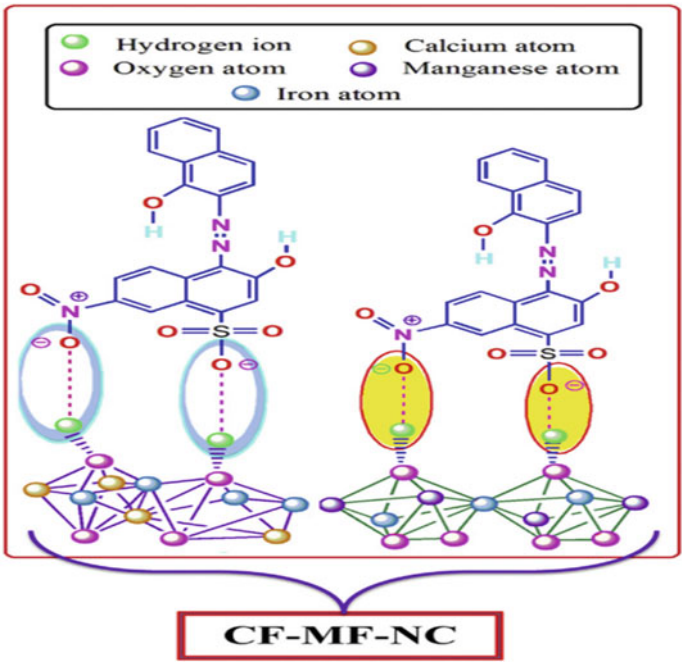

Fig. 2.7 Mechanism of adsorption EBT dye on the active sites of CF-MF-NC [98]. Copyright 2019. Reproduced with permission from Elsevier

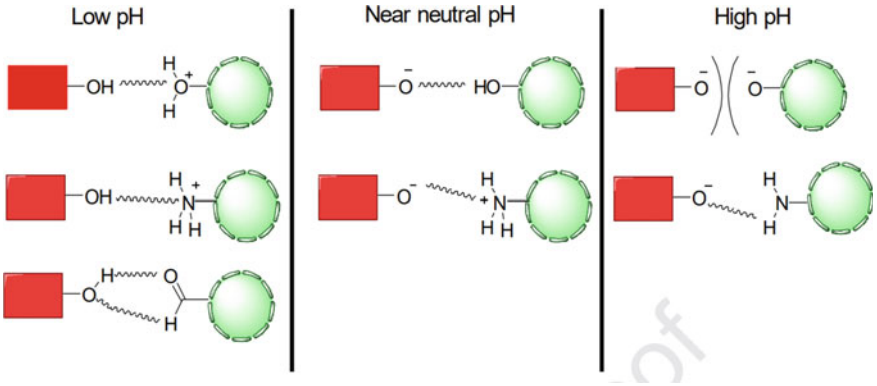

Fig. 2.8 Mechanisms for the adsorption of EBT dye on polypeptidylated Hb/iron oxide (1:1) adsorbent. Here in the figure the round green shape represents the adsorbent, and red rectangular shape indicates the dye molecules [99]. Copyright 2020. Reproduced with permission from Elsevier

Maximum adsorption of both these dyes was observed at pH range of 3–4 and contact time of 100 min.

2.5 Conclusion

This chapter summarized that the advancement of magnetic iron oxide-based nanocomposites showed potential adsorbents toward the cationic and anionic dyes removal because of their characteristics such as magnetic separation from aqueous solution, high adsorption limit, high surface area, and great recyclability. The characterization of iron oxide was also discussed. Different parameters such as optimum pH, time, kinetics, isotherm, and maximum adsorption capacity were compared in detail. The percentage removal of cationic dyes was observed in higher pH and of anionic dyes was observed in lower pH. The maximum adsorption of cationic dyes such as methylene blue was 90.9 mg/g, crystal violet was 556.6 mg/g, methyl violet was 153.85, and malachite green was 973 mg/g. The maximum adsorption of anionic dyes such as Congo red was 500 mg/g, methyl orange was 167.7 mg/g, Eriochrome black T was 416.6 mg/g, Reactive Black 5 was 17.98, acid red was 888.8 mg/g, and Remazol Red was 808.43 mg/g. Most of the adsorbents follow pseudo-second-order kinetics model which means a chemical bond is formed in between adsorbent and adsorbate. Moreover, the research reported that most of the cationic and anionic dyes adsorbed on iron oxide-based materials through $\pi-\pi$ interaction, hydrogen bonding, and electrostatic bonding.

References

1. Widiyastuti W, Fahrudin Rois M, Suari NMIP, Setyawan H (2020) Activated carbon nanofibers derived from coconut shell charcoal for dye removal application. Adv Powder Technol 31:3267–3273. https://doi.org/10.1016/j.apt.2020.06.012
2. Rong N, Chen C, Ouyang K et al (2021) Adsorption characteristics of directional cellulose nanofiber/chitosan/montmorillonite aerogel as adsorbent for wastewater treatment. Sep Purif Technol 274:119120. https://doi.org/10.1016/j.seppur.2021.119120
3. Qiu B, Duan F (2019) Synthesis of industrial solid wastes/biochar composites and their use for adsorption of phosphate: from surface properties to sorption mechanism. Colloids Surf A Physicochem Eng Asp 571:86–93. https://doi.org/10.1016/j.colsurfa.2019.03.041
4. Rehman R, Jamil A, Alakhras F (2022) Sorptive removal of diamond green dye by acid treated *Punica granatum* peels in eco-friendly way. Int J Phytoremediation 24:245–254. https://doi.org/10.1080/15226514.2021.1932732
5. Joshi S, Garg VK, Kataria N, Kadirvelu K (2019) Applications of Fe_3O_4@AC nanoparticles for dye removal from simulated wastewater. Chemosphere 236. https://doi.org/10.1016/j.chemosphere.2019.07.011
6. Hasdi ND (2020) Reviewing methods to prepare activated carbon from various sources. Nanoscale Res Lett 14:1–17

7. Panis C, Candiotto LZP, Gaboardi SC et al (2022) Widespread pesticide contamination of drinking water and impact on cancer risk in Brazil. Environ Int 165. https://doi.org/10.1016/j.envint.2022.107321
8. Iloms E, Ololade OO, Ogola HJO, Selvarajan R (2020) Investigating industrial effluent impact on municipal wastewater treatment plant in Vaal, South Africa. Int J Environ Res Public Health 17:1–18. https://doi.org/10.3390/ijerph17031096
9. Raj D, Shaji E (2017) Fluoride contamination in groundwater resources of Alleppey, southern India. Geosci Front 8:117–124. https://doi.org/10.1016/j.gsf.2016.01.002
10. Das TR, Patra S, Madhuri R, Sharma PK (2018) Bismuth oxide decorated graphene oxide nanocomposites synthesized via sonochemical assisted hydrothermal method for adsorption of cationic organic dyes. J Colloid Interface Sci 509:82–93. https://doi.org/10.1016/j.jcis.2017.08.102
11. Calisto V, Ferreira CIA, Oliveira JABP et al (2015) Adsorptive removal of pharmaceuticals from water by commercial and waste-based carbons. J Environ Manage 152:83–90. https://doi.org/10.1016/j.jenvman.2015.01.019
12. Kumar Sahoo S, Kumar Panigrahi G, Prakash Dhal J et al (2023) A greener approach to synthesize magnetically separable and photocatalytic recyclable g-C_3N_4-Fe_3O_4 nanomaterial for removing toxic organic dyes from water. Inorg Chem Commun 154:110969. https://doi.org/10.1016/j.inoche.2023.110969
13. Radoor S, Karayil J, Parameswaranpillai J, Siengchin S (2020) Removal of anionic dye Congo red from aqueous environment using polyvinyl alcohol/sodium alginate/ZSM-5 zeolite membrane. Sci Rep 10:1–15. https://doi.org/10.1038/s41598-020-72398-5
14. Sahoo JK, Hota A, Singh C et al (2021) Rice husk and rice straw based materials for toxic metals and dyes removal: a comprehensive and critical review. Int J Environ Anal Chem 1–23. https://doi.org/10.1080/03067319.2021.2003349
15. Tian H, Hu Y, Xu X et al (2019) Enhanced wastewater treatment with high o-aminophenol concentration by two-stage MABR and its biodegradation mechanism. Bioresour Technol 289:121649. https://doi.org/10.1016/j.biortech.2019.121649
16. Shen C, Pan Y, Wu D et al (2019) A crosslinking-induced precipitation process for the simultaneous removal of poly(vinyl alcohol) and reactive dye: the importance of covalent bond forming and magnesium coagulation. Chem Eng J 374:904–913. https://doi.org/10.1016/j.cej.2019.05.203
17. Cseri L, Topuz F, Abdulhamid MA et al (2021) Electrospun adsorptive nanofibrous membranes from ion exchange polymers to snare textile dyes from wastewater. Adv Mater Technol 6:2000955. https://doi.org/10.1002/admt.202000955
18. Cinperi NC, Ozturk E, Yigit NO, Kitis M (2019) Treatment of woolen textile wastewater using membrane bioreactor, nanofiltration and reverse osmosis for reuse in production processes. J Clean Prod 223:837–848. https://doi.org/10.1016/j.jclepro.2019.03.166
19. Januário EFD, Vidovix TB, Bergamasco R, Vieira AMS (2021) Performance of a hybrid coagulation/flocculation process followed by modified microfiltration membranes for the removal of solophenyl blue dye. Chem Eng Process Process Intensif 168. https://doi.org/10.1016/j.cep.2021.108577
20. Li K, Xu L, Zhang Y et al (2019) A novel electro-catalytic membrane contactor for improving the efficiency of ozone on wastewater treatment. Appl Catal B Environ 249:316–321. https://doi.org/10.1016/j.apcatb.2019.03.015
21. Ramutshatsha-Makhwedzha D, Nomngongo PN (2022) Application of ultrafiltration membrane technology for removal of dyes from wastewater. In: Muthu SS, Khadir A (eds) Membrane based methods for dye containing wastewater: recent advances. Springer Singapore, Singapore, pp 37–47
22. Moosavi S, Lai CW, Gan S et al (2020) Application of efficient magnetic particles and activated carbon for dye removal from wastewater. ACS Omega 5:20684–20697. https://doi.org/10.1021/acsomega.0c01905
23. Ye W, Liu R, Chen X et al (2020) Loose nanofiltration-based electrodialysis for highly efficient textile wastewater treatment. J Memb Sci 608:118182. https://doi.org/10.1016/j.memsci.2020.118182

24. Khan MA, Momina SMR et al (2020) Removal of Rhodamine B from water using a solvent impregnated polymeric Dowex 5WX8 resin: statistical optimization and batch adsorption studies. Polymers (Basel) 12:1–12. https://doi.org/10.3390/polym12020500
25. Yadav A, Sharma P, Panda AB, Shahi VK (2021) Photocatalytic TiO_2 incorporated PVDF-co-HFP UV-cleaning mixed matrix membranes for effective removal of dyes from synthetic wastewater system via membrane distillation. J Environ Chem Eng 9:105904. https://doi.org/10.1016/j.jece.2021.105904
26. Ebiad MA, Abd El-Hafiz DR, Masod MB (2020) β-FeOOH/C nanocomposite for elemental mercury removal as a new approach to environmental and natural gas processes. J Nat Gas Sci Eng 80. https://doi.org/10.1016/j.jngse.2020.103383
27. Liu WX, Song S, Ye ML et al (2022) Nanomaterials with excellent adsorption characteristics for sample pretreatment: a review. Nanomaterials 12. https://doi.org/10.3390/nano12111845
28. Nayak V, Singh KR, Singh AK, Singh RP (2021) Potentialities of selenium nanoparticles in biomedical science. New J Chem 45:2849–2878. https://doi.org/10.1039/d0nj05884j
29. Pourtalebi Jahromi L, Ghazali M, Ashrafi H, Azadi A (2020) A comparison of models for the analysis of the kinetics of drug release from PLGA-based nanoparticles. Heliyon 6. https://doi.org/10.1016/j.heliyon.2020.e03451
30. Li Y, Wang Z, Sun L et al (2019) Nanoparticle-based sensors for food contaminants. TrAC Trends Anal Chem 113:74–83. https://doi.org/10.1016/j.trac.2019.01.012
31. Dheyab MA, Aziz AA, Jameel MS, Oladzadabbasabadi N (2022) Recent advances in synthesis, modification, and potential application of tin oxide nanoparticles. Surf Interfaces 28:101677. https://doi.org/10.1016/j.surfin.2021.101677
32. Khan S, Dewang Y, Raghuwanshi J et al (2022) Nanoparticles as fuel additive for improving performance and reducing exhaust emissions of internal combustion engines. Int J Environ Anal Chem 102:319–341. https://doi.org/10.1080/03067319.2020.1722810
33. Fernández-Garcia M, Rodriguez JA (2009) Metal oxide nanoparticles. Encycl Inorg Chem. https://doi.org/10.1002/0470862106.ia377
34. Lahneman DJ, Kim H, Jiang H et al (2023) Electronic and optical properties of strain-locked metallic Ti_2O_3 films. Curr Appl Phys 47:9–14. https://doi.org/10.1016/j.cap.2022.12.006
35. Bhuiyan MSH, Miah MY, Paul SC et al (2020) Green synthesis of iron oxide nanoparticle using *Carica papaya* leaf extract: application for photocatalytic degradation of remazol yellow RR dye and antibacterial activity. Heliyon 6:e04603. https://doi.org/10.1016/j.heliyon.2020.e04603
36. Baylan N, İlalan İ, İnci İ (2020) Copper oxide nanoparticles as a novel adsorbent for separation of acrylic acid from aqueous solution: synthesis, characterization, and application. Water Air Soil Pollut 231. https://doi.org/10.1007/s11270-020-04832-3
37. Islam MA, Ali I, Karim SMA et al (2019) Removal of dye from polluted water using novel nano manganese oxide-based materials. J Water Process Eng 32:100911. https://doi.org/10.1016/j.jwpe.2019.100911
38. Alagarsamy A, Chandrasekaran S, Manikandan A (2022) Green synthesis and characterization studies of biogenic zirconium oxide (ZrO_2) nanoparticles for adsorptive removal of methylene blue dye. J Mol Struct 1247:131275. https://doi.org/10.1016/j.molstruc.2021.131275
39. Masoudian N, Rajabi M, Ghaedi M (2019) Titanium oxide nanoparticles loaded onto activated carbon prepared from bio-waste watermelon rind for the efficient ultrasonic-assisted adsorption of Congo red and phenol red dyes from wastewaters. Polyhedron 173:114105. https://doi.org/10.1016/j.poly.2019.114105
40. Sharma S, Hasan A, Kumar N, Pandey LM (2018) Removal of methylene blue dye from aqueous solution using immobilized *Agrobacterium fabrum* biomass along with iron oxide nanoparticles as biosorbent. Environ Sci Pollut Res 25:21605–21615. https://doi.org/10.1007/s11356-018-2280-z
41. Qadri S, Ganoe A, Haik Y (2009) Removal and recovery of acridine orange from solutions by use of magnetic nanoparticles. J Hazard Mater 169:318–323. https://doi.org/10.1016/j.jhazmat.2009.03.103

42. Zhu J, Ng KYS, Deng D (2014) Micro single crystals of hematite with nearly 100% exposed {104} facets: preferred etching and lithium storage. Cryst Growth Des 14:2811–2817. https://doi.org/10.1021/cg5000777
43. Reddy KR, Park W, Sin BC et al (2009) Synthesis of electrically conductive and superparamagnetic monodispersed iron oxide-conjugated polymer composite nanoparticles by in situ chemical oxidative polymerization. J Colloid Interface Sci 335:34–39. https://doi.org/10.1016/j.jcis.2009.02.068
44. Shakya A, Agarwal T (2019) Removal of Cr(VI) from water using pineapple peel derived biochars: adsorption potential and re-usability assessment. J Mol Liq 293:111497. https://doi.org/10.1016/j.molliq.2019.111497
45. Akhbarizadeh R, Shayestefar MR, Darezereshki E (2014) Konkurrierende Entfernung von Metallen aus Abwasser mit Hilfe von Maghemit-Nanopartikeln: Ein Vergleich zwischen künstlichem Abwasser und Sauerwasser. Mine Water Environ 33:89–96. https://doi.org/10.1007/s10230-013-0255-3
46. Ngomsik AF, Bee A, Talbot D, Cote G (2012) Magnetic solid-liquid extraction of Eu(III), La(III), Ni(II) and Co(II) with maghemite nanoparticles. Sep Purif Technol 86:1–8. https://doi.org/10.1016/j.seppur.2011.10.013
47. Panda SK, Aggarwal I, Kumar H et al (2021) Magnetite nanoparticles as sorbents for dye removal: a review. Environ Chem Lett 19:2487–2525. https://doi.org/10.1007/s10311-020-01173-9
48. Kim HJ, Lee JM, Choi JH et al (2021) Synthesis and adsorption properties of gelatin-conjugated hematite (α-Fe_2O_3) nanoparticles for lead removal from wastewater. J Hazard Mater 416:125696. https://doi.org/10.1016/j.jhazmat.2021.125696
49. Jabbar KQ, Barzinjy AA, Hamad SM (2022) Iron oxide nanoparticles: preparation methods, functions, adsorption and coagulation/flocculation in wastewater treatment. Environ Nanotechnol Monit Manag 17:100661. https://doi.org/10.1016/j.enmm.2022.100661
50. Chang M, Shih Y (2018) Synthesis and application of magnetic iron oxide nanoparticles on the removal of Reactive Black 5: reaction mechanism, temperature and pH effects. J Environ Manage 224:235–242. https://doi.org/10.1016/j.jenvman.2018.07.021
51. Priya VS, Basha SK, Kumari VS (2023) Kinetics and adsorption performance of biosorbent starch/poly(vinyl alcohol)/graphene oxide nanocomposite for the removal of dyes. J Umm Al-Qura Univ Appl Sci. https://doi.org/10.1007/s43994-023-00063-4
52. Shah N, Khan I, Ahmad H et al (2021) Synthesis and characterization of starch coated natural magnetic iron oxide nanoparticles for the removal of methyl orange dye from water. Lett Appl NanoBioSci 10:2750–2759. https://doi.org/10.33263/LIANBS104.27502759
53. Mohanta J, Kumari R, Dey B, Dey S (2021) Highly porous iron-zirconium-zinc ternary metal oxide scaffold: facile synthesis and efficient removal of malachite green from water. J Chem Eng Data 66:297–307. https://doi.org/10.1021/acs.jced.0c00681
54. Mohanta J, Dey B, Dey S (2020) Magnetic cobalt oxide nanoparticles: sucrose-assisted self-sustained combustion synthesis, characterization, and efficient removal of malachite green from water. J Chem Eng Data 65:2819–2829. https://doi.org/10.1021/acs.jced.0c00131
55. Ladio H, Oladejo J, Saka A et al (2023) Heliyon effective removal of malachite green from local dyeing wastewater using zinc-tungstate based materials. Heliyon 9:e19167. https://doi.org/10.1016/j.heliyon.2023.e19167
56. Sarkar S, Tiwari N, Basu A et al (2021) Sorptive removal of malachite green from aqueous solution by magnetite/coir pith supported sodium alginate beads: kinetics, isotherms, thermodynamics and parametric optimization. Environ Technol Innov 24:101818. https://doi.org/10.1016/j.eti.2021.101818
57. Bibi S, Ahmad A, Anjum MAR et al (2021) Photocatalytic degradation of malachite green and methylene blue over reduced graphene oxide (rGO) based metal oxides (rGO-Fe_3O_4/TiO_2) nanocomposite under UV-visible light irradiation. J Environ Chem Eng 9. https://doi.org/10.1016/j.jece.2021.105580
58. Arora C, Kumar P, Soni S et al (2020) Efficient removal of malachite green dye from aqueous solution using *Curcuma caesia* based activated carbon. Desalin Water Treat 195:341–352. https://doi.org/10.5004/dwt.2020.25897

59. Abbasi M, Sabzehmeidani MM, Ghaedi M et al (2021) Synthesis of grass-like structured Mn–Fe layered double hydroxides/PES composite adsorptive membrane for removal of malachite green. Appl Clay Sci 203:105946. https://doi.org/10.1016/j.clay.2020.105946
60. Zadvarzi SB, Khavarpour M, Vahdat SM et al (2021) Synthesis of Fe_3O_4@chitosan@ZIF-8 towards removal of malachite green from aqueous solution: theoretical and experimental studies. Int J Biol Macromol 168:428–441. https://doi.org/10.1016/j.ijbiomac.2020.12.067
61. Karbasaki SS, Bagherzade G, Maleki B, Ghani M (2021) Fabrication of sulfamic acid functionalized magnetic nanoparticles with denderimeric linkers and its application for microextraction purposes, one-pot preparation of pyrans pigments and removal of malachite green. J Taiwan Inst Chem Eng 118:342–354. https://doi.org/10.1016/j.jtice.2020.12.025
62. Mohammadi SZ, Mofidinasab N, Karimi MA, Mosazadeh F (2020) Fast and efficient removal of Pb(II) ion and malachite green dye from wastewater by using magnetic activated carbon-cobalt nanoparticles. Water Sci Technol 82:829–842. https://doi.org/10.2166/wst.2020.375
63. Niknam L, Davoudi S (2022) Removal studies of methyl orange dye using *Ricinus communis*-capeed Fe_3O_4 NPs from aqueous solutions. J Phys Theoret Chem 18:37–54
64. Bakhshi Nejad S, Mohammadi A (2020) Epoxy-triazinetrione-functionalized magnetic nanoparticles as an efficient magnetic nanoadsorbent for the removal of malachite green and Pb(II) from aqueous solutions. J Chem Eng Data 65:2731–2742. https://doi.org/10.1021/acs.jced.0c00063
65. Dehbi A, Dehmani Y, Omari H et al (2020) Comparative study of malachite green and phenol adsorption on synthetic hematite iron oxide nanoparticles (α-Fe_2O_3). Surf Interfaces 21:100637. https://doi.org/10.1016/j.surfin.2020.100637
66. Hasan I, Bhatia D, Walia S, Singh P (2020) Removal of malachite green by polyacrylamide-g-chitosan γ-Fe_2O_3 nanocomposite—an application of central composite design. Groundw Sustain Dev 11:100378. https://doi.org/10.1016/j.gsd.2020.100378
67. Arabkhani P, Asfaram A (2020) Development of a novel three-dimensional magnetic polymer aerogel as an efficient adsorbent for malachite green removal. J Hazard Mater 384:121394. https://doi.org/10.1016/j.jhazmat.2019.121394
68. Eltaweil AS, Ali Mohamed H, Abd El-Monaem EM, El-Subruiti GM (2020) Mesoporous magnetic biochar composite for enhanced adsorption of malachite green dye: characterization, adsorption kinetics, thermodynamics and isotherms. Adv Powder Technol 31:1253–1263. https://doi.org/10.1016/j.apt.2020.01.005
69. De Marco C, Mauler RS, Daitx TS et al (2020) Removal of malachite green dye from aqueous solutions by a magnetic adsorbent. Sep Sci Technol 55:1089–1101. https://doi.org/10.1080/01496395.2019.1585455
70. Dey S, Mohanta J, Dey B (2020) Sucrose-triggered, self-sustained combustive synthesis of magnetic nickel oxide nanoparticles and efficient removal of malachite green from water. ACS Omega 5:16510–16520. https://doi.org/10.1021/acsomega.0c00999
71. Yarahmadi H (2023) Catalytic degradation of organic dyes using eggshell-derived hydroxyapatite coated by silver nanoparticles. J Environ Sci Stud 8:6775–6795
72. Abu Sharib ASAA, Bonilla-Petriciolet A, Selim AQ et al (2021) Utilizing modified weathered basalt as a novel approach in the preparation of Fe_3O_4 nanoparticles: experimental and theoretical studies for crystal violet adsorption. J Environ Chem Eng 9. https://doi.org/10.1016/j.jece.2021.106220
73. Abdullah NH, Shameli K, Abdullah EC, Abdullah LC (2020) Low cost and efficient synthesis of magnetic iron oxide/activated sericite nanocomposites for rapid removal of methylene blue and crystal violet dyes. Mater Charact 163:110275. https://doi.org/10.1016/j.matchar.2020.110275
74. Geramizadegan A (2022) Removal studies of methyl orange dye using asparagus plant-capped Fe_3O_4 NPs from aqueous solutions. J Phys Theoret Chem 18:1–18
75. Valizadeh K, Bateni A, Sojoodi N et al (2022) Magnetized inulin by Fe_3O_4 as a bio-nano adsorbent for treating water contaminated with methyl orange and crystal violet dyes. Sci Rep 12:1–13. https://doi.org/10.1038/s41598-022-26652-7

76. Barakat MAE, Kumar R, Seliem MK et al (2020) Exfoliated clay decorated with magnetic iron nanoparticles for crystal violet adsorption: modeling and physicochemical interpretation. Nanomaterials 10:1–19. https://doi.org/10.3390/nano10081454
77. Ahmed M, Mashkoor F, Nasar A (2020) Development, characterization, and utilization of magnetized orange peel waste as a novel adsorbent for the confiscation of crystal violet dye from aqueous solution. Groundw Sustain Dev 10:100322. https://doi.org/10.1016/j.gsd.2019.100322
78. Pietrzyk P, Borowska EI, Hejduk P et al (2023) Green composites based on volcanic red algae Cyanidiales, cellulose, and coffee waste biomass modified with magnetic nanoparticles for the removal of methylene blue. Environ Sci Pollut Res 30:62689–62703. https://doi.org/10.1007/s11356-023-26425-3
79. Ali H, Ismail AM (2023) Fabrication of magnetic Fe_3O_4/polypyrrole/carbon black nanocomposite for effective uptake of Congo red and methylene blue dye: adsorption investigation and mechanism. J Polym Environ 31:976–998. https://doi.org/10.1007/s10924-022-02663-3
80. De Souza APN, Licea YE, Colaço MV et al (2021) Green iron oxides/amino-functionalized MCM-41 composites as adsorbent for anionic azo dye: kinetic and isotherm studies. J Environ Chem Eng 9. https://doi.org/10.1016/j.jece.2021.105062
81. Zafari SH, Saadatjou N, Shaabani B (2021) Fe–Cu binary oxides as low-cost adsorbents and their application in photocatalytic removal of Acid Red 14, Methyl Orange and Malachite Green from aqueous solutions. J Appl Chem 15:2021
82. Simonescu CM, Tătăruş A, Culiţă DC et al (2021) Comparative study of $CoFe_2O_4$ nanoparticles and $CoFe_2O_4$-chitosan composite for Congo red and methyl orange removal by adsorption. Nanomaterials 11:1–24. https://doi.org/10.3390/nano11030711
83. Altintig E, Alsancak A, Karaca H et al (2022) The comparison of natural and magnetically modified zeolites as an adsorbent in methyl violet removal from aqueous solutions. Chem Eng Commun 209:555–569. https://doi.org/10.1080/00986445.2021.1874368
84. Ansari Mojarad A, Tamjidi S, Esmaeili H (2022) Clay/starch/Fe_3O_4 nanocomposite as an efficient adsorbent for the removal of methyl violet dye from aqueous media. Int J Environ Anal Chem 102:8159–8180. https://doi.org/10.1080/03067319.2020.1845665
85. Foroutan R, Mohammadi R, Ahmadi A et al (2022) Impact of ZnO and Fe_3O_4 magnetic nanoscale on the methyl violet 2B removal efficiency of the activated carbon oak wood. Chemosphere 286:131632. https://doi.org/10.1016/j.chemosphere.2021.131632
86. Sharma VT, Halanur MM, Kamath SV et al (2020) Fe–Al based nanocomposite reinforced hydrothermal carbon: efficient and robust absorbent for anionic dyes. Chemosphere 259:127421. https://doi.org/10.1016/j.chemosphere.2020.127421
87. Fungaro DA (2011) Adsorption of anionic dyes from aqueous solution on zeolite from fly ash-iron oxide magnetic nanocomposite. J At Mol Sci 2:305–316. https://doi.org/10.4208/jams.032211.041211a
88. Lamichhane N, Sharma S, Parul et al (2021) Iron oxide-based magneto-optical nanocomposites for in vivo biomedical applications. Biomedicines 9:1–28. https://doi.org/10.3390/biomedicines9030288
89. Tan L, Xu J, Xue X et al (2014) Multifunctional nanocomposite Fe_3O_4@SiO_2-mPD/SP for selective removal of Pb(II) and Cr(VI) from aqueous solutions. RSC Adv 4:45920–45929. https://doi.org/10.1039/c4ra08040h
90. Yadav S, Asthana A, Chakraborty R et al (2020) Cationic dye removal using novel magnetic/activated charcoal/β-cyclodextrin/alginate polymer nanocomposite. Nanomaterials 2–7
91. Sahoo JK, Paikra SK, Mishra M, Sahoo H (2019) Amine functionalized magnetic iron oxide nanoparticles: synthesis, antibacterial activity and rapid removal of Congo red dye. J Mol Liq 282:428–440. https://doi.org/10.1016/j.molliq.2019.03.033
92. Williams KFE, Johnson CE, Thomas MF (1998) Mössbauer spectroscopy measurement of iron oxidation states in float composition silica glasses. J Non Cryst Solids 226:19–23. https://doi.org/10.1016/S0022-3093(98)00361-5
93. Mahmud N, Benamor A (2023) Magnetic iron oxide kaolinite nanocomposite for effective removal of Congo red dye: adsorption, kinetics, and thermodynamics studies. Water Conserv Sci Eng 8. https://doi.org/10.1007/s41101-023-00207-x

94. Koohi P, Rahbar-Kelishami A, Shayesteh H (2021) Efficient removal of Congo red dye using Fe_3O_4/NiO nanocomposite: synthesis and characterization. Environ Technol Innov 23:101559. https://doi.org/10.1016/j.eti.2021.101559
95. Sahoo SK, Dhal JP, Panigrahi GK (2020) Magnesium oxide nanoparticles decorated iron oxide nanorods: synthesis, characterization and remediation of Congo red dye from aqueous media. Compos Commun 22:100496. https://doi.org/10.1016/j.coco.2020.100496
96. Barakat MA, Kumar R, Lima EC, Seliem MK (2021) Facile synthesis of muscovite–supported Fe_3O_4 nanoparticles as an adsorbent and heterogeneous catalyst for effective removal of methyl orange: characterisation, modelling, and mechanism. J Taiwan Inst Chem Eng 119:146–157. https://doi.org/10.1016/j.jtice.2021.01.025
97. Wang Z, Li Y, Xie X, Wang Z (2021) Bifunctional $MnFe_2O_4$/chitosan modified biochar composite for enhanced methyl orange removal based on adsorption and photo-Fenton process. Colloids Surf A Physicochem Eng Asp 613:126104. https://doi.org/10.1016/j.colsurfa.2020.126104
98. Bhowmik M, Kanmani M, Debnath A, Saha B (2019) Sono-assisted rapid adsorption of anionic dye onto magnetic $CaFe_2O_4$/$MnFe_2O_4$ nanocomposite from aqua matrix. Powder Technol 354:496–504. https://doi.org/10.1016/j.powtec.2019.06.009
99. Essandoh M, Garcia RA, Gayle MR, Nieman CM (2020) Performance and mechanism of polypeptidylated hemoglobin (Hb)/iron oxide magnetic composites for enhanced dye removal. Chemosphere 247:125897. https://doi.org/10.1016/j.chemosphere.2020.125897
100. Raghu MS, Yogesh Kumar K, Prashanth MK et al (2017) Adsorption and antimicrobial studies of chemically bonded magnetic graphene oxide-Fe_3O_4 nanocomposite for water purification. J Water Process Eng 17:22–31. https://doi.org/10.1016/j.jwpe.2017.03.001
101. El-Desouky MG, Hassan N, Shahat A et al (2021) Synthesis and characterization of porous magnetite nanosphere iron oxide as a novel adsorbent of anionic dyes removal from aqueous solution. Biointerface Res Appl Chem 11:13377–13401. https://doi.org/10.33263/BRIAC115.1337713401

Dr. Jitendra Kumar Sahoo completed his Ph.D from NIT Rourkela in the field of Nano and Environmental Chemistry. In 2019, he joined as an Assistant Professor in Chemistry at GIET University, Gunupur, Rayagada, Odisha, India. He has established a Nano & Environmental Laboratory at GIET University. He received B.Sc., M.Sc. and Ph.D. degrees in Chemistry. His Ph.D. thesis was on the "Iron Oxide Based Magnetic Nanocomposites: Removal of Inorganic and Organic Water Contaminants and Antimicrobial Properties". He has expertise in the field of wastewater treatment, graphene-based materials, nanomaterials, photocatalysis, adsorption of inorganic and organic contaminates synthesis of novel magnetic nanomaterials, and antibacterial activity. He has got many collaborative works with eminent professors from IIT, NIT and CSIR Laboratory of India and foreign professors as well. He has taught various courses to undergraduate and postgraduate students. He is a frequent speaker at national and international conferences and is an Editorial Board member in the Environmental Protection Research Journal. He has authored many book chapters with Cambridge Press, Stadium Press, Springer and Elsevier. He has a good number of publications to his credit in many peer-reviewed, high-impact journals of international repute. He has received the Young Scientist Award in 2021 for his contribution and honourable achievements in innovative research. He received the Incredible Young Researchers of India Award in 2022 from Record Owner.

Dr. Harekrushna Sahoo is currently serving as a faculty of Chemistry at NIT Rourkela (a premier academic institute in India). Before joining NIT Rourkela, he had his postdoctoral research tenure at multiple places (UMASS-Amherst [USA], TUD Dresden [Germany], and MBC Dresden [Germany]). He completed his PhD in 2007 from Jacobs University Bremen (Germany) in a research group advised by Prof. Werner M. Nau in the field of peptide chemistry and fluorescence spectroscopy. During his postdoc tenure, he was exposed to the field of protein and

membrane along with advanced optical spectroscopic techniques. Currently, he is working in multiple research fields such as protein dynamics, extracellular matrix, nanocomposites, and environmental chemistry. To make his research work wider and more visible, he is collaborating with national and international faculties. To his credit, he has many publications which include research and review articles, book chapters and edited books.

Chapter 3
Iron Oxide-Based Nanozymes and Their Applications

Shraban Kumar Sahoo, Gagan Kumar Panigrahi, Jitendra Kumar Sahoo, Anupama Sahoo, Silpa Subhalaxmi, Dipti Mayee Sahoo, and Priyanka Patel

Abstract In the past ten years, interest in nanozymes, which are nanomaterials with inherent enzyme-like capabilities, has skyrocketed because of their potential to overcome the drawbacks of conventional enzymes, such as their low stability, high cost, and difficult storage. Iron oxide-based nanozymes, among other forms of nanozymes, have magnetic properties (superparamagnetic), are biocompatible, and are stable. Iron oxide-based nanozymes are frequently used for many biomedical applications because of the aforementioned features. The basic concepts of iron oxide-based nanozymes and their biological applications are the main emphasis of this chapter. Also briefly covered are recent findings and the outlook for iron oxide-based nanozymes.

Keywords Iron oxide · Nanozymes · Biomedical applications · Nanotechnology

3.1 Introduction

The manipulation, study, and comprehension of material properties at the nanoscale level are the focus of nanotechnology. One nanometer (nm) is one billionth of a meter (m). Over the past 20 years, interdisciplinary fields inspired by nanotechnology and nanoscience have made contributions to chemistry, physics, material science, and biomedical sciences [1–5]. The Nanotechnology Revolution aided in the creation of an environment that allowed chemists and other specialists in the fields of physics, biology, and engineering to cooperate until they reached a point of

S. K. Sahoo (✉) · G. K. Panigrahi (✉) · A. Sahoo · S. Subhalaxmi · D. M. Sahoo · P. Patel
School of Applied Sciences, Centurion University of Technology and Management, Bhubaneswar, Odisha, India
e-mail: shraban.sahoo@cutm.ac.in

G. K. Panigrahi
e-mail: gagan.panigrahi@cutm.ac.in

J. K. Sahoo
Department of Chemistry, GIET University, Gunupur, Odisha, India

H. Sahoo and J. K. Sahoo (eds.), *Iron Oxide-Based Nanocomposites and Nanoenzymes*, Nanostructure Science and Technology, https://doi.org/10.1007/978-3-031-44599-6_3

collaboration with material and industrial scientists, allowing scientists and specialists in all fields to advance their research quickly [6–8]. Over the last three decades, scientists have focused their research on simulating the functioning and structural features of natural enzymes [9]. The overarching objective was to develop "artificial enzymes" that imitate the fundamental activities of biologically occurring enzymes while also having better features such as cost-effectiveness and stability. Nanozyme research intends to merge features of nanomaterials and take inspiration from biological enzymes to create the artificial enzymes of upcoming generation, which is an emerging topic connecting nanotechnology and biology [9–11].

Biological enzymes are macromolecular catalysts that catalyze natural biochemical processes. Although each enzyme serves a specific job, it has various disadvantages, which limit its use in broad-spectrum applications. To accomplish catalytic tasks, biological enzymes need specified physiological conditions. Some of the key downsides are low strength in extreme environmental conditions of the enzymes and also the large cost of manufacturing, separation, and refinement. As a result, numerous ways have recently been developed as a substitute to natural enzymes, with the production of complexes, molecules, and nanoparticles that mimic their intrinsic catalytic properties [12–14]. Nanozymes are the nanomaterials which are inherited with properties like natural enzyme those have exploded in popularity since the last decade due to the potential to get over the normal enzyme restrictions such as high cost, limited stability, and problematic storage [15]. Nanozymes are the nanoparticles that have the characteristics of an enzyme. Because of the rapid growth and improved knowledge of nanotechnology and nanoscience, nanozymes have the capability to act as direct surrogates for natural enzymes by reproducing and further altering the active centers of biological enzymes. It possesses the same kinetics (e.g., Michaelis–Menten equation) and catalytic mechanism (e.g., ordered, ping-pong, or random reaction) as a natural enzyme. It has inhibitors and activators to control how active it is. The nanozyme's catalytic activity is obtained without the change of any extra natural enzymes or chemical catalysts [16, 17]. The activity of nanozymes is dramatically simulated by typical nanoscale parameters such as shape, size, and surface, which gives a superior technique for modifying its activity. Nanozymes, like normal enzymes, frequently have active centers or electron-transport structures. Nanozyme has enzymatic or catalytic activity due to its active site. Nanozyme has the potential being used like the replacement of the enzyme for human health and surpasses natural enzymes in a variety of areas, including durability, cheap cost, and ease of manufacture. Nanozymes have substantial advantages over biological enzymes, leading to a surge in the development of artificial biocatalysts. These advantages include simple production techniques, smooth surface modification and dependable catalytic performance of nanomaterials [9, 12–14]. In today's nanotechnology, nanozymes are being studied extensively to develop a variety of applications in immunoassays, theranostics, biosensing, disease diagnosis and therapy, oxidative stress protection, cell/tissue development, and pollution removal. Nanozymes have lower specificity and selectivity than biological enzymes, although having more reactivity. This drawback

can be overcome if nanozymes are utilized for catalytic activities involving small molecules (e.g., oxygen radicals), where the steric characteristics of native enzymes is less significant [18–20].

Many metal oxide-based nanomaterials have also been investigated for their ability to replicate the functions of functional enzymes seen in natural defense systems. Metal oxide nanostructures have a lot of charge on their surfaces, which explains why they have such good electron characteristics. Metal oxide-based nanozymes, as a result, show up in the fields of fuel cells, sensing and electrocatalysis. In addition, as potential replacements for natural bioenzymes, they were found to be more stable and resilient under harsh circumstances than natural enzymes. Their uses are additionally broadened by their noteworthy physicochemical qualities (e.g., excellent optical and photothermal exchange abilities and high surface energy), as well as their ease of manufacture and storage [21, 22]. Surprisingly, the physicochemical characteristics and catalytic activities of metal oxide nanoparticles may be tailored without difficulty to meet convenient requirements. Surface modification, for example, has been identified as a possible technique for improving the biocompatibility of these nanozymes. Through proper management of synthetic circumstances, the structural design linked with catalytic efficiency is adaptable. As a result of this ascendency, metal- and metal oxide-related nanozyme research has increasingly expanded beyond the environment to the medicine, food, chemical industry, biomedicine, agriculture, and other industries [12, 19, 21, 22]. Metal oxide nanozymes have long been regarded as potential artificial enzymes because to their high surface energy and surface-to-volume ratio. The most prevalent metal oxide nanozymes, such as Co_3O_4, Mn_3O_4, Fe_3O_4, Mn_2O_3, Fe_2O_3, and CeO_2, have all been shown to exhibit activities like multi-enzymes. They also have a number of unique features, including fluorescence quenching, dielectric, and magnetic properties. Metal oxide-based nanozymes have a cheaper cost and a shorter manufacturing procedure than precious metal nanomaterials [23, 24]. Furthermore, their biopharmaceutical application has expanded due to their less biological toxicity and good accumulation in tissues. Natalio et al. investigated the intrinsic activity of V_2O_5 nanowires like peroxidase enzyme generated by a hydrothermal technique, demonstrating that V_2O_5 nanowires functioned similarly to naturally occurring vanadium haloxidase, that could help to avoid marine biological contamination [25]. CeO_{2-x} nanorods were manufactured by a hydrothermal technique, mimic haloperoxidase enzyme, that is, based on Ce^{4+}/Ce^{3+} redox couples, which was created by Herget et al. [26]. Wang et al. investigated the influence of chloride ions on the suppression and eradication of biofilms by CuO peroxidase using the CuO-Fenton reaction (peroxidase) [27]. Karim et al. discovered that CuO nanorods were manufactured via a solution-based technique that possesses peroxidase activity, and they used visible light as an external "trigger" to modulate the antibacterial activity of the CuO nanorods nanozyme [28]. Iron oxide NPs (IO-NPs), which primarily contain magnetite, i.e., iron(II, III) oxide, Fe_3O_4, and hematite, i.e., iron(III) oxide, Fe_2O_3 NPs, have been the focus of metal oxide research. This is because IO-NPs have the capacity to decrease reactive oxygen species (ROS) [11].

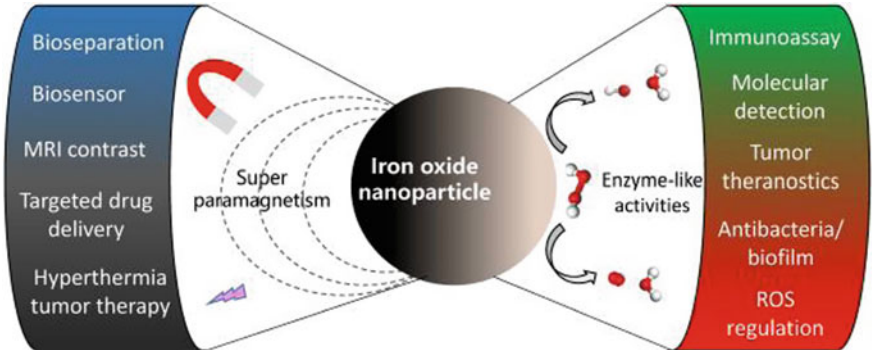

Fig. 3.1 Magnetic properties and enzyme-like activities of iron oxide nanoparticles for various applications [29]

One of the most common nanozymes is iron oxide nanoparticles (IO-NPs). In vivo cell monitoring, magnetic resonance imaging (MRI), hyperthermia, drug or gene delivery, and magnetic targeting are just a few of the biomedical uses for these [29]. The vast range of applications for IO-NPs, including electrochemical applications, data storage, and environmental clean-up, drew a lot of attention. Iron oxide NPs are commonly used in diagnostics (e.g., imaging, detection, or biosensing) due to their inherent magnetic characteristics (superparamagnetic) as well as their biocompatibility and stability. When exposed to an alternating magnetic field, IO-NPs can cause local heat enhancement, which is particularly useful for the reduction of cancer cells, those, unlike healthy cells, cannot survive in the temperature of 42–49 °C [29–31]. To be ready for diagnosis or therapy, cells of interest must be labeled with a rather high number of IO-NPs in each case, raising the issue of toxicity concern. In 2007, ferromagnetic (Fe_3O_4) nanoparticles were revealed to have inherent activity like peroxidase, exhibiting catalytic action comparable to horseradish peroxidase (HRP). Other nanozymes have been investigated using the analytical methods developed for iron oxide nanoenzymes characterization, particularly for kinetics and mechanism experiments to identify catalytic characteristics. Figure 3.1 shows the activities of iron oxide nanomaterials like enzyme with different utilizations.

3.2 Enzymatic Activities of (Iron Oxide Nanozyme) IONzyme

IONzyme is now being used to imitate two enzyme activity from the oxidoreductase family: peroxidase and catalase. While hydrogen peroxide is used by both enzymes as a substrate, only peroxidase produces free radicals that can be used to react with

a hydrogen donor (AH_2), while catalase produces oxygen (Eqs. 3.1 and 3.2). In aerobically respiring species, both peroxidase and catalase are important in avoiding cellular oxidative damage.

$$H_2O_2 + AH_2 \xrightarrow{\text{Peroxidase}} A + 2H_2O \tag{3.1}$$

$$2H_2O_2 \xrightarrow{\text{Catalase}} O_2 + 2H_2O \tag{3.2}$$

(a) **Peroxidase enzyme-like activity**: The first enzyme-like characteristics discovered in IONzyme were the activity like peroxidase enzyme, which catalyzes the standard colorimetric process using chromogenic reagents and hydrogen peroxide (H_2O_2). This characteristic is present in both Fe_3O_4 and Fe_2O_3 nanomaterials; however, the former is generally more active than the latter. Free radicals are produced as an intermediate, by catalyzed reaction of H_2O_2, and those subsequently react with a hydrogen donor (typically chromogenic molecules) to produce H_2O and oxidized donor [17]. The ideal conditions for catalysis of iron oxide nanozyme are the same as HRP, with a temperature range of 37–40 °C and a pH range of 3–6.5 in an acidic buffer. When 3,3′,5,5′-tetramethylbenzidine (TMB) was used as the hydrogen donor, an excessive quantity of H_2O_2 might hold back the colorimetric reaction. The peroxide concentration must be within a certain range for both HRP and iron oxide nanozyme catalysis and to retain activity. O-phenylenediamine (OPD), TMB, 2,2′-azino-bis (3-ethylbenzothiazoline-6-sulfonicacid) (ABTS), and 3,3′-diaminobenzidine (DAB) are just a few of the chromogenic substrates that IONzyme may catalyze. Aside from chromogenic substrates, biomolecules such as polysaccharides, nucleic acids, proteins, and lipids can also be the targets. In biological systems, peroxidases have a variety of important activities, including detoxification of reactive oxygen species (e.g., glutathione peroxidase) and fighting in opposition to infections (e.g., myeloperoxidase). The enzyme peroxidase is frequently utilized in clinical and bioanalytical chemistry, where it is conjugated to an antibody and used to enzymatically catalyze colorimetric substrates for signaling or imaging [10, 21, 22, 29].

(b) **Catalase-like activity**: IONzyme has activity like peroxidase as well as catalase in the decomposition of H_2O_2 into O_2 and H_2O. Under basic and neutral pH (pH 7–10), dimercaptosuccinic acid (DMSA)-coated Fe_3O_4 and Fe_2O_3 nanoparticles converted H_2O_2 to O_2, according to the Gu group. Fe_3O_4 has stronger catalase-like activity than Fe_2O_3, similar to peroxidase-like catalysis. IONzyme has so far been able to conduct the two actions stated above while maintaining correct pH regulation [10, 21, 22, 29].

3.3 Applications of Iron Oxide-Based Nanozyme

3.3.1 Iron-Based Nanozymes for Tumor/Cancer Treatment

Iron-based nanomaterials are some of the most effective nanomedicines. They were originally used in translational research, and the FDA has authorized numerous iron-containing nanoformulations for clinical use. Iron-based nanozymes have often showed a number of therapeutically beneficial features, many of which are particularly significant for tumor treatment [9, 29]. From a physiochemical standpoint, earlier research has shown that after being stored at room temperature, the nanoparticles that are based on iron can be stable for 40 days and also that their catalytic efficacy can be maintained after numerous treatment sessions.

Additionally, iron-based nanozymes have high biocompatibility that helps to the effectiveness and safety of treatment. Furthermore, because of their controlled magnetic characteristics, iron-based nanozymes might be effectively deposited into tumor tissues, increasing the therapeutic index. Furthermore, as compared to natural enzymes, iron-based nanozymes have enhanced resistance to environmental stress for instance acidic or basic conditions and severe temperatures. Additionally, iron-based nanozymes exhibit high morphological uniformity and are simple to manufacture at a low cost. Because of the benefits listed above, iron-based nanozymes have made major contributions to the advancement of nanocatalytic cancer treatment [9–11].

Iron-based nanozymes have the potential to mimic a variety of enzymes in vivo with their varied catalytic activities. This, together with the magnetic receptivity, variable surface chemistry, and superior biocompatibility of nanoparticles based on iron, has led to an increased use of iron-based nanozymes in the detection and treatment of a wide range of tumor indications (Fig. 3.2). Cai et al., for example, revealed the iron core in ferromagnetic H-ferritin nanoparticles has catalytic activity similar to peroxidase and could be employed to stain tumor tissues immunohistochemically. The authors found that xenografted tumor tissues incubated with ferrimagnetic H-ferritin nanoparticles turned brown due to the nanozyme-catalyzed oxidation of 3,3′-diaminobenzidine tetrahydrochloride substrates in the presence of excessive H_2O_2, whereas normal tissues were stained purple by hematoxylin [33]. Meanwhile, catalase-like iron-based nanozymes have been reported to degrade tumor H_2O_2 to create extra oxygen, which might be used to improve ultrasound imaging of the tumor region [34]. In terms of therapeutic applications, current research focuses mostly on the use of iron-based nanozymes as Fenton nanocatalysts or oxygen producers, which will be explored in the section below.

Iron-based nanozymes with catalase-mimicking characteristics have also been investigated for reducing hypoxia-induced resistance to cancer treatment. In a recent work, a hybrid nanosphere containing Fe^{3+} was used to overcome tumor hypoxia by decomposing endogenous H_2O_2. This strategy's viability and prospective therapeutic benefits were proven.

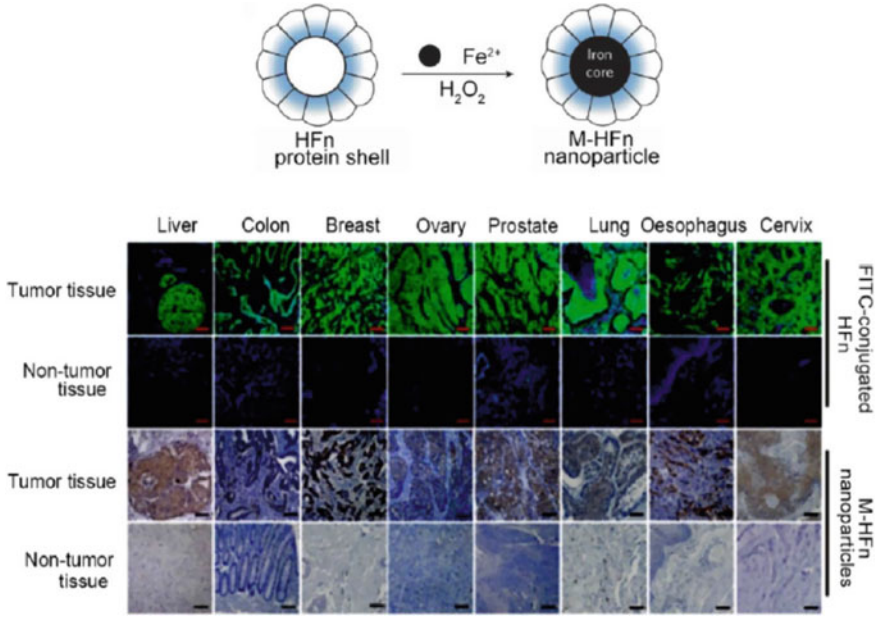

Fig. 3.2 IONzyme activity for tumor using magneto ferritin. Reproduced with permission from the Royal Society of Chemistry [32]

Aside from the iron-based nanozymes' promising antitumor effectiveness, it is also important to look at their possible effects on the recipient host's health in the short and long term. As a result, iron-based nanozymes should be non-toxic to normal tissues, disintegrate in biological settings, and finally be removed from the body when the therapeutic activities are completed. The biocompatibility and biosafety of enzymes and nanozymes are crucial in assuring their continued clinical use. Nonetheless, iron-based nanozymes are a new technology in its early stages of development, and the majority of their interactions with the biological environment are unknown, necessitating ongoing research into their pharmacokinetics, metabolism, absorption, therapeutic sustainability, excretion, distribution, and toxicity at the molecular, cellular, and systemic levels [10, 35].

3.3.2 Cardioprotection

Iron oxide nanoparticles were also examined for their cardioprotective properties. Iron oxide NPs were found to protect hearts in vitro and in vivo against ischemia injury from various studies. Myocardial ischemia can be explained as a lack of blood supply to the heart, which is one of the most common causes of myocardial injury. This causes myocardial hypoxia that can lead to angina pectoris, coronary artery

heart disease, or even a heart attack. There is currently no treatment for myocardial ischemia damage that has been proved to be successful, and current treatment comprises the administration of a variety of pharmacological medications such as free-radical scavengers, antioxidants, calcium channel blockers, and anti-apoptotic agents [14, 19, 21, 23, 25]. Although, one of the most significant difficulties is that pharmacologic medications intend just one method, but myocardial ischemia damage is linked to a number of other pathogenic pathways. The cardioprotective effect of iron oxide NPs was investigated as an alternate strategy. The activity of the iron oxide NPs was compared to that of two pharmaceutical medications often used to treat myocardial ischemia injury: verapamil, a calcium channel blocker, and *Salvia miltiorrhiza* extract, an antioxidant. The researchers used a rat coronary artery ligature model to investigate the cardioprotective effect of 2,3-dimercaptosuccinic acid (DMSA)-modified iron oxide NPs in a variety of tiny sizes [14, 19, 21, 23, 25, 36]. The cardioprotective impact of the iron oxide NPs was greater than that of both *Salvia miltiorrhiza* extract and verapamil, following ischemia reperfusion, as evaluated by left ventricular developed pressure. The cardioprotective effect was shown to be dependent on the size of the iron oxide NPs, but not on their surface charge.

Iron oxide NPs were used to stimulate cardiac mesenchymal stem cells (cardiac MSCs, cMSCs) by Han and colleagues. The MSCs were labeled with superparamagnetic iron oxide NPs by Parivar's team. Superparamagnetic iron oxide NPs are widely employed in MRI for cell tracking and contrast, as well as for cell magnetization in tissue engineering and medication targeting. To produce iron oxide NP-labeled MSCs, polyethylene glycol (PEG)ylated iron oxide NPs were manufactured and applied to the MSCs for 48 h. The iron oxide NP-labeled MSCs were then injected into the heart of a rat model of heart failure. A neodymium magnet was put over the heart for 48 h for the magnet-dependent iron oxide NP-labeled MSCs. In comparison with the unlabeled MSCs and the magnet-independent groups, the magnetic-dependent group had a higher restoration of the injected proportion. Because a larger percentage of iron oxide NPs were kept in the heart, the cardiomyocytes were preserved, and the formation of fibrosis following heart failure was reduced.

3.3.3 Wound Healing

Because of the negative and positive effects of oxygen and H_2O_2 on wound healing, iron oxide NPs that can catalyze H_2O_2 have been investigated for wound-healing applications. It was discovered that incorporating iron oxide NPs into three-dimensional (3D) cellular spheroids stimulated ECM synthesis. It was also feasible to change the composition of iron oxide NP by adjusting its concentration and properties. Magnetic iron oxide NPs (magnetoferritin) boosted the production of all the proteins that make up the ECM, while varying the iron oxide NP concentration had an influence on both collagen IV and elastin formation. Hu and colleagues employed iron oxide NPs in wound dressings manufactured from electrospun poly(vinyl alcohol) (PVA) membranes [37]. Because of its large surface-to-volume ratio as well as

porosity, which allow for significant water absorption and robust oxygen permeability, a polymeric PVA mesh was chosen as the scaffold. By combining spindle-shaped iron oxide NPs with a PVA solution and electrospinning them, they were synthesized and incorporated into the scaffold fibers. The as-prepared fibers were TEM imaged with concentrations of iron oxide NPs that are homogeneously incorporated. The results, as indicated by a colorimetric test and an oxygen-sensitive electrode, suggest that the iron oxide NP-containing PVA fibers had catalytic activity at all concentrations investigated. In the presence of H_2O_2 at harmful amounts, the effect of the iron oxide NPs on the scaffolds was studied in terms of fibroblast proliferation. More than 90% cell survival was observed after incubation with H_2O_2-disclosed nanofibrous dressings containing iron oxide NPs for overnight period, indicating that the catalytic scaffolds provided a superior environment for cell growth. Importantly, cells treated with bare scaffolds showed full apoptosis. The iron pxide NP PVA membranes have potential for wound-healing dressings because of their ability to reduce H_2O_2 concentrations to harmless levels.

3.3.4 Antibacteria and Biofilm Elimination

IONzyme combines with H_2O_2 in the catalytic process to produce free radicals as intermediate products; those are very harmful to bacteria because of targeting proteins, cell membranes, and nucleic acids, causing bacterial dysfunction. H_2O_2 is a typical biocidal chemical that can be used for a variety of cleaning and disinfecting applications, as well as like an antibacterial agent in good hygiene and in medical treatments [9, 14, 18, 38]. The mechanism is also based on the reaction of hydrogen peroxide with cellular constituents, but for resistant bacteria, the effectiveness is generally less. In terms of mechanism of the ping-pong reaction, an iron oxide nanozyme with activity like peroxidase enzyme may aid in the enhancement of antimicrobial properties of H_2O_2. In the previous studies, the enhanced impact was established on methicillin-resistant *Staphylococcus aureus* (MRSA) and *Escherichia coli* (*E. coli*). The antibacterial capability had demonstrated to be effective for wound healing in bacteria-infected wounds, as well as other treatment techniques against multidrug-resistant bacteria [9–11, 14, 18, 29, 38].

Enhancing H_2O_2 catalysis to create radicals also opens up the possibility of eradicating biofilm, a type of bacterium community that aids in the development of drug resistance by preventing antibiotics or other biocides from penetrating the organic matrix used for protection. Through improved oxidative breakdown of biofilm components (oligosaccharides, proteins, and nucleic acids) in the presence of hydrogen peroxide, Fe_3O_4 nanozyme with activity like peroxidase enzyme could amplify the effectiveness of H_2O_2 in breakdown and prevention of biofilm. The Fe_3O_4 nanozyme can break nucleic acids (DNA), proteins, and polysaccharides into minute pieces when combined with H_2O_2. IONzyme or H_2O_2 administered independently, on the other hand, failed to balance the oxidative destruction. The Fe_3O_4 NP-H_2O_2 system's capacity to cleave biomolecules allows it to proficiently break

the matrix of existing biofilm and avoid development of new biofilms, killing both planktonic bacteria and those within the biofilm, resulting in a unique technique for biofilm removal and other uses. This method had previously proved successful in the removal of dental biofilms. In vivo, IONzyme combined with H_2O_2 successfully inhibited the beginning and harshness of tooth caries while protecting normal biological tissues. These findings suggested that nanozymes could be used as a viable alternative treatment for the common biofilm-related disease [9–11, 14, 18, 29, 38].

3.4 Conclusion and Perception

It has been ten years since iron oxide nanoparticles' inherent enzyme-like activity was discovered. As a new generation of enzyme mimics, iron oxide nanozyme's catalytic activity and kinetics have been thoroughly studied to better understand the mechanisms. By attempting to control specific parameters, such as size, dopants, surface modification, morphology, nanostructure, or integration with other nanomaterials, we can then rationally design the appropriate nanozymes for potential implementation. IONzyme is a platform with multifunctionality and adaptability that may be functionalized with additional labels or compounds. It has significantly more stability than conventional enzyme mimetics or natural enzymes. These advantages have made it possible to use iron oxide nanoparticles in a new way that does not rely on magnetism. In clinic and biomedical applications such as cancer imaging, gene transfer, DNA extraction, and cell sorting, magnetic iron oxide materials have long been used. All of these applications make use of the magnetism of these materials. The enzyme-like actions will be useful for pathogen detection and immunoassay, boil removal, cancer detection and therapy, and ROS modulations at various levels for neuroprotection, cell differentiation, and cardioprotection. These nanozymes can also break down influenza virus by inducing lipid peroxidation in the viral envelope. These advantages have made it possible to use iron oxide nanoparticles in a new way that does not rely on magnetism. In clinic and biomedical applications such as cancer imaging, gene transfer, DNA extraction, and cell sorting, magnetic iron oxide materials have long been used. All of these applications make use of the magnetism of these materials. The enzyme-like actions will be useful for pathogen detection and immunoassay, boil removal, cancer detection and therapy, and ROS modulations at various levels for neuroprotection, cell differentiation, and cardioprotection. These nanozymes can also break down influenza virus by inducing lipid peroxidation in the viral envelope. There must be a detailed investigation of the final effect on biological systems that are ROS-sensitive, such as immunological activation, brain development, stem cell proliferation and differentiation, cardiac stress, and cancer growth. Therefore, serious efforts are needed to solve the underlying issues and boost iron oxide nanozyme activity for biological applications in vitro and in vivo.

Acknowledgements All authors appreciatively acknowledge the Centurion University of Technology and Management (CUTM), Odisha, India, for providing research facilities.

References

1. Li Z, Lin Z (2017) Noble metal–metal oxide nanohybrids with tailored nanostructures for efficient solar energy conversion, photocatalysis and environmental remediation. Energy Environ Sci 10:402–434. https://doi.org/10.1039/c6ee02265k
2. Ray C, Pal T (2017) Recent advances of metal–metal oxide nanocomposites and their tailored nanostructures. J Mater Chem A 5:9465–9487. https://doi.org/10.1039/c7ta02116j
3. Korotcenkov G, Cho BK (2017) Metal oxide composites in conductometric gas sensors: achievements and challenges. Sens Actuators B Chem 244:182–210. https://doi.org/10.1016/j.snb.2016.12.117
4. Zhong BL, Hu J, Liang H et al (2006) Self-assembled 3D flowerlike iron oxide nanostructures and their application in water treatment. Adv Mater 18:2426–2431. https://doi.org/10.1002/adma.200600504
5. Song H, Zhang L, He C et al (2011) Graphene sheets decorated with SnO_2 nanoparticles: in situ synthesis and highly efficient materials for cataluminescence gas sensors. J Mater Chem 21:5972–5977. https://doi.org/10.1039/c0jm04331a
6. Ventola CL, Bharali DJ, Mousa SA (2010) The nanomedicine revolution: part 1: emerging concepts. Pharm Ther 128:512–525
7. Roco MC, Bainbridge WS (2005) Societal implications of nanoscience and nanotechnology: maximizing human benefit. J Nanopart Res 7:1–13. https://doi.org/10.1007/s11051-004-2336-5
8. Roco MC (2003) Nanotechnology: convergence with modern biology and medicine. Curr Opin Biotechnol 14:337–346. https://doi.org/10.1016/S0958-1669(03)00068-5
9. Li M, Zhang H, Hou Y et al (2020) State-of-the-art iron-based nanozymes for biocatalytic tumor therapy. Nanoscale Horiz 5:202–217. https://doi.org/10.1039/c9nh00577c
10. Sutrisno L, Hu Y, Hou Y et al (2020) Progress of iron-based nanozymes for antitumor therapy. Front Chem 8:1–9. https://doi.org/10.3389/fchem.2020.00680
11. Shi C, Li Y, Gu N (2020) Iron-based nanozymes in disease diagnosis and treatment. ChemBioChem 21:2722–2732. https://doi.org/10.1002/cbic.202000094
12. Korschelt K, Tahir MN, Tremel W (2018) A step into the future: applications of nanoparticle enzyme mimics. Chemistry 24:9703–9713. https://doi.org/10.1002/chem.201800384
13. Ragg R, Tahir MN, Tremel W (2016) Solids go bio: inorganic nanoparticles as enzyme mimics. Eur J Inorg Chem 2016:1906–1915. https://doi.org/10.1002/ejic.201501237
14. Shang Y, Liu F, Wang Y et al (2020) Enzyme mimic nanomaterials and their biomedical applications. ChemBioChem 21:2408–2418. https://doi.org/10.1002/cbic.202000123
15. Cheng H, Zhang L, He J et al (2016) Integrated nanozymes with nanoscale proximity for in vivo neurochemical monitoring in living brains. Anal Chem 88:5489–5497. https://doi.org/10.1021/acs.analchem.6b00975
16. Jiang B, Duan D, Gao L et al (2018) Standardized assays for determining the catalytic activity and kinetics of peroxidase-like nanozymes. Nat Protoc 13:1506–1520. https://doi.org/10.1038/s41596-018-0001-1
17. Chen Z, Yin J, Zhou Y et al (2012) Dual enzyme-like activities of iron oxide nanoparticles and their implication for diminishing cytotoxicity. ACS Nano 4001–4012
18. Dong H, Fan Y, Zhang W et al (2019) Catalytic mechanisms of nanozymes and their applications in biomedicine. Bioconjug Chem 30:1273–1296. https://doi.org/10.1021/acs.bioconjchem.9b00171
19. Liang M, Yan X (2019) Nanozymes: from new concepts, mechanisms, and standards to applications. Acc Chem Res 52:2190–2200. https://doi.org/10.1021/acs.accounts.9b00140
20. Sun H, Zhou Y, Ren J, Qu X (2018) Kohlenstoff-Nanozyme: Enzymatische Eigenschaften, Katalysemechanismen und Anwendungen. Angew Chem 130:9366–9379. https://doi.org/10.1002/ange.201712469
21. Alizadeh N, Salimi A (2021) Multienzymes activity of metals and metal oxide nanomaterials: applications from biotechnology to medicine and environmental engineering. J Nanobiotechnol 1–31. https://doi.org/10.1186/s12951-021-00771-1

22. Duygu Y, Gökçal B, Büber E et al (2021) A new nanozyme with peroxidase-like activity for simultaneous phosphoprotein isolation and detection based on metal oxide affinity chromatography: monodisperse-porous cerium oxide microspheres. Chem Eng J 403. https://doi.org/10.1016/j.cej.2020.126357
23. Wang X, Guo W, Hu Y et al (2016) Metal oxide-based nanomaterials for nanozymes
24. Liu Q, Zhang A, Wang R et al (2021) A review on metal- and metal oxide-based nanozymes: properties, mechanisms, and applications. Springer Singapore
25. Natalio F, André R, Hartog AF et al (2012) Vanadium pentoxide nanoparticles mimic vanadium haloperoxidases and thwart biofilm formation. Nat Nanotechnol 7:530–535. https://doi.org/10.1038/nnano.2012.91
26. Herget K, Hubach P, Pusch S et al (2017) Haloperoxidase mimicry by CeO_{2-x} nanorods combats biofouling. Adv Mater 29:1–8. https://doi.org/10.1002/adma.201603823
27. Wang L, Hou J, Liu S et al (2019) CuO nanoparticles as haloperoxidase-mimics: chloride-accelerated heterogeneous Cu-Fenton chemistry for H_2O_2 and glucose sensing. Sens Actuators B Chem 287:180–184. https://doi.org/10.1016/j.snb.2019.02.030
28. Karim MN, Singh M, Weerathunge P et al (2018) Visible-light-triggered reactive-oxygen-species-mediated antibacterial activity of peroxidase-mimic CuO nanorods. ACS Appl Nano Mater 1:1694–1704. https://doi.org/10.1021/acsanm.8b00153
29. Gao L, Fan K, Yan X (2017) Iron oxide nanozyme: a multifunctional enzyme mimetic for biomedical applications. Theranostics 7:3207–3227. https://doi.org/10.7150/thno.19738
30. Vallabani NVS, Vinu A, Singh S, Karakoti A (2020) Tuning the ATP-triggered pro-oxidant activity of iron oxide-based nanozyme towards an efficient antibacterial strategy. J Colloid Interface Sci 567:154–164. https://doi.org/10.1016/j.jcis.2020.01.099
31. Mansur AAP, Mansur HS, Carvalho SM (2022) Engineered hybrid nanozyme catalyst cascade based on polysaccharide-enzyme-magnetic iron oxide nanostructures for potential application in cancer therapy. Catal Today 388–389:187–198. https://doi.org/10.1016/j.cattod.2020.06.083
32. Wu L, Qu X (2015) Cancer biomarker detection: recent achievements and challenges. Chem Soc Rev 44:2963–2997. https://doi.org/10.1039/c4cs00370e
33. Cai Y, Cao C, He X et al (2015) Enhanced magnetic resonance imaging and staining of cancer cells using ferrimagnetic H-ferritin nanoparticles with increasing core size. Int J Nanomed 10:2619–2634. https://doi.org/10.2147/IJN.S80025
34. Wang C, Yang J, Dong C, Shi S (2020) Glucose oxidase-related cancer therapies. Adv Ther 3:1–29. https://doi.org/10.1002/adtp.202000110
35. Tibbitt MW, Dahlman JE, Langer R (2016) Emerging frontiers in drug delivery. J Am Chem Soc 138:704–717. https://doi.org/10.1021/jacs.5b09974
36. Lockwood DJ. Nanozymology
37. Hu M, Korschelt K, Daniel P et al (2017) Fibrous nanozyme dressings with catalase-like activity for H_2O_2 reduction to promote wound healing. ACS Appl Mater Interfaces 9:38024–38031. https://doi.org/10.1021/acsami.7b12212
38. Hosta-Rigau L (2019) Engineering and regenerative medicine

Chapter 4
Photocatalytic Degradation of Aqueous Organic Pollutants Using Iron Oxide-Based Photocatalysts

Yagna Prakash Bhoi and Weixin Huang

Abstract Pollution of water bodies arose due to invade of pollutants from various sector of society such as industries, agricultural field and domestic effluent water, etc. Heavy metals, pathogens and recalcitrant organic chemicals are typical examples of deleterious elements that adversely affect the health of aquatic environment. The removal of such pollutants has become an urgent need across the globe, which brings the discovery of various water treatment techniques in order to get clean water. In past few decade, outstanding result has been achieved in the field of water desalination. The application of heterogeneous photocatalysis route for the cleaning of water is reflected as one of the potential and sustainable approach since it makes use of renewable solar light as source of energy. In this chapter, we will discuss the application of iron oxide-based photocatalysts towards the removal of pollutants from aqueous source. Various research approaches progressed to improve the photocatalytic ability of iron oxide will be discussed in detail. The discussion of this chapter particularly focussed on the evolution of composite/heterostructure of iron oxide-based photocatalysts and their photocatalytic applications towards the removal of aqueous pollutants.

Keywords Photocatalysis · Water pollutant · Solar energy · Iron oxide nanocomposite

4.1 Introduction

The water pollution and its impact on the all life on the earth is a global concern. The discharged water from the chemical and agrochemical industries contains substantially huge amount of toxic and carcinogenic organic chemicals such as VOC, pesticides, dyes, etc., which infused into water bodies. This water pollution is one of the

Y. P. Bhoi (✉) · W. Huang
Hefei National Laboratory for Physical Sciences at Microscale, Department of Chemical Physics, University of Science and Technology of China, Jinzhai Road 96, Hefei 230026, P.R. China
e-mail: yagnapbhoi@gmail.com

H. Sahoo and J. K. Sahoo (eds.), *Iron Oxide-Based Nanocomposites and Nanoenzymes*, Nanostructure Science and Technology, https://doi.org/10.1007/978-3-031-44599-6_4

responsible factor for many water-borne diseases and scarcity of portable water. In this perspective, development of low-cost and high efficient water treatment technologies to treat and recycle the wastewater in a sustainable way is prime importance in order to get portable water for our society. Various methodologies were developed in recent past, which includes wet air oxidation, UV photolysis, adsorption and biodegradation methods are available for wastewater treatment [1–3]. The adsorption or coagulation techniques are among the widely used desalination technique in order to remove organic and inorganic pollutants from contaminated water [2]. However, these techniques simply concentrate the pollutants by transferring them to other phases. Sedimentation, filtration, chemical and membrane technologies are some examples of some conventional water treatment techniques, which suffers with the limitations like high operational cost and could produce toxic by-products into the environment. It is highly essential to develop advanced water treatment technology, which can mineralize the organic pollutants completely by a simple and easy experimentation process, less expense of energy and cost. In this perspective, the complete mineralization of organic pollutants by heterogeneous photocatalytic process using solar light as energy source and semiconductor nanoparticles as catalyst is a sustainable strategy to deal.

4.2 Fundamental of Photocatalysis

Photocatalysis is the science, which employed a catalyst and light as energy source to speed up chemical reactions and photocatalyst is a material that is capable of absorbing light, producing electron–hole pairs that enable chemical transformations of the reactants and regenerate after each cycle. When light energy with greater than the band gap energy (E_g) of the photocatalyst falls on the photocatalyst surface, the electron gets excited to the conduction band (CB) leaving a hole in the valance band (VB). The electron hole migrates to the surface of the photocatalyst and participate in reaction with different substrate. On the other hand, some of the electron hole recombines themselves, which leads to the poor photocatalytic activity of the catalyst (Fig. 4.1). The splitting of water by Fujishima and Honda over TiO_2 surface in the presence of light and electricity put the foundation for the semiconductor-based photocatalysis [4]. Until now TiO_2 is the most widely studied photocatalyst with promising field of applications such as environmental cleaning, self-cleaning surfaces, air and water purification, sterilization, hydrogen evolution, and photoelectrochemical conversion of energy, etc. [4]. TiO_2 is a wide band gap photocatalyst with band gap of 3.2 eV. Although, TiO_2 photocatalyst possess advantages such as high oxidation ability, excellent chemical stability, nontoxicity and inexpensive, it suffers limitations like fast recombination of photogenerated electron–hole pair and poor utilization of solar spectrum [4, 5]. Moreover, the solar spectrum comprises only 5–7% of UV light, while 46% and 47% of the solar spectrum has visible light and infrared radiation, respectively [6].

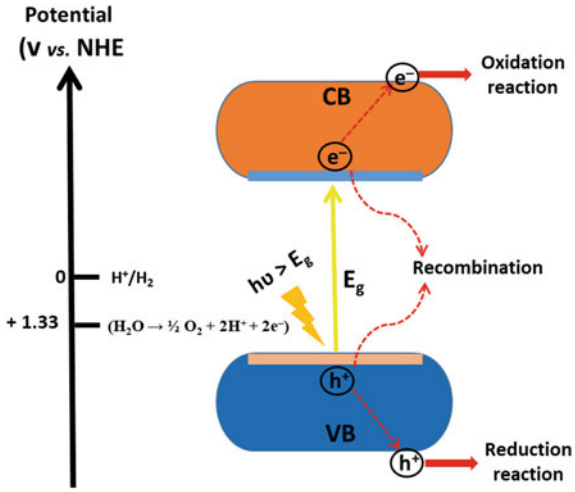

Fig. 4.1 General schematic representation for the working principle of a photocatalyst

In recent past, several research efforts has been put in order to design photocatalyst, which can able to absorb visible light of solar spectrum. MoS_2, CdS, Fe_2O_3, Bi_2WO_6, $Bi_2W_2O_9$, $BiFeO_3$ and bismuth oxyhalides (BiOX, X = Cl, Br, I) are few examples of metal oxide and metal sulphide-based visible light active photocatalyst widely studied for the degradation of a wide range of harmful aqueous organic pollutants into CO_2 and H_2O [7–13]. The pristine photocatalysts suffers with a poor separation of charge carriers, which leads to a poor photocatalytic efficiency of the photocatalysts. With time, noticeable research attempts have been devoted in order to minimize the recombination process of charge carriers and to enhance the light absorption ability of the photocatalyst, by adopting several strategies such as decoration of noble metal nanoparticles over photocatalyst surface, doping, and composite/heterojunction formation by coupling with suitable a semiconductor [14, 15]. Fe_2TiO_5/α-Fe_2O_3/TiO_2, α-NiS/Bi_2O_3, Bi_2S_3/$BiFeO_3$, CuS/$Bi_2O_2CO_3$, Bi_3S_3/β-Bi_2O_3/$ZnIn_3S_4$, CuS/$BiFeO_3$, CuS/$Bi_4Ti_3O_{12}$, Bi_2S_3/$Bi_2W_2O_9$, CuS/$Bi_2W_2O_9$, Bi_2O_3/$CuBi_2O_4$, UiO-66/$CdIn_2S_4$, SnS_2/$Bi_4Ti_3O_{12}$, CdS/BiOBr/$Bi_2O_2CO_3$ and CdS/$Bi_{20}TiO_{32}$/$Bi_4Ti_3O_{12}$ are few examples of recently studied heterojunction photocatalytic systems with improved light absorption and charge carrier separation ability [12, 16–27].

4.3 Iron Oxide-Based Photocatalyst

The iron oxides are composed of Fe and O. Among eight different form of iron oxides, the hematite (α-Fe_2O_3), magnetite (Fe_3O_4) and maghemite (γ-Fe_2O_3) are widely studied oxides due to their unique biochemical, magnetic and catalytic properties. The Fe_2O_3 exists in three of different crystalline structures, such as hematite (α-Fe_2O_3), maghemite (γ-Fe_2O_3) and ε-Fe_2O_3 [6, 28]. The α- and γ-phases are extensively studied materials, while β-Fe_2O_3 phase is less studied material because of

the difficulty in the preparation of single-phase material. Rhombohedral–hexagonal α-Fe_2O_3 is highly stable and has significant potentials in photocatalytic applications, as it is nontoxic, inexpensive, earth abundance, corrosion resistance property with a suitable band gap value ($E_g = 2.0–2.2$ eV) to harvest visible light of the solar spectrum, whereas the maghemite is a metastable phase between hematite and magnetite. It has similar crystal structure as magnetite and chemical composition similar to hematite. In the hematite crystal structure, iron occupies the octahedral sites where oxygen is hexagonally close packed. On the other hand in both maghemite and magnetite, iron present in both octahedral and tetrahedral sites and oxygen cubically close packed. The ε-Fe_2O_3 is a transition phase between hematite and maghemite, which attract research attention owing to its unique magnetic properties. Seeing the extensively used of both hematite and maghemite form of Fe_2O_3 than the other polymorphs, this study is focussed on their utilizations in the field of heterogeneous photocatalysis towards the degradation of various persistent organic contaminants from aqueous medium.

Song and co-worker prepare α-Fe_2O_3 nanodisks by the assembly of single-crystalline nanoplates with layered structures by using a silicate-anion-assisted hydrothermal method. The silicate anions believe to adsorb selectively onto the {0001} plane of α-Fe_2O_3 nanoplates and induce the self-assembly of the plates to give the layered nanodisks structure. The α-Fe_2O_3 nanodisks display enhanced visible light absorption with excellent photocatalytic activity for the degradation of methylene blue under visible light irradiation [29]. Heidari and co-worker reported the synthesis of porous network-like α-Fe_2O_3 and α/γ-Fe_2O_3 nanoparticles by a simple solution combustion method and evaluated the photocatalytic activity towards the degradation of methylene blue (MB) dye under. The Fe_2O_3 materials calcined at 700 and 800 °C contains diffraction peaks for only α-Fe_2O_3, where Fe_2O_3 material obtains after a calcination at 450 °C, which contains both the α and γ-Fe_2O_3 for of Fe_2O_3. The higher photocatalytic efficiency of the α/γ-Fe_2O_3 heterophase material may be account for the formation of junction between α-Fe_2O_3 and γ-Fe_2O_3 phases, which reduced the recombination of photogenerated electrons, and holes [30]. Jing and co-workers studied the photocatalytic activity of pure α-Fe_2O_3 as well as phosphate-modified α-Fe_2O_3. They have employed the simple one-pot water-organic two-phase separated hydrolysis-solvothermal (HST) method for the preparation of α-Fe_2O_3 nanoparticles. The phosphate-modified α-Fe_2O_3 exhibits high visible photocatalytic activity for the degradation of liquid-phase phenol and gas-phase acetaldehyde. After surface modification with phosphate, the surface –Fe–OH substituted with –Fe–O–P–OH groups, which significantly promote O_2 adsorption over the catalyst surface. The enhanced photocatalytic activity is due to the enhancement in charge carriers separation ability after the modification with phosphate groups [31]. By using electron beam evaporation through a normal thin film deposition and oblique angle deposition (OAD), Fe_2O_3 thin films and nanorod arrays fabricated by Larsen and co-workers [32]. The growth of the materials aligns towards the (110) direction. Under visible light, the Fe_2O_3 thin film samples shows more photocatalytic efficiency towards the degradation of methylene blue dye. Whereas the Fe_2O_3 nanorod inactivate more efficiently to the *Escherichia coli* O157:H7 bacteria as compared to

the Fe_2O_3 thin films. Bahnemann and co-workers demonstrated the generation of H_2O_2 species during the photocatalytic oxidations of organic compounds by using α-Fe_2O_3 photocatalyst. In a comparison study, the ZnO and TiO_2 photocatalysts found to be more active in the generation of H_2O_2 and in the degradation of chlorinated hydrocarbon molecules as compared to the α-Fe_2O_3 photocatalyst [33]. Hameed and co-workers successfully fabricated the α-Fe_2O_3 and γ-Fe_2O_3 polymorphs by using a simple surfactant (Triton X) aided hydrogel synthetic route. The photocatalytic properties of both the form of Fe_2O_3 were studied for the mineralization of 2-chlorophenol and 2-nitrophenol pollutants under the visible light as well as under natural sunlight illumination. Both the polymorphs showed a considerably high activity for the degradation of the phenolic compounds under solar light as compared to visible light irradiation. A significant improvement in the photocatalytic activity under visible light was noticed when the polymorphs were pre-exposed to sunlight preceding to the photocatalytic tests. The higher photocatalytic activity of the exposed polymorphs as compared to the unexposed one is due to the introduction of defects sites which traps the excited electrons during the photocatalysis mechanism [34]. Wang and co-workers fabricated a dodecahedral α-Fe_2O_3 nanoparticle with 6 (012) and (104) exposed facets, respectively. The coexistence of these different facets account for a better photocatalytic ability in comparison with the crystals having single exposed facet. They have also demonstrated that the separation of charge carriers between anisotropic facets also has a significant contribution on photocatalytic degradation of Rhodamine B and methylene blue organic dyes [35]. Ramakrishna and co-workers prepared pure α-Fe_2O_3 with nanobraids and nanoporous like structures using an electrospinning synthesis method followed by annealing at 500 °C for 5 h. Both of the nanobraids and nanoporous display excellent photocatalytic degradation activity for Congo red dye with 91.2% and 90.2% degradation, respectively after 140 min of irradiation under visible light. They have demonstrated the significant role of porous surface and small particle size of the α-Fe_2O_3 towards the excellent photocatalytic activity. The superoxide radicals ($O_2^{\cdot -}$), H^+ ion, hydroperoxyl radicals ($^{\cdot}HO_2$), hydroxyl radicals are generated by the reaction of water and oxygen on the photogenerated hole and electron are responsible for the degradation of Congo red dye over the photocatalyst surface [36]. Zheng and co-workers successfully fabricated dendritic α-Fe_2O_3 nanostructures with controlled dimension and morphology by a facile solvothermal synthesis method in the presence of 1-N-butyl-3-methylimidazolium benzoate ([Bmim][PhCOO]) ionic liquid. A change in the molar ratio of [Bmim][PhCOO] to $K_3[Fe(CN)_6]$ from 0:1 to 2:1, and 5:1 can bring the dendrite structure to hexagonal nanoplates and rods. The ionic liquid plays a crucial role in deciding the formation of α-Fe_2O_3 with different morphologies. The α-Fe_2O_3 with rod morphology exhibit superior photocatalytic activity towards visible light-induced degradation of Rhodamine B (RhB) dye as compared to the dendrites and plates structured α-Fe_2O_3 materials. The degree of crystallinity and exposed crystal facets of α-Fe_2O_3 materials accounts for improving the photocatalytic activity [37].

Song and co-workers recently fabricated a snowflake-like α-Fe_2O_3 materials by using a simple single-step hydrothermal approach and studied there photocatalytic activity towards the degradation of a wide variety of organic pollutants such as crystal violet, Rhodamine 6G, methyl orange, etc. The α-Fe_2O_3 snowflakes exhibit a superior photocatalytic activity towards degrading cationic organic dyes (crystal violet, Rhodamine 6G) than for the anionic dye (methyl orange) degradation [38]. Shim and co-workers synthesized porous natured Fe_2O_3 nanorod by a two-step process. First ferrous oxalate dihydrate ($FeC_2O_4{\cdot}2H_2O$) precursor synthesized by a chemical solution processes and second the ferrous oxalate dehydrate on annealing in air at 500 °C for 2 h to get the porous Fe_2O_3 nanorod. The ferrous oxalate dihydrate nanorods precursor has the length 3–9 μm and diameter of between 110 and 150 nm. After thermal annealing, the nanorods structured remain intact in the Fe_2O_3 materials. The Fe_2O_3 nanorod exhibited excellent photocatalytic degradation ability for a wide range of organic pollutants such as RhB, methylene blue (MB), p-nitrophenol (pNP), eosin B and methyl orange (MO), respectively. The porous structures believe to provide more active reaction sites and also facilitates the efficient separation of photogenerated electrons and holes which is accountable for the excellent photocatalytic efficiency of the prepared porous Fe_2O_3 nanorods [39]. Zhou and co-workers has prepared γ-Fe_2O_3 nanoparticles with spherical morphology by using an oxidizing environment via a solution synthesis method by changing the pH and reaction temperature. The spherical nanoparticles has a particle size around 17–55 nm and a BET surface area of 14.357 m^2/g. The pH of the reaction media crucially influence the particle size of the nanomaterials. With increase in the pH value from 6 to 12, the particle size also increases. The as-synthesized γ-Fe_2O_3 nanoparticles show potential photocatalytic activity towards the degradation of Orange I dye under UV and visible light illumination. The γ-Fe_2O_3 nanoparticles prepared at pH 6 at a reaction temperature 60 °C with smallest particle size show highest photocatalytic efficiency than other synthesized γ-Fe_2O_3 nanoparticles [40]. Fardood and co-workers synthesized hematite (α-Fe_2O_3) nanoparticles by a simple, environment-friendly and less-expensive sol–gel synthesis method in the presence of a bio template (Arabic gum). The average particle size of the prepared materials is 45–50 nm. The α-Fe_2O_3 materials evaluated as a potential photocatalyst with a photocatalytic activity of 90% degradation of Congo red dye after a 90 min of irradiation time [41]. Wang and co-workers fabricated hollow microspherical α-Fe_2O_3 nanostructure material by ionic liquid-assisted solvothermal method followed by calcination at 250 °C for 6 h. The α-Fe_2O_3 have a specific surface area up to 220 m^2/g. The α-Fe_2O_3 microspheres show excellent photocatalytic activity towards the degradation of Rhodamine B dye. The as-synthesized α-Fe_2O_3 microspheres exhibit a photocatalytic activity 2–3 times higher than the α-Fe_2O_3 nanoparticles. The higher specific surface area, porous nature and hollow nanostructure play crucial role in the enhanced photocatalytic activity of the α-Fe_2O_3 microspheres [42]. Zhu and co-workers prepared hierarchical α-Fe_2O_3 hollow microspheres using a surfactant-free solvothermal synthesis method and post-thermal treatment at 450 °C for 2 h. The prepared photocatalyst evaluated as a potential catalyst for the degradation of salicylic acid under UV light irradiation [43]. Wang and co-workers fabricated α-Fe_2O_3 nanospheres/microsphere by using

a surfactant and template-free two-step synthesis procedure, hydrothermal treatment followed by a thermal decomposition. The α-Fe_2O_3 nanospheres/microsphere composed of interlinked elongated nanoparticle and nanospheres/microsphere has a diameter around 5 μm, and the elongated particle size is below 30 nm. The α-Fe_2O_3 nanospheres/microsphere is mesoporous in nature, with a pore size distribution between 2 and 50 nm with specific surface area of 20 m^2/g. The photocatalytic activity of the as-synthesized α-Fe_2O_3 nanospheres/microsphere evaluated for the degradation of Rhodamine 6G dye under visible light illumination. The α-Fe_2O_3 nanospheres/microsphere exhibit a photocatalytic efficiency 2 times that of nanosized α-Fe_2O_3 particles and around 12 times higher than the micron-sized particles. The higher photocatalytic activity of the α-Fe_2O_3 nanospheres/microsphere was due to combined contribution of the high specific surface area and the porous architecture [44]. Wang and co-workers develop a facile solvothermal route to prepare 3D porous flower-like α-Fe_2O_3 nanomaterial with hierarchical architecture without using any structural templates. Two-dimensional α-Fe_2O_3 nanopetals organize themselves in a hierarchical fashion in order to give the 3D porous flower-like structure. The depth morphological analysis reveals that the nanopetals has a thickness between 20 and 50 nm and width of 300–500 nm; moreover, these nanopetals composed of nanobricks with 100 nm in length and 30 nm in diameter. The 3D α-Fe_2O_3 materials has high specific surface area (∼ 52.51 m^2/g) with the presence of numerous mesopores and macropores that facilitate the efficient transportation of the substrate during the catalytic reaction. The photocatalytic activity of the 3D α-Fe_2O_3 nanomaterial explored by the mineralization of Rhodamine B dye under UV light irradiation [45]. Geng and co-workers prepared α-Fe_2O_3 with flue-like 3D porous nanoarchitectures by using a Ni^{2+}/surfactant-assisted solvothermal method at 200 °C for 24 h. The α-Fe_2O_3 material has a specific surface area of 88.82 m^2/g with potential photocatalytic activity towards the degradation of methylene blue dye under visible light. They have closely demonstrated the influence of the Fe^{3+} and Ni^{2+} ion ratio on the morphology of the α-Fe_2O_3 materials. At a molar ratio of Fe^{3+} to Ni^{2+} ion at 1:2 in the solution gives rise to a micro-balls constituted of fine α-Fe_2O_3 nanorods, while at molar ratio of 1:3 gives the 3D flue-like structure and the micro-balls structure again regain on further changing in the molar ratio to 1:4. The 3D flue-like α-Fe_2O_3 shows highest photocatalytic ability for the degradation of methylene blue dye as compared α-Fe_2O_3 nanoparticles and P25 photocatalyst under visible light illumination [46]. The pristine Fe_2O_3 photocatalyst has some limitations such as rapid recombination of photogenerated electron–hole pair and poor response to solar spectrum, which result in poor photocatalytic performances. Within short span of time, a lot of research effort have been devoted to prepare novel hybrid materials such as modification with noble metal, doping and formation of binary and ternary composite/heterojunction material. These strategies believe to suppress the recombination process of charge carriers and enhance the light photocatalytic efficiency as a whole. In the subsequent text, we will discussed the hybrid, doped and noble metal-modified Fe_2O_3 photocatalyst and their photocatalytic applications.

Generally, doping of foreign elements (metal or non-metal) significantly alter the physical parameters, chemical reactivity and redox behaviour of the host material. The doping with non-metal such as nitrogen and sulphur widely studied. The main purpose of non-metal doping in Fe_2O_3, TiO_2 or with metal oxide photocatalysts is to alter the band gap value by mixing the oxygen 2p orbital with that of non-metal. The doping of non-metals believe to creating a trap state (separate band) in between the valence band and conduction band which controls the electron–hole recombination and delay the recombination process so that the photogenerated electron–hole pair could be available for the redox reaction. Parida and co-workers prepare α-Fe_2O_3 material co-doped with S and N by using co-precipitation method. They have used thiourea both as precipitating agent and as the sulphur and nitrogen source. The S and S–N co-doping induced growth along the (104) plane, whereas the N doping induced along the (110) crystal plane. After S and N doping, the specific surface area increases significantly than the un-doped pristine α-Fe_2O_3; on the other hand, the highest surface area has been noticed for the S–N co-doped sample (57.85 m^2/g). This observation indicates the significant contribution of minute amount of sulphate ion in the samples. The doped sample shows improved visible light response than the pure α-Fe_2O_3 sample. The photocatalytic activity of the un-doped and doped sample was evaluated for the degradation of Rhodamine B dye under natural sunlight. A maximum degradation efficiency of 95% was obtained after a reaction time of 4 h [47]. Almazroai and co-workers prepared S-doped α-Fe_2O_3 nanomaterial by microwave irradiation (300 W for 20 min) using thiourea as sulphur precursor. The crystallinity of the α-Fe_2O_3 nanomaterial has found to decrease after S doping on the α-Fe_2O_3 lattice. After the sulphur-doping enhancement in the visible light absorption, intensity was noticed with a small decrease in the band gap value. This enhancement in the absorbance intensity of the doped photocatalyst can be attributed to the charge transition between the p-orbitals of the S atom and the conduction band (CB) of the α-Fe_2O_3 nanomaterial. The S-doped α-Fe_2O_3 nanomaterial display improved photocatalytic degradation efficiency than the pristine α-Fe_2O_3 nanomaterial [48]. Suganthi and co-workers fabricated metal (M = Cu, Ni and Co)-doped iron oxide (α-Fe_2O_3) nanoparticle by chemical precipitation followed by calcination. The specific surface area and mesoporosity of the Fe_2O_3 increases after doping with metal was observed. The metal-doped α-Fe_2O_3 exhibits higher photocatalytic activity than the pristine α-Fe_2O_3 nanomaterial towards the degradation of Acid Red-27 organic dye under visible light illumination. Among the metal-doped α-Fe_2O_3 materials, the Cu-doped α-Fe_2O_3 exhibits highest photocatalytic activity [49]. Gao and co-workers prepared multiple metal-doped Fe_3O_4@Fe_2O_3 nanoparticles from Waelz slag, an iron containing hazardous waste. They have employed acidolysis, sol–gel and calcination in order to prepare the multiple metal (Al, Zn, Cu and Mn)-doped Fe_3O_4@Fe_2O_3 nanoparticles from the waste slog. The photocatalytic activities of the synthesized multiple-metal-doped Fe_3O_4@Fe_2O_3 nanoparticles as well as the pristine Fe_2O_3 nanoparticles were compared for the photocatalytic degradation of methyl orange dye under UV and simulated sun light irradiation. It was observed that all of the doped Fe_3O_4@Fe_2O_3 nanoparticles shows improved photocatalytic activities as compared

to the pristine Fe_2O_3 [50]. So far, TiO_2 and ZnO are widely studied UV-active photocatalyst. However, there UV light response and poor separation of charge carriers limits their practical utility. Hence, a lot of research effort has been made in recent past in order to make heterojunction and composite by combining with different suitable visible light active semiconductor photocatalyst. α-Fe_2O_3 is a narrow band gap visible light active photocatalyst and its suitable band alignment makes α-Fe_2O_3 an ideal candidate to combine with other wide band gap semiconductor with improved light absorption and charge carrier separation ability. In the subsequent text, we will discuss the research progress in the preparation of composite/heterojunction of α-Fe_2O_3 with various semiconducting photocatalytic materials.

Omri and co-workers recently fabricated α-Fe_2O_3/TiO_2 nanocomposite material containing 10 and 50 mol% of TiO_2 by using a simple precipitation method. The α-Fe_2O_3/TiO_2 nanocomposite materials were characterized using various analytical instruments and studied as photocatalyst to degrade methylene blue dye (MB) under visible light. A maximum of 92% of MB dye degradation was recorded after 120 min of irradiation by using α-Fe_2O_3/TiO_2 composite material 50 mol% of TiO_2, whereas the pure α-Fe_2O_3 and TiO_2 exhibited relatively lower photocatalytic efficiency than the composite materials. Under the visible light, the TiO_2 material is unable to generate electron–hole pair, whereas the α-Fe_2O_3 material produce electron–hole pair. After material contact, the excited electron from the conduction band (CB) of α-Fe_2O_3 migrate to the CB of TiO_2, whereas the hole accumulate in the valance band (VB). This process minimize the recombination process of photogenerated electron–hole pair. The improved visible light absorption and charge carrier separation properties are account for the higher photocatalytic activity of the α-Fe_2O_3/TiO_2 nanocomposite material [51]. Qu and co-workers prepared α-Fe_2O_3/TiO_2 dendritic heterostructure nanomaterials in a two-step processes, first TiO_2 nanofiber prepared by electrospinning method and in second step the α-Fe_2O_3 nanomaterial deposited over the TiO_2 nanofiber by hydrothermal method. Four different sets of α-Fe_2O_3/TiO_2 dendritic heterostructure materials were prepared containing different amount of α-Fe_2O_3. From morphology, it is clearly seen that the heterostructure are comprises of TiO_2 nanofiber (diameter 70 nm) and α-Fe_2O_3 nanorods (length 100–200 nm and diameter ~ 30 nm), and the TiO_2 nanofibers are homogeneously covered by the α-Fe_2O_3 nanorods giving a typical branched and dendritic heterostructure configuration. The heterostructure materials exhibit enhanced visible light absorption feature. The photocatalytic activity of the α-Fe_2O_3/TiO_2 dendritic heterostructure nanomaterials demonstrated towards the degradation of a wide range of organic dye pollutants such as Congo red (CR), methylene blue (MB), methyl orange (MO) and eosin red (ER). All the heterostructure materials show enhanced degradation efficiency than the parent TiO_2 and commercial α-Fe_2O_3 materials. The enhanced photocatalytic activity of the heterostructured material is due to improved visible light response, charge carrier separation and efficient generation of hydroxyl radical [52]. Fu and co-workers fabricated magnetic γ-Fe_2O_3 nanosheets/mesoporous black TiO_2 hollow spherical heterojunctions material by employing a metal-ion intervened hydrothermal process followed by high-temperature hydrogenation technique. The hybrid γ-Fe_2O_3/b-TiO_2 hollow structure material have high specific surface area of $\sim 63\ m^2/g$ and a pore size

of 10.5 nm. The resulting hybrid material contains oxygen vacancies which influence the recombination process of electron–hole pairs and extend the lifetime of the charge carriers, by this means improving the photocatalytic performance of the photocatalyst. The photocatalytic activity of the hybrid γ-Fe_2O_3/b-TiO_2 heterojunctions material has been studied by degrading tetracycline pollutant. The hybrid γ-Fe_2O_3/b-TiO_2 display the photocatalytic degradation efficiency about three times greater than that of the pristine photocatalyst. The high photocatalytic property of hybrid γ-Fe_2O_3/b-TiO_2 heterojunctions is account to the narrow bandgap nature which extending the photo response from visible light to near infrared regions and the efficient separation and trapping of charge carrier due to generation of vacancies [53]. Jeevanandam and co-workers have synthesized TiO_2@α-Fe_2O_3 core–shell nanoheterostructured material by using a simple thermal decomposition technique. Microscopic studies confirm the deposition of the uniform α-Fe_2O_3 shell on the surface of TiO_2 spheres. The photocatalytic application of the TiO_2@α-Fe_2O_3 core–shell nanoheterostructured material was explored towards the degradation of RhB dye under sunlight illumination. The nanoheterostructured material displays enhanced photocatalytic ability than the pristine TiO_2 and α-Fe_2O_3 materials. This enhanced photocatalytic activity of the heterostructured material can be ascribed to the facile transfer of electrons from TiO_2 and α-Fe_2O_3 phase, which reduce the recombination processes of electron–hole pair over the photocatalyst surface [54].

The zinc oxide (ZnO) is an n-type wide band gap semiconductor, low price and non-toxic nature and a very good photocatalyst photocatalysis. Zhang and co-workers fabricate of magnetic 3D γ-Fe_2O_3@ZnO core–shell nanomaterial by using hydrothermal sintering followed by atomic layer deposition (ALD) method. ZnO shell layer was uniformly deposited on the γ-Fe_2O_3 core. The band alignment of the γ-Fe_2O_3 and ZnO photocatalyst are so aligned in a manner to give the characteristic feature of a type-II heterojunction photocatalyst. The photocatalytic activity of the synthesized core–shell nanomaterial was evaluated for ciprofloxacin degradation under simulated sun light illumination. The hydroxyl radical and the hole contribute significantly on the degradation of ciprofloxacin is noticed. The γ-Fe_2O_3@ZnO core–shell nanomaterial displays enhanced photocatalytic efficiency than the pristine γ-Fe_2O_3 and ZnO counterpart. The improved photocatalytic activity of the heterostructured material is due to the formation of type-II heterojunction and the core–shell structure, which facilitate the efficient migration and separation of the charge carrier [55]. Carmalt and co-workers fabricate α-Fe_2O_3/ZnO heterojunction films by using aerosol-assisted chemical vapour deposition technique. The band alignment and electron migration gives a characteristic feature of a type-I heterojunction system. The prepared α-Fe_2O_3/ZnO heterojunction films exhibit remarkably improved photocatalytic efficiency towards the degradation of stearic acid under UVA light, which is 16 times higher than that of the α-Fe_2O_3 and 2.5 times than that of the ZnO photocatalysts. Upon irradiation photogenerated electrons migrate from the CB of ZnO layer to the α-Fe_2O_3 layer that increase the life time of the electron which is responsible for the enhanced photocatalytic property of the α-Fe_2O_3/ZnO heterojunction films [56]. Mohapatra and co-workers fabricated a ternary α-Fe_2O_3/$ZnFe_2O_4$/

ZnO nanohybrid material by using a microwave-assisted co-precipitation and co-precipitation and thermal annealing synthesis technique. The co-precipitation method gives raise to nanoparticle where microwave-assisted synthesis gives nanodisks like morphology of the ternary photocatalyst. The ternary α-Fe_2O_3/$ZnFe_2O_4$/ZnO photocatalyst materials were examined as photocatalyst towards the degradation of methylene blue and malachite green dyes under solar light. The material prepared by using microwave-assisted synthesis shows highest photocatalytic activity than the material obtained by co-precipitation method. A maximum of 93.2% of MB degradation noticed after 32 min of irradiation using the α-Fe_2O_3/$ZnFe_2O_4$/ZnO nanodisks. The hydroxyl radical plays a crucial role in the degradation of the organic dyes which was confirmed from the radical scavenger experiment. They have proposed a cascade movement of electron across the CB band of the three component of the ternary photocatalyst, which efficiently reduce the recombination rate of the photogenerated charge carriers. This property may accountable for the improved photocatalytic activity of the synthesized ternary photocatalytic material [57]. Hota and co-workers have fabricated Fe_2O_3/$ZnFe_2O_4$, $ZnFe_2O_4$/ZnO and Fe_2O_3/$ZnFe_2O_4$/ZnO binary and ternary composite photocatalyst systems by using a simple hydrothermal method followed by calcination at 500 °C. All the synthesized nanocomposite materials display improved visible response as compared to the Fe_2O_3 material. The Fe_2O_3/$ZnFe_2O_4$/ZnO ternary composite material has the highest specific surface area of 49.464 m^2/g, which is much higher than that of the pure Fe_2O_3 and the binary composite material. The photocatalytic activity of the synthesized composite materials was evaluated for the degradation of malachite green (MG) dye under natural sunlight. A maximum of 96.92% of degradation of MG dye was achieved after 90 min of irradiation using the Fe_2O_3/$ZnFe_2O_4$/ZnO ternary composite material. They have proposed a cascade migration of electron across the CB of the different component of the ternary photocatalyst, which significantly reduce the recombination process of charge carriers [58].

Graphic carbon nitride (g-C_3N_4) has been emerged as a potential visible light active photocatalyst with a band gap of 2.7 eV due to high chemical stability, suitable band alignment, natural abundance and easy synthesis. However, low specific surface area, moderate band gap value and poor separation of photogenerated charge carriers limits its practical applications. So many research approaches have been made in recent past in order to prepare composite and heterojunction with Fe_2O_3, which has a suitable band alignment to prepare hybrid material with improved visible light response and charge carrier separation properties. Lu and co-workers has recently fabricated a series of α-Fe_2O_3/g-C_3N_4 hybrid materials and studied their photocatalytic activity towards tetracycline degradation under visible light. The α-Fe_2O_3/g-C_3N_4 hybrid materials were prepared by the calcination of Fe-based metal organic framework (Fe-MOF) and melamine. They have demonstrated the uniform distribution of α-Fe_2O_3 nanoparticles (3–5 nm) over the porous g-C_3N_4 nanosheet. The existence of close microscopic contact between these two phases further confirmed

from the TEM analysis. The α-Fe_2O_3/g-C_3N_4 hybrid material displays higher photocatalytic activity than the bulk g-C_3N_4 photocatalyst. The band alignment of both the component of the hybrid α-Fe_2O_3/g-C_3N_4 material are aligned in a type-II fashion, and this is responsible for the enhanced charge carrier separation and photocurrent density. The improved visible light absorption, greater specific surface area and efficient charge carrier separation property of the α-Fe_2O_3/g-C_3N_4 hybrid material are responsible for the enhanced photocatalytic activity [59]. Prakasam and co-workers prepared g-C_3N_4/α-Fe_2O_3 hybrid nanocomposites material by changing the mass ratio of both the components by using a simple one-step hydrothermal method. The photocatalytic activity of the hybrid material evaluated by degrading Congo red (CR) and malachite green (MG) dye under visible light. The FESEM study of g-C_3N_4/α-Fe_2O_3 composite material clearly indicates the incorporation of α-Fe_2O_3 nanoparticles over the g-C_3N_4 nanosheet. The absorption edge of both the pristine g-C_3N_4 and α-Fe_2O_3 materials commence around 455 and 460 nm, respectively. A considerable red shift in the absorption edge was observed for the hybrid material indicating the better visible light absorption and decrease in the band gap value of the photocatalyst. The hybrid material exhibits 87 and 95% of CR and MG dyes degradation after 100 min of irradiation time, which is around 2 times higher than that of the pristine g-C_3N_4 photocatalyst. The type-II nature of the electron–hole migration in the heterojunction is responsible for the higher photocatalytic activity of the hybrid photocatalyst [60]. Li and co-workers prepared a cocoon-shaped magnetic Fe_2O_3/g-C_3N_4 nanocomposite material by two-step hydrothermal synthesis. The cocoon-shaped Fe_2O_3 dispersed uniformly over the porous and layered g-C_3N_4 surface. The Fe_2O_3/g-C_3N_4 composite photocatalyst exhibits better photocatalytic efficiency for the degradation of Rhodamine B dye than the pristine Fe_2O_3 and g-C_3N_4 counterpart [61]. Li and co-workers prepared a Z-scheme g-C_3N_4/α-Fe_2O_3 heterojunction photocatalytic system with enhanced charge carrier separation and photocatalytic activity. They have demonstrated the establishment of the Fe–O–C bond in the heterojunction system, which believe to induce facile migration of electron across the grain boundary. The improved visible light response and facile migration of electron makes the heterojunction photocatalyst a better one than the pristine counterpart towards visible light-induced degradation of methylene blue dye [62]. Due to narrow band gap nature and suitable band alignment of the Fe_2O_3 semiconducting nanoparticle, it is not only involve in making hybrid photocatalyst with TiO_2, ZnO and g-C_3N_4 but also a lot of new Fe_2O_3-based hybrid materials with improved photocatalytic activity that has been evolved with time. The Fe_2O_3-based hybrid materials, their synthesis method, photocatalytic application and their photocatalytic efficiency is presented in Table 4.1.

Table 4.1 Photocatalytic applications of different Fe_2O_3-based photocatalyst

Materials	Methods	Photocatalytic application	Photocatalytic performance	References
TiO_2/Fe_2O_3/CNTs	Sol–gel and calcination	Tetracycline degradation	89.41% in 90 min	[63]
$SiO_2/TiO_2/Fe_2O_3$	Mechanochemical	Methylene blue degradation	97% in 22 h	[64]
$Ag_3PO_4–TiO_2–Fe_2O_3$	Solid state blending	Orange II	86.71% in 30 min	[65]
Fe_2O_3/g-C_3N_4@N-TiO_2	Electrochemical anodization, calcination	Bisphenol-A degradation	100% in 80 min	[66]
Fe_2O_3 @SiO_2 @TiO_2	Solvothermal, layer-by-layer assembly	Phenol degradation	100% in 1 h	[67]
α-Fe_2O_3@TiO_2 core–shell	Hydrothermal synthesis	Acid orange 7 degradation	98.6% in 90 min	[68]
$Fe_2O_3–TiO_2$	Template-assisted dipping/ adsorbing-calcining strategy	Methyl blue degradation	95% in 25 min	[69]
g-C_3N_4/γ-Fe_2O_3/TiO_2	Sol–gel	Cefixime trihydrate degradation	98.09% in 90 min	[70]
α-Fe_2O_3@TiO_2 core–shell	Hetero-epitaxial growth	Rhodamine B degradation	60% in 5 h	[71]
Fe_2O_3 @TiO_2@nanometal (Au, Ag)	Sol–gel	Methylene blue degradation	92% in 2 h	[72]
$TiO_2/Au/Fe_2O_3$	Metal-organic framework (MOF) route	2,4 dichlorophenol	94% in 90 min	[73]
TiO_2 and γ-Fe_2O_3@GO/PANI-NT	Co-precipitation, hydrolysis-calcination	Rhodamine B degradation	94% in 140 min	[74]
Carbon/TiO_2/Fe_2O_3	Hydrolysis and hydrothermal procedures	Methylene blue degradation	97% in 100 min	[75]
α-$Fe_2O_3–TiO_2$/fly ash	Sol–gel	Rhodamine B degradation	100% in 1 h	[76]
Fe_2O_3/TiO_2	Sol–gel	4-chlorophenol degradation	100% in 180 min	[77]
$Fe_2O_3/ZnO/ZnFe_2O_4$	Hydrothermal and annealing	Rhodamine B degradation	95.7% in 60 min	[78]
CuO/Fe_2O_3/ZnO	Sol–gel combustion	Bisphenol A degradation	97.5% in 180 min	[79]
Zeolite-supported $ZnO/Fe_2O_3/MnO_2$	One-step impregnation method	Methylene blue degradation	93% in 120 min	[80]

(continued)

Table 4.1 (continued)

Materials	Methods	Photocatalytic application	Photocatalytic performance	References
Fe_2O_3/ZnO	Solution-combustion technique	Rhodamine 6G degradation	100% in 4 h	[81]
Cu–Fe_2O_3/Ni–ZnO	Hydrothermal, precipitation and calcination	Tetracycline degradation	94% in 2 h	[82]
γ-Fe_2O_3/g-C_3N_4	Thermal heating and hydrothermal treatment	Tetracycline degradation	73.8% in 120 min	[83]
g-C_3N_4–Fe_2O_3	Calcination	Methyl orange degradation	99% in 120 min	[84]
$BaTiO_3$/α-Fe_2O_3	Thermal annealing	Rhodamine B degradation	> 95% in 120 min	[85]
$KNbO_3$/α-Fe_2O_3	Hydrothermal method	Methylene blue degradation	89% in 90 min	[86]
α-Fe_2O_3/RGO	Hydrothermal method	Phenol degradation	62% in 150 min	[87]
α-Fe_2O_3/CdS	Wet-chemical method	Methylene blue degradation	86.7% in 120 min	[88]
SnO_2/α-Fe_2O_3	Chemical vapour deposition	Methylene blue degradation	100% in 2.5 h	[89]
SnO_2/α-Fe_2O_3–PB (Prussian blue) thin films	Electrochemical and annealing	Rhodamine B and Congo red degradation	~ 80% CR and ~ 82% RhB in 120 min	[90]
α-Fe_2O_3/Ag/AgX (X = Cl, Br, I)	In-situ oxidation reaction and self-assembly process	Rhodamine B degradation	100% in 60 min	[91]
α-Fe_2O_3/rGO	Hydrothermal method	Rhodamine 6G degradation	90.5% in 4 h	[92]
$CaFe_2O_4$/Fe_2O_3	Hydrothermal and co-precipitation method	Methyl orange degradation	99% in 60 min	[93]
NiO–Fe_2O_3–CdO	Precipitation and calcination	Methyl orange degradation	84.25% in 60 min	[94]
ZnS/Fe_2O_3/Ag	Hydrothermal method	Eosin blue degradation	93% in 60 min	[95]
Fe_2O_3/Mn_2O_3	Sol–gel method	Parathion degradation	90% in 15 min	[96]
α-Fe_2O_3@rGO/PAN	Hydrothermal method	Methylene blue degradation	98.5% in 2 h	[97]
Ag/AgBr@Fe_2O_3	Solvothermal method	Methyl orange degradation	94.4% in 12 min	[98]

(continued)

Table 4.1 (continued)

Materials	Methods	Photocatalytic application	Photocatalytic performance	References
$SrTiO_3/Fe_2O_3$	Hydrothermal and electrospinning technique	Tetracycline degradation	82.7% in 140 min	[99]
$Ag_3PO_4/\alpha\text{-}Fe_2O_3$	Hydrothermal method	Rhodamine B degradation	95% in 10 min	[100]
Fe_2O_3/Cu_2O	Hydrothermal method	Rhodamine B degradation	91.25% in 120 min	[101]
$Fe_2O_3@WO_3$	Hydrothermal method and precipitation	Rhodamine B degradation	98% in 75 min	[102]
$\alpha\text{-}Fe_2O_3/Ag_6Si_2O_7$	Wet chemical method	Methylene blue degradation	98% in 30 min	[103]
$Fe_2O_3/CuBi_2O_4$	Hydrothermal method	Tetracycline degradation	80% in 120 min	[104]
Fe_2O_3/Ag_3VO_4	Solvothermal and precipitation method	Rhodamine B degradation	96.1% in 60 min	[105]
CeO_2/Fe_2O_3	Co-precipitation method	Eosin yellow degradation	98% in 25 min	[106]
Fe_2O_3/BiOCl	Hydrothermal method	Methyl orange-Rhodamine B mixed dye degradation	90% in 30 min	[107]
$CuO/\alpha\text{-}Fe_2O_3/\gamma\text{-}Al_2O_3$	Precipitation method	Methyl orange degradation	98% in 240 min	[108]
$SnO_2–Fe_2O_3–rGO$	Hydrothermal method	Crystal violet degradation	96.3% in 120 min	[109]
$\alpha\text{-}Fe_2O_3/BiVO_4$	Hydrothermal method	Tetracycline degradation	> 80% in 120 min	[110]
$Fe_2TiO_5/\alpha\text{-}Fe_2O_3/TiO_2$	Combustion synthesis	Methylene blue degradation	> 95% in 120 min	[16]
$\alpha\text{-}Fe_2O_3/BiFeO_3$	Hydrothermal method	Rhodamine B degradation	60% in 4 h	[111]
$FeWO_4/Fe_2O_3$ di-modified WO_3	Hydrothermal method	Methylene blue degradation	95% in 10 min	[112]
$\gamma\text{-}Fe_2O_3@SiO_2@AgBr$:Ag	Solvothermal, Stöber method	Acid orange 7 degradation	> 90% in 20 min	[113]
$\alpha\text{-}Fe_2O_3$-doped Ti_3C_2 MXene	Ultrasonic assisted self-assembly method	Rhodamine B degradation	98% in 120 min	[114]
$\alpha\text{-}Fe_2O_3$@UiO-66	Wet chemical method and calcination	Methylene blue degradation	> 95% in 60 min	[115]
Fe_2O_3/Bi_2S_3	Hydrothermal method	Methylene blue degradation	~ 90% in 5 h	[116]

(continued)

Table 4.1 (continued)

Materials	Methods	Photocatalytic application	Photocatalytic performance	References
γ-Fe_2O_3/BiOI	Sol–gel, microwave hydrothermal method	Methyl orange degradation	86.3% in 120 min	[117]
Ag_2CO_3/α-Fe_2O_3	Precipitation and hydrothermal method	Malachite green degradation	~ 90% in 120 min	[118]
ZnS/Fe_2O_3	Hydrothermal method	Methylene blue degradation	90.17% in 4 h	[119]
C_3N_4@$CoFe_2O_4$/Fe_2O_3	Hydrothermal and calcination method	Tetracycline degradation	99.7% in 80 min	[120]
P3HT/α-Fe_2O_3	Electrophoretic deposition	Tetracycline degradation	97% in 90 min	[121]

4.4 Conclusions

In this chapter, we emphasized the photocatalytic applications of iron oxide and iron oxide-based materials towards the degradation of various persistent aqueous organic pollutants such as dyes, pesticides and phenolic compounds. In terms of synthesis, this chapter provides an overview of morphology control preparation of phase pure iron oxide as well as single-step and multiple-step preparation of iron oxide-based hybrid materials. We believe that this chapter gives an idea in order to prepare iron oxide-based hybrid materials and their applications in the emerging field of research such as electronic, energy and environment.

Acknowledgements The authors are thankful to Prof. Braja Gopal Mishra, Dr. Dibyananda Majhi and Krishnendu Das, Department of Chemistry, National Institute of Technology Rourkela, Odisha, India, for their timely help and valuable discussions.

References

1. Zou LY, Li Y, Hung YT (2007) Wet air oxidation for waste treatment. In: Wang LK, Hung YT, Sharma NK (eds) Advanced physicochemical treatment technologies. Handbook of environmental engineering, vol 5. Humana Press. https://doi.org/10.1007/978-1-59745-173-4_13
2. Saxena R, Saxena M, Lochab A (2020) Recent progress in nanomaterials for adsorptive removal of organic contaminants from wastewater. ChemistrySelect 5:335–353. https://doi.org/10.1002/slct.201903542
3. Jain M, Khan AS, Sharm K, Jadhao PR, Pant KK, Ziora ZM, Blaskovich MAT (2022) Current perspective of innovative strategies for bioremediation of organic pollutants from wastewater. Bioresour Technol 344:126305. https://doi.org/10.1016/j.biortech.2021.126305
4. Nakata K, Fujishima A (2012) TiO_2 photocatalysis: design and applications. J Photochem Photobiol C Photochem Rev 13:169–189. https://doi.org/10.1016/j.jphotochemrev.2012.06.001
5. Hitam CNC, Jalil AA (2020) A review on exploration of Fe_2O_3 photocatalyst towards degradation of dyes and organic contaminants. J Environ Manage 258:110050. https://doi.org/10.1016/j.jenvman.2019.110050
6. Wu W, Jiang C, Roy VAL (2015) Recent progress in magnetic iron oxide–semiconductor composite nanomaterials as promising photocatalysts. Nanoscale 7:38–58. https://doi.org/10.1039/C4NR04244A
7. Lai MTL, Lee KM, Yang TCK, Pan GT, Lai CW, Chen CY, Johan MR, Juan JC (2021) The improved photocatalytic activity of highly expanded MoS_2 under visible light emitting diodes. Nanoscale Adv 3:1106. https://doi.org/10.1039/D0NA00936A
8. Cheng L, Xiang Q, Liao Y, Zhang H (2018) CdS-based photocatalysts. Energy Environ Sci 11:1362–1391. https://doi.org/10.1039/C7EE03640J
9. Mishra M, Chun DM (2015) α-Fe_2O_3 as a photocatalytic material: a review. Appl Catal A 498:126–141. https://doi.org/10.1016/j.apcata.2015.03.023
10. Bhoi YP, Rout DP, Mishra BG (2016) Photocatalytic chemoselective aerobic oxidation of thiols to disulfides catalyzed by combustion synthesized bismuth tungstate nanoparticles in aqueous media. J Clust Sci 27:267–284. https://doi.org/10.1007/s10876-015-0928-0

11. Bhoi YP, Mishra BG (2018) Synthesis, characterization, and photocatalytic application of type-II CdS/$Bi_2W_2O_9$ heterojunction nanomaterials towards aerobic oxidation of amines to imines. Eur J Inorg Chem 2648–2658. https://doi.org/10.1002/ejic.201800221
12. Bhoi YP, Mishra BG (2018) Photocatalytic degradation of alachlor using type-II CuS/$BiFeO_3$ heterojunctions as novel photocatalyst under visible light irradiation. Chem Eng J 344:391–401. https://doi.org/10.1016/j.cej.2018.03.094
13. Yang Y, Zhang C, Lai C, Zeng G, Huang D, Cheng M, Wang J, Chen F, Zhou C, Xiong W (2018) BiOX (X = Cl, Br, I) photocatalytic nanomaterials: applications for fuels and environmental management. Adv Colloid Interface Sci 254:76–93. https://doi.org/10.1016/j.cis.2018.03.004
14. Marschall R (2014) Semiconductor composites: strategies for enhancing charge carrier separation to improve photocatalytic activity. Adv Funct Mater 24:2421–2440. https://doi.org/10.1002/adfm.201303214
15. Wang Y, Wang Q, Zhan X, Wang F, Safdar M, He J (2013) Visible light driven type II heterostructures and their enhanced photocatalysis properties: a review. Nanoscale 5:8326–8339. https://doi.org/10.1039/C3NR01577G
16. Bhoi YP, Fang F, Zhou X, Li Y, Sun X, Wang J, Huang W (2020) Single step combustion synthesis of novel Fe_2TiO_5/α-Fe_2O_3/TiO_2 ternary photocatalyst with combined double type-II cascade charge migration processes and efficient photocatalytic activity. Appl Surf Sci 525:146571. https://doi.org/10.1016/j.apsusc.2020.146571
17. Majhi D, Samal PK, Das K, Gouda SK, Bhoi YP, Mishra BG (2019) α-NiS/Bi_2O_3 nanocomposites for enhanced photocatalytic degradation of tramadol. ACS Appl Nano Mater 2(1):395–407. https://doi.org/10.1021/acsanm.8b01974
18. Majhi D, Bhoi YP, Samal PK, Mishra BG (2018) Morphology controlled synthesis and photocatalytic study of novel CuS-$Bi_2O_2CO_3$ heterojunction system for chlorpyrifos degradation under visible light illumination. Appl Surf Sci 455:891–902. https://doi.org/10.1016/j.apsusc.2018.06.051
19. Bhoi YP, Majhi D, Das K, Mishra BG (2019) Visible-light-assisted photocatalytic degradation of phenolic compounds using Bi_2S_3/$Bi_2W_2O_9$ heterostructure materials as photocatalyst. ChemistrySelect 4(12):3423–3431. https://doi.org/10.1002/slct.201900450
20. Majhi D, Das K, Bariki R, Padhan S, Mishra A, Dhiman R, Dash P, Nayak B, Mishra BG (2020) A facile reflux method for in situ fabrication of a non-cytotoxic Bi_2S_3/β-Bi_2O_3/$ZnIn_2S_4$ ternary photocatalyst: a novel dual Z-scheme system with enhanced multifunctional photocatalytic activity. J Mater Chem A 8:21729–21743. https://doi.org/10.1039/D0TA06129H
21. Das K, Majhi D, Bhoi YP, Mishra BG (2019) Combustion synthesis, characterization and photocatalytic application of CuS/$Bi_4Ti_3O_{12}$ p–n heterojunction materials towards efficient degradation of 2-methyl-4-chlorophenoxyacetic acid herbicide under visible light. Chem Eng J 362:588–599. https://doi.org/10.1016/j.cej.2019.01.060
22. Bhoi YP, Behera C, Majhi D, Equeenuddin SM, Mishra BG (2018) Visible light-assisted photocatalytic mineralization of diuron pesticide using novel type II CuS/$Bi_2W_2O_9$ heterojunctions with a hierarchical microspherical structure. New J Chem 42:281–292. https://doi.org/10.1039/C7NJ03390G
23. Majhi D, Mishra AK, Das K, Bariki R, Mishra BG (2021) Plasmonic Ag nanoparticle decorated Bi_2O_3/$CuBi_2O_4$ photocatalyst for expeditious degradation of 17α-ethinylestradiol and Cr(VI) reduction: insight into electron transfer mechanism and enhanced photocatalytic activity. Chem Eng J 413:127506. https://doi.org/10.1016/j.cej.2020.127506
24. Bariki R, Majhi D, Das K, Behera A, Mishra BG (2020) Facile synthesis and photocatalytic efficacy of UiO-66/$CdIn_2S_4$ nanocomposites with flowerlike 3D-microspheres towards aqueous phase decontamination of triclosan and H_2 evolution. Appl Catal B 270:118882. https://doi.org/10.1016/j.apcatb.2020.118882
25. Das K, Majhi D, Bariki R, Mishra BG (2020) SnS_2/$Bi_4Ti_3O_{12}$ heterostructure material: a UV-visible light active direct Z-scheme photocatalyst for aqueous phase degradation of diazinon. ChemistrySelect 5(4):1567–1577. https://doi.org/10.1002/slct.201904532

26. Majhi D, Das K, Mishra A, Dhiman R, Mishra BG (2020) One pot synthesis of CdS/BiOBr/$Bi_2O_2CO_3$: a novel ternary double Z-scheme heterostructure photocatalyst for efficient degradation of atrazine. Appl Catal B 260:118222. https://doi.org/10.1016/j.apcatb.2019.118222
27. Das K, Bariki R, Majhi D, Mishra A, Das KK, Dhiman R, Mishra BG (2022) Facile synthesis and application of CdS/$Bi_{20}TiO_{32}$/$Bi_4Ti_3O_{12}$ ternary heterostructure: a synergistic multi-heterojunction photocatalyst for enhanced endosulfan degradation and hydrogen evolution reaction. Appl Catal B 303:120902. https://doi.org/10.1016/j.apcatb.2021.120902
28. Kharisov BI, Dias HVR, Kharissova OV, Perez VMJ, Pereza BO, Flores BM (2012) Iron-containing nanomaterials: synthesis, properties, and environmental applications. RSC Adv 2:9325–9358. https://doi.org/10.1039/C2RA20812A
29. Qu J, Yu Y, Cao CY, Song WG (2013) α-Fe_2O_3 nanodisks: layered structure, growth mechanism, and enhanced photocatalytic property. Chem Eur J 19:11172–11177. https://doi.org/10.1002/chem.201301295
30. Ghasemifard M, Heidari G, Ghamari M, Fathi E, Izi M (2019) Synthesis of porous network-like α-Fe_2O_3 and α/γ-Fe_2O_3 nanoparticles and investigation of their photocatalytic properties. Nanotechnol Russ 14:353–361. https://doi.org/10.1134/S1995078019040062
31. Sun W, Meng Q, Jing L, Liu D, Cao Y (2013) Facile synthesis of surface-modified nanosized α-Fe_2O_3 as efficient visible photocatalysts and mechanism insight. J Phys Chem C 117:1358–1365. https://doi.org/10.1021/jp309599d
32. Basnet P, Larsen GK, Jadeja RP, Hung YC, Zhao Y (2013) α-Fe_2O_3 nanocolumns and nanorods fabricated by electron beam evaporation for visible light photocatalytic and antimicrobial applications. ACS Appl Mater Interfaces 5:2085–2095. https://doi.org/10.1021/am303017c
33. Kormann C, Bahnemann DW, Hoffmann MR (1989) Environmental photochemistry: is iron oxide (hematite) an active photocatalyst? A comparative study: α-Fe_2O_3, ZnO, TiO_2. J Photochem Photobiol A Chem 48(1):161–169. https://doi.org/10.1016/1010-6030(89)87099-6
34. Aslam M, Qamar MT, Rehman AU, Soomro MT, Ali S, Ismail IMI, Hameed A (2018) The evaluation of the photocatalytic activity of magnetic and nonmagnetic polymorphs of Fe_2O_3 in natural sunlight exposure: a comparison of photocatalytic activity. Appl Surf Sci 451:128–140. https://doi.org/10.1016/j.apsusc.2018.04.219
35. Wang C, Zhu C, Ren X, Shi J, Wang L, Lv B (2019) Anisotropic photogenerated charge separations between different facets of a dodecahedral α-Fe_2O_3 photocatalyst. CrystEngComm 21:6390–6395. https://doi.org/10.1039/C9CE01143A
36. Sundaramurthy J, Kumar PS, Kalaivani M, Thavasi V, Mhaisalkara SG, Ramakrishna S (2012) Superior photocatalytic behaviour of novel 1D nanobraid and nanoporous α-Fe_2O_3 structures. RSC Adv 2:8201–8208. https://doi.org/10.1039/c2ra20608k
37. Xie S, Jia H, Lu F, Sun N, Yu J, Liu S, Zheng L (2015) Controlled synthesis of α-Fe_2O_3 nanostructures with the assistance of ionic liquid and their distinct photocatalytic performance under visible-light irradiation. CrystEngComm 17:1210–1218. https://doi.org/10.1039/c4ce02033b
38. Wang FL, Song X, Teng Y, Xia J, Xu ZY, Wang WP (2019) Synthesis, structure, magnetism and photocatalysis of α-Fe_2O_3 nanosnowflakes. RSC Adv 9:35372–35383. https://doi.org/10.1039/c9ra07490b
39. Liu X, Chen K, Shim JJ, Huang J (2015) Facile synthesis of porous Fe_2O_3 nanorods and their photocatalytic properties. J Saudi Chem Soc 19(5):479–484. https://doi.org/10.1016/j.jscs.2015.06.009
40. Liang C, Liu H, Zhou J, Peng X, Zhang H (2015) One-step synthesis of spherical γ-Fe_2O_3 nanopowders and the evaluation of their photocatalytic activity for Orange I degradation. J Chem 8. Article ID 791829. https://doi.org/10.1155/2015/791829
41. Fardood ST, Moradnia F, Moradi S, Forootan R, Zare FY, Heidari M (2019) Eco-friendly synthesis and characterization of α-Fe_2O_3 nanoparticles and study of their photocatalytic activity for degradation of Congo red dye. Nanochem Res 4(2):140–147. https://doi.org/10.22036/ncr.2019.02.005

42. Yin H, Zhao Y, Hua Q, Zhang J, Zhang Y, Xu X, Long Y, Tang J, Wang F (2019) Controlled synthesis of hollow α-Fe_2O_3 microspheres assembled with ionic liquid for enhanced visible-light photocatalytic activity. Front Chem 7:58. https://doi.org/10.3389/fchem.2019.00058
43. Xu JS, Zhu YJ (2011) α-Fe_2O_3 hierarchically hollow microspheres self-assembled with nanosheets: surfactant-free solvothermal synthesis, magnetic and photocatalytic properties. CrystEngComm 13:5162. https://doi.org/10.1039/c1ce05252g
44. Liu G, Deng Q, Wang H, Ng DHL, Kong M, Cai W, Wang G (2012) Micro/nanostructured α-Fe_2O_3 spheres: synthesis, characterization, and structurally enhanced visible-light photocatalytic activity. J Mater Chem 22:9704. https://doi.org/10.1039/c2jm31586f
45. Zhu LP, Bing NC, Wang LL, Jin HY, Liao GH, Wang LJ (2012) Self-assembled 3D porous flowerlike α-Fe_2O_3 hierarchical nanostructures: synthesis, growth mechanism, and their application in photocatalysis. Dalton Trans 41:2959. https://doi.org/10.1039/c2dt11822j
46. Geng B, Tao B, Li X, Wei W (2012) Ni^{2+}/surfactant-assisted route to porous α-Fe_2O_3 nanoarchitectures. Nanoscale 4:1671. https://doi.org/10.1039/c2nr12102f
47. Pradhan GK, Sahu N, Parida KM (2013) Fabrication of S, N co-doped α-Fe_2O_3 nanostructures: effect of doping, OH radical formation, surface area, [110] plane and particle size on the photocatalytic activity. RSC Adv 3:7912–7920. https://doi.org/10.1039/C3RA23088K
48. Almazroai LS, Maliabari LA (2020) Microwave synthesis of sulfur-doped α-Fe_2O_3 and testing in photodegradation of methyl orange. J Chin Chem Soc 67(10). https://doi.org/10.1002/jccs.202000035
49. Satheesh R, Vignesh K, Suganthi A, Rajarajan M (2014) Visible light responsive photocatalytic applications of transition metal (M = Cu, Ni and Co) doped α-Fe_2O_3 nanoparticles. J Environ Chem Eng 2:1956–1968. https://doi.org/10.1016/j.jece.2014.08.016
50. Li N, He Y, Yi Z, Gao L, Zhai F, Chattopadhyay K (2020) Multiple-metal-doped Fe_3O_4@Fe_2O_3 nanoparticles with enhanced photocatalytic performance for methyl orange degradation under UV/solar light irradiation. Ceram Int 46:19038–19045. https://doi.org/10.1016/j.ceramint.2020.04.234
51. Mansour H, Omri K, Bargougui R, Ammar S (2020) Novel α-Fe_2O_3/TiO_2 nanocomposites with enhanced photocatalytic activity. Appl Phys A 126:151. https://doi.org/10.1007/s00339-020-3320-3
52. Li X, Lin H, Chen X, Niu H, Liu J, Zhang T, Qu F (2016) Dendritic α-Fe_2O_3/TiO_2 nanocomposites with improved visible light photocatalytic activity. Phys Chem Chem Phys 18:9176–9185. https://doi.org/10.1039/c5cp06681f
53. Ren L, Zhou W, Sun B, Li H, Qiao P, Xu Y, Wu J, Lin K, Fu H (2019) Defects-engineering of magnetic γ-Fe_2O_3 ultrathin nanosheets/mesoporous black TiO_2 hollow sphere heterojunctions for efficient charge separation and the solar-driven photocatalytic mechanism of tetracycline degradation. Appl Catal B 240:319–328. https://doi.org/10.1016/j.apcatb.2018.08.033
54. Mahajan J, Jeevanandam P (2018) Synthesis of TiO_2@α-Fe_2O_3 core–shell heteronanostructures by thermal decomposition approach and their application towards sunlight driven photodegradation of Rhodamine B. New J Chem 42:2616–2626. https://doi.org/10.1039/c7nj04892k
55. Li N, Zhang J, Tian Y, Zhao J, Zhang J, Zuo W (2017) Precisely controlled fabrication of magnetic 3D γ-Fe_2O_3@ZnO core-shell photocatalyst with enhanced activity: ciprofloxacin degradation and mechanism insight. Chem Eng J 308:377–385. https://doi.org/10.1016/j.cej.2016.09.093
56. Jiamprasertboon A, Kafizas A, Sachs M, Ling M, Alotaibi AM, Lu Y, Siritanon T, Parkin IP, Carmalt CJ (2019) Heterojunction α-Fe_2O_3/ZnO films with enhanced photocatalytic properties grown by aerosol-assisted chemical vapour deposition. Chem Eur J 25(48):11337–11345. https://doi.org/10.1002/chem.201902175
57. Choudhary S, Bisht A, Mohapatra S (2021) Microwave-assisted synthesis of α-Fe_2O_3/$ZnFe_2O_4$/ZnO ternary hybrid nanostructures for photocatalytic applications. Ceram Int 47:3833–3841. https://doi.org/10.1016/j.ceramint.2020.09.243

58. Dhal JP, Mishra BG, Hota G (2015) Hydrothermal synthesis and enhanced photocatalytic activity of ternary $Fe_2O_3/ZnFe_2O_4/ZnO$ nanocomposite through cascade electron transfer. RSC Adv 5:58072. https://doi.org/10.1039/c5ra05894e
59. Wang B, Liu X, Dai S, Lu H (2020) α-Fe_2O_3 nanoparticles/porous g-C_3N_4 hybrids synthesized by calcinations of Fe-based MOF/melamine mixtures for boosting visible-light photocatalytic tetracycline degradation. ChemistrySelect 5:3303–3311. https://doi.org/10.1002/slct.201904388
60. Sumathi M, Prakasam A, Anbarasan PM (2019) A facile microwave stimulated g-C_3N_4/α-Fe_2O_3 hybrid photocatalyst with superior photocatalytic activity and attractive cycling stability. J Mater Sci Mater Electron 30:10985–10993. https://doi.org/10.1007/s10854-019-01439-1
61. Yu X, Yang X, Li G (2018) Magnetically separable Fe_2O_3/g-C_3N_4 nanocomposites with cocoon-like shape: magnetic properties and photocatalytic activities. J Electron Mater 47(1):672–676. https://doi.org/10.1007/s11664-017-5835-8
62. Yu Q, Yang K, Li H, Li X (2021) Z-scheme α-Fe_2O_3/g-C_3N_4 with the Fe–OC–bond toward enhanced photocatalytic degradation. Colloids Surf A Physicochem Eng Asp 616:126269. https://doi.org/10.1016/j.colsurfa.2021.126269
63. Lu C, Guan W, Zhang G, Ye L, Zhou Y, Zhang X (2013) TiO_2/Fe_2O_3/CNTs magnetic photocatalyst: a fast and convenient synthesis and visible-light-driven photocatalytic degradation of tetracycline. Micro Nano Lett 8(10):749–752. https://doi.org/10.1049/mnl.2013.0428
64. Kucio K, Charmas B, Pasieczna-Patkowska S, Zięzio M (2020) Mechanochemical synthesis of nanophotocatalysts $SiO_2/TiO_2/Fe_2O_3$: their structural, thermal and photocatalytic properties. Appl Nanosci 10:4733–4746. https://doi.org/10.1007/s13204-020-01462-3
65. Ana L, Meng Y, Wang T, Xiong C, Yan Z, Xu Z (2020) Highly efficient and easily recoverable Ag_3PO_4–TiO_2–Fe_2O_3 magnetic photocatalyst with wide spectral range for water treatment. Russ J Phys Chem A 94(5):1067–1072. https://doi.org/10.1134/S0036024420050027
66. Kong X, Lia J, Yang C, Tang Q, Wang D (2020) Fabrication of Fe_2O_3/g-C_3N_4@N-TiO_2 photocatalyst nanotube arrays that promote bisphenol A photodegradation under simulated sunlight irradiation. Sep Purif Technol 248:116924. https://doi.org/10.1016/j.seppur.2020.116924
67. Szeto W, Li J, Huang H, Xu J, Leung DYC (2015) Novel urchin-like Fe_2O_3@SiO_2@TiO_2 microparticles with magnetically separable and photocatalytic properties. RSC Adv 5:55363. https://doi.org/10.1039/c5ra08070c
68. Liu J, Yang S, Wu W, Tian Q, Cui S, Dai Z, Ren F, Xiao X, Jiang C (2015) 3D flowerlike α-Fe_2O_3@TiO_2 core–shell nanostructures: general synthesis and enhanced photocatalytic performance. ACS Sustain Chem Eng 3:2975–2984. https://doi.org/10.1021/acssuschemeng.5b00956
69. Luo H, Yu S, He F, Li L, Zhong M, Dong N, Su B (2021) An important phenomenon in Fe_2O_3–TiO_2 photocatalyst: ion-inter-doping. Solid State Sci 113:106538. https://doi.org/10.1016/j.solidstatesciences.2021.106538
70. Jahanshahi R, Sobhani S, Sansano JM (2020) High performance magnetically separable g-C_3N_4/γ-Fe_2O_3/TiO_2 nanocomposite with boosted photocatalytic capability towards the cefixime trihydrate degradation under visible-light. ChemistrySelect 5:10114–10127. https://doi.org/10.1002/slct.202002682
71. Xia Y, Yin L (2013) Core–shell structured α-Fe_2O_3@TiO_2 nanocomposites with improved photocatalytic activity in the visible light region. Phys Chem Chem Phys 15:18627–18634. https://doi.org/10.1039/c3cp53178c
72. Kim SE, Woo JY, Kang SY, Min BK, Lee JK, Lee SW (2016) A facile general route for ternary Fe_2O_3@TiO_2@nanometal (Au, Ag) composite as a high-performance and recyclable photocatalyst. J Ind Eng Chem 43:142–149. https://doi.org/10.1016/j.jiec.2016.07.060
73. Li Y, Yang B, Liu B (2021) MOF assisted synthesis of TiO_2/Au/Fe_2O_3 hybrids with enhanced photocatalytic hydrogen production and simultaneous removal of toxic phenolic compounds. J Mol Liq 322:114815. https://doi.org/10.1016/j.molliq.2020.114815

74. Ghavami M, Kassaee MZ, Mohammadi R, Koohi M, Haerizadeh BN (2014) Polyaniline nanotubes coated with TiO_2&γ-Fe_2O_3@graphene oxide as a novel and effective visible light photocatalyst for removal of Rhodamine B from water. Solid State Sci 38:143–149. https://doi.org/10.1016/j.solidstatesciences.2014.09.010
75. Wang M, Han J, Yuan G, Guo R (2019) Carbon/TiO_2/Fe_2O_3 hybrid shells toward efficient visible light photocatalysts. New J Chem 43:11282–11287. https://doi.org/10.1039/C9NJ01742A
76. Liu S, Zhu J, Guo X, Ge J, Wu H (2015) Preparation of α-Fe_2O_3–TiO_2/fly ash cenospheres photocatalyst and its mechanism of photocatalytic degradation. Colloids Surf A Physicochem Eng Asp 484:434–440. https://doi.org/10.1016/j.colsurfa.2015.08.033
77. Palanisamy B, Babu CM, Sundaravel B, Anandan S, Murugesan V (2013) Sol–gel synthesis of mesoporous mixed Fe_2O_3/TiO_2 photocatalyst: application for degradation of 4-chlorophenol. J Hazard Mater 252–253:233–242. https://doi.org/10.1016/j.jhazmat.2013.02.060
78. Li X, Jin B, Huang J, Zhang Q, Peng R, Chu S (2018) Fe_2O_3/ZnO/$ZnFe_2O_4$ composites for the efficient photocatalytic degradation of organic dyes under visible light. Solid State Sci 80:6–14. https://doi.org/10.1016/j.solidstatesciences.2018.03.016
79. Shekoohiyan S, Rahmani A, Chamack M, Moussavia G, Rahmanian O, Alipour V, Giannakis S (2020) A novel CuO/Fe_2O_3/ZnO composite for visible-light assisted photocatalytic oxidation of Bisphenol A: kinetics, degradation pathways, and toxicity elimination. Sep Purif Technol 242:116821. https://doi.org/10.1016/j.seppur.2020.116821
80. Tedla H, Díaz I, Kebede T, Taddesse AM (2015) Synthesis, characterization and photocatalytic activity of zeolite supported ZnO/Fe_2O_3/MnO_2 nanocomposites. J Environ Chem Eng 3:1586–1591. https://doi.org/10.1016/j.jece.2015.05.012
81. Pradhan GK, Martha S, Parida KM (2012) Synthesis of multifunctional nanostructured zinc–iron mixed oxide photocatalyst by a simple solution-combustion technique. ACS Appl Mater Interfaces 4:707–713. https://doi.org/10.1021/am201326b
82. Li Y, Liu K, Zhang J, Yang J, Huang Y, Tong Y (2020) Engineering the band-edge of Fe_2O_3/ZnO nanoplates via separate dual cation incorporation for efficient photocatalytic performance. Ind Eng Chem Res 59:18865–18872. https://doi.org/10.1021/acs.iecr.0c03388
83. Li C, Yu S, Che H, Zhang X, Han J, Mao Y, Wang Y, Liu C, Dong H (2018) Fabrication of Z-scheme heterojunction by anchoring mesoporous γ-Fe_2O_3 nanospheres on g-C_3N_4 for degrading tetracycline hydrochloride in water. ACS Sustain Chem Eng 6:16437–16447. https://doi.org/10.1021/acssuschemeng.8b03500
84. Babar S, Gavade N, Shinde H, Mahajan P, Lee KH, Mane N, Deshmukh A, Garadkar K, Bhuse V (2018) Evolution of waste iron rust into magnetically separable g-C_3N_4–Fe_2O_3 photocatalyst: an efficient and economical waste management approach. ACS Appl Nano Mater 1:4682–4694. https://doi.org/10.1021/acsanm.8b00936
85. Cui Y, Briscoe J, Wang Y, Tarakina NV, Dunn S (2017) Enhanced photocatalytic activity of heterostructured ferroelectric $BaTiO_3$/α-Fe_2O_3 and the significance of interface morphology control. ACS Appl Mater Interfaces 9:24518–24526. https://doi.org/10.1021/acsami.7b03523
86. Farooq U, Chaudhary P, Ingole PP, Kalam A, Ahmad T (2020) Development of uuboidal $KNbO_3$@α-Fe_2O_3 hybrid nanostructures for improved photocatalytic and photoelectrocatalytic applications. ACS Omega 5:20491–20505. https://doi.org/10.1021/acsomega.0c02646
87. Pradhan GK, Padhi DK, Parida KM (2013) Fabrication of α-Fe_2O_3 nanorod/RGO composite: a novel hybrid photocatalyst for phenol degradation. ACS Appl Mater Interfaces 5:9101–9110. https://doi.org/10.1021/am402487h
88. Shi Y, Li H, Wang L, Shen W, Chen H (2012) Novel α-Fe_2O_3/CdS cornlike nanorods with enhanced photocatalytic performance. ACS Appl Mater Interfaces 4:4800–4806. https://doi.org/10.1021/am3011516
89. Kang J, Kuang Q, Xie ZX, Zheng LS (2011) Fabrication of the SnO_2/α-Fe_2O_3 hierarchical heterostructure and its enhanced photocatalytic property. J Phys Chem C 115:7874–7879. https://doi.org/10.1021/jp111419w

90. Jana S, Mondal A (2014) Fabrication of SnO_2/α-Fe_2O_3, SnO_2/α-Fe_2O_3–PB heterostructure thin films: enhanced photodegradation and peroxide sensing. ACS Appl Mater Interfaces 6:15832–15840. https://doi.org/10.1021/am5030879
91. Sun L, Wu W, Tian Q, Lei M, Liu J, Xiao X, Zheng X, Ren F, Jiang C (2016) In situ oxidation and self-assembly synthesis of dumbbell-like α-Fe_2O_3/Ag/AgX (X = Cl, Br, I) heterostructures with enhanced photocatalytic properties. ACS Sustain Chem Eng 4:1521–1530. https://doi.org/10.1021/acssuschemeng.5b01473
92. Zhang L, Bao Z, Yu X, Dai P, Zhu J, Wu M, Li G, Liu X, Sun Z, Chen C (2016) Rational design of α-Fe_2O_3/reduced graphene oxide composites: rapid detection and effective removal of organic pollutants. ACS Appl Mater Interfaces 8:6431–6438. https://doi.org/10.1021/acsami.5b11292
93. Fu Y, Shan S, Chen F, Hu J (2020) Constructing an efficient p–n heterojunction photocatalyst $CaFe_2O_4$/Fe_2O_3 nanocomposite for degradation of methyl orange. J Mater Sci Mater Electron 31:17967–17979. https://doi.org/10.1007/s10854-020-04349-9
94. Mukhtar F, Munawar T, Nadeem MS, Hasan M, Hussain F, Nawaz MA, Iqbal F (2020) Multi metal oxide NiO–Fe_2O_3–CdO nanocomposite-synthesis, photocatalytic and antibacterial properties. Appl Phys A 126:588. https://doi.org/10.1007/s00339-020-03776-z
95. Sunkara JR, Botsa SM (2020) ZnS/Fe_2O_3/Ag ternary nanocomposite photocatalyst for the degradation of dyes under visible light. Russ J Phys Chem A 94(2):392–400. https://doi.org/10.1134/S0036024420020144
96. Mai NVN, Lim DT, Bac NQ, Chi NTH, Dung DT, Pham NN, Nhiem DN (2019) Fe_2O_3/Mn_2O_3 nanoparticles: preparations and applications in the photocatalytic degradation of phenol and parathion in water. J Chin Chem Soc 1–4. https://doi.org/10.1002/jccs.201900033
97. Sun K, Wang L, Wu C, Deng J, Pan K (2017) Fabrication of α-Fe_2O_3@rGO/PAN nanofiber composite membrane for photocatalytic degradation of organic dyes. Adv Mater Interfaces 1700845. https://doi.org/10.1002/admi.201700845
98. Huang S, Xu Y, Chen Z, Xie M, Xu H, He M, Li H, Zhang Q (2015) A core–shell structured magnetic Ag/AgBr@Fe_2O_3 composite with enhanced photocatalytic activity for organic pollutant degradation and antibacterium. RSC Adv 5:71035. https://doi.org/10.1039/c5ra13403j
99. Liu C, Wu G, Chen J, Huang K, Shi W (2016) Fabrication of a visible-light-driven photocatalyst and degradation of tetracycline based on the photoinduced interfacial charge transfer of $SrTiO_3$/Fe_2O_3 nanowires. New J Chem 40:5198–5208. https://doi.org/10.1039/c5nj03167b
100. Gao Y, Ma H, Han C, Gui C, Deng C (2022) Preparation of Ag_3PO_4/α-Fe_2O_3 hybrid powders and their visible light catalytic performances. RSC Adv 12:6328. https://doi.org/10.1039/d1ra09256a
101. Abhilash MR, Akshatha G, Srikantaswamy S (2019) Photocatalytic dye degradation and biological activities of the Fe_2O_3/Cu_2O nanocomposite. RSC Adv 9:8557. https://doi.org/10.1039/c8ra09929d
102. Bai S, Zhang K, Sun J, Luo R, Li D, Chen A (2014) Surface decoration of WO_3 architectures with Fe_2O_3 nanoparticles for visible-light-driven photocatalysis. CrystEngComm 16:3289–3295. https://doi.org/10.1039/c3ce42410c
103. Liu J, Wu W, Tian Q, Dai Z, Wu Z, Xiao X, Jiang C (2016) Anchoring of $Ag_6Si_2O_7$ nanoparticles on α-Fe_2O_3 short nanotubes as a Z-scheme photocatalyst for improving their photocatalytic performances. Dalton Trans 45:12745–12755. https://doi.org/10.1039/c6dt02499h
104. Li M, Tang Y, Shi W, Chen F, Shia Y, Gu H (2018) Design of visible-light-response core–shell Fe_2O_3/$CuBi_2O_4$ heterojunctions with enhanced photocatalytic activity towards the degradation of tetracycline: Z-scheme photocatalytic mechanism insight. Inorg Chem Front 5:3148–3154. https://doi.org/10.1039/c8qi00906f
105. Xu Y, Jing L, Chen X, Ji H, Xu H, Li H, Li H, Zhang Q (2016) Novel visible-light-driven Fe_2O_3/Ag_3VO_4 composite with enhanced photocatalytic activity toward organic pollutants degradation. RSC Adv 6:3600. https://doi.org/10.1039/c5ra22912j

106. Arul NS, Mangalaraj D, Ramachandran R, Gracec AN, Han JI (2015) Fabrication of CeO_2/Fe_2O_3 composite nanospindles for enhanced visible light driven photocatalysts and supercapacitor electrodes. J Mater Chem A 3:15248–15258. https://doi.org/10.1039/c5ta02630j
107. Li N, Hua X, Wang K, Jin Y, Xu J, Chen M, Teng F (2014) In situ synthesis of uniform Fe_2O_3/BiOCl p/n heterojunctions and improved photodegradation properties for mixture dyes. Dalton Trans 43:13742–13750. https://doi.org/10.1039/c4dt01999g
108. Kanwal A, Sajjad S, Leghari SAK, Yousaf Z (2021) Cascade electron transfer in ternary CuO/α-Fe_2O_3/γ-Al_2O_3 nanocomposite as an effective visible photocatalyst. J Phys Chem Solids 151:109899. https://doi.org/10.1016/j.jpcs.2020.109899
109. Botsa SM, Naidu GP, Ravichandra M, Rani SJ, Anjaneyulu RB, Ramana ChV (2020) Flower like SnO_2–Fe_2O_3–rGO ternary composite as highly efficient visible light induced photocatalyst for the degradation of organic pollutants from contaminated water. J Mater Res Technol 9(6):12461–12472. https://doi.org/10.1016/j.jmrt.2020.08.087
110. Ma C, Lee J, Kim Y, Seo WC, Jung H, Yang W (2021) Rational design of α-Fe_2O_3 nanocubes supported $BiVO_4$ Z-scheme photocatalyst for photocatalytic degradation of antibiotic under visible light. J Colloid Interface Sci 581:514–522. https://doi.org/10.1016/j.jcis.2020.07.127
111. Zhang R, Liu S, Kong F, Tong J, Ruan L, Duan Q, Zhou J, Zhang X (2020) α-Fe_2O_3/$BiFeO_3$ composites as visible-active photocatalysts and their optical response mechanism. J Phys Chem Solids 141:109329. https://doi.org/10.1016/j.jpcs.2019.109329
112. Wang H, Wang C, Cui X, Qina L, Ding R, Wang L, Liu Z, Zheng Z, Lv B (2018) Design and facile one-step synthesis of $FeWO_4/Fe_2O_3$ di-modified WO_3 with super high photocatalytic activity toward degradation of quasiphenothiazine dyes. Appl Catal B 221:169–178. https://doi.org/10.1016/j.apcatb.2017.09.011
113. Tian B, Wang T, Dong R, Bao S, Yang F, Zhang J (2014) Core–shell structured α-Fe_2O_3@SiO_2@AgBr: Ag composite with high magnetic separation efficiency and excellent visible light activity for acid orange 7 degradation. Appl Catal B 147:22–28. https://doi.org/10.1016/j.apcatb.2013.08.028
114. Zhang H, Li M, Cao J, Tang Q, Kang P, Zhu C, Ma M (2018) 2D α-Fe_2O_3 doped Ti_3C_2 MXene composite with enhanced visible light photocatalytic activity for degradation of Rhodamine B. Ceram Int 44:19958–19962. https://doi.org/10.1016/j.ceramint.2018.07.262
115. Zhang R, Du B, Li Q, Cao Z, Feng G, Wang X (2019) α-Fe_2O_3 nanoclusters confined into UiO-66 for efficient visible-light photodegradation performance. Appl Surf Sci 466:956–963. https://doi.org/10.1016/j.apsusc.2018.10.048
116. Helal A, Harraz FA, Ismail AA, Sami TM, Ibrahim IA (2017) Hydrothermal synthesis of novel heterostructured Fe_2O_3/Bi_2S_3 nanorods with enhanced photocatalytic activity under visible light. Appl Catal B Environ 213:18–27. https://doi.org/10.1016/j.apcatb.2017.05.009
117. Niu J, Zhang Z, Dai P, Yao B, Yu X, Zhang Q, Yang R (2018) Facile synthesis of γ-Fe_2O_3/BiOI microflowers with enhanced visible light photocatalytic activity. Mater Des 150:29–39. https://doi.org/10.1016/j.matdes.2018.04.001
118. Guo R, Qi X, Zhang X, Zhang H, Cheng X (2019) Synthesis of Ag_2CO_3/α-Fe_2O_3 heterojunction and it high visible light driven photocatalytic activity for elimination of organic pollutants. Sep Purif Technol 211:504–513. https://doi.org/10.1016/j.seppur.2018.10.011
119. Liu Q, Cao J, Jia Y, Li X, Li W, Zhu Y, Liu X, Li J, Yang J, Yang Y (2020) Construction of a direct Z-scheme ZnS quantum dot (QD)-Fe_2O_3 QD heterojunction/reduced graphene oxide nanocomposite with enhanced photocatalytic activity. Appl Surf Sci 506:144922. https://doi.org/10.1016/j.apsusc.2019.144922
120. Lv SW, Liu JM, Zhao N, Li CY, Yang FE, Wang ZH, Wang S (2020) MOF-derived $CoFe_2O_4$/Fe_2O_3 embedded in g-C_3N_4 as high-efficient Z scheme photocatalysts for enhanced degradation of emerging organic pollutants in the presence of persulfate. Sep Purif Technol 253:117413. https://doi.org/10.1016/j.seppur.2020.117413
121. Zhu H, Chen Z, Hu Y, Gong L, Li D, Li Z (2020) A novel immobilized Z-scheme P3HT/α-Fe_2O_3 photocatalyst array: study on the excellent photocatalytic performance and photocatalytic mechanism. J Hazard Mater 389:122119. https://doi.org/10.1016/j.jhazmat.2020.122119

Chapter 5
Iron Oxide-Functionalized Graphene Nanocomposites for Supercapacitor Application

Meenaketan Sethi, U. Sandhya Shenoy, and D. Krishna Bhat

Abstract The wonder material graphene after its discovery in 2004 has attracted enormous research attention globally in various domains such as energy, environment, biomedical, food packaging, to name a few. Graphene is a 2D carbon nanomaterial and possesses excellent properties such as high electrical conductivity, high surface area, good thermal and chemical stability, wide potential window and rich surface chemistry. Due to its high surface area and electronic conductivity, it has been widely used as an electrode in supercapacitors. Generally, carbon-based material like graphene falls under the category of electrochemical double-layer capacitors (EDLCs), and the EDLC phenomena depend on the electrode/electrolyte interface transport and storage of the developed electrical charge. Graphene-based materials provide high specific capacitance, high power density and long cyclic stability. In contrast, pseudocapacitive materials, e.g. iron oxide-based materials (Fe_2O_3, Fe_3O_4), render high energy density, comparatively low power density and cyclic stability. However, the combination of EDLC and pseudocapacitive materials will be a good choice to ameliorate the capacitance, cyclability, energy and power density to improve the electrochemical performance as a whole. In this chapter, we briefly describe about supercapacitors, the use of different graphene forms, iron oxide nanomaterial and its composites with graphene designed in order to increase the electrochemical performance of the supercapacitors.

Keywords Iron oxides · Graphene · Nanocomposite · Supercapacitor · EDLC · Pseudocapacitor

M. Sethi · D. K. Bhat (✉)
Department of Chemistry, National Institute of Technology Karnataka, Surathkal, Mangalore 575025, India
e-mail: denthajekb@gmail.com; kishan@nitk.edu.in

U. S. Shenoy
Department of Materials Science and Engineering, Institute of Engineering and Technology, Srinivas University, Mukka, Mangalore 574146, India
e-mail: sandhyashenoy347@gmail.com

H. Sahoo and J. K. Sahoo (eds.), *Iron Oxide-Based Nanocomposites and Nanoenzymes*, Nanostructure Science and Technology, https://doi.org/10.1007/978-3-031-44599-6_5

5.1 Introduction to Supercapacitors

Capacitors are devices in which electric charges are accumulated on the electrodes with lateral repulsive force and without involving redox chemical changes [1]. Capacitors are classified into three types by their mode of charge storage: (i) electrostatic, (ii) electrolytic and (iii) electrochemical capacitors. In an electrostatic capacitor, vacuum or a dielectric material is sandwiched between two conducting metal plates. Capacitance arises from the electrostatic charge separation between these two conducting metal plates. A thin film of an oxide such as Al_2O_3 and Ta_2O_5 is sandwiched between two conducting metal plates in electrolytic capacitors. Capacitance arises from the buildup of electrostatic charges between two interfaces. Electrochemical capacitors (ECs) on the other hand are complementary to batteries and fuel cells, which bridge the gap between batteries and conventional capacitors. As the magnitude of capacitance of ECs is very high, these devices are also known as supercapacitors or ultracapacitors [2, 3]. A supercapacitor is an ideal electrochemical capacitor that stores the charge on the electroactive surface using the reversible adsorption of electrolyte ions of the active materials electrostatically [4, 5]. Supercapacitors can store and deliver energy at high rates in comparison to batteries and fuel cells due to long cyclic stability and rapid charging and discharging at high power densities [5].

Based on the charge storage mechanisms, supercapacitors are of three types as shown in Fig. 5.1. (a) Electrical double-layer capacitors (EDLCs), where the electrical charge is stored at the interface between the electrode and electrolyte; (b) redox electrochemical capacitors, where capacitance arises from reversible Faradaic reactions taking place at the interface of electrode/electrolyte; (c) hybrid capacitors which combine the capacitive and pseudocapacitive electrode and hence exhibit better performance [1, 6].

Supercapacitors store and discharge energy very quickly and hence are used in several different applications. Supercapacitors complement a primary energy source like an internal combustion engine, fuel cell or battery, which cannot repeatedly provide quick bursts of power. The future horizon looks promising for supercapacitors as a green, alternative energy resource. The supercapacitors can be efficiently utilized in a host of application spheres such as, for the acceleration of hybrid vehicles, wherein power is derived from regenerative braking systems, to start the vehicles in cold weather or when batteries are drained, when burst power is needed for lifting loads, to help power electrical systems, starter systems and power steering in hybrid and electric cars apart from providing starting power in start–stop systems and in systems where quick discharge and charge of power is required such as, power grid, solid-state memory drives and electronic toys.

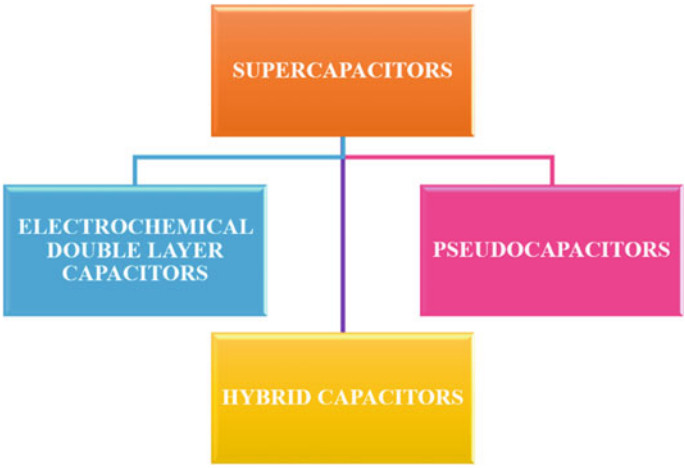

Fig. 5.1 Types of supercapacitors

5.2 Working Principle

A conventional capacitor has a sandwich structure consisting of two conducting electrodes (generally made of metal) separated by an insulating dielectric material such as air, oiled paper, mica, glass, porcelain, or titanate. For an electrostatic charge to develop along the electrodes of a capacitor, work must be done by an external driving force. When an external voltage is applied across the two electrodes, opposite charges assemble on the surfaces of each electrode. When the external voltage difference is removed, both the charges remain in their corresponding electrodes. The voltage difference between the two electrodes is called the cell voltage of the capacitor. The charges are kept separated by the dielectric, thus producing an electric field that permits the capacitor to store and delivery energy. This is illustrated in Fig. 5.2.

For a conventional capacitor, capacitance 'C' is proportional to the electrode surface area 'A' and inversely proportional to the distance 'D' between the electrodes as expressed by the following Eq. (5.1)

$$C = \frac{\varepsilon_0 \varepsilon_r A}{D} \tag{5.1}$$

where 'ε_0' is the dielectric constant (or permittivity) of free space and 'ε_r' is the dielectric constant of the insulating material between the electrodes. In electrochemical capacitor, the electrical energy is stored in an electrochemical double layer (Helmholtz layer) formed at the electrode/electrolyte interface. At the electrode surface, positive and negative ionic charges within the electrolyte accumulate and counterbalance the electronic charge. The concentration of the electrolyte and the size of the ions decide the thickness of the double layer which is usually in the order of 5–10 Å for concentrated electrolytes. This is illustrated in Fig. 5.3.

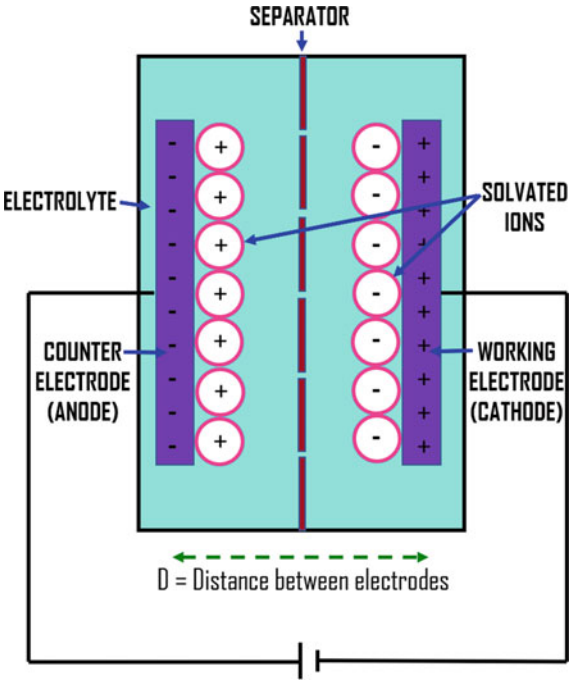

Fig. 5.2 Schematic view of a conventional capacitor

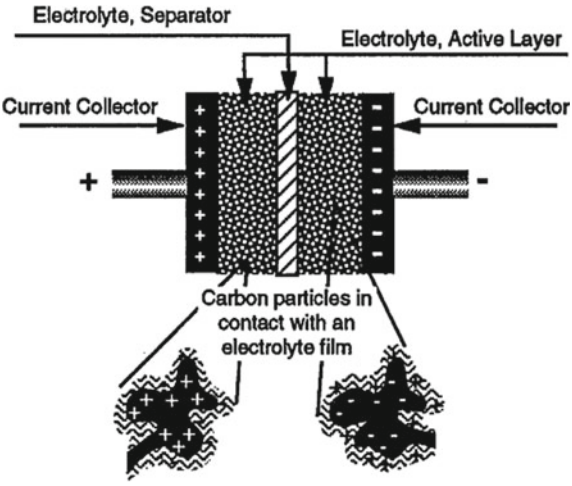

Fig. 5.3 Schematic view of an electrochemical capacitor. Reproduced with permission from Elsevier [7]

Energy density and power density are the two vital properties of any energy storage devices. The energy density is the maximum quantity of energy that can be stored, while power density is a measure of how quick the stored energy can be delivered. The maximum energy stored 'E_m' and maximum usable power 'P_m' for a capacitor are calculated by Eqs. (5.2) and (5.3).

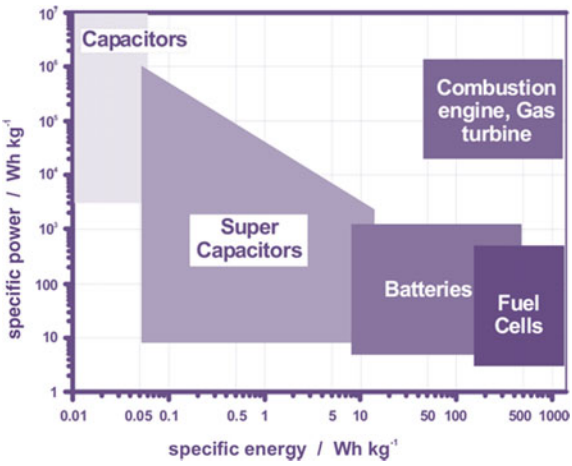

Fig. 5.4 Ragone plot of energy devices. Reproduced with permission from Elsevier [4]

$$E_{\mathrm{m}} = \frac{CV^2}{2} \tag{5.2}$$

$$P_{\mathrm{m}} = \frac{V^2}{4R} \tag{5.3}$$

where 'V' is the applied voltage, 'C' is the specific capacitance and 'R' is the equivalent series resistance (ESR). An ideal energy storage system must have high energy and high power density apart from high capacitance, large voltage window and low ESR values.

Figure 5.4 shows a Ragone plot of different energy storage devices with power densities plotted against energy densities. Electrochemical capacitors currently fill the gap between batteries and conventional solid-state and electrolytic capacitors. Despite greater capacitance than conventional capacitors, electrochemical capacitors have lower energy densities in comparison to mid and high-end batteries. In the recent years, due to extensive research on new electrode materials, improved understanding of ion behaviour and the design of new hybrid systems combining capacitive and pseudocapacitive electrodes, increased performance of ECs is observed.

5.3 Types of Supercapacitors

5.3.1 Electrochemical Double-Layer Capacitors (EDLCs)

The electrochemical double layer theory, which is the foundation of electrochemistry, was first established by Helmholtz and developed further by Gouy, Chapman, Graham and Stern. It investigates the electrochemical processes occurring at an electrostatic

interface between the charged electrode material and the electrolyte. An electrostatic charge accumulation is achieved on either side of the electrode conductor, when it is placed in contact with the solid or liquid ionic conductor, leading to the development of an electrical double layer. In electrical double layer, charge transfer is not occurring across the interface and the current observed during this process is essentially a displacement current due to the arrangement of charges. Therefore, this process is non-Faradaic in nature. A schematic of an electrical double layer (EDL), i.e. Helmholtz layer and a more fundamental model of the EDL, is shown in Fig. 5.5 indicating the different size of the ions and their reactivity at the negative electrode surface.

An EDLC consists of two electrodes which are immersed in an electrolyte with a separator between the electrodes. The electrode materials used for the fabrication are carbon-based materials because these materials possess high surface area, high electronic conductivity, high chemical and electrochemical stability with porosity in the diameter range of nanometer [4]. EDLCs utilize the double layer to store the charge electrostatically, and there is no charge transfer between electrode and electrolyte. EDLCs can attain higher energy densities than the conventional capacitors which is attributed to the double layers with a high surface area and higher contact between the electrodes [1, 7, 8].

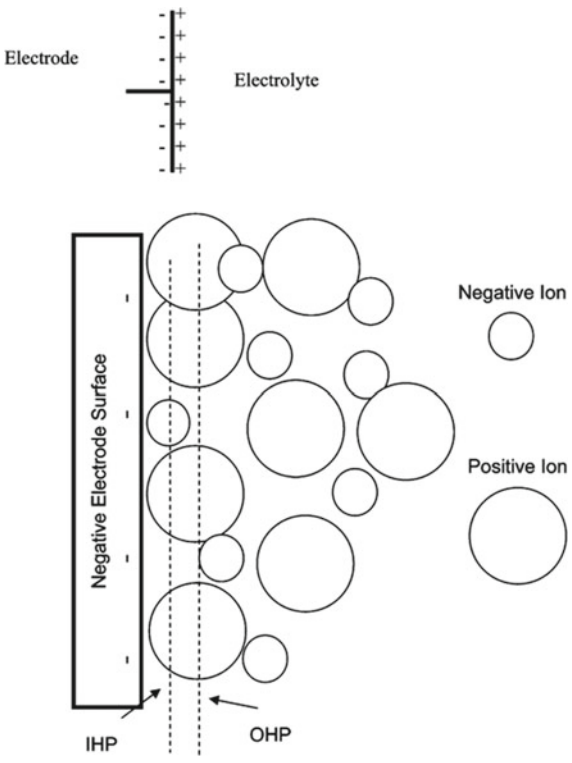

Fig. 5.5 Schematic representation of electrochemical double-layer capacitor. Reproduced with permission from Elsevier [4]

The double-layer capacitance of each electrode is calculated according to Eq. (5.1). Due to the smaller thickness of the double layer (fraction of nm in liquid electrolytes), the charged electrode/electrolyte interface has a high a real specific capacitance of 15–30 $\mu F\ cm^{-2}$. With electrodes having a large surface area ($> 1000\ m^2\ g^{-1}$) such as activated carbon, felts, and xerogels, capacitances as large as 200–300 $F\ g^{-1}$ can be achieved, which is far superior to the conventional capacitor [9]. Further, non-Faradaic processes are not associated with any chemical or compositional changes as there is no transfer of charge between electrolyte and electrode. Hence, EDLCs exhibit a great degree of reversibility in cyclical charge/discharge process with stable performance characteristics and have demonstrated cycle lives in excess of 500,000 cycles. Carbon and its various other forms are widely used as electrodes for EDLC with studies focused on increasing the surface area and reducing the matrix resistivity [10]. Different materials based on carbon which can be used for charge storage in EDLC electrodes are activated carbons, carbon nanofibres, carbon nanotubes, graphene, porous graphene, etc.

5.3.1.1 Activated Carbons

It is a type of carbonaceous material that possesses high surface area (internal porosity), which may be obtained by thermal or chemical treatment. The process by which the surface area can be increased is known as 'activation', and the resulting broad group of materials is known as activated carbon. Generally, physical activation is carried out at elevated temperatures between 750 and 1100 °C using oxidants, such as steam [11], carbon dioxide [12] or mixture of these gases [13]. Impregnating the precursor with activating agents, such as phosphoric acid [14], zinc chloride [15] and later pyrolysing between 400 and 800 °C in the absence of oxygen are the usual means of chemical activation. Due to its low cost (as it can be produced from carbonaceous materials, such as wood, coconut shell) and higher specific surface area than other carbon-based materials, activated carbon is widely used as electrode material in EDLCs. It utilizes a complex porous structure composed of micropores, mesopores and macropores to achieve the desired high surface area [16]. Activation does not produce any significant change in the morphology, dimension and electrical conductivity but leads to formation of new micropores and higher surface areas along with more number of basic oxygen groups [17].

5.3.1.2 Carbon Nanofibres

Carbon nanofibres (CNFs) are carbon materials with a cylindrical shape like carbon nanotubes (CNTs) but with structural and textural characteristics different from CNTs. CNFs are obtained from thermosetting of organic molecules such as cellulose, phenolic resins, polyacrylonitrile and pitch-based substrates. After extrusion, the nanofibre will be activated in a controlled oxidizing environment to obtain required

size and porosity. The pores obtained on the fibre surface provide a good accessibility to ions. High adsorption capacities and high adsorption rates have led CNFs to be widely used in EDLCs. CNFs usually exhibit diameters in the range of 100–300 nm with lengths up to 200 μm. They can be categorized into (i) high graphitic fibres and (ii) low graphitic fibres. The former can be obtained either by a catalytic vapour-grown procedure with a metal catalyst floating in the reaction media [18] or by catalytic chemical vapour deposition with the metal catalyst on a support [19]. These CNFs show a high electrical conductivity on the order of 1 S cm^{-1} for the compacted pellets and a low specific surface area of 10–50 m^2 g^{-1}. Their specific capacitance is very low (1–10 F g^{-1}) due to their low surface area. However, capacitance retention of these fibres at high currents is very high. However, activation can increase the specific surface area up to 100 m^2 g^{-1} leading to a moderate increase in specific capacitance value, i.e. 100 F g^{-1}.

Graphitic carbon nanofibres of second category may be obtained by (a) blending of polymers in which the polymer acts as the carbon source and provides porosity [20], (b) electrospinning of precursors [21], (c) using an anodic alumina as a template, which leads to CNFs with marked mesoporosity [22], (d) electrochemical decomposition of chloroform [23] and (e) flames of ethanol [24]. These CNFs possesses conductivity of 0.1 S cm^{-1} for compacted pellets, but their specific surface area is much higher (100–500 m^2 g^{-1}) giving a higher specific capacitance. The limitation of activated carbon fibres is that they are generally more expensive than the products of powder carbon [10].

5.3.1.3 Carbon Nanotubes

Carbon nanotubes became one of the most special materials since its discovery by Iijima and Ichihashi [25]. These have received great attention in the field of the fundamental research to applied perspectives. Numerous studies were carried out on CNTs due to its novel hollow tube structure, dimensions in the nanorange, high specific surface area and an excellent conductivity. CNTs are of two types namely single-walled (SWCNT) and multiwalled (MWCNT). Recent research trends show that there is an increasing interest in using CNTs as electrode materials for EDLCs [26]. Electrodes made from SWCNT show a high specific capacitance (180 F g^{-1}) and high-power density [27]. But electrodes made from MWCNT show a capacitance (135 F g^{-1}) less than SWCNT [9]. The high capacitance of SWCNT may be attributed to its high surface area accessible to electrolyte and good mechanical strength. Comparative study of the specific capacitance achieved with CNTs and activated carbon shows that the later one shows higher specific capacitance [28]. ECs made from CNT films (directly grown or by casting of colloidal suspension on to current collectors) show close rectangular CV curve even at a high scan rate of 1000 mV s^{-1} [29]. The high cost of production limits its application, but it can be used as conductive agent, in conjugation with other active materials for fabricating electrodes.

5.3.1.4 Graphene

Carbon atoms arranged in a monolayer honeycomb network is known as graphene. Graphene, a rising 2D honeycomb layer of sp^2-bonded carbon atoms is considered as mother of all carbon dimensionalities [30]. It is the planar thinnest known material in the world and the strongest ever measured [31]. Instead of its planar structure, graphene can be rolled into one dimensional CNTs, which is further subdivided depending on the number of graphene layers into SWCNTs and MWCNTs, also wrapped into zero-dimensional spherical fullerenes (Fig. 5.6) [32]. Graphene was first prepared by scotch tape method by attaching a tape onto graphite face and peeling off the tape [33]. It is important to clarify that graphene nanosheet (GNS) refers to graphene in its standard form, i.e. a single layer of graphene. In addition to single layer graphene, few layer graphene (FLG) has also been studied [34, 35]. Before synthesis of graphene nanosheets, it should be oxidized to graphene oxide (GO) and reduced chemically or electrochemically [36]. The synthetic process determines not only the properties but also its application in a particular field which has led to immense interest in research field. The extensive use of this material is due to the spectacular properties like high electrical and thermal conductivity [37], high specific surface area [38] and high mechanical strength [39]. Due to these properties, they are used in many technological applications such as in nanocomposites [40], sensors [41], nanoelectronics [42], batteries [43], supercapacitors [44, 45] and hydrogen storage [46].

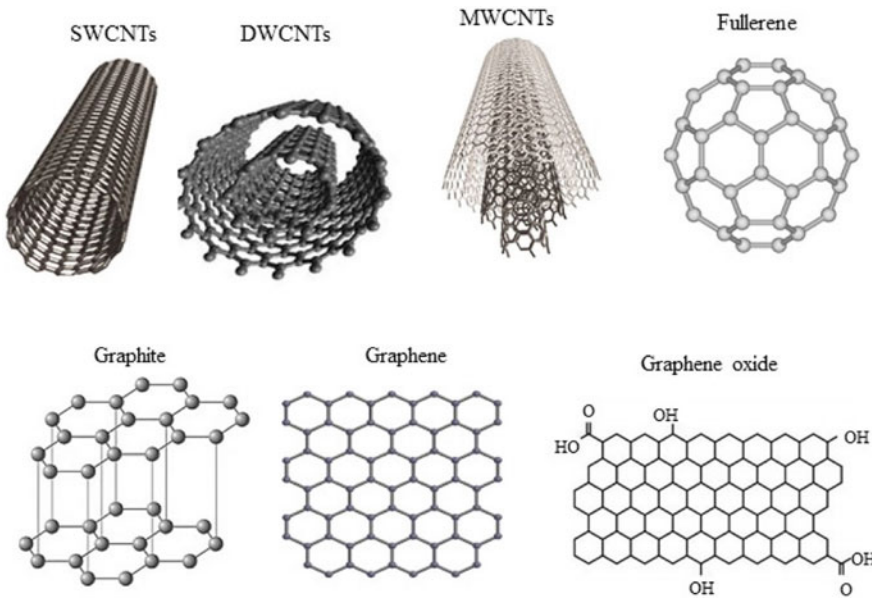

Fig. 5.6 Various structures of carbon materials. Reproduced with permission from Elsevier [32]

Numerous bottom–up such as chemical vapour deposition [CVD]; epitaxial growth onto metal catalyst substrates and arc discharge method and top down such as micromechanical cleavage, reduction of graphite oxide, sonication and exfoliation approaches have been adopted to synthesize graphene-based materials. But the widely accepted one is the chemical exfoliation method, i.e. oxidation of graphite to graphene oxide and subsequent reduction of graphene oxide to graphene. Graphene-based supercapacitors have high specific capacitances ranging from 197 to 350 F g^{-1} in aqueous electrolytes [45, 47].

5.3.1.5 Porous Graphene

Porous graphene is a new kind of spongy planar sheet material resembling graphene with some hole/pores created by the removal of sp^2 carbon atoms. Depending on their pore diameters, they are categorized as microporous (diameter < 2 nm), mesoporous (diameter from 2 to 50 nm) and macroporous (diameter > 50 nm) material [48]. Depending on the fabrication methods used, the pore size varies from atomic to nanoscale dimensions. The mesoporous and macroporous structures are used in chromatographic separations, as catalyst for water and air purification and as electrochemical capacitors [49, 50].

The pioneering work on porous graphene was first done by Bieri et al. [51]. They used cyclohexa-m-phenylene as a precursor and produced a 2D polyphenylene networks with regular distribution of pores of single atom wide and subnanometer periodicity by the aryl–aryl coupling on a metal surface. The 2D polyphenylene porous graphene is shown in Fig. 5.7. The structure of the precursor CHP resembles graphene, and in porous graphene the phenyl rings are missing periodically. Structurally graphene's unit cell consists of two carbon atoms, whereas in polyphenylene, the unit cell consists of 3 × 3 supercells of 2 C_6H_3 rings linked by C–C bonds [51].

Till date, the preparation of porous graphene includes chemical bottom–up approach through the surface assisted aryl–aryl coupling reaction [52], etching of graphene sheets by MnO_2 [53] and in-situ hydrothermal polymerization/carbonization of biomass [34]. Physical methods of preparation involve electron beam irradiation [54], helium ion bombardment [55] and laser irradiation [56]. Such methods involve a greater number of steps to produce porous network and requires expensive conductive substrate. Further, the yield is also very poor, and sometimes microporous structure is produced which hinders its practical applications.

5.3.2 Pseudocapacitors

Pseudocapacitors store charge Faradaically, through the transfer of charge between electrode and electrolyte in comparison to EDLCs, which store charge electrostatically. Processes like electrosorption, redox reactions and intercalation help in the

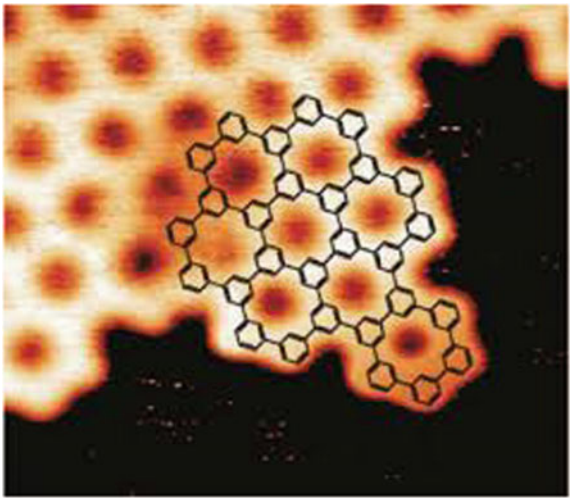

Fig. 5.7 STM image of 2D polyphenylene model for porous graphene. Reproduced with permission from Royal Society of Chemistry [51]

accomplishment of this which allows the pseudocapacitors to achieve greater capacitances and energy densities [57, 58]. The charges transferred in these reactions are voltage dependent. The capacitance can be calculated using the following Eq. (5.4).

$$C = \frac{Q_{\text{tot}}}{V_{\text{tot}}} \tag{5.4}$$

where the 'Q_{tot}' and 'V_{tot}' are the total charge and voltage change for a charge or discharge of the electrode. The most widely used electrode materials for pseudocapacitors are transition metal oxides or hydroxides [59] and electronically conducting polymers [60].

5.3.2.1 Conducting Polymers

Conducting polymers are known to possess a relatively high capacitance, conductivity, energy and power density values. In addition to this, they have low ESR value and are cost-effective in comparison to other carbon-based materials [61]. But the major disadvantage is the lack of cycling stability due to high mechanical stress during the oxidation and reduction reactions [8, 60]. In addition to this, dearth of efficient n-doped-type materials based on conducting polymers has hindered the development of conducting polymer pseudocapacitors for practical applications [62].

5.3.2.2 Metal Oxides

Metal oxides are suitable electrode material for supercapacitor due to abundant availability, low cost, environmentally friendly and easy synthetic process [59]. Generally, metal oxides provide high surface redox properties leading to high energy density in Faradaic supercapacitors [1]. The achieved high energy density in metal oxides is far more than carbon-based materials, and it also has high stability than polymeric substrates. Metal oxides exhibit Faradaic electrochemical reactions between electrode materials and ions within an appropriate potential window [63]. The primary criteria for the metal oxides to be used as an electrode material are (a) it must be electronically conductive, (b) metals must possess variable oxidation states and (c) there must be provision for intercalation of protons into the oxide lattice on reduction and out of the lattice on oxidation, allowing easy interconversion of O^{2-} and OH^{-} [2]. Some of the finest pseudocapacitive materials, such as RuO_2, MnO_2, ZnO, MoO_2, SnO_2, Co_3O_4, NiO, Fe_2O_3, Fe_3O_4, V_2O_5, MoO_3, TiO_2 and WO_3, are used as an electrode material for supercapacitor. In the recent years, Fe_2O_3 and Fe_3O_4 have emerged as new type of pseudocapacitive electrode material due to their low-cost, ecofriendly nature and high abundance [64, 65].

5.3.3 Hybrid Capacitors

Combining the double-layer capacitor and pseudocapacitor a new type of capacitor named as hybrid capacitors can be generated. This capacitor provides high power and energy density in comparison to the conventional capacitors. This system also shows high-rate capability and cycling stability. Based on their electrode configuration they are grouped into three types: composite, asymmetric and battery type, respectively [6].

5.3.3.1 Composite

Composite electrodes are fabricated by the integration of carbon-based precursors with either conducting polymers or metal oxide nanostructures containing both physical and chemical charge storage processes jointly in a single electrode. Incorporation of carbon-based materials provides better contact between the electrolyte and pseudocapacitive material due to higher surface area leading to a double layer of high capacitance. Further, the pseudocapacitive materials also increase the capacitance through Faradaic reactions [66, 67].

5.3.3.2 Asymmetric

Combination of Faradaic processes and non-Faradaic processes by pairing of an EDLC electrode with a pseudocapacitor electrode led to the generation of asymmetric supercapacitor. In particular, the coupling of an activated carbon negative electrode with a conducting polymer positive electrode has attained enormous attention [68]. Due to the unavailability of an efficient, negatively charged material, conducting polymer material has limited success in pseudocapacitor field. But the application of a negatively charged, activated carbon electrode solved this problem. While conducting polymer electrodes generally have higher capacitances and lower resistance than activated carbon electrodes, they have lower maximum voltages and less cycling stability. Asymmetric hybrid capacitors strike a compromise to achieve higher energy and power densities with better cycling stability.

5.3.3.3 Battery Type

Battery-type hybrids are an answer to the demand for supercapacitors with higher energy densities and batteries with higher power densities obtained by combining a supercapacitor electrode with a battery electrode. These are characterized by higher life cycle with excellent recharging capacities. The gap between the supercapacitors and batteries is bridged by using activated carbon as one electrode and nickel hydroxide or lead dioxide as another [69]. Full potential of these hybrid materials can be exploited by further research [70].

5.4 Electrolytes

One of the important components of EC is the electrolyte. These exist in contact with the active material and also reside partially inside the separator [2]. A good electrolyte should be economic and of high purity and possess large voltage window, low resistivity and high electrochemical stability. It should also have low viscosity, volatility and toxicity. The electrolytes ideally should have high ionic concentration and low solvated ionic radicals. Electrolytes belong to three major kinds, namely (a) aqueous, (b) organic and (c) ionic liquids.

5.4.1 Aqueous Electrolytes

Aqueous electrolytes deliver higher ionic concentration, lower resistance in addition to smaller ionic radius which leads to higher capacitance and power density of the ECs. Electrolytes like H_2SO_4, KOH, Na_2SO_4 and NH_4Cl hold an advantage of having simple synthetic procedure for obtaining highly pure material. But the major

drawback in improving the energy and power density while using aqueous electrolyte is the small potential window of about 1.2 V.

5.4.2 Organic Electrolytes

High-voltage window of around 3.5 V of organic electrolyte makes it a potential replacement of aqueous electrolyte. Solvents such as acetonitrile, propylene carbonate, salts based on tetrafluoroborates are commonly used [2]. Although acetonitrile has a power to dissolve higher concentration of salts its toxicity is known to affect the environment adversely. On the other hand, propylene carbonate is an ecofriendly electrolyte with wide range of voltage window and operating temperatures. The major disadvantage of organic electrolytes is the charge-induced depletion and safety concerns associated with the usage. In addition to it, high precautions must be taken to keep the water content below 3–5 ppm to avoid reduction in the voltage of the ECs [2].

5.4.3 Ionic Liquids

Ionic liquids (ILs) are obtained by providing heat to the salts to acquire them in molten state by counterbalancing the crystal lattice energy [2]. They exhibit low vapour pressure and flammability and possess high chemical and thermal stability. Higher conductivity of around 10 mS cm^{-1} and wide window of stable electrochemical activity of 2–6 V make them potential candidates as electrolytes for ECs [71, 72]. In addition, they provide a well-recognized ion size due to lack of solvation shell. While the quaternary ammonium salts are used for room temperature studies, sulphonium and phosphonium salts are used for lower temperatures [73].

5.5 Separator

A separator is used to prevent the electrical contact between the electrodes. However, it should allow the rapid transfer of ionic charge by being permeable to the ions. High electrical resistance and low thickness are the desired features for a separator. Paper or polymer-based separators are often used in ECs in combination with aqueous and organic electrolytes.

5.6 Electrode Characterization and Device Fabrication

The three-electrode setup consists of (a) reference electrode which is usually saturated calomel electrode or Ag/AgCl electrode, (b) counterelectrode which is usually a platinum wire and (c) working electrode which is usually sheet of Ni or stainless steel coated with the electroactive material under consideration. The ink is prepared by mechanically mixing the electroactive material with another material like acetylene black to improve the conductance, in presence of a binder in a definite ratio [35, 45, 50]. This is later coated on to the sheet or carbon paper or carbon cloth or Ni foam using various techniques like Doctor's blade technique or layer brush coating technique to get a working electrode. The symmetrical supercapacitor setup consists of stainless steel panels which act as current collectors, separator which is usually filter paper soaked in the electrolyte, working electrode in contact with the electrolyte which could be either aqueous, organic or ionic liquid [45, 74, 75].

The electrodes and the device are characterized by cyclic voltammetry (CV), galvanostatic charge–discharge (GCD) and electrochemical impedance spectra (EIS) to study the electrochemical properties [74–79].

The specific capacitance values from the CV curves and GCD curves can be calculated according to Eqs. (5.5) and (5.6), respectively.

$$C_s = \frac{nA}{\Delta V \times m \times v} \tag{5.5}$$

$$C_s = n \times \frac{I \times \Delta t}{m \times \Delta V} \tag{5.6}$$

The specific capacity can be calculated from the GCD data for 3-electrode system and supercapacitor device by using Eqs. (5.7) and (5.8), respectively.

$$Q_s = \frac{I \times \Delta t}{m} \tag{5.7}$$

$$Q_s = C_s \times \Delta V \tag{5.8}$$

The energy and power density can be calculated according to Eqs. (5.9) and (5.10), respectively.

$$E = \frac{1}{2} C_s \Delta V^2 \frac{1000}{3600} \tag{5.9}$$

$$P = \frac{E}{\Delta t} \times 3600 \tag{5.10}$$

where C_s is specific capacitance (F g^{-1}), Q_s is the specific capacity (C g^{-1}), E is energy density (W h kg^{-1}), P is power density (W kg^{-1}), A is the integrated area of

the CV curve, ΔV is the maximum potential window (V), m is the deposited mass on one single electrode (g) and ν is the scan rate (V s^{-1}), $\frac{I}{m}$ is the applied current density, and Δt is the discharging time. For 3-electrode system, $n = 1$ and for 2-electrode system $n = 2$ (owing to the formation of series capacitance in symmetrical supercapacitor device) [3, 50, 59, 67].

The coulombic efficiency η (%) can be determined from the GCD curves using Eq. (5.11).

$$\eta\,(\%) = \frac{\Delta t_{\mathrm{d}}}{\Delta t_{\mathrm{c}}} \times 100 \tag{5.11}$$

where Δt_{d} and Δt_{c} are the discharging and charging times, respectively.

The individual contributions to the total capacitance can be estimated by using Eq. (5.12) [80, 81].

$$C_{\mathrm{s}}(T) = C_{\mathrm{EDLC}} + C_{\mathrm{P}} \tag{5.12}$$

where $C_{\mathrm{s}}(T)$ is the total specific capacitance, C_{EDLC} and C_{P} are the respective contribution of double-layer capacitance and pseudocapacitance [50, 59].

5.7 Synthesis of Graphene Oxide (GO) and Graphene

The pioneering work on the synthesis of graphene oxide was done by Brodie [82], where he treated graphite with $KClO_3$ in 1:3 weight ratios in strong fuming nitric acid; however the major drawbacks of this method was longer reaction time of 4 days, extensive purification process, generation of toxic and explosive gases which stifled further study. Later in, 1898, Staudenmaier proposed a simplified method for GO synthesis in one reaction vessel by taking fuming nitric acid, H_2SO_4 with $KClO_3$ in multiple proportions [83]. However, the reaction time was still 4 days, and evolution of explosive ClO_2 gas was observed during the synthesis [83]. Therefore, these two methods were unsuitable for the oxidation of graphite.

In 1958, Hummers and colleagues developed a safe method for the synthesis of GO, which has been widely accepted for the large-scale GO synthesis [84]. In this method, oxidation was done in a reaction vessel by using an anhydrous mixture of H_2SO_4, $NaNO_3$, and $KMnO_4$ as oxidizing agents. Also, the reaction temperature and time were very less [84]. The advantages of Hummers' protocol include formation of no toxic and explosive gases, and the use of strong oxidant, i.e. $KMnO_4$ ensures the reduction in duration of completion of reaction from several days to few hours. However, some limitations such as formation of NO_2/N_2O_4 due to introduction of $NaNO_3$, removal of Na^+ and NO^{3-} ions from wastewater, while purification process and incomplete oxidation process resulting in graphite-core/GO-shell particles are observed. After 40 years, Kovtyukhova and colleagues prepared graphite oxide by using Hummers' protocol with some modifications, named as modified Hummers'

method [85]. The authors stated that before GO synthesis, an additional pre-oxidation step was necessary, otherwise incomplete oxidation of graphite-core/GO-shell particles was observed. The pre-oxidation was carried out by treating graphite with H_2SO_4 and 1:1 weight ratio of $K_2S_2O_8$:P_2O_5. Later, Stankovich et al. prepared GO by using Hummers' method and sonicated to form a stable graphene oxide suspension [86]. The reduction of graphene oxide to graphene sheets was carried out by using hydrazine hydrate over a period of 24 h. Later in 2010, Marcano's group reported an improved version of the Hummers method [87]. Removing $NaNO_3$ and treating graphite with a 9:1 mixture of concentrated H_2SO_4 and H_3PO_4 in one reaction vessel leading to a high degree of oxidation with no release of toxic gases. The oxidation product was also larger in quantity, which is a significant achievement for the large-scale graphene oxide synthesis. In recent years, further modification of Hummer's method was carried out by Bhat's group, wherein graphite flakes were stirred with H_2SO_4 and to the cooled solution $KMnO_4$ was added. Later, H_2O_2 was added to obtain GO [75, 88, 89]. This method was a modification of an earlier procedure, wherein $NaNO_3$ was added prior to the addition of $KMnO_4$ [90]. Thus, formation of oxides of nitrogen was eliminated making the procedure safer and applicable for large-scale production. They also reported GO synthesis by modifying the method reported by Marcano's group by addition of H_2O_2 at a later stage resulting in pure and large quantities of GO product [3, 50].

5.8 Fe_2O_3-Graphene Composites for Supercapacitor Applications

5.8.1 Hydro/Solvothermal Method

Hydrothermal method is a fascinating route for the synthesis of nanomaterials and by adopting this route various nanostructures of α-Fe_2O_3 such as nanotubes, nanocubes, nanodots, nanoplates, nanoring like structures have been prepared, and its composites with graphene have been studied thoroughly (Fig. 5.8). The electrochemical data from several works revealed enhancement in the specific capacitance value of the composite structures in comparison to the components due to the synergistic effect. Some of these are summarized below. The α-Fe_2O_3 nanotubes–RGO composite prepared by Lee's group exhibited a capacitance value of 215 F g^{-1} in comparison to 30 F g^{-1} exhibited by the nanotubes at a scan rate of 2.5 mV s^{-1} with only 8% reduction in value after 700 cycles and remained totally unchanged up to 2000 cycles at a high current density of 5 A g^{-1} [91]. The excellent electrochemical performance of the composites was attributed to the high surface area of hollow α-Fe_2O_3 nanotubes and the incorporation of RGO which boosted the conductive pathway for the fast and reversible reaction. Another attempt was made by Chaudhari's group to synthesize cube like structure of α-Fe_2O_3 on multimodal porous carbon with very high surface area for supercapacitor applications [92]. The prepared composite has

delivered double the capacitance value in comparison to porous carbon and four times higher value than that of α-Fe_2O_3. The enhanced electrochemical performance of the composite was mainly accredited to the high structural stability, conductivity and porosity. Hydrothermal method was adopted by Zhao and co-workers for the doping of hetero atoms (N-doping) and the prepared N-doped graphene/Fe_2O_3 nanoparticles composite study showed that nitrogen doping in the graphene composite ameliorated the capacitance value to 260 F g^{-1} at a high current density of 2 A g^{-1} in comparison to a value of 150.4 F g^{-1} obtained for graphene/Fe_2O_3 [93]. Additionally, 82.5% initial capacitance value was retained after 1000 cycles at a current density of 2 A g^{-1} by the N-doped graphene/Fe_2O_3 nanocomposite in comparison to 61.4% by graphene/Fe_2O_3. The superior electrochemical performance of the N-doped composite was primarily ascribed to the good electronic conductivity induced by the extra lone pair of electrons from nitrogen (pyrrolic) and more active sites. Similarly, Liu's group studied the effect of N-doping in the amelioration of electrochemical performance of supercapacitors and synthesized Fe_2O_3 nanodots-N-doped graphene through solvothermal method [94]. The synthesized electrode material depicted excellent electrochemical performance in KOH electrolyte with a high specific capacitance value of 274 F g^{-1} at a current density of 1 A g^{-1} and even retained capacitance value of 140 F g^{-1} at a current density of 50 A g^{-1}. Also, the electrode material showed superior cyclic stability up to 100,000 cycles with 75% initial capacitance retention at a high current density of 5 A g^{-1}. Such an excellent electrochemical performance is mainly attributed to the good combination of Fe_2O_3 nanodots and appropriate doping of nitrogen in the composite, which offered plenty of electroactive sites for the electron transfer and diffusion and reduced the volume change during the charge–discharge cycles. Wang's group aimed to increase the electrochemical performance of the anode materials in supercapacitors [95]. Single-crystalline Fe_2O_3 nanoparticles grown over graphene hydrogel by hydrothermal route displayed a high specific capacitance value of 908 F g^{-1} at a current density of 2 A g^{-1} and 622 F g^{-1} at a higher current density of 50 A g^{-1}, whereas the Fe_2O_3 nanoparticles and graphene hydrogel displayed a capacitance value of 91 F g^{-1} and 272 F g^{-1} at a current density of 2 A g^{-1}, respectively. The anode material displayed a retention value of 75% after 200 cycles at a scan rate of 20 mV s^{-1}. The retention value of Fe_2O_3 nanoparticles was only 51%. The observed superior electrochemical performance of the composite structure is mainly ascribed to the synergistic effect from the constituent materials. Song's group fabricated nano-Fe_2O_3 and 3D graphene aerogel composite through hydrothermal method for the utility in supercapacitors [96]. The prepared supercapacitor depicted a capacitance value of 81.3 F g^{-1} at a current density of 1 A g^{-1} and 62.7 F g^{-1} at a current density of 10 A g^{-1} in a wide potential window in aqueous 0.5 M Na_2SO_4 electrolyte. Yang and co-workers synthesized porous α-Fe_2O_3-graphene composites to enhance the electrochemical performance in supercapacitors [97]. The hydrothermal route led to a high specific surface area and high pore volume, which resulted in high capacitance value of 344 F g^{-1} at a current density of 3 A g^{-1} and retention of 97% of its initial capacitance value after 50,000 cycles at a high current density of 10 A g^{-1}, suggesting its utility in high-performance supercapacitor applications. The high electrochemical performance of

the composite structure is mainly ascribed to the synergetic effect of optimal loading of porous α-Fe_2O_3 nanostructures and crumpled structure of graphene nanosheets, which facilitated the smooth passage of electrolyte ions, shortened ion diffusion path length and enhanced electrical conductivity. The nanoplate kind α-Fe_2O_3 structures decorated on interconnected RGO sheets prepared through a facile hydrothermal method by Quan and co-researchers have shown superior electrochemical properties as compared to α-Fe_2O_3 nanoplates [98]. The composite depicted a high capacitance value of 903 F g^{-1} in comparison to 347 F g^{-1} by the α-Fe_2O_3 nanoplates at a current density of 1 A g^{-1}. 70% initial capacitance retention value by the composite after 1000 cycles at a high current density of 5 A g^{-1} was ascribed to high surface area with mesoporous structure and high electrical conductivity of the electrode material. Gao and co-workers adopted a solvothermal method to prepare quasi-hexagonal nanoplates-graphene nanocomposite structure with high surface area compared to Fe_2O_3 nanoplates [99]. A high capacitance value of 1083 F g^{-1} is shown by the material at a current density of 2 A g^{-1}. With tenfold increase in the current density electrode material showed 199 F g^{-1} capacitance, which is 18.4% of the initial value, suggesting the good rate capability. The composite material displayed capacitance retention of 75% after 1000 cycles at a high current density of 4 A g^{-1}, whereas the Fe_2O_3 only retained 21% after 1000 cycles. Zhu and co-workers prepared thumb ring like α-Fe_2O_3 and RGO composites through hydrothermal method as an anode for supercapacitors [100]. The composite delivered a good capacitance value of 255 F g^{-1} at a current density of 0.5 A g^{-1} with 90% retention value after 10,000 cycles at a high current density of 10 A g^{-1} in a potential window of 1.2 V. Zhang's group prepared core–shell nanostructures of 3D graphene anchored on Fe_2O_3@C through a scalable and simple one-pot hydrothermal process followed by annealing [101]. The highly conductive 3D carbon network enabled fast ion and electron transport. In addition to it, the remarkable specific surface area contributed to a good performance with high specific capacitance, enhanced rate capability and excellent cyclic stability. The composite electrode material showed a capacitance value of 211 F g^{-1} at a current density of 0.5 A g^{-1} and 177 F g^{-1} at a current density of 20 A g^{-1} with no decay in the initial capacitance value after 2500 cycles. It is worth noting that by changing the compounds or adjusting the heating strategy, various types and structures of 3D carbon composite materials can be developed. Gao's group adopted a hydrothermal method followed by thermal reduction method to prepare graphene-Fe_2O_3 nanoparticle composite [102]. The microscopic results displayed the anchoring of iron oxide nanoparticles over the graphene surface providing rich redox active sites for the electrochemical process. Owing to the availability of plenty of redox chemical sites, the electrode material displayed a high capacitance value of 378.7 F g^{-1} at a current density of 1.5 A g^{-1} and retained 88.8% initial capacitance retention value after 3000 cycles at the same current density. Furthermore, the prepared asymmetric supercapacitor by using graphene as positive electrode and graphene-Fe_2O_3 composite as negative electrode has displayed high energy and power density at higher applied current densities, suggesting its excellent power capabilities. The supercapacitor device retained 78% of its initial value after 3000 cycles at a high current density of 5 A g^{-1}. The superior electrochemical performance of the composite electrode is

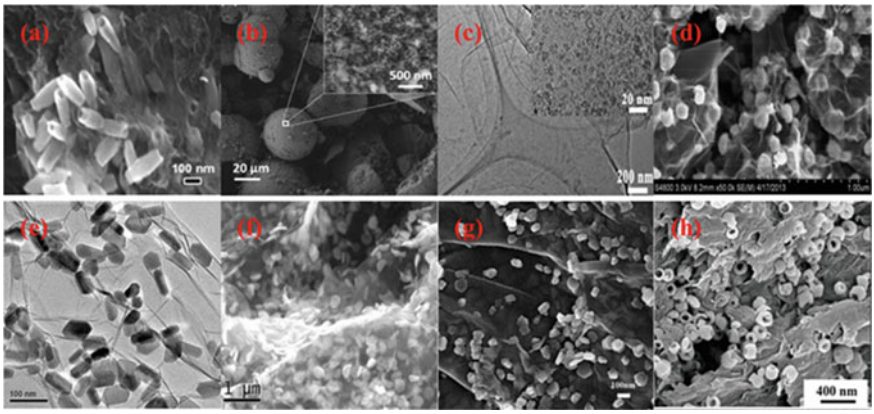

Fig. 5.8 **a** FESEM image of α-Fe_2O_3 nanotubes–RGO composite. Reproduced with permission from Royal Society of Chemistry [91]. **b** Fe_2O_3 nanoparticles over graphene surface. Reproduced with permission from Elsevier [93]. **c** TEM image of Fe_2O_3 nanodots@nitrogen-doped graphene. Reproduced with permission from American Chemical Society [94]. **d** FESEM image of Fe_2O_3 nanoparticles grown over graphene hydrogel. Reproduced with permission from Elsevier [95]. **e** TEM image of α-Fe_2O_3 nanostructures on RGO sheets. Reproduced with permission from American Chemical Society [97]. **f** FESEM image of α-Fe_2O_3 nanoplates on RGO sheets. Reproduced with permission from Elsevier [98]. **g** FESEM image of quasi-hexagonal Fe_2O_3 nanoplates on graphene sheets. Reproduced with permission from Elsevier [99]. **h** α-Fe_2O_3 nanostructures on RGO sheets. Reproduced with permission from American Chemical Society [100]

mainly ascribed to the sufficient number of accessible active sites for electrochemical reaction, which provided a pathway for smooth passage of electrolyte ions diffusion into the interior pores.

5.8.2 Self-assembly Method

Self-assembly technique is one of the most fascinating synthetic techniques in nanoscience. In this route, the nanostructures are designed at the atomic and molecular level. Lin's group synthesized mesoporous carbon/iron oxide composites by cooperative self-assembly method (Fig. 5.9) and fabricated a symmetrical supercapacitor device [103]. The resulted nanocomposites (neat mesoporous carbon) have shown a high surface area and high pore volume, which led to a capacitance value of 235 F g^{-1} at a current density of 0.5 A g^{-1} and retained 51% of the initial capacitance value at a current density of 10 A g^{-1} in 1 M Na_2SO_3 electrolyte. The fabricated supercapacitor has exhibited more than 95% initial retention value after 380 cycles at a current density of 1 A g^{-1}. Similarly, Zhang's group adopted colloidal electrostatic self-assembly method followed by hydrothermal reduction method to prepare 2D-layered α-Fe_2O_3–RGO flexible films for electrochemical capacitors [104]. The prepared composite material displayed a high gravimetric capacitance

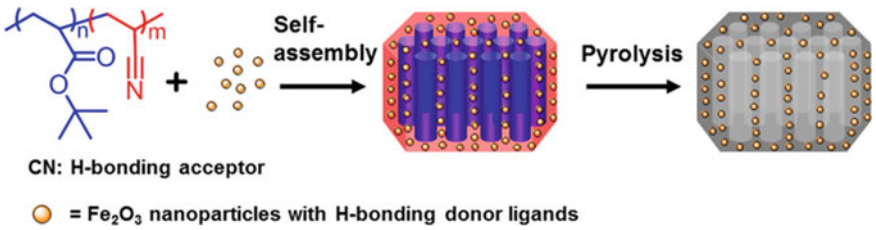

Fig. 5.9 Self-assembly method for the preparation of Fe_2O_3–RGO composite structure. Reproduced with permission from American Chemical Society [103]

value of 714 F g^{-1} at a current density of 1 A g^{-1}, whereas α-Fe_2O_3 has shown only 274 F g^{-1}. The fabricated symmetrical supercapacitor by using this composite has exhibited retention of 79% capacitance value after a long 1000 charge–discharge cycles at a high current density of 2.5 mA cm^{-2}. Wu's research group adopted metal ion induced self-assembly followed by calcination method to produce novel ultrasmall amorphous Fe_2O_3 nanodot-graphene aerogel nanocomposite structure with a high surface area of 261.7 m^2 g^{-1} with improved energy storage properties [105]. The high surface area and good pore volume provided more electroactive sites for ion transport, resulting in a high capacitance value (347 F g^{-1}) and high capacitance retention value of 94% after 2500 cycles at 5 A g^{-1} along with high energy and power density value in a wide potential window of 1.5 V. The method opened up a new strategy to design new electrode materials of high surface area for energy storage devices.

5.8.3 Thermal Decomposition Route

Thermal decomposition route is an attractive one for the synthesis of ultrafine nanoparticles. Xia's group synthesized hematite quantum dots functionalized on graphene sheets for high energy density supercapacitors [106]. The large surface area of the Fe_2O_3/FGS composites undoubtedly shortened the ion diffusion path and led to improved pseudocapacitive performance of the composite electrodes with a capacitance value of 347 F g^{-1} at a scan rate of 10 mV s^{-1}. As an asymmetric supercapacitor electrode material with MnO_2 the supercapacitor device (2 V) displayed a high energy density value of 50.7 W h kg^{-1} while maintaining a power density of 100 W kg^{-1}. Apart from this, the device retained 95% of the capacitance after 5000 cycles at a current density of 0.5 A g^{-1}.

5.8.4 Template-Assisted Method

Ordered mesoporous carbon/Fe_2O_3 nanocomposites were successfully synthesized by Hu and co-workers for high-performance supercapacitors [107]. The template-assisted method led to the formation of a mesoporous network with high specific surface area. The obtained capacitance value for the composite was 264 F g^{-1} at a scan rate of 5 mV s^{-1} with 90% retention of the capacitance after 1000 cycles. The synergistic effects of the dual-template method demonstrated in this work had a significant impact on the design of electrode materials on both the mesoscale porous structure and macroscale morphology and could be applied to other electrochemical energy storage systems to improve both energy density and power density.

5.8.5 Wet Chemical Route

Sun's group prepared Fe_2O_3-graphene nanosheet composite through wet chemical method by engineering highly porous nanostructures using ionic liquids to ameliorate energy density and power density values [108]. The composite electrode displayed a capacitance value of 143 F g^{-1} at a current density of 0.2 A g^{-1} as compared to Fe_2O_3, which displayed a capacitance value of 53.5 F g^{-1}. The prepared asymmetric supercapacitor (4 V) by using Fe_2O_3-graphene nanosheet composite and activated polyaniline-derived carbon nanorods displayed a high energy density value of 177 W h kg^{-1} at a power density of 200 W kg^{-1}.

5.8.6 Gas Liquid Diffusion Method

Huang's group synthesized flexible and transparent supercapacitor electrode made up of biographene-wrapped Fe_2O_3 nanowire networks through a bio-inspired gas liquid diffusion method [109]. The flexible film showed an aerial capacitance of 3.3 mF cm^{-2} at a scan rate of 10 mV s^{-1}, which was higher than the value of graphene films. The composite film had high power density of 191.3 W cm^{-3}, an energy density of 8 mW h cm^{-3} and superior cycling stability up to 10,000 cycles with 92% retention of initial capacitance value. The superior electrochemical performance of the flexible electrode was mainly ascribed to the nanowire structure of Fe_2O_3, and the wrapping of graphene on the nanowires, which not only improved the capacitance but also improved the cyclic stability by enhancing the ion transport rate through the 3D structure (Fig. 5.10).

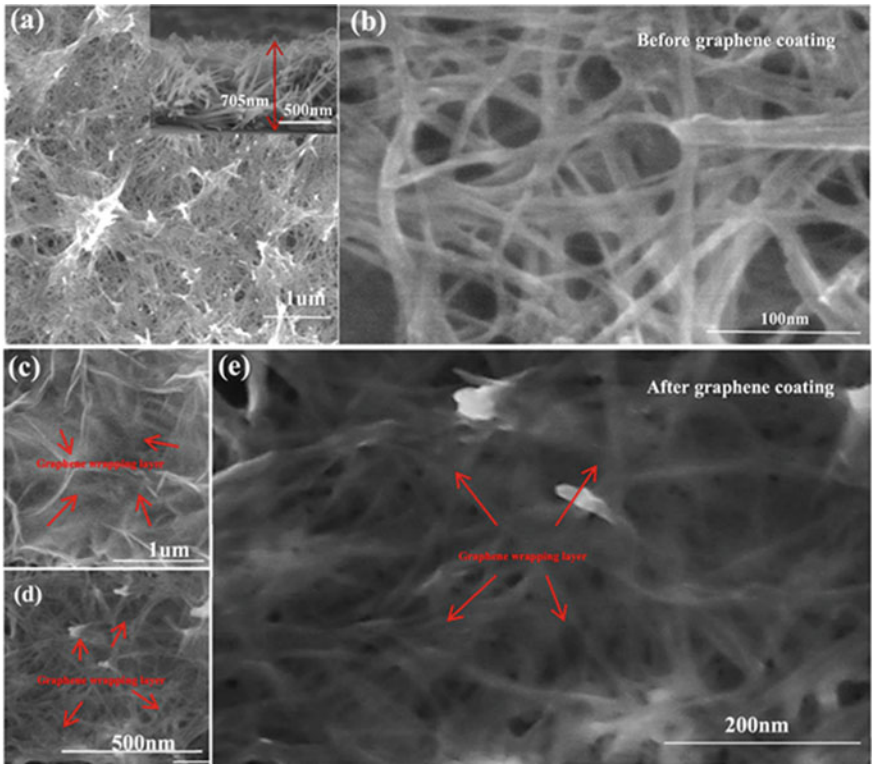

Fig. 5.10 **a** Low- and **b** high-resolution SEM micrographs of Fe_2O_3 nanowire; **c**, **d** low- and **e** high-resolution SEM micrograph of Fe_2O_3 nanowire@graphene surface. Reproduced with permission from IOP Science [109]

5.8.7 Electrochemical Method

Yang's group prepared electrochemically reduced graphene oxide sheet iron oxide composites and used it as binder-free electrode material for supercapacitors [110] [Fig. 5.11]. The obtained composite material has shown good mechanical strength and displayed a good capacitance value of 235 F g^{-1} at a scan rate of 10 mV s^{-1}, and initial capacitance retention value of 92% after 2000 cycles at a current density of 1 A g^{-1}.

5.8.8 Microwave Method

Saraf and co-workers adopted a two-step process consisting of precipitation of starting precursors followed by microwave heating for the formation of reduced

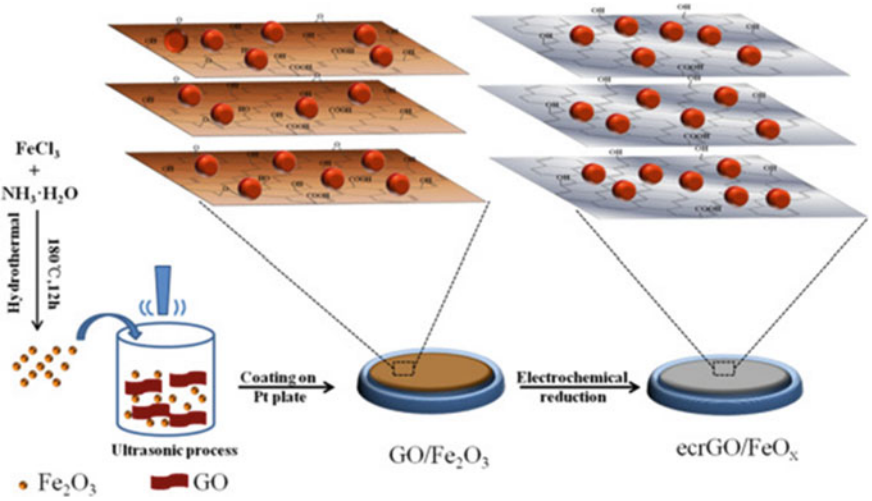

Fig. 5.11 Schematic illustration for the fabrication of electrochemical synthesized RGO/Fe_2O_3 electrodes. Reproduced with permission from Elsevier [110]

graphene oxide-Fe_2O_3 nanocomposites [111] [Figs. 5.12 and 5.13]. The composite structure rendered excellent capacitance value of 577.5 F g^{-1} at a current density of 2 A g^{-1} and produced a high capacitance value of 437.5 F g^{-1} at a current density of 10 A g^{-1}, which suggests the good rate capability of the electrode material. Further, the electrode material displayed 85.7% retention of initial capacitance value after 1000 cycles at a current density of 2 A g^{-1}. The electrode material delivered high energy and power density values in high current range.

5.8.9 Mechanical Agitation Method

Chen's group synthesized α-Fe_2O_3–RGO composites through in-situ process followed by mechanical agitation method [112]. The microscopic analysis revealed that the α-Fe_2O_3 nanoparticles densely covered the RGO sheets, forming a compact structure. The composite structure of α-Fe_2O_3 and RGO not only prevented the agglomeration of nanoparticles and restacking of RGO sheets but also sustained the severe volume change during the repeated electrochemical cycles. The nanocomposites gave a high capacitance value of 920 F g^{-1} at a current density of 2 A g^{-1}. The obtained good electrochemical result is mainly ascribed to the synergetic effect of the components of the composite.

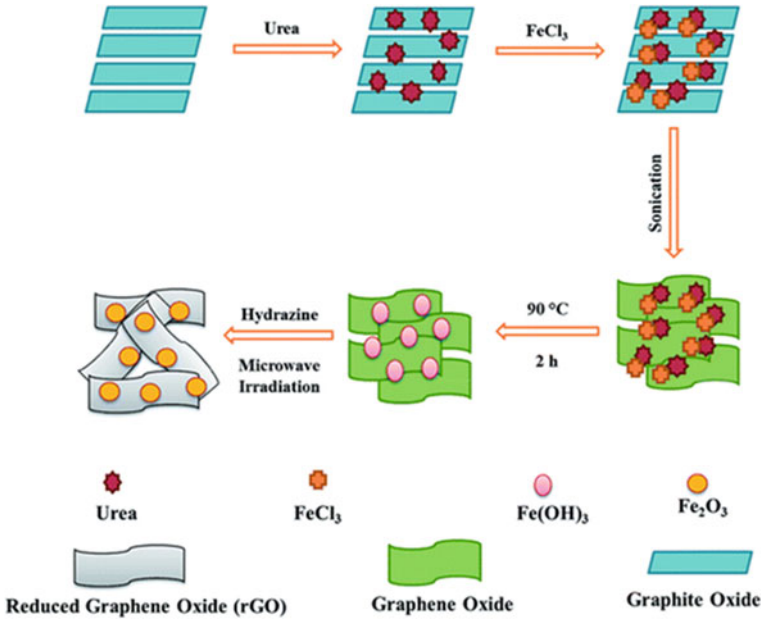

Fig. 5.12 Schematic representation of synthesis of RGO–Fe_2O_3 composite. Reproduced with permission from Royal Society of Chemistry [111]

5.8.10 Novel Intercalation Method

Haridas and co-workers fabricated a hybrid supercapacitor consisting of Fe_2O_3 nanorods and graphene sheets through a novel intercalation method followed by calcination of the intermediates in air [64] [Fig. 5.14]. The hybrid composites possessed a high conductivity value of 3.1×10^6 S cm^{-1}. The high electrical conductivity and low resistivity of the hybrid composite structure resulted in a high capacitance value of 1135 mF cm^{-2} at a scan rate of 5 mV s^{-1} and 815 mF cm^{-2} at a current density of 0.5 mA cm^{-2} with 55% retention of capacitance after 10,000 cycles at a high current density of 4 mA cm^{-2}.

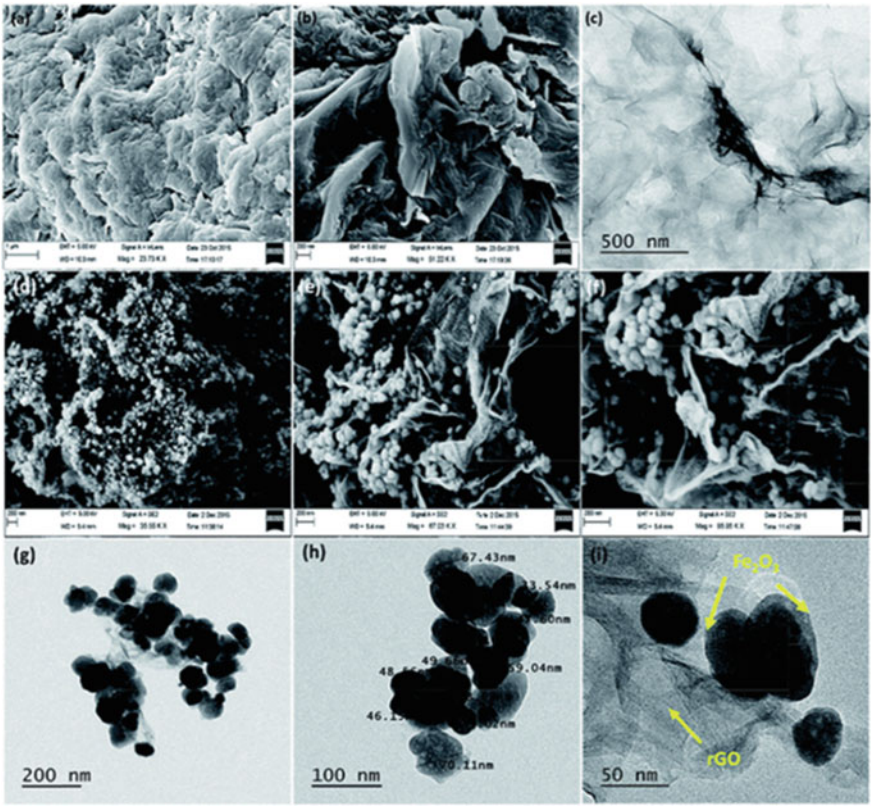

Fig. 5.13 **a**, **b** FESEM images of RGO at different magnifications; **c** TEM image of RGO; **d**–**f** FESEM images of RGO–Fe_2O_3 composite at different magnifications; **g**–**i** TEM image of RGO–Fe_2O_3 composite at different magnifications. Reproduced with permission from Royal Society of Chemistry [111]

5.9 Fe_3O_4-Graphene Composites for Supercapacitor Applications

5.9.1 Hydro/Solvothermal Method

Shi's group adopted a facile solvothermal method for the synthesis of Fe_3O_4 nanoparticles decorated over RGO sheets [113]. The composite electrode material has depicted a high capacitance value of 480 F g^{-1} at a high current density of 5 A g^{-1} with excellent energy and power density values. The composite electrode has retained 100% of its initial capacitance value after 1000 cycles at a current density of 5 A g^{-1}, suggesting its utility in high-performance electrochemical supercapacitors. Similarly, Wang and co-workers adopted a hydrothermal method for the preparation of Fe_3O_4-graphene composites without the use of surfactants or templates [114]. The addition

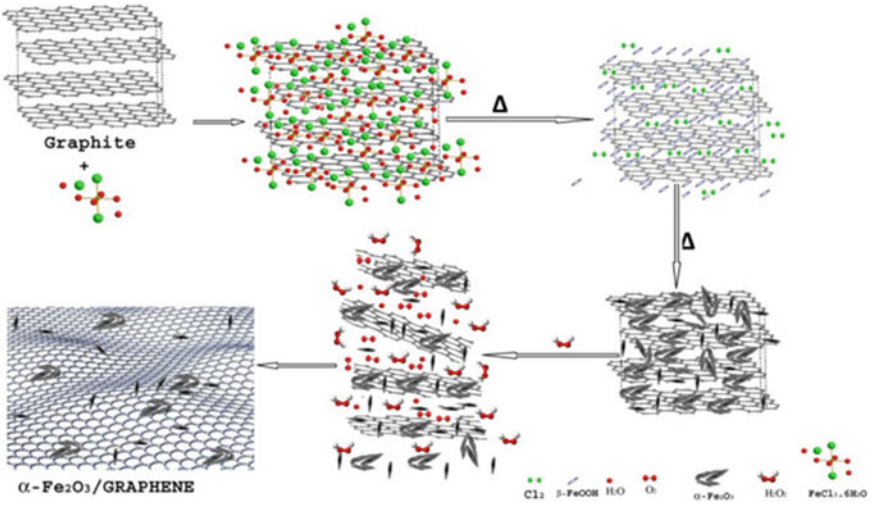

Fig. 5.14 Schematic representation of the formation of α-Fe_2O_3/graphene nanosheets. Reproduced with permission from Elsevier [64]

of graphene sheets increased the surface area of hybrid composite (49.5 $m^2\ g^{-1}$) in comparison to Fe_3O_4 (19.25 $m^2\ g^{-1}$). The increase in surface area of the composite led to increase in specific capacitance value of the composite structure to 220 F g^{-1} at a current density of 0.5 A g^{-1} as compared to Fe_3O_4 (65.4 F g^{-1}). Wasiński's group studied the effect of loading of double-layer electroactive materials on the enhancement in the capacitance values [115]. They adopted a solvothermal method to combine the electrochemical double-layer materials as positive electrode and battery-type materials as negative electrode to form a hybrid composite structure in order to enhance the capacitance, energy and power density values. The high conductive RGO sheets acted as a positive electrode and Fe_3O_4 nanoparticles acted as a negative electrode. They found that the 30 wt.% loading of graphene displayed a high capacitance value of 83 F g^{-1} as compared to the 10 and 20 wt.% loading. Beyond 30 wt.% loading they observed a decrease in the capacitance value due to the agglomeration of the constituent materials. Li's group synthesized a hybrid composite structure consisting of Fe_3O_4 nanoparticles on RGO sheets through a novel hydrothermal method [116]. The high surface area and mesoporous structure of the composite led to a good capacitance value of 241 F g^{-1} at a current density of 1 A g^{-1} with good initial capacitance retention of 79% after 1000 cycles at a high current density of 10 A g^{-1}. Mezgebe's group studied the electrochemical performance of Fe_3O_4–RGO nanocomposite synthesized through hydrothermal method [117]. The obtained nanocomposite had a BET surface area of 27.6 $m^2\ g^{-1}$ with pore volume of 0.184 cc g^{-1}. The obtained composite structure had a capacitance value of 116.4 F g^{-1} at a current density of 1 A g^{-1} in 1 M H_2SO_4 electrolyte. Lin and co-workers deposited Fe_3O_4 nanosheet arrays on graphene surface through in-situ hydrothermal method followed by plasma-enhanced CVD heating for the enhancement of electrochemical

performance of the supercapacitors [118]. The fabricated anode material had a high capacitance value of 732 F g^{-1} at a current density of 2 A g^{-1} with excellent rate capability of 54% at a high current density of 50 A g^{-1}. The cyclic stability test performed at a high current density of 20 A g^{-1} showed retention of 90.4% of the initial capacitance value after 10,000 cycles, whereas the Fe_3O_4 electrode displayed only 61.8% retention. Pal's group adopted a simple one-pot hydrothermal method for the synthesis of Fe_3O_4–RGO hybrid material and studied the effect of applied magnetic field on the electrochemical performance of the hybrid composite [119]. The hybrid composite had a capacitance value of 868.9 F g^{-1} (451 F g^{-1}) with applied magnetic field (without applied magnetic field). The external magnetic field (0.125 T) had huge impact on the enhancement of electrochemical properties along with high surface area which allowed the deep penetration of electrolyte ions into the electrode thus ameliorating the electrochemical performance. Sheng's group deposited Fe_3O_4 nanospheres onto graphene surface through hydrothermal process for high energy density supercapacitors [120]. The fabricated supercapacitor displayed a high capacitance value of 268 F g^{-1} at a scan rate of 2 mV s^{-1} with 99% retention of initial capacitance value after 10,000 cycles at a high cycling rate of 200 mV s^{-1}. The hybrid composite promoted the electron transport and ion diffusion/transport, resulting in the remarkable enhancement of the electrochemical performance. Khan's group prepared Fe_3O_4 nanodiscs embedded on reduced graphene oxide through a facile hydrothermal method [121]. The composite was tested as a negative electrode in aqueous KOH electrolyte, and it displayed a capacitance value of 1149 F g^{-1} in comparison to a value of 920 F g^{-1} for Fe_3O_4 nanodiscs at a current density of 1.5 A g^{-1}. Apart from this, excellent cyclic stability was shown by the composite material with 97.53% retention of initial capacitance compared to 87.8% for the Fe_3O_4 nanodiscs after 10,000 cycles at a current density of 10 A g^{-1}. Liao and co-workers utilized solvothermal route for synthesis of Fe_3O_4 graphene nanocomposite with a good surface area and porous structure [65]. The composite material had a good capacitance value of 300 F g^{-1} at a current density of 0.4 A g^{-1}, which was higher compared to the Fe_3O_4 nanomaterial and graphene sheets. The electrode material retained 93% of its initial capacitance after 500 discharge cycles at a low current density of 0.4 A g^{-1}. Although the electrode material displayed a good gravimetric capacitance value, it failed in the long-term cyclic stability study owing to the agglomeration effect, which restricted the smooth passage of electrolyte ions into the electroactive surface lowering the electrochemical performance. Figure 5.15 depicts the anchoring of various nanostructures on graphene surface in the hybrid composites.

5.9.2 Chemical Vapour Deposition Method

Shi and co-workers prepared iron oxide impregnated hollow carbon spheres for supercapacitor electrode material (Fig. 5.16) [122]. Due to the pore size which was found to be optimum and cavity which was partially filled, electrolyte ions exhibited

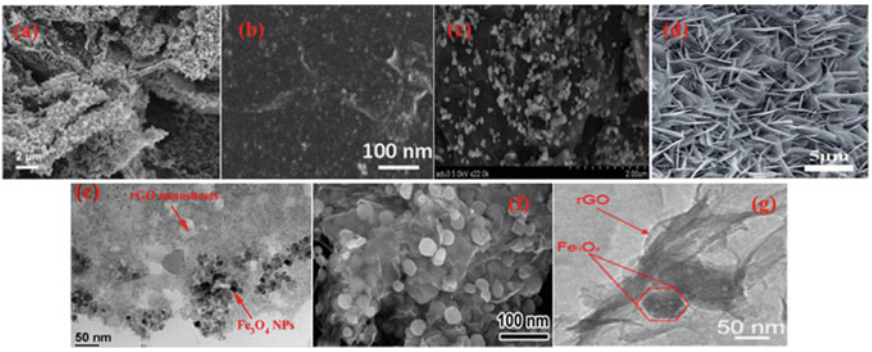

Fig. 5.15 **a** SEM image of Fe_3O_4 nanoparticles/RGO composite. Reproduced with permission from Elsevier [114]. **b** High-magnification SEM image of Fe_3O_4–RGO composite. Reproduced with permission from Elsevier [116]. **c** SEM image of RGO/Fe_3O_4 composite. Reproduced with permission from Elsevier [117]. **d** SEM image of graphene@Fe_3O_4 nanosheets. Reproduced with permission from Royal Society of Chemistry [118]. **e** TEM image of Fe_3O_4/RGO sheets. Reproduced with permission from IOP Science [119]. **f** SEM image of graphene-Fe_3O_4 nanocomposites. Reproduced with permission from Elsevier [120]. **g** TEM image of Fe_3O_4/RGO nanocomposites. Reproduced with permission from Elsevier [121]

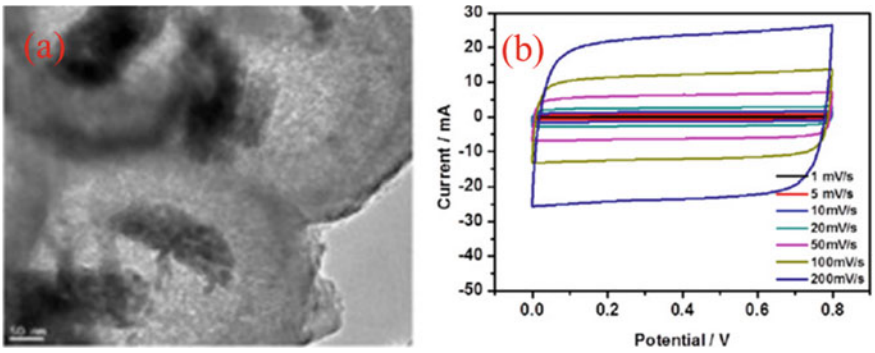

Fig. 5.16 **a** TEM image of hollow carbon sphere-Fe_3O_4 nanocomposite; **b** CV curves showing the EDLC behaviour of the composite. Reproduced with permission from Elsevier [122]

easy and reversible transport through the porous composite leading to a capacitance value of 193 F g^{-1} at a scan rate of 1 mV s^{-1} and retained 94.75% of initial capacitance values after 10,000 cycles in 5 M LiCl electrolyte.

5.9.3 Electrochemical Process

Qu's group synthesized 2D sandwich like Fe_3O_4@graphene nanocomposites through electrochemical process [123]. The obtained nanocomposite displayed good surface

area along with high capacitance value of 349 F g^{-1} at a current density of 0.5 A g^{-1}. Also, the prepared electrode retained 95% of its initial capacitance value after 1000 cycles at current density of 2 A g^{-1}. The excellent electrochemical performance of the nanocomposite is mainly attributed to the 2D sandwich like structure of Fe_3O_4, which uniformly anchored on the graphene sheets, prevented the aggregation of both the nanostructures and helped in the increase of electrical conductivity and overall electrochemical properties. Li's group deposited Fe_3O_4 nanoparticles on functional exfoliated graphene sheets over a carbon paper to prepare a binder-free electrode with porous structure and good conductivity [124]. A high capacitance value of 470 F g^{-1} is delivered by the composite structure at a current density of 1 A g^{-1} with 91.9% initial capacitance retention after 5000 cycles at a current density of 1 A g^{-1}.

5.9.4 Microwave Method

Low-cost microwave method was adopted by Karthikeyan's group to synthesize Fe_3O_4-graphene composite to fabricate a symmetrical supercapacitor device of 1 V [125]. The supercapacitor device displayed a capacitance value of 88 F g^{-1} at a low current density of 0.25 A g^{-1}. However, the device showed a high cyclic stability up to 100,000 cycles at a high current density of 3.75 A g^{-1} with 99.5% retention of initial capacitance value. Apart from high cyclic stability rate, the device also produced good energy and power density values, suggesting its utility for the practical applications. Kumar and group synthesized interconnected 3D network of Fe_3O_4/RGO nanosheet composite for high-performance supercapacitor electrode material through microwave approach [126]. The specific capacitance of the composite was estimated to be 455 F g^{-1} at a current density of 3.6 A g^{-1}, which is superior compared to the Fe_3O_4 nanoparticles. The composite electrode retained 91.4% initial capacitance value after 9600 cycles at an applied current density of 3.8 A g^{-1}.

5.9.5 Reflux Method

Qi's group synthesized Fe_3O_4/RGO nanocomposites through a facile hydrolysis route followed by post-annealing method [127]. The nanocomposite provided a good capacitance value of 350.6 F g^{-1} at a scan rate of 1 mV s^{-1}, and with 100-fold increase in scan rate, the capacitance value was 157.6 F g^{-1}, which showed the material had good rate capability. In addition to this, the electrode material retained 100% initial capacitance value after 10,000 cycles at a high scan rate of 100 mV s^{-1}. Liu and group fabricated a negative flexible paper supercapacitor, which possessed a high surface area of 346 m^2 g^{-1} with mesoporous structure [128]. The wet chemical synthesis followed by vacuum drying led to the formation of Fe_3O_4 nanoparticles uniformly deposited over the graphene surface by covalent bonding. The intact hybrid structure resulted in good capacitance value of 368 F g^{-1} at a current density of 1 A g^{-1} and at

a current density of 5 A g^{-1}; the capacitance value was 225 F g^{-1}, which is 61% of the former capacitance value. The cyclic stability test of the hybrid material revealed 66.6% retention of initial capacitance value at a high current density of 5 A g^{-1} after 1000 cycles. Sarno and group synthesized FLG-Fe_3O_4 nanohybrid composite for supercapacitor application [129]. The prepared composite gave a capacitance value of 227 F g^{-1} at a current density of 0.23 A g^{-1} along with high energy density and power density values. It also retained 95% of its initial capacitance value after 1000 cycles at a high current density of 20 A g^{-1}. The excellent electrochemical performance of this nanohybrid composite was due to the favourable function of FLG for anchoring nanosized Fe_3O_4 particles, which prevented the aggregation of nanoparticles and provided effective pathways for the electron transport.

5.9.6 Electrophoretic Deposition Method

Ghasemi's group adopted electrophoretic deposition method to synthesize RGO–Fe_3O_4 films [130]. A specific capacitance of 154 F g^{-1} at current density of 1 A g^{-1} was observed which was higher than that of RGO (81 F g^{-1}) in 0.5 M Na_2SO_4 electrolyte. The electrochemical behaviour of RGO–Fe_3O_4/SS electrodes was improved with the addition of three kind of surfactant, i.e. sodium dodecyl sulphate (SDS), cetyltrimethylammonium bromide (CTAB), t-octyl phenoxy polyethoxyethanol (Triton X-100) to Na_2SO_4 aqueous solution. The RGO–Fe_3O_4/SS in Na_2SO_4 electrolyte containing Triton X-100 showed maximum specific capacitance of 236 F g^{-1} at 1 A g^{-1} with retention of 97% initial capacitance after 500 cycles. Yang's group studied the electrochemical performance of porous edge-functionalized graphitic carbon nitride/iron oxide nanoparticle composites prepared through electrophoretic deposition method [131]. The synthesized binder-free electrodes, graphitic carbon nitride/iron oxide nanoparticles on Ni foam current collector delivered a specific capacity of 197 mA h g^{-1} at a current density of 0.5 A g^{-1}. In comparison to 77 mA h g^{-1} delivered by Fe_3O_4. The capacitance retention of the composite was 88.5% after 4000 cycles in comparison to 60.8% of Fe_3O_4 at an applied current density of 3 A g^{-1}.

5.9.7 Self-assembly Method

Yan's research group synthesized irregular hexagonal-Fe_3O_4 sheets-RGO composite through a colloidal electrostatic assembly process followed by a heat treatment process (Fig. 5.17) [132]. The porous composite electrode displayed a BET surface area of 173.3 m^2 g^{-1} with mesoporous structure. A capacitance value of 193 F g^{-1} at a current density of 0.3 A g^{-1}, and 112.3 F g^{-1} at a current density of 2 A g^{-1} which is 58.2% after 6.7-fold increase in the current density was obtained suggesting its

Fig. 5.17 Schematic representation of colloidal electrostatic assembly process for the synthesis of hexagonal-Fe_3O_4 sheets-RGO composite. Reproduced with permission from Elsevier [132]

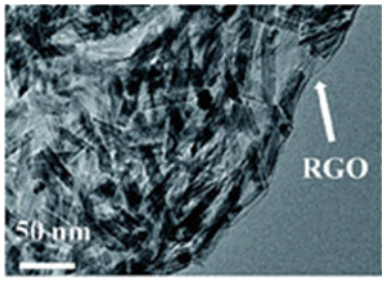

Fig. 5.18 TEM image of Fe_3O_4 nanorods-RGO composite. Reproduced with permission from Royal Society of Chemistry [133]

good rate capability. The cyclic stability test at a current density of 1 A g^{-1} for 1000 cycles revealed that around 83.2% of the initial capacitance value was retained.

5.9.8 Wet Chemical Route

Das and co-workers adopted a wet chemical route for the synthesis of Fe_3O_4 nanorods-RGO composite for enhancement of the electrochemical properties [133]. The hybrid composite showed a high capacitance value of 315 C g^{-1} at a current density of 5 A g^{-1}. The electrode material also displayed high initial capacitance retention (95%) after 2000 cycles at an applied current density of 5 A g^{-1} (Fig. 5.18).

5.9.9 Bio-inspired Green Method

Madhuvilakku's group adopted a biosurfactant assisted green one-pot method for the fabrication of flower-like Fe_3O_4 anchored on RGO sheets to form a hybrid composite (Fig. 5.19) [134]. The synergetic effect and fast redox reaction owing to the short ion diffusion path led to a high capacitance value of 425 F g^{-1} at a current density of 1.5 A g^{-1}, which is more as compared to Fe_3O_4 (144.8 F g^{-1}) and RGO sheets (159 F g^{-1}). Although the hybrid composite showed a high capacitance value, it did

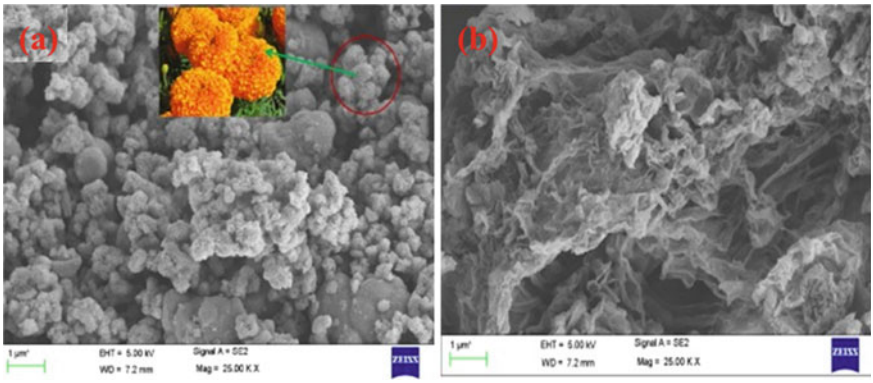

Fig. 5.19 **a** FESEM image of Fe_3O_4 nanoflowers; **b** Fe_3O_4/RGO nanocomposite. Reproduced with permission from Elsevier [134]

not fare well in cyclic stability test as it retained 80% of the initial capacitance value after only 750 cycles.

5.9.10 Graphenothermal Method

Rosaiah's group adopted a cost-effective graphenothermal method to synthesize flower-like RGO–Fe_3O_4 nanoparticle composite, which displayed a high surface area of 141.3 $m^2\ g^{-1}$ with mesoporous structure [135]. The nanocomposite electrode exhibited a high capacitance value of 498 F g^{-1} at a high scan rate of 10 mV s^{-1} and 454.3 F g^{-1} at a current density of 1 A g^{-1}. The nanocomposite electrode also retained 94% of the initial capacitance value after 10,000 discharge cycles at a current density of 3 A g^{-1}. The excellent electrochemical performance displayed by the composite structure as compared to the constituents was due to the high surface area and mesoporous structure of the composite.

5.9.11 Chemical Reduction Method

Aruna Devi and co-workers studied the electrochemical performance of Fe_3O_4–RGO nanocomposites for supercapacitor applications prepared by one-step chemical reduction method (Fig. 5.20) [136]. It was found that the high concentration of $Fe(NO_3)_3$ led to a capacitance value of 416 F g^{-1} as compared to low Fe concentration, which showed a capacitance value of 398 F g^{-1}. The high specific capacitance values of the Fe_3O_4/RGO nanocomposites obtained are due to the combined effect of RGO possessing EDLC behaviour and Fe_3O_4 possessing pseudocapacitive behaviour causing fast Faradaic reaction. Apart from high capacitance value,

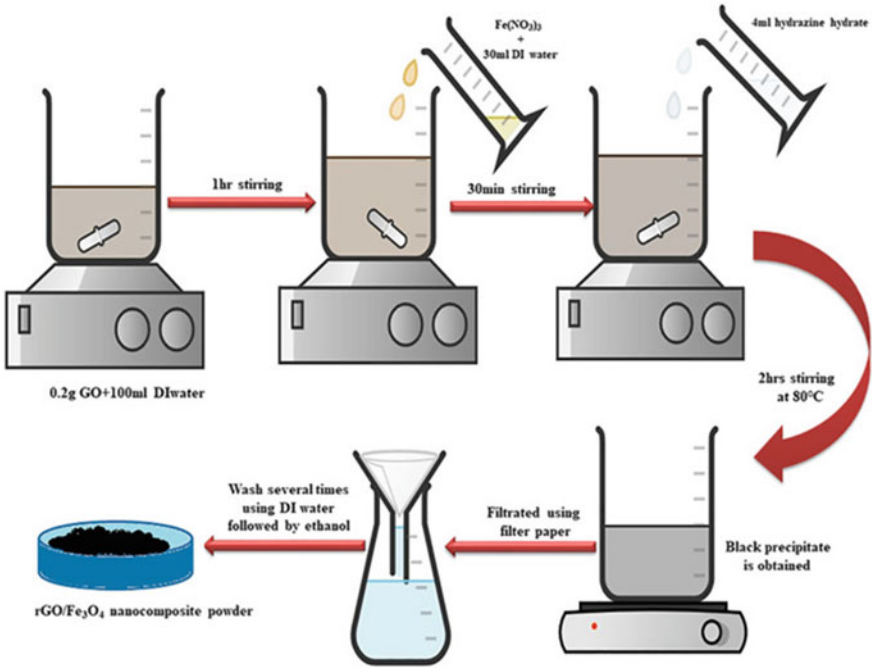

Fig. 5.20 Schematic illustration for the synthesis of RGO–Fe_3O_4 nanocomposite. Reproduced with permission from Elsevier [136]

the electrode material was able to retain 88.6% initial capacitance value after 1000 cycles at a high current density of 5 A g^{-1}.

5.10 Conclusions

This book chapter presents the basics of supercapacitors, their types and materials used as electrodes in the fabrication of supercapacitors. Owing to the discovery of graphene and its spectacular properties, this material has been widely accepted by researchers across the globe. The high electron mobility, high surface area, high mechanical and Young's modulus help in the enhancement of capacitance value. However, the presence of van der Waal's forces makes the graphene sheets to come closer which would lead to the agglomeration of sheets. To overcome this issue, the introduction of foreign molecules was found to be an attractive approach. In this chapter, various methods implemented to introduce iron oxide nanostructures into graphene derivatives to form hybrid composites have been discussed. The incorporation of foreign moieties led to increase in the electrochemical performance of the hybrid composites by many folds with high cyclic stability at high applied current

density. The electrode materials exhibited high electrochemical activity and cyclic stability due to the synergistic effects of the components of the nanocomposite materials. The impressive electrochemical accomplishment of various composite materials is attributed to the increase in active surface area and electronic conductivity. The published works suggest that these graphene-based nanocomposites with iron oxides are potential candidates as electrode materials for the supercapacitor applications.

References

1. Conway BE (1999) Electrochemical supercapacitors: scientific fundamentals and technological applications. Kluwer Academic Publishers, Plenum Press, New York
2. Wang G, Zhang L, Zhang J (2012) A review of electrode materials for electrochemical supercapacitors. Chem Soc Rev 41:797–828
3. Sethi M, Shenoy US, Bhat DK (2021) Simple solvothermal synthesis of porous graphene-NiO nanocomposites with high cyclic stability for supercapacitor application. J Alloy Compd 854:157190
4. Winter M, Brodd RJ (2004) What are batteries, fuel cells, and supercapacitors? Chem Rev 104(10):4245–4270
5. Simon P, Gogotsi Y (2008) Materials for electrochemical capacitors. Nat Mater 7(11):845–854
6. Hadjipaschalis I, Poullikkas A, Efthimiou V (2009) Overview of current and future energy storage technologies for electric power applications. Renew Sustain Energy Rev 13(6–7):1513–1522
7. Kötz R, Carlen MJEA (2000) Principles and applications of electrochemical capacitors. Electrochim Acta 45(15–16):2483–2498
8. Burke A (2000) Ultracapacitors: why, how, and where is the technology. J Power Sources 91(1):37–50
9. Frackowiak E, Beguin F (2001) Carbon materials for the electrochemical storage of energy in capacitors. Carbon 39(6):937–950
10. Pandolfo AG, Hollenkamp AF (2006) Carbon properties and their role in supercapacitors. J Power Sources 157(1):11–27
11. Satya Sai PM, Ahmed J, Krishnaiah K (1997) Production of activated carbon from coconut shell char in a fluidized bed reactor. Ind Eng Chem Res 36(9):3625–3630
12. Linares-Solano A, Salinas-Martínez de Lecea C, Cazorla-Amorós D, Martín-Gullón I (2000) Porosity development during CO_2 and steam activation in a fluidized bed reactor. Energy Fuels 14(1):142–149
13. Daud WMAW, Ali WSW (2004) Comparison on pore development of activated carbon produced from palm shell and coconut shell. Bioresour Technol 93(1):63–69
14. Jagtoyen M, Derbyshire F (1998) Activated carbons from yellow poplar and white oak by H_3PO_4 activation. Carbon 36(7–8):1085–1097
15. Aygün A, Yenisoy-Karakaş S, Duman I (2003) Production of granular activated carbon from fruit stones and nutshells and evaluation of their physical, chemical and adsorption properties. Microporous Mesoporous Mater 66(2–3):189–195
16. IUPAC (1972) Manual of symbols and terminology. Pure Appl Chem 31
17. Barranco V, Lillo-Rodenas MA, Linares-Solano A, Oya A, Pico F, Ibañez J, Agullo-Rueda F, Amarilla JM, Rojo JM (2010) Amorphous carbon nanofibers and their activated carbon nanofibers as supercapacitor electrodes. J Phys Chem C 114(22):10302–10307
18. Kim SH, Kim YI, Park JH, Ko JM (2009) Cobalt-manganese oxide/carbon-nanofiber composite electrodes for supercapacitors. Int J Electrochem Sci 4(11):1489–1496
19. Houweling ZS, Verlaan V, Ten Grotenhuis GT, Schropp REI (2009) Formation of isolated carbon nanofibers with hot-wire CVD using nanosphere lithography as catalyst patterning technique. Thin Solid Films 517(12):3566–3569

20. Suarez-Garcia F, Vilaplana-Ortego E, Kunowsky M, Kimura M, Oya A, Linares-Solano A (2009) Activation of polymer blend carbon nanofibres by alkaline hydroxides and their hydrogen storage performances. Int J Hydrogen Energy 34(22):9141–9150
21. Seo MK, Park SJ (2009) Electrochemical characteristics of activated carbon nanofiber electrodes for supercapacitors. Mater Sci Eng B 164(2):106–111
22. Wang K, Birjukovs P, Erts D, Phelan R, Morris MA, Zhou H, Holmes JD (2009) Synthesis and characterisation of ordered arrays of mesoporous carbon nanofibres. J Mater Chem 19(9):1331–1338
23. Adhyapak PV, Maddanimath T, Pethkar S, Chandwadkar AJ, Negi YS, Vijayamohanan K (2002) Application of electrochemically prepared carbon nanofibers in supercapacitors. J Power Sources 109(1):105–110
24. Bao Q, Bao S, Li CM, Qi X, Pan C, Zang J, Lu Z, Li Y, Tang DY, Zhang S, Lian K (2008) Supercapacitance of solid carbon nanofibers made from ethanol flames. J Phys Chem C 112(10):3612–3618
25. Iijima S, Ichihashi T (1993) Single-shell carbon nanotubes of 1-nm diameter. Nature 363(6430):603–605
26. Frackowiak E (2007) Carbon materials for supercapacitor application. Phys Chem Chem Phys 9(15):1774–1785
27. An KH, Kim WS, Park YS, Choi YC, Lee SM, Chung DC, Bae DJ, Lim SC, Lee YH (2001) Supercapacitors using single-walled carbon nanotube electrodes. Adv Mater 13(7):497–500
28. Emmenegger C, Mauron P, Sudan P, Wenger P, Hermann V, Gallay R, Züttel A (2003) Investigation of electrochemical double-layer (ECDL) capacitors electrodes based on carbon nanotubes and activated carbon materials. J Power Sources 124(1):321–329
29. Du C, Pan N (2006) Supercapacitors using carbon nanotubes films by electrophoretic deposition. J Power Sources 160(2):1487–1494
30. Geim AK, Novoselov KS (2007) The rise of graphene. Nat Mater 6(3):183–191
31. Geim AK (2009) Graphene: status and prospects. Science 324:1530–1534
32. Lalabadi MA, Hashemi H, Feng J, Jafari SM (2020) Carbon nanomaterials against pathogens; the antimicrobial activity of carbon nanotubes, graphene/graphene oxide, fullerenes, and their nanocomposites. Adv Colloid Interface Sci 284:102250
33. Novoselov KS, Geim AK, Morozov SV, Jiang D, Zhang Y, Dubonos SV, Grigorieva IV, Firsov AA (2004) Electric field effect in atomically thin carbon films. Science 306(5696):666–669
34. Zhang L, Zhang F, Yang X, Long G, Wu Y, Zhang T, Leng K, Huang Y, Ma Y, Yu A, Chen Y (2013) Porous 3D graphene-based bulk materials with exceptional high surface area and excellent conductivity for supercapacitors. Sci Rep 3(1):1–9
35. Subramanya B, Bhat DK (2015) Novel one-pot green synthesis of graphene in aqueous medium under microwave irradiation using a regenerative catalyst and the study of its electrochemical properties. New J Chem 39(1):420–430
36. Brownson DA, Gorbachev RV, Haigh SJ, Banks CE (2012) CVD graphene vs. highly ordered pyrolytic graphite for use in electroanalytical sensing. Analyst 137(4):833–839
37. Avouris P, Chen ZH, Perebeinos V (2007) Carbon based electronics. Nat Nanotechnol 2:605–615
38. Xia J, Chen F, Li J, Tao N (2009) Measurement of the quantum capacitance of graphene. Nat Nanotechnol 4(8):505–509
39. Lee C, Wei X, Kysar JW, Hone J (2008) Measurement of the elastic properties and intrinsic strength of monolayer graphene. Science 321(5887):385–388
40. Liu L, Yu Y, Yan C, Li K, Zheng Z (2015) Wearable energy-dense and power-dense supercapacitor yarns enabled by scalable graphene–metallic textile composite electrodes. Nat Commun 6(1):1–9
41. Schedin F, Geim AK, Morozov SV, Hill EW, Blake P, Katsnelson MI, Novoselov KS (2007) Detection of individual gas molecules adsorbed on graphene. Nat Mater 6(9):652–655
42. Son YW, Cohen ML, Louie SG (2006) Half-metallic graphene nanoribbons. Nature 444(7117):347–349

43. Sun B, Wang B, Su D, Xiao L, Ahn H, Wang G (2012) Graphene nanosheets as cathode catalysts for lithium-air batteries with an enhanced electrochemical performance. Carbon 50(2):727–733
44. Velasco A, Ryu YK, Boscá A, Ladrón-de-Guevara A, Hunt E, Zuo J, Pedrós J, Calle F, Martinez J (2021) Recent trends in graphene supercapacitors: from large area to microsupercapacitors. Sustain Energy Fuels 5(5):1235–1254
45. Subramanya B, Bhat DK (2015) Novel eco-friendly synthesis of graphene directly from graphite using 2,2,6,6-tetramethylpiperidine 1-oxyl and study of its electrochemical properties. J Power Sources 275:90–98
46. Jindal H, Oberoi AS, Sandhu IS, Chitkara M, Singh B (2021) Graphene for hydrogen energy storage—a comparative study on GO and rGO employed in a modified reversible PEM fuel cell. Int J Energy Res 45(4):5815–5826
47. Peng YY, Liu YM, Chang JK, Wu CH, Ger MD, Pu NW, Chang CL (2015) A facile approach to produce holey graphene and its application in supercapacitors. Carbon 81:347–356
48. Zdravkov B, Čermák J, Šefara M, Janků J (2007) Pore classification in the characterization of porous materials: a perspective. Open Chem 5(2):385–395
49. Bantawal H, Sethi M, Shenoy US, Bhat DK (2019) Porous graphene wrapped $SrTiO_3$ nanocomposite: Sr–C bond as an effective coadjutant for high performance photocatalytic degradation of methylene blue. ACS Appl Nano Mater 2(10):6629–6636
50. Sethi M, Bantawal H, Shenoy US, Bhat DK (2019) Eco-friendly synthesis of porous graphene and its utilization as high performance supercapacitor electrode material. J Alloy Compd 799:256–266
51. Bieri M, Treier M, Cai J, Ait-Mansour K, Ruffieux P, Gröning O, Gröning P, Kastler M, Rieger R, Feng X, Müllen K, Fasel R (2009) Porous graphenes: two-dimensional polymer synthesis with atomic precision. Chem Commun 45:6919–6921
52. Li Y, Zhou Z, Shena P, Chen Z (2010) Two dimensional polyphenylene: experimentally available porous graphene as a hydrogen purification membrane. Chem Commun 46(21):3672–3674
53. Fan Z, Zhao Q, Li T, Yan J, Ren Y, Feng J, Wei T (2012) Easy synthesis of porous graphene nanosheets and their use in supercapacitors. Carbon 50(4):1699–1703
54. Fischbein MD, Drndić M (2008) Electron beam nanosculpting of suspended graphene sheets. Appl Phys Lett 93(11):113107
55. Bell DC, Lemme MC, Stern LA, Williams JR, Marcus CM (2009) Precision cutting and patterning of graphene with helium ions. Nanotechnology 20(45):455301
56. Koenig SP, Wang L, Pellegrino J, Bunch JS (2012) Selective molecular sieving through porous graphene. Nat Nanotechnol 7(11):728–732
57. Conway BE (1991) Transition from "supercapacitor" to "battery" behaviour in electrochemical energy storage. J Electrochem Soc 138(6):1539–1548
58. Mastragostino M, Arbizzani C, Soavi F (2001) Polymer-based supercapacitors. J Power Sources 97:812–815
59. Sethi M, Shenoy US, Muthu S, Bhat DK (2020) Facile solvothermal synthesis of $NiFe_2O_4$ nanoparticles for high-performance supercapacitor applications. Front Mater Sci 14(2):120–132
60. Wang H, Jiang N, Zhang Q, Xie G, Tang N, Liu L, Xie Z (2021) Facilely tunable redox behaviors in donor–node–acceptor polymers toward high-performance ambipolar electrode materials. Macromolecules 54(7):3469–3477
61. Arbizzani C, Mastragostino M, Soavi F (2001) New trends in electrochemical supercapacitors. J Power Sources 100(1–2):164–170
62. Arbizzani C, Mastragostino M, Meneghello L (1996) Polymer-based redox supercapacitors: a comparative study. Electrochim Acta 41(1):21–26
63. Allado K, Liu M, Jayapalan A, Arvapalli D, Nowlin K, Wei J (2021) Binary MnO_2/Co_3O_4 metal oxides wrapped on superaligned electrospun carbon nanofibers as binder free supercapacitor electrodes. Energy Fuels 35(9):8396–8405

64. Haridas V, Sukhananazerin A, Pullithadathil B, Narayanan BN (2021) Ultrahigh specific capacitance of α-Fe_2O_3 nanorods incorporated defect free graphene nanolayers. Energy 221:119743
65. Liao J, Li Y, Wang Z, Lv L, Chang L (2021) In-situ preparation of Fe_3O_4/graphene nanocomposites and their electrochemical performances for supercapacitor. Mater Chem Phys 258:123995
66. Sahoo MK, Rao GR (2018) Fabrication of $NiCo_2S_4$ nanoball embedded nitrogen doped mesoporous carbon on nickel foam as an advanced charge storage material. Electrochim Acta 268:139–149
67. Sethi M, Shenoy US, Bhat DK (2020) Porous graphene–$NiCo_2O_4$ nanorod hybrid composite as a high performance supercapacitor electrode material. New J Chem 44(10):4033–4041
68. Li K, Wang X, Wang X, Liang M, Nicolosi V, Xu Y, Gogotsi Y (2020) All-pseudocapacitive asymmetric MXene-carbon-conducting polymer supercapacitors. Nano Energy 75:104971
69. William JJ, Babu IM, Muralidharan G (2021) Nickel bismuth oxide as negative electrode for battery-type asymmetric supercapacitor. Chem Eng J 422:130058
70. Hira SA, Park KH (2021) Nitrogen-doped zeolitic imidazolate framework and particle-reduced graphene oxide composites as electrochemical sensors and battery-type supercapacitors. ACS Appl Nano Mater 4(8):7870–7878
71. Ohno H, Fukumoto K (2008) Progress in ionic liquids for electrochemical reaction matrices. Electrochemistry 76(1):16–23
72. Snook GA, Kao P, Best AS (2011) Conducting-polymer-based supercapacitor devices and electrodes. J Power Sources 196(1):1–12
73. Galiński M, Lewandowski A, Stępniak I (2006) Ionic liquids as electrolytes. Electrochim Acta 51(26):5567–5580
74. Mishra AK, Ramaprabhu S (2011) Functionalized graphene-based nanocomposites for supercapacitor application. J Phys Chem C 115(29):14006–14013
75. Sethi M, Shenoy US, Bhat DK (2020) A porous graphene–$NiFe_2O_4$ nanocomposite with high electrochemical performance and high cycling stability for energy storage applications. Nanoscale Adv 2(9):4229–4241
76. Sethi M, Bhat DK (2019) Facile solvothermal synthesis and high supercapacitor performance of $NiCo_2O_4$ nanorods. J Alloy Compd 781:1013–1020
77. Sun Z, Li F, Ma Z, Wang Q, Qu F (2021) Battery-type phosphorus doped FeS_2 grown on graphene as anode for hybrid supercapacitor with enhanced specific capacity. J Alloy Compd 854:157114
78. Brousse T, Bélanger D, Long JW (2015) To be or not to be pseudocapacitive? J Electrochem Soc 162(5):A5185
79. Zhang X, Zhu M, Ouyang T, Chen Y, Yan J, Zhu K, Ye K, Wang G, Cheng K, Cao D (2019) $NiFe_2O_4$ nanocubes anchored on reduced graphene oxide cryogel to achieve a 1.8 V flexible solid-state symmetric supercapacitor. Chem Eng J 360:171–179
80. Biswas S, Sharma V, Mandal D, Chowdhury A, Chakravarty M, Priya S, Gowda CC, De P, Singh I, Chandra A (2020) Hollow nanostructures of metal oxides as emerging electrode materials for high performance supercapacitors. Cryst Eng Commun 22(9):1633–1644
81. Sharma V, Biswas S, Sundaram B, Haldar P, Dubey B, Chandra A (2019) Electrode materials with highest surface area and specific capacitance cannot be the only deciding factor for applicability in energy storage devices: inference of combined life cycle assessment and electrochemical studies. ACS Sustain Chem Eng 7(5):5385–5392
82. Brodie BC XIII (1859) On the atomic weight of graphite. Philos Trans R Soc Lond 149:249–259
83. Staudenmaier L (1898) Verfahren zur darstellung der graphitsäure. Ber Dtsch Chem Ges 31(2):1481–1487
84. Hummers WS Jr, Offeman RE (1958) Preparation of graphitic oxide. J Am Chem Soc 80(6):1339–1339
85. Kovtyukhova NI, Ollivier PJ, Martin BR, Mallouk TE, Chizhik SA, Buzaneva EV, Gorchinskiy AD (1999) Layer-by-layer assembly of ultrathin composite films from micron-sized graphite oxide sheets and polycations. Chem Mater 11(3):771–778

86. Stankovich S, Dikin DA, Dommett GH, Kohlhaas KM, Zimney EJ, Stach EA, Piner RD, Nguyen ST, Ruoff RS (2006) Graphene-based composite materials. Nature 442(7100):282–286
87. Marcano DC, Kosynkin DV, Berlin JM, Sinitskii A, Sun Z, Slesarev A, Alemany LB, Lu W, Tour JM (2010) Improved synthesis of graphene oxide. ACS Nano 4(8):4806–4814
88. Sadiq MMJ, Shenoy US, Bhat DK (2016) Novel RGO/$ZnWO_4$/Fe_3O_4 nanocomposite as high performance visible light photocatalyst. RSC Adv 6:61821–61829
89. Sadiq MMJ, Shenoy US, Bhat DK (2017) Enhanced photocatalytic performance of N-doped RGO-$FeWO_4$/Fe_3O_4 ternary nanocomposite in environmental applications. Mater Today Chem 4:133–141
90. Sadiq MMJ, Shenoy US, Bhat DK (2018) Novel NRGO-$CoWO_4$-Fe_2O_3 nanocomposite as an efficient catalyst for dye degradation and reduction of 4-nitrophenol. Mater Chem Phys 208:112–122
91. Lee KK, Deng S, Fan HM, Mhaisalkar S, Tan HR, Tok ES, Loh KP, Chin WS, Sow CH (2012) α-Fe_2O_3 nanotubes-reduced graphene oxide composites as synergistic electrochemical capacitor materials. Nanoscale 4(9):2958–2961
92. Chaudhari NK, Chaudhari S, Yu JS (2014) Cube-like α-Fe_2O_3 supported on ordered multimodal porous carbon as high performance electrode material for supercapacitors. ChemSusChem 7(11):3102–3111
93. Zhao P, Li W, Wang G, Yu B, Li X, Bai J, Ren Z (2014) Facile hydrothermal fabrication of nitrogen-doped graphene/Fe_2O_3 composites as high performance electrode materials for supercapacitor. J Alloy Compd 604:87–93
94. Liu L, Lang J, Zhang P, Hu B, Yan X (2016) Facile synthesis of Fe_2O_3 nano-dots@nitrogen-doped graphene for supercapacitor electrode with ultralong cycle life in KOH electrolyte. ACS Appl Mater Interfaces 8(14):9335–9344
95. Wang H, Xu Z, Yi H, Wei H, Guo Z, Wang X (2014) One-step preparation of single-crystalline Fe_2O_3 particles/graphene composite hydrogels as high performance anode materials for supercapacitors. Nano Energy 7:86–96
96. Song Z, Liu W, Xiao P, Zhao Z, Liu G, Qiu J (2015) Nano-iron oxide (Fe_2O_3)/three-dimensional graphene aerogel composite as supercapacitor electrode materials with extremely wide working potential window. Mater Lett 145:44–47
97. Yang S, Song X, Zhang P, Gao L (2015) Heating-rate-induced porous α-Fe_2O_3 with controllable pore size and crystallinity grown on graphene for supercapacitors. ACS Appl Mater Interfaces 7(1):75–79
98. Quan H, Cheng B, Xiao Y, Lei S (2016) One-pot synthesis of α-Fe_2O_3 nanoplates-reduced graphene oxide composites for supercapacitor application. Chem Eng J 286:165–173
99. Gao Y, Wu D, Wang T, Jia D, Xia W, Lv Y, Cao Y, Tan Y, Liu P (2016) One-step solvothermal synthesis of quasi-hexagonal Fe_2O_3 nanoplates/graphene composite as high performance electrode material for supercapacitor. Electrochim Acta 191:275–283
100. Zhu Y, Cheng S, Zhou W, Jia J, Yang L, Yao M, Wang M, Zhou J, Wu P, Liu M (2017) Construction and performance characterization of α-Fe_2O_3/rGO composite for long-cycling-life supercapacitor anode. ACS Sustain Chem Eng 5(6):5067–5074
101. Zhang M, Sha J, Miao X, Liu E, Shi C, Li J, He C, Li Q, Zhao N (2017) Three-dimensional graphene anchored Fe_2O_3@C core-shell nanoparticles as supercapacitor electrodes. J Alloy Compd 696:956–963
102. Gao W, Li Y, Zhao J, Zhang Z, Tang W, Wang J, Wu Z, Li Z (2022) Design and preparation of graphene/Fe_2O_3 nanocomposite as negative material for supercapacitor. Chem Res Chin Univ 38(4):1097–1104
103. Lin Y, Wang X, Qian G, Watkins JJ (2014) Additive-driven self-assembly of well-ordered mesoporous carbon/iron oxide nanoparticle composites for supercapacitors. Chem Mater 26(6):2128–2137
104. Zhang H, Lu C, Chen C, Xie L, Zhou P, Kong Q (2017) 2D layered α-Fe_2O_3/rGO flexible electrode prepared through colloidal electrostatic self-assembly. ChemElectroChem 4(8):1990–1996

105. Wu C, Zhang Z, Chen Z, Jiang Z, Li H, Cao H, Liu Y, Zhu Y, Fang Z, Yu X (2021) Rational design of novel ultra-small amorphous Fe_2O_3 nanodots/graphene heterostructures for all-solid-state asymmetric supercapacitors. Nano Res 14(4):953–960
106. Xia H, Hong C, Li B, Zhao B, Lin Z, Zheng M, Savilov SV, Aldoshin SM (2015) Facile synthesis of hematite quantum-dot/functionalized graphene-sheet composites as advanced anode materials for asymmetric supercapacitors. Adv Funct Mater 25(4):627–635
107. Hu J, Noked M, Gillette E, Han F, Gui Z, Wang C, Lee SB (2015) Dual-template synthesis of ordered mesoporous carbon/Fe_2O_3 nanowires: high porosity and structural stability for supercapacitors. J Mater Chem A 3(43):21501–21510
108. Sun S, Lang J, Wang R, Kong L, Li X, Yan X (2014) Identifying pseudocapacitance of Fe_2O_3 in an ionic liquid and its application in asymmetric supercapacitors. J Mater Chem A 2(35):14550–14556
109. Huang X, Zhang H, Li N (2017) Symmetric transparent and flexible supercapacitor based on bio-inspired graphene-wrapped Fe_2O_3 nanowire networks. Nanotechnology 28(7):075402
110. Yang Q, Bi R, Yung KC, Pecht M (2017) Electrochemically reduced graphene oxides/nanostructured iron oxides as binder-free electrodes for supercapacitors. Electrochim Acta 231:125–134
111. Saraf M, Natarajan K, Mobin SM (2017) Microwave assisted fabrication of a nanostructured reduced graphene oxide (rGO)/Fe_2O_3 composite as a promising next generation energy storage material. RSC Adv 7(1):309–317
112. Chen L, Liu D, Yang P (2019) Preparation of α-Fe_2O_3/RGO composites toward supercapacitor applications. RSC Adv 9(23):12793–12800
113. Shi W, Zhu J, Sim DH, Tay YY, Lu Z, Zhang X, Sharma Y, Srinivasan M, Zhang H, Hng HH, Yan Q (2011) Achieving high specific charge capacitances in Fe_3O_4/reduced graphene oxide nanocomposites. J Mater Chem 21(10):3422–3427
114. Wang Q, Jiao L, Du H, Wang Y, Yuan H (2014) Fe_3O_4 nanoparticles grown on graphene as advanced electrode materials for supercapacitors. J Power Sources 245:101–106
115. Wasiński K, Walkowiak M, Półrolniczak P, Lota G (2015) Capacitance of Fe_3O_4/rGO nanocomposites in an aqueous hybrid electrochemical storage device. J Power Sources 293:42–50
116. Li L, Gao P, Gai S, He F, Chen Y, Zhang M, Yang P (2016) Ultra small and highly dispersed Fe_3O_4 nanoparticles anchored on reduced graphene for supercapacitor application. Electrochim Acta 190:566–573
117. Mezgebe MM, Yan Z, Wei G, Gong S, Zhang F, Guang S, Xu H (2017) 3D graphene-Fe_3O_4-polyaniline, a novel ternary composite for supercapacitor electrodes with improved electrochemical properties. Mater Today Energy 5:164–172
118. Lin J, Liang H, Jia H, Chen S, Guo J, Qi J, Qu C, Cao J, Fei W, Feng J (2017) In situ encapsulated Fe_3O_4 nanosheet arrays with graphene layers as an anode for high-performance asymmetric supercapacitors. J Mater Chem A 5(47):24594–24601
119. Pal S, Majumder S, Dutta S, Banerjee S, Satpati B, De S (2018) Magnetic field induced electrochemical performance enhancement in reduced graphene oxide anchored Fe_3O_4 nanoparticle hybrid based supercapacitor. J Phys D Appl Phys 51(37):375501
120. Sheng S, Liu W, Zhu K, Cheng K, Ye K, Wang G, Cao D, Yan J (2019) Fe_3O_4 nanospheres in situ decorated graphene as high-performance anode for asymmetric supercapacitor with impressive energy density. J Colloid Interface Sci 536:235–244
121. Khan AJ, Khan A, Javed MS, Arshad M, Asim S, Khalid M, Siyal SH, Hussain S, Hanif M, Liu Z (2020) Surface assembly of Fe_3O_4 nanodiscs embedded in reduced graphene oxide as a high-performance negative electrode for supercapacitors. Ceram Int 46(11):19499–19505
122. Shi X, Zhang S, Chen X, Tang T, Mijowska E (2017) Effect of iron oxide impregnated in hollow carbon sphere as symmetric supercapacitors. J Alloy Compd 726:466–473
123. Qu Q, Yang S, Feng X (2011) 2D sandwich-like sheets of iron oxide grown on graphene as high energy anode material for supercapacitors. Adv Mater 23(46):5574–5580
124. Li Y, Yu J, Chen S, Huang Z, Wang L (2018) Fe_3O_4/functional exfoliation graphene on carbon paper nanocomposites for supercapacitor electrode. Ionics 24(9):2697–2704

125. Karthikeyan K, Kalpana D, Amaresh S, Lee YS (2012) Microwave synthesis of graphene/magnetite composite electrode material for symmetric supercapacitor with superior rate performance. RSC Adv 2(32):12322–12328
126. Kumar R, Singh RK, Vaz AR, Savu R, Moshkalev SA (2017) Self-assembled and one-step synthesis of interconnected 3D network of Fe_3O_4/reduced graphene oxide nanosheets hybrid for high-performance supercapacitor electrode. ACS Appl Mater Interfaces 9(10):8880–8890
127. Qi T, Jiang J, Chen H, Wan H, Miao L, Zhang L (2013) Synergistic effect of Fe_3O_4/reduced graphene oxide nanocomposites for supercapacitors with good cycling life. Electrochim Acta 114:674–680
128. Liu M, Sun J (2014) In situ growth of monodisperse Fe_3O_4 nanoparticles on graphene as flexible paper for supercapacitor. J Mater Chem A 2(30):12068–12074
129. Sarno M, Cirillo C, Ponticorvo E, Ciambelli P (2015) Synthesis and characterization of FLG/Fe_3O_4 nanohybrid supercapacitor. Chem Eng Trans 43:727–732
130. Ghasemi S, Ahmadi F (2015) Effect of surfactant on the electrochemical performance of graphene/iron oxide electrode for supercapacitor. J Power Sources 289:129–137
131. Yang Z, Liu Q, Zhang L, Dai J, Shen Z (2020) Green one-pot synthesis of binder-free porous edge-functionalized graphitic carbon nitride/iron oxide nanoparticles nanocomposite as an outstanding electrode for supercapacitors. J Energy Storage 32:101909
132. Yan F, Ding J, Liu Y, Wang Z, Cai Q, Zhang J (2015) Fabrication of magnetic irregular hexagonal-Fe_3O_4 sheets/reduced graphene oxide composite for supercapacitors. Synth Met 209:473–479
133. Das AK, Sahoo S, Arunachalam P, Zhang S, Shim JJ (2016) Facile synthesis of Fe_3O_4 nanorod decorated reduced graphene oxide (RGO) for supercapacitor application. RSC Adv 6(108):107057–107064
134. Madhuvilakku R, Alagar S, Mariappan R, Piraman S (2017) Green one-pot synthesis of flowers-like Fe_3O_4/rGO hybrid nanocomposites for effective electrochemical detection of riboflavin and low-cost supercapacitor applications. Sens Actuators B Chem 253:879–892
135. Rosaiah P, Zhu J, Hussain OM, Qiu Y (2019) Facile and cost-effective synthesis of flower-like RGO/Fe_3O_4 nanocomposites with ultra-long cycling stability for supercapacitors. Ionics 25(2):655–664
136. Aruna Devi N, Nongthombam S, Sinha S, Bhujel R, Rai S, Ishwarchand Singh W, Swain BP (2020) Investigation of chemical bonding and supercapacitivity properties of Fe_3O_4-rGO nanocomposites for supercapacitor applications. Diam Relat Mater 104:107756

Chapter 6
Iron Oxide Nanozyme in Biomedicine

Amit Kumar, Diptikanta Acharya, Sagarika Satapathy, and Sushil Kumar Sahu

Abstract Iron oxide nanoparticles with intrinsic enzymatic properties are considered as iron oxide nanozymes (IONzymes). IONzymes are bridging the gap between nanotechnology and biomedicine. Their catalytic actions mimic those of natural enzymes such as peroxidase and catalase. IONzymes are synthesized chemically and are less expensive than the preparation of natural enzymes. They are stable over a wide range of pH and temperature, an advantage over natural enzymes. In addition to IONzyme's enzymatic properties, their magnetic properties provide opportunities for developing of bioseparation assays, imaging tools, targeted drug delivery and hyperthermia therapy in the field of biomedicine.

Keywords IONzymes · Nanotechnology · Biomedicine · Peroxidase · Catalase · Drug delivery

6.1 Introduction

Iron oxide particles show the properties of remanence and coercivity. Remanence refers to the amount of magnetization retained by iron oxide at zero driving field, and coercivity is the amount of driving field needed to demagnetize it [1]. Iron oxide nanoparticles are paramagnetic or superparamagnetic in nature, which is a superior characteristic over iron oxide particles [2]. So, they quickly aggregate and re-disperse by applying and removing an external magnetic field, respectively [3]. Due to this property, iron oxide nanoparticles have multiple biomedical applications,

A. Kumar
Department of Human and Molecular Genetics, Virginia Commonwealth University, School of Medicine, Richmond, VA 23298, USA

D. Acharya · S. Satapathy
Department of Biotechnology, GIET University, Gunupur, Rayagada, Odisha 765022, India

S. K. Sahu (✉)
Department of Zoology, Siksha-Bhavana, Visva-Bharati University, Santiniketan, West Bengal 731235, India
e-mail: sushilkumar.sahu@visva-bharati.ac.in

H. Sahoo and J. K. Sahoo (eds.), *Iron Oxide-Based Nanocomposites and Nanoenzymes*, Nanostructure Science and Technology, https://doi.org/10.1007/978-3-031-44599-6_6

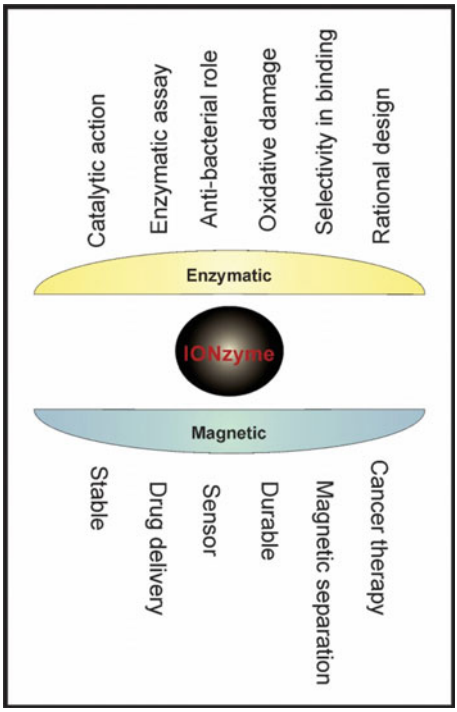

Fig. 6.1 Enzyme-like activities and magnetic properties of iron oxide nanoparticles (IONzymes) for biomedical applications

which include but are not limited to biosensors [4, 5], bioseparation [6, 7], targeted drug delivery [8, 9], magnetic resonance imaging [10] and hyperthermia therapy [11, 12]. Haematite (Fe_2O_3) and magnetite (Fe_3O_4) nanoparticles are considered as iron oxide nanozymes (IONzymes) due to their enzymatic properties. The first reported nanozyme was Fe_3O_4 nanoparticles, which possess horseradish peroxidase (HRP)-like catalytic activity [13]. Subsequently, different metals and metal oxides having enzymatic activities similar to peroxidase, oxidase, catalase and superoxide dismutase were studied [14–16]. Here, we present the catalytic activities of IONzyme and their applications in biomedicine (Fig. 6.1).

6.2 Enzymatic Activities of IONzyme

IONzyme is considered an enzyme mimetic as it possesses catalytic mechanisms similar to natural enzymes [17]. They mimic the properties of enzymes such as peroxidase and catalase of the oxidoreductase family [13, 18]. Both contain a non-protein part (or cofactor), i.e. haem. Peroxidase acts on hydrogen peroxide (H_2O_2) and gives rise to free radicals, whereas catalase acts on H_2O_2 to give rise to oxygen. Both of them play a crucial role in preventing oxidative damage in aerobic organisms.

(1) **IONzymes as peroxidase:**

IONzymes (nanomaterials of Fe_2O_3 and Fe_3O_4) mimic peroxidase activity (Eq. 6.1). Fe_3O_4 nanomaterial has been reported to exhibit better activity than Fe_2O_3 nanomaterial [19, 20]. IONzymes show optimum peroxidase activity at 37–40 °C in an acidic (pH 3–6.5) medium [18]. They can act on polysaccharides, lipids, proteins, and nucleic acids and peroxidize all these substrates [19, 21]. Activators of IONzymes are AMP, ADP and ATP [22], and inhibitors are free radical quenchers such as sodium azide, ascorbic acid, hypotaurine and catecholamines [17, 23].

$$H_2O_2 \xrightarrow{\text{Peroxide}} 2A + 2H_2O \tag{6.1}$$

(2) **IONzymes as Catalase:**

IONzymes also mimic catalase activity (Eq. 6.2). It has been shown that maghemite (γ-Fe_2O_3) and Fe_3O_4 nanoparticles decompose H_2O_2 both at neutral and basic pH [18, 19].

$$2H_2O_2 \xrightarrow{\text{Catalase}} O_2 + 2H_2O \tag{6.2}$$

6.3 Kinetics and Mechanism of Action of IONzyme

IONzymes follow Michaelis–Menten kinetics as in Eq. 6.3 [24].

$$v = (V_{max}[S])/(K_m + [S]) \tag{6.3}$$

where 'v' is the initial velocity of the reaction, 'V_{max}' is the maximal rate of the reaction, '$[S]$' is the concentration of the substrate, and 'K_m' is the Michaelis–Menten constant.

$$K_{cat} = V_{max}/[E] \tag{6.4}$$

where 'K_{cat}' is the catalyst rate constant that describes the limiting rate of any enzyme-catalysed reaction at saturation (Eq. 6.4).

The determinations of V_{max}, K_m and K_{cat} for IONzymes are apparently determined based on the peroxidase reaction. Tetramethyl benzidine-hydrogen peroxide (TMB-H_2O_2) is a chromogenic substrate for HRP. This substrate produces a soluble blue colour in the presence of HRP. This reaction can be stopped with an equal volume of 1N sulfuric acid. The optical density of the resulting yellow colour can be read at 450 nm. HRP can be replaced with IONzyme, which has a greater affinity for TMB than the native enzyme. IONzyme's surface has abundant iron in contrast to the one iron in the HRP molecule, which may be attributed to its higher affinity.

For the measurement of catalase activity, oximetry is preferred. An oxygen electrode senses the rate of O_2 generation. The reaction rate of catalase is positively correlated with the amount of molecular oxygen generated in the solution. However, it may be affected by external factors such as temperature, diffusion and oxygen in the air. Catalase can be replaced with IONzyme to perform the above process [25, 26].

A haem group and a coordinated iron are present in the active sites of the enzymes peroxidase and catalase. This helps with electron transfer during redox reactions. In an IONzyme, the superficial surface may act as an active site. The affinity of IONzyme towards H_2O_2 can be enhanced by manipulating the surface of IONzyme by molecular coating, imprinting or grafting other substances on its surface [24, 27].

6.4 Synthesis of IONzyme

IONzyme synthesis is achieved using the chemical methods, co-precipitation, solvothermal preparation, sol–gel, oxidative hydrolysis, thermal decomposition and Massart hydrolysis [27]. However, shape, size, morphology, nanostructure and activity change from one method to another. Biogenic methods of IONzyme synthesis like bacterial magnetosomes are possible, and they produce uniform-size IONzymes with better dispersity and biocompatibility than chemical methods [28, 29]. Additionally, modification of IONzyme's surface or its integration into other substances can be done to form multifunctional hybrid nanocomplexes to facilitate its further applications. For example, iron oxide is integrated onto the surface of graphene oxide and hydrogel [30, 31]. It is hard to compare IONzymes produced by different available methods and find the best one.

6.5 Properties of IONzyme

(1) **Stability**: IONzymes are more stable in comparison to natural enzymes like peroxidase and catalase in a broad range of pH and temperature. For instance, Fe_3O_4 nanozyme is stable at pH 1–12, with temperatures 4–90 °C although the catalytic activity reduces at a pH below 5 and above 40 °C [32–34].

(2) **Tunability**: IONzymes can be tuned to enhance their activity by modulating their shape, size and surface. Usually, the smaller the size of IONzymes, the superior the catalytic activity [35]. The activity of IONzymes could be improved by doping with other elements like gold (Au), silver (Ag) and platinum (Pt). Au–Fe_3O_4 nanoparticles (NPs) have more peroxidase-like activity than Fe_3O_4 NPs due to the synergistic effect of Fe_3O_4 NPs and Au NPs. Also, polarization effects from Au to Fe_3O_4 occur. Ag-nanowire coated on Fe_3O_4 NPs gives enhanced peroxidase-like activity compared to Fe_3O_4 NPs. Pt–Fe_3O_4 NPs show enhanced catalytic activity compared to Fe_3O_4 nanoparticles. Iron oxide NPs integrated

into carbon nanomaterials exhibit better peroxidase activity than pure iron oxide nanoparticles [24, 36, 37]. Surface modifications of IONzyme may substantially increase, decrease or reduce its activity depending upon the microenvironment and nature of the substrate. Fe_3O_4 NPs modified with polyethylene glycol decrease enzyme activity, but modifications with dextran have no substantial effect. Likewise, the surface charge of IONzyme may increase or decrease its activity. Heparin-coated negative surface charges of iron oxide nanoparticles showed nearly sixfold higher peroxidase activity than those with ethyleneimine-coated positive surface charges using TMB as the substrate. However, positive surface charges showed more than 11-fold higher peroxidase activity than those with negative surfaces using 2,2′-Azinobis [3-ethylbenzothiazoline-6-sulfonic acid]-diammonium salt (ABTS) as the substrate. ABTS is a chromogenic substrate for HRP that yields a green end product after reacting with peroxidase. Catalytic efficiency was further increased by lowering the size of NPs [24]. Integration of biomolecules can enhance the IONzyme's activity. For instance, the peroxidase-like activity of DNA-capped iron oxide nanoparticles and casein-coated magnetic nanoparticles has more effect than that of naked nanoparticles using the TMB system [38].

(3) **Multifunctionality**: IONzyme has the property of superparamagnetism, and enzymatic activity is an additional nanoscale feature. Hence, both of these properties allow IONzymes for multi-purpose performance. IONzyme mimics peroxidase activity in acidic pH and catalase activity in neutral pH [19]. So, these activities can be regulated by changing pH in a cancer microenvironment or a biofilm formed by dysbiotic microbiota. Moreover, IONzyme can be used as a vehicle to load numerous molecules into a pathway to perform cascade reactions [39].

6.6 Applications of IONzyme in biomedicine

In the area of biomedicine, the enzymatic activity of IONzyme has been widely reported. The peroxidase-like activity of IONzyme provides an opportunity for designing colorimetric assays. Free radicals generated by it help kill microbes and cells via the ROS-mediated signalling pathway.

(1) **Enzyme alternative for immunoassay and pathogen detection**

IONzymes can be used instead of peroxidase in assays based on peroxidase activity. For example, IONzymes can be use in place of HRP-based detection in enzyme-linked immunosorbent assays (ELISA) and other similar assays by conjugating antibodies to them (Fig. 6.2).

Similarly, the superparamagnetism properties of IONzyme help enrich a small amount of antigens and improve the sensitivity of the assay. For example, chitosan-modified magnetic nanoparticles successfully detect a very small amount (1 ng/ml) of carcinoembryonic antigen. This immunoassay has been reported to detect

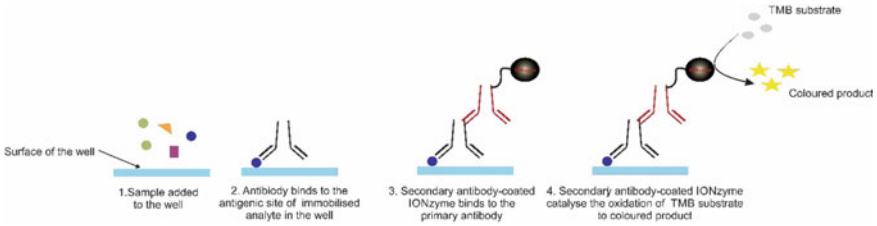

Fig. 6.2 IONzymes for immunoassay. The antibody recognizes the antigenic site of the analyte and is then detected by the second antibody-coated IONzymes, which catalyse the oxidation of colorimetric (TMB) substrates to give rise to a coloured product

IgG, human chorionic gonadotropin, epidermal growth factor receptor and human epidermal growth factor receptor [18]. IONzyme can be used to develop a lateral flow-based diagnostic test kit. This has been successfully achieved to detect glycoproteins of the Ebola virus and is more sensitive than the standard colloidal gold strip. A similar method has been used to detect the new bunyavirus. IONzyme's surface is coated with a forward primer and a biotinylated reverse primer, which can amplify the target DNA during PCR. This can bind to a streptavidin-coated surface and produce a signal via the catalysis of IONzyme. This assay can detect *Vibrio cholerae* with a minimum of 10^3 colony-forming units/mL and show directions for detecting other bacterial DNAs in food and water. IONzyme's surface, coated with aptamers, has the potential to identify target molecules with high specificity. This method has been reported to detect *Listeria monocytogenes* in food [40].

(2) **Enzyme cascades and substrate-based detection**

Multiple enzymes can be brought together onto the IONzyme surface to execute a cascade of enzymatic reactions to react with the substrate, followed by its detection indirectly by analysing the product. Glucose oxidase was bonded with Fe_3O_4 nanoparticles. Then, glucose was catalysed by glucose oxidase to produce H_2O_2. H_2O_2 was catalysed by IONzymes due to its peroxidase activity. By using a chromogenic substrate, a colour signal can be formed in proportion to the concentration of glucose [19, 39]. This glucose detection method was reflected in many other reports [24, 41, 42]. Similarly, different oxidases that can produce H_2O_2 as an intermediate in a cascade of reactions can be bonded to IONzyme to detect the corresponding substrates. In this regard, galactose oxidase for galactose, cholesterol oxidase for cholesterol and alcohol oxidase for alcohol have been reported to be used in IONzyme base detection [43, 44]. Integrating of a series of natural enzymes into IONzyme to participate in a cascade reaction offers a novel approach to developing assays for detecting any molecules present in the cascade.

(3) **Diagnosis of tumour and its therapy**

IONzyme shows promising applications for the diagnosis of tumours and their therapy. For tumour diagnosis, an IONzyme called magnetoferritin (MFt) nanoparticles, a superparamagnetic protein, can be used. MFt nanoparticles were encapsulated inside the shell of human heavy-chain ferritin. Upon delivery, this binds to

cancerous cells overexpressing transferrin receptor 1. The peroxidase activities of IONzyme allow the oxidation of target substrates in the presence of H_2O_2, resulting in the formation of coloured products. The coloured product can be seen in the solid tumour [45]. In a therapeutic approach, IONzyme can be used to kill cancer cells by catalysing H_2O_2 and producing toxic radicals in the tumour microenvironment. For this, delivery of H_2O_2 into the target tissue in vivo or integrating an enzyme that can produce H_2O_2 using a substance in the target tissue as a substrate may be considered. This approach has been tested using Fe_3O_4 nanozyme and H_2O_2 in a mouse model of cervical cancer [46]. Iron present in the nanomaterials produces a lot of ROS, resulting in the death of cancer cells, or induces polarization of macrophages in tumour tissues to reduce their further growth without administration of H_2O_2 from outside [47, 48]. Such anti-cancer effects may be attributed to the enzymatic action of iron in nanomaterials, which is similar to IONzyme. It is crucial to understand the safety of IONzyme in terms of its distribution, kinetics, action and clearance in an animal model. Fe_3O_4 nanoparticles coated with dextran were localized mostly in the liver, lung and spleen and less in the kidney, lymph nodes and thymus. Usually, nanoparticles are taken up by the reticuloendothelial system and circulated to the liver, lung and spleen.

(4) **Anti-bacteria and biofilm elimination**

IONzymes have the potential to kill bacteria and reduce biofilm formation [49]. H_2O_2 gives rise to free radicals in the presence of IONzyme, which can destroy bacterial cells by attacking their membrane proteins or genetic material in the nucleus. The free radicals inhibit bacterial biofilm formation. The peroxidase-like activity of IONzyme facilitates increasing the anti-bacterial action of H_2O_2. The increased effect has been reported on *Escherichia coli* and *Staphylococcus aureus* [46, 50]. These anti-bacterial properties are helpful to kill multiple-drug-resistant bacteria, inhibit sepsis and heal injuries. Free radical production and peroxidase activity in the presence of Fe_3O_4 nanozyme lead to oxidative damage of the components of biofilm, such as oligosaccharides, nucleic acids and proteins. The action of IONzyme and H_2O_2 independently is not efficient, but synergistic effects work better for oxidative degradation [18]. The Fe_3O_4 nanoparticles and H_2O_2 work as a system to cleave biomolecules, resulting in the degradation of existing biofilms and preventing the formation of new ones. This approach has been reported to target microorganisms in the oral microenvironment to inhibit the formation of plaque and dental caries [51]. The peroxidase-like action of IONzyme breaks glucans in the biofilm matrix into glucose and kills microbes like *Streptococcus mutans*. It also reduces the demineralization of teeth in an acidic environment created by dysbiotic microbiota. These reports suggested the potential of nanozymes as a compelling option for managing of biofilm-related illnesses.

6.7 Conclusion

IONzyme is regarded as an enzyme mimetic of the new generation due to its strong catalytic properties. The kinetics of IONzyme were subsequently investigated to elucidate its mechanism of action and improved by manipulating its size, shape, surface, dopants and combination with other nanoparticles. This facilitates sensibly designing the appropriate nanozymes for practical appliances. Compared to natural enzymes and other mimetic of natural enzymes, IONzymes are more stable. Also, they are multifunctional and versatile since they can be modified by additional labelling to function on multiple platforms in terms of assay development and therapy. These properties have shown a new direction for using magnetism-independent iron oxide nanomaterials. It has been reported that magnetic iron oxide materials can be used in the field of biomedicine in some specific instances, like DNA isolation, delivery of genes to the target, sorting of desired cells and imaging of solid tumours. For instance, we can sort T-cells to be used in chimeric antigen receptor (CAR) T-cell therapy, an important immunotherapy for treating cancer. These uses are based on their magnetic properties. IONzymes, to which the enzyme-like properties bring further advantages like immunoassays, detection of microbes, diagnosis and therapy of tumours, biofilm removal, and free radical modulations at different levels for cellular differentiation and development. As yet, several IONzymes and their applications have been addressed, but several insight challenges still need to be addressed. A standard procedure is needed to calculate and compare the activities of different IONzymes from independent preparations. Specific activity is one way to evaluate enzyme activity. More specific evaluation is needed for calculating the K_M, K_{cat} or K_{cat}/K_M in the same reaction conditions in terms of substrate quantity, temperature, pH and buffer.

IONzymes are not natural, and their interaction, affinity and action are not the same as those of natural enzymes; the method to improve their selectivity is still incomplete. The feature of interaction at the molecular level between enzyme and substrate may help to synthesize IONzymes with enhanced selectivity. Molecular imprinting is one way to improve the IONzyme's selectivity. Enzyme-mimicking activities of IONzyme are studied mostly in catalase and peroxidase. Numerous natural enzymes utilize iron as a cofactor to execute catalytic activities. Therefore, it is vital, though difficult, to design IONzyme with a preferred action. The probable clue remains in understanding the detailed structure and functions of natural enzymes. In vivo activities of IONzyme and their correlation with catalytic activity, therapeutic effect, and biocompatibility still need to be clearly understood. Iron oxide nanoparticles got clinical permission for magnetic resonance imaging (MRI) of tumours in vivo. However, its biocompatibility and intrinsic peroxidase and catalase-like activities need to be carefully evaluated. Influences on reactive oxygen species-sensitive events in vivo need to be investigated. These include immune activation and repression, the development of nerves and the nervous system, heart regulation, stem cell lineage maintenance, differentiation and growth. Overall, great efforts are needed to address and overcome the fundamental challenges and advance IONzyme's activity for both in vitro and in vivo applications.

References

1. Maldonado-Camargo L, Unni M, Rinaldi C (2017) Magnetic characterization of iron oxide nanoparticles for biomedical applications. Methods Mol Biol 1570:47–71
2. Wahajuddin S (2012) Arora, superparamagnetic iron oxide nanoparticles: magnetic nanoplatforms as drug carriers. Int J Nanomed 7:3445–3471
3. Dulinska-Litewka J, Lazarczyk A, Halubiec P, Szafranski O, Karnas K, Karewicz A (2019) Superparamagnetic iron oxide nanoparticles-current and prospective medical applications. Materials **12**:617
4. Lee DY, Kang S, Lee Y, Kim JY, Yoo D, Jung W, Lee S, Jeong YY, Lee K, Jon S (2020) PEGylated bilirubin-coated Iron oxide nanoparticles as a biosensor for magnetic relaxation switching-based ROS detection in whole blood. Theranostics 10:1997–2007
5. Kaushik A, Khan R, Solanki PR, Pandey P, Alam J, Ahmad S, Malhotra BD (2008) Iron oxide nanoparticles-chitosan composite based glucose biosensor. Biosens Bioelectron 24:676–683
6. Abarca-Cabrera L, Fraga-Garcia P, Berensmeier S (2021) Bio-nano interactions: binding proteins, polysaccharides, lipids and nucleic acids onto magnetic nanoparticles. Biomater Res 25:12
7. Fahmy SA, Alawak M, Brussler J, Bakowsky U, El Sayed MMH (2019) Nanoenabled bioseparations: current developments and future prospects. Biomed Res Int 2019:4983291
8. Turrina C, Berensmeier S, Schwaminger SP (2021) Bare iron oxide nanoparticles as drug delivery carrier for the short cationic peptide lasioglossin. Pharmaceuticals 14:405
9. Shen L, Li B, Qiao Y (2018) Fe_3O_4 nanoparticles in targeted drug/gene delivery systems. Materials 11:324
10. Shen Z, Wu A, Chen X (2017) Iron oxide nanoparticle based contrast agents for magnetic resonance imaging. Mol Pharm 14:1352–1364
11. Ullah Khan A, Chen L, Ge G (2021) Recent development for biomedical applications of magnetic nanoparticles. Inorg Chem Commun **134**:108995
12. Wabler M, Zhu W, Hedayati M, Attaluri A, Zhou H, Mihalic J, Geyh A, DeWeese TL, Ivkov R, Artemov D (2014) Magnetic resonance imaging contrast of iron oxide nanoparticles developed for hyperthermia is dominated by iron content. Int J Hyperther **30**:192–200 (North American Hyperthermia Group)
13. Gao L, Zhuang J, Nie L, Zhang J, Zhang Y, Gu N, Wang T, Feng J, Yang D, Perrett S, Yan X (2007) Intrinsic peroxidase-like activity of ferromagnetic nanoparticles. Nat Nanotechnol 2:577–583
14. Niu X, Liu B, Hu P, Zhu H, Wang M (2022) Nanozymes with multiple activities: prospects in analytical sensing. Biosensors **12**
15. Singh S (2019) Nanomaterials exhibiting enzyme-like properties (nanozymes): current advances and future perspectives. Front Chem 7:46
16. Zhang Y, Jin Y, Cui H, Yan X, Fan K (2019) Nanozyme-based catalytic theranostics. RSC Adv 10:10–20
17. Huang Y, Ren J, Qu X (2019) Nanozymes: classification, catalytic mechanisms, activity regulation, and applications. Chem Rev 119:4357–4412
18. Gao L, Fan K, Yan X (2017) Iron oxide nanozyme: a multifunctional enzyme mimetic for biomedical applications. Theranostics 7:3207–3227
19. Chen Z, Yin JJ, Zhou YT, Zhang Y, Song L, Song M, Hu S, Gu N (2012) Dual enzyme-like activities of iron oxide nanoparticles and their implication for diminishing cytotoxicity. ACS Nano 6:4001–4012
20. Li Y, Wang Z, Liu R (2021) Superparamagnetic alpha-Fe_2O_3/Fe_3O_4 heterogeneous nanoparticles with enhanced biocompatibility. Nanomaterials 11:834
21. Wang L, Min Y, Xu D, Yu F, Zhou W, Cuschieri A (2014) Membrane lipid peroxidation by the peroxidase-like activity of magnetite nanoparticles. Chem Commun 50:11147–11150
22. Yang YC, Wang YT, Tseng WL (2017) Amplified peroxidase-like activity in iron oxide nanoparticles using adenosine monophosphate: application to urinary protein sensing. ACS Appl Mater Interf 9:10069–10077

23. Liu CH, Yu CJ, Tseng WL (2012) Fluorescence assay of catecholamines based on the inhibition of peroxidase-like activity of magnetite nanoparticles. Anal Chim Acta 745:143–148
24. Yu F, Huang Y, Cole AJ, Yang VC (2009) The artificial peroxidase activity of magnetic iron oxide nanoparticles and its application to glucose detection. Biomaterials 30:4716–4722
25. Fan K, Wang H, Xi J, Liu Q, Meng X, Duan D, Gao L, Yan X (2016) Optimization of Fe_3O_4 nanozyme activity via single amino acid modification mimicking an enzyme active site. Chem Commun 53:424–427
26. Li W, Fan GC, Gao F, Cui Y, Wang W, Luo X (2019) High-activity Fe_3O_4 nanozyme as signal amplifier: a simple, low-cost but efficient strategy for ultrasensitive photoelectrochemical immunoassay. Biosens Bioelectron 127:64–71
27. Vallabani NVS, Singh S (2018) Recent advances and future prospects of iron oxide nanoparticles in biomedicine and diagnostics. 3 Biotech **8**:279
28. Mirabello G, Lenders JJ, Sommerdijk NA (2016) Bioinspired synthesis of magnetite nanoparticles. Chem Soc Rev 45:5085–5106
29. Guo FF, Yang W, Jiang W, Geng S, Peng T, Li JL (2012) Magnetosomes eliminate intracellular reactive oxygen species in *Magnetospirillum gryphiswaldense* MSR-1. Environ Microbiol 14:1722–1729
30. Zhang L, Yu X, Hu H, Li Y, Wu M, Wang Z, Li G, Sun Z, Chen C (2015) Facile synthesis of iron oxides/reduced graphene oxide composites: application for electromagnetic wave absorption at high temperature. Sci Rep 5:9298
31. Belda Marin C, Egles C, Humblot V, Lalatonne Y, Motte L, Landoulsi J, Guenin E (2021) Gold, silver, and iron oxide nanoparticle incorporation into silk hydrogels for biomedical applications: elaboration, structure, and properties. ACS Biomater Sci Eng **7**:2358–2371
32. Park Y, Whitaker RD, Nap RJ, Paulsen JL, Mathiyazhagan V, Doerrer LH, Song YQ, Hurlimann MD, Szleifer I, Wong JY (2012) Stability of superparamagnetic iron oxide nanoparticles at different pH values: experimental and theoretical analysis. Langmuir 28:6246–6255
33. Paolone A, Angelucci M, Panero S, Betti MG, Mariani C (2014) Thermal stability and reduction of iron oxide nanowires at moderate temperatures. Beilstein J Nanotechnol 5:323–328
34. Dani RK, Schumann C, Taratula O (2014) Temperature-tunable iron oxide nanoparticles for remote-controlled drug release. AAPS PharmSciTech 15:963–972
35. Magro M, Vianello F (2019) Bare iron oxide nanoparticles: surface tunability for biomedical, sensing and environmental applications. Nanomaterials **9**
36. Wang C, Qian J, Wang K, Yang X, Liu Q, Hao N, Dong X, Huang X (2016) Colorimetric aptasensing of ochratoxin A using Au@Fe_3O_4 nanoparticles as signal indicator and magnetic separator. Biosens Bioelectron 77:1183–1191
37. Lee JW, Jeon HJ, Shin HJ, Kang JK (2012) Superparamagnetic Fe_3O_4 nanoparticles-carbon nitride nanotube hybrids for highly efficient peroxidase mimetic catalysts. Chem Commun 48:422–424
38. Liu B, Liu J (2015) Accelerating peroxidase mimicking nanozymes using DNA. Nanoscale 7:13831–13835
39. Wei H, Wang E (2008) Fe_3O_4 magnetic nanoparticles as peroxidase mimetics and their applications in H_2O_2 and glucose detection. Anal Chem 80:2250–2254
40. Zhang L, Huang R, Liu W, Liu H, Zhou X, Xing D (2016) Rapid and visual detection of Listeria monocytogenes based on nanoparticle cluster catalyzed signal amplification. Biosens Bioelectron 86:1–7
41. Wang Y, Zhou B, Wu S, Wang K, He X (2015) Colorimetric detection of hydrogen peroxide and glucose using the magnetic mesoporous silica nanoparticles. Talanta 134:712–717
42. Liu Q, Li H, Zhao Q, Zhu R, Yang Y, Jia Q, Bian B, Zhuo L (2014) Glucose-sensitive colorimetric sensor based on peroxidase mimics activity of porphyrin-Fe_3O_4 nanocomposites, Materials science & engineering. Mater Sci Eng C 41:142–151
43. Kim MI, Shim J, Li T, Woo MA, Cho D, Lee J, Park HG (2012) Colorimetric quantification of galactose using a nanostructured multi-catalyst system entrapping galactose oxidase and magnetic nanoparticles as peroxidase mimetics. Analyst 137:1137–1143

44. Il Kim M, Shim J, Parab HJ, Shin SC, Lee J, Park HG (2012) A convenient alcohol sensor using one-pot nanocomposite entrapping alcohol oxidase and magnetic nanoparticles as peroxidase mimetics, J Nanosci Nanotechnol 12:5914–5919
45. Fan K, Cao C, Pan Y, Lu D, Yang D, Feng J, Song L, Liang M, Yan X (2012) Magnetoferritin nanoparticles for targeting and visualizing tumour tissues. Nat Nanotechnol 7:459–464
46. Zhang D, Zhao YX, Gao YJ, Gao FP, Fan YS, Li XJ, Duan ZY, Wang H (2013) Anti-bacterial and in vivo tumor treatment by reactive oxygen species generated by magnetic nanoparticles. J Mater Chem B 1:5100–5107
47. Kim SE, Zhang L, Ma K, Riegman M, Chen F, Ingold I, Conrad M, Turker MZ, Gao M, Jiang X, Monette S, Pauliah M, Gonen M, Zanzonico P, Quinn T, Wiesner U, Bradbury MS, Overholtzer M (2016) Ultrasmall nanoparticles induce ferroptosis in nutrient-deprived cancer cells and suppress tumour growth. Nat Nanotechnol 11:977–985
48. Zanganeh S, Hutter G, Spitler R, Lenkov O, Mahmoudi M, Shaw A, Pajarinen JS, Nejadnik H, Goodman S, Moseley M, Coussens LM, Daldrup-Link HE (2016) Iron oxide nanoparticles inhibit tumour growth by inducing pro-inflammatory macrophage polarization in tumour tissues. Nat Nanotechnol 11:986–994
49. Thukkaram M, Sitaram S, Kannaiyan SK, Subbiahdoss G (2014) Anti-bacterial efficacy of iron-oxide nanoparticles against biofilms on different biomaterial surfaces. Int J Biomater 2014:716080
50. Pan WY, Huang CC, Lin TT, Hu HY, Lin WC, Li MJ, Sung HW (2016) Synergistic anti-bacterial effects of localized heat and oxidative stress caused by hydroxyl radicals mediated by graphene/iron oxide-based nanocomposites. Nanomed Nanotechnol Biol Med 12:431–438
51. Gao L, Liu Y, Kim D, Li Y, Hwang G, Naha PC, Cormode DP, Koo H (2016) Nanocatalysts promote *Streptococcus mutans* biofilm matrix degradation and enhance bacterial killing to suppress dental caries in vivo. Biomaterials 101:272–284

Chapter 7
Nanoscale Zerovalent Iron and Its Composites for the Removal of Toxic Pollutants from Water

Uttam Kumar Sahu and Shengyan Pu

Abstract Organic chlorinated compounds and carcinogenic heavy metals like arsenic in surface and groundwater are a worldwide problem. Therefore, these studies focus on the removal of chlorinated hydrocarbons (CHCs) and heavy metals (arsenic) from an aqueous environment by using only nano zerovalent iron (nZVI) and biochar-supported nZVI. Here, biochar is prepared from naturally occurring environmentally friendly materials and then nZVI decorated on its surface through a chemical reduction process. The composite materials have been used for CHCs and arsenic removal with variations in solution parameters. The mechanism of interaction between adsorbate and adsorbent has also been discussed. Here, nZVI decorated biochar can be a potential adsorbent for wastewater treatment.

Keywords Chlorinated hydrocarbons · Arsenic · nZVI · Adsorption · Removal

7.1 Introduction

7.1.1 Water Pollution

Water is a renewable source, but the feasibility of freshwater is not renewable. A specific number of people in the world are suffering due to this lack of freshwater. Yet again, this water demand increases rapidly with population growth worldwide. A World Health Organization (WHO) survey revealed that only 2.6 billion people accessed drinking water in 1990. Still, it increased to 663 million in 2015, and by 2030, this ratio will increase very spontaneously and highly

U. K. Sahu (✉) · S. Pu
State Key Laboratory of Geohazard Prevention and Geoenvironment Protection, Chengdu University of Technology, 1#, Dongsanlu, Erxianqiao, Chengdu 610059, Sichuan, People's Republic of China
e-mail: sahuuttam02@gmail.com

U. K. Sahu
Department of BSH, GIET University, Gunupur, Odisha 765022, India

H. Sahoo and J. K. Sahoo (eds.), *Iron Oxide-Based Nanocomposites and Nanoenzymes*, Nanostructure Science and Technology, https://doi.org/10.1007/978-3-031-44599-6_7

affect the living organism [1]. The toxic, carcinogenic materials like chlorinated hydrocarbons (CHCs), perchloroethylene (PCE), polychlorinated biphenyls (PCBs), dichloroethane (DCE), trichloroethylene (TCE), hexachloroethane (HCA), and vinyl chloride (VC)) [2–4], heavy metals [5] (arsenic (As(III) and As(V))) are presented in water, which are not good and create problems for living beings. These toxic pollutants in water are mainly caused by growth in globalisation, increased population, and high-speed development in the industrialisation sector. The concentration or intensity of the above poisonous materials is so high that only 40% of people worldwide can access clean or pure water. By 2030, the availability of fresh drinking water will be less than 10%. Again, various problems arise due to the intake of this toxic water, including diseases like sickness, fever, change in colour of urine, headache, irritations in the skin, respiratory problems, anaemia, eye inflammations, kidney disease, hypertension, bladder irritation, nervous disorders, cardiovascular issues, neurological, endocrine disorders, heart disease, and lung cancer [2, 5].

To reduce the concentration level of the above pollutants, electrochemical processes [6] such as chemical precipitation [7], membrane filtration [8], reverse osmosis [9], adsorption [10], photocatalytic degradation [10], and ion-exchange [10] are applied by the different research groups. But the adsorption process gains visibility due to its easy maintenance, low cost, and efficient, non-toxic process. A number of carbon-based materials like biochar [11], clay minerals [12], and nanosized metal oxide [13] are frequently applied to remove pollutants from the wastewater system. In recent times, zerovalent iron oxide [10] has been widely used as an adsorbent for pollutants removal by chemical reduction processes, and its removal performance is thrilling and convincing. As compared to others, nanosized zerovalent iron oxide nanoparticles have greater redox potential and good adsorptive properties to remove toxic material from water.

There are different types of iron oxide nanoparticles (Fe_2O_3, Fe_3O_4, and nano zerovalent iron (nZVI)), which are used singly or supported with other materials that have been used for phenols, heavy metals, CHCs, and dye removal from aqueous environments. However, Fe_2O_3 and Fe_3O_4 have a lower ability and also mineralise with contaminants. Therefore, nano zerovalent iron (nZVI) is used for wastewater applications due to its low cost, abundance, and good reduction potential (ORP) of 0.44 [14]. Hence, a lot of studies have been done where halogenated organic compounds [15] and heavy metals (arsenic) [16] are effectively removed by using nZVI and show good results for its small particle size and outstanding chemical reactivity [16, 17]. The only problem with the nZVI is agglomeration, which reduced the active binding sites and decreased its efficiency. Hence, to check agglomeration, nZVIO has been decorated in the novel with other materials. The main reaction mechanism is the transfer of electrons (e) from ZVI to toxic materials, which are transformed into non-toxic elements.

The main objective of this review chapter is the preparation and application of nZVI and nZVI-based composites. The major objectives are (1) to explain the synthesis of the nZVI and nZVI-based bio-composites; (2) to explain the details of the solution parameter conditions for the removal of toxic heavy metal ions and halogenated hydrocarbon pollutants from wastewater; (3) to analyse the adsorption mechanisms of contaminants on nZVI nanoparticles; and (4) to give expected future research and conclusions.

7.1.2 Synthesis of Single nZVI Nanoparticles

There are two ways to synthesise nZVI nanoparticles: physical and chemical methods. But the physical method is very costly, time-consuming, and low-yielding. Therefore, the researcher has chosen the chemical method (mainly liquid-phase reduction) because of its easy operation and good yield to produce nZVI nanoparticles [10]. In liquid-phase reduction, the sodium borohydride process is mainly used to synthesise nZVI particles. An iron salt ($FeCl_3 \cdot 6H_2O$) solution is shaken at 150 rpm in a three-necked flask under a nitrogen atmosphere for 6 h at 80 °C. Then, $NaBH_4$ solutions have been added to it at regular intervals. Thereafter, washed with water, dried, and zerovalent iron nanoparticles are prepared as given in Eq. 7.1.

$$Fe^{3+} + 3BH_4^- + 3H_2O = Fe^0 + 3B(OH)_3 + 4.5H_2 \tag{7.1}$$

Researchers have produced different shapes and sizes of nZVI particles in the above-explained process. The particle sizes of 1–100 nm with chain-like nZVI particles [18], spherical nanoparticles [19], and quasi-spherical amorphous nZVI particles [20] have been successfully synthesised.

7.1.3 Synthesis of NZVI-Based Composite Materials

Single nZVIO particles show aggregation due to their nanosize and high surface energy, which limits their practical applications. To reduce the aggregation and increase the surface area, several nZVI-based composites have been prepared by using layered double hydroxides [21], graphene [22], clay minerals [23], polymers [24], and biochar [10] through a different process. This synthesis process contains inert gas condensation, thermal decomposition, chemical vapour deposition, hydrogenation of metallic oxides, pulsed laser ablation, template methods, and thermal reduction. However, biochar is considered one of the best supporting materials as it is a plant-based material, easily available everywhere, has good thermal stability, is non-toxic, and is low in cost.

7.2 Environmental Applications of nZVI-Based Biochar for the Removal of Contaminants from Water

Presently, the rapid use and synthesis of nZVI nanoparticles show their ability and potential for environmental applications for wastewater treatment. But as discussed above, the single nZVI nanoparticles show aggregation, which limits their practical applications. Hence, nZVIO has been modified with biochar prepared from different plant materials. The obtained nZVIO decorated biochar has a higher removal efficiency than single nZVI nanoparticles. The nZVI-based adsorbent will be an effective and promising adsorbent to remove toxic substances (CHCs and heavy metals) from the aqueous environment.

7.2.1 Chlorinated Hydrocarbons (CHCs)

Generally, groundwater is polluted due to chlorinated hydrocarbons (CHCs). The different types of CHCs are hexachloroethane (HCA), perchloroethylene (PCE), vinyl chloride (VC), polychlorinated biphenyls (PCBs), trichloroethylene (TCE), and dichloroethane (DCE). These chlorinated compounds are very toxic and harmful to both humans and animals [3, 4]. Hence, to remove or degrade this contaminant, single nZVI and biochar decorated nZVI have been used as promising materials as influential electron donors from the surface of iron to hydrocarbons for the reductive degradation of chlorinated compounds. Shan et al. applied the nZVI-Ni@BC composite for the elimination of trichloroethylene and found 99% degradation at pH 4 [25]. Semerad et al. applied nZVI/BC for chloroethene removal, and, here, they found that 99% of chlorine compounds were removed in 30 days [26]. Similarly, in another work, biochar was prepared from *Nephelium lappaceum* (Rambutan) fruit peel, and nZVI was decorated on its surface [27]. This composite was able to dechlorinate 96–99% at 120 min and pH 4.

7.2.2 Heavy Metals

Like organic pollutants, heavy metals are present in water and make it unusable for living beings and aquatic life. These heavy metals are non-biodegradable and carcinogenic. There are different types of heavy metals, such as arsenic, lead, chromium, mercury, copper, cadmium, and nickel. But amongst these, arsenic is very toxic and occupies the number one position in the toxic metal list, so we chose arsenic as a target heavy metal in this study. In groundwater, arsenic is mainly present in arsenite (As(III)) and arsenate (As(V)) forms [28]. National agencies like WHO and USAPA

have set the maximum amount of arsenic in drinking water to be less than 10 g/L. Therefore, nZVI and nZVI decorated materials have been used to remove arsenic in recent years.

Zhang et al. use single nZVI to remove As(III) through the oxidation-adsorption process, where electrons transfer from nZVI to As(III) which oxidises As(V), then adsorb on the surface of nZVI [29]. Similar results were observed by Yin et al. when nZVI was used to oxidise As(III) to As(V) [29]. About 99% of As(V) and 70.9% of As(III) were removed from the aqueous solution through the chemisorption process by using nZVI. Again, the same mechanism has been found by Liu et al., but they decorated nZVI on the graphene-like biochar surface [30]. The composite had a very high surface area and reduced As(III) to As(V) and As(V) was easily attached to the biochar surface. The adsorption capacity obtained was 363 mg/g. Mao et al. synthesised biochar from solid waste, put it on its surface, and applied it for arsenic removal [31]. About 90% of As(III) was removed in the optimum conditions of 20 mg/L of initial arsenic concentration, pH 7, and a contact time of 10 min, respectively. The adsorption capacity obtained was 121 mg/g. Zhu et al. also found an adsorption capacity of 18 and 12 mg/g for As(III) and As(V) by using activated-supported nZVI [29]. Here, arsenic removal by adsorbent proceeded with a pseudo-second-order kinetic model and was endothermic. The maximum amount of arsenic was removed at pH 7 and had a contact time of 72 h. The 0.1 M NaOH solution was used for regeneration studies. Xu et al. used carbonising biomass for biochar preparation, and 18.5–30.9% of Fe was loaded on its surface in the form of nZVI [32]. The adsorption was done in a large pH range, is highly efficient, and can be applied for several cycles without loss in efficiency. The maximum adsorption capacities of As(III) and As(V) were 129.24 mg/g and 127.15 mg/g, respectively.

7.3 Conclusions and Future Research Expected

Here, the review explains the synthesis of nZVIO and nZVIO decorated biochar, its application for heavy metal (arsenic) and chlorinated hydrocarbon removal from water, and the mechanism of target pollutants removal by reduction and adsorption processes. The effects of various experimental conditions have been explained thoroughly. In recent times, a lot of work has been done using nZVI for the above toxic substance removal, but still, there should be more discussions on the influence of environmental conditions, details of the adsorption mechanism, and large-scale application cost analysis studies. Therefore, future studies should be done to establish the interaction mechanism of nZVI with heavy metals and chlorinated hydrocarbons in groundwater and surface water, which will be highly beneficial for situ remediation.

References

1. Stephens GL, Slingo JM, Rignot E, Reager JT, Hakuba MZ, Durack PJ et al (2020) Earth's water reservoirs in a changing climate. Proc R Soc A Math Phys Eng Sci 476:1–33
2. Mishakov IV, Bauman YI, Brzhezinskaya M, Netskina OV, Shubin YV, Kibis LS et al (2022) Water purification from chlorobenzenes using heteroatom-functionalized carbon nanofibers produced on self-organizing Ni–Pd catalyst. J Environ Chem Eng 10:107873
3. Mangayayam MC, Perez JPH, Alonso-de-Linaje V, Dideriksen K, Benning LG, Tobler DJ (2022) Sulfidation extent of nanoscale zerovalent iron controls selectivity and reactivity with mixed chlorinated hydrocarbons in natural groundwater. J Hazard Mater 431:1–25
4. Wu YZ, Li HX, Xu ZL, Li P, Zhan ZM, Li PP et al (2022) Ceramic hollow fiber NF membrane incorporating UiO-66 for the chlorinated hydrocarbons removal. Chem Eng J 435:20–22
5. Rathi BS, Kumar PS (2021) A review on sources, identification and treatment strategies for the removal of toxic arsenic from water system. J Hazard Mater 418:126299
6. Kim J, Yoon S, Choi M, Min KJ, Park KY, Chon K et al (2022) Metal ion recovery from electrodialysis-concentrated plating wastewater via pilot-scale sequential electrowinning/chemical precipitation. J Clean Prod 330:129879
7. Hassani A, Malhotra M, Karim AV, Krishnan S, Nidheesh PV (2022) Recent progress on ultrasound-assisted electrochemical processes: a review on mechanism, reactor strategies, and applications for wastewater treatment. Environ Res 205:112463
8. Waqas S, Harun NY, Bilad MR, Samsuri T, Md Nordin NAH, Shamsuddin N et al (2022) Response surface methodology for optimization of rotating biological contactor combined with external membrane filtration for wastewater treatment. Membranes **12**:271
9. Guo Y, Liu C, Liu H, Zhang J, Li H, Zhang C (2022) Contemporary antibiofouling modifications of reverse osmosis membranes: State-of-the-art insights on mechanisms and strategies. Chem Eng J 429:132400
10. Sahu UK, Ji W, Liang Y, Ma H, Pu S (2022) Mechanism enhanced active biochar support magnetic nano zero-valent iron for efficient removal of Cr(VI) from simulated polluted water. J Environ Chem Eng 10:107077
11. Gupta M, Savla N, Pandit C, Pandit S, Gupta PK, Pant M et al (2022) Use of biomass-derived biochar in wastewater treatment and power production: a promising solution for a sustainable environment. Sci Total Environ 825:153862
12. Haclosmanoglu GG, Mejias C, Martin J, Santos JL, Alonso E (2022) Antibiotic adsorption by natural and modified clay minerals as designer adsorbents for wastewater treatment: a comprehensive review. J Environ Manage 317:115397
13. Ganzoury MA, Ghasemian S, Zhang N, Yagar M, de Lannoy CF (2022) Mixed metal oxide anodes used for the electrochemical degradation of a real mixed industrial wastewater. Chemosphere 286:131600
14. Fan Z, Zhang Q, Gao B, Li M, Liu C, Qiu Y (2019) Removal of hexavalent chromium by biochar supported nZVI composite: batch and fixed-bed column evaluations, mechanisms, and secondary contamination prevention. Chemosphere 217:85–94
15. Venkateshaiah A, Silvestri D, Wacławek S, Ramakrishnan RK, Krawczyk K, Saravanan P et al (2022) A comparative study of the degradation efficiency of chlorinated organic compounds by bimetallic zero-valent iron nanoparticles. Environ Sci Water Res Technol 8:162–172
16. Mortazavian S, An H, Chun D, Moon J (2018) Activated carbon impregnated by zero-valent iron nanoparticles (AC/nZVI) optimized for simultaneous adsorption and reduction of aqueous hexavalent chromium: material characterizations and kinetic studies. Chem Eng J 353:781–795
17. Zhang S, Lyu H, Tang J, Song B, Zhen M, Liu X (2019) A novel biochar supported CMC stabilized nano zero-valent iron composite for hexavalent chromium removal from water. Chemosphere 217:686–694
18. Ghosh A, Dutta S, Mukherjee I, Biswas S, Chatterjee S, Saha R (2017) Template-free synthesis of flower-shaped zero-valent iron nanoparticle: role of hydroxyl group in controlling morphology and nitrate reduction. Adv Powder Technol 28:2256–2264

19. Wang W, Jin Z, Li T, Zhang H, Gao S (2006) Preparation of spherical iron nanoclusters in ethanol-water solution for nitrate removal. Chemosphere **65**:1396–1404
20. Wang T, Lin J, Chen Z, Megharaj M, Naidu R (2014) Green synthesized iron nanoparticles by green tea and eucalyptus leaves extracts used for removal of nitrate in aqueous solution. J Clean Prod 83:413–419
21. Lv X, Qin X, Wang K, Peng Y, Wang P, Jiang G (2019) Nanoscale zero valent iron supported on MgAl-LDH-decorated reduced graphene oxide: Enhanced performance in Cr(VI) removal, mechanism and regeneration. J Hazard Mater 373:176–186
22. Bagheri M, Jafari SM, Eikani MH (2021) Ultrasonic-assisted production of zero-valent iron-decorated graphene oxide/activated carbon nanocomposites: chemical transformation and structural evolution. Mater Sci Eng C 118:111362
23. Khandelwal N, Tiwari E, Singh N, Darbha GK (2021) Heterogeneously porous multiadsorbent clay-biochar surface to support redox-sensitive nanoparticles: applications of novel clay–biochar–nanoscale zerovalent iron nanotrident (C-BC-nZVI) in continuous water filtration. ACS ES&T Water. 1:641–652
24. Ma B, Yao J, Chen Z, Liu B, Kim J, Zhao C et al (2022) Superior elimination of Cr(VI) using polydopamine functionalized attapulgite supported nZVI composite: behavior and mechanism. Chemosphere 287:131970
25. Shan A, Idrees A, Zaman WQ, Abbas Z, Ali M, Rehman MSU et al (2021) Synthesis of nZVI-Ni@BC composite as a stable catalyst to activate persulfate: trichloroethylene degradation and insight mechanism. J Environ Chem Eng 9:104808
26. Semerád J, Ševců A, Nguyen NHA, Hrabák P, Špánek R, Bobčíková K et al (2021) Discovering the potential of an nZVI-biochar composite as a material for the nanobioremediation of chlorinated solvents in groundwater: degradation efficiency and effect on resident microorganisms. Chemosphere 281:130915
27. Batool S, Shah AA, Abu Bakar AF, Maah MJ, Abu Bakar NK (2022) Removal of organochlorine pesticides using zerovalent iron supported on biochar nanocomposite from *Nephelium lappaceum* (Rambutan) fruit peel waste. Chemosphere 289:133011
28. Kanematsu M, Young TM, Fukushi K, Green PG, Darby JL (2013) Arsenic(III, V) adsorption on a goethite-based adsorbent in the presence of major co-existing ions: modeling competitive adsorption consistent with spectroscopic and molecular evidence. Geochim Cosmochim Acta 106:404–428
29. Zhang T, Zhao Y, Kang S, Bai H, Gu W, Fang D et al (2021) Mechanical activation of zero-valent iron (ZVI) in the presence of $CaCO_3$: improved reactivity of ZVI for enhancing As(III) removal from water. J Clean Prod 286:124926
30. Liu K, Li F, Cui J, Yang S, Fang L (2020) Simultaneous removal of Cd(II) and As(III) by graphene-like biochar-supported zero-valent iron from irrigation waters under aerobic conditions: synergistic effects and mechanisms. J Hazard Mater 395:112623
31. Mao W, Zhang L, Zhang Y, Guan Y (2022) Simultaneous removal of arsenite and cadmium by a manganese-crosslinking sodium alginate modified biochar and zerovalent iron composite from aqueous solutions. Environ Sci Nano 9:214–228
32. Xu L, Shu Z, Feng L, Zhou J, Li T, Zhao Z et al (2022) Fresh biomass derived biochar with high-load zero-valent iron prepared in one step for efficient arsenic removal. J Clean Prod 352:131616

Chapter 8
Oxide Phases in Bismuth Ferrite (BFO)—Key for Photovoltaic Application

Dillip Pattanayak, Samita Pattanayak, and Chinmaya Rout

Abstract Iron oxides have gained recognition in the twenty-first century for their innumerable applications in a variety of sectors, including nano-biotechnology, biomedical engineering, and many more. Iron oxides' super-paramagnetic characteristic and smaller size are the main factors in their widespread application. There are numerous polymorphic forms of iron oxide that display various magnetic properties, catalytic activity, biocompatibilities, and other multifunctional qualities. Iron oxide possesses five unpaired electrons and is ferromagnetic by nature, with M_s value 1.7 emu/g, according to magnetic experiments. Five are arranged in a 3D shell that is half filled in Fe^{3+}. The Fe^{3+} magnetic moments are connected anti-ferromagnetically between adjacent planes and ferromagnetically inside the pseudo cubic (111) planes. A shifting magnetic field in the iron oxide-based materials allows an electric current to flow through conductive material. This induced electrical current can be measured with a magnetoelectric sensor. In ferromagnetic materials like Fe_2O_3, spin creation is introduced, which created the device application known as spintronics.

Keywords BFO · Octahedral · Polarisation · Multiferroelectric

8.1 Introduction

Iron oxide is the mineral component that is most abundant in nature. It displays a variety of crystal structures, each with distinct structural as well as magnetic characteristics. They commonly take the forms of hematite, magnetite, and maghemite [6]. The close interaction of iron cations in octahedral or tetrahedral interstitial spaces with oxygen anions in planes explains the crystal structure of the three oxides. Due to its distinctive crystal structure, the crystallographic phase of iron oxide known

D. Pattanayak (✉) · C. Rout
Department of Physics, GIET University, Gunupur, Rayagada, Odisha 765022, India
e-mail: dkp.phy@gmail.com

S. Pattanayak
Department of Physics, Odisha University of Technology and Research, Bhubaneswar, Odisha 751003, India

H. Sahoo and J. K. Sahoo (eds.), *Iron Oxide-Based Nanocomposites and Nanoenzymes*, Nanostructure Science and Technology, https://doi.org/10.1007/978-3-031-44599-6_8

as magnetite (Fe_3O_4) is one of the most fascinating. There are four unique crystal polymorphs, each with a different magnetic property. The two primary forms of iron oxide, hematite and maghemite, are found in nature, although other oxides, such beta (–Fe_2O_3) and epsilon (–Fe_2O_3), are typically made in laboratories [6]. Iron oxides are most frequently found in rocks and soils, and hematite, also known as –Fe_2O_3, is the most common form of iron oxide. It is an oxide that exhibits weak magnetic characteristics at ambient temperature and can be either ferromagnetic or antiferromagnetic. It possesses paramagnetic characteristics above the Curie temperature, the Néel temperature, or the Curie–Weiss equation, respectively. Two-thirds of the octahedral interstices in –Fe_2O_3 are filled with Fe^{+3} ions in alternate layers, and the rhombohedral structure is of the corundum type. The hexagonal crystallographic structure that makes up the ion O^{-2} reticle is tightly packed; other forms of iron oxide are transformed into hematite, which is very stable under environmental circumstances and simpler to synthesise than other forms of oxide. A typical ferromagnetic mineral called g-Fe_2O_3 called maghemite is thermally unstable and turns into hematite at higher temperatures. According to Zboril et al., the crystal structure of its spinel is identical to that of magnetite, with the exception of vacancies in the cation sub-lattice. Fe(III) ions occupy two-thirds of the sites, which are filled in an orderly fashion with one vacant site followed by two full sites. Due of their rapid magnetisation, G-Fe_2O_3 and magnetite (Fe_3O_4) both exhibit significant magnetic responses, when subjected to an external magnetic field. They oxidise to –Fe_2O_3 at temperatures over 673 K because they are metastable oxides in an oxidising atmosphere. Fe_2O_3 is a peculiar iron oxide with a body-centred cubic structure and two non-equivalent octahedral crystallographic positions for the Fe^{+3} ions. It is the only kind of iron oxide that displays paramagnetic behaviour at room temperature. The Neel magnetic transition temperature is between 100 and 119 K; below this temperature, –Fe_2O_3 is magnetically organised in an anti-Ferro fashion. It changes into either g-Fe_2O_3 or α-Fe_2O_3, depending on the thermodynamic stability, when heated. The orthorhombic crystal structure of the epsilon form of iron oxide results from the tightly packed arrangement of four layers of oxygen (–Fe_2O_3). Consider g-Fe_2O_3, a polymorphous intermediate that resembles both g-Fe_2O_3 and –Fe_2O_3, as well as –Fe_2O_3. There are two magnetic transitions that –Fe_2O_3 passes through, one at about 495 K (the Curie temperature) and the other at about 110 K. One of the most important objectives of study into the solid chemical state of iron is to comprehend the processes and dynamics of the polymorphous transformation (kinetics of the transition crystalline phase) of iron oxides (2012 Callister Jr). Moreover, for these problems, it is equally crucial to comprehend the mechanism underlying any prospective uses of Fe_2O_3 in combination with other substances like bismuth. The most stable multiferroic material that exhibits both ferroelectric and antiferromagnetic properties in a single phase is $BiFeO_3$ (BFO). The mechanism of BFO-related material for prospective device application is given a special emphasis in this chapter.

8.2 About BFO

In multiferroelectricity, there are multiple primary ferroic order parameters present in a single material, including ferromagnetism, ferroelectricity, ferroelasticity, and ferrotoroidicity. Of these, ferromagnetism (or anti-ferromagnetism) and ferroelectricity are the two most intentional multiferroics that have been observed. Therefore, such materials have a wide range of potential applications that can be investigated in device application in spintronics, information storage devices, high sensitivity AC magnetic field sensors, electrically tunable microwave devices like filters, oscillators, and phase shifters, advance multifunctional devices with quick speed having efficiency, etc. $BiFeO_3$ is the most exceptional and eminent inorganic chemical compound that exists in a single phase at room temperature and has a rhombohedrally deformed ABO_3-type perovskite structure [22] (BFO). For many device applications, it is still possible to modify the structural, microstructural, electrical, and magnetic properties of perovskite oxide by substituting either on the A site, B site, or both while maintaining the original structure [24, 34, 41]. Perovskite has multiferroic characteristics at room temperature, with a lattice constant of $a = 5.63$, a rhombohedral angle of 89.45°, and a space group of R3c [45]. According to calculations made by Kreiselt et al. [15], BFO has a high curie temperature (T_C) of roughly 1143 K, a phase transition that is G-type antiferromagnetic, a high Neel temperature (T_N) of roughly 647 K, and high intrinsic polarisation (100 $\mu C/cm^2$) that is aligned with the (1 1 1) direction. Typically, in an ideal ABO_3 structure, "A" stands for a larger metal cation (12-fold coordination), which is located at the cube's corner, "B" for a smaller metal cation (sixfold coordination), which is located in the middle, and "O" for a negatively charged anion, which is located at the cube's face centre. At room temperature, many oxides display slightly distorted fluctuations with less symmetry. The ferromagnetic (FM) or ferroelectric (FE) properties of perovskites are related to some structural aberrations in those materials. The structural deformation of the perovskite structure is measured by the ratio of the A to B cation size for metal ions. The Goldsmith's tolerance factor (t) was used to calculate and identify the compatibility of an ion with the perovskite crystal structure (Wang et al.; [19]. The displacement of the Bi^{3+} from Centro symmetric positions as a result of the Bi^{3+} lone pair (6 s orbital) and O_2 (2p orbital) hybridisation is what results in the ferroelectric polarisation in BFO. Despite the high values of (T_C) and (T_N) for BFO (unique multiferroic material), the majority of researchers are interested in using at least two switchable states, such as polarisation, magnetisation, and strain, for multifunctional devices (Kreiselt et al.). Due to the fact that a single BFO material has both ferromagnetic and ferroelectric characteristics, an electric field can alter the magnetisation while an external magnetic field can alter the electric polarisation. This phenomenon is known as the magnetoelectric effect (ME), and the materials that exhibit it are referred to as magnetoelectrics. Due to urgent prospective uses and ecologically friendly electronics such as spintronics, multifunctional low-power sensors, actuators, and transducers, as well as the possibility of mutual control of magnetic and electric properties, this possibility is the focus of the majority of research [10]. However, the main drawback of $BiFeO_3$ is high dielectric loss and higher leakage current, which are caused by the oxygen

vacancy at the Bi site of BFO and restrict the material's ability to be employed for device manufacturing [38, 55]. By applying an electric field at ambient temperature to create the proper ferroelectric hysteresis loop, the semiconducting behaviour and high leakage current of the BFO material are constrained [16].

Ion replacement is the most effective way to get around these problems, making it a possible contender for use in devices.

8.3 Mechanism for Device Application

8.3.1 Crystal Structure of BFO

The majority of crystal oxides of the ABO_3 class share the same structure as the perovskite mineral ($CaTiO_3$). The ideal perovskite structure has a Pm3m space group and a cubic unit cell with a side of about 3.9 A_0. The most typical perovskite structure is the BFO ($BiFeO_3$) bulk ceramic perovskite structure seen in Fig. 8.1. It belongs to the space group R3c at room temperature, with a rhombohedral symmetry structure, a lattice constant of 5.63, and a rhombohedral angle of 89.45. The "A" and "B" ions each contains octahedral oxygen coordination, and the oxygen ions are linked to six cations (4A + 2B). A bigger metal cation (+ve) is located at the cube's corner in the perovskite structure, B represents a positive metal cation in the centre, and O is a negatively charged anion located at the cube's face. The ferroelectric polarisation property is led by the A site, or Bi^{3+}, through structural distortions brought on by its stereo-chemically active lone pairs of electrons. The magnetisation property is led by the B site, or Fe^{3+}, with its five 3D electrons. The A and B ions must be big enough to form 12-fold and sixfold (octahedral) anion coordination, respectively ($r_A > 0.9$ A° and $r_B > 0.51$ A°), as this is a crucial requirement for the stability of the perovskite structure. For metal ions, the ratio between cation sizes A and B measures structural deformation. Goldsmith's tolerance factor was used to calculate and determine the compatibility of an ion with the perovskite crystal structure [16, 38] (t).

$$t = \frac{(r_A + r_O)}{\sqrt{2}(r_B + r_O)}$$

t is equal to one for the ideal perovskite structure and ranges between 0.75 and 1 for other structures. If either $t < 1$ or $t > 1$ occurs, the structural distortion occurs. Though they have a specific place in the rhombohedral BFO structure, the substitution of another element will cause a significant change in the physical and structural characteristics of Bi^{3+} and Fe^{3+}. The material structure and its many components are changed when there is partial substitution of captions at site A, site B, or concurrently at both, which results in a variety of odd features including multiferroicity [8, 46] piezoelectricity [39], superconductivity [21], ionic conduction, dielectric and optical properties, insulator metal transition properties, and ferroelectricity [4, 13, 32].

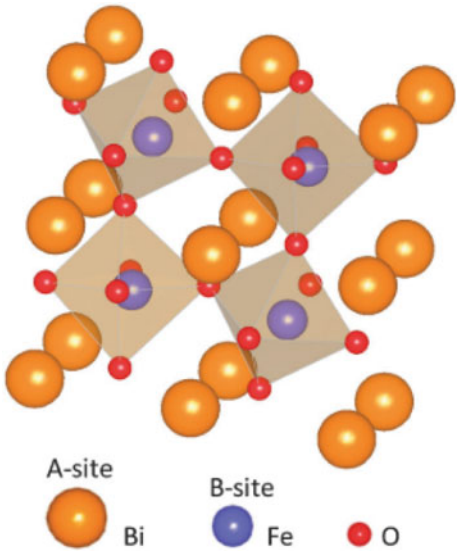

Fig. 8.1 Perovskite crystal structure of $BiFeO_3$

8.3.2 Ion Substitution in BFO Bulk Ceramic

The common method for altering ion substitutions on either the Bi or Fe sites in BFO bulk ceramics, or both, in order to improve the electrical characteristics. When an ion is substituted at the Bi site, the ferroelectric and piezoelectric properties are changed by lowering leakage current. The effects of ion replacements, especially those involving rare earth ions, are detailed in detail below for each site in BFO.

8.3.2.1 Substitution for Bi Site

The rare earth ion (Bi_{3+}) in the BFO has a partially filled f-shell that is close to the core area and is shielded by a stable outer shell of 5s and 5p orbitals. The rare earth ions fill the vacant space between the oxygen octahedrons, affecting the bond by providing an electron to the B site and affecting the bond's bond angle. However Bi^{3+} in BFO has 6s electron in the outer shell resulting reaction phenomena in terms of spatial position and electron energy level. It produces covalent bond with neighbouring oxygen ion (Bi_{6sp}–O_{2p}) or makes 6s lone pair (shown Fig. 8.2).

Since polarisation is generated by the Bi site, the ferroelectric and magnetic characteristics of BFO ceramic bulks are both significantly impacted by the appropriate ion substitution. It has been noted that rare earth element doping enhances the electrical characteristics of BFO ceramics. When rare earth elements are substituted (e.g. Sm [36, 37, 42, 56], Nd [49, 51], Dy [37, 54], La (Ying, [50]), Ce [28], Ho [11, 40], Yb, Eu, Gd, Tb, and Pr) in the Bi site, it is possible to successfully control the leakage current of BFO ceramics, enhancing the piezoelectric and ferroelectric properties. In

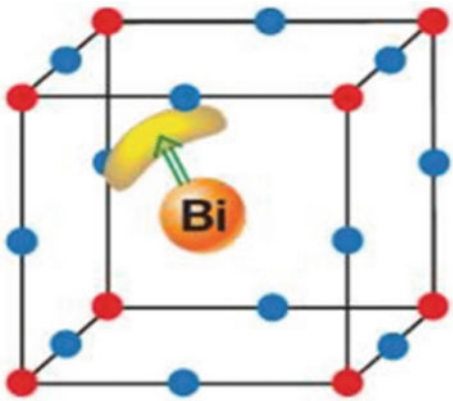

Fig. 8.2 Ordering of lone pairs (yellow" lobes") of Bi^{3+} ions (orange), contributes to the polarisation (green arrow) [Ref: D. Khomskii, Physics 2, 20 (2009)]

the case of BFO ($Bi_{1-x-y}Sm_xLa_yFeO_3$) ceramics, for instance, Wu et al. observed that co-substitution of La and Sm at the Bi^{3+} site revealed that for high value of d33 of 50 pC/N will decrease leakage current. A moderately high remnant polarisation Pr value of 10–50 pC/cm^2 was also noted when Sm, Dy, Eu, Gd, Tb, and other elements were substituted on BFO ceramics. The BFO's ferroelectric and piezoelectric characteristics will surely be improved by the rare earth replacement for the leakage current. Phase structural alterations brought about by ion substitution at the Bi site may potentially be significant. Therefore, it is crucial to look into how various ion substitutions affect the phase structure of BFO ceramics. Rare earth elements undergo a phase change from rhombohedral structure to others when doped with BFO compounds. The kind and amount of doped rare earth elements have a significant impact on the phase structures. Yuan and Or [50], Anbusathaiah et al. [3], Ceramics et al. [7], Levin et al. [17], Sun et al. [44], Karpinsky et al. [14], and others all mention this. For example, according to Yuan et al., the phase transformation of the $Bi_{1-x}Nd_xFeO_3$ ceramics occurs from rhombohedral structure ($x = 0$) to triclinic structure ($x =$ 0.05–0.15) and finally to pseudo-tetragonal structure ($x = 0.175$–0.2). The magnetic behaviour was impacted by the slow collapse of the space-modulated spin structure. The ferroelectric characteristics deteriorate as x grows due to the presence of non-ferroelectric phases. Between $x = 0$ and 0.12, $Bi_{1-x}Sm_xFeO_3$ ceramics exhibit a rhombohedral structure. Between $x = 0.125$ and 0.20, triclinic and orthorhombic phases are seen, and at $x = 0.25$, a paraelectric orthoferrite-type phase is visible. The ceramic system of $Bi_{1-x-y}Sm_xLa_yFeO_3$ with triclinic phase showed increased d33 of 50 pC/N by additional La doping. Other rare earth elements like Dy, Nd, Eu, Gd, and Tb have also been studied in relation to their effects on BFO phase transitions. To change the phase structure and create the improved characteristics, additional Group II elements like Sr, Ba, and Ca may be added. For instance, the basic R3c structure in $Bi_{1-x}Ba_xFeO_3$ was twisted into a monoclinic or tetragonal structure when x changed. The magnetic behaviour (Ms = 0.75 emu/g) was enhanced by the pseudo-tetragonal structure's shape. The suppression of the inhomogeneous magnetic spin structure and the rise in canting angle may have caused the transition of rhombic structures

into triclinic ones after the addition of Sr. It was shown, however, that other elements, such as Ce, Yb, Pr, and Ho, could not cause phase changes in BFO ceramics. The decrease in leakage current caused by these elements was largely responsible for the enhancement of the ferroelectric characteristics [11, 26–28, 30, 40, 53]. The effects of phase structures on the piezoelectric properties of Sm or Eu modified BFO ceramics have recently undergone additional development utilising the quenched method. In contrast to mixed phases or other phases, which result in a lower d33, pure R phases have been developed in ceramics, and this has resulted to a higher d33 of 45–46 pC/N. Accordingly, when Sm and Eu were utilised to alter BFO in ceramic form, the R phase did indeed show increased piezoelectric activity. To improve the piezoelectric performance of BFO ceramics in this situation, "MPB" (morphotropic phase boundary) may not be required. The current results indicate that an MPB for the A site modified BFO ceramics that is comparable to that in PZT is difficult to produce. Their electrical properties, especially the behaviour of the ferroelectric and piezoelectric materials, were significantly impacted by the leakage current. The type of replacement ion is therefore crucial for the alteration of the characteristic.

8.3.2.2 Substitution for Fe Site

InBFO, Fe^{3+} ions exist at B site which is surrounded by six oxygen neighbouring anions resulting FeO_6 octahedral. The empty spaces at A site are occupied by Bi^{3+} ions. Such an ABO_3 structure is produced by doping the B site with a transition metal ion and doping the A site with trivalent rare earth ions or divalent alkali earth ions. When different researched elements (such Ho, Co, Zn, Mn, Sc, Nb, and Ni) are substituted on the Fe site, the phase structure of BFO ceramics is preserved. Similar to how the Bi site substitution affects the structural phase and relevant (electrical and magnetic) properties of BFO ceramic, the ion replacement on the Fe site does as well. On BFO ceramics, however, the replacement of Ti caused the occurrence of the R (rhombohedral)–O (orthorhombic) phase boundary. In contrast to the Bi site replacement, the Fe site of the BFO's ion replacement often led to lower ferroelectric and piezoelectric behaviour while still having some increased magnetic behaviour. According to the information, secondary phases created by dopants, such as Co, Nb, Sc, Zn, Zr, and Ni, may be the reason of the decreased electrical properties (ferroelectric and piezoelectric). The BFO's magnetic properties could be enhanced by substituting some magnetic elements (such Co and Ni) at the Fe position. By way of illustration, the FM super-exchange interaction between Fe^{3+}–O–Ni^{2+} enhanced the remnant magnetisation (M_r) of BFO ceramic bulk from 0.006 to 0.10 emu/g when Ni was substituted. Another example is how the Co substitution significantly enhanced the magnetic properties of $BiFe_{0.95}Co_{0.05}O_3$ (Mr-0.7 emu/g) by resulting in a distorted rhombohedral structure with compressive lattice distortion. While switching out the Fe site for an appropriate magnetic element may usually improve the magnetic properties, it is still challenging to balance the magnetic and ferroelectric properties in BFO ceramics.

8.3.2.3 Substitution for Both Bi and Fe Sites

If ions are simultaneously substituted on the Bi and Fe sites of BFO ceramic bulk, the physical properties and phase structure of the materials are changed. The Bi^{3+} 6 s lone pair electrons and partially filled d orbitals of Fe, respectively, in the BFO, generate ferroelectrical and magnetic properties. As a result, the electrical (i.e. ferroelectric and piezoelectric) and magnetic properties can be promoted by appropriate chemical alterations in both sites. The authors reported, for example, that both Nd and Mn replacements on $Bi_{0.85}Nd_{0.15}Fe_{0.98}Mn_{0.02}O_3$ ceramics exhibit a structural phase change from the rhombohedral (R3c) phase to the tetragonal (P4mm) phase, and better ferroelectric characteristics are being noted. The BFO-based ceramics RT by La and Ti, R-Pbnm by Ca and Nb, R-pseudo-tetragonal by Ba and Ti, and R–O by Pr and Ti all have both sites doped and have also reported distinct phase boundaries. Some elemental combinations, such as La and (Nb, Zr, Tb), Mg, (Ho, Ca, Pr, Gd) and Ti, Zn and Ni, Ca and Mg, Ho and Ni, Y and Zr, Ba and Ni, and Sm and Co, however, do not significantly alter the phase structure of BFO. Piezoelectric and ferroelectric technologies fail. Recent research has shown that improving the piezoelectric activity of BFO ceramics by substituting certain elements for the Bi and Fe sites is possible as long as the leakage current is maintained under control [24]. $Bi_{0.925}La_{0.05}A_{0.025}FeO_3$ (i.e. A: Sm, Yb, Ho, Y, Nd, Pr, Dy, Gd) and $Bi_{0.925}La_{0.05}Sm_{0.025}Fe_{0.95}M_{0.05}O_3$ (i.e. M: Sc, In, Al, Ga, Ni, Co) ceramics, for instance, showed that the kinds of A and M ions seemed to affect the piezoelectric behaviour. While the majority of the M ions, including In, Al, Ga, Ni, and Co, were unable to help prevent the formation of impurity phases, this led to a decline in piezoelectricity; some of these ions, including A = Sm, Yb, Ho, and Y, could result in both a single-phase structure and reasonably good piezoelectricity [45]. $Ca_{0.15}Bi_{0.85}Mn_{0.05}Fe_{0.95}O_3$nanofibers demonstrated a higher saturation magnetisation, probably as a result of greater double exchange interaction of Fe^{3+}–O–Fe^{2+} that improves the photo-response.

8.4 Distinguished Properties of BFO Responsible for Device Application

8.4.1 Ferroelectric Properties

Perovskite oxides like $BaTiO_3$, $PbZrO_3$, and their doped compounds are important for ferroelectricity for their specific temperature. The phase transition that causes ferroelectricity is usually described by a soft-mode model which is proficient in ceramics for electronic industry and engineering. When electric field is applied, ferroelectric material exhibit spontaneous polarisation which is key for application in the field of multipurpose sensors, dynamic random access memory (DRAM, RAM, and RFID cards, input devices for imaging tunable capacitors, etc.).

8.4.2 Piezoelectricity

Pierre and Paul-Jacques Curie two brothers in 1880 revealed the existence of piezoelectricity in different crystals like quartz, tourmaline, and Rochelle salt. Piezoelectricity is the capacity of some materials to generate an electric charge in response to applied mechanical stress. It has a perovskite crystal structure of A^{2+} B^{4+} O^{2}-3 general formula in which A denotes a large divalent metal ion such as barium or lead and B denotes a tetravalent metal ion such as titanium or zirconium. Perovskite materials having piezoelectric properties have important applications like motors sensing devices [25], optic modulators, energy harvesting devices, used on solar panels, speakers, voltage multipliers, gauge, lighters, etc.

8.4.3 Photo-Catalytic Activity

Perovskite also exhibits outstanding catalytic activity and high chemical stability. The structural stability of perovskites enables the production of compounds from elements with significant oxygen deprivation. High surface activity to oxygen reduction ratio is partly responsible for high catalytic activity. It is used in cleaning catalysts, intelligent automobile catalysts, and exhaust gas catalysts for vehicles, among other things. Perovskites containing Cu, Co, Mn, or Fe demonstrated outstanding direct catalytic activity at high temperatures.

8.5 Application of BFO

The advantages of good execution make BFO materials extremely promising for designing and fostering a wide variety of gadgets with new capabilities. Uses of electronics, spintronics, and photonics technologies will be the main topic of this section.

8.5.1 For Electronics

Bismuth ferrite-based nanomaterials combine ferromagnetism and ferroelectricity at ambient temperature, which makes them an excellent candidate for use in high-thickness ferroelectric devices like non-volatile memory (Wang et al.; [18]). However, a reliable reversible switchable with slow operating speed, stability, and persistence is required by the quick high-density, non-volatile data storage, and logic

devices (Ma et al.; Wang et al.; [52]). Different adjustments were made to the BFO-based nanomaterials in order to change the ferroelectric resistive exchange. An atomically tetragonal BFO ultrathin film was used by Wang et al. to achieve this by monitoring the behaviour of ferroelectric polarisation switching (Wang et al.). Figure 8.3 represents the piezoresponse force microscopy (PFM) images and switchability of the ferroelectric polarisation. Strong hysteresis behaviour and a butterfly-like shape were seen in BFO films as thin as 2 (u.c) indicating persistent ferroelectric performance. The powerful reversibly switchable is supported even more by the superb PFM images. Additionally, when a BFO film is employed at room temperature, the burrowing electro opposition influence shown in ferroelectric burrow crossings can reach 370%. Ferroelectric-based non-volatile memory might be made smaller thanks to these brilliant displays, which were acquired in atomically thick BFO film as a result of ionic movements in oxide electrode and surface charges.

A prototype for an electric-optical memory was put forth by Lu et al. [20] using Ti-doped BFO films. This technology allows for both optical and electric modes of reading and writing. The control can be successfully repeated because the resistance state allows the photovoltaic open-circuit voltage to be controlled. The films exhibit fibre-type RS impact. They also found that the doping of Ti benefited high execution, opening up a promising approach for the creation of next-generation memory devices. Another group of devices understands strong, reversibly switchable states with significant thickness using ferroelectric space barriers (Ma et al.; [18, 35]). Nanoscale topological defects known as ferroelectric domain barriers have the ability to separate and independently govern spontaneous topological forms. For high-density and

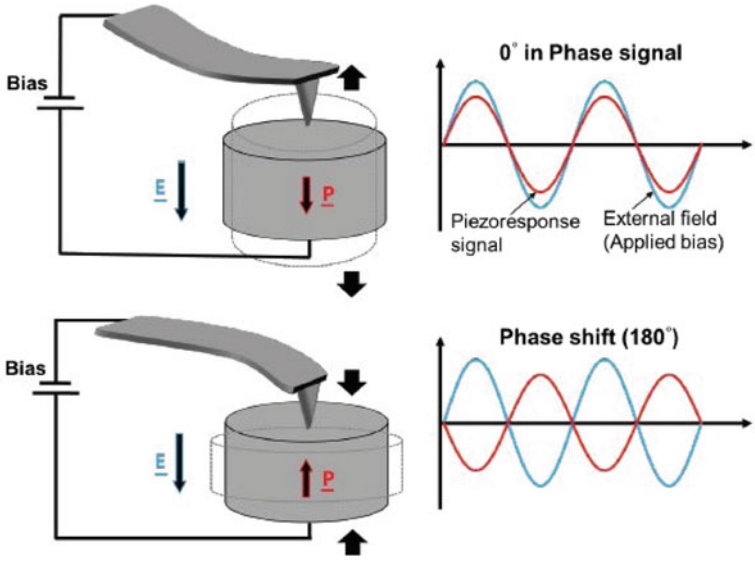

Fig. 8.3 Piezoresponse force microscopy (PFM) images and switchability of the ferroelectric polarisation

well-ordered BFO nano-islands and nano-dots, the use of BFO nanostructures as non-volatile memory has been proposed. A non-volatile ferroelectric domain wall memory prototype was presented by Sharma et al. in [35]. With low voltages of 3 V, this device can be read out non-destructively and has a good OFF–ON ratio (103). Additionally, there is a scale that is smaller than 100 nm. It also has strong endurance and excellent retention capabilities (104 and 103 cycles, respectively). The square BFO nano-island self-assembled array served as the foundation for the cross-bar memory device presented by Ma et al. They discovered that square-shaped BFO nano-islands contain domains with charged DWs that have cross-shaped shapes. Every time an electric field was employed to adjust the ferroelectric polarisation, the regions may alternate between centre-convergent and centre-divergent states, where all polar vectors directed in one direction or the other. Following the centre-type domains' transition to divergent states, a three-order rise in conductance was also observed. It was then that they understood that there was a reversible exchange of electric fields between the two stable community type area states. For a long time, this device exhibits 100 cycles of exchange stability and polarisation stability. Contrary to popular belief, the majority of ferroelectric-based non-volatile memories swapping speeds announced are on the microsecond time scale. It was still not possible for BFO non-volatile memory devices to meet the switching speeds and endurance requirements for the intrinsic ferroelectric switching in universal memory, which might take place at the nanosecond level. As a result, BFO non-volatile memory technologies that have fast switching and outstanding switching endurance still merit further research. Ferroelectric memory employs the photovoltaic effect of BFO, according to Wang et al. [9]. The fact that V_{oc} and I_{sc} reversed in less than 10 ns suggested a quick writing speed. The viability of creating a ferroelectric memory based on the sun effect was further demonstrated by the development of a 16-cell prototype memory. Energy capacity nanoparticles with enhanced power and energy thickness are becoming more and more necessary as interest in energy grows. Recent advances have led to significant gains in energy storage. Features of BFO-based nanoparticles energy densities and efficiencies of up to 100–150 J cm^{-3} and 80–88%, respectively, are theoretically expected for a $Bi_{1-x}Nd_xFeO_3$ system, according to Xu et al. [47]. Wang et al. [43] developed a doped BFO-BTO ceramic energy storage device by attaining an electrically homogenous microstructure. An energy discharge of up to 10.5 J cm^{-3} is possible with an efficiency of 87%. Additionally, two-dimensional electron gas was made using nanomaterials based on BFO (2DEG). Zhang et al. demonstrated that ferroelectric triggered interfacial 2DEG using a BFO-TbScO3 (BFO/TSO) heterostructure. It is easy to see that there is a noticeably polarisation-dependent anisotropic conductivity at the BFO/TSO interface. The conductivity of the 109° domain stripes was also found to be higher than that of the direction parallel to them. Hypothetical modelling predicts that the domain structure-induced p-type directed channels will swap the polarisation subordinate interfacial conductivity. An insulating interface is created at the p–n junction by the construction of a recurring potential barrier for free carriers, which also generates electrons or holes along the 109° domain stripes. Through the manipulation of ferroelectric polarisation, this discovery paved a brand-new way for the creation of high-tech gadgets that can

control two-dimensional anisotropic electronic transport. Li et al. also looked at the elastic dynamics of the BFO's transition from the rhombohedral to the tetragonal phase [12]. Around this transition, they discovered that Young's modulus values concurrently reduced by almost 30%, while the piezoresponse was multiplied by two to three. This incredibly stretchy material is electrically controlled. The large elastic stiffness with electrical control and associated electromechanical features improves the potential applications of BFO towards frequency-agile electroacoustic systems.

8.5.2 For Spintronics Devices

The magnetoelectric coupling property at ambient temperature makes it possible to control the attractive ways that BFO-based nanomaterials behave in an electric field. BFO-based materials are thus now a competitor for spintronic device applications [1, 5]. To explore the possibilities for BFO-based nanomaterials in electrically written spintronic devices, Allison et al. proposed a large magneto-resistive device based on BFO utilising spin valve exchange. The device's STO/SRO/BFO-Mn/BFO/CoFeB/Cu/Co structure was used to assess a 1% large magneto-resistance signal. The applied voltages also controlled the trading disposition. In fact, the unstable BFO/CoFeB interfaces prevented the growth of the weak magneto-resistance signal. The underlying physical mechanism for the thermal stability of the BFO/CoFeB contact was later investigated by Zhang et al. [53]. It was established that the primary factor affecting thermal stability was the differentiation of oxygen vacancies brought on by BFO polarisation course. In order to raise the large magneto-resistance value to 4.2%, a workable plan of action was also suggested. The impact of stress on the enormous magneto-resistive reaction was the main topic of Sando et al. studies [33]. They discovered that pseudo-collinear anti-ferromagnetism at high strain can be caused by tractable and compressive loads, illustrating the tendency for magnetic response to change with strain. The trade coupling between the antiferromagnetic request and the ferromagnetic over layer was then examined by Saenrang et al. in order to further research BFO-based spintronic devices. The Co magnetisation and the BFO antiferromagnetic request were seen to trade coupling spontaneously. The substrate step edges are where the Co uniaxial anisotropy axis is placed in the down state, whereas in the up state, it turns nearly 90°. You can repeat this furious and dependable exchange 100 times. Manipatruni et al. recently demonstrated that voltage controls unidirectional anisotropy in CoFe/BFO heterostructure [23]. At the junction between the huge magneto-resistance and the BFO, a significant, electrically switchable exchange bias is seen. Figure 8.4 shows switchable exchange ferroelectric and magnetic bias in hysteresis loop. In order to develop exchange bias, this is required. In order to accomplish this, the horizontal sections of the large magneto-resistance stack must shrink. They also discovered that a bipolar electric field might be used to reverse the exchange bias. These investigations provide insight on how to reduce the energy required switching out magnetoelectric devices.

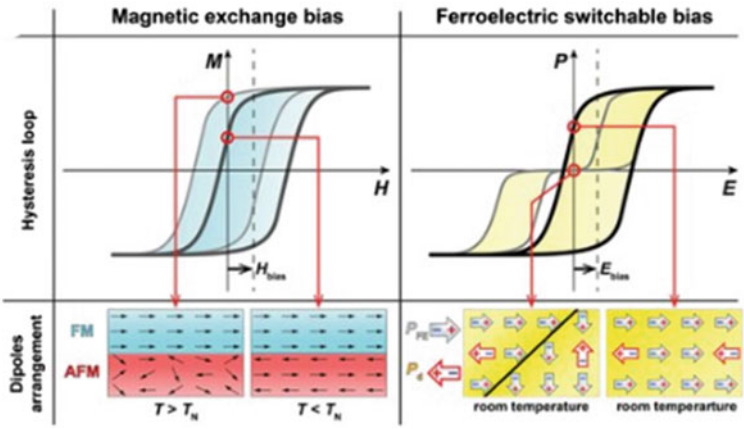

Fig. 8.4 Switchable exchange ferroelectric and magnetic bias in hysteresis loop

8.5.3 For Optics

Growing interest in perfect and sustainable electricity has led to the development of ferroelectric photovoltaic nanoparticles, which can transform solar cell energy into electrical power. BFO-based nanomaterials have unique qualities above ordinary ferroelectric nanoparticles, including a small bandgap, enhanced carrier transport, and light-absorbing capabilities. Therefore, employing BFO nanoparticles to construct ferroelectric PV systems is crucial. Outstanding research using BFO nanoparticles in the field of solar application has been produced by Yang et al. [3, 31, 48]. A self-powered ITO/BFO/Ag photodetector was created using the photovoltaic-pyroelectric coupled effect to investigate potential uses for the BFO photodetector [52]. The photodetector used in this experiment picked up a photocurrent of about 10 nA. The pyroelectric effect can change the height of the Schottky barrier, increasing photocurrent. The relationship was established between the current signal of the sharp peak in the *I*–*t* curves and the photovoltaic and pyroelectric effects. Only the photovoltaic effect may explain why the terrace had a steady current. The pyroelectric current had gradually depleted by the time the steady state of the light-induced temperature was established, leaving just the photovoltaic current. Then, to quickly identify 450-nm light, a self-powered photodetector array was developed. Nearly every channel displays the same shade of green when there is no light illumination. Channel 5 clearly showed a different image when only pixel 5 was illuminated with the 450-nm light. The photodetector is shown to be capable of instantaneous detection of 450-nm light. The enhancement of photovoltaic performance is also greatly impacted by temperature, they discovered. A 16-unit self-powered photodetector array was created to examine how temperature affects the photovoltaic impact of BFO [29]. The BFO photodetector's photovoltaic performance is illustrated in connection to the effects of applying different temperatures by sensing output current and voltage

signals in two states—heating and cooling. In heated environments, the output current can be increased, yet cooling environments can improve the voltage responsiveness. Improved photocurrent in photovoltaic activities is influenced by temperature and thermal optical effects. In specifically for possible use in photodetector systems, these studies offer methods to enhance the ferroelectric nanoparticles' photovoltaic effect. A surprising photovoltaic effect of the BFO at the nanoscale was also proven. The photovoltaic effect in BFO single crystals was investigated using AFM by Marin Alexe et al. [7]. They discovered that it was feasible to multiply the photovoltaic impact by seven. The term "tip augmentation" refers to this nanoscale enhancement. Because of the clever top electrode design, a point-contact geometry with nanoscale dimensions is created, which is ideal for collecting photoexcited particles. This work may provide a better understanding of the physical mechanisms underlying the photovoltaic properties of BFO-based nanomaterials. The strain gradient regulates the local morphotropic phase boundaries as well as the optical response of BFO, as was before mentioned. The optical response of BFO thin films was altered by Sando et al. using epitaxial strain engineering [2]. They discovered that under tension, the optical index varied dramatically. This indicates a high effective elastoptic coefficient for the system. Additionally, they discovered piezochromism, a shift in the optical bandgap caused by stress in other nanomaterials. Due to the electric-controlled piezochromism's potential for reversibility and persistence, this discovery broadens the BFO's potential applications to photonics and acousto-optic devices. The ferroic ordering can also be carefully controlled under all-optical light at room temperature, according to Liou et al. The significant energy difference between the coupling strengths of the order parameter and the sun spectrum makes it difficult to properly alter ferroic orders using optical techniques, as was already mentioned. The prospect of light-induced tuning of ferroelectricity, magnetism, and ferroelasticity is made possible by the finding of relatively low phase transition barriers in mixed-phase BFOs with tetragonal and rhombohedral phases. Using light at ambient temperature, researchers were able to regulate the distinct ferroic ordering in an epitaxial mixed-phase $BiFeO_3$ thin film. The results show that light illumination can affect the domain transformation as well as the R–T phase distribution. It is feasible to do precise sequential laser writing and other laser-related activities by using light to reversibly change the piezoelectric property. Additionally, they discovered that light-induced thermal and flexoelectric effects can influence the associated ferroic ordering. These investigations offer insight into the optical control of various capabilities as well as theoretical and practical support for the prospective use of BFO-based materials in optoelectronic applications.

8.6 Conclusion

Due to the volatility of bismuth and the oxygen vacancy created during sintering, a single-phase BFO is challenging to make. An appropriate rare earth or transitional element dopant must be substituted at the A site or B site, or we can do both sides of

the doping, in order to obtain a stable form of BFO. This gives us more control over the BFO's stability, which is essential for many photovoltaic applications, and the ability to modify the band gap of the BFO. The BFO composite with a nanostructure, on the other hand, has better characteristics that could make it a candidate for photovoltaic usage.

References

1. Allibe J, Bouzehouane K, Daumont C et al (2012) Room temperature electrical manipulation of giant magnetoresistance in spin valves exchange-biased with $BiFeO_3$
2. Altmann J, Tung J, Archie EA, Alberts SC (2016) Longevity in wild baboons. Nat Commun 7:1–7. https://doi.org/10.1038/ncomms11181
3. Anbusathaiah V, Kan BD, Pa L et al (2010) Universal behavior and electric-field-induced structural transition in rare-earth-substituted $BiFeO_3$ 1108–1115. https://doi.org/10.1002/adfm.200902017
4. Arlt G, Hennings D, De With G (1985) Dielectric properties of fine-grained barium titanate ceramics. J Appl Phys 58:1619–1625. https://doi.org/10.1063/1.336051
5. Baek SH, Jang HW, Folkman CM et al (2010) Ferroelastic switching for nanoscale non-volatile magnetoelectric devices 9:309–314. https://doi.org/10.1038/nmat2703
6. Bumajdad A, Ali S, Mathew A (2011) Characterization of iron hydroxide/oxide nanoparticles prepared in microemulsions stabilized with cationic/non-ionic surfactant mixtures. J Colloid Interface Sci 355:282–292. https://doi.org/10.1016/j.jcis.2010.12.022
7. Ceramics RB, Troyanchuk IO, Karpinsky D V et al (2011) Phase transitions, magnetic and piezoelectric properties of rare-earth-substituted $BiFeO_3$ ceramics. 4506:4502–4506. https://doi.org/10.1111/j.1551-2916.2011.04780.x
8. Dong S, Liu JM (2012) Recent progress of multiferroic perovskite manganites. Mod Phys Lett B 26:1–26. https://doi.org/10.1142/S0217984912300049
9. Guo R, You L, Zhou Y et al (2013) Photovoltaic effect. Nat Commun 4:1–5. https://doi.org/10.1038/ncomms2990
10. Hill NA (2000) Why are there so few magnetic ferroelectrics? J Phys Chem B 104:6694–6709. https://doi.org/10.1021/jp000114x
11. Jeon N, Rout D, Kim IW et al (2011) Enhanced multiferroic properties of single-phase BiFeO3 bulk ceramics by Ho doping Enhanced multiferroic properties of single-phase BiFeO 3 bulk ceramics 072901:2011–2014. https://doi.org/10.1063/1.3552682
12. Kalinin S V, Balke N (2015) Giant elastic tunability in strained $BiFeO_3$ near an electrically induced phase transition 1–9. https://doi.org/10.1038/ncomms9985
13. Kamalasanan MN, Chandra S, Joshi PC, Mansingh A (1991) Structural and optical properties of sol-gel-processed $BaTiO_3$ ferroelectric thin films. Appl Phys Lett 59:3547–3549. https://doi.org/10.1063/1.105653
14. Karpinsky DV, Troyanchuk IO, Tovar M et al (2013) Evolution of crystal structure and ferroic properties of La-doped $BiFeO_3$ ceramics near the rhombohedral-orthorhombic phase boundary. J Alloys Compd 555:101–107. https://doi.org/10.1016/j.jallcom.2012.12.055
15. Kreiselt J, Glazer AM, Jones G et al (2000) An x-ray diffraction and Raman spectroscopy investigation of A-site substituted perovskite compounds: the $(Na_{1-x}K_x)0.5Bi_{0.5}TiO_3$ ($0 \leq x \leq 1$) solid solution. J Phys Condens Matter 12:3267–3280. https://doi.org/10.1088/0953-8984/12/14/305
16. Lecture A (1929) Crystal structure and chemical
17. Levin I, Tucker MG, Wu H et al (2011) Displacive phase transitions and magnetic structures in Nd-substituted $BiFeO_3$ 2166–2175

18. Li Z, Wang Y, Tian G et al (2017) High-density array of ferroelectric nanodots with robust and reversibly switchable topological domain states 1–9
19. Liu Y, Nagra AS, Erker EG et al (2000) $BaSrTiO_3$ interdigitated capacitors for distributed phase shifter applications. IEEE Microw Guid Wave Lett 10:448–450. https://doi.org/10.1109/75.888828
20. Lu Z, Yang X, Jin C et al (2018) Nonvolatile electric-optical memory controlled by conductive filaments in Ti-doped $BiFeO_3$ 1700551:1–6. https://doi.org/10.1002/aelm.201700551
21. Maeno Y, Hashimoto H, Yoshida K et al (1994) Superconductivity in a layered perovskite without copper. Nature 372:532–534
22. Maleki H, Simchi A, Imani M, Costa BFO (2012) Size-controlled synthesis of superparamagnetic iron oxide nanoparticles and their surface coating by gold for biomedical applications. J Magn Magn Mater 324:3997–4005. https://doi.org/10.1016/j.jmmm.2012.06.045
23. Manipatruni S, Nikonov DE, Lin C et al (2018) Voltage control of unidirectional anisotropy in ferromagnet-multiferroic system 1–9
24. Mohapatra M, Anand S (2011) Synthesis and applications of nano-structured iron oxides/hydroxides—a review. Int J Eng Sci Technol 2:127–146. https://doi.org/10.4314/ijest.v2i8.63846
25. Moubarak PM, Member S, Ben-tzvi P, Zaghloul ME (2012) A self-calibrating mathematical model for the direct piezoelectric effect of a new MEMS tilt sensor. IEEE Sens J 12:1033–1042
26. Pradhan SK (2013) Influence of iron deficiency on electric and magnetic behavior of Ho doped $BiFeO_3$ electroceramic 1720–1726. https://doi.org/10.1007/s10854-012-1003-3
27. Pradhan SK, Das J, Rout PP et al (2010) Effect of holmium substitution for the improvement of multiferroic properties of $BiFeO_3$. J Phys Chem Solids 71:1557–1564. https://doi.org/10.1016/j.jpcs.2010.08.001
28. Pradhan SK, Roul BK (2012) Electrical behavior of high resistivity Ce-doped $BiFeO_3$ multiferroic. Phys B Phys Condens Matter 407:2527–2532. https://doi.org/10.1016/j.physb.2012.03.061
29. Qi J, Ma N, Ma X et al (2018) Functional inorganic materials and devices enhanced photocurrent in $BiFeO_3$ materials by coupling temperature and thermo-phototronic effects for self-powered UV photodetector system. Beijing Inst Nanoenergy Nanosyst Chinese. https://doi.org/10.1021/acsami.8b02543
30. Rao TD, Karthik T, Srinivas A, Asthana S (2012) Study of structural, magnetic and electrical properties on Ho-substituted $BiFeO_3$. Solid State Commun 152:2071–2077. https://doi.org/10.1016/j.ssc.2012.08.007
31. Ru M, Bife YBC (2022) Math-Net Ru 145:1255–1258
32. Samara GA (1971) Pressure and temperature dependence of the dielectric properties and phase transitions of the ferroelectric perovskites: Pbtio3 and batio3. Ferroelectrics 2:277–289. https://doi.org/10.1080/00150197108234102
33. Sando D, Agbelele A, Rahmedov D et al (2013) Crafting the magnonic and spintronic response of $BiFeO_3$ films by epitaxial strain. Nat Mater 12:1–6. https://doi.org/10.1038/nmat3629
34. Schmid H (1994) Multi-ferroic magnetoelectrics. Ferroelectrics 162:317–338. https://doi.org/10.1080/00150199408245120
35. Sharma P, Zhang Q, Sando D et al (2017) Nonvolatile ferroelectric domain wall memory. IEEE Sens J 1–9
36. Sm B, Chen X, Wang J et al (2012) Structure, ferroelectric and piezoelectric properties of multiferroic 541:173–176. https://doi.org/10.1016/j.jallcom.2012.06.094
37. Sun C, Wang Y, Yang Y et al (2012) Various temperatures. Mater Lett 72:160–163. https://doi.org/10.1016/j.matlet.2011.12.119
38. Tidrow SC (2014) Mapping comparison of goldschmidt's tolerance factor with perovskite structural conditions. Ferroelectrics 470:13–27. https://doi.org/10.1080/00150193.2014.922372
39. Uchino K (2015) Glory of piezoelectric perovskites. Sci Technol Adv Mater 16:46001. https://doi.org/10.1088/1468-6996/16/4/046001
40. Uniyal P, Yadav KL (2012) Enhanced magnetoelectric properties in $Bi_{0.95}Ho_{0.05}FeO_3$ polycrystalline ceramics. J Alloys Compd 511:149–153. https://doi.org/10.1016/j.jallcom.2011.09.012

41. Van Aken BB, Rivera JP, Schmid H, Fiebig M (2007) Observation of ferrotoroidic domains. Nature 449:702–705. https://doi.org/10.1038/nature06139
42. Walker J, Budic B, Bryant P et al (2015) Robust polarization and strain behavior of sm-modified $BiFeO_3$ piezoelectric ceramics. IEEE Trans Ultrason Ferroelectr Freq Control 62:83–87. https://doi.org/10.1109/TUFFC.2014.006663
43. Wang G, Li J, Zhang X et al (2019) Environmental science ultrahigh energy storage density lead-free multilayers by controlled electrical homogeneity 3. https://doi.org/10.1039/c8ee03287d
44. Wang H, Liu ZR, Yoong HY et al Direct observation of room-temperature out-of-plane ferroelectricity and tunneling electroresistance at the two-dimensional limit. Nat Commun 1–8. https://doi.org/10.1038/s41467-018-05662-y
45. Wang KF, Liu JM, Ren ZF (2009) Multiferroicity: the coupling between magnetic and polarization orders. Adv Phys 58:321–448. https://doi.org/10.1080/00018730902920554
46. Weston L, Cui XY, Ringer SP, Stampfl C (2016) Multiferroic crossover in perovskite oxides. Phys Rev B 93:1–11. https://doi.org/10.1103/PhysRevB.93.165210
47. Xu B (2017) Designing lead-free antiferroelectrics for energy storage. https://doi.org/10.1038/ncomms15682
48. Xu B, Wang D, Íñiguez J, Bellaiche L (2014) Finite-temperature properties of rare-earth-substituted $BiFeO_3$ multiferroic solid solutions 1–7. https://doi.org/10.1002/adfm.201403811
49. Yuan GL, Or SW (2014) Enhanced piezoelectric and pyroelectric effects in single-phase multiferroic $Bi_{1-x}Nd_xFeO_3$ ($x = 0 - 0.15$) ceramics enhanced piezoelectric and pyroelectric effects in single-phase multiferroic 3:98–101. https://doi.org/10.1063/1.2169905
50. Yuan GL, Or SW (2006) Multiferroicity in polarized single-phase $Bi_{0.875}Sm_{0.125}FeO_3$ ceramics 024109:0–5. https://doi.org/10.1063/1.2220642
51. Yuan GL, Or SW, Liu JM, Liu ZG (2006) Structural transformation and ferroelectromagnetic behavior in single- phase $Bi_{1-x}Nd_xFeO_3$ multiferroic 052905:1–4. https://doi.org/10.1063/1.2266992
52. Zavaliche F, Zhao T, Zheng H et al (2007) Electrically assisted magnetic recording in multiferroic nanostructures. IEEE Sens J 3–7
53. Zhang Q, You L, Shen X et al (2015) Polarization-mediated thermal stability of metal/oxide heterointerface 6934–6938. https://doi.org/10.1002/adma.201502754
54. Zhang S, Wang L, Chen Y et al (2012) Observation of room temperature saturated ferroelectric polarization in Dy substituted $BiFeO_3$ ceramics Observation of room temperature saturated ferroelectric polarization in Dy substituted $BiFeO_3$ ceramics 074105:https://doi.org/10.1063/1.3702405
55. Zheng H, Wang J, Lofland SE et al (2004) Multiferroic $BaTiO_3$–$CoFe_2O_4$ nanostructures. Science 303:661–663. https://doi.org/10.1126/science.1094207
56. Zheng T, Wu J (2015) Enhanced piezoelectric activity in high-temperature $Bi_{1-x-y}Sm_xLa_yFeO_3$ lead-free ceramics. J Mater Chem C 3:3684–3693. https://doi.org/10.1039/c5tc00363f

Chapter 9
A Perspective on Environmental and Disposal Assessment of Magnetic Sorbents

Nishesh Kumar Gupta, Herlys Viltres, and Carolina Leyva

Abstract While adsorption is an age-old technique for the treatment of contaminated water, the involvement of magnetic phase separation is relatively new. Magnetism in adsorbents (or magnetic adsorbents) has eased the recovery of micro/nano-adsorbents post-adsorption. Magnetic adsorbents could lower the operation time/cost and improve the overall efficacy of the adsorption process. In this book, most of the chapters have highlighted the use of magnetic adsorbents in water remediation applications. This chapter is focused on the regeneration strategies and disposal assessment of magnetic adsorbents and eluents post-exhaustion. Moreover, the chapter has been updated with some accounts of repurposing strategies for exhausted magnetic adsorbents.

Keywords Green strategies · Magnetic adsorbents · Regeneration · Repurposing

9.1 Introduction

In general, adsorbents are judged based on their robustness and efficacy for pollutant uptake [1, 32]. Apart from the efficacy, ease of recyclability and the extent to which an adsorbent could be recycled are equally important, which are often ignored

N. K. Gupta (✉)
Department of Environmental Research, University of Science and Technology (UST), Daejeon 34113, Korea
e-mail: guptan@kict.re.kr

Department of Environmental Research, Korea Institute of Civil Engineering and Building Technology (KICT), Goyang 10223, Korea

H. Viltres
School of Engineering Practice and Technology, McMaster University, 1280 Main Street West, Hamilton, ON L8S 4L8, Canada

C. Leyva
Instituto Politécnico Nacional, Centro de Investigación en Ciencia Aplicada y Tecnología Avanzada, Mexico City, Mexico

H. Sahoo and J. K. Sahoo (eds.), *Iron Oxide-Based Nanocomposites and Nanoenzymes*, Nanostructure Science and Technology, https://doi.org/10.1007/978-3-031-44599-6_9

in the published works [26]. In wastewater treatment facilities, the cost of sludge processing and disposal is significantly higher than the cost of the adsorbent. Thus, the commercialization of magnetic adsorbents for wastewater treatment relies on the regeneration process and management of fully used adsorbents. Another feature that the studies lack is the environmental significance of the magnetic adsorbents-based treatment processes. The use of toxic chemicals or high energy input in the regeneration process needs to be criticized in the interest of achieving sustainability. At the same time, the disposal of toxic spent adsorbents in the landfills should be strictly monitored and guided by environmental norms. Reuse and disposal are two different aspects of waste management. Though regeneration of adsorbents is always an energy-intensive process, the choice of the regeneration process and the economic value of pollutants may balance the equation. Disposal is the process of discarding spent adsorbents either by burning in incinerations (applicable for organic adsorbent-pollutant systems) or in landfills. Since magnetic adsorbents cannot be incinerated, a landfill is considered the only viable option. In the subsequent sections, we have discussed different approaches for regeneration and disposal (Fig. 9.1).

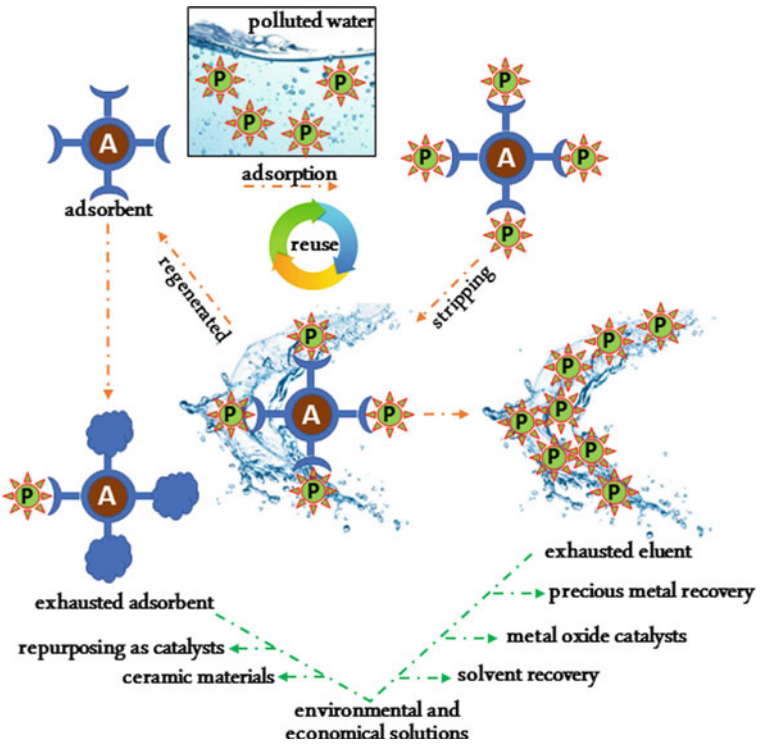

Fig. 9.1 A schematic representation of the adsorption process as an economical and greener initiative

9.2 Regeneration and Reuse of Spent Adsorbents

The regeneration of a spent magnetic adsorbent is a crucial process to cover the environmental and monetary cost of the adsorbent. An ideal regeneration process should revert the adsorption process and restore the physicochemical properties of the adsorbent. In the regeneration process, adsorbed pollutants are stripped out of the adsorbent and a limited number of adsorption sites are made available for the next cycle. The choice of the regeneration process is based on the physicochemical properties of pollutants, stability of adsorbent, and economic constraints. For heavy metal-loaded magnetic adsorbents, stripping agents (eluents) are recommendable. The eluents are either acid/base solutions or solutions of complexing agents, which could extract heavy metals into the solution phase [26]. The strength of eluents depends on the nature of adsorbate–adsorbent interactions, contact time, and temperature. For extracting organic pollutants from the spent adsorbent, the use of polar solvents like ethanol and methanol is recommendable [35]. In some studies, regeneration methods like thermal regeneration and ultrasonication have been reported, which are less tedious and suitable for stable adsorbents. The reusability of magnetic adsorbents for the removal of heavy metals and organic pollutants has been listed in Table 9.1. In general, the choice of using acid/base solutions for the desorption process is largely based on adsorbent–adsorbate interactions as a function of pH. In the pH-dependent adsorption profiles, the pH at which the pollutant uptake is the least is considered a suitable pH to desorb it. The adsorbed cations of heavy metals are stripped using strong acidic solutions due to the competitive nature of protons for the adsorption sites [39, 43, 44]. The use of strong acids for desorption lowers the structural stability of the adsorbent, which is due to the dissolution of magnetic nanoparticles. In some cases, where heavy metals are adsorbed via an ion-exchange mechanism, the use of electrolytic solution (KCl/NaCl) is preferred. The choice of using electrolyte solution for desorption of Tl(I) from magnetic Prussian blue derivative adsorbent was reported by Yeisy et al. [29]. The study reported the use of HNO_3, NaOH, and KCl as three elution agents, where pH swing does not affect Tl(I) desorption (Fig. 2a). Though HNO_3 could desorb 26% of the adsorbed Tl(I) through proton exchange, KCl was the best eluent with a 97% desorption efficacy (Fig. 2b). The oxyanions (arsenate and chromate) are usually desorbed with strong basic solutions (NaOH) [6, 25]. Chen et al. reported the use of 0.5 mol L^{-1} NaOH solution for the elution of chromate from spent polyethyleneimine-functionalized Fe_3O_4 [6]. The pH-dependent adsorption profile showed very low chromate uptake at pH 12, which made 0.5 mol L^{-1} NaOH solution, an ideal choice for the desorption studies. For this reason, the adsorbent was used for 20 cycles with a 13% loss in the uptake capacity after the 20th cycle.

The method of pH swing is equally applicable to the stripping of organic pollutants from spent adsorbents. Since organic charged dyes are adsorbed by electrostatic interaction, pH variation using an acid/base could give a better desorption efficacy [42, 50].

Table 9.1 Reusability of magnetic adsorbents for heavy metals and organic pollutants removal

Adsorbent	Pollutant	Eluent	%Ads (1st cycle)	%Ads (*n*th cycle)
Fe_3O_4 decorated with β-cyclodextrins-functionalized graphene oxide [25]	As(V)	NaOH	99	61 (5)
Diethyl-4-(4-amino-5-mercapto-4*H*-1,2,4-triazol-3-yl)phenyl phosphonate-capped biogenic Fe_3O_4 [43]	Cd(II)	HCl	91	77 (5)
EDTA-cross-linked magnetic chitosan DTPA-cross-linked magnetic chitosan [49]	Cd(II)	HNO_3	99 99	87 (10) 82 (10)
Fe_3O_4/MnO_2 [24]	Cd(II)	HNO_3	95	83 (5)
Polyethyleneimine-functionalized Fe_3O_4 [6]	Cr(VI)	NaOH	100	87 (20)
Magnetic iron oxide@$CaCO_3$ [21]	Cr(VI)	HCl	100	95 (5)
Fe_3O_4–walnut shell [39]	Pb(II)	HCl	79	60 (10)
Fe_3O_4@diaminophenol and formaldehyde-based polymer [44]	Pb(II)	HNO_3	92	81 (5)
3,4-Dihydroxyphenethylcarbamodithioate-capped Fe_3O_4 [45]	Hg(II)	HNO_3	93	83 (5)
Magnetic Prussian blue derivative [29]	Tl(I)	KCl	100	95 (6)
Magnetic@chitosan/halloysite [42]	Congo red	NaOH	100	90 (6)
Tryptophan-functionalized Fe_3O_4 [40]	Congo red	Ethanol	98	87 (5)
Magnetic bacterial cellulose nanofiber/graphene oxide polymer aerogel [2]	Malachite green	Acetic acid/methanol	93	63 (7)
Fe_3O_4@graphene oxide nanohybrids [13]	Rhodamine B Methylene blue	Ethanol	100 100	86 (8) 66 (5)
$CoFe_2O_4$/graphene oxide [15]	Methylene blue	400 °C	96	79 (4)
Ce–MOF@Fe_3O_4@activated carbon composite [35]	Methylene blue Indigo carmine	Methanol	100 100	96 (4) 87 (4)
Magnetic hollow carbon microspheres [30]	Rhodamine B	NaOH + 400 °C	98	92 (6)
Carbon dot-modified magnetic carbon nanotubes [9]	Carbamazepine	Acetonitrile	77	75 (7)
Magnetic carbon microspheres [8]	Sulfonamide	pH 10 + ultrasonication	94	75 (5)
Hypercrosslinked magnetic resin Q100 [50]	Tetracycline	NaOH	100	95 (10)

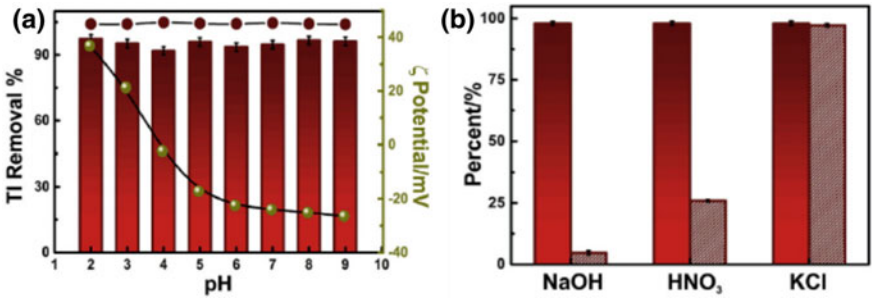

Fig. 9.2 **a** Tl(I) removal versus pH (*right axis:* ζ potential); **b** Tl(I) recovery percent versus Eluting solution for magnetic Prussian blue derivative adsorbent. Reproduced with permission from Elsevier (2021) [29]

Organic solvents like ethanol and methanol are also recommended as eluents either in the form of pure solvents [2] or acid/basic solvents [13] due to their high solubility in polar organic solvents. As compared to solvent stripping, thermal regeneration is a simplistic approach to eliminating organic pollutants from spent adsorbents. For a thermally stable adsorbent, heating at an elevated temperature could volatilize the adsorbed organic pollutants. Gupta et al. demonstrated the use of thermal regeneration of methylene blue-adsorbed $CoFe_2O_4$/graphene oxide by heating at 400 °C for 1 h in an inert atmosphere [15]. The nanocomposite adsorbent retained 80% of its dye uptake capacity even after the 4th cycle. In another study, the combined effect of pH variation and thermal regeneration was used to desorb rhodamine B from magnetic hollow carbon microspheres. The spent adsorbent was treated with 1.0 mol L^{-1} NaOH solution and heated at 400 °C for 1 h in an inert atmosphere. The method successfully regenerated the adsorbent with a 6% loss in the performance after the 6th cycle, which made it suitable for more adsorption–desorption cycles [30]. Thus, the development of regeneration strategies is largely dependent on the chemical/thermal stability of the adsorbent, the strength of interactions, the chemical state of pollutants, and so on. More information on the regeneration of adsorbents and recovery could be found in the published specialized reviews [14, 26, 34].

9.3 Disposal of Spent Stripping Solutions

The regeneration of spent adsorbents by solvent stripping methods generates large volumes of toxic organic/inorganic solutions, which need to be managed as per the rules set by the environmental protection agencies. So far, research works are the least concerned with the management of spent eluents. The most judicious way is the use of the same eluent for multiple cycles to produce solutions with a high concentration of heavy metals, which are like ore leachates. Heavy metals like copper, platinum, palladium, and nickel have a high monetary value due to their widespread use. The

heavy metals from the spent solutions could be extracted by different metallurgical technologies like flotation with pyrometallurgy [38], solvometallurgy, and electrolysis [3]. Even multi-elemental solutions could be processed by varying the pH to extract precious metals [47]. Moreover, heavy metals are used as catalysts and co-catalysts in different industrial processes like catalytic cracking, syngas production, and Fischer–Tropsch process [4, 27]. These spent solutions can be converted to metal oxide catalysts by precipitation and thermal treatment, which will be an alternative way to convert waste into value-added products [10]. Many of the heavy metals (e.g., arsenate, chromate, and mercury) are costlier to recover than their market value but are highly toxic to living beings. Spent solutions, rich in such heavy metals are concentrated, encapsulated, and disposed of in well-maintained landfill sites [33]. Organic solvents used as dye-stripping agents like acetone, methanol, and ethanol have a low boiling point of 56, 65, and 78 °C, respectively. The dye-rich organic solvents could be regenerated by evaporation to recover the stripping solvents and dyes. Though the evaporation process is energy-intensive, the use of acetone as the stripping agent in combination with the concentrated solar radiation as the heating source could be a cost-cutting solution for the management of dye-rich spent solvents. Most of the suggested methods are yet to be reported in the literature in detail. The research work dealing with wastewater treatment is largely focused on answering whether the fabricated adsorbent can adsorb. If yes, then how much? Whether it could be reused and if yes, then for how many cycles? But it is expected that in the future studies, researchers will be more interested in exploring disposal strategies for exhausted eluents.

9.4 Disposal of Exhausted Adsorbents

After numerous cycles of adsorption-regeneration, the pollutant uptake capacity of an adsorbent reaches a point where it is no more economically feasible to reuse it. The spent adsorbent is replaced by a fresh one and the spent adsorbent is treated as a highly toxic solid waste. Dumping of these toxic exhausted adsorbents in open spaces poses severe risks to human health and the environment, especially in countries where waste segregation and disposal strategies are limited [5]. Even improper disposal of exhausted adsorbents in landfills or poor maintenance after disposal could generate the issue of secondary pollution of groundwater or soil [51]. Thus, it is critical to construct suitable waste-disposal mechanisms from the environmental perspective. However, the concept of finding an alternative application for a waste product is more valuable than finding a new path for disposal. Gupta et al. reported an alternative application of exhausted CuO after the H_2S desulfurization process. The study reported better methylene blue photodegradation efficiency for exhausted materials compared to the fresh CuO (Fig. 9.3) [16]. A mesoporous silica (MCM-41) was developed for the removal of chromate from waste solutions. The Cr-loaded MCM-41 was calcined in air at 550 °C for 6 h to produce the Cr/MCM-41 catalyst, which was used for the catalytic degradation of methyl mercaptan (a volatile organosulfur

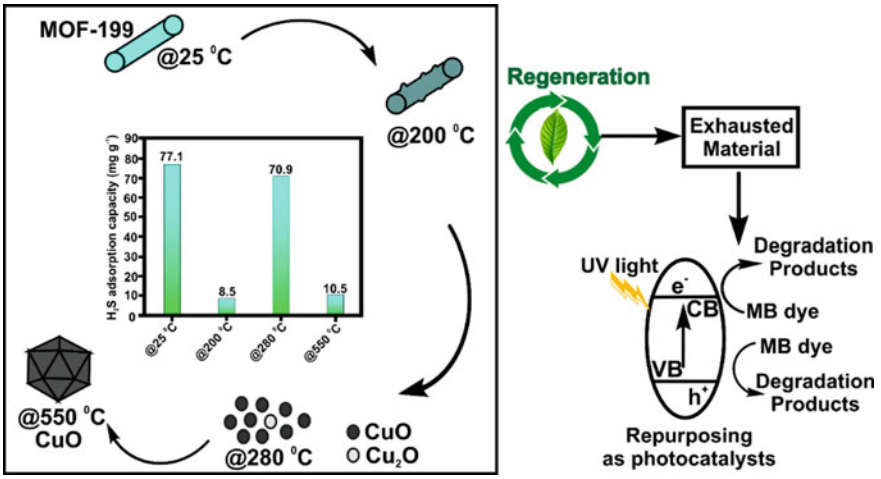

Fig. 9.3 The exhausted CuO was repurposed for dye photodegradation as an environmentally benign route to provide value to the waste. Reproduced with permission from the American Chemical Society (2021) [16]

compound with an obnoxious odor) [19]. The waste-to-wealth concept has been used for the conversion of spent Pb-loaded hydrochar to a carbonaceous anode for lithium-ion batteries [48].

On a similar note, reports on the waste-to-wealth concept are available for spent magnetic adsorbents as well. A magnetic mesoporous silica/poly(m-aminothiophenol) nanocomposite was fabricated for Hg(II) removal [11]. The adsorbent showed a remarkable sorption capacity of 243 mg g^{-1} within 10 min of agitation. The adsorbent was reused for 5 cycles with a retention of 76% of its initial adsorption capacity. The spent adsorbent was repurposed as a catalyst for the conversion of phenylacetylene to acetophenone with a 97% yield. Further modifications were made to the material to develop a magnetic network polymer composite by introducing poly(m-aminothiophenol) and chitosan onto the magnetic nanoparticle using tannic acid as a cross-linking agent. The material possessed a Hg(II) removal capacity of 245.5 mg g^{-1} with excellent reusability and selectivity. Moreover, the exhausted adsorbent catalyzed the transformation of different phenylacetylene derivatives into corresponding acetophenone with ~ 98–99% yield [12]. In another study, the fabricated magnetic mesoporous silica/chitosan composite was studied for Hg(II) removal [20]. The adsorbent has an uptake capacity of 437.8 mg g^{-1} with the retention of 87% of its initial adsorption capacity after the 6th adsorption-regeneration cycle. The spent adsorbent was used as a thermal catalyst for the conversion of phenylacetylene to acetophenone with a yield of 98.3%.

Cruz et al. have reported a novel concept of turning waste into wealth on two fronts [7]. The natural organic matter (NOM)-rich water from a waterfall was used for the synthesis of $CoFe_2O_4$/NOM as an adsorbent for the removal of chromate. The adsorbent was reusable, where the adsorption performance was 82% in the 5th cycle

as compared to 96% in the 1st cycle. The spent adsorbent was used as a catalyst for the reduction of 4-nitrophenol in the presence of $NaBH_4$ as the reducing agent, where a conversion efficiency of 99.9% was recorded within 3 s. The catalyst was studied for two additional cycles, where the conversion efficiency was still 99.9% within 30 s. Apart from excellent reusability, the material showed insignificant leaching of chromium and iron in the solution phase. On the same concept, an adsorbent and subsequently a catalyst was developed using waste biomass [28]. Fir sawdust was used as a bio-sorbent for the adsorption of Cu(II) and Fe(III) ions. This metal-loaded biomass was pyrolyzed to yield Cu–Fe_3O_4–carbon material, which found application as a reusable catalyst for the reduction of 4-nitrophenol.

A low-cost Fe_3O_4/Carbon composite, developed for the adsorptive capture of chromate from wastewater, was repurposed as an anode material for potassium-ion batteries after chromate adsorption. The redox reaction between Cr(VI) and Cr(III) was responsible for the K-storage mechanism. Thus, more adsorption on chromate was favorable for improving the K-storage capacity of the material [31]. Zn–Al–La layered double hydroxide is an inorganic synthetic clay, which showed a high uptake behavior for amaranth (azo dye). After dye adsorption, the spent material was calcined (to form a carbonaceous composite material) and repurposed as a photocatalyst for the degradation of ibuprofen [41]. On the same line, spent magnetic adsorbents could be used as suitable photocatalysts for the degradation of organic pollutants. Specifically, transition heavy metals along with iron oxide in these adsorbents are excellent UV–visible responsive photocatalysts [17, 18]. Thus, spent magnetic adsorbents could be used for alternative applications of catalysis that comply with the principles of industrial symbiosis with extraordinary environmental benefits.

Spent adsorbents rich in heavy metals could be repurposed to produce ceramic materials, which works as an alternative method for stabilizing toxic metals and at the same time serves the purpose of construction material. One such example was the use of lime activated fly ash for adsorptive removal of heavy metals (Pb, Zn, and As) and subsequent valorization of exhausted adsorbent as an additive in construction material [23]. Rathore and Mondal have reported the stabilization of arsenic-loaded adsorbents namely, thermally treated laterite, acid–base treated laterite, and aluminum oxide/hydroxide nanoparticles as clay bricks. Brick properties like density, water absorption, shrinkage, compressive strength, and efflorescence complied with the Indian standards set for construction materials. Moreover, the maximum amount of arsenic in the brick leachate was well below the United State Environmental Protection Agency permissible limit of 5.0 mg L^{-1} [36, 37]. Though stabilization of spent magnetic adsorbent as clay bricks has not been studied, Verbinnen et al. developed a novel method to stabilize heavy metals and oxyanions forming elements (Cr, Ni, Cu, Zn, As, Cd, and Pb) by adsorbing it on zeolite- or perlite-supported magnetite. This was followed by mixing the spent adsorbent with industrial sludge (sludge/adsorbent ratio of 97/3) at 1100 °C for 0.5 h. Based on the study, the leaching of toxic metals from the ceramic was below the regulatory limits [46]. The production of lime and cement used for the solidification/stabilization of spent adsorbents

before being dumped in landfills has a high carbon footprint due to CO_2 release [22]. Stabilization of spent adsorbents as bricks and ceramics saves raw clay materials and lowers the environmental impact and cost of the landfill process.

9.5 Conclusion

Repurposing of spent adsorbents is a new concept, which needs to be explored more often to make the overall adsorption process, environmentally benign and affordable. In the literature, only a handful of research works have been dedicated to the cause. Nevertheless, the idea that has cropped up in these studies is worth reporting in the context of the environmental sustainability of the process. While the researchers are dedicated to exploring regeneration techniques, finding alternative applications for the exhausted adsorbents is highly lucrative and novel. With the enrichment of the literature with such studies in the future, it will be easier to judge the environmental applicability of the adsorption processes.

References

1. Abdel Maksoud MIA, Elgarahy AM, Farrell C, Al-Muhtaseb AH, Rooney DW, Osman AI (2020) Insight on water remediation application using magnetic nanomaterials and biosorbents. Coord Chem Rev 403:213096. https://doi.org/10.1016/j.ccr.2019.213096
2. Arabkhani P, Asfaram A (2020) Development of a novel three-dimensional magnetic polymer aerogel as an efficient adsorbent for malachite green removal. J Hazard Mater 384:121394. https://doi.org/10.1016/j.jhazmat.2019.121394
3. Binnemans K, Jones PT (2017) Solvometallurgy: an emerging branch of extractive metallurgy. J Sustain Metall 3(3):570–600. https://doi.org/10.1007/s40831-017-0128-2
4. Biswas S, Pal A, Pal T (2020) Supported metal and metal oxide particles with proximity effect for catalysis. RSC Adv 10(58):35449–35472. https://doi.org/10.1039/D0RA06168A
5. Chaukura N, Gwenzi W, Tavengwa N, Manyuchi MM (2016) Biosorbents for the removal of synthetic organics and emerging pollutants: opportunities and challenges for developing countries. Environ Dev 19:84–89. https://doi.org/10.1016/j.envdev.2016.05.002
6. Chen B, Zhao X, Liu Y, Xu B, Pan X (2015) Highly stable and covalently functionalized magnetic nanoparticles by polyethyleneimine for Cr(VI) adsorption in aqueous solution. RSC Adv 5(2):1398–1405. https://doi.org/10.1039/C4RA10602D
7. Cruz DRS, Santos BTJ, Cunha GC, Romão LPC (2017) Green synthesis of a magnetic hybrid adsorbent ($CoFe_2O_4$/NOM): removal of chromium from industrial effluent and evaluation of the catalytic potential of recovered chromium ions. J Hazard Mater 334:76–85. https://doi.org/10.1016/j.jhazmat.2017.03.062
8. Dai K, Wang F, Jiang W, Chen Y, Mao J, Bao J (2017) Magnetic carbon microspheres as a reusable adsorbent for sulfonamide removal from water. Nanoscale Res Lett 12(1):528. https://doi.org/10.1186/s11671-017-2295-2
9. Deng Y, Ok YS, Mohan D, Pittman CU, Dou X (2019) Carbamazepine removal from water by carbon dot-modified magnetic carbon nanotubes. Environ Res 169:434–444. https://doi.org/10.1016/j.envres.2018.11.035
10. Fan X, Song C, Lu X, Shi Y, Yang S, Zheng F, Huang Y, Liu K, Wang H, Li Q (2021) Separation and recovery of valuable metals from spent lithium-ion batteries via concentrated sulfuric acid

leaching and regeneration of $LiNi_{1/3}Co_{1/3}Mn_{1/3}O_2$. J Alloys Compd 863:158775. https://doi.org/10.1016/j.jallcom.2021.158775
11. Fu Y, Sun Y, Chen Z, Ying S, Wang J, Hu J (2019) Functionalized magnetic mesoporous silica/poly(m-aminothiophenol) nanocomposite for Hg(II) rapid uptake and high catalytic activity of spent Hg(II) adsorbent. Sci Total Environ 691:664–674. https://doi.org/10.1016/j.scitotenv.2019.07.153
12. Fu Y, Sun Y, Zheng Y, Jiang J, Yang C, Wang J, Hu J (2021) New network polymer functionalized magnetic-mesoporous nanoparticle for rapid adsorption of Hg(II) and sequential efficient reutilization as a catalyst. Sep Purif Technol 259:118112. https://doi.org/10.1016/j.seppur.2020.118112
13. Ganesan V, Louis C, Damodaran SP (2018) Graphene oxide-wrapped magnetite nanoclusters: a recyclable functional hybrid for fast and highly efficient removal of organic dyes from wastewater. J Environ Chem Eng 6(2):2176–2190. https://doi.org/10.1016/j.jece.2018.03.026
14. Gkika DA, Mitropoulos AC, Kyzas GZ (2022) Why reuse spent adsorbents? The latest challenges and limitations. Sci Total Environ 822:153612. https://doi.org/10.1016/j.scitotenv.2022.153612
15. Gupta A, Viltres H, Gupta NK (2020) Sono-adsorption of organic dyes onto $CoFe_2O_4$/Graphene oxide nanocomposite. Surf Interfaces 20:100563. https://doi.org/10.1016/j.surfin.2020.100563
16. Gupta NK, Bae J, Kim KS (2021) From MOF-199 microrods to CuO nanoparticles for room-temperature desulfurization: regeneration and repurposing spent adsorbents as sustainable approaches. ACS Omega 6:25631–25641. https://doi.org/10.1021/acsomega.1c03712
17. Gupta NK, Ghaffari Y, Bae J, Kim KS (2020) Synthesis of coral-like α-Fe_2O_3 nanoparticles for dye degradation at neutral pH. J Mol Liq 301:112473. https://doi.org/10.1016/j.molliq.2020.112473
18. Gupta NK, Ghaffari Y, Kim S, Bae J, Kim KS, Saifuddin M (2020) Photocatalytic degradation of organic pollutants over MFe_2O_4 (M = Co, Ni, Cu, Zn) nanoparticles at neutral pH. Sci Rep 10(1):4942. https://doi.org/10.1038/s41598-020-61930-2
19. He D, Zhang L, Zhao Y, Mei Y, Chen D, He S, Luo Y (2018) Recycling spent Cr adsorbents as catalyst for eliminating methylmercaptan. Environ Sci Technol 52(6):3669–3675. https://doi.org/10.1021/acs.est.7b06357
20. He H, Meng X, Yue Q, Yin W, Gao Y, Fang P, Shen L (2021) Thiol-ene click chemistry synthesis of a novel magnetic mesoporous silica/chitosan composite for selective Hg(II) capture and high catalytic activity of spent Hg(II) adsorbent. Chem Eng J 405:126743. https://doi.org/10.1016/j.cej.2020.126743
21. Islam MS, Choi WS, Nam B, Yoon C, Lee H-J (2017) Needle-like iron oxide@$CaCO_3$ adsorbents for ultrafast removal of anionic and cationic heavy metal ions. Chem Eng J 307:208–219. https://doi.org/10.1016/j.cej.2016.08.079
22. Kajaste R, Hurme M (2016) Cement industry greenhouse gas emissions—management options and abatement cost. J Cleaner Prod 112:4041–4052. https://doi.org/10.1016/j.jclepro.2015.07.055
23. Karanac M, Đolić M, Veljović Đ, Rajaković-Ognjanović V, Veličković Z, Pavićević V, Marinković A (2018) The removal of Zn^{2+}, Pb^{2+}, and As(V) ions by lime activated fly ash and valorization of the exhausted adsorbent. Waste Manage 78:366–378. https://doi.org/10.1016/j.wasman.2018.05.052
24. Kim E-J, Lee C-S, Chang Y-Y, Chang Y-S (2013) Hierarchically structured manganese oxide-coated magnetic nanocomposites for the efficient removal of heavy metal ions from aqueous systems. ACS Appl Mater Interfaces 5(19):9628–9634. https://doi.org/10.1021/am402615m
25. Kumar ASK, Jiang S-J (2017) Synthesis of magnetically separable and recyclable magnetic nanoparticles decorated with β-cyclodextrin functionalized graphene oxide an excellent adsorption of As(V)/(III). J Mol Liq 237:387–401. https://doi.org/10.1016/j.molliq.2017.04.093
26. Lata S, Singh PK, Samadder SR (2015) Regeneration of adsorbents and recovery of heavy metals: a review. Int J Environ Sci Technol 12(4):1461–1478. https://doi.org/10.1007/s13762-014-0714-9

27. Lee DW, Yoo BR (2014) Advanced metal oxide (supported) catalysts: synthesis and applications. J Ind Eng Chem 20(6):3947–3959. https://doi.org/10.1016/j.jiec.2014.08.004
28. Liu W-J, Tian K, Jiang H, Yu H-Q (2014) Harvest of Cu NP anchored magnetic carbon materials from Fe/Cu preloaded biomass: their pyrolysis, characterization, and catalytic activity on aqueous reduction of 4-nitrophenol. Green Chem 16(9):4198. https://doi.org/10.1039/C4GC00599F
29. López YC, Ortega GA, Martínez MA, Reguera E (2021) Magnetic Prussian blue derivative like absorbent cages for an efficient thallium removal. J Cleaner Prod 283:124587. https://doi.org/10.1016/j.jclepro.2020.124587
30. Lu F, Huang C, You L, Wang J, Zhang Q (2017) Magnetic hollow carbon microspheres as a reusable adsorbent for rhodamine B removal. RSC Adv 7(38):23255–23264. https://doi.org/10.1039/C7RA03045B
31. Ma J, Liu C (2021) Turning waste into treasure: Reuse of contaminant-laden adsorbents (Cr(vi)-Fe_3O_4/C) as anodes with high potassium-storage capacity. J Colloid Interface Sci 582:1107–1115. https://doi.org/10.1016/j.jcis.2020.08.110
32. Mehta D, Mazumdar S, Singh SK (2015) Magnetic adsorbents for the treatment of water/wastewater—a review. J Water Process Eng 7:244–265. https://doi.org/10.1016/j.jwpe.2015.07.001
33. Mohan D, Pittman CU (2007) Arsenic removal from water/wastewater using adsorbents—a critical review. J Hazard Mater 142(1–2):1–53. https://doi.org/10.1016/j.jhazmat.2007.01.006
34. Patel H (2021) Review on solvent desorption study from exhausted adsorbent. J Saudi Chem Soc 25(8):101302. https://doi.org/10.1016/j.jscs.2021.101302
35. Paz R, Viltres H, López YC, Kumar Gupta N, Levya C (2021) Fabrication of magnetic cerium-organic framework-activated carbon composite for charged dye removal from aqueous solutions. J Mol Liq 337:116578. https://doi.org/10.1016/j.molliq.2021.116578
36. Rathore VK, Mondal P (2017) Stabilization of arsenic and fluoride bearing spent adsorbent in clay bricks: preparation, characterization and leaching studies. J Environ Manage 200:160–169. https://doi.org/10.1016/j.jenvman.2017.05.081
37. Rathore VK, Mondal P (2017) Competitive adsorption of arsenic and fluoride onto economically prepared aluminum oxide/hydroxide nanoparticles: multicomponent isotherms and spent adsorbent management. Ind Eng Chem Res 56(28):8081–8094. https://doi.org/10.1021/acs.iecr.7b01139
38. Ruismäki R, Rinne T, Dańczak A, Taskinen P, Serna-Guerrero R, Jokilaakso A (2020) Integrating flotation and pyrometallurgy for recovering graphite and valuable metals from battery scrap. Metals 10(5):680. https://doi.org/10.3390/met10050680
39. Safinejad A, Chamjangali MA, Goudarzi N, Bagherian G (2017) Synthesis and characterization of a new magnetic bio-adsorbent using walnut shell powder and its application in ultrasonic assisted removal of lead. J Environ Chem Eng 5(2):1429–1437. https://doi.org/10.1016/j.jece.2017.02.027
40. Sahoo JK, Paikra SK, Mishra M, Sahoo H (2019) Amine functionalized magnetic iron oxide nanoparticles: synthesis, antibacterial activity and rapid removal of Congo red dye. J Mol Liq 282:428–440. https://doi.org/10.1016/j.molliq.2019.03.033
41. Shen X, Zhu Z, Zhang H, Di G, Chen T, Qiu Y, Yin D (2020) Carbonaceous composite materials from calcination of azo dye-adsorbed layered double hydroxide with enhanced photocatalytic efficiency for removal of Ibuprofen in water. Environ Sci Eur 32(1):77. https://doi.org/10.1186/s12302-020-00351-4
42. Vahidhabanu S, Adeogun AI, Babu BR (2019) Biopolymer-Grafted, magnetically tuned halloysite nanotubes as efficient and recyclable spongelike adsorbents for anionic azo dye removal. ACS Omega 4(1):2425–2436. https://doi.org/10.1021/acsomega.8b02960
43. Venkateswarlu S, Yoon M (2015) Rapid removal of cadmium ions using green-synthesized Fe_3O_4 nanoparticles capped with diethyl-4-(4 amino-5-mercapto-4H-1,2,4-triazol-3-yl)phenyl phosphonate. RSC Adv 5(80):65444–65453. https://doi.org/10.1039/C5RA10628A
44. Venkateswarlu S, Yoon M (2015) Core–shell ferromagnetic nanorod based on amine polymer composite (Fe_3O_4@DAPF) for fast removal of Pb(II) from aqueous solutions. ACS Appl Mater Interfaces 7(45):25362–25372. https://doi.org/10.1021/acsami.5b07723

45. Venkateswarlu S, Yoon M (2015) Surfactant-free green synthesis of Fe_3O_4 nanoparticles capped with 3,4-dihydroxyphenethylcarbamodithioate: stable recyclable magnetic nanoparticles for the rapid and efficient removal of Hg(II) ions from water. Dalton Trans 44(42):18427–18437. https://doi.org/10.1039/C5DT03155A
46. Verbinnen B, Block C, Van Caneghem J, Vandecasteele C (2015) Recycling of spent adsorbents for oxyanions and heavy metal ions in the production of ceramics. Waste Manage 45:407–411. https://doi.org/10.1016/j.wasman.2015.07.006
47. Yang C, Li J, Tan Q, Liu L, Dong Q (2017) Green process of metal recycling: coprocessing waste printed circuit boards and spent tin stripping solution. ACS Sustain Chem Eng 5(4):3524–3534. https://doi.org/10.1021/acssuschemeng.7b00245
48. Yu J, Tang T, Cheng F, Huang D, Martin JL, Brewer CE, Grimm RL, Zhou M, Luo H (2021) Exploring spent biomass-derived adsorbents as anodes for lithium ion batteries. Mater Today Energy 19:100580. https://doi.org/10.1016/j.mtener.2020.100580
49. Zhao F, Repo E, Sillanpää M, Meng Y, Yin D, Tang WZ (2015) Green synthesis of magnetic EDTA- and/or DTPA-cross-linked chitosan adsorbents for highly efficient removal of metals. Ind Eng Chem Res 54(4):1271–1281. https://doi.org/10.1021/ie503874x
50. Zhou Q, Li Z, Shuang C, Li A, Zhang M, Wang M (2012) Efficient removal of tetracycline by reusable magnetic microspheres with a high surface area. Chem Eng J 210:350–356. https://doi.org/10.1016/j.cej.2012.08.081
51. Zhu W, Yang X, He J, Wang X, Lu R, Zhang Z (2021) Investigation and systematic risk assessment in a typical contaminated site of hazardous waste treatment and disposal. Front Public Health 9:764788. https://doi.org/10.3389/fpubh.2021.764788

Chapter 10
Synthesis, Morphology and Environmental Applications of Iron Oxide-Based Nanoarchitectures

Tushar Kanta Sahu and Mohammad Qureshi

Abstract Iron oxide-based nanostructured materials have been extensively studied and developed for various environmental applications in last few decades. Herein, we discussed about various synthesis techniques used to synthesize iron oxide-based nanostructures with different morphologies and their environmental applications. Furthermore, the importance of understanding and controlling the morphology is discussed to realize more efficient environmental applications.

Keywords Iron oxide · Synthesis · Morphology · Nanoarchitectures · Environment · Applications

10.1 Introduction

Iron oxide-based nanomaterials have excellent potential for different environmental applications due to their abundance, low cost and non-toxicity. Although the oxide form of iron is known to have many different phases, among them magnetite (Fe_3O_4), hematite (α-Fe_2O_3) and maghemite (γ-Fe_2O_3) have been widely explored due to their stability, ease in synthesis and magnetic properties. These iron-based oxides have been investigated for various applications such as biomedicine, environmental remediation, catalysis, energy harvesting and energy storage devices due to their tunable optical, electronic and magnetic properties. The morphology control starting from 0 to 3D plays a crucial role in tuning the properties and performance of iron oxide-based materials which not only depend on their chemical composition and characteristic crystallographic structure, but also on their morphology, crystal size and the exposed facets [1–3]. In this chapter, we will briefly discuss about synthesis, morphology and environmental applications of iron oxides nanoarchitectures.

T. K. Sahu · M. Qureshi (✉)
Department of Chemistry, IIT Guwahati, Guwahati, Assam, India
e-mail: mq@iitg.ac.in

H. Sahoo and J. K. Sahoo (eds.), *Iron Oxide-Based Nanocomposites and Nanoenzymes*, Nanostructure Science and Technology, https://doi.org/10.1007/978-3-031-44599-6_10

10.2 Preparation Methods for Iron Oxide Nanoarchitectures

Preparation methods play a key role in controlling the nanostructures of iron oxides, including the regulation of the sizes, structures and morphologies. Various synthetic protocols are known in literature for the morphological synthesis of iron oxides among which hydrothermal, chemical co-precipitation, sol–gel, microemulsion, sonochemical, thermal decomposition and electrochemical decomposition are mostly used.

10.2.1 Hydrothermal/Solvothermal Methods

Hydrothermal method is generally used to crystallize substances in a sealed container from their aqueous solution at high temperature (100–250 °C) and high vapour pressure (0.3–4 MPa) [4]. The conditions of the reaction are very crucial during the hydrothermal process as solvent type, temperature and reaction duration affect the final products. For example, with higher water contents and prolonged reaction duration, the size of the Fe_3O_4 particles increases. The nucleation and grain growth process can control the size of the particles during hydrothermal process [5]. Also, different iron oxide nanoarchitectures can be synthesized using surface directing agents and various solvent mixtures [6–10]. The only difference between a hydrothermal and solvothermal method is that aqueous solution is used in hydrothermal, whereas non-aqueous solution is used in solvothermal during the crystallization process. Both of these synthetic protocols are crucial for synthesis of different morphological iron oxides [11].

10.2.2 Sol–Gel Methods

In sol–gel method, the molecular precursors in solution undergo hydroxylation followed by condensation which results in a ‘sol’ stage from the nanometric particles. With the removal of solvents or by some chemical reaction, three-dimensional metal oxide is formed in wet ‘gel’. As these sol–gel processes are generally performed at room temperature further heat treatment is needed to obtain the final crystalline structure [12, 13]. The parameters such as hydrolysis, condensation, kinetics, pH of the precursor, properties of the gel and agitation influence the synthesis procedure and final structures [14]. The main advantages of this method are that we can have a good control over particle size, monodispersity, homogeneity, predetermined structure and pure amorphous phase [15, 16].

10.2.3 Co-precipitation Method

Co-precipitation is the facile and conventional method for the preparation of metal oxide-based nanoparticles. This method involves the reaction of metal salts in aqueous medium in suitable acidic/basic conditions with the presence of as mild oxidant [17, 18]. The factors such as pH of the solution, reaction temperature, stirring rate and ionic strength decide the size and shape of nanoparticles [19]. For example, iron oxide needs basic pH condition for precipitation [17]. Generally, the crystallinity of iron oxide nanoparticles is very low in this method which can be improved by heat treatment after the synthesis [20]. The adjustment of experimental conditions to obtain monodispersed nanoparticles with stable size and its scale-up is the major drawbacks of this process [11, 19].

10.2.4 Microemulsion

Microemulsion system uses simple and mild reaction conditions where we can easily control the particle size, morphology and homogeneity. Components of microemulsion system consist of an aqueous phase, hydrocarbons, surfactants and co-surfactants [21]. In this process, two immiscible phases such as water and oil undergo isotropic dispersion in the presence of a surfactant, where it forms a monolayer in between the interface of water and oil [16]. More specifically, the hydrophobic part of the surfactant dissolves in the oil phase, whereas the hydrophilic part dissolves in aqueous phase. The lamellar phase generally helps in particle growth, nucleation and agglomeration [22]. The main advantage of this method is that a diverse range of controlled iron oxide nanoparticles with different shape and size can be obtained. However, the adverse effects of residual surfactants on the properties of the synthesized iron oxides and difficulty in scale-up procedures is the disadvantage associated with this method [23, 24].

10.2.5 Thermal Decomposition

Thermal decomposition method is an effective technique in terms of size and morphology control of the iron oxide nanoarchitectures. It includes decomposition of organometallic iron precursors including metallic acetate, acetylacetonates and carboxylic acids of organic surfactants which is generally decomposed at higher temperature to form iron oxides [25]. Thermal decomposition method has many advantages such as production of highly monodispersed particles with a narrow size distribution, however the main disadvantage is that as synthesized nanoparticles are generally dissolved only in nonpolar solvents [26].

It should be noted that the methods of preparation have a significant role on the size of the particle and forms of the materials, distribution of size, surface chemistry and therefore on their properties and applications. Besides, the preparation method also commands the level of structural defects, their distribution and the amount of impurities possibly present in the synthesized materials [27].

In the following sections, we will discuss the recent development and various strategies for obtaining different morphologies of iron oxide.

10.3 Morphology of Iron Oxide

In this part of the chapter, synthesis of iron oxide-based nanoarchitectures starting from 0 to 3D architectures is discussed. As we know, morphology plays a crucial role in enhancing the efficiency of iron oxide base nanoarchitectures for different environmental applications. In principle, 0D morphology generally refers to nanoparticles with same dimensions on each axis with size less than 100 nm. When the dimension in one of the particular directions is greater than other dimensions, it is referred to 1D morphology such as nanorods, nanotubes and nanowires. The 2D morphology generally refers to nanoplates, nanodiscs and nanoplates. The 3D morphology typically includes different hierarchical structures such as urchin-like, flower-like and star-like nanostructures. In this section, we will briefly discuss about the synthetic methods for fabrication of iron oxide nanoarchitectures and different parameters that influences the formation and growth of these nanostructures.

10.3.1 0D Morphology

Iron oxide nanoparticles are the commonly known 0D nanoarchitecture which are widely studied due to their ease in synthesis and utilizations in biomedical and catalytic applications. For efficient utilization in various applications, iron oxide nanoparticles should have a narrow size distribution, high magnetic response, better stability and dispersity in solutions. To achieve the abovementioned properties, many factors such as choice of precursor, solvent, reducing agent, reaction temperature, and reaction time are very crucial.

Co-precipitation is the most popular synthetic method for the synthesis of iron oxide nanoparticles in aqueous medium. The phase of iron oxide nanoparticles can be tuned by employment of different bases to the iron precursors [18]. For example, by addition of Na_2CO_3 to iron precursor solution, highly monodispersed α-FeOOH particles with size around 60 nm can be obtained, whereas addition of NaOH instead of Na_2CO_3 leads to the formation of α-Fe_2O_3 particles with higher size of around 230 nm. This is due to the capabilities of bases to maintain a constant pH of the solution during precipitation. Specifically, the molar ratio of OH to Fe decides the final particle size and elongation by controlling the rate of hydrolysis, whereas carbonate

ions help to maintain a constant pH throughout the entire reaction [28]. Although precipitation method is mostly convenient for Fe_3O_4 nanoparticles, it is relatively difficult to control the particle size of others iron oxide-based nanoparticles.

Besides co-precipitation method, hydrothermal and solvothermal synthetic methods are suitable for the preparation of iron oxide nanoparticles with control over size, phase and morphology by changing the reaction parameters [29]. For example, with increasing the concentration of iron precursor, the size of the resulting Fe_3O_4 nanoparticles decreases. This is because the nucleation and growth rate of Fe_3O_4 particles is strongly affected by concentration of Fe(II) in the precursor solution [30, 31]. The higher initial concentration of precursor leads to the formation of a large number of seed nuclei which leads to smaller particles size [32].

Ultra-large-scale monodispersed iron oxide nanocrystals also can be synthesized by varying the experimental conditions using inexpensive and non-toxic metal salts as reactants. Firstly, iron-oleate complex precursor is formed by reaction between iron chloride and sodium oleate. The thermal decomposition of this iron-oleate complex precursor in a high boiling solvent results in monodispersed iron oxide nanocrystals. The size of these nanocrystals can be controlled by using various solvents such as trioctylamine (b.p. 365 °C), 1-eicosene (b.p. 330 °C), 1-octadecene (b.p. 317 °C), octyl ether (b.p. 287 °C) and 1-hexadecene (b.p. 274 °C). Also, by varying the concentration of oleic acid, the size of the nanocrystals can be further fine-tuned [33]. Figure 10.1 shows TEM images of typical iron oxide nanoparticles with uniform size distributions.

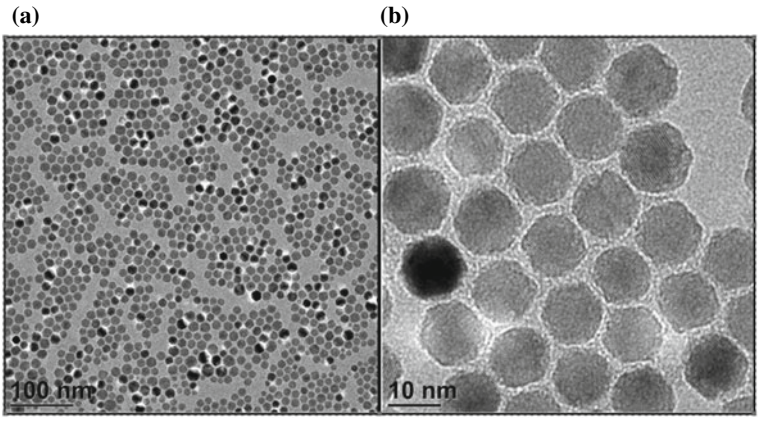

Fig. 10.1 Transmission electron microscope (TEM) image of iron oxide nanoparticles with two different magnifications (**a**, **b**). Obtained from Ref. [8]. Copyright Springer Nature

10.3.2 1D-Nanoarchitectures

1D nanostructures are mostly studied due to their enhanced electron and mass transport properties as they have a higher length along the longitudinal direction as compared to any other axis. Nucleation and subsequent anisotropic growth in one specific direction gives rise to formation of 1D nanostructures. It is necessary to control the growth rates of different facets of the crystals kinetically during the synthesis process. For this kinetic control, various surfactants and additives are often used. For instance, some specific surfactants block the growth on *x*-axis and *y*-axis planes by adsorption and enables selective growth in *z*-axis direction for generation of 1D nanostructures [34]. 1D iron oxide nanostructures such as nanowires, nanorods, nanotubes and nanospindles are mainly synthesized by both template-assisted and template-free methods [35–40].

Annealing of β-FeOOH nanorods in air at temperature more than 350 °C results in the formation of uniform α-Fe_2O_3 and Fe_3O_4 nanorods, where β-FeOOH nanorods are generally produced through hydrothermal method using $FeCl_3$ at 80 °C [41, 42]. Preparation of iron oxide nanotubes generally needs a template-assisted method. After the preparation of a coating layer over the template, the metal-based template is etched through NaOH solution and undergo subsequent high-temperature annealing to form iron oxide nanotubes. The arrangement of Fe_2O_3 nanotubes is similar to the metal-template matrix [43, 44]. α-Fe_2O_3 nanowires can be synthesized in large scale by solvothermal method using organic chains as a mediating template and annealing at high temperature [45]. Figure 10.2 shows SEM and TEM images of different 1D iron oxide nanoarchitectures such as nanowires, nanorods, nanotubes and nanospindles.

10.3.3 2D Nanoarchitectures

Owing to their unique properties such as high surface to volume ratio and unique physicochemical, optical and electronic properties, 2D nanostructures have attracted significant research interests in the recent years. These attractive properties of 2D nanostructures made them attractive for various environmental applications. 2D nanostructures morphologies of iron oxides such as nanoplates and nanosheets have been successfully synthesized using various methods, including hydrothermal, thermal decomposition, thermal oxidation and electrodeposition [46–50].

Hexagonal magnetite (Fe_3O_4) nanoplates can be synthesized trough hydrothermal method by using β-cyclodextrin as a reducing agent and urea as a modifier. Herein, urea is used as a growth modifier for controlling the shape of iron oxides as it can undergo hydrolysis slowly and can adjust the pH of the solution [51]. Fe_3O_4 nanoplates can also be synthesized by one-step hydrothermal route by Schikorr reaction. In this reaction, $Fe(OH)_2$ is oxidized by protons of water to form Fe_3O_4 and H_2 under anaerobic conditions. In addition, use of elthylene glycol as a solvent

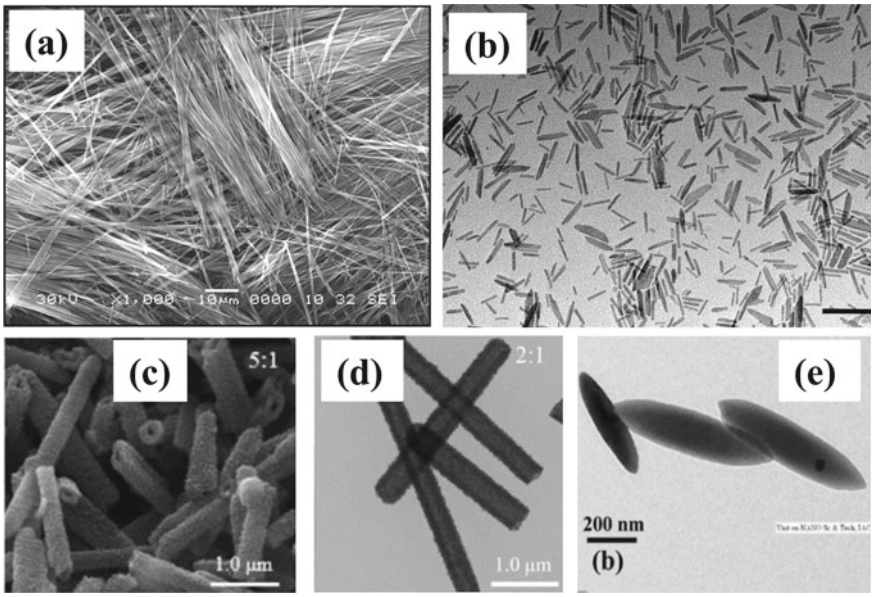

Fig. 10.2 **a** Scanning electron microscope (SEM) image of α-Fe_2O_3 nanowires. Reprinted with permission from Ref. [45], copyright American Chemical Society, **b** TEM image of Fe_3O_4 Nanorods. Reprinted with permission from Ref. [40], copyright American Chemical Society. **c** SEM image of α-Fe_2O_3 nanotubes, **d** TEM image of α-Fe_2O_3 nanotubes. Reprinted with permission from Ref. [44], copyright Springer Nature. **e** TEM image of spindle like α-Fe_2O_3. Reprinted with permission from Ref. [35], copyright IOP Science

besides water can adjust the morphology and thickness of the product [47]. Hematite nanodiscs with (001) exposed can be synthesized by one-pot solvothermal method. During the synthesis, the concentrations of OH^- and H^+ play crucial role on the final morphology of the product. The nanodiscs morphology is due to the anisotropic packing of the ions in Fe_2O_3 crystals, where (001) facet is densest and stable [52]. Silicate anions and citric acid are the commonly used capping agents for the formation of disc and prism type iron oxide nanostructures due to their selective adsorption towards {001} facet of iron oxide seeds during the hydrothermal synthesis [50, 53]. Figure 10.3 shows SEM and TEM images of different 2D iron oxide nanoarchitectures such as nanodiscs, nanoplates and nanosheets.

10.3.4 3D Iron Oxide Nanoarchitectures

3D nanoarchitectures are generally formed by integration of 1D and 2D nanoscale building blocks such as nanowire, nanorod, nanosheet and nanoplates. These hierarchical architectures have unique properties as a result of combined features of

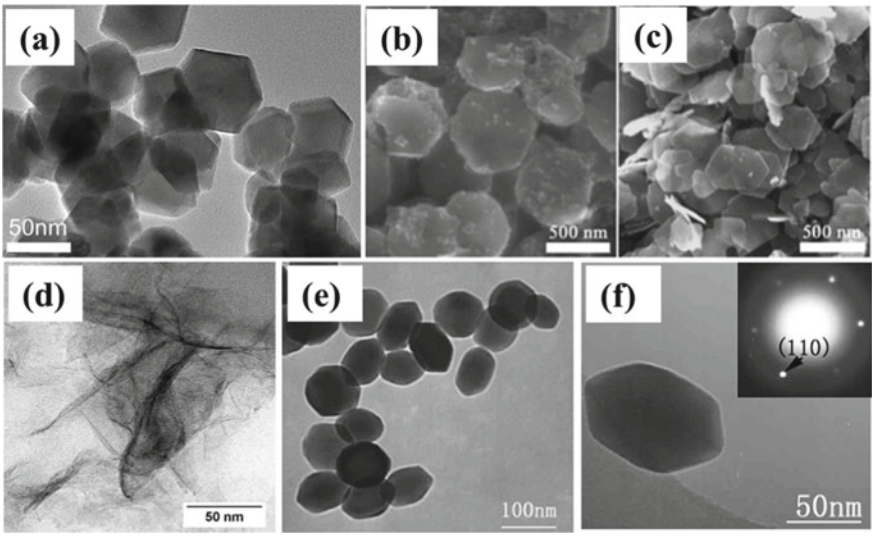

Fig. 10.3 **a** TEM image of hexagonal Fe_3O_4 nanoplates. Reprinted from Ref. [47], copyright SpringerOpen. **b** SEM image of α-Fe_2O_3 nanoplates formed using NaOH, **c** SEM image of α-Fe_2O_3 nanoplates formed using CH_3CH_2COONa. Reprinted with permission from Ref. [52], copyright Royal Society of Chemistry. **d** TEM image of γ-Fe_2O_3 nanosheets. Reprinted with permission from Ref. [48], copyright American Chemical Society. **e** TEM image of hexagonal Fe_2O_3 nanoplates and **f** TEM image of a Fe_2O_3 nanoplate with corresponding SAED pattern. Reprinted with permission from Ref. [53], copyright American Chemical Society

nanoscale building blocks that are distinct from the features of single nanoarchitectures. These 3D nanoarchitectures are utilized in various environmental applications such as catalysis, chemical and biological sensors.

Many synthetic strategies like ultrasonic irradiation, solvothermal and polyol-assisted self-assembly process are known for the synthesis of various 3D iron oxide nanostructures with distinct shapes, such as urchin-like, flower-like, chestnut-like, dendrites-like, stars-like and peant-like morphology [54–62].

3D nanotubular sea urchin-shaped iron oxide nanostructures can be synthesized by a simple and rapid sonochemical method with template-free approach. This urchin-like nanostructure is composed of spherical core with perpendicular 1D tubular structure with high surface area. Also, the interconversion from γ-Fe_2O_3 phase to α-Fe_2O_3 phase can be easily achieved by following a post calcination procedure [54]. 3D γ-Fe_2O_3 and Fe_3O_4 chestnut-like nanostructures can be synthesized by annealing the Fe_2O_3 chestnut-like amorphous core/γ-phase shell nanoarchitectures at different temperatures in a nitrogen atmosphere. Firstly, Fe_2O_3 chestnut-like nanostructures is synthesized by solvethermal method using DMS as solvent along with tin and iron precursor [55]. 3D flower-like iron oxide nanostructures can be produced by an ethylene glycol-mediated self-assembly process. Use of ferric chloride precursor, urea and tetrabutylammonium bromide (TBAB) with ethylene glycol with a 30 min reflux at 195 °C followed by calcination leads to the formation of either α-Fe_2O_3,

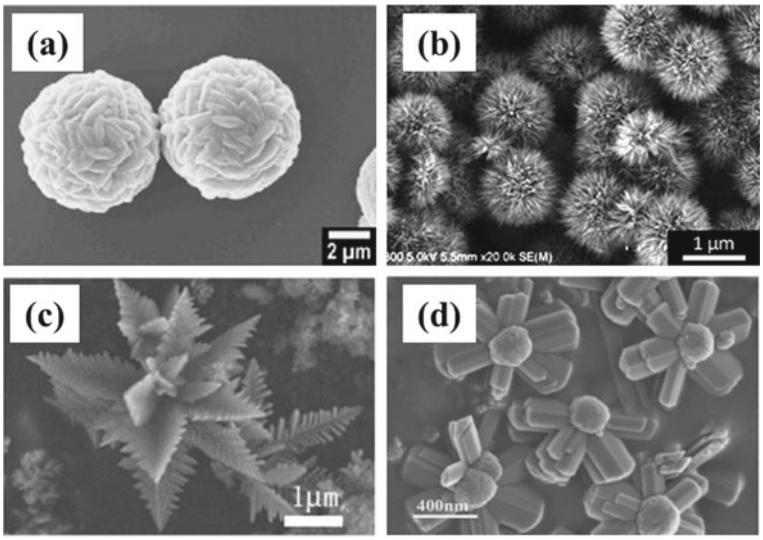

Fig. 10.4 SEM image of 3D iron oxide with **a** Flower-like nanostructures. Reprinted with permission from Ref. [62], copyright Elsevier. **b** Chestnut-like Nanostructures. Reprinted with permission from Ref. [55], copyright American Chemical Society. **c** Multi-leaf α-Fe_2O_3 nanostructures. Reprinted with permission from Ref. [57], copyright Elsevier and **d** Star-like nanostructures. Reprinted with permission from Ref. [58], copyright Elsevier

χ-Fe_2O_3 or Fe_3O_4 by controlling the calcination temperatures. The original flower-like morphology is maintained even after the calcination process [56]. Figure 10.4 shows SEM images of different 3D iron oxide nanoarchitectures such as flowers-like, urchin-like, multi-leaf-like and star-like morphology.

10.4 Environmental Applications of Iron Oxide Nanostructures

Iron oxide nanostructures with various morphology and high tailorabilities have many potentials towards environmental applications such as catalysis, sensors, biomedical and water remediation fields. In this section, we will briefly discuss about the potentials of various iron oxide-based nanostructures for different applications.

10.4.1 Removal of Heavy Metals

Contamination of natural water sources by heavy metals due to industrial and geographical reasons makes it unhealthy for consumption. Heavy metal contamination is a great concern because of their toxic effect on human beings, animals as well as plants, and their removal is necessary [63]. Iron oxide nanomaterials are known for its efficient heavy metal adsorption properties due to its high surface area, surface reactivity and strong magnetic behaviour [56, 64–67]. Iron oxide with different nanoarchitectures is being widely used as effective adsorbents for the adsorption and removal of heavy metals such as arsenic, chromium, mercury, lead, copper and cadmium [68–79].

10.4.2 Removal of Organic Contaminants

Besides heavy metal adsorption, iron oxide is also known for the efficient removal of organic contaminants such as industrial dyes, pesticides and hydrocarbons from water through adsorption and photocatalytic degradation. In adsorption process, the dyes are not destroyed, they only transfer from one phase to another. However, in degradation process, the dyes and pollutants are converted into organic acids with low-molecular-mass and even into CO_2, water and small inorganic molecules [80]. Iron oxide nanoparticles degrades the pollutants in Fenton-like reaction systems which effectively decompose hydrogen peroxide (H_2O_2) to free hydroxyl radicals (·OH) [81]. In this process, dyes such as methyl blue, azo dye, rhodamine B, methyl orange, chlorinated hydrocarbons and phenols have been efficiently removed from water through iron oxide nanoarchitectures materials [82–85].

10.4.3 Carbon Monoxide (CO) Oxidation

Air pollutants such as NO_x, CO, SO_x, NH_3 and many volatile organic compounds are harmful for both human beings and environment. Among these air pollutants, CO is most toxic and can cause severe health issues upon exposure. So, efficient oxidation of CO through catalyst is highly desired [86]. Among different catalytic materials, iron oxide nanomaterials have great potential for oxidation of CO due to its high surface area, surface reactivity and dual functionality as oxidant as well as catalyst [87]. It is also found that nanoscale iron oxide is more significant as a catalyst and as a reagent compared to non-nanoscale iron oxide for oxidation of CO [88].

10.4.4 Biosensors

Due to its simple preparation methods, non-toxicity and biocompatibility, iron oxide nanostructure materials have attracted a great attention towards biosensors. Functionalized iron oxide nanoparticles have been utilized in biofuel cells, bioelectronic devices andelectrochemical biosensors [89–91]. Iron oxide is known to be effectively selective towards the electrochemical sensing of dopamine which is inexpensive and highly sensitive towards dopamine detection [92–95].

Beside abovementioned environmental applications iron oxide nanostructures have been used in various others applications such as photocatalytic water splitting, pollutant sensors, artificial leaf for CO_2 sequestration, biomimetic carbonation, mineral carbonation, N_2O decomposition, methane combustion, drug delivery and bio imaging [42, 96, 97].

10.5 Conclusions

Owing to their abundance, cost-effectiveness, low toxicity, magnetic behaviour and ease in preparation, iron oxide nanoarchitectures have been explored significantly for various applications. Fabrication of iron oxide nanomaterials with different morphology starting from 0 to 3D in a controlled manner has also been attained through various synthetic methods such as hydrothermal, sol–gel, co-precipitation, thermal decomposition, sonochemical and microemulsion. All these preparation methods have both advantages and disadvantages owing to their control over size, shape and morphology. Relatively due to their magnetic properties and high surface area, iron oxide has been used in many environmental applications. Use of iron oxide nanomaterials instead of rare-earth-based nanomaterials has proven to be cost-effective and efficient alternative for many applications. Although magnetic iron oxide nanomaterials show many distinctive properties, further research is needed for clarity over the toxicity level and biocompatibility of iron oxides.

References

1. Zhao J, Yang P, Chen H, Li J, Che Q, Zhu Y, Shi R (2015) Effect of sequential morphology adjustment of hematite nanoplates to nanospindles on their properties and applications. J Mater Chem C 3:2539–2547. https://doi.org/10.1039/C4TC02752C
2. Yang S, Xu Y, Sun Y, Zhang G, Gao D (2012) Size-controlled synthesis, magnetic property, and photocatalytic property of uniform α-Fe_2O_3 nanoparticles via a facile additive-free hydrothermal route. CrystEngComm 14:7915–7921. https://doi.org/10.1039/c2ce25929j
3. Wang X, Wang J, Cui Z, Wang S, Cao M (2014) Facet effect of α-Fe_2O_3 crystals on photocatalytic performance in the photo-fenton reaction. RSC Adv 2014(4):34387–34394. https://doi.org/10.1039/C4RA03866E

4. Wang X, Zhuang J, Peng Q, Li YD (2005) A general strategy for nanocrystal synthesis. Nature 437:121–124. https://doi.org/10.1038/nature03968
5. Denkbaş EB, Çelik E, Erdal E, Kavaz D, Akbal Ö, Kara G, Bayram C (2016) Magnetically based nanocarriers in drug delivery. Nanobiomater Drug Deliv 9:285–331 (William Andrew Publishing)
6. Kongsat P, Kudkaew K, Tangjai J, O'Rear EA, Pongprayoon T (2021) Synthesis of structure-controlled hematite nanoparticles by a surfactant-assisted hydrothermal method and property analysis. J Phys Chem Solids 148:109685. https://doi.org/10.1016/j.jpcs.2020.109685
7. Ramesh R, Rajalakshmi M, Muthamizhchelvan C, Ponnusamy S (2012) Synthesis of Fe_3O_4 nanoflowers by one pot surfactant assisted hydrothermal method and its properties. Mater Lett 70:73–75. https://doi.org/10.1016/j.matlet.2011.11.085
8. Wierzbinski KR, Szymanski T, Rozwadowska N, Rybka JD, Zimna A, Zalewski T, Nowicka-Bauer K, Malcher A, Nowaczyk M, Krupinski M, Fiedorowicz M, Bogorodzki P, Grieb P, Giersig M, Kurpisz MK (2018) Potential use of superparamagnetic iron oxide nanoparticles for in vitro and in vivo bioimaging of human myoblasts. Sci Rep 8(1):1–17. https://doi.org/10.1038/s41598-018-22018-0
9. Rajendran R, Muralidharan R, Santhana Gopalakrishnan R, Chellamuthu M, Ponnusamy SU, Manikandan E (2011) Controllable synthesis of single-crystalline Fe_3O_4 nanorice by a one-pot, surfactant-assisted hydrothermal method and its properties. Eur J Inorg Chem 2011:5384–5389. https://doi.org/10.1002/ejic.201100840
10. Zou G, Xiong K, Jiang C, Li H, Wang Y, Zhang S, Qian Y (2005) Magnetic Fe_3O_4 nanodisc synthesis on a large scale via a surfactant-assisted process. Nanotechnology 16:1584–1588. https://doi.org/10.1088/0957-4484/16/9/030
11. Ahmed KAM (2014) Formation Fe_2O_3 nanowalls through solvent-assisted hydrothermal process and their application for Titan Yellow GR dye degradation. J Korean Chem Soc 58:205–209. https://doi.org/10.5012/jkcs.2014.58.2.205
12. da Silva AK, Sobieski E, Viana LH, Lanças FM, Nazario CED (2016) Extração em Fase Sólida Magnética (MSPE): fundamentos e Aplicações. Sci Chromatogr 8:239–256. https://doi.org/10.4322/sc.2016.036
13. Lam UT, Mammucari R, Suzuki K, Foster NR (2008) Processing of iron oxide nanoparticles by supercritical fluids. Ind Eng Chem Res 47(3):599–614. https://doi.org/10.1021/ie070494+
14. Kojima K, Miyazaki M, Mizukami F, Maeda K (1997) Selective formation of spinel iron oxide in thin films by complexing agent-assisted sol-gel processing. J Sol-Gel Sci Technol 8(1–3):77–81. https://doi.org/10.1007/BF02436821
15. Ennas G, Musinu A, Piccaluga G et al (1998) Characterization of iron oxide nanoparticles in an Fe_2O_3–SiO_2 composite prepared by a sol-gel method. Chem Mat 10(2):495–502. https://doi.org/10.1021/cm970400u
16. Hasany S, Ahmed I, Rajan J, Rehman A (2012) Systematic review of the preparation techniques of iron oxide magnetic nanoparticles. Nanosci Nanotechnol 2(6):148–158. https://doi.org/10.5923/j.nn.20120206.01
17. Tavakoli A, Sohrabi M, Kargari A (2007) A review of methods for synthesis of nanostructured metals with emphasis on iron compounds. Chem Papers 61(3):151–170. https://doi.org/10.2478/s11696-007-0014-7
18. Wu S, Sun A, Zhai F et al (2011) Fe_3O_4 magnetic nanoparticles synthesis from tailings by ultrasonic chemical co-precipitation. Mat Lett 65(12):1882–1884. https://doi.org/10.1016/j.matlet.2011.03.065
19. Varanda LC, Morales MP, Jafelicci M Jr, Serna CJ (2002) Monodispersed spindle-type goethite nanoparticles from Fe^{III} solutions. J Mater Chem 12:3649–3653. https://doi.org/10.1039/B207190H
20. Hernández-Hernández AA, Álvarez-Romero GA, Contreras-López E, Aguilar-Arteaga K, Castañeda-Ovando A (2017) Food analysis by microextraction methods based on the use of magnetic nanoparticles as supports: recent advances. Food Anal Methods 10(9):2974–2993. https://doi.org/10.1007/s12161-017-0863-9

21. Scano A, Cabras V, Pilloni M, Ennas G (2019) Microemulsions: the Renaissance of ferrite nanoparticle synthesis. J Nanosci Nanotechnol 19(8):4824–4838. https://doi.org/10.1166/jnn.2019.16876
22. Solans C, Izquierdo P, Nolla J, Azemar N, Garcia-Celma MJ (2005) Nano-emulsions. Curr Opin Colloid Interface Sci 10(3–4):102–110. https://doi.org/10.1016/j.cocis.2005.06.004
23. Pileni MP (1993) Reverse micelles as microreactors. J Phys Chem 97(27):6961–6973. https://doi.org/10.1021/j100129a008
24. Soenen SJ, De Cuyper M (2009) Assessing cytotoxicity of (iron oxide-based) nanoparticles: an overview of different methods exemplified with cationic magnetoliposomes. Contrast Media Mol Imaging 4(5):207–219. https://doi.org/10.1002/cmmi.282
25. Tartaj P, del Puerto Morales M, Veintemillas-Verdaguer S, González-Carreño T, Serna CJ (2003) The preparation of magnetic nanoparticles for applications in biomedicine. J Phys D Appl Phys 36(13):R182. https://doi.org/10.1088/0022-3727/36/13/202
26. Sun S, Zeng H (2002) Size-controlled synthesis of magnetite nanoparticles. J Am Chem Soc 124(28):8204–8205
27. Wu W, He Q, Jiang C (2008) Magnetic iron oxide nanoparticles: synthesis and surface functionalization strategies. Nanoscale Res Lett 3:397–415
28. Teja SA, Koh PY (2009) Synthesis, properties, and applications of magnetic iron oxide nanoparticles. Prog Cryst Growth Charact Mater 55(1–2):22–45. https://doi.org/10.1016/j.pcrysgrow.2008.08.003
29. Tanaka S, Kaneti YV, Septiani NLW, Dou SX, Bando Y, Hossain MSA, Kim J, Yamauchi Y (2019) A review on iron oxide-based nanoarchitectures for biomedical, energy storage, and environmental applications. Small Methods 3(5):1800512
30. Wu W, Wu Z, Yu T, Jiang C, Kim WS (2015) Recent progress on magnetic iron oxide nanoparticles: synthesis, surface functional strategies and biomedical applications. Sci Technol Adv Mater 16(2):023501
31. Ge S, Shi X, Sun K, Li C, Uher C, Baker JR Jr, Banaszak Holl MM, Orr BG (2009) Facile hydrothermal synthesis of iron oxide nanoparticles with tunable magnetic properties. J Phys Chem C 113(31):13593–13599
32. Hui C, Shen C, Yang T, Bao L, Tian J, Ding H, Li C, Gao HJ (2008) Large-scale Fe_3O_4 nanoparticles soluble in water synthesized by a facile method. J Phys Chem C 112(30):11336–11339
33. Park J, An K, Hwang Y, Park JG, Noh HJ, Kim JY, Park J-H, Hwang N-M, Hyeon T (2004) Ultra-large-scale syntheses of monodisperse nanocrystals. Nat Mater 3(12):891–895
34. Hiramatsu H, Osterloh FE (2004) A simple large-scale synthesis of nearly monodisperse gold and silver nanoparticles with adjustable sizes and with exchangeable surfactants. Chem Mater 16(13):2509–2511
35. Mitra S, Das S, Mandal K, Chaudhuri S (2007) Synthesis of a α-Fe_2O_3 nanocrystal in its different morphological attributes: growth mechanism, optical and magnetic properties. Nanotechnology 18(27):275608
36. Jia C-J, Sun L-D, Luo F, Han X-D, Heyderman LJ, Yan Z-G, Yan C-H, Zheng K, Zhang Z, Takano M, Hayashi N, Eltschka M, Kläui M, Rüdiger U, Kasama T, Cervera-Gontard L, Dunin-Borkowski R-E, Tzvetkov G, Raabe J (2005) Single-crystalline iron oxide nanotubes. Angew Chem 117(28):4402–4407
37. Almeida TP, Fay M, Zhu Y, Brown PD (2009) Process map for the hydrothermal synthesis of α-Fe_2O_3 nanorods. J Phys Chem C 113(43):18689–18698
38. Liu H, Wang G, Park J, Wang J, Liu H, Zhang C (2009) Electrochemical performance of α-Fe_2O_3 nanorods as anode material for lithium-ion cells. Electrochim Acta 54(6):1733–1736
39. Li Z, Lai X, Wang H, Mao D, Xing C, Wang D (2009) Direct hydrothermal synthesis of single-crystalline hematite nanorods assisted by 1, 2-propanediamine. Nanotechnology 20(24):245603
40. Das R, Alonso J, Nemati Porshokouh Z, Kalappattil V, Torres D, Phan MH, Garaio E, García JA, Llamazares JLS, Srikanth H (2016) Tunable high aspect ratio iron oxide nanorods for enhanced hyperthermia. J Phys Chem C 120(18):10086–10093

41. Kaneti YV, Zakaria QM, Zhang Z, Chen C, Yue J, Liu M, Xiang X, Yu A (2014) Solvothermal synthesis of ZnO-decorated α-Fe_2O_3 nanorods with highly enhanced gas-sensing performance toward n-butanol. J Mater Chem A 2(33):13283–13292
42. Sahu TK, Shah AK, Banik A, Qureshi M (2019) Enhanced surface and bulk recombination kinetics by virtue of sequential metal and nonmetal incorporation in hematite-based photoanode for superior photoelectrochemical water oxidation. ACS Appl Energy Mater 2(6):4325–4334
43. Chen J, Xu L, Li W, Gou X (2005) α-Fe_2O_3 nanotubes in gas sensor and lithium-ion battery applications. Adv Mater 17(5):582–586
44. Ma L, Ma H, Gao N, Wang J, Zhang X (2016) Controllable synthesis of α-Fe_2O_3 nanotubes with high surface area: preparation, growth mechanism, and its catalytic performance for the selective catalytic reduction of NO with NH_3. J Mater Sci 51(4):1959–1965
45. Wang G, Gou X, Horvat J, Park J (2008) Facile synthesis and characterization of iron oxide semiconductor nanowires for gas sensing application. J Phys Chem C 112(39):15220–15225
46. Palchoudhury S, Xu Y, Rushdi A, Holler RA, Bao Y (2012) Controlled synthesis of iron oxide nanoplates and nanoflowers. Chem Commun 48(85):10499–10501
47. Ma M, Zhang Y, Guo Z, Gu N (2013) Facile synthesis of ultrathin magnetic iron oxide nanoplates by Schikorr reaction. Nanoscale Res Lett 8(1):1–7
48. Niu S, McFeron R, Godinez-Salomon F, Chapman BS, Damin CA, Tracy JB, Augustyn V, Rhodes CP (2017) Enhanced electrochemical lithium-ion charge storage of iron oxide nanosheets. Chem Mater 29(18):7794–7807
49. Jun YW, Choi JS, Cheon J (2006) Shape control of semiconductor and metal oxide nanocrystals through nonhydrolytic colloidal routes. Angew Chem Int Ed 45(21):3414–3439
50. Qu J, Yu Y, Cao CY, Song WG (2013) α-Fe_2O_3 nanodisks: layered structure, growth mechanism, and enhanced photocatalytic property. Chemistry 19(34):11172–11177
51. Xu Z, Wei Z, He P, Duan X, Yang Z, Zhou Y, Jia D (2017) Seed-mediated growth of ultra-thin triangular magnetite nanoplates. Chem Commun 53(80):11052–11055
52. Lu J, Peng Q, Wang Z, Nan C, Li L, Li Y (2013) Hematite nanodiscs exposing (001) facets: synthesis, formation mechanism and application for Li-ion batteries. J Mater Chem A 1(17):5232–5237
53. Wu J, Zhang H, Du N, Ma X, Yang D (2006) General solution route for nanoplates of hexagonal oxide or hydroxide. J Phys Chem B 110(23):11196–11198
54. Lee SC, Jeong Y, Kim YJ, Kim H, Lee HU, Lee YC, Lee SM, Kim HJ, An HR, Ha MG, Lee GW, Lee YS, Lee G (2018) Hierarchically three-dimensional (3D) nanotubular sea urchin-shaped iron oxide and its application in heavy metal removal and solar-induced photocatalytic degradation. J Hazard Mater 354:283–292
55. Mou F, Guan J, Ma H, Xu L, Shi W (2012) Magnetic iron oxide chestnutlike hierarchical nanostructures: preparation and their excellent arsenic removal capabilities. ACS Appl Mater Interfaces 4(8):3987–3993
56. Zhong LS, Hu JS, Liang HP, Cao AM, Song WG, Wan LJ (2006) Self-Assembled 3D flowerlike iron oxide nanostructures and their application in water treatment. Adv Mater 18(18):2426–2431
57. Liang J, Li L, Kang H (2013) Solvothermal synthesis, growth mechanism, and magnetic property of self-assembled 3D multileaf α-Fe_2O_3 superstructures. Powder Technol 235:475–478
58. Song F, Guan J, Fan X, Yan G (2009) Single-crystal star-like arrayed particles of hematite: synthesis, formation mechanism and magnetic properties. J Alloy Compd 485(1–2):753–758
59. Cao M, Liu T, Gao S, Sun G, Wu X, Hu C, Wang ZL (2005) Single-crystal dendritic micropines of magnetic α-Fe_2O_3: large-scale synthesis, formation mechanism, and properties. Angew Chem Int Ed 44(27):4197–4201
60. Cho YS, Huh YD (2009) Preparation of hyperbranched structures of α-Fe_2O_3. Bull Korean Chem Soc 30(6):1413–1415
61. An Z, Zhang J, Pan S, Song G (2012) Novel peanut-like α-Fe_2O_3 superstructures: oriented aggregation and Ostwald ripening in a one-pot solvothermal process. Powder Technol 217:274–280

62. Liang H, Chen W, Yao Y, Wang Z, Yang Y (2014) Hydrothermal synthesis, self-assembly and electrochemical performance of α-Fe_2O_3 microspheres for lithium ion batteries. Ceram Int 40(7):10283–10290
63. Xu P, Zeng GM, Huang DL, Feng CL, Hu S, Zhao MH, Lai C, Wei Z, Huang C, Xie GX, Liu ZF (2012) Use of iron oxide nanomaterials in wastewater treatment: a review. Sci Total Environ 424:1–10
64. Hu H, Wang Z, Pan L (2010) Synthesis of monodisperse Fe_3O_4 @ silica core–shell microspheres and their application for removal of heavy metal ions from water. J Alloy Compd 492(1–2):656–661
65. Nassar NN (2010) Rapid removal and recovery of Pb (II) from wastewater by magnetic nanoadsorbents. J Hazard Mater 184(1–3):538–546
66. Mahdavian AR, Mirrahimi MAS (2010) Efficient separation of heavy metal cations by anchoring polyacrylic acid on superparamagnetic magnetite nanoparticles through surface modification. Chem Eng J 159(1–3):264–271
67. Pradeep T (2009) Noble metal nanoparticles for water purification: a critical review. Thin Solid Films 517(24):6441–6478
68. Sahu TK, Arora S, Banik A, Iyer PK, Qureshi M (2017) Efficient and rapid removal of environmental malignant arsenic (III) and industrial dyes using reusable, recoverable ternary iron oxide-ORMOSIL-reduced graphene oxide composite. ACS Sustain Chem Eng 5(7):5912–5921
69. Hao L, Liu M, Wang N, Li G (2018) A critical review on arsenic removal from water using iron-based adsorbents. RSC Adv 8(69):39545–39560
70. Ilankoon N (2014) Use of iron oxide magnetic nanosorbents for Cr (VI) removal from aqueous solutions: a review. J Eng Res Appl 4(10):55–63
71. Choi WS, Lee HJ (2022) Nanostructured materials for water purification: adsorption of heavy metal ions and organic dyes. Polymers 14(11):2183
72. Gong Y, Huang Y, Wang M, Liu F, Zhang T (2019) Application of iron-based materials for remediation of mercury in water and soil. Bull Environ Contam Toxicol 102(5):721–729
73. Vélez E, Campillo GE, Morales G, Hincapié C, Osorio J, Arnache O, Uribe JI, Jaramillo F (2016) Mercury removal in wastewater by iron oxide nanoparticles. J Phys Conf Ser 687(1):012050 (IOP Publishing)
74. Gholami A, Moghadassi AR, Hosseini SM, Shabani S, Gholami F (2014) Preparation and characterization of polyvinyl chloride-based nanocomposite nanofiltration-membrane modified by iron oxide nanoparticles for lead removal from water. J Ind Eng Chem 20(4):1517–1522
75. Lingamdinne LP, Koduru JR, Rao Karri R (2019) Green synthesis of iron oxide nanoparticles for lead removal from aqueous solutions. Key Eng Mater 805:122–127 (Trans Tech Publications Ltd)
76. Ehrampoush MH, Miria M, Salmani MH, Mahvi AH (2015) Cadmium removal from aqueous solution by green synthesis iron oxide nanoparticles with tangerine peel extract. J Environ Health Sci Eng 13(1):1–7
77. Suda A, Makino T (2016) Functional effects of manganese and iron oxides on the dynamics of trace elements in soils with a special focus on arsenic and cadmium: a review. Geoderma 270:68–75
78. Tamez C, Hernandez R, Parsons JG (2016) Removal of Cu (II) and Pb (II) from aqueous solution using engineered iron oxide nanoparticles. Microchem J 125:97–104
79. Ghaemi N, Madaeni SS, Daraei P, Rajabi H, Zinadini S, Alizadeh A, Heydari R, Beygzadeh M, Ghouzivand S (2015) Polyethersulfone membrane enhanced with iron oxide nanoparticles for copper removal from water: application of new functionalized Fe_3O_4 nanoparticles. Chem Eng J 263:101–112
80. Litter MI, Slodowicz M (2017) An overview on heterogeneous Fenton and photoFenton reactions using zerovalent iron materials. J Adv Oxid Technol 20(1):1–19
81. Wang W, Cheng Y, Kong T, Cheng G (2015) Iron nanoparticles decoration onto three-dimensional graphene for rapid and efficient degradation of azo dye. J Hazard Mater 299:50–58

82. Xu W, Yang T, Liu S, Du L, Chen Q, Li X, Dong J, Zhang X, Lu S, Gong Y, Zhou L, Liu Y, Tan X, Tan X (2022) Insights into the synthesis, types and application of iron nanoparticles: the overlooked significance of environmental effects. Environ Int 158:106980
83. Jabbar KQ, Barzinjy AA, Hamad SM (2022) Iron oxide nanoparticles: preparation methods, functions, adsorption and coagulation/flocculation in wastewater treatment. Environ Nanotechnol Monitor Manage 17:100661
84. Fei J, Cui Y, Zhao J, Gao L, Yang Y, Li J (2011) Large-scale preparation of 3D self-assembled iron hydroxide and oxide hierarchical nanostructures and their applications for water treatment. J Mater Chem 21(32):11742–11746
85. Edla R, Tonezzer A, Orlandi M, Patel N, Fernandes R, Bazzanella N, Date K, Kothari DC, Miotello A (2017) 3D hierarchical nanostructures of iron oxides coatings prepared by pulsed laser deposition for photocatalytic water purification. Appl Catal B Environ 219:401–411
86. Date M, Haruta M (2001) Moisture effect on CO oxidation over Au/TiO_2 catalyst. J Catal 201(2):221–224
87. Li L, Fan M, Brown RC, Van Leeuwen J, Wang J, Wang W, Song Y, Zhang P (2006) Synthesis, properties, and environmental applications of nanoscale iron-based materials: a review. Crit Rev Environ Sci Technol 36(5):405–431
88. Li P, Miser DE, Rabiei S, Yadav RT, Hajaligol MR (2003) The removal of carbon monoxide by iron oxide nanoparticles. Appl Catal B 43(2):151–162
89. Sleutels TH, Ter Heijne A, Buisman CJ, Hamelers HV (2012) Bioelectrochemical systems: an outlook for practical applications. Chemsuschem 5(6):1012–1019
90. Turner AP (2013) Biosensors: sense and sensibility. Chem Soc Rev 42(8):3184–3196
91. Nöll T, Nöll G (2011) Strategies for "wiring" redox-active proteins to electrodes and applications in biosensors, biofuel cells, and nanotechnology. Chem Soc Rev 40(7):3564–3576
92. Rani GJ, Babu KJ, Rajan MJ (2016) *Watsonia meriana* flower like Fe_3O_4/reduced graphene oxide nanocomposite for the highly sensitive and selective electrochemical sensing of dopamine. J Alloy Compd 688:500–512
93. Zhang Y, Gao W, Zuo L, Zhang L, Huang Y, Lu H, Fan W, Liu T (2016) In Situ growth of Fe_2O_3 nanoparticles on highly porous graphene/polyimide-based carbon aerogel nanocomposites for effectively selective detection of dopamine. Adv Mater Interfaces 3(15):1600137
94. Liu H, Xiong R, Zhong P, Li G, Liu J, Wu J, Liu Y, He Q (2020) Nanohybrids of shuttle-like α-Fe_2O_3 nanoparticles and nitrogen-doped graphene for simultaneous voltammetric detection of dopamine and uric acid. New J Chem 44(47):20797–20805
95. Auffan M, Rose J, Bottero JY, Lowry GV, Jolivet JP, Wiesner MR (2009) Towards a definition of inorganic nanoparticles from an environmental, health and safety perspective. Nat Nanotechnol 4(10):634–641
96. Magro M, Baratella D, Bonaiuto E, de Roger AJ, Vianello F (2018) New perspectives on biomedical applications of iron oxide nanoparticles. Curr Med Chem 25(4):540–555
97. Campos EA, Pinto DVBS, Oliveira JISD, Mattos EDC, Dutra RDCL (2015) Synthesis, characterization and applications of iron oxide nanoparticles—a short review. J Aerosp Technol Manag 7:267–276

Chapter 11
Role of Magnetic Nanomaterials in Environmental Remediation

Melaku Masresha Woldeamanuel, Shibani Mohapatra, Soumyaranjan Senapati, Tapan Kumar Bastia, Alok Kumar Panda, and Prasanta Rath

Abstract "Nanomaterials," or substances having a diameter of less than 100 nm, have piqued the interest of scientists. The number of studies on magnetic nanomaterials has increased extraordinarily over the previous two decades. Recently, ecologists have developed a keen interest in the development of nanomaterials that are both economical to produce as well as benign to both the environment and the biosphere. There is a lot of interest in ferrite nanomaterials for use in environmental remediation due to the materials' unique magnetic properties, which can be tuned to a wide variety of functionalization. This chapter summarizes magnetic nanomaterials and their potential uses in environmental remediation. Environmental remediation benefits from the use of magnetic nanomaterials since they can remove pollutants and biological contaminants rapidly. New applications are being developed for magnetic nanomaterials with unusual optical, magnetic, thermal, and mechanical properties of magnetic nanomaterials. Magnetic nanoparticles can transform magnetic energy into thermal energy, opening the door to a wide range of analytical methods. The easy separation of magnetic nanoparticles by a magnet and their reusability makes them highly efficient. In addition, the difficulties of employing adsorbent materials, the time required, and the volume of the samples can be overcome by using them. In this chapter, the use of magnetic nanomaterials in various environmental remediation applications and their mechanism of action has been outlined.

Keywords Environmental remediation · Water remediation · Magnetic nanoparticles · Toxic metals · Dyes · Pesticides

Melaku Masresha Woldeamanuel and Shibani Mohapatra contributed equally as first author.

M. M. Woldeamanuel · S. Mohapatra · S. Senapati · T. K. Bastia · A. K. Panda · P. Rath (✉)
Environmental Science Laboratory, School of Applied Sciences, Kalinga Institute of Industrial Technology, Deemed to be University, Bhubaneswar 751024, India
e-mail: prathfch@kiit.ac.in

H. Sahoo and J. K. Sahoo (eds.), *Iron Oxide-Based Nanocomposites and Nanoenzymes*, Nanostructure Science and Technology, https://doi.org/10.1007/978-3-031-44599-6_11

11.1 Introduction

Nanoscience mainly deals with nanoparticles (NPs), which range from around 1–100 nm and can be made from a variety of materials. These NPs have very specific and unique properties as compared to their bulk forms and hence are used in a variety of applications ranging from the development of devices and sensors to applications in biotechnology and environmental remediation. To classify them, geometrical characteristics such as morphology and composition, uniformity, and agglomeration are taken into consideration. In addition, nanostructures can be spherical, flat, needle-like, or random in orientation, and they can be D, ^{1}D, ^{2}D, or ^{3}D. (e.g., nanotubes and nanowires) [1, 2]. Nanomaterials are mainly obtained in powder, colloidal, and suspension forms and come in a variety of morphologies [3]. Nanomaterials can be a combination of two or more materials and in such cases, they are known as composites. Composites are made up of polymers, metals, ceramics, alloys, etc. Polymers, metals, ceramics, and alloys are examples of single-material composites [4]. Their chemical and electrostatic properties can be achieved through a variety of methods, including gas-phase processes, mechanical processes, vapor deposition synthesis, and co-precipitation, as well as by dispersing them uniformly in a matrix [5]. To achieve proper uniformity, chemical synthesis methods are often preferred over others. Nanomaterials based on their composition can be divided into a number of categories, such as monometallic, bimetallic, trimetallic, metal oxide, magnetic hybrid, semiconductor, composite, etc. [6].

This chapter focuses on magnetic nanomaterials which are increasingly common in an extensive range of fields, including, environmental remediation and biotechnology [5, 7–15]. There are a plethora of applications for magnetic nanomaterials, each with its own set of advantages. Magnetic nanoparticles have a wide range of uses, each with a unique set of benefits. They are utilized in a wide range of products, such as supercapacitors, batteries (fuel and solar cells included), biosensors, antimicrobial materials, and sharp memory products [16]. In addition to this, bioactive proteins and magnetic nanomaterials have been utilized in recent developments in the fields of point-of-care diagnosis, environmental remediation, and food safety [17]. With regard to mechanical engineering, it has long been established that the use of magneto-ferric oxide as well as other types of magnetic materials in concrete results in increased durability as well as sustainability [18]. This chapter also highlights the basic utility of magnetic nanomaterials in biotechnology with respect to environmental remediation [19].

11.1.1 The Evolution of Nanomaterials: A Historical Overview

Nanoscale smoke particles were created by early humans as a result of their use of fire [20]. Nanomaterials, on the other hand, were discovered much later in the history of

science. In 1857, Michael Faraday published his findings on the synthesis of colloidal gold particles, which was one of the earliest scientific publications on the subject [3, 20]. Nanostructured catalysts, on the other hand, have been under investigation for more than seven decades. Precipitated silica nanoparticles and flaming silica nanoparticles were being developed and commercialized in the United States and Germany during the early 1940s as alternatives to ultrafine carbon black for use in rubber reinforcements in the United States and Germany, respectively [21]. In the 1960s and 1970s, researchers discovered metallic nano powders for magnetic recording tapes, which were later commercialized. Using the now widely used inert-gas evaporation process, Granqvist and Buhrman published the first paper on nanocrystals in 1976, which was considered groundbreaking [22]. According to recent research, Maya blue paint has been discovered to be a nanostructured hybrid material that can be used in a variety of applications. Although authentic samples from Jaina Island have not yet been identified, investigations into them have revealed that the material is composed of needle-shaped palygorskite (clay) crystals that combine to form superlattices with periods as short as 1.4 nm [23].

Nanophase engineering is now applying to a growing number of structural and functional materials, both inorganic and organic, allowing us to manipulate their mechanical, catalytic (electrical and magnetic), optical (optical-electronic), and electrical properties. Manufacturing nanophase or cluster-assembled materials is a common practice, and it involves first creating distinct, smaller clusters that are then fusing them together to form a bulk-like material or embedding them into a compact liquid or solid matrix material during the manufacturing process [2].

11.1.2 Nanoparticles with Magnetic Properties

Magnetic nanoparticles have the advantage of being non-electrical and requiring less sample than conventional techniques (filtration and centrifugation) [24, 25]. Most of the arsenic-tainted water is found in outlying areas where power is scarce. Magnetic nanoparticles are the best method for treating wastewater in these areas. A powder made of Fe_3O_4 nanoparticles and iminodiacetic acid has been used to remove ~ 84.9% of the Cd and ~ 72% of the Pb [26]. The use of this magnetic nanoparticle is beneficial because it simplifies the chelation and subsequent magnetic separation of heavy metals [27]. Magnetic nanoparticles find excellent application in biomedicine and biotechnology. Internal (in vivo) and external (ex vivo) administrations are the most common methods of delivery in these applications. Magnetic nanoparticles are used for therapeutic (drug delivery and hyperthermia) and diagnostic (nuclear magnetic resonance imaging) purposes. Diagnostic applications are the primary focus of in vitro research [28, 29].

Increasing numbers of scientific studies on nanomagnetic materials with drug-delivery functions have been conducted in recent years. These studies have been focused on developing, characterizing, and improving nanomagnetic materials with high-specificity surface functionalization. Modern technology is heavily reliant on

these materials because they are used in so many industrial products and processes across a wide range of different industries [30]. Different magnetic materials have a wide range of unique properties that can be used in a variety of applications. Magnetic nanoparticles can exist in a variety of structures in polymorphic materials, which are distinguished by their ability to change shape. In addition to other physical characteristics such as magnetic character and chemical properties such as the bonds between atoms or ions, particle size, and the degree of hydration also varies. As a rule, particles of super-paramagnetic iron oxide are classified according to their size, which is less than 10 nm. This is because mono-domain magnetic particles with a size less than 10 nm prevent saturation magnetization or complete pairing of the spins [31]. When compared to other magnetic materials based on oxides or pure metals, iron oxides as magnetic materials having superior biocompatibility find wide applications in biotechnology. The two iron oxides which are used in biomedical applications are magnetite (Fe_2O_3) and magnetite (Fe_3O_4) [32].

The magnetic nanoparticles used for biotechnological purposes must have high magnetic moments, chemical stability under physiological conditions, and low toxicity, low production costs. It is important to note that the size and shape of nanoparticles, as well as their degree of crystallinity and dispersibility, have a significant impact on their performance in therapeutic and diagnostic techniques, such as magnetic resonance imaging (MRI) and hyperthermia. These parameters have a strong relationship with them because of the manner in which they are prepared. Magnets coated with carbon powder are currently being evaluated for their potential application in a variety of fields. Carbon nanotubes can coat these nanoparticles, preserving their magnetic properties while also binding to a variety of other substances, such as metals, catalysts, polymers, and organic compounds. This coating acts as a wrapper around the nanoparticles [33].

11.1.3 Classification of Magnetic Nanomaterials—Based on Properties

Metal nanoparticles, metal oxide nanoparticles, and metal alloy nanoparticles are the three most common types of magnetite nanoparticles (NPs) currently in use in research and development. FeCo, FePt, and others are examples of metal alloy nanoparticles, whereas cobalt oxides ($CoFe_2O_4$) and ferrites ($MnO{\cdot}6ZnO{\cdot}4Fe_2O_4$) are examples of metal oxide nanoparticles. Metal oxide Fe_2O_3 and Fe_3O_4 nanoparticles are the most widely used magnetic nanoparticles [17]. These nanoparticles are easy to prepare and can have their particle size and shape precisely controlled. Incorporating metallic elements such as manganese (Mn) and zinc (Zn) into the structure of iron oxide nanoparticles allows them to be transformed into a variety of ferrite nanoparticles ($Mn_3Zn_7Fe_2O_4$, $MnO{\cdot}6ZnO{\cdot}4Fe_2O_4$, and so on). They are particularly well suited for magnetic resonance imaging due to their higher relaxation rate and stronger magnetism, which makes them ideal for MRI application [34]. Another

characteristic of magnetic NPs is that they exhibit interesting surface activity. Its specific surface area makes it well suited for transporting numerous DNA fragments, drugs, and chemically modified compounds. Modifications allow them to be used as an effective vector. Secondly, the biocompatibility of most modified magnetic NPs is excellent [35]. The metamagnetic domain structure is common to most magnetic materials. A single magnetic domain structure is formed when magnetic materials are reduced to the nanoscale, resulting in paramagnetic material [36].

This disordered and super-paramagnetic spin can be rapidly magnetized by an alternate magnetic field and can move in an alternating direction with the magnetic field if the magnetic material has a critical size. When the magnetic field is removed, the magnetization of the material is zero, indicating that the material does not exhibit magnetism when there is no external magnetic field present in the environment. When subjected to an external magnetic field, super-paramagnetic materials exhibit a magnetic susceptibility that is significantly greater than general paramagnetic materials. This indicates that they are more susceptible to magnetic fields. In addition, because magnetic nanoparticles (MNPs) can produce thermal effects when subjected to alternating magnetic fields, they can be used in tumor thermotherapy [37]. The groundwork and modification of numerous nanoparticles have taken a significant amount of time and effort on the part of researchers to overcome this resistance. Iron oxide nanoparticles have several advantages over conventional nanoparticles, including their biodegradability and low cytotoxicity, as well as the fact that they can be altered by a variety of substances and interact with many specific ligands or antibodies. They have been used with MRI and tumor thermotherapy [38].

11.1.4 General Applications of Magnetic Nanomaterials

In biotechnology and environmental remediation, magnetic nanomaterials (MNMs) offer a broad variety of uses [39, 40] and high amounts of organic–inorganic chemicals in environmental matrices might be removed in this way [17, 41–45]. Heavy metals, colors, oils, medications, insecticides, and nutritional components are among the substances found in these complexes [13, 17, 45]. Particles chemical composition, granulometric uniformity, crystal structure, magnetic behavior, surface structure, adsorption properties, solubility, and low self-toxicity must meet strict requirements for biotechnology applications in terms of their physical, chemical, and pharmacological characteristics as well as [11, 35] reported by Mohammed et al. electrostatic attraction, co-precipitation, and strong reductive reactivity are all possible reactions between magnetic nanoparticles and contaminating molecules [46]. Magnetic nanoparticles may also be used in water purification as non-absorbents or immobilization carriers to improve the efficacy of contaminant removal [15, 45]. As a result of their small size at the nanometer scale, relatively large surface area (10–500 m^2/g), super-paramagnetic, and biocompatibility with biomolecules, these applications offer significant environmental advantages, such as higher removal efficiency (usually greater than 85%), faster kinetics (such as first and second-order kinetics),

as well as stronger reactivity with numerous contaminants (both organic and inorganic) [47]. In the selective and highly effective adsorption of dangerous metal ions from complex matrices, such as Pb^{2+}, Cd^{2+}, Cu^{2+}, Zn^{2+}, Ni^{2+}, and As^{3+}, magnetic nanoparticles are an essential application [17, 48, 49]. Acid-resistant and very effective at neutral pH adsorption capacity, diethylenetriamine modified chitosan MNPs can remove rare-earth metal ions like Dy^{3+}, Nd^{3+}, and Er^{3+} [50]. MNPs may also successfully remove radioactive metal ions. Using MNPs of CeO_2–TiO_2–Fe_2O_3, radioactive uranium (U) may be removed from aqueous solution with an efficiency of around 96% [51]. The removal of colors from industrial wastewater, such as those from the dyeing, textile, tannery, and painting industries, is another key use for MNPs in remediation [52]. The use of bare MNPs, such as maghemite, magnetite, and ferrite NPs, as new adsorbents for dye separation has been described. Maghemite [53] and MIONs may remove both anionic and cationic dyes [54]. Dyes may be removed using surface coating MNPs and magnetic core–shell nanocomposites. If you are looking to extract Acid Black 1 from diverse aqueous environments, for example, a new magnetic adsorbent of Fe_3O_4/Al_2O_3 hybrid composite has been produced electrochemically using Fe_3O_4 [55]. Cationic methylene blue is electrostatically attracted to $ZnFe_2O_4$ NPs that have been modified with anionic sodium dodecyl sulfate surfactant (SDS). Adsorption capacity of 699.30 mg/g was achieved at pH = 12 [56].

Human health and the ecological system are gravely jeopardized due to the persistence and hydrophobicity of oil in soils and groundwater [57]. MNPs coated with a surface coating may remove more than 85% of oil from wastewater. Oil-field wastewater is treated using MNPs with three different layers of filtration: ferro ferric oxide as the core, nonporous silica as the interlayer, and mesoporous silica as the outside [58]. An external magnetic field has recently been employed to separate emulsified oil droplets quickly and obtain high oil removal efficiency (92.3%) using polyoxyallcylated *N*, *N*-dimethylethanolamine-Fe_3O_4-MNPs [59]. Surface-coated hydrophobic MNPs have a great attraction for oil and are capable of removing oils of any viscosity from the water surface regardless of their density [60]. Groundwater, vadose zones, and soils have been plagued by the presence of pharmaceuticals during the previous several decades [61, 62]. The synthesis of MNPs for the removal of pharmaceuticals from environmental matrices is only the subject of a small number of investigations. Nickel ferrite NPs have absorption capacities of 30.4 mg/g (at a pH of 6) and 25.0 mg/g (at a pH of 4) that make them promising dipyrone adsorbents [63]. Tetracycline may be adsorbed by Chitosan–Fe_3O_4 MNPs, and this adsorption exhibits pseudo-second-order kinetics [64]. Following Freundlich and Langmuir isotherms and pseudo-second-order kinetic models, it is possible to remove amoxicillin as adsorbents using magnetic Fe_3O_4@C NPs [65]. As a consequence, certain MNPs are devoted to the remediation of pesticides, which have a high persistence in the environment and hence require an extraordinarily long time for natural attenuation in soils, resulting in significant harm and dangers to human and ecosystem health [66, 67]. Polymer nanoparticles (NPs) with molecularly imprinted molecular patterns may be used to remove di-(2-ethylhexyl) phthalate from water using surface imprinting technology and the sol–gel technique, according to new research [68]. The removal effectiveness of isomeric endrin and dieldrin pesticides is 86.0 and

74.0% for graphene oxide/MION nanocomposites, demonstrating a unique stereoselective removal behavior [69]. The extraction efficiency of several pesticides, such as parathion, fenthion, phoxim, temephos, and paraquat, has been shown to be improved by MNPs treated with ionic liquids [70]. Adsorption and recovery of nutrients from industrial wastewater facilities, such as nitrate and phosphate, has recently been applied to MNPs. Al-doped MNPs, for example, have good phosphate removal effectiveness in chicken washing and urban wastewater [71]. Adsorbents made of ($MgFe_2O_4$)/biochar magnetic composites have the potential to recover phosphate from wastewater. They are very efficient and reusable [55]. Magnetic activated carbons have a 76.29% adsorption effectiveness for nitrate ions at pH = 4 and an equilibrium period of 20 min [72].

Magnetic nanoparticles are used to construct a variety of environmental remediation systems, which makes them even more intriguing [73]. It is now possible to better understand and control nanomagnetic phenomena, which can apply to a wide range of industrial applications ranging from engine seals to bank checks. Nanomagnetic phenomena are now better understood and controlled [74]. Several useful inventions, such as powerful permanent magnets and magnetic storage systems capable of storing large amounts of information, are the outcome of this technology. The surface effects at the nanoscale can be beneficial or detrimental depending on its application [5]. Recording industry has addressed this issue extensively because even the tiniest "bit" of information can be constrained, and it is also possible that these systems are limited by magnetic interactions [75, 76]. This chapter describes the most recent developments in nanomagnetic materials research and their uses in environmental remediation and biotechnology.

11.2 Magnetic Nanomaterials in Environmental Remediation

Toxins such as heavy metal ions, pesticides, and chemical toxins are a huge concern to the ecosystem since they are found in water, food, and the atmosphere. Magnetic nanoparticles can address these environmental concerns [24, 77, 78]. Because of nano biosensors, such as magnetic nano biosensors, environmental remediation has reached a new level. Pollution from metallurgical industries (such as heavy metal waste (Pb, Cd, Hg, etc.)) is caused by the poisonous nature of heavy metals. Another major contributor to environmental pollution is the widespread and excessive use of pesticides to increase agricultural yields. Pesticide residues are detected in water and food, which can have an impact on human health. To combat these problems, nanomaterial-based immuno- and genosensors are powerful instruments [79]. Quantum Dots (QD)-based magnetic nano biosensors have been used to monitor environmental pollutants such as pesticides, heavy metal ions, and chemical toxins. Quasi-dielectric (Qd)-based magnetic nano biosensors are extremely effective as metal sensors for toxic heavy metal ion detection in water, and they are required due

to the fact that heavy metal contamination is the primary source of water pollution [11, 80]. Hg^{2+} has been detected in water samples using ZnS QD magnetic nanomaterial-based sensors. According to a new investigation, Dithizone-functionalized CdSe/CdS NPs have been reported to be an ultra-sensitive technique for the detection of Pb^{2+}. Also, ZnS-QDs and Mn^{2+}-QD magnetic nano biosensors have been used to detect several pesticides like cyphenothrin, pentachlorophenol, acetamiprid, and pyrethroids [81–83].

Many studies have shown that carbon-based magnetic nanomaterial biosensors can be used to detect and monitor environmental pollutants such as heavy metal ions, explosives, pathogens, and pesticides due to the unique electrical and physical properties of these sensors [84, 85]. A waterborne virus that causes diarrhea has been detected using magnetic nano biosensors and rGO field-effect transistors. Pb^{2+} can be detected in water using DNA-wrapped metallic SWCNT electrochemical magnetic biosensors [83, 86]. The body's own sensors Plant and animal growth are inhibited by pesticides in agriculture, resulting in increased agricultural output. Toxic to humans and animals alike, organophosphates are the most hazardous pollutants for human health. Organophosphorus hydrolase, butyrylcholinesterase, tyrosine, and acetylcholinesterase are only a few of the enzymes used in carbon nanotube-based enzymatic magnetic biosensors to detect pesticides. Organophosphorus pesticide triazophos has been detected using biosensors based on multiwalled carbon nanotubes and chitosan [13, 87].

Liposomes containing potassium ferrocyanide-labeled molecules have been utilized by Viswanathan et al. for environmental remediation and biomedical diagnostics applications. It has been reported that the adsorption mechanisms of Fe_3O_4 are extremely effective at removing arsenic from water [88]. In another study, Li et al. used a dye-coded AgNP magnetic nano biosensor to detect environmental pollutants such as Cu^{2+} and Hg^{2+} ions [89]. Magnetic nanoparticles designed from polymer-based materials have excellent encapsulation properties, making them particularly well suited for environmental remediation applications. The detection of As^{3+} and As^{5+} ions in groundwater has been accomplished by using iron oxyhydroxide nanoparticles (NPs) on cellulose polymer matrix-based biosensors have developed a nano biosensor based on chitosan–Au that can detect Zn^{2+} and Cu^{2+} ions [90, 91].

Among other things, magnetic nanomaterials are used in a variety of applications such as catalysis and oil processing; sensors; medicine; food; energy storage; and construction materials. The production, transformation, and exportation of natural and synthetic nanomaterials on a daily basis have a negative impact on the environment, as has been demonstrated. Artificial nanomaterials are being released into the environment, water sources, soil, and landfill waste streams as a result of the widespread use of these materials. Drilling for natural gas and enhanced oil recovery have been made possible through the use of carbon-based nanostructures such as graphite and graphene, as well as other materials such as fullerene, carbon nanotubes, and diamonds, as well as carbon black and other carbon-based materials [13, 74]. Only a few magnetic nanomaterials can be easily degraded by the environment, which is why they have become commonplace in our daily lives despite their environmental sensitivity. Researchers are experimenting with iron nanoparticles as well

as nanocomposite synthesis techniques that incorporate plant and microorganism sources such as cellulose, biopolymers, hemoglobin, and glucose in order to improve environmental applications. Although magnetic nanomaterials are widely used in the environment, including the air, soil, and water, the possibility that they are toxic to aquatic life cannot be ruled out [92, 93]. Electrochemical, magnetic, and optoelectronic nanomaterials derived from molten salt synthesis can be found in a wide range of applications, including medicine and electronics [94].

The exposure to lead poisoning, which is a toxic heavy metal, is putting the public's health at risk in developing countries, especially. To detect lead ions in environmental media (such as soil, water, food, and other food-contact surfaces), a fluorescent magnetic nanomaterial has been developed [95, 96]. Electrochemical sensors based on carbonaceous magnetic nanomaterials (dihydroxy benzene isomers) have been reported [97] for the simultaneous electrochemical sensing of multiple-environmental contaminants. However, while rapid urbanization and industrialization have improved the well-being of many people, they are depleting the planet's natural resources and endangering the lives of all living things. When released into an aqueous system, magnetic nanomaterials, according to Hasanpour and Hatami have the potential to remove heavy metal ions and radionuclides from the environment [98]. According to the researchers, molecularly imprinted Polymers (MIPs) based on carbon-based magnetic nanomaterials are used to detect a wide range of environmental pollutants [99]. For example, 2D titanium carbide is a type of MXene magnetic nanomaterial that can degrade organic pollutants via photocatalysis [99]. Dye, heavy metals, and pathogen contamination pollute water, resulting in both human and animal health complications. Water sources, such as rivers, ponds, and lakes that have become polluted, can be cleaned using nanoscale adsorbents [100].

For the cleanup of oil spills and the protection of oceanic life from water pollution, which can disrupt the ecological framework of marine biodiversity, new materials are being developed. These new materials include magnetic nanocomposites and nanofluids, functionalized super-paramagnetic iron oxide nanoparticles and polymers, and magnetic nano adsorbents, all of which are being developed to clean up oil spills and protect oceanic life from water pollution. This has the potential to significantly improve oil recovery from oceanic spills as a result of the use of nanomaterials in this manner [101]. Carbon dots, carbon nanotubes, graphene, and carbon electrodes are being used to identify and analyze biological, environmental, and food samples [102]. Biologically active chemicals that disrupt the endocrine system pose a serious threat to the health of humans and animals. For the detection of estrogens in food and the environment, a variety of nanomaterial-based fabricated biosensors based on the detection of Hg^{2+} ions are used. Nano biosensors have shown potential in a variety of applications. Mercury is a toxic heavy metal that has a negative impact on the health [103]. Toxic gases in the air are harmful to both humans and animals, and the problem must be addressed immediately, regardless of how long it takes. The application of magnetic nanomaterials for organic pollutant removal from water is the most effective alternative for combating water pollution caused by industrial development, population growth, and climate change throughout the world using carbon-based magnetic nanomaterials or nanocomposites as a magnetic

field source [104]. It has been discovered that these materials can detect and remove lead (II) ions. Unusual sorbents based on carbon nanomaterials are widely used in the removal of contaminants from water and soil. Toxic metals chromium and arsenic are both present, and nanomaterials can be used to remove these toxins from the environment (wastewater) [105]. Carbonaceous nanomaterials have also been investigated for their ability to remove Cr and As ions from wastewater [106].

Environmental pollution has increased in recent years because of an increase in the number of industries that release hazardous waste into the environment. Therefore, new water treatment methods based on the use of adsorptive materials such as carbon and adsorbents are urgently needed to remove both inorganic and organic contaminants from water. According to Yu et al. magnetic nanomaterials such as MXene can remove both inorganic and organic contaminants from water [107]. Zeidman et al. removed antibiotics from the aqueous phase by using synthetic silica-based nanocomposite materials [108]. Using synthetic silica-based nanocomposite materials. Cheng et al. reported that the photocatalytic degradation of heavy metal and organic dye ions could be accomplished by using engineered magnetic nanomaterials [10]. According to Lunge et al. nanomaterials such as metal or carbon-based materials are emerging adsorbents used in water treatment processes [109]. It is possible that the antibiotic chloramphenicol will be harmful to human health if used in large quantities in the environment. The detection of chloramphenicol was accomplished through the use of an electrochemical aptamer sensor. Rare-earth elements are removed from waste through the use of efficient nanomaterials in the adsorption process.

The detection of chloramphenicol was achieved using an electrochemical aptamer sensor [7, 110]. The removal of rare-earth elements from wastewater is accomplished through the use of efficient nanomaterials in the adsorption process [7, 111]. Toxicity, manifested in the form of toxic chemicals originating from both natural and man-made sources, is a worldwide issue. There is a widespread problem with harmful substances, which may come from both natural and man-made sources. In research by Basheer, carbon nanoparticles were utilized as adsorbents in the treatment of wastewater [112] To give an example, several articles on nano adsorbents for water purification by removing heavy metal ions from wastewater have been published in recent years [45, 113, 114] and are available online.

11.2.1 Wastewater Treatment Using Magnetic Nanomaterials

However, researchers are working to find new ways to prevent agricultural waste from spreading into the environment and causing harm to human health because of the presence of pesticides and other non-biodegradable organic and inorganic contaminants. Even at extremely low concentrations, these water contaminants can cause respiratory, cardiovascular, and even irreversible organ damage, according to the Environmental Protection Agency.

Adsorbents that have at least one dimension below 100 nm, as well as tunable nanomorphology's and multifunctionalities, have emerged as highly promising candidates for the removal of toxic metal elements and organic contaminants found at extremely low concentrations in wastewater, according to recent research [12]. Water remediation processes benefit greatly from the high specific surface area and variety of surface functionalizations of these materials. Functionalized magnetic nanoparticles (MNPs) have been used as adsorbents to remove harmful metal ions from wastewater and agricultural waste [115].

Aqueous solutions containing magnetic materials can be recovered after the adsorption process is complete and the adsorbent has been removed. With their large surface area, they can develop electrostatic interactions and cation-interactions, as well as hydrophobic interactions and metal ion complexation. To degrade organic pollutants in agricultural wastewater, a combination of adsorption and catalytic performance can be used [116].

11.2.2 Magnetic Nanoparticle for Removal of Toxic Metal Ions

By using Magnetic Nanoparticle to Remove Toxic Metal Ions, many scientists are working to find a solution to the wastewater problem, which is a major health concern that impacts all living things. Even at low concentrations, various toxic metals like Pb^{2+}, Ni^{2+}, Zn^{2+}, Cr^{3+}, Cu^{2+}, and Cd^{2+} wreak havoc on the environment and human health and well-being. In order to develop new technologies that efficiently remove toxic metals from agricultural wastewater, numerous studies have been carried out [24, 90, 117–119]. Coagulation/flocculation and electrochemical treatment are just some of the cutting-edge methods currently being investigated in this field. The adsorption technique appears to be the most convenient because of its simplicity, high availability, and low cost [120].

One of the most important issues in this case is the regeneration and separation of adsorbent from wastewater. Magnetic nanomaterials have been proven to be a highly effective and dependable solution for the removal of hazardous metal ions from wastewater [115]. A magnetic field can be used to remove the adsorbent from water because of its magnetic properties. A variety of factors must be taken into consideration when determining the most effective method for removing metal ions from water, including the amount of metal ions present, operating costs, and even how the water is produced [120]. A metal ion adsorbent material must have the following features and needs in order to be regarded effective: low pH adsorption, metal ion desorption ease, quick desorption/adsorption rate, high adsorption capacity, regeneration, and reuse, as well as excellent mechanical properties [121]. Chemical waste, industrial wastewater, and agricultural waste may all be treated using a variety of adsorbers to remove metal ions that are detrimental to the environment. Some examples of these adsorbers include: Cu(II), Ni(II), Zn(II), Cd(II), and Hg(II).

Because of its high toxicity, lack of biodegradability, and high abundance in sewage, lead (Pb) is unquestionably one of the most hazardous heavy metals for the environment and living organisms. Pb is widely used in a variety of applications, including electroplating, microelectronics, battery manufacturing, metal coloring, and others. Because of a combination of factors, including its widespread use, high demand, and toxic properties, it is considered being one of the most dangerous heavy metals for biological systems. There has been a great deal of research into how to remove lead (II) from water [122].

Fatemeh et al. reported the removal of Pb(II) from aqueous solutions using amine magnetic Fe_3O_4 nanoparticles (MBA-Fe_3O_4) in aqueous solutions. After they were synthesized using a solvent-based method, the surface of the magnetic nanoparticles was grafted with melamine to improve their magnetic properties. Under ideal conditions, the endothermal and spontaneous metal ion adsorption processes were able to remove 85.6% of the lead from the solution (II). Five cycles of adsorption and desorption revealed that only 7% of the adsorption capacity of these adsorbents has been lost during the experiment [123]. Maghemite nanotubes synthesized by microwave irradiation. Maghemite nanotubes have been used for metal ion removal from groundwater [124]. The nanotubes had maximum adsorption capacities of 111.11, 84.95, and 71.42 mg/g of maghemite.

Pannenrselvan et al. showed Ni(II) ions can be removed from aqueous solutions using a magnetic-based adsorbent, which they called the Ni(II) adsorbent [125]. In another study, tea waste has been coated with Fe_3O_4 nanoparticles [109]. The dependence of the adsorbent on pH, initial Ni(II) concentration, and temperature has also been investigated in the same study. The tea waste coated Fe_3O_4 magnetic nanoparticles exhibit dated an adsorption capacity of 38.3 mg/g, indicating a significant improvement in Ni^{2+} removal from agricultural biomass waste [126].

Using the co-precipitation method developed by Gautam et al., synthesized Fe_3O_4 super-paramagnetic nanoparticle having a size range of 5–15 nm and with a high magnetic field. These nanoparticles are highly effective Ni(II) adsorbents, having adsorbing capacity in the range of 209–362 mg/g. In addition, these NPs are inexpensive, and are easy to separate and have an adsorption capacity of nearly 85% during the first four cycles [127]. The presence of Cr (VI) ions, which are extremely toxic to humans and aquatic life, has been linked to a variety of health issues. Using Ppy-mPD composite nanomaterials, which are composed of modified polypyrrole and m-phenylenediamine, the scientists could remove Cr from the sample (VI). In the field, they were created through the process of oxidative polymerization [128]. The Ppy-mPD/Fe_3O_4 magnetic nanocomposites had an adsorption capacity of 555.6 mg/g when compared to other materials. Dai et al. developed a magnetic adsorbent for the removal of Cr(III) from wastewater that is both cost-effective and environmentally friendly. They used AL-DA/Fe_3O_4 NPs as the magnetic adsorbent [129]. In this study, the functionalization of alkaline lignin with dopamine molecules has been achieved using a nanoprecipitation procedure. It is possible to regenerate and reuse these materials five times with their magnetic properties. The adsorption capacity of these materials after five desorption cycles is found to be 44.56 mg/g.

In addition to chromium, cadmium is also a very toxic metal as a variety of industrial products, such as cadmium batteries, pigments, and solar panels, are all made from the element. Water containing more than 0.003 mg/L of Cd(II) has been set by the World Health Organization and the Environmental Protection Agency as safe for consumption. Cd(II) exposure has been linked to kidney damage, high blood pressure, and extensive organ damage, among other things [130]. The ability of magnetite nanoparticles coated with citric acid to remove Cd(II) from aqueous media has been investigated using citric acid-coated magnetite nanoparticles. In this study, it is seen that at 298 °C, the adsorption capacity of the material is 0.2 g/L of an adsorbent, with a removal efficacy of ~ 96% at 40 min [121]. Bio-magnetic membrane capsules created by cross-linking a polyvinyl alcohol and sodium alginate matrix with phytogenic magnetic nanoparticles (BMMCs) have been used as substrates for the removal of toxins such as Pb(II) and Cd(II) from water with a binding capacity of 548 and 611 mg/g, respectively. Each of the adsorbents was regenerated with HNO_3 and used seven times, in order to maintain their initial adsorption capacity [131].

11.2.3 Pesticides and Antibiotic Removal by Magnetic Nanoparticles

Organic compounds are being used in agricultural practices, which have resulted in serious environmental concerns. Because of the non-biodegradability and toxicity of agricultural chemicals such as pesticides and antibiotics, they accumulate in the environment, including water and soil causing contamination. Using functional magnetic nanomaterials as adsorbents to remove harmful organic contaminants from agricultural wastewater has been investigated by several research groups. Electrostatic interactions, stacking, donor–acceptor, hydrophobic, and other types of interactions are commonly used to explain adsorption of dyes on the NPs. In order to remove pesticides from agricultural wastewater, various magnetic nano adsorbents have been developed [132]. There are numerous applications for these substances, including pest control, disease prevention, and increased crop quality and yield. Additional information about pesticide removal from agricultural wastewater using MNP mediation is provided in a brief description [133]

A monolithic Fe_2O_3/TiO_2 nano photocatalyst developed by Singh et al. has been used for the degradation of Fibronil [109, 134]. The degradation efficiency of Fibronil reached a maximum of 88.71% under optimized experimental conditions. Fortunately, the Fe_3O_4 monolith could be reused for a further four runs before it lost its photo catalytic efficient [135]. It has recently been reported that the surface of magnetic (Fe_3O_4) chitosan decorated with Co–Ni nanoparticles exhibited excellent water remediation activity as well as showed high adsorption capacity for the pesticide 2,4-DCPOA (2,4-D) [136]. The authors achieved optimal experimental conditions for pesticide degradation by modulating the concentration of oxidant (H_2O_2),

catalyst, and pH. Two metals (Co and Ni) synergistically worked together to achieve ~ 95.50% decomposition of 2,4-D in a bimetallic Co–Ni@CS@Fe_3O_4 magnetic nanoparticle.

In another study, eight triazole fungicides have been extracted from environmental water samples using carbon nanospheres coated with Fe_3O_4. All of the extracts had high extraction percentages of nearly 80% or above [137].

Zr-based magnetic metal organic frameworks (MMOFs) have been created by immobilizing the UiO-66 MOF on Fe_3O_4/SiO_2 NP cores and then annealing the resulting structure. This magnetic nanomaterial synthesized adsorbed TCS and TCC, two fungicides that are commonly found in wastewater, groundwater, and drinking water. Hydrogen bonding and hydrophobic interactions between the fungicides and MMOFs played an important role during the adsorption process [115]. In this study, the adsorption capacity of the nanomaterial for TCS and TCC are 476.27 mg/g and 602.40 mg/g, respectively. Antibiotics are substances that stop bacteria from multiplying and spreading in animals and humans. Environments are contaminated because of the widespread use of antibiotics in agriculture. Adsorbents containing magnetically functionalized materials have been used to remove antibiotics from wastewater, including tetracycline, sulfonamide, quinolones, and sulfamethoxazole [138]. Various materials can be used to create magnetic devices, including microspheres, magnetic molecularly imprinted polymers, magnetic nanoparticles, and magnetic carbon-based materials, magnetic molecularly imprinted ferrites (MOF), and covalent organic frameworks. Microspheres are the most common type of magnetic device, and they can be made from any type of material 1 [139]. To detect sulfadimidine, sulfadimidine, sulfathiazole, and sulfathiazole from water, Fe_3O_4@SiO_2@Fe–pamoate ternary single-core double-shell magnetic microspheres have been used. The detection limits of 0.08–0.12 mg/mL have been achieved with the aid of this magnetic microsphere. The water samples contained high concentrations of all antibiotics, ranging from 86.3 to 99.7% [140].

Imprinted molecular polymers with molecular recognition, thermo responsiveness, and super paramagnetism have been discovered in magnesia, silica, and polymer by Xu et al. The antibiotic sulfamethazine has been used as a model for the development of these materials. The batch experiments showed that temperature and contact time played a vital role in the adsorption of the magnetic material on the magnetic nanomaterial. The release of the antibiotic from the magnetic material increases with the increase in the temperature beyond the LCSTS [141]. In another study, magnetic nanocomposites with surface-oxidized cobalt wrapped in carbon nanotubes have been used to remove organic waste and dye rhodium B from water [142]. Yang and coworkers have recently developed Fe_3O_4-N-doped carbon sphere activated with peroxymonosulfate that removed and catalytically degraded tetracycline from the solution [143]. This magnetic material removed ~ 97% of tetracycline as compared to peroxymonosulfate only. Lead (Pb) is one of the most toxic heavy metals for the environment and living organisms because of its high toxicity, lack of biodegradability, and abundance in waste. It is used in a variety of applications, including electroplating, microelectronics, battery manufacturing, metal coloring, and many

others. Besides its toxic properties, it is considered being among the most toxic heavy metals. The removal of Pb(II) from aqueous media has thus been a subject of active research [122].

For the removal of Pb(II) from drinking water, Fatemeh et al. developed a nanoparticle made of melamine and Fe_3O_4 amines (MBA-Fe_3O_4) which was used in the study by solvo thermal method, and the amine-grafting procedure [144]. The magnetic nanomaterial synthesized removed ~ 85% of lead ion. The efficiency of the nanomaterial decreased by 7% after five consecutive adsorption–desorption cycles. Microwave synthesized maghemite nanotubes removed copper, zinc, and lead from water by the processes of electrolysis. The nanomaterial exhibited a maximum adsorption efficiency for of 111.11, 84.95, and 71.42 mg/g for all the three metals. When the concentration of Ni(II) ions in drinking water rises above 0.01 mg/L, which occurs because of various industrial waste products released from processes used in battery manufacturing and electronics manufacturing, it can pose serious health problems [124, 145]. Pannenrselvan and coworkers have shown that magnetic adsorbents can remove Ni(II) ion from water. They achieved an adsorption capacity of 38.3 mg/g [126]. In another study at pH 6.5, using magnetic nanomaterial a maximum adsorption of 548 and 611 mg/g for lead and chromium ions, respectively have been reported. In the same study when the adsorbents are treated with HNO_3 and then used repeatedly for seven cycles, their capacity returned to the level it had been before treatment [146]. Agricultural practices rely heavily on organic compounds which lead to serious environmental concerns in recent decades. Because of their toxicity and non-biodegradability, they are classified as non-selective toxins. Pesticides and antibiotics are just a couple of examples of the agricultural chemicals available today [147].

To remove the harmful organic contaminants, more than a dozen research groups are investigating the use of functional magnetic nanomaterials as adsorbents in agricultural wastewater. The development of electrostatic interactions is primarily responsible for the adsorption in the majority of cases. Some examples of such phenomena include stacking, donor–acceptor interactions, hydrophobic interactions, and other phenomena with a similar nature. Pesticides and herbicides are widely used in agriculture for a variety of purposes, including the control and repulsion of pests, the prevention of plant diseases, and the improvement of crop quality and yield, among others [148]. Singh and coworkers developed a ferromagnetic Fe_2O_3/TiO_2 monolithic photocatalyst for fibronil photodegradation [134]. Other than in agriculture, this pesticide is widely used in the veterinary and domestic fields, as well as in the food industry. The photocatalytic performance of the above-mentioned catalyst in the degradation of fibronil has been evaluated using UV–Vis spectrophotometry. Under optimal experimental conditions, the maximum fipronil degradation efficiency of 88.71% has been, which is the highest ever recorded [149]. Researchers recently discovered that the synthesis of magnetic (Fe_3O_4) chitosan, which is then coated with Co–Ni nanoparticles, resulted in an effective nano catalyst, having the ability to degrade the pesticide 2,4-DCPOA, among other contaminants. The degradation efficacy of the nano catalyst at optimized condition is ~ 95.50% and this magnetic nano catalyst can be recovered and reused.

The self-assembly of carbon nanosphere surfaces with Fe_3O_4 nanoparticles resulted in an innovative magnetic adsorbent. This magnetic nanomaterial has the ability to adsorb triazole fungicides from the wastewater with the adsorption efficiency of more than 80%. These nanomaterials can be recycled and reused for several adsorption–desorption cycles [129]. In another study, with the aid of solvothermal method, a zirconium based magnetic metal organic framework having a core-shell Fe_3O_4/SiO_2 nanoparticle has been designed which has the ability to adsorb triclosan and triclocarban fungicides [150]. These fungicides are mainly found in wastewater as well as drinking water. The adsorption interaction between the nanomaterial and the fungicides is mainly dominated by hydrogen bonding and hydrophobic interactions. In the same study, they have shown that the adsorption–desorption cycles can be repeated for eleven cycles. These nanomaterials have very high adsorption capacities of 476.27 mg/g and 602.40 mg/g, for triclosan and triclocarban, respectively [151] (Fig. 11.1).

An antibiotic is a compound that is used to prevent the growth and spread of bacteria in both animals and humans. The widespread use of antibiotics in agriculture has resulted in significant environmental contamination [138]. In another study, a ternary core-shell magnetic nanoparticle composed of $Fe_3O_4@SiO_2@Fe$–pamoate removed five sulfonamide antibiotic compounds both from drinking and river water [153] (Fig. 11.2).

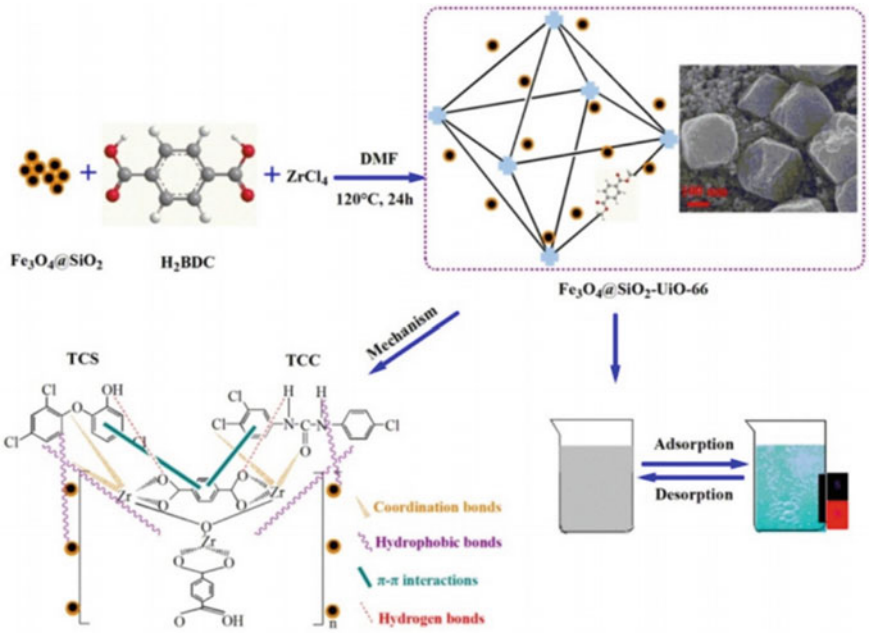

Fig. 11.1 The use of MMOFs for the efficient adsorption removal of two fungicides from aqueous environments has been demonstrated (adapted from permission from Elsevier [152])

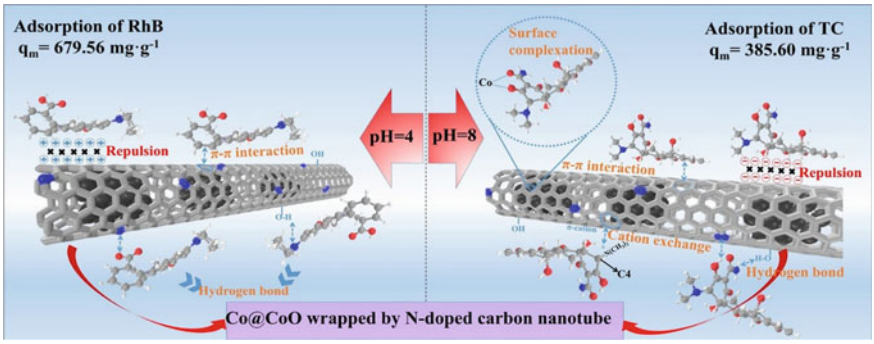

Fig. 11.2 **a** Schematic diagram of adsorption of RhB (on the left) and TC (on the right) on Co@CoO/NC (Adapted with permission from Elsevier [154])

A chitosan-iron complex composite activated with peroxymonosulfate is able to remove and degrade tetracycline from wastewater [155]. Similarly, a Fe_3O_4-N-doped carbon sphere composite is able to extract ~ 97% of chromium from wastewater [156]. The catalyst is composed of a carbon sphere composite made of a chitosan–iron complex that is biodegradable and environmentally friendly. By activating peroxymonosulfate, which we accidentally discovered, we were able to remove and catalytically degrade the tetracycline and other antibiotics (TC). The magnetic Fe_3O_4-N-doped carbon sphere composite catalyst removed 97% of the total chromium in a 25 °C environment, whereas PMS alone removed only 50%.

With this catalyst's outstanding adsorption and catalytic efficiency, tetracycline may be safely and efficiently extracted from water. Decomposition rates of functionalized magnetic carbon porous frameworks rose from 0.133 to 96% when they were brought into the system 10 min after H_2O_2 was injected, but only 13% degradation rates were detected when H_2O_2 was not present. The authors argue that in order for catalytic degradation to occur, TC molecules must collect in holes of porous materials with a high specific surface area. A constrained microenvironment is created as a consequence of this, according to the authors. ·OH and other reactive radical species generated by Fe^{2+} and Au(0) catalytic centers contribute in the breakdown of target substances as well as hydrogen peroxide activation by Fe(II) and Au(0) [157]. The rate of decomposition increased from 0.133 to 96% when functionalized magnetic carbon porous frameworks were introduced into the system 10 min after H_2O_2 was introduced, whereas only a 13% degradation rate could be observed after 30 min of operation when H_2O_2 was not present. The authors argue that in order for catalytic degradation to occur, TC molecules must collect in holes of porous materials with a high specific surface area. According to the authors, this creates a microenvironment that is more constrained. ·OH and other reactive radical species generated by Fe(II) and Au(0) catalytic centers contribute in the breakdown of target substances as well as hydrogen peroxide activation by Fe(II) and Au(0) [158].

11.3 Summary and Future Prospectives

The inherent properties of magnetic nanoparticles have a lot of benefit in enhancing and remediating the environment. In this chapter, most work is focused on remediation of various types of water such as wastewater, groundwater, industrial water, etc. in removing various types of pollutants, such as toxic metal ions, dyes, pesticides, etc. Almost all the water remediation works are based on the adsorption of the contaminant on the nanoparticle or the magnetic nanomaterials. In addition, some of the research works are focused on synthesizing various magnetic nanocomposites which have better removal capacity than the simple magnetic nanoparticle. Although a lot of work has been done on the laboratory scale in water and environmental remediation but in the field that conditions may be different. Therefore, the translation of the laboratory work into the real applications is the need of the hour. But before field applications, a lot of research gaps are still there in understanding the mechanism of the action of the magnetic materials in environmental remediation and the potential reusability and toxicity of the synthesized magnetic nanomaterials toward the various organisms existing in the environment.

References

1. Khan I, Saeed K, Khan I (2019) Nanoparticles: properties, applications and toxicities. Arab J Chem 12(7):908–931
2. (2006) Chapter 1 Nanotechnology and nanomaterials. In: Studies in interface science. Elsevier, pp 1–69. https://doi.org/10.1016/S1383-7303(06)80002-5
3. Jeevanandam J et al (2018) Review on nanoparticles and nanostructured materials: history, sources, toxicity and regulations. Beilstein J Nanotechnol 9:1050–1074
4. Sen M (2020) Nanocomposite materials. In: Sen M (ed) Nanotechnology and the environment. IntechOpen
5. Baig N, Kammakakam I, Falath W (2021) Nanomaterials: a review of synthesis methods, properties, recent progress, and challenges. Mater Adv 2(6):1821–1871
6. Basavegowda N, Baek K-H (2021) Multimetallic nanoparticles as alternative antimicrobial agents: challenges and perspectives. Molecules 26(4):912
7. Alsaiari NS et al (2021) The application of nanomaterials for the electrochemical detection of antibiotics: a review. Micromachines 12(3):308
8. Baby R et al (2022) Nanomaterials for the treatment of heavy metal contaminated water. Polymers 14(3):583
9. Carneiro P, Morais S, Pereira MC (2019) Nanomaterials towards biosensing of Alzheimer's disease biomarkers. Nanomaterials 9(12):1663
10. Cheng Z et al (2021) Nanomaterials for cancer therapy: current progress and perspectives. J Hematol Oncol 14(1):85
11. Hashem A et al (2021) Nanomaterials based electrochemical nucleic acid biosensors for environmental monitoring: a review. Appl Surf Sci Adv 4:100064
12. Lu F, Astruc D (2018) Nanomaterials for removal of toxic elements from water. Coord Chem Rev 356:147–164
13. Malakar A et al (2021) Nanomaterials in the environment, human exposure pathway, and health effects: a review. Sci Total Environ 759:143470
14. Maleki Dizaj S et al (2021) Nanomaterials for chronic kidney disease detection. Appl Sci 11(20):9656

15. Yang J et al (2019) Nanomaterials for the removal of heavy metals from wastewater. Nanomaterials 9(3):424
16. Abdel Maksoud MIA et al (2021) Advanced materials and technologies for supercapacitors used in energy conversion and storage: a review. Environ Chem Lett **19**(1):375–439
17. Ali A et al (2021) Review on recent progress in magnetic nanoparticles: synthesis, characterization, and diverse applications. Front Chem 9:629054
18. Soto-Bernal JJ et al (2015) Effects of static magnetic fields on the physical, mechanical, and microstructural properties of cement pastes. Adv Mater Sci Eng 2015:1–9
19. Chen X, Charrier M, Srubar WV (2021) Nanoscale construction biotechnology for cementitious materials: a prospectus. Front Mater 7. https://doi.org/10.3389/fmats.2020.594989
20. Bayda S et al (2019) The history of nanoscience and nanotechnology: from chemical-physical applications to nanomedicine. Molecules 25(1):112
21. Barhoum A et al (2022) Review on natural, incidental, bioinspired, and engineered nanomaterials: history, definitions, classifications, synthesis, properties, market, toxicities, risks, and regulations. Nanomaterials 12(2):177
22. Granqvist C, Buhrman R (1976) Ultrafine metal particles. J Appl Phys 47(5):2200–2219
23. European Commission. Directorate General for, Reasearch and Innovation (2012) Nanotechnologies: principles, applications, implications and hands on activities (a compendium for educators). Publications Office, LU
24. Liosis C et al (2021) Heavy metal adsorption using magnetic nanoparticles for water purification: a critical review. Materials 14(24):7500
25. Nisticò R et al (2018) Sustainable magnet-responsive nanomaterials for the removal of arsenic from contaminated water. J Hazard Mater 342:260–269
26. Morales-Amaya CG et al (2021) Ferrous magnetic nanoparticles for arsenic removal from groundwater. Water 13(18):2511
27. Fan L et al (2016) Chelating capture and magnetic removal of non-magnetic heavy metal substances from soil. Sci Rep 6(1):21027
28. Anik MI et al (2021) Recent progress of magnetic nanoparticles in biomedical applications: a review. Nano Select 2(6):1146–1186
29. Baghban R et al (2021) Were magnetic materials useful in cancer therapy? Biomed Pharmacother 144:112321
30. Materón EM et al (2021) Magnetic nanoparticles in biomedical applications: a review. Appl Surf Sci Adv 6:100163
31. Ali A et al (2016) Synthesis, characterization, applications, and challenges of iron oxide nanoparticles. Nanotechnol Sci Appl 9:49–67
32. Sangaiya P, Jayaprakash R (2018) A review on iron oxide nanoparticles and their biomedical applications. J Supercond Novel Magn 31(11):3397–3413
33. Mourdikoudis S, Pallares RM, Thanh NTK (2018) Characterization techniques for nanoparticles: comparison and complementarity upon studying nanoparticle properties. Nanoscale 10(27):12871–12934
34. Slavu LM, Rinaldi R, Di Corato R (2021) Application in nanomedicine of manganese-zinc ferrite nanoparticles. Appl Sci 11(23):11183
35. Akbarzadeh A, Samiei M, Davaran S (2012) Magnetic nanoparticles: preparation, physical properties, and applications in biomedicine. Nanoscale Res Lett 7(1):144
36. Nisticò R, Cesano F, Garello F (2020) Magnetic materials and systems: domain structure visualization and other characterization techniques for the application in the materials science and biomedicine. Inorganics 8(1):6
37. Kafrouni L, Savadogo O (2016) Recent progress on magnetic nanoparticles for magnetic hyperthermia. Prog Biomater 5(3–4):147–160
38. Tran H-V et al (2022) Multifunctional iron oxide magnetic nanoparticles for biomedical applications: a review. Materials 15(2):503
39. Hussain CM (2016) Chapter 19. Magnetic nanomaterials for environmental analysis. In: Hussain CM, Kharisov B (eds) Detection science. Royal Society of Chemistry, Cambridge, pp 1–13

40. Tartaj P et al (2005) Advances in magnetic nanoparticles for biotechnology applications. J Magn Magn Mater 290–291:28–34
41. Guo T et al (2018) The recent advances of magnetic nanoparticles in medicine. J Nanomater 2018:1–8
42. Mohseni M et al (2012) The role of nanotechnology in automotive industries. In: Carmo J (ed) New advances in vehicular technology and automotive engineering. InTech
43. Mutanda T et al (2020) Biotechnological applications of microalgal oleaginous compounds: current trends on microalgal bioprocessing of products. Front Energy Res 8:598803
44. Tahir MB et al (2022) Role of nanotechnology in photocatalysis. Encyclopedia of smart materials. Elsevier, pp 578–589
45. Wadhawan S et al (2020) Role of nanomaterials as adsorbents in heavy metal ion removal from waste water: a review. J Water Process Eng 33:101038
46. Mohammed L et al (2017) Magnetic nanoparticles for environmental and biomedical applications: a review. Particuology 30:1–14
47. Tang SCN, Lo IMC (2013) Magnetic nanoparticles: essential factors for sustainable environmental applications. Water Res 47(8):2613–2632
48. Ge F et al (2012) Effective removal of heavy metal ions Cd^{2+}, Zn^{2+}, Pb^{2+}, Cu^{2+} from aqueous solution by polymer-modified magnetic nanoparticles. J Hazard Mater 211–212:366–372
49. Hasanzadeh R et al (2017) Effective removal of toxic metal ions from aqueous solutions: 2-Bifunctional magnetic nanocomposite base on novel reactive PGMA-MAn copolymer@Fe_3O_4 nanoparticles. J Colloid Interface Sci 490:727–746
50. Liu E et al (2017) Preparation of diethylenetriamine-modified magnetic chitosan nanoparticles for adsorption of rare-earth metal ions. New J Chem 41(15):7739–7750
51. El-sherif RM, Lasheen TA, Jebril EA (2017) Fabrication and characterization of CeO_2–TiO_2–Fe_2O_3 magnetic nanoparticles for rapid removal of uranium ions from industrial waste solutions. J Mol Liq 241:260–269
52. Bayramoglu G, Altintas B, Arica MY (2009) Adsorption kinetics and thermodynamic parameters of cationic dyes from aqueous solutions by using a new strong cation-exchange resin. Chem Eng J 152(2–3):339–346
53. Afkhami A, Moosavi R (2010) Adsorptive removal of Congo red, a carcinogenic textile dye, from aqueous solutions by maghemite nanoparticles. J Hazard Mater 174(1–3):398–403
54. Qadri S, Ganoe A, Haik Y (2009) Removal and recovery of acridine orange from solutions by use of magnetic nanoparticles. J Hazard Mater 169(1–3):318–323
55. Jung K-W et al (2017) Synthesis of a novel magnetic Fe_3O_4/γ-Al_2O_3 hybrid composite using electrode-alternation technique for the removal of an azo dye. Appl Surf Sci 423:383–393
56. Zhang R et al (2019) Highly effective removal of pharmaceutical compounds from aqueous solution by magnetic Zr-based MOFs composites. Ind Eng Chem Res 58(9):3876–3884
57. Alegbeleye OO, Opeolu BO, Jackson VA (2017) Polycyclic aromatic hydrocarbons: a critical review of environmental occurrence and bioremediation. Environ Manage 60(4):758–783
58. Liu Z et al (2012) Oil-field wastewater purification by magnetic separation technique using a novel magnetic nanoparticle. Cryogenics 52(12):699–703
59. Duan M et al (2017) Core-shell composite nanoparticles with magnetic and temperature dual stimuli-responsive properties for removing emulsified oil. Adv Powder Technol 28(5):1291–1297
60. Dutra GVS et al (2017) Obtaining superhydrophopic magnetic nanoparticles applicable in the removal of oils on aqueous surface. Mater Chem Phys 200:204–216
61. Gomes AR et al (2017) Review of the ecotoxicological effects of emerging contaminants to soil biota. J Environ Sci Health Part A 52(10):992–1007
62. Ma L et al (2018) Impacts of irrigation water sources and geochemical conditions on vertical distribution of pharmaceutical and personal care products (PPCPs) in the vadose zone soils. Sci Total Environ 626:1148–1156
63. Springer V, Pecini E, Avena M (2016) Magnetic nickel ferrite nanoparticles for removal of dipyrone from aqueous solutions. J Environ Chem Eng 4(4):3882–3890

64. Raeiatbin P, Açıkel YS (2017) Removal of tetracycline by magnetic chitosan nanoparticles from medical wastewaters. Desalin Water Treat 73:380–388
65. Kakavandi B et al (2014) Magnetic Fe_3O_4@C nanoparticles as adsorbents for removal of amoxicillin from aqueous solution. Water Sci Technol 69(1):147–155
66. Hirsch-Ernst K et al (2009) Current issues in pesticide exposure and health risk—risk assessment of multiple residues and endocrine disrupting pesticides. Toxicol Lett 189:S30
67. Odukkathil G, Vasudevan N (2013) Toxicity and bioremediation of pesticides in agricultural soil. Rev Environ Sci Bio/Technol 12(4):421–444
68. Li C et al (2017) Preparation of magnetic molecularly imprinted polymer nanoparticles by surface imprinting by a sol-gel process for the selective and rapid removal of di-(2-ethylhexyl) phthalate from aqueous solution. J Sep Sci 40(7):1621–1628
69. Shrivas K et al (2017) Removal of endrin and dieldrin isomeric pesticides through stereoselective adsorption behavior on the graphene oxide-magnetic nanoparticles. Environ Sci Pollut Res 24(32):24980–24988
70. Latifeh F, Yamini Y, Seidi S (2016) Ionic liquid-modified silica-coated magnetic nanoparticles: promising adsorbents for ultra-fast extraction of paraquat from aqueous solution. Environ Sci Pollut Res 23(5):4411–4421
71. Xu J, Luu L, Tang Y (2017) Phosphate removal using aluminum-doped magnetic nanoparticles. Desalin Water Treat 58:238–249
72. Arbabi M et al (2017) Nitrate removal from aqueous solution by almond shells activated with magnetic nanoparticles. Desalin Water Treat 80:344–351
73. Patra JK et al (2018) Nano based drug delivery systems: recent developments and future prospects. J Nanobiotechnol 16(1):71
74. Samrot AV et al (2021) A review on synthesis, characterization and potential biological applications of superparamagnetic iron oxide nanoparticles. Curr Res Green Sustain Chem 4:100042
75. Peddis D et al (2014) Magnetic interactions. Frontiers of nanoscience. Elsevier, pp 129–188
76. Wallyn AV (2019) Synthesis, principles, and properties of magnetite nanoparticles for in vivo imaging applications—a review. Pharmaceutics 11(11):601
77. Briffa J, Sinagra E, Blundell R (2020) Heavy metal pollution in the environment and their toxicological effects on humans. Heliyon 6(9):e04691
78. Mitra S et al (2022) Impact of heavy metals on the environment and human health: Novel therapeutic insights to counter the toxicity. J King Saud Univ Sci 34(3):101865
79. Salek Maghsoudi A et al (2021) Recent advances in nanotechnology-based biosensors development for detection of arsenic, lead, mercury, and cadmium. Int J Nanomed 16:803–832
80. Gaviria-Arroyave MI, Cano JB, Peñuela GA (2020) Nanomaterial-based fluorescent biosensors for monitoring environmental pollutants: a critical review. Talanta Open 2:100006
81. Duan J, Zhan J (2015) Recent developments on nanomaterials-based optical sensors for Hg^{2+} detection. Sci China Mater 58(3):223–240
82. Mokhtarzadeh A et al (2017) Nanomaterial-based biosensors for detection of pathogenic virus. Trends Anal Chem 97:445–457
83. Zhao Q et al (2013) Dithizone functionalized CdSe/CdS quantum dots as turn-on fluorescent probe for ultrasensitive detection of lead ion. J Hazard Mater 250–251:45–52
84. Koczorowski T, Cerbin-Koczorowska M, Rębiś T (2021) Azaporphyrins embedded on carbon-based nanomaterials for potential use in electrochemical sensing—a review. Nanomaterials 11(11):2861
85. Kuna L et al (2019) Peptic ulcer disease: a brief review of conventional therapy and herbal treatment options. J Clin Med 8(2):179
86. Sengupta J, Hussain CM (2021) Graphene-based field-effect transistor biosensors for the rapid detection and analysis of viruses: a perspective in view of COVID-19. Carbon Trends 2:100011
87. Duhan JS et al (2017) Nanotechnology: the new perspective in precision agriculture. Biotechnol Rep 15:11–23

88. Dutta S et al (2020) Hollow polyaniline microsphere/Fe_3O_4 nanocomposite as an effective adsorbent for removal of arsenic from water. Sci Rep 10(1):4982
89. Li M et al (2013) Detection of lead (II) with a "turn-on" fluorescent biosensor based on energy transfer from CdSe/ZnS quantum dots to graphene oxide. Biosens Bioelectron 43:69–74
90. Kuhn R et al (2022) Applications of environmental nanotechnologies in remediation, wastewater treatment, drinking water treatment, and agriculture. Appl Nano 3(1):54–90
91. Sugunan A et al (2005) Heavy-metal ion sensors using chitosan-capped gold nanoparticles. Sci Technol Adv Mater 6(3–4):335–340
92. Mondal P, Anweshan A, Purkait MK (2020) Green synthesis and environmental application of iron-based nanomaterials and nanocomposite: a review. Chemosphere 259:127509
93. Saif S, Tahir A, Chen Y (2016) Green synthesis of iron nanoparticles and their environmental applications and implications. Nanomaterials 6(11):209
94. Gupta SK, Mao Y (2021) Recent developments on molten salt synthesis of inorganic nanomaterials: a review. J Phys Chem C 125(12):6508–6533
95. Gupta R, Xie H (2018) Nanoparticles in daily life: applications, toxicity and regulations. J Environ Pathol Toxicol Oncol 37(3):209–230
96. Hyder A et al (2022) Identification of heavy metal ions from aqueous environment through gold, silver and copper nanoparticles: an excellent colorimetric approach. Environ Res 205:112475
97. Avan AA, Filik H (2020) Simultaneous electrochemical sensing of dihydroxybenzene isomers at multi-walled carbon nanotubes aerogel/gold nanoparticles modified graphene screen-printed electrode. J Electroanal Chem 878:114682
98. Hasanpour M, Hatami M (2020) Application of three dimensional porous aerogels as adsorbent for removal of heavy metal ions from water/wastewater: a review study. Adv Coll Interf Sci 284:102247
99. Bagheri AR et al (2021) Molecularly imprinted polymers-based adsorption and photocatalytic approaches for mitigation of environmentally-hazardous pollutants—a review. J Environ Chem Eng 9(1):104879
100. Hairom NHH et al (2021) A review of nanotechnological applications to detect and control surface water pollution. Environ Technol Innov 24:102032
101. Zhang X et al (2020) Powerful combination of 2D g-C_3N_4 and 2D nanomaterials for photocatalysis: recent advances. Chem Eng J 390:124475
102. Pandey RR, Chusuei CC (2021) Carbon nanotubes, graphene, and carbon dots as electrochemical biosensing composites. Molecules 26(21):6674
103. Iavicoli I et al (2013) The effects of nanomaterials as endocrine disruptors. Int J Mol Sci 14(8):16732–16801
104. Pinto M et al (2020) Application of magnetic nanoparticles for water purification. Environ Adv 2:100010
105. Yang Z et al (2019) A review on reverse osmosis and nanofiltration membranes for water purification. Polymers 11(8):1252
106. Lal S, Singhal A, Kumari P (2020) Exploring carbonaceous nanomaterials for arsenic and chromium removal from wastewater. J Water Process Eng 36:101276
107. Yu S et al (2022) MXenes as emerging nanomaterials in water purification and environmental remediation. Sci Total Environ 811:152280
108. Zeidman AB et al (2020) Removal of antibiotics in aqueous phase using silica-based immobilized nanomaterials: a review. Environ Technol Innov 20:101030
109. Lunge S, Singh S, Sinha A (2014) Magnetic iron oxide (Fe_3O_4) nanoparticles from tea waste for arsenic removal. J Magn Magn Mater 356:21–31
110. Dong X et al (2020) Ultrasensitive detection of chloramphenicol using electrochemical aptamer sensor: a mini review. Electrochem Commun 120:106835
111. Zahra QA et al (2021) Advances in gold nanoparticles-based colorimetric aptasensors for the detection of antibiotics: an overview of the past decade. Nanomaterials 11(4):840
112. Basheer AA (2018) New generation nano-adsorbents for the removal of emerging contaminants in water. J Mol Liq 261:583–593

113. Mudhoo A, Sillanpää M (2021) Magnetic nanoadsorbents for micropollutant removal in real water treatment: a review. Environ Chem Lett 19(6):4393–4413
114. Nik Abdul Ghani NR, Jami MS, Alam MZ (2021) The role of nanoadsorbents and nanocomposite adsorbents in the removal of heavy metals from wastewater: a review and prospect. Pollution 7(1)
115. Manyangadze M et al (2020) Enhancing adsorption capacity of nano-adsorbents via surface modification: a review. S Afr J Chem Eng 31:25–32
116. Ray PC, Yu H, Fu PP (2009) Toxicity and environmental risks of nanomaterials: challenges and future needs. J Environ Sci Health C 27(1):1–35
117. Kausar F et al (2022) Nanomaterials for removal of heavy metals from wastewater. Nanobiosorbents for decontamination of water, air, and soil pollution. Elsevier, pp 135–161
118. Shang Y et al (2019) Applications of nanotechnology in plant growth and crop protection: a review. Molecules 24(14):2558
119. Yang L et al (2019) Recent advances in the pharmacological activities of dioscin. Biomed Res Int 2019:1–13
120. Qasem NAA, Mohammed RH, Lawal DU (2021) Removal of heavy metal ions from wastewater: a comprehensive and critical review. NPJ Clean Water 4(1):36
121. De Gisi S et al (2016) Characteristics and adsorption capacities of low-cost sorbents for wastewater treatment: a review. Sustain Mater Technol 9:10–40
122. Tchounwou PB et al (2012) Heavy metal toxicity and the environment. In: Luch A (ed) Molecular, clinical and environmental toxicology. Springer Basel, Basel, pp 133–164
123. Ganapathe LS et al (2020) Magnetite (Fe_3O_4) nanoparticles in biomedical application: from synthesis to surface functionalisation. Magnetochemistry 6(4):68
124. Roy A, Bhattacharya J (2012) Removal of Cu(II), Zn(II) and Pb(II) from water using microwave-assisted synthesized maghemite nanotubes. Chem Eng J 211–212:493–500
125. Shi R-J et al (2022) Multifunctional cellulose and cellulose-based (nano) composite adsorbents. Front Bioeng Biotechnol 10:891034
126. Panneerselvam P, Morad N, Tan KA (2011) Magnetic nanoparticle (Fe_3O_4) impregnated onto tea waste for the removal of nickel(II) from aqueous solution. J Hazard Mater 186(1):160–168
127. Hariani PL et al (2013) Synthesis and properties of Fe_3O_4 nanoparticles by co-precipitation method to removal procion dye. Int J Environ Sci Dev 4(3):336–340
128. Oliveira H (2012) Chromium as an environmental pollutant: insights on induced plant toxicity. J Bot 2012:1–8
129. Spanos A et al (2021) Functionalized magnetic nanomaterials in agricultural applications. Nanomaterials 11(11):3106
130. Wang A et al (2020) Functionalized magnetic nanosized materials for efficient biodiesel synthesis *via* acid–base/enzyme catalysis. Green Chem 22(10):2977–3012
131. Acelas N et al (2021) Evaluating the removal of the antibiotic cephalexin from aqueous solutions using an adsorbent obtained from palm oil fiber. Molecules 26(11):3340
132. Hassaan MA, El Nemr A (2020) Pesticides pollution: classifications, human health impact, extraction and treatment techniques. Egypt J Aquatic Res 46(3):207–220
133. Huang H et al (2014) Anacardic acid induces cell apoptosis associated with induction of ATF4-dependent endoplasmic reticulum stress. Toxicol Lett 228(3):170–178
134. Singh J et al (2019) Synthesis of Fe_2O_3/TiO_2 monoliths for the enhanced degradation of industrial dye and pesticide via photo-Fenton catalysis. J Photochem Photobiol A 376:32–42
135. Bhardwaj U et al (2012) Persistence of fipronil and its risk assessment on cabbage, *Brassica oleracea var. capitata L.* Ecotoxicol Environ Safety **79**:301–308
136. Freire TM et al (2020) Magnetic porous controlled Fe_3O_4—chitosan nanostructure: an ecofriendly adsorbent for efficient removal of azo dyes. Nanomaterials 10(6):1194
137. Garcia-Segura S, Brillas E (2017) Applied photoelectrocatalysis on the degradation of organic pollutants in wastewaters. J Photochem Photobiol C 31:1–35
138. Manyi-Loh C et al (2018) Antibiotic use in agriculture and its consequential resistance in environmental sources: potential public health implications. Molecules 23(4):795

139. Poonia K et al (2022) Magnetic molecularly imprinted polymer photocatalysts: synthesis, applications and future perspective. J Indus Eng Chem **113**:S1226086X22002714
140. Socas-Rodríguez B et al (2020) Recent applications of magnetic nanoparticles in food analysis. Processes 8(9):1140
141. Shi S, Fan Y, Huang Y (2013) Facile low temperature hydrothermal synthesis of magnetic mesoporous carbon nanocomposite for adsorption removal of ciprofloxacin antibiotics. Ind Eng Chem Res 52(7):2604–2612
142. Roshan S et al (2019) Molecularly imprinted polymer-silica hybrid particles for biomimetic recognition of target drugs. Adv Polym Technol 2019:1–7
143. Yang J et al (2019) Nanomaterials for the removal of heavy metals from wastewater. Nanomaterials 9(3):E424
144. Jamshidiyan M, Shirani AS, Alahyarizadeh G (2017) Solvothermal synthesis and characterization of magnetic Fe_3O_4 nanoparticle by different sodium salt sources. Mater Sci Pol 35(1):50–57
145. Karami H (2013) Heavy metal removal from water by magnetite nanorods. Chem Eng J 219:209–216
146. He Y et al (2019) Efficient removal of Pb(II) from aqueous solution by a novel ion imprinted magnetic biosorbent: adsorption kinetics and mechanisms. PLoS ONE 14(3):e0213377
147. Kaur H, Garg H (2015) Pesticides: environmental impacts and management strategies. In: Soloneski S (ed) Pesticides—toxic aspects. InTech
148. Ambaye TG et al (2021) Mechanisms and adsorption capacities of biochar for the removal of organic and inorganic pollutants from industrial wastewater. Int J Environ Sci Technol 18(10):3273–3294
149. Fatimah I, Sumarlan I, Alawiyah T (2015) Fe(III)/TiO_2—montmorillonite photocatalyst in photo-fenton-like degradation of methylene blue. Int J Chem Eng 2015:1–9
150. Meng W et al (2021) Fe_3O_4 magnetic cores coated with metal-organic framework shells as collectable composite nanoparticle vehicles for sustained release of the pesticide imidacloprid. ACS Appl Nano Mater 4(6):5864–5870
151. Huang Y, Shen D, Wang Z (2022) Preparation of citric acid-sewage sludge hydrochar and its adsorption performance for Pb(II) in aqueous solution. Polymers 14(5):968
152. Ma J et al (2020) Preparation of magnetic metal-organic frameworks with high binding capacity for removal of two fungicides from aqueous environments. J Ind Eng Chem 90:178–189
153. Wo R et al (2019) Preparation and characterization of functionalized metal-organic frameworks with core/shell magnetic particles (Fe_3O_4@SiO_2@MOFs) for removal of congo red and methylene blue from water solution. J Chem Eng Data 64(6):2455–2463
154. Yang G et al (2021) Surface oxidized nano-cobalt wrapped by nitrogen-doped carbon nanotubes for efficient purification of organic wastewater. Sep Purif Technol 259:118098
155. Di Pietro P et al (2016) Gold and silver nanoparticles for applications in theranostics. Curr Top Med Chem 16(27):3069–3102
156. Chen Z et al (2017) Synthesis of magnetic Fe_3O_4/CFA composites for the efficient removal of U(VI) from wastewater. Chem Eng J 320:448–457
157. Gopal G et al (2020) A review on tetracycline removal from aqueous systems by advanced treatment techniques. RSC Adv 10(45):27081–27095
158. Zhou L et al (2014) Preparation and characterization of magnetic porous carbon microspheres for removal of methylene blue by a heterogeneous Fenton reaction. ACS Appl Mater Interf 6(10):7275–7285

Chapter 12
Applications and Working Mechanism of Fe_2O_3 Nanoparticle and Its Composite for Wastewater Treatment

Manoj Kumar Sahu, Hari Sankar Mohanty, Raj Kishore Patel, and Sudarshan Khudwakar

Abstract The impacts of various added substances on the morphology and related photocatalytic properties of different hematite (α-Fe_2O_3) nanostructures were examined. α-Fe_2O_3 croissant-like designs and finished microspheres were framed by aqueous treatment at 120 °C for 6 h within the sight of NaCl, Na_2SO_4, and $Na_2C_2O_4$ as added substances, separately. After heat treatment in air, the photocatalytic movement of the α-Fe_2O_3 powder was surveyed by degrading methyl orange (MO) under UV light with hydrogen peroxide (H_2O_2) as an activator. The α-Fe_2O_3 progressive designs displayed the best photocatalytic activity with a 76.5% evacuation or degradation of dye molecules. This is credited to the high surface region of the iron oxide like morphology, which gives more dynamic locales for the degradation of dyes. The activation energy has also been well compared to the kinetic and isotherm models in the review, which shows that degradation of dyes on the outer layer of iron oxide is much more effective.

Keywords Iron oxide · Nanoparticles · Degradation · Dyes · Wastewater

M. K. Sahu (✉)
Department of Chemistry, GIET University, Gunupur, Odisha 765022, India
e-mail: manojsahu.pdm@gmail.com

H. S. Mohanty
Department of Physics, GIET University, Gunupur, Odisha 765022, India

R. K. Patel
Department of Chemistry, National Institute of Technology, Rourkela 769008, India

S. Khudwakar
Department of Civil and Environmental Engineering, California State University, 800 N. State College Blvd., Fullerton, CA 92831, USA

H. Sahoo and J. K. Sahoo (eds.), *Iron Oxide-Based Nanocomposites and Nanoenzymes*, Nanostructure Science and Technology, https://doi.org/10.1007/978-3-031-44599-6_12

12.1 Introduction

Water is the most precious resource and is crucial for all living creatures in its pure state on earth. It plays a key role in the world economy. An exclusively broad spectrum of hazardous contaminants is released into the watercourse due to rapid urbanization, industrialization, population growth, and long-term droughts, which has grown to be a serious issue worldwide [1–4]. So far, industries have generated a huge amount of miscellaneous carcinogenic contents, and the disposal of these untreated contaminants has been observed to be the main source of water pollution [5, 6]. This may lead to major social evils such as drinking water deficits [7], water evaporation [8], and surface water contamination [7]. The most important factors contributing to this global water pollution are industrial sewage containing hazardous dyes and heavy metals, along with some poisonous chemicals. In fact, these untreated industries discharged the contaminants that contaminate surface water as well as groundwater by spreading their toxicity and causing severe protozoan infections, fungal attacks, and other deadly diseases in aquatic organisms [9–11]. These pollutants, which have tempted increasing concerns about wastewater, can cause adverse ecological problems for wildlife and the environment, such as health effects and mutagenic effects in human beings, aquatic beings, and other living beings [12]. Moreover, the release of these miscellaneous dyes as well as a number of toxic natural contaminants in soils and aqueous environments has made the global water source's condition of inferior quality [13].

Commonly, dyes are classified into two major types such as: herbal/natural and synthetic/artificial dyes. Natural dyes are derived from plant resources such as leaves, roots, wood, berries, fungi, bark, and lichens, whereas synthetic dyes are produced from chemicals, earth minerals, and petroleum derivatives [3, 4]. Artificial dyes are considerably used in sports as well as in paper; in printing, they are used as colorants, and they are also used in the beauty and leather industries too [14]. It has been previously affirmed that dyes were comprehensively used in textile industries (~200,000 tons/year), and without a precise remediation method, they were tended to release into the sewage [2, 15].

In general, dyes possess a very complicated shape with a high molecular weight, are water-soluble, degradation-resistant, potentially carcinogenic as well as mutagenic, and also have the tendency to inhibit sunlight penetration and reduce photosynthetic reactions [6]. The water pollutants may be labeled into numerous principal types, which include natural and inorganic contaminants, vitamins, agricultural waste, pathogens, suspended solids, radioactive wastes, and thermal pollution as well [16].

Generally, there have been various treatment methods implemented to eliminate hazardous organic contaminants from aqueous solutions over the past decades [17]. Several chemical, physico-chemical, and biological techniques, such as membrane separation [18], flocculation [19], adsorption [20], coagulation [21], fungal decolonization [22], degradation [23–26], and ultra-chemical treatments [27], have been widely implemented for the successful removal of dyes from wastewater. Among

those methods, chemical degradation by the advanced oxidation process (AOP) has been proven to be the most efficient one for the resolution of these hazardous chemicals due to their refractory and persistent structure [28]. This process has also been demonstrated to be much more efficient, non-toxic, cost-effective, easy-handling, energy-saving, and eco-friendly in nature.

In the present scenario, nanotechnology has materialized as a cutting-edge technology and a state-of-the-art with broad applications in every field of life. At present, scientists and researchers are putting more focus on the fabrication of nanocomposite, and various techniques are also being implemented for this purpose [29]. Physical methods and chemical techniques are conventionally applied to prepare these nanosheets. Furthermore, magnetic nanocomposites consist of a significant group of inorganic materials and propose a number of applications in research fields by virtue of their unique and distinctive properties [30].

Magnetic nanostructures hold the capability to remove these finely shaped nanoparticles of toxic dyes, heavy metals, and colloids, which cause a very problematic situation when they are supposed to be removed by those pre-conventional techniques. Among those several magnetic nanocomposites, iron oxide has been considered to be the most efficient as well as convenient for the adsorption technique due to its very small size and ferromagnetic nature [31]. They have the potential to remove several heavy metal ions, such as lead, cadmium, copper, or chromium, as well as dyes and pesticides, simultaneously from wastewater [32]. In current times, the application of magnetic nanoadsorbents for the decontamination process has become very efficient and has received considerable demand and attention due to their easy separation ability [33–38]. The iron oxide possesses many kinds of phases, such as FeOOH, FeO, Fe_4O_5, Fe_3O_4, Fe_4O_3, $Fe(OH)_3$, polymorphs of Fe_2O_3 (α-Fe_2O_3, and γ-Fe_2O_3), and so on. Among these, maghemite (γ-Fe_2O_3), hematite (α-Fe_2O_3), and magnetite (Fe_3O_4) are of greater interest for their drinking water treatment, electrical, magnetic properties, optical properties, ferrofluid technology, magneto caloric refrigerant, gas sensing, etc. [39–42]. This compound has a lot of influence and impact on the remediation of water, such as fast and easy production, rapid uptake, high adsorptive capacity, easy separation, etc.

Over the last few years, the elimination of different organic dyes has grown to be a global concern considering their carcinogenic effects on the environment. Approximately 70–80% of total illnesses in women and children in developing countries are initiated by different water contaminants, according to WHO and UNICEF reports from 2000. The several toxic things caused by dyes are shown in Fig. 12.1. Thus, in this session, different applications of Fe_2O_3 in the removal of organic dyes and pesticides are discussed.

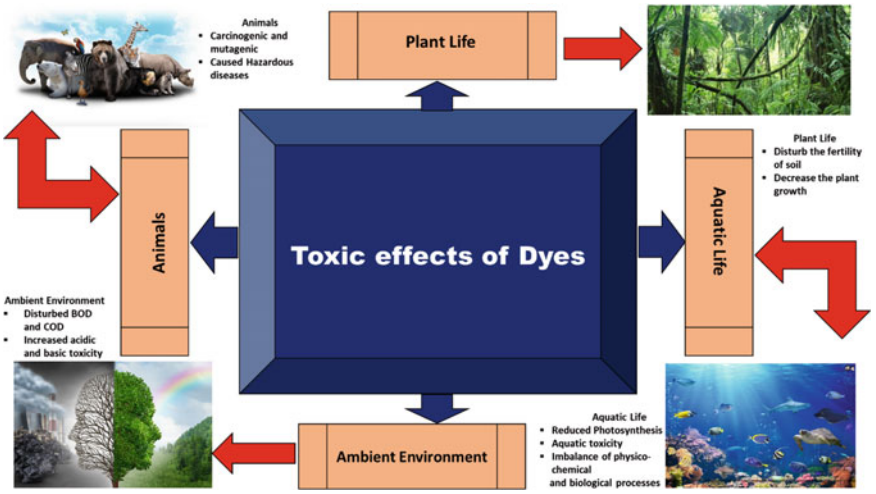

Fig. 12.1 Toxic things caused by dyes on environment and living beings

12.2 Removal of Organic Dyes

A dye is a substance that imparts color through physical or chemical binding. The chromophoric units present in the dye develop a color to which auxochromes are attached. Dyes are used in various applications in our day-to-day lives that release toxic organic and inorganic chemicals from industries wastewater, resulting in harmful effects on the environment. Therefore, it is essential to protect the environment from the toxic effluents released into the water body by treating them through different physical, chemical, and biological treatments. In the following sections, the adsorptive and photocatalytic removal of dyes using various classes of adsorbents and catalysts and their adsorptive and photocatalytic mechanisms are presented.

Guo et al. synthesized a heterogeneous Fenton catalyst i.e., α-Fe_2O_3/$Cu_2O(SO_4)$, which was highly efficient as well as a novel reagent for the removal of organic dye in the field of advanced oxidation processes (AOPs). It had become a widespread investigation which resulted in the formation of $Cu_2O(SO_4)$-Fe_9 [43] composite showing brilliant catalytic removal efficiency for the degradation of orange II. Considering its effectiveness, it showed the rate of removal of about 98.9% at 50 mg/L Orange II in 100 ml (under the condition of 0.3 g/L $Cu_2O(SO_4)$-Fe_9 catalyst, 3 mm H_2O_2, and pH = 3.5). In this concern, PL spectra were used to measure the dissociation efficiency of photon-generated carriers. The intensity of this PL spectra indicated that the $Cu_2O(SO_4)$-Fe_9 nanocomposite excited the dissociation of carriers by showing the peaks as $Cu_2O(SO_4) > \alpha$-$Fe_2O_3 > Cu_2O(SO_4)$-Fe_9. Again a number of scavengers like 1,4-benzoquinone, isopropanol, CCl_4, and CH_3OH were added to the photo-fenton system to adsorb the superoxide, hydroxyl radicals, electrons, and holes respectively. When the rate of degradation of Orange II was compared without and along with the scavengers, it was found that when isopropanol (10 mM) was added to the system,

the degradation efficiency of Orange II was decreased to 21.4% from 98.9% within 15 min. Based on this decreasing efficiency, the catalytic mechanism was analyzed as shown below.

$$Fe^{3+}_{surf} - OH + H_2O_2 \rightarrow (H_2O_2)_S \tag{12.1}$$

$$(H_2O_2)_S \leftrightarrow Fe^{2+}_{surf} - \cdot O_2H + H_2O \tag{12.2}$$

$$Fe^{2+}_{surf} - \cdot O_2H \leftrightarrow Fe^{2+}_{surf} - \cdot O_2H \tag{12.3}$$

$$(H_2O_2)_S \leftrightarrow Fe^{2+}_{surf} - \cdot O_2H + H_2O \tag{12.4}$$

$$Fe^{2+}_{surf} + H_2O_2 \rightarrow Fe^{3+}_{surf} - OH + \cdot OH \tag{12.5}$$

$$Fe^{2+}_{surf} - OH + \cdot O_2H \rightarrow Fe^{2+}_{surf} + H_2O + O_2 \tag{12.6}$$

$$Fe^{3+} + H_2O_2 \rightarrow Fe^{2+} + \cdot O_2^- + 2H^+ \tag{12.7}$$

$$Fe^{2+} + H_2O_2 + H^+ \rightarrow Fe^{3+} + \cdot OH + H_2O \tag{12.8}$$

First of all, surface complex precursor was formed between $Fe^{3+}_{surf} - OH$ and H_2O_2 which may be considered as the initiation step (Eqs. 12.1–12.4). For the oxidation of organic pollutants, more number of hydroxyl radicals were needed which was produced by the dissociation of peroxide and reduction of Fe by interface electron transfer (Eqs. 12.5–12.6). The amount of Fe^{2+} on the surface of catalyst was increased to 38.7% from 26.1%. At the same time, these cyclic reactions for Cu^{2+}/Cu^{+} and Fe^{3+}/Fe^{2+} were carried out under acidic circumstances (Eqs. 12.7–12.8). And it was observed that the combined effect of Cu and Fe in the above reaction became very helpful in enhancing the hydroxyl radical production for the degradation of H_2O_2. It was also inferred from the above study that orange II was very well-attacked by Cu_2O (SO_4)-Fe_9 nanocomposite.

Another researcher Mai et al. reported the AOP reaction of Fenton system modified with Fe_2O_3 and $NaHSO_3$. This novel nanocomposite showed a very well-organized synergistic effect for the removal of Orange II and azo dye. In this study, the radical species produced were %OH and $\%SO_4^-$ showing very high competence to oxidize and degrade organic contaminants. In this concern, hydroxyl radical was formed by activating $NaHSO_3$ with Fe^{3+} reduced to Fe^{2+}. The removal efficiency was found to be 90% in 20 min when the pH was adjusted between 8 and 10. The experimental result and the pathways of the experiment are shown by the following equations.

$$\equiv Fe^{3+} + HSO_3^- + OH^- \rightarrow \equiv Fe^{2+} + \cdot SO_3^- + H_2O \tag{12.9}$$

$$\cdot SO_3^- + \cdot O_2 \rightarrow SO_5^- \tag{12.10}$$

$$\cdot SO_5^- + 2 \equiv Fe^{2+} + H_2O \rightarrow 2 \equiv Fe^{3+} + \cdot SO_4^- + OH^- \tag{12.11}$$

$$\cdot SO_5^- + HSO_3^- \rightarrow \cdot SO_4^- + \cdot SO_4^{2-} + H_2O \tag{12.12}$$

$$\cdot SO_3^- + Fe^{2+} + H^+ \rightarrow Fe^{3+} + HSO_3^- (pH < 6) \tag{12.13}$$

$$\cdot SO_4^- + Fe^{2+} \rightarrow Fe^{3+} + SO_4^{2-} \tag{12.14}$$

$$\cdot OH^- + Fe^{2+} \rightarrow Fe^{3+} + OH^- \tag{12.15}$$

$$\cdot SO_4^- + HSO_3^- \rightarrow \cdot SO_3^- + SO_4^- + H_2O \tag{12.16}$$

$$\cdot SO_4^- + \cdot SO_4^- \rightarrow S_2O_8^{2-} \rightarrow 2SO_4^{2-} \tag{12.17}$$

$$\cdot SO_3^- + \cdot SO_3^- \rightarrow S_2O_6^{2-} \rightarrow 2SO_3^{2-} \rightarrow 2SO_4^{2-} \tag{12.18}$$

First of all, HSO_3^- was accumulated on Fe_2O_3 catalyst surface and it was studied under both acidic and alkaline conditions (Eq. 12.9). The $\cdot SO_3^-$ which was supported by dissolved oxygen generated the powerful oxidizing peroxy-sulfate ion $\cdot SO_5$ (Eq. 12.10) which was further reacted to Fe^{2+} along with HSO_3 (Eqs. 12.11–12.12) generating the stability and catalytic activity. This overall mechanism of degradation by $\cdot SO_4$ and $\cdot OH$ was found to be more consistent for Orange II with the formation of organic intermediates along with CO_2 and H_2O.

The core–shell nanocomposites of $Fe@Fe_2O_3$ were synthesized by Yang et al. for the degradation of Orange II dye. This heterogeneous catalyst was found to be very effective in the reaction of Fenton to degrade organic pollutants as well as dyes [44]. The efficiency of this nanocomposite was increased when this $Fe@Fe_2O_3$ was assisted by $NaHSO_3$. This combined form of the experimental nanocomposite was inferred for the removal of Orange II dye in both acidic as well as in alkaline medium. The mechanism of degradation process is shown below.

$$\equiv Fe^{3+} + 2HSO_3^- + 2OH^- \rightarrow \equiv Fe^{2+} + 2SO_3^{-\cdot} + H_2O \tag{12.19}$$

$$SO_3^{-\cdot} + O_2 \rightarrow \cdot SO_5^{-\cdot} \tag{12.20}$$

$$SO_5^{-\cdot} + HSO_3^- \rightarrow SO_4^{-\cdot} + SO_4^{2-} + H^+ \tag{12.21}$$

$$Fe^0 + 2Fe^{III} \rightarrow 3Fe^{II} \tag{12.22}$$

$$Fe^{II}OFe^{III} \rightarrow Fe^{III}OFe^{II} \tag{12.23}$$

$$Fe^{II}OFe^{III} + O_2 \rightarrow O_2^{-\cdot} \tag{12.24}$$

$$2O_2^{-\cdot} + 2H^+ \rightarrow H_2O_2 + O_2 \tag{12.25}$$

$$\equiv Fe^{2+} + H_2O_2 \rightarrow \equiv Fe^{3+} + OH^{\cdot} + OH^- \tag{12.26}$$

This process involves solid–liquid interface of $Fe@Fe_2O_3$ nanocomposites. First of all, the HSO_3^- radical species assembled on the surface of $Fe@Fe_2O_3$ catalyst. After that, SO_5^- was produced as a result of reaction of $\cdot SO_3^-$ and dissolved O_2^-. The $\cdot SO_5^-$ so obtained treated with HSO_3^- to obtain $\cdot SO_4$ (Eqs. 12.19–12.21). This Fenton catalyst could persuade electron transfer in between the Fe_2O_3 shell and Fe core which accelerated the generation of $\cdot O_2^-$ (Eqs. 12.22–12.24). The generation of radical resulted in the removal of Orange II. This mechanism was well-established for the removal of Orange II dye.

MgO/α-Fe_2O_3 nanocomposite was prepared by Allawi et al. with the help of hydrothermal process, and photo-oxidation operations were carried out for the degradation of MB dye. The study is mainly based on two assumptions i.e., (1) the decrease in recombination possibility of electron–hole pairs and (2) the increase in absorption of photon by MgO. So this study was made on combined photocatalytic outcome of MgO-Fe_2O_3 nanocomposite [45]. The mechanism of the reaction of as follows:

$$MgO/Fe_2O_3 + h\nu(\text{Vis Region}) \rightarrow MgO/Fe_2O_3\left(H^+ + e^-\right) \tag{12.27}$$

$$H^+ + H_2O(OH^{\cdot}) \rightarrow (OH^{\cdot}) + h^+ \tag{12.28}$$

$$h^+ + \text{Dye} \rightarrow \text{Dye}^{\cdot+}(\text{Oxidation of Dyes}) \tag{12.29}$$

$$e^- + O_2 \rightarrow O_2^{\cdot-} + \text{Semiconductor} \tag{12.30}$$

$$\text{Dye} + O_2^{\cdot-} \rightarrow \text{Degradation Products} \tag{12.31}$$

The result of degradation of MB dye was found to be 91.7% at pH 12 which was designated to be very cost-effective as well as efficient photocatalyst for mineralization of dye pollution.

Bouziani et al. synthesized the heterogeneous nanocomposite α-Fe_2O_3/TiO_2 by sol–gel method to integrate the photocatalytic activity of titanium oxide. The α-Fe_2O_3/TiO_2 nanocomposite showed great photocatalytic efficiency for the degradation of methylene blue i.e., 90% in 180 min of photo-illumination [46]. The process involved the generation of active species like ·OH, $\cdot O_2^-$, holes. The mechanism of the process is:

$$\mathrm{TF6} + h\nu \rightarrow \mathrm{TF6}\left(h^+ + e^-\right) \tag{12.32}$$

$$\mathrm{O_2} + e^- \rightarrow \mathrm{O_2^{-\cdot}} \tag{12.33}$$

$$\mathrm{O_2^{-\cdot}} + \mathrm{H^+} \rightarrow \mathrm{HO_2^{\cdot}} \tag{12.34}$$

$$2\mathrm{HO_2^{\cdot}} \rightarrow \mathrm{O_2} + \mathrm{H_2O_2} \tag{12.35}$$

$$\mathrm{H_2O_2} + \mathrm{O_2^{-\cdot}} \rightarrow \mathrm{OH^{\cdot}} + \mathrm{OH^-} + \mathrm{O_2} \tag{12.36}$$

$$\mathrm{H_2O_2} + h\nu \rightarrow 2\mathrm{OH^-} \tag{12.37}$$

A well-organized photocatalyst for the decolorization of MB dye was studied by Hojamberdiev et al. The Porolas-Fe_2O_3 nanocomposite (1%) was prepared using the precursor iron nitrate which was more amorphous as compared to 7% of the same nanocomposite. The heterogeneous photodecomposition on the nanomaterial surface by UV photo-irradiation [47].

$$\mathrm{H_2O} \rightarrow \mathrm{H^+} + \mathrm{OH^-} \tag{12.38}$$

$$e^{\mathrm{CB}-} + \mathrm{O_2} \rightarrow \mathrm{O_2^{\cdot -}} \tag{12.39}$$

$$\mathrm{O_2^{\cdot -}} + \mathrm{H_{aq}^+} \rightarrow \mathrm{HO_2^{\cdot}} \tag{12.40}$$

$$\mathrm{HO_2^{\cdot}} + \mathrm{HO_2^{\cdot}} \leftrightarrow \mathrm{H_2O_2} + \mathrm{O_2} \tag{12.41}$$

$$h^{\mathrm{VB}+} + \mathrm{OH_{aq}^-} \rightarrow \mathrm{OH^{\cdot -}} \tag{12.42}$$

$$\mathrm{MB^{\cdot}} + \mathrm{MB^{\cdot +}} + \mathrm{O_2^{\cdot -}}, \mathrm{HO_2^{\cdot}}, \mathrm{H_2O_2}, \mathrm{OH^{\cdot -}} \rightarrow \text{Degradation Products} \tag{12.43}$$

Mohamed et al. studied a *Z*-scheme photocatalytic system which simulated the photosynthesis by recombination of charge carrier and having great redox capacities. They produced the Fe_2O_3/GO/WO_3 3*Z*-Scheme nanocomposite [48] which was seen

to be very effective for the decolorization of MB and CV dyes. The mechanism of the reaction in α-Fe_2O_3/WO_3 system includes the electron–hole generation under solar light. The photo-generated electrons and photo-generated holes lead to the increase in oxidizing and reducing abilities of Fe_2O_3 and WO_3. These radical species generated in this reaction were responsible for the degradation of organic pollutant like methylene blue. The result of this study revealed that the efficiency of this nanocomposite for the removal of MB was 95.4% in 120 min. This process was found to be a green synthesis of $Fe_2O_3/GO/WO_3$ nanocomposite with the utilization of solar light.

The nanocomposite Fe_2O_3/Graphene/CuO (FGC), which is known to be a visible photo-sensitive material was successfully synthesized by Nuengmatcha et al. using a very simple solvothermal method. In this context, the photocatalytic activity of FGC was evaluated for the removal of MB when the nanocomposite was subjected to act in presence of visible light. It was found that the nanocomposite showed very great efficiency as compared to other types of catalysts. Furthermore, the mechanism of photocatalytic property of this hybrid composite was also studied. The synthesis of Fe_2O_3/graphene/CuO (FGC) [49] photocatalyst in a visible light system showed very good photocatalytic activity and brilliant magnetic separation capability. This method was very well-established for the removal of MB dye with an efficiency of more than 90% in 5 cycles. When FGC nanocomposites were used as a catalyst the valence band (VB) electrons of CuO were shifted to its conduction band (CB). This excitation results in the generation of electron–hole pairs (e^-/h^+) that mainly cause the photocatalytic as well as a redox reaction. As grapheme showed brilliant electronic conductivity and possessed large surface area, it behaved as electron transporter and acceptor. These reacted with O_2 which was dissolved in water and transformed to $O_2^{-\cdot}$ radical species. At the same time, the holes reacted to OH^-/H_2O absorbed on the surface of FGC to form ·OH. These radical species had a strong ability to oxidize and degrade MB to CO_2, H_2O with other byproducts. Following figure shows the mechanism of degradation of MB using this method.

Narendhran et al. [50] synthesized $Fe_2O_3/FeWO_4/WO_3$ nanostructures to examine the photocatalytic effect on methyl orange under UV–VIS irradiation method. When the nanoparticles were exposed to visible light, the band intensity of absorbed dye decreased. The hetero compound showed an efficiency of 98% within 160 min which was very high as compared to the individual reagents. These nanoparticles were synthesized by hydrothermal and precipitation method and no surfactant was added in the synthesis process. Santana et al. [51] synthesized a Fenton-like nanocomposite i.e., Fe_2O_3/MCM-41 for the photocatalytic degradation of methyl orange it showed a degradation efficiency of 70% in 120 min. The reaction mechanism of this reaction was as that of Fenton-like process which involves the production of hydroxyl radicals from hydrogen peroxide (H_2O_2) along with non-selective and highly oxidative OH radicals. These OH radical species showed brilliant efficiency toward degradation of organic pollutant like methyl orange. This study shows that Fe_2O_3/MCM-41 catalyst showed promising approach for the removal of MB dye.

Friendy and Sillanpaa synthesized a novel α-Fe_2O_3/Graphene nanomaterial for the removal of Rhodamine B (RhB) by visible light. α-Fe_2O_3/Gr nanocomposite [30] showed a brilliant catalytic activity with 98% toward the degradation of RhB under visible light. The series of disintegration process was performed to evaluate the reusability of the photocatalyst. This overall study showed that the nanocomposite was very effective, efficient, reusable, and eco-friendly. A novel nanocomposite was reported by Ouachtak et al. [12] for the adsorption of Rhodamine B by co-precipitation method and the nanocomposite was named as ν-Fe_2O_3@Mt or magnetic montmorillonite nanostructure. The adsorption property of RhB on ν-Fe_2O_3@Mt surface was measured. It was well-fitted with a great efficiency for the removal of RhB.

Jasmindar et al. [52] prepared a mesoporous Fe_2O_3/g-C_3N_4 nanomaterial for the removal of RhB. This novel nanocomposite showed an efficiency of 94.7% catalytic activity in 140 min. Due to the porous nature of Fe_2O_3/g-C_3N_4 monoliths, with higher charge separation ability, this leads to increase the catalytic property. This nanocomposite was found to be very effective and reusable. However, the nanocomposite was found to be very difficult to synthesize. The mechanism of the reaction involved the formation of holes (h^+), superoxides ($O_2^{-\cdot}$), and hydroxide radical species. This radical was used to decolorize the harmful RhB dye. Following figure shows the mechanism of the proposed reaction.

Another researcher Yang and Li studied the ZnO/Fe_2O_3 nanomaterial for the degradation of RhB in presence of UV-Light. The nanocomposite was synthesized by co-precipitation method. It showed brilliant photocatalytic activity for the degradation of RhB [53] when applied to external magnetic field, the magnetic saturation was sufficiently high. And the nanocomposite was found to be very efficient, eco-friendly, and showed outstanding photocatalytic activity. The following figure shows the mechanism of the reaction. Hasan et al. prepared a Υ-Fe_2O_3 nanomaterial for the removal of malachite green. The process was carried out by polymerization of oxidative free radical with acrylamide monomer. The novel material PACT@Υ-Fe_2O_3 nanocomposite [54] was utilized on the removal of MG with an efficiency of 77% in 170.28 min. as the conventional methods for the removal of dyes were found to be due to excessive cost, a most favorable approach could be adopted for its moderate approach, easy-handling and low cost as well. The optimization of various kind of processes could be maintained by the association of central composite design with response to surface methodology. The experimental process concludes toward degradation of MG with an easy access.

Jiang et al. synthesized novel Fe_2O_3 hollow box with double shell structure for the adsorption of MG by template-engage process. This nanocomposite was formed from diatomite@FeOOH [55] using the diatomite@MnO_2 material by a very simple route. The mechanism involved the introduction of Fe_2O_3/H_2O_2 in the solution of MG under irradiation of visible light. The Fe_2O_3 nanostructures are uniformly spreaded on the framework which was found to be 100% efficient in 60 min for the removal of MG in presence of H_2O_2. It exhibited great catalytic efficiency even after 5 cycles. This implies the nanomaterial can be taken as one of the promising catalysts used for the degradation of MG. Dehbi et al. used iron oxide nanoparticle from Fe $(NO_3)_3 \cdot 9H_2O$

and NH_4OH for the removal of malachite green (MG). The elimination efficiency was found to be 86.13% in 45 min using iron oxide. The nanocomposite was seen to be very recognized by thermodynamics stability. This α-Fe_2O_3 nanocomposite [56] was used as an efficient photocatalyst for the removal of MG.

Again another researcher introduced the application of Υ-Fe_2O_3 nanocomposite [57] for the removal of BTEX. The process was followed by photocatalytic degradation of semiconductors by gaining energy of the electrons present in the valence band (VB) and excited to CB. These electron–hole pairs (e^- and h^+) and hydroxyl radical were used for the degradation of BTEX in simpler compounds. The Υ–C nanomaterial was found to be very useful, cost-effective, and eco-friendly for the removal of BTEX. Ismail et al. [58] reported a very simple process to synthesize very efficient photocatalyst i.e., CNT-α-Fe_2O_3 nanocomposite for the removal of Bismarck Brown R dye (BBR). This nanomaterial showed an effectiveness of 98% for dye degradation when there was a synergistic effect of CNT and Fe_2O_3 interface. The main purpose of this study was to prepare an efficient photo-active mesoporous nano hybrid such as CNT-α-Fe_2O_3 with high sensitivity toward UV–VIS light. This nanomaterial can also be used as electrochemical sensor electrode. The photocatalyst showed remarkable efficiency for the removal of BBR dye.

Ghaffari et al. studied the AOPs for degrading organic dyes from wastewater. The process was followed by photocatalysis of fenton reactions with a very high efficiency. This involved a combined nanocomposite of Fe_2O_3/Mn_2O_3 [59] fabrication using the method of surfactant mediated co-precipitation. The recyclability was seen for seven cycles of catalytic reaction. The organic dye removal onto FMNC was found to be very efficient and sensitive for UV–VIS light.

Chen et al. [60] proposed a novel nanostructure for the degradation of organic contaminants which was a functionalized biochar of Fe_2O_3/TiO_2 (Fe_2O_3/TiO_2-BC). The preparation of the composite involves pyrolysis process, and the removal process involves oxidation and fenton-like reaction. In this context the MB (75%), RhB (60%) and MO (40%) were removed. Overall this system possesses brilliant potential for the degradation of organic pollutants. Liu et al. [61] reported a novel nanocomposite such as α-Fe_2O_3 having a silkworm–cocoon structure with brilliant adsorption capacity of 99.2–100% efficiency in the removal of several heavy metals along with various organic dyes such as CR, MO, etc. In this study, simple hydrothermal process to synthesize the nanocomposite and fenton-like photo-catalysis for the degradation of organic pollutants. This catalyst was well organized and possess high efficiency in the removal process even if at very low temperature and concentration. The overall study became very promising, cost-effective adsorbent for wastewater treatment. A hierarchically structured nanocomposite of Υ-Fe_2O_3-PPy [62] was prepared by Gopal et al. for the decolorization of cationic and anionic dyes. It was known to be an eco-friendly, low cost, and earth abundant composite for removing MB. These Υ-Fe_2O_3 nanocomposites possess very strong magnetic properties, high adsorption ability, and high surface area. This eco-friendly Fe_2O_3-PPy nanostructure was applied successfully in the removal of organic dyes.

12.3 Removal of Pesticides and Other Organic Pollutants

Along with the rapid progress of urbanization and industrialization, environmental pollution also increases rapidly. The wastewater from the developing industries is discharged into the water bodies, which contain different organic pollutants. Among them, different kinds of organic pollutants, such as pharmaceutical products, phenols, benzene compounds, antibiotics, and halogenated hydrocarbons, are toxic and harmful. Thus, it is necessary to discover an eco-friendly and high-productivity method to change organic pollutants into non-toxic and harmless products.

Singh et al. investigated the monolithic catalyst for the removal of industrial pesticides and dyes through a photo-Fenton-like system. This process involved the advanced oxidation process with the generation of hydroxyl radical (·OH) radical resulted in the degradation of pesticides as well as dyes. The novel nanocomposites formed in this process were Fe_2O_3/TiO_2 [63]. The mechanism of the system was found to be as like fenton system with the wide generation of various radical species. The nanocomposite obtained in this process was very cost-effective, non-toxic, and chemically stable in nature. It showed 95.7% efficiency in 150 min for reactive brilliant red X-33 dye and the herbicide 2,4-dichlorophynoxyacetic acid was removed with an efficiency of 18% in 1 h. Sun et al. [11] investigated the degradation of organic pollutant using a magnesium Mg-dopped $CuO–Fe_2O_3$ nanomaterials. Mg doping increased the catalytic activity of novel nanocomposite and the efficiency for degradation of phenol was found to be 84.36% in 45 min using 3.2% Mg doped $CuO-Fe_2O_3$ nano sheet modified with persulfate system (PS). This novel nanocomposite was prepared by hydrothermal method and inferred to be a cost-effective and eco-friendly photocatalyst.

Salari et al. reported the photocatalytic degradation of organic pollutant in aqueous solution under UV–VIS light. In this contest, the $Fe_2O_3/MoO_3/AgBr$ nanocomposite [64] was prepared by facile method. Various parameters such as amount of photocatalyst calcinations temperature, dye concentration pH of the solution, and contact time were observed. It was inferred that the photocatalytic activity was increased with maximum peak at pH = 6.5. The experiment followed Langmuir Hinshelwood isotherm and Pseudo-first-order kinetics. Guo et al. [65] synthesized Ca-doped-Fe_2O_3 nanocomposites and used for the degradation of organic pollutants. They prepared low cost and environment-friendly calcium-doped α-Fe_2O_3 (Ca-Fe_2O_3) with abundant oxygen vacancies by precipitation method and used for the degradation of Rhodamine B (RhB). RhB was efficiently degraded by the 5% Ca-Fe_2O_3/PMS system over a pH values of (3.0–10.0), and the catalyst shows good constancy, flexibility, and less iron leaching. They reported that the process fitted well with the pseudo-first-order kinetics model.

Huang et al. synthesized magnetic $CuS/Fe_2O_3/Mn_2O_3$ nanocomposite via a facile Strategy and investigated the degradation of peroxymonosulfate (PMS) for ciprofloxacin (CIP) from aqueous solution. They reported that the magnetic CuS/Fe_2O_3/Mn_2O_3 nanocomposite [66] possessed higher catalytic activity for degradation of ciprofloxacin than bare CuS and Fe_2O_3/Mn_2O_3 composite. The degradation

process of ciprofloxacin was best fitted with the pseudo-first-order kinetic model and the highest rate was reached 0.10083 min^{-1} at the optimized conditions i.e., catalyst doses 0.6 $g{\cdot}L^{-1}$, PMS of 0.6 $g{\cdot}L^{-1}$, pH of the solution 5.84, initial concentration of 0.2 $g{\cdot}L^{-1}$ and time 120 min, the degradation efficiency was reported to be 88 and 48.6% corresponding to degradation and mineralization of ciprofloxacin, respectively. Ahmed et al. [67] studied the removal of Ciprofloxacin from wastewater via Pickering Emulsion Liquid Membrane Stabilized by Magnetic Nano-Fe_2O_3. They prepared the nanocomposite by ultrasonication for adsorption of Ciprofloxacin. They investigated the high rate of adsorption reached to 98.85% and minimum emulsion crack of 0.06% within 10 min addition time taken at the optimal operating conditions: 12,700 rpm homogenizer speed, 0.7 (%w/v) nano-Fe_2O_3 particles concentration, 6% (v/v) TBP concentration at emulsification time of 7 min and 0.1 M HCl in the internal phase.

Anfar et al. [68] prepared the Fe_2O_3/biochar by the process of green synthesis in microwave. They investigated the adsorption under different experimental parameters time (0–120 min), initial concentration (10–500 mg/L), pH (2–12). They reported the ultrasound-assisted adsorption capacity of salicylic acid, naproxen, and ketoprofen (SA, Nap, and Keto) from wastewater. For the removal (adsorption) of SA, Nap, and Keto the fitted kinetics and isotherm are pseudo-second-order model and Langmuir isotherm and maximum adsorption rate of SA, Nap, and Keto reaches to 683, 533, and 444 mg g^{-1}, respectively. Ding et al. [69] studied the degradation of salicylic acid from wastewater by using the α-Fe_2O_3/MXene. They prepared α-Fe_2O_3/MXene by facile hydrothermal method which is good degradation of salicylic acid from wastewater. The degradation rate of salicylic acid was reported 97% at 0.2 g/L FM-2 catalyst (17.1 wt.% of α-Fe_2O_3 loading) and 0.2 g/L PMS under neutral conditions.

Niu et al. [70] synthesized persulfate activated with magnetic γ-Fe_2O_3/CeO_2 by oxidation-precipitation method. They reported effective removal of tetracycline from wastewater by degradation process. They investigated γ-Fe_2O_3–CeO_2 had high crystallinity and good magnetism which leads good removal efficiency of tetracycline. The percentage of removal of tetracycline was reached to 84% under condition of a wide pH application range (pH 3–pH 9). Shan et al. synthesized magnetically recyclable $La_2O_2CO_3$/γ-Fe_2O_3 by using calcinating La-Fe binary MOF precursors as an adsorbent. They examined the adsorption of phosphate from wastewater by $La_2O_2CO_3$/γ-Fe_2O_3 [71]. Batch adsorption experiments showed that $La_2O_2CO_3$/γ-Fe_2O_3 (2:1) adsorbent exhibited a remarkable phosphate sorption capacity of 134.82 mg P/g, a fast sorption kinetic, strong selectivity for phosphate in the presence of co-existing anions, and a wide applicable pH range of 3–9. They reported the adsorption rate reached to 83.1%. Experimental data showed that the adsorption process followed Langmuir model and kinetics followed pseudo-second-order.

Wang et al. [10] prepared γ-Fe_2O_3@BC by pyrolysis of the pomelo peel-based biochar at a temperature of 400 °C and loaded with γ-Fe_2O. They studied the adsorption of norfloxacin from wastewater by using γ-Fe_2O_3@BC. The experimental study revealed that adsorption of norfloxacin followed the pseudo-second-order kinetic model. Again the experimental study confirmed the adsorption isotherm followed the Sips mode. García-Muñoz et al. investigated the wastewater treatment

by removing norfloxacin via degradation. They used mesoporous Fe_2O_3–TiO_2 [72] for the wastewater treatment which was prepared via structure-directing-surfactant method. They reported the best results were obtained with catalysts that had a surface Fe_2O_3 content of 3% (w/w), where the breakdown of H_2O_2 led to the maximum norfloxacin running down rate. They examined using 405 nm LED light, Fe_2O_3–TiO_2 improved the process efficiency and under UV illumination at 405 nm and with a stoichiometric amount of H_2O_2, almost complete norfloxacin removal and almost total mineralization were achieved in 120 min at 298 K and pH = 7.

Abdel-Wahab et al. [73] studied the treatment of pharmaceutical wastewater containing paracetamol by the help of magnetic flower-like TiO_2/Fe_2O_3 core–shell. They synthesized the magnetic flower-like TiO_2/Fe_2O_3 core–shell nanocomposite which was ultrasonically assisted by sol–gel method with some alterations. They mentioned that paracetamol was completely degraded after 90 min with 50% TiO_2/Fe_2O_3 under light irradiation and 66% paracetamol mineralization had occurred. They investigated the attack of the –OH radical on the aromatic ring which was supposed to be the initial point for photo-degradation of paracetamol. By experimental data, the kinetics study indicated that degradation fitted with pseudo-first-order reaction. Chahm et al. [74] reported the adsorption of ibuprofen from wastewater with the help of O-carboxymethyl-N-laurylchitosan/γ-Fe_2O_3. For the adsorption mechanism, they studied Langmuir, Freundlich, and Sips isotherms and kinetics of pseudo-first-order, pseudo-second-order, and intra-particle diffusion model. They reported the maximum adsorption of ibuprofen was found to be 395 mg/g at 25 °C and pH 7.0 which was well-fit for Sips isotherms and pseudo-second-order kinetics.

Lin et al. investigated the treatment of wastewater by using $Ag/TiO_2/Fe_2O_3$. They reported the removal of deleterious and recalcitrant compounds by using this novel nanoparticle [75]. The maximum TOC removal at optimum conditions of light wavelength (254 nm), pH (4.68), photocatalyst dosage (480 mg/L), and initial TOC concentration (11,126.5 mg/L) was calculated using a numerical optimization approach of 9.78% and validated with experimental results of 9.42%. Ding et al. [76] studied the anode and cathode of an electrochemical/electro-Fenton oxidation (EC/EF) device to degrade atrazine were boron-doped diamond (BDD) and Fe@Fe_2O_3 core–shell nanowires loaded active carbon fiber (Fe@Fe_2O_3/ACF), respectively. Fe@Fe_2O_3 could activate molecular oxygen 31 to produce more ·OH via Fenton reaction, preferring atrazine degradation, according to an active 30 species trapping experiment.

He et al. [77] were studied the treatment of municipal wastewater. They prepared Fe@Fe_2O_3 nanomaterial combined with polydiallyldimethylammonium chloride (PDMDAAC) and H_2SO_4 for sludge dewatering and found that the nanocomposite was very effective. Cao et al. studied the wastewater treatment which contains refractory pollutants via adsorption and catalytic oxidation. They performed the adsorption experiment by use of γ-Fe_2O_3/Bentonite [78] Modified which was prepared via a facile and eco-friendly reaction. They investigated the removal of BPA (bisphenol A). The experimental data showed that Langmuir isotherm well-fitted with adsorption with adsorption capacity of 77.36 mg/g. BPA photocatalytic degradation by product had a reaction rate constant of 0.00104 min^{-1}. They reported the catalytic activity

of the material still reached 91% after 5 experiment repeatedly. Pan et al. examined the degradation of bisphenol A (BPA) from wastewater. They used Aldehyde-modified *a*-Fe_2O_3/graphitic carbon nitride (α-Fe_2O_3-DBD/g-C_3N_4) [79] prepared by complexation reaction for the degradation of bisphenol A. They reported under 180 min of photocatalytic irradiation, the mineralization rate of BPA over 1.6% and α-Fe_2O_3-DBD/g-C_3N_4 was 52.2%, which is 6.14 times higher than that over g-C_3N_4.

Gao et al. synthesized heterogeneous Fenton-like catalyst which was used to treat the wastewater. By the use of sol–gel technique and sufficient oxygen vacancies (OVs) promoted the synthesis of Fe_2O_3–CeO_2 photocatalyst. They degraded sulfamerazine from wastewater with an efficient manner. They reported that the Fe_2O_3–CeO_2 catalyst [80] was confirmed to have very good activity and stability after 75 min at pH 3.0 and temperature 45 °C in an Oxygen atmosphere and in these conditions, the Fenton-like reaction achieved complete SMR conversion. The main active species of the reaction were surface-bound OH radicals. In the Fenton-like method, OVs on the surface of the Fe_2O_3–CeO_2 catalyst highly improved the formation of OH under the atmosphere of O_2. Huo et al. [81] developed *Z*-scheme α-Fe_2O_3/MIL-101(Cr) hybrid materials for the treatment of wastewater under the irradiation of UV–VIS light. They reported the degradation of carbamazepine from contaminated water. They prepared the *Z*-scheme α-Fe_2O_3/MIL-101(Cr) structure via hydrothermal method. The experimental data indicated that the carbamazepine was completely adsorbed from contaminated water after 180 min irradiation over the optimum α-Fe_2O_3 (0.3)/MIL-101(Cr) hybrid.

Yan et al. studied the treatment of wastewater by removing nitrobenzene from aqueous solution. The degradation of nitrobenzene was done by preparing Si-doped α-Fe_2O_3 nanocomposites [82]. The adsorption experiment suggested that pH of the solution is 6.5. They reported best Si/Fe ratio of Si-doped α-Fe_2O_3 catalyst was 0.5 in present and suggested that a heavy dose of Si-doped α-Fe_2O_3 makes high removal of nitrobenzene. Gao et al. [83] studied degradation of phenol from wastewater by using magnetic Fe_2O_3–ZrO_2. They synthesized the nanocomposite by sol–gel method. Hydroxyl and superoxide radicals were generated by the Fe_2O_3–ZrO_2 photocatalyst they reported. In the heterogeneous system, complete phenol conversion and 56% TOC removal were attained after 210 min at 60 °C at neutral pH. Wang et al. investigated the degradation of 4-chlorophenol and 4-nitrophenol for the treatment of wastewater. They prepared the nanocomposite oleophilic Fe_2O_3/polystyrene fibers [84] via electrospinning and γ-Ray irradiation methods. The photocatalytic degradation of 4-CP and 4-NP were stated to be 80 and 75% in the 6th cycling and the composite fiber showed the batter recyclability of about 90%. Salih et al. [85] prepared the hematite (α-Fe_2O_3) nanocomposite by a modified method i.e., solution combustion and applied for the degradation of pollutants present in petroleum refinery wastewater using hematite (α-Fe_2O_3) and reported the biodegradability rate of BOD/COD was increased from 0.074 to 0.604. The removal rate was observed to be 90.85% for 90 min at a catalyst concentration of 5 gL^{-1}, pH of 7.5, and H_2O_2/COD ratio of 1 mg g^{-1} (Table 12.1).

Table 12.1 Removal capacity of different materials

Materials	Organic contaminant	Process of removal	pH	Maximum removal capacity	Author
Peroxymonosulfate activated CuS/Fe_2O_3/Mn_2O_3 Magnetic nanocomposite	Ciprofloxacin	Degradation	5.8	88%	[66]
α-Fe_2O_3/$Cu_2O(SO_4)$ composite	Orange II	Degradation	3.5	98.9%	[43]
Maghemite nanoparticles (γ-Fe_2O_3-NPs)	Textile and tanning wastewater effluents	Degradation	–	89.4%	[86]
Polyethersulfone-maghemite (PES/γ-Fe_2O_3) composite membranes	Oil–water mixtures	Self-cleaning and anti-fouling	–	81.7%	[13]
Fe_2O_3/Mn_2O_3	Organic dyes	Photodegradation	–	80–97%	[59]
A three-dimensional electrochemical oxidation system with a—Fe_2O_3/PAC	Ammonium nitrogen	Degradation	–	95.30%	[87]
Fe_2O_3/biochar	Nonsteroidal Anti-inflammatory Drugs (NSAIDs) (salicylic acid, naproxen, and ketoprofen)	Adsorption	3.2	Salicylic acid (99.52%), Naproxen (95.86%), and Ketoprofen (93.45%)	[68]
Haematite α-Fe_2O_3	Pollutants present in Petroleum refinery	Photocatalytic degradation	–	90.85%	[85]
MgO/α-Fe_2O_3 Nanocomposite	Methylene Blue	Degradation	12	91.7%	[45]
Fe_2O_3/TiO_2 functionalized biochar	Dye	Degradation	6	65%	[60]
Novel α-Fe_2O_3/MXene nanocomposite	Salicylic acid	Degradation	7.4	97%	[69]
α-Fe_2O_3/graphene	RhB	Degradation	–	~ 98%	[30]
Hierarchically structured γ-Fe_2O_3-PPy	Cationic dye	Adsorption	11	98%	[62]
Polyacrylamide-g-chitosan γ-Fe_2O_3 nanocomposite	Malachite green	Filtration	–	73%	[54]

(continued)

Table 12.1 (continued)

Materials	Organic contaminant	Process of removal	pH	Maximum removal capacity	Author
Fenton-like system of Fe_2O_3 and $NaHSO_3$	Orange II	Degradation	5	90%	[88]
$Fe_2O_3/WO_3/FeWO_4$	Methyl orange	Photocatalytic degradation	–	98%	[50]
Persulfate activated with magnetic γ-Fe_2O_3/CeO_2 catalyst	Tetracycline	Degradation	3–9	84%	[70]
Fe_2O_3	Anionic dye	Adsorption	3		[89]
Magnetic montmorillonite composite γ-Fe_2O_3@Mt	Rhodamine B dye	Adsorption	5.5		[12]
Fe_2O_3/MCM-41	Methyl orange	Degradation			[51]
Mesoporous magnetic Fe_2O_3/g-C3N4 monoliths	Rhodamine B	Degradation	7	94.7%	[52]
Mg doped CuO-Fe_2O_3 composites	Organic pollutants	Degradation	3–11	84.36%	[11]
γ-Fe_2O_3@BC	Norfloxacin	Adsorption	3–5	61.43%	[10]
Mn_3O_4–FeS_2/Fe_2O_3	Orange II	Degradation	2.8	99.0%	[90]
Magnetic flower-like TiO_2/Fe_2O_3 core–shell	Paracetamol	Photocatalytic degradation		100%	[73]
O-carboxymethyl-Nlaurylchitosan/ γ-Fe_2O_3	Ibuprofen	Adsorption	7	99%	[74]
Magnetic Fe_2O_3–ZrO_2	Phenol	Degradation	7	56%	[83]
Fe_2O_3 nano sheet	Malachite green	Degradation		99.9%	[55]
$Ag/TiO_2/Fe_2O_3$	Confectionery wastewater	Degradation	4.68	9.24%	[75]

(continued)

Table 12.1 (continued)

Materials	Organic contaminant	Process of removal	pH	Maximum removal capacity	Author
α-Fe_2O_3	Congo red (CR), methyl orange (MO)	Adsorption	–	99.2 and 83.9%	[61]
ZnO/Fe_2O_3	Rhodamine B	Degradation	–	97.6	[53]
Magnetic γ-Fe_2O_3/CeO_2	Tetracycline	Degradation	3–9	84%	[70]
Fe_2O_3	COD	Electro-Fenton process	2.84	67.65	[91]
Fe@Fe_2O_3/ACF	Atrazine	Degradation	3	100	[76]
Fe@Fe_2O_3/H_2SO_4/PDMDAAC	Sludge dewatering	Degradation	2.9	78.1	[77]
Fe_2O_3/MoO_3/AgBr	Organic pollutant	Degradation	6.5	60%	[64]
Fe@Fe_2O_3	Orange II	Degradation	3	90%	[44]
Mesoporous Fe_2O_3–TiO_2	Norfloxacin	Degradation	7	60%	[72]
α-Fe_2O_3/TiO_2	Methylene Blue (MB) and Phenol (Ph)	Degradation		90% of MB and 50% of Ph	[46]
γ-Fe_2O_3/Bentonite Modified	Bisphenol A (BPA)	Adsorption	2–6	91%	[78]
α-Fe_2O_3/Carbon Nanotubes	Bismarck Brown R (BBR) Dye	Adsorption		98%	[58]
α-Fe_2O_3	Malachite green	Adsorption		86.13%	[56]
Fe_2O_3–CeO_2	Sulfamerazine	Degradation	3	100%	[80]
Ca-doped—Fe_2O_3	Organic pollutants	Degradation	3.0–10.0	91, 99 and 99%	[65]
Amorphous Fe_2O_3	Methylene blue (MB)	Adsorption		96–98%	[47]
Z-scheme α-Fe_2O_3/MIL-101(Cr) hybrid	Carbamazepine	Degradation		100%	[81]
γ-Fe_2O_3/α-MnO_2	Organic contaminant (Rhodamine B)	Adsorption	5.27	92.79%	[92]
Cu-doped Fe@Fe_2O_3	Tetracycline	Degradation	3.0–4.0	98.1%	[93]

(continued)

Table 12.1 (continued)

Materials	Organic contaminant	Process of removal	pH	Maximum removal capacity	Author
Fe_2O_3/GO/WO_3	MB and CV and phenol	Degradation		95.4% of phenol	[48]
Magnetic Nano-Fe_2O_3	Ciprofloxacin	Adsorption	8	98.85%	[67]
Fe_2O_3/graphene/CuO	Methylene blue	Degradation	1–11	78.80%	[49]
α-Fe_2O_3-DBD/g-C_3N_4	Bisphenol A	Degradation			[79]
magnetic Fe_2O_3	Lead ions	Adsorption	3	97.2%	[94]
γ-Fe_2O_3	COD	Degradation	2–8	90.94%	[57]
Fe_2O_3/TiO_2	Industrial dye and pesticide (RbX)	Degradation	3	88.71%	[63]
Oleophilic Fe_2O_3/polystyrene fibers	4-chlorophenol and 4-nitrophenol	Degradation	4.3	80 and 75%	[84]
Si-doped α-Fe_2O_3	Nitrobenzene	Degradation	6.5		[82]

12.4 Conclusion

This chapter explains the recent investigations on photocatalytic degradation of various organic as well as azo dyes. The decoration of these dye particles has been found to be very well-established due to the large surface area of iron oxide nanocomposite and its magnetic properties. To give a superior comprehension of the impact of various photocatalytic frameworks and the impact of planning methods on morphological properties for improved iron oxide execution, general data on photocatalytic corruption, a few instances of the Fenton oxidation process, and different amalgamation courses of various morphologies of iron oxide have been incorporated. To sum up, utilizing appropriate help materials, a very scattered photocatalyst with a high surface region, abundant dynamic destinations, and better contamination particle adsorption could be understood. Moreover, acquiring a useful old-style heterojunction or *Z*-plot heterojunction requires a cautious choice of a semiconductor photocatalyst with a sufficient band hole to be combined with iron oxide. The expanded reaping of noticeable light because of diminished band holes decreased charge recombination, and more successful charge transporter partitions show that both heterojunctions were well planned. However, it's actually quite important that there are still a large number of associated concerns and examination chances to be investigated in the future. To the best of our knowledge, there hasn't been any exploration of surface imperfections like oxygen opportunities and metal blemishes for further developing Fe_2O_3 performance. Several studies have been distributed to date on the examination of deformity areas for adjusting the band hole while supporting charge division and, in this manner, helping photocatalytic performance. Both metal deformities and oxygen opening can change the electronic band structure by shaping mid-hole states beneath the CB, modifying the band hole energy for apparent light gathering and charge transporter detachment at the same time. Several methods have been accounted for producing imperfection locales, including warming under vacuum or at high temperatures, illuminating with UV, lessening treatment, plasma-treating, and so on. Furthermore, the expansion of an alternate valence-state metal dopant would bring about the development of surface defects. In different examinations, oxygen openings and metal imperfections were made on the outer layer of photocatalysts through a self-doping strategy without the utilization of any impurity materials, and disorganized layers were created.

References

1. Tornero V, Hanke G (2016) Chemical contaminants entering the marine environment from sea-based sources: a review with a focus on European seas. Mar Pollut Bull 112(1–2):17–38
2. León O, Muñoz-Bonilla A, Soto D, Pérez D, Rangel M, Colina M, Fernández-García M (2018) Removal of anionic and cationic dyes with bioadsorbent oxidized chitosans. Carbohydr Polym 194:375–383

3. Mohd Adnan MA, Muhd Julkapli N, Amir MNI, Maamor A (2019) Effect on different TiO_2 photocatalyst supports on photodecolorization of synthetic dyes: a review. Int J Environ Sci Technol 16(1):547–566
4. Pavithra KG, Jaikumar V (2019) Removal of colorants from wastewater: a review on sources and treatment strategies. J Ind Eng Chem 75:1–19
5. Cinperi NC, Ozturk E, Yigit NO, Kitis M (2019) Treatment of woolen textile wastewater using membrane bioreactor, nanofiltration and reverse osmosis for reuse in production processes. J Clean Product 223:837–848
6. Jusoh NWC, Jalil AA, Triwahyono S, Setiabudi HD, Sapawe N, Satar MAH, Karim AH, Kamarudin NHN, Jusoh R, Jaafar NF, Salamun N, Efendi J (2013) Sequential desilication-isomorphous substitution route to prepare mesostructured silica nanoparticles loaded with ZnO and their photocatalytic activity. Appl Catal A Gen 468:276–287
7. Brillas E, Martínez-Huitle CA (2015) Decontamination of wastewaters containing synthetic organic dyes by electrochemical methods: an updated review. Appl Catal B Environ 166:603–643
8. Bhattacharyya S, Das P, Datta S (2019) Removal of ranitidine from pharmaceutical waste water using activated carbon (AC) prepared from waste lemon peel. In: Ghosh SK (ed) Waste water recycling management. Springer, New York, pp 123–142
9. Wen B, Li J, Lin Y, Liu X, Fu J, Miao H, Zhang Q (2011) A novel preparation method for γ-Fe_2O_3 nanoparticles and their characterization. Mater Chem Phys 128(1–2):35–38
10. Wang J, Zhang M, Zhou R, Li J, Zhao W, Zhou J (2020) Adsorption characteristics and mechanism of norfloxacin in water by γ-Fe_2O_3@BC. Water Sci Technol 82(2):242–254
11. Sun M, Lei Y, Cheng H, Ma J, Qin Y, Kong Y, Komarneni S (2020) Mg doped CuO–Fe_2O_3 composites activated by persulfate as highly active heterogeneous catalysts for the degradation of organic pollutants. J Alloys Comp 825:154036–154047
12. Ouachtak H, El Haouti R, El Guerdaoui A, Haounati R, Amaterz E, Addi AA, Akbal F, Taha ML (2020) Experimental and molecular dynamics simulation study on the adsorption of Rhodamine B dye on magnetic montmorillonite composite γ-Fe_2O_3@Mt. J Mol Liquids 309:113142–113160
13. Ouda M, Ibrahim Y, Banat F, Hasan SW (2020) Oily wastewater treatment via phase-inverted polyethersulfone-maghemite (PES/γ-Fe_2O_3) composite membranes. J Water Process Eng 37:101545–101555
14. Lai X, Guo R, Xiao H, Lan J, Jiang S, Cui C, Ren E (2019) Rapid microwave-assisted bio-synthesized silver/dandelion catalyst with superior catalytic performance for dyes degradation. J Hazard Mater 371:506–512
15. Jalil AA, Satar MAH, Triwahyono S, Setiabudi HD, Kamarudin NHN, Jaafar NF, Sapawe N, Ahamad R (2013) Tailoring the current density to enhance photocatalytic activity of CuO/HY for decolorization of malachite green. J Electroanal Chem 701:50–58
16. Chen X, Ji D, Wang X, Zang L (2017) Review on Nano zerovalent Iron (nZVI): from modification to environmental applications. In: IOP conference series on earth environment science, p 12004
17. Grégorio C, Eric L (2019) Advantages and disadvantages of techniques used for wastewater treatment. Environ Chem Lett 17:145–155
18. Lei C, Pi M, Jiang C, Cheng B, Yu J (2017) Synthesis of hierarchical porous zinc oxide (ZnO) microspheres with highly efficient adsorption of Congo red. J Colloid Interface Sci 490:242–251
19. Chen Y, Liu Y, Li Y, Wu Y, Chen Y, Liu Y, Zhang J, Xu F, Li M, Li L (2020) Synthesis, application and mechanisms of Ferro-Manganese binary oxide in water remediation: a review. Chem Eng J 388:124313–124327
20. Zhang F, Chen X, Wu F, Ji Y (2016) High adsorption capability and selectivity of ZnO nanoparticles for dye removal. Colloids Surf A Physicochem Eng Aspects 509:474–483
21. Zhang S, Li B, Wang X, Zhao G, Hu B, Lu Z, Wen T, Chen J, Wang X (2020) Recent developments of two-dimensional graphene-based composites in visible-light photocatalysis for eliminating persistent organic pollutants from wastewater. Chem Eng J 390:124642–124654

22. Bharathi D, Ranjithkumar R, Chandarshekar B, Bhuvaneshwari V (2019) Preparation of chitosan coated zinc oxide nanocomposite for enhanced antibacterial and photocatalytic activity: as a bionanocomposite. Int J Biol Macromol 129:989–996
23. Tao Q, Bi J, Huang X, Wei R, Wang T, Zhou Y, Hao H (2021) Fabrication, application, optimization and working mechanism of Fe_2O_3 and its composites for contaminants elimination from wastewater. Chemosphere 263:127889–127909
24. Kataria N, Garg VK (2018) Green synthesis of Fe_3O_4 nanoparticles loaded sawdust carbon for cadmium(II) removal from water: regeneration and mechanism. Chemosphere 208:818–828
25. Mosleh S, Rahimi MR, Ghaedi M, Dashtian K, Hajati S, Wang S (2017) Ag_3PO_4/AgBr/Ag-HKUST-1-MOF composites as novel blue LED light active photocatalyst for enhanced degradation of ternary mixture of dyes in a rotating packed bed reactor. Chem Eng Process Process Intens 114:24–38
26. Chauhan AK, Kataria N, Garg VK (2020) Green fabrication of ZnO nanoparticles using *Eucalyptus* spp. leaves extract and their application in wastewater remediation. Chemosphere 247:125803–125815
27. Yuan X, Zhou C, Jin Y, Jing Q, Yang Y, Shen X, Tang Q, Mu Y, Du AK (2016) Facile synthesis of 3D porous thermally exfoliated g-C_3N_4 nanosheet with enhanced photocatalytic degradation of organic dye. J Colloid Interface Sci 468:211–219
28. Li R, Jia Y, Bu N, Wu J, Zhen Q (2015) Photocatalytic degradation of methyl blue using Fe_2O_3/TiO_2 composite ceramics. J Alloys Comp 643:88–93
29. Pang Y, Li Z, Jiao X, Chen D, Li C (2020) Metal-organic framework derived porous α-Fe_2O_3/C nano-shuttles for enhanced visible-light photocatalysis. ChemistrySelect 5(3):1047–1053
30. Frindy S, Sillanpää M (2020) Synthesis and application of novel α-Fe_2O_3/graphene for visible-light enhanced photocatalytic degradation of RhB. Mater Des 188:108461–108473
31. Zhang H, Wei X, Liu L, Zhang Q, Jiang W (2019) The role of positively charged sites in the interaction between model cell membranes and γ-Fe_2O_3 NPs. Sci Total Environ 673:414–423
32. Sehlleier YH, Hardt S, Schulz C, Wiggers H (2016) A novel magnetically-separable porous iron-oxide nanocomposite as an adsorbent for methylene blue (MB) dye. J Environ Chem Eng 4(4):3779–3787
33. Othman NH, Alias NH, Shahruddin MZ, Abu Bakar NF, Nik Him NR, Lau WJ (2018) Adsorption kinetics of methylene blue dyes onto magnetic graphene oxide. J Environ Chem Eng 6(2):2803–2811
34. Amer R, Hadi H (2022) Application of CTAB-coated magnetic nanoparticles for solid-phase extraction of thiamine hydrochloride from pharmaceutical formulations and urine samples. Arab J Sci Eng 47:429–440
35. Kanwal A, Bhatti HN, Iqbal M, Noreen S (2017) Basic dye adsorption onto clay/$MnFe_2O_4$ composite: a mechanistic study. Water Environ Res 89(4):301–311
36. Ianoş R, Păcurariu C, Muntean SG, Muntean E, Nistor MA, Nižňanský D (2018) Combustion synthesis of iron oxide/carbon nanocomposites, efficient adsorbents for anionic and cationic dyes removal from wastewaters. J Alloys Compd 741:1235–1246
37. Lilhare S, Mathew SB, Singh AK, Carabineiro SAC (2021) Calcium alginate beads with entrapped iron oxide magnetic nanoparticles functionalized with methionine—a versatile adsorbent for arsenic removal. Nanomaterials 11(5):1345–1355
38. Ge YL, Zhang YF, Yang Y, Xie S, Liu Y, Maruyama T, Deng ZY, Zhao X (2019) Enhanced adsorption and catalytic degradation of organic dyes by nanometer iron oxide anchored to single-wall carbon nanotubes. Appl Surf Sci 488:813–826
39. Samrot AV, Ali HH, Selvarani J, Faradjeva E, Kumar S (2021) Adsorption efficiency of chemically synthesized superparamagnetic iron oxide nanoparticles (SPIONs) on crystal violet dye. Curr Res Green Sustain Chem 4:100066–100080
40. Rajabi M, Mahanpoor K, Moradi O (2019) Preparation of PMMA/GO and PMMA/GO-Fe_3O_4 nanocomposites for malachite green dye adsorption: kinetic and thermodynamic studies. Compos B Eng 167:544–555
41. Qiu Y, Xu X, Xu Z, Liang J, Yu Y, Cao X (2020) Contribution of different iron species in the iron-biochar composites to sorption and degradation of two dyes with varying properties. Chem Eng J 389:124471–124483

42. Kausar A, Bhatti HN, Iqbal M, Ashraf A (2017) Batch versus column modes for the adsorption of radioactive metal onto rice husk waste: conditions optimization through response surface methodology. Water Sci Technol 76(5):1035–1043
43. Guo X, Xu Y, Zha F, Tang X, Tian H (2020) α-Fe_2O_3/$Cu_2O(SO_4)$ composite as a novel and efficient heterogeneous catalyst for photo-Fenton removal of Orange II. Appl Surf Sci 530:1–11
44. Yang Y, Sun M, Zhou J, Ma J, Komarneni S (2020) Degradation of orange II by Fe@Fe_2O_3 core shell nanomaterials assisted by $NaHSO_3$. Chemosphere 244:125588–125600
45. Allawi F, Juda AM, Radhi SW (2020) Photocatalytic degradation of methylene blue over MgO/α-Fe_2O_3 nano composite prepared by a hydrothermal method. In: AIP conference on the proceedigns, pp 030020–030037
46. Bouziani A, Park J, Ozturk A (2020) Synthesis of α-Fe_2O_3/TiO_2 heterogeneous composites by the sol–gel process and their photocatalytic activity. J Photochem Photobiol A Chem 400:112718–112732
47. Hojamberdiev M, Kadirova ZC, Daminova SS, Yubuta K, Razavi-Khosroshahi H, Sharipov KT, Miyauchi M, Teshima K, Hasegawa M (2019) Amorphous Fe_2O_3 nanoparticles embedded into hypercrosslinked porous polymeric matrix for designing an easily separable and recyclable photocatalytic system. Appl Surf Sci 466:837–846
48. Mohamed HH (2019) Rationally designed Fe_2O_3/GO/WO3 Z-scheme photocatalyst for enhanced solar light photocatalytic water remediation. J Photochem Photobiol A Chem 378:74–84
49. Nuengmatcha P, Porrawatkul P, Chanthai S, Sricharoen P, Limchoowong N (2019) Enhanced photocatalytic degradation of methylene blue using Fe_2O_3/graphene/CuO nanocomposites under visible light. J Environ Chem Eng 7(6):103438–103458
50. Narendhran S, Shakila PB, Manikandan M, Vinoth V, Rajiv P (2020) Spectroscopic investigation on photocatalytic degradation of methyl orange using Fe_2O_3/WO_3/$FeWO_4$ nanomaterials. Spectrochim Acta A Molecul Biomolecul Spectrosc 232:118164–118171
51. Sidney Santana C, Freire Bonfim DP, da Cruz IH, da Silva Batista M, Fabiano DP (2021) Fe_2O_3/MCM-41 as catalysts for methyl orange degradation by Fenton-like reactions. Environ Prog Sustain Energy 40(2):1–9
52. Singh J, Basu S (2020) Synthesis of mesoporous magnetic Fe_2O_3/g-C_3N_4 monoliths for Rhodamine B removal. Microp Mesop Mater 303:110299–110307
53. Yang Y, Li X, Zhao R, Yang J, Sun Q, Chen X, Wu X (2018) The study on degradation and separation of RhB under UV light by magnetically ZnO/Fe_2O_3 nanoparticles. Phys Status Solidi A Appl Mater Sci 215(23):1–7
54. Hasan I, Bhatia D, Walia S, Singh P (2020) Removal of malachite green by polyacrylamide-g-chitosan γ-Fe_2O_3 nanocomposite-an application of central composite design. Groundwater Sustain Develop 11:100378–100390
55. Jiang D, Bin X, Liu X, Xu X, Zhang YX (2018) Double-shell Fe_2O_3 hollow box-like structure for enhanced photo-Fenton degradation of malachite green dye. J Phys Chem Solids 112:209–215
56. Dehbi A, Dehmani Y, Omari H, Lammini A, Elazhari K, Abdallaoui A (2020) Hematite iron oxide nanoparticles (α-Fe_2O_3): synthesis and modelling adsorption of malachite green. J Environ Chem Eng 8(1):103394–103410
57. Sheikholeslami Z, Kebria DY, Qaderi F (2020) Application of γ-Fe_2O_3 nanoparticles for pollution removal from water with visible light. J Molecul Liquids 299:1–10
58. Ismail AA, Ali AM, Harraz FA, Faisal M, Shoukry H, Al-Salami AE (2019) A facile synthesis of α-Fe_2O_3/carbon nanotubes and their photocatalytic and electrochemical sensing performances. Int J Electrochem Sci 14(1):15–32
59. Ghaffari Y, Gupta NK, Bae J, Kim KS (2020) One-step fabrication of Fe_2O_3/Mn_2O_3 nanocomposite for rapid photodegradation of organic dyes at neutral pH. J Molecul Liquids 315:113691–113707
60. Chen XL, Li F, Chen HY, Wang HJ, Li GG (2020) Fe_2O_3/TiO_2 functionalized biochar as a heterogeneous catalyst for dyes degradation in water under Fenton processes. J Environ Chem Eng 8(4):103905–103915

61. Liu H, Wang Z, Li H, Wang H, Yu R (2018) Controlled synthesis of silkworm cocoon-like α-Fe_2O_3 and its adsorptive properties for organic dyes and Cr(VI). Mater Res Bull 100:302–307
62. Gopal RA, Song M, Yang D, Lkhagvaa T, Chandrasekaran S, Choi D (2020) Synthesis of hierarchically structured ϒ-Fe_2O_3-PPy nanocomposite as effective adsorbent for cationic dye removal from wastewater. Environ Pollut 267:115498–115507
63. Singh J, Sharma S, Aanchal and S. Basu, (2019) Synthesis of Fe_2O_3/TiO_2 monoliths for the enhanced degradation of industrial dye and pesticide via photo-Fenton catalysis. J Photochem Photobiol A Chem 376:32–42
64. Salari H, Kohantorabi M (2020) Fabrication of novel $Fe_2O_3/MoO_3/AgBr$ nanocomposites with enhanced photocatalytic activity under visible light irradiation for organic pollutant degradation. Adv Powder Technol 31(1):493–503
65. Guo S, Wang H, Yang W, Fida H, You L, Zhou K (2020) Scalable synthesis of Ca-doped α-Fe_2O_3 with abundant oxygen vacancies for enhanced degradation of organic pollutants through peroxymonosulfate activation. Appl Catal B Environ 262:118250–118265
66. Huang Y, Chao Nengzi L, Zhang X, Gou J, Gao Y, Zhu G, Cheng Q, Cheng X (2020) Catalytic degradation of ciprofloxacin by magnetic $CuS/Fe_2O_3/Mn_2O_3$ nanocomposite activated peroxymonosulfate: Influence factors, degradation pathways and reaction mechanism. Chem Eng J 388:124274–124287
67. Mohammed AA, Atiya MA, Hussein MA (2020) Studies on membrane stability and extraction of ciprofloxacin from aqueous solution using pickering emulsion liquid membrane stabilized by magnetic nano-Fe_2O_3. Colloids Surf A Physicochem Eng Aspects 585:124044–124060
68. Anfar Z, Zbair M, Ait Ahsiane H, Jada A, El Alem N (2020) Microwave assisted green synthesis of Fe_2O_3/biochar for ultrasonic removal of nonsteroidal anti-inflammatory pharmaceuticals. RSC Adv 10(19):11371–11380
69. Ding M, Chen W, Xu H, Shen Z, Lin T, Hu K, Lu C, Xie Z (2020) Novel A-Fe_2O_3/MXene nanocomposite as heterogeneous activator of peroxymonosulfate for the degradation of salicylic acid. J Hazard Mater 382:121064–121073
70. Niu L, Zhang G, Xian G, Ren Z, Wei T, Li Q, Zhang Y, Zou Z (2021) Tetracycline degradation by persulfate activated with magnetic γ-Fe_2O_3/CeO_2 catalyst: performance, activation mechanism and degradation pathway. Sep Purif Technol 259:118156–118167
71. Shan S, Wang W, Liu D, Zhao Z, Shi W, Cui F (2020) Remarkable phosphate removal and recovery from wastewater by magnetically recyclable $La_2O_2CO_3/\gamma$-Fe_2O_3 nanocomposites. J Hazard Mater 397:122597–122609
72. García-Muñoz P, Zussblatt NP, Pliego G, Zazo JA, Fresno F, Chmelka BF, Casas JA (2019) Evaluation of photoassisted treatments for norfloxacin removal in water using mesoporous Fe_2O_3–TiO_2 materials. J Environ Manag 238:243–250
73. Abdel-Wahab AM, Al-Shirbini AS, Mohamed O, Nasr O (2017) Photocatalytic degradation of paracetamol over magnetic flower-like TiO_2/Fe_2O_3 core-shell nanostructures. J Photochem Photobiol A Chem 347:186–198
74. Chahm T, Rodrigues CA (2017) Removal of ibuprofen from aqueous solutions using O-carboxymethyl-N-laurylchitosan/γ-Fe_2O_3. Environ Nanotechnol Monit Manag 7:139–148
75. Lin YP, Mehrvar M (2018) Photocatalytic treatment of an actual confectionery wastewater using $Ag/TiO_2/Fe_2O_3$: optimization of photocatalytic reactions using surface response methodology. Catalysts 8(10):1–17
76. Ding X, Wang S, Shen W, Mu Y, Wang L, Chen H, Zhang L (2017) Fe@Fe_2O_3 promoted electrochemical mineralization of atrazine via a triazinon ring opening mechanism. Water Res 112:9–18
77. He DQ, Luo HW, Huang BC, Qian C, Yu HQ (2016) Enhanced dewatering of excess activated sludge through decomposing its extracellular polymeric substances by a Fe@Fe_2O_3-based composite conditioner. Bioresour Technol 218:526–532
78. Cao Y, Zhou G, Zhou R, Wang C, Chi B, Wang Y, Hua C, Qiu J, Jin Y, Wu S (2020) Green synthesis of reusable multifunctional γ-Fe_2O_3/bentonite modified by doped TiO_2 hollow spherical nanocomposite for removal of BPA. Sci Total Environ 708:134669–134690

79. Pan L, Cao S, Liu R, Chen H, Jiang F, Wang X (2019) Graphitic carbon nitride grown in situ on aldehyde-functionalized α-Fe_2O_3: all-solid-state Z-scheme heterojunction for remarkable improvement of photo-oxidation activity. J Colloid Interf Sci 548:284–292
80. Gao P, Chen X, Hao M, Xiao F, Yang S (2019) Oxygen vacancy enhancing the Fe_2O_3–CeO_2 catalysts in Fenton-like reaction for the sulfamerazine degradation under O_2 atmosphere. Chemosphere 228:521–527
81. Huo Q, Qi X, Li J, Liu G, Ning Y, Zhang X, Zhang B, Fu Y, Liu S (2019) Preparation of a direct Z-scheme A-Fe_2O_3/MIL-101(Cr) hybrid for degradation of carbamazepine under visible light irradiation. Appl Catal B Environ 255:117751–117762
82. Yan P, Shen J, Yuan L, Kang J, Wang B, Zhao S, Chen Z (2019) Catalytic ozonation by Si-doped A-Fe_2O_3 for the removal of nitrobenzene in aqueous solution. Separat Purif Technol 228:115766–115776
83. Gao P, Song Y, Hao M, Zhu A, Yang H, Yang S (2018) An effective and magnetic Fe_2O_3–ZrO_2 catalyst for phenol degradation under neutral pH in the heterogeneous Fenton-like reaction. Separat Purif Technol 201:238–243
84. Wang JC, Li Y, Li H, Cui ZH, Hou Y, Shi W, Jiang K, Qu L, Zhang YP (2019) A novel synthesis of oleophylic Fe_2O_3/polystyrene fibers by Γ-Ray irradiation for the enhanced photocatalysis of 4-chlorophenol and 4-nitrophenol degradation. J Hazard Mater 379:120806–120815
85. Yousif Mohamed Salih F, Sakhile K, Shaik F, Lakkimsetty NR (2020) Treatment of petroleum wastewater using synthesised haematite (α-Fe_2O_3) photocatalyst and optimisation with response surface methodology. Int J Environ Anal Chem 1:1–20
86. Fouda A, Hassan SED, Saied E, Azab MS (2021) An eco-friendly approach to textile and tannery wastewater treatment using maghemite nanoparticles (γ-Fe_2O_3-NPs) fabricated by *Penicillium expansum* strain (K–w). J Environ Chem Eng 9(1):104693–104712
87. Yuan M, Yan F, Chen Y, Luo J, Li Z (2020) A three-dimensional electrochemical oxidation system with α-Fe_2O_3/PAC as the particle electrode for ammonium nitrogen wastewater treatment. RSC Adv 10(15):8773–8779
88. Mei Y, Zeng J, Sun M, Ma J, Komarneni S (2020) A novel Fenton-like system of Fe_2O_3 and $NaHSO_3$ for Orange II degradation. Separat Purif Technol 230:115866–115872
89. Noreen S, Mustafa G, Ibrahim SM, Naz S, Iqbal M, Yaseen M, Javed T, Nisar J (2020) Iron oxide (Fe_2O_3) prepared via green route and adsorption efficiency evaluation for an anionic dye: kinetics, isotherms and thermodynamics studies. J Mater Res Technol 9(3):4206–4217
90. Xu Y, Guo X, Zha F, Tang X, Tian H (2020) Efficient photocatalytic removal of orange II by a Mn_3O_4–FeS_2/Fe_2O_3 heterogeneous catalyst. J Environ Manag 253:109695–109705
91. Davarnejad R, Azizi J (2016) Alcoholic wastewater treatment using electro-Fenton technique modified by Fe_2O_3 nanoparticles. J Environ Chem Eng 4(2):1–8
92. Li J, Guo R, Ma Q, Chao Nengzi L, Cheng X (2019) Efficient removal of organic contaminant via activation of potassium persulfate by γ-Fe_2O_3/α-MnO_2 nanocomposite. Separat Purif Technol 227:115669–115678
93. Luo T, Feng H, Tang L, Lu Y, Tang W, Chen S, Yu J, Xie Q, Ouyang X, Chen Z (2020) Efficient degradation of tetracycline by heterogeneous electro-Fenton process using Cu-doped Fe@Fe_2O_3: mechanism and degradation pathway. Chem Eng J 382:122970–122981
94. Salman HM, Mohammed AA (2019) Extraction of lead ions from aqueous solution by co-stabilization mechanisms of magnetic Fe2O3 particles and nonionic surfactants in emulsion liquid membrane. Colloids Surf A Physicochem Eng Aspects 568:301–310

Chapter 13
Iron Oxide-Based Heterogeneous Catalysts for Environmental Applications

M. Roshni, S. Anaina, and D. Jagadeesan

Abstract Heterogenous catalysts based on iron are widely used in environmental remediation reactions due to their abundance and less toxicity. The prospects of upscaling and the risks of leaching during the treatment processes are important considerations to choose iron-based materials. Particularly, various forms of iron oxides, doped forms, iron oxyhydroxides in bulk and nanoforms are increasingly used for catalysis of environmental remediation. In this chapter, we have given the overview of these minerals and general variety of their usage in environmental catalysis. The applications of these iron-based materials in environmentally important reactions such as oxidation of volatile organic compounds (VOCs) and CO, selective catalytic reduction of NO_x and Fenton reaction are described.

Keywords Iron oxides · Thermal catalysis · Photocatalysis · Photothermal catalysis · Plasma catalysis · VOC oxidation · CO oxidation · Selective catalytic reduction of NOx · Fenton process

13.1 Introduction

Iron is the fourth most abundant element on earth constituting nearly 5 wt% of the earth's crust. The most dominant forms of iron are oxyhydroxide, oxides and sulfides. It is not only an important component of the functional proteins in living systems but has been an integral part of the civilizations since the iron age [1]. Iron oxide-based materials have been used in catalysis, biomedicine, environmental

M. Roshni · S. Anaina · D. Jagadeesan (✉)
Department of Chemistry, Indian Institute of Technology Palakkad, Ahalia Integrated Campus, Kozhipara, Palakkad, Kerala 678 557, India
e-mail: d.jagadeesan@iitpkd.ac.in

D. Jagadeesan
Environmental Sciences and Sustainable Engineering Centre (ESSENCE), Indian Institute of Technology Palakkad, Ahalia Integrated Campus, Kozhipara, Palakkad, Kerala 678 557, India

H. Sahoo and J. K. Sahoo (eds.), *Iron Oxide-Based Nanocomposites and Nanoenzymes*, Nanostructure Science and Technology, https://doi.org/10.1007/978-3-031-44599-6_13

remediation and energy storage devices due to their unique chemical, thermal, optical, electronic and magnetic properties. Among the 16 available oxide forms, haematite (α-Fe_2O_3), maghemite (γ-Fe_2O_3) and magnetite (Fe_3O_4) are the most studied ones. Haematite is the most stable form, which acts as a precursor for other oxides. It is an *n*-type semiconductor with a bandgap of 2.1–2.3 eV, whereas magnetite has very low resistivity and lower bandgap of 0.1 eV. Owing to its high abundance, low toxicity, high sensitivity/activity and high corrosion resistance, haematite is most widely used. In α-Fe_2O_3, Fe^{3+} occupies two thirds of octahedral sites with oxygen in hexagonal close packed arrangements, while in Fe_3O_4, oxide ions are in cubic close packed array resulting in an inverse spinel structure with Fe^{2+} in half of octahedral sites and Fe^{3+} in remaining octahedral and tetrahedral sites. The second most stable oxide of iron is γ-Fe_2O_3, which has a cubic spinel structure, where oxygen ions are in cubic close packed array and Fe^{3+} occupies the octahedral and tetrahedral sites [2] (Fig. 13.1).

An ever-increasing population coupled with aspirations for higher living standards has a direct or indirect impact on the air quality. Natural events and anthropogenic activities also release air pollutants in significant amounts making respiratory diseases as one of the major causes for death in recent years. The management of air quality is a perennial challenge that not only requires strict enforcement of policy level decisions but also development and deployment of new and efficient technologies to continuously monitor and curb it at the source. As clean air is an absolute necessity for a healthy living, the necessity to mitigate contaminants from the air has assumed enormous significance in recent decades. VOCs, CO, NO_x and particulate matter arising from the combustion of fossil fuels by stationary and mobile sources are major pollutants that must be mitigated. CO is not only a toxic gas upon inhalation but also aids in the formation of ground level ozone, which leads to severe environmental pollution. Similarly, brownish nitrogen oxides are also poisonous and affect respiratory system. Along with VOCs, NO_x creates photochemical smog during hot summer. The reaction between VOC and NO_x occurs in the presence of sunlight producing brownish haze. In the recent years, air pollution has significantly increased even indoors. In developing countries, indoor air pollution has outgrown outdoor pollution such that it causes 2 million deaths every year [3]. Indoor air contains particulate matter and VOCs, which originates from construction materials, cooking, furniture and different packing materials, which are considered as serious air pollutants. Different government agencies have their own measures and policies to

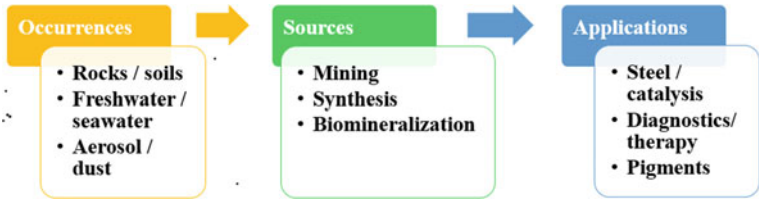

Fig. 13.1 Occurrence, sources and general applications of iron oxide [1]

reduce and mitigate gaseous emissions. For mitigating the emissions, thermal incineration systems or catalytic systems can be used. Catalytic systems are more preferred over incineration because of low energy demand. Lots of research worldwide are trying to develop an efficient thermal/photo/plasma/electrocatalytic system, which can mitigate air pollutants at the ambient conditions. Iron-based catalytic materials have successfully found their way to play a reliable role in the technologies to purify the polluted environment.

Brief Introduction to Catalytic Process

According to IUPAC, a catalyst is a substance that increases the rate of a reaction without altering the standard Gibbs energy change of a reaction. Catalysis can be of two types depending on the phase in which reactants and catalyst exists. If both reactant and catalyst exist in different phases, catalysis is known as heterogeneous catalysis. If not, it is homogenous catalysis. Most of the industrial processes are heterogeneous catalysis, which in general contains catalysts in solid phase and reactant in gas or liquid phase. Heterogeneous catalysts are more robust over a range of harsh reaction conditions. They are also separable making them prepared over homogeneous catalyst. The steps involved are adsorption, surface reaction and termination. Adsorption can be physisorption or chemisorption depending on the energetics of interaction between catalysts and reactant molecule. Physisorption is uneventful as far as reactions are concerned. Chemisorption of intermediate strength has relevance to catalysis.

On the surface of the catalyst, there are certain regions known as active sites, which directly participate in the reaction. They are usually under-coordinated surface atoms or defects, which can satisfy their coordination by bonding with the reactant molecule. This step is normally understood as chemisorption and invariably causes the activation of certain bonds on the reactant molecule. Activation of a molecule is understood in terms of weakening (or elongation) of the bonds that eventually breaks and combines with other reactants or surface adsorbed species to form new intermediates or products. Desorption of the newly formed product and regeneration of the active sites are crucial parts to complete a catalytic cycle. According to Sabatier's principle, the energy of interaction between the catalytic surface (adsorbent) and reactant (adsorbate) should be optimum for an eventful chemical reaction [4]. Number and nature of the active sites are critical parameters in evaluating catalytic performances, which are indicated by turn over numbers or frequency and selectivity of products. Catalysts are developed based on deep understanding of the chemical processes involved in the synthesis of the catalyst structure of active sites and energetics of the surface chemical reactions leading to products. Catalytic activity is also often found to be directly proportional to the surface area [5]. The process of heterogeneous catalysis relies on the adsorbate-adsorbent interactions, catalyst surface morphology, size of the particles, defects, etc.

Catalytic Oxidation Technology

In general, catalytic oxidation follows four steps. The first step is the adsorption step, where the reactant molecules (VOC/CO_x/NO_x) and oxygen adsorb onto the

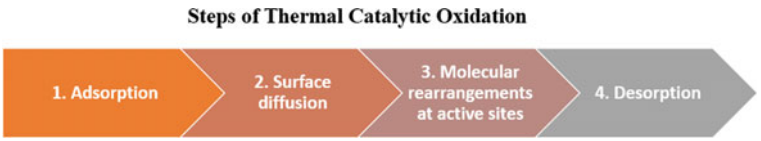

Fig. 13.2 Steps of thermal catalytic oxidation [6]

active sites of the catalyst. The second step involves the surface diffusion of atoms to adjacent adsorption/active sites. Molecular rearrangements or the reaction between oxygen and reactant molecule occur in the third step resulting in the oxidation products of the original reactant molecule. The last step is desorption of the products of the reaction from the surface of the catalyst [6] (Fig. 13.2).

There are three kinetic models proposed to explain the mechanisms of catalytic VOC oxidation. They are:

a. Langmuir–Hinshelwood (L–H) Mechanism: L–H mechanism proposes that both oxygen and the other reactant (e.g., VOCs) are adsorbed on to the surface and react to form the products (e.g., carbon dioxide and water). The rate determining step is the step in which reaction occurs between adsorbed oxygen and adsorbed reactant molecules. It can be of two types, single site and dual site based on same or different active site at which oxygen and reactant got absorbed.
b. Eley–Rideal (E–R) Mechanism: Either oxygen or reactant gets adsorbed onto the surface, which reacts with the molecule present in the atmosphere. So, the reaction occurs between either the adsorbed oxygen with reactants in air or between adsorbed reactants and oxygen in air which is the slowest step and hence the rate determining step.
c. Mars van Krevalan (MVK) Mechanism: According to the model, the reaction is triggered by the interaction of reactants and surface lattice oxygen in two consecutive steps. In the first step, the surface oxygen sites get reduced by reacting with reactant molecule and these sites will be regenerated either by the consumption of gaseous oxygen or by transfer of bulk oxygen to the surface in the second step [7] (Fig. 13.3).

Types of Catalysis Using Iron Oxides and General Materials Consideration

Depending on the nature of energy inputs, the reactive species might be different which can open a new reaction pathway on the surface of the catalyst. In the context of environmental catalysis, following types of catalytic reactions are known.

a. Photocatalysis: Photocatalysis is a catalytic oxidation of VOCs/NO_x/CO using a catalyst and light energy, particularly the visible region of the sunlight. Photocatalysts are mainly semiconductor nanoparticles with a specific band gap suitable enough to produce high energy excitons (photo-induced electron–hole pair) when light is shined on them. Absorption edge (λ_g) is related to the band gap (E_g) of the photocatalyst ($\lambda_g = 1240/E_g$). The photo-generated excitons can then produce reactive radicals, which can react with reactants such as VOCs to completely

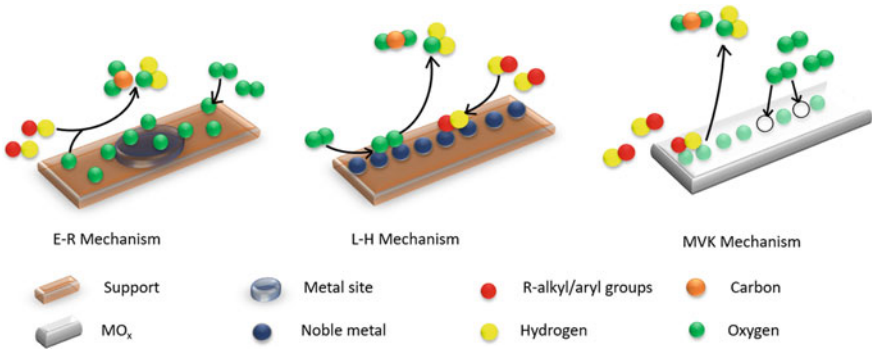

Fig. 13.3 Different mechanisms of thermal catalytic oxidation. Adapted from ref [7] with permission from Elsevier

oxidize them. Mitigation of reactants by photocatalysis is dependent on the quantity of photon flux available. On the other hand, deactivation of the catalysts is caused by surface contamination or aggregation of active sites. Photocatalysts are poised to treat the indoor pollution effectively when used in combination with construction materials such as window glasses, whereby visible spectrum of the sunlight or indoor light source can be utilized. A photocatalyst material that can efficiently utilize visible light without undergoing photo-induced damage is a challenge [8, 9].

b. Photothermal catalysis: Thermo-catalytic oxidation of reactants such as VOCs consumes relatively less energy compared to thermal oxidation. For the conventional photocatalysis, utilization efficiency of solar energy is small even after modification of the catalysts. In photo-thermo-catalysis, both thermal and photo processes are combined, whereby catalytic efficiency and durability of thermo-catalysis combined with low energy utilization of photocatalysis are expected to coexist. The thermal effects of vis-IR are utilized in photocatalysis to increase reaction efficiency or a broad range of solar spectrum is explored which simultaneously induces thermochemical and photochemical processes which synergistically catalyze the reaction [10] (Fig. 13.4).

It can be divided into two types based on the reaction pathway:

Photo-assisted thermal catalysis: Photothermal conversion can be defined as the conversion of sunlight into heat energy by collection and absorption system. Generally, there are three kinds of materials which can be used such as narrow band gap photocatalysts that can be excited by IR light, visible/near-IR plasmonic photocatalysts which carry out photochemical reactions by using plasmonic hot electrons, defective materials which can handle both light and heat like non-plasmonic oxide materials. Graphene is one of the materials which shows photothermal activity and some materials such as Mn-based catalysts doped with Fe, Cu and Mg [12]. Surface plasmon resonance effect is another process by which noble metals (Au, Ag and Pt)

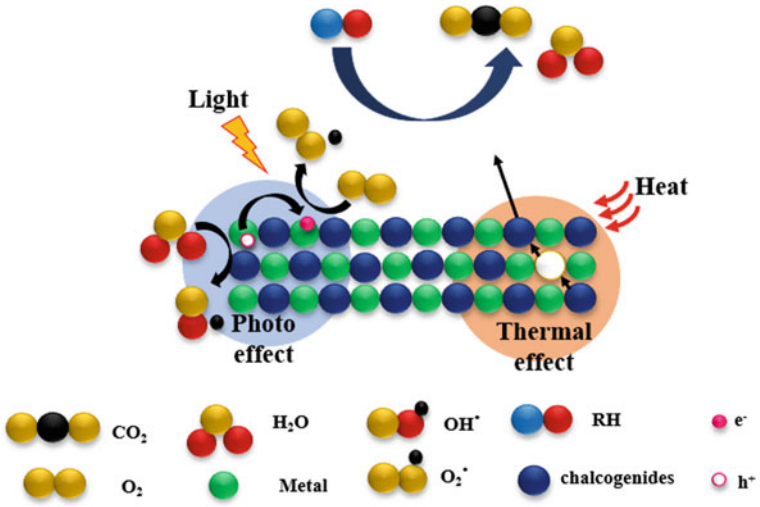

Fig. 13.4 Diagram representing photo-thermal catalysis Adapted from ref [11] with permission from Wiley VCH GmbH

absorb light and scatter it. Incorporating these metals into the catalyst will improve light harvesting ability hence the photo-thermo catalytic activity.

Photo-thermal synergistic catalysis: The advantages of both thermal catalysis and photocatalysis are combined to have the synergistic effect, which enhances the catalytic performance. A semiconductor material with narrow band gap usually shows excellent performance [13].

c. Plasma catalysis: When a gas is exposed to an electric field of desired magnitude, it will get ionized to ions and electrons. The partially ionized gas with electrons, ions and neutral species interacts with each other giving rise to reactive environment called plasma. In plasma catalysis, both plasma and catalyst enhance the reaction rate independently and inter dependably. Plasma initiates a few processes on the surface such as sputtering, [14] etching [15, 16] formation of hotspots and charging. The interdependence of plasma and catalysts known as synergistic behavior, which improves energy efficiency, conversion percentile and selectivity for the reaction. At the plasma catalyst interface, plasma establishes an electric field and changes the gas composition by producing reactive species, ions, electrons and photons to the surface, whereas catalyst lowers activation energy for some reactions. At the interdependent state, plasma alters the surface morphology or work function of the catalyst and dielectric constant, or morphology of the catalyst affect energy distribution in plasma. Vibrationally excited species are important because they influence plasma surface interactions more. Generally, for a nanoparticle to be active, the requirements are size, faceting, uncoordinated surface atoms and other defects, active sites, strain, oxidation state, charge transfer, etc. During plasma catalysis, all these factors will be modified by plasma

thus effecting the catalytic activity. The requirements of a material to be tried for plasma catalysis can be summarized as having a large contact area for strong interaction and a higher dielectric constant of the catalyst. A shorter distance between plasma and catalyst facilitates the reaction of the short-lived radicals to the maximum. Most of the active catalysts are transition metals [17]. Plasma catalysis not only prevents coke formation and catalytic poisoning which are inevitable in thermal catalysis but synergism in plasma catalysis even modifies the reaction pathway (Fig. 13.5).

Synthesis of Iron Oxide-Based Catalysts

Proper identification of experimental conditions for the preparation of catalysts is extremely important for the activity of nanoparticles [2]. Iron oxide nanoparticles and nanocrystals are considered as 0 D architectures of iron oxide, used mostly for biomedical and catalytic applications. Desirable features of nanoparticles like narrow particle size distribution, good dispersion and stability can be achieved by optimizing reaction conditions like choice of iron precursor, solvent, concentration of reducing agent, pH, reaction temperature and time. Co-precipitation is often used to prepare iron oxide nanoparticles in water which involves adding a base to the precursor solution which contains Fe(II) or Fe(III) ions to promote the precipitation of ferrihydrites and subsequent dehydration generates iron oxide nanoparticles. Employing different

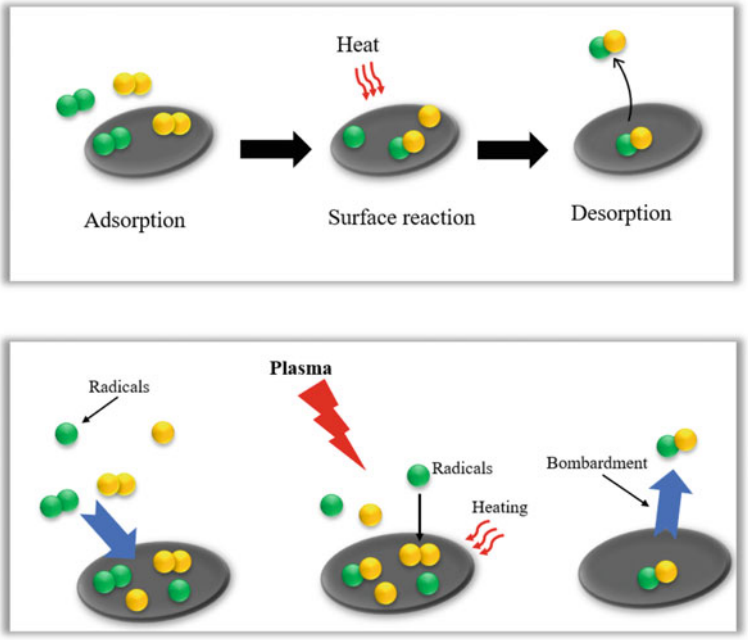

Fig. 13.5 Diagram differentiating thermal and plasma catalysis [17]

bases, ionic medium, pH and iron precursors the formation of desired phase of iron oxide can be achieved [18]. Solvothermal methods have the added advantages of being low cost, high yield and greater control over the phases and requirement of moderate temperature. In a typical solvothermal synthesis by adjusting concentrations of ferrous chloride and ratio of ethanol/water mixture, particle size can be tuned from 15 to 31 nm. Higher particle concentrations of $FeCl_2$ create more nuclei and finally to smaller particles and more the amount of ethanol in the solvent also created smaller particles by inhibiting the particle growth [19].

13.2 Catalytic Oxidation of VOCs by Iron Oxide-Based Catalysts

Air pollutants are mainly of two types: *Particulate pollutants, which can be removed by adsorption techniques,* and *Gaseous pollutants* (in sub ppm levels), which consists of VOCs as a major share. Among them, VOCs are not easily removable and their mitigation has been under the special focus for several years. The European Union defines any organic compound having an initial boiling point $\leq$ 250 °C measured at standard atmospheric pressure of 101.3 kPa as VOCs. They are acknowledged as hazardous to human health as well as to the environment mainly because of its high volatility, persistence in the environment, ability to spread over long distances from the point of release and ability to get transformed to other hazardous compounds by chemical reactions, often under normal atmospheric conditions. In India, the Clean Air Act 1990 (Amendment) and the Factory Act 1986 (Amendment) limit the emission of hazardous chemicals including VOCs [20]. Due to the current scenario of strict regulations on the concentration of VOCs in indoor as well as outdoor environment, either recovery techniques or oxidative techniques are applied. Recovery techniques involve both separation of the VOCs and particulate matter from the air followed by its recovery from the adsorbents. Adsorption, membrane separation and condensation methods come under the category of recovery techniques. Adsorption method is suitable only for dilute VOC emissions like the removal of solvent vapors in the atmosphere. Membrane separation and absorption methods are expensive because of the maintenance of the setup. Condensation is useful for VOCs with higher boiling points where the oversaturation is achieved by cooling or pressurizing the gas stream. The major disadvantage associated with these methods includes the lack of solutions to dispose of the VOCs recovered from the adsorbent. On the other hand, oxidative techniques involve the complete oxidation of the VOCs into carbon dioxide and water. Thermal incineration is a viable alternative despite being highly energy-demanding. The important disadvantage of the incineration method is the production of incompletely oxidized volatile byproducts, which invariably happens. This certainly aggravates air pollution instead of mitigating it. Hence, catalytic oxidation is a very powerful technology to completely oxidize the volatiles to relatively harmless carbon dioxide and H_2O at reasonable temperatures.

Belessi et al. carried out kinetic studies of the deep oxidation of CH_4 on oxide solids $La_{0.7}Ce_{0.3}FeO_3$, $La_{0.7}Sr_{0.3}FeO_3$, $La_{0.7}Sr_{0.1}Ce_{0.2}FeO_3$ oxide solids having mixed oxide and perovskite phases. From the kinetic analyses of the reaction rate, it is found that adsorbed oxygen in dissociative form reacted with gaseous methane, following the Eley–Rideal model. The existence of a $SrFeO_{3\pm x}$ perovskite crystal phase, which can uptake large amounts of oxygen accounts for the large value of heat of adsorption of oxygen, $\lambda_{O_2} = 53–211$ KJmol^{-1} [21].

Catalytic oxidation of VOCs by Fe-based materials using thermal, photo, photothermal, and plasma techniques is summarized in Tables 13.1, 13.2 and 13.3. Low-temperature catalytic activity is shown by Fe–Ce mixed oxides on SBA-15(Sl no 4) hence even better than supported Au catalyst (SI no 32). The higher activity can be due to the better dispersion of metal oxides over the porous structure of the material. Higher conversion with lower specific input energy (SEI = plasma power (kW)/flow rate(*L*/min)*X* 60 s/min) was shown by Fe-doped Mn octahedral sieves. Modifying defects and surface area of the catalysts by various methods improved the production of active species in plasma and oxygen mobility on the surface to enhance the mitigation efficiency of the catalysts for various VOC oxidation. Generally, iron oxides show good activity among the other oxides in the oxidation of chlorinated VOCs with the added advantages of high efficiency, low cost and environmental friendliness. Recently, studies were carried out with Fe–Mn mixed oxides for the oxidation of toluene, formaldehyde, chlorobenzene and dichlorobenzene [23, 58]. Among those, chlorinated VOCs are more important because of their contributions to the production of secondary organic aerosols, peroxyacetyl nitrate, tropospheric ozone and the greenhouse effect. Noble metal catalysts have the disadvantage of chlorinated compounds due to deactivation by HCl, Cl_2 poisoning and chlorination of products other than oxidation [22]. Ru is known to be resistant to Cl poisoning by promoting deacon reaction. It is known that supports do affect the catalytic activity by altering the crystallite dimensions and thermal stability of the metal species. Wang et al. studied the possible application of Ru doped on mesostructured Fe–Mn oxides. The mesoporous Fe–Mn bimetallic oxide with a metal atomic ratio of 1:2 was prepared by oxalate pyrolysis without any template followed by metal impregnation for doping with Ru. The XRD data did not show any active phases of Ru and no significant diffraction peaks of Mn which means that the active phase of Ru is stabilized in the mesoporous substrate by strong metal-support interactions [23]. In a recent study by Fan et al., HCHO oxidation was carried out using Fe–Ce–O catalyst supported on mesoporous silica prepared by simple impregnation-calcination resulting in the formation of small solid solution particles with good dispersion in confined spaces. CeO_2 materials are routinely investigated along with other transition metal oxides for VOC oxidation but suffer from having a low surface area and limited efficacy for low-temperature oxidation. Many methods were explored to lower the activation barrier such as doping other metal atoms and creating more oxygen vacancies. Activity achieved at a low temperature of 60 °C was associated with the presence of Fe content which along with the calcination temperature influenced the activity by increasing oxygen vacancy [25]. Xiaodong et al. tried mesoporous Ti-doped iron oxide for the degradation of ortho-dichlorobenzene. Surprisingly, the Ti-doped iron

oxide was showing better activity compared to the individual counterparts, which can be due to the presence of Ti^{4+} which had a higher affinity toward chlorinated VOCs, and iron oxide which showed a better oxidation power. It has also been proven that TiO_2 alone has a slower activity which proves the active component is iron oxide. The study mostly concentrates on regulating the composition and hence the structure of the TiO_2–Fe_2O_3 system to gain more knowledge about the interface interactions between both. It was prepared by CTAB as the structure-directing agent [22]. For example, Bismuth ferrite with a rhombohedrally distorted perovskite structure is a multiferroic compound that exhibits ferroelectricity and weak ferromagnetism above room temperature. Due to the narrow band gap energy (2.2 eV) and excellent chemical stability, these materials have applications in visible light photocatalysis. However, the electrical and multiferroic potential applications of BFO magnetic nanoparticles are hindered due to the following properties such as weak ferroelectricity, remanent polarization, high leakage current density, poor ferroelectric reliability and inhomogeneous weak magnetization. The substitution of any of the A-site and B-site had significant improvement in the multiferroic and photocatalytic properties [60].

Materials Consideration for Heterogeneous Catalysts for VOC Oxidation

If the VOC is an *N*-containing one, then there is a chance for the generation of nitrogen oxides, and if it is *S*-containing, the formation of metal sulfates is inevitable and which leads to the deactivation of catalysts. The key step for catalytic oxidation is the adsorption of the compound onto the surface of the catalyst with subsequent activation. In activating oxygenated VOCs, the abundance of OH groups on the surface plays a significant role. Introducing alkali metal salts onto the supported metal increases the concentration of –OH groups. For example, using noble metal catalysts for chlorinated VOCs has the disadvantage of easy deactivation as well as generating polychlorinated pollutants as byproducts. Even though increasing the acidity of the support decreases the selectivity toward polychlorinated byproducts, the application of noble metal catalysts for chlorinated VOCs is not advisable. Hence, selecting a catalyst also depends on the functional groups present, and in the case of a mixture of compounds, the mutual chemical interaction plays a crucial role in the choice of metal, support, precursor, preparation method, reaction conditions and catalytic reactor to be chosen. Hence, designing new catalysts which are active at low temperatures with high selectivity and low cost is critically important in practical applications.

Supported Noble Metal Catalysts (SNMCs) and Transition Metal Oxides (TMOs) are in general used as catalysts where the former have superior activity, selectivity and ease of regeneration despite being costly. So, the noble metal atoms are dispersed on a support which can be simple oxides such as silica or alumina, transition metal oxides or molecular sieves. Based on the involvement in chemical transformation, supports are classified into active or inert. Active support gets involved in catalytic oxidation, whereas inert support does not show any catalytic activity but provides surface and pore structure for the uniform dispersion of active metal catalysts. The presence of these supports not only reduces the amount of noble metal used, which is an economical advantage but also increases the dispersion of active sites thereby

Table 13.1 Catalysts for VOC oxidation by thermal catalysis

S. No.	Catalyst	VOC	T (K)	Conversion (%)	References
1	Ti-doped iron oxide	1,2-Dichlorobenzene	623	100	[22]
2	Ru-doped porous Fe–Mn oxide	Chlorobenzene	470	90	[23]
3	PtPdFe nanoparticle	Propene	383	50	[24]
4	Fe-Ce mixed oxide supported on SBA-15	Formaldehyde	333	100	[25]
5	Mn incorporated mesoporous ferrihydrite	Acetaldehyde and toluene	353	99	[26]
6	Fe zeolites	Toluene and ethanol	649 (Toluene) and 530 (Ethanol)	98	[27]
7	Ce_{1-x} $Fe_xO_{2-\delta}$	Methane	773	100	[28]
8	Iron molybdate	Methanol	503	100	[29]
9	Fe/SBA-15	Methane thiol	713	100	[30]
10	Co–Fe layered double oxide/Fe mesh	Toluene	620	90	[31]
11	$Au/FeO_x/CeO_x$	Methanol and toluene	433 (Methanol) and 583 (Toluene)	100	[32]
12	Fe/MnO_x	1-Methoxy-2-propyl acetate	533	100	[33]
13	Iron titanate	Chlorobenzene	573	100	[34]
14	Pt/Iron oxide	Xylene	498	100	[35]
15	Fe(III) intercalated titanium phosphate	Acetone, methanol and diethyl ether	483 (Acetone), 533 (Methanol), 543 (Diethyl ether)	100	[36]
16	Ferric sludge	Propane and toluene	633 (Propane) and 493 (Toluene)	100	[37]
17	MnO_2 decorated $Co_3Fe_1O_x$	Toluene	516	90	[38]
18	Iron–titanium–hafnium oxide	Ethyl acetate	700	100	[39]

(continued)

Table 13.1 (continued)

S. No.	Catalyst	VOC	T (K)	Conversion (%)	References
19	Fe-pillared montmorillonite	Toluene and chlorobenzene	673 (Toluene) and 723 (Chloro benzene)	100	[40]
20	Fe–Mn mixed oxides	Ethanol, ethyl acetate and toluene	492 (Ethanol), 518 (Ethyl acetate) and 566 (Toluene)	80	[41]
21	Iron oxide impregnated on clay	Toluene	623	100	[42]
22	$0.25Pt_1/meso\text{-}Fe_2O_3$	Benzene	471	90	[43]
23	Au/Fe_2O_3	Isopropanol, ethanol, acetone and toluene	473(Methanol), 523(Ethanol) and 473(Isopropanol)	100	[44]
24	Fe_2O_3	Chlorobenzene	673	90	[45]
25	Fe-Ti binary oxides	Ethyl acetate	725	100	[46]
26	Fe–Mn mixed metal oxides	Chlorobenzene	470	90	[47]
27	Mesoporous Fe_2O_3	Acetone and methanol	462 (Acetone) and 481 (Methanol)	90	[48]
28	MnFe mixed oxide	Ethanol and propane	493 (Ethanol) and 623 (Propane)	100	[49]
29	Co-Fe spinel oxide	Ethanol	548	100	[50]
30	$Cu_yCo_{3-y}FeO_x$	Toluene	523	100	[51]
31	Cu-oxo-Fe/silica	Toluene	723	80	[52]
32	$Au/\alpha\text{-}Fe_2O_3$	Formaldehyde	343	100	[53]
33	Iron oxide/porous clay heterostructures	Toluene	471	90	[54]
34	Fe–Mn mixed oxides	1,2-Di chlorobenzene	673	100	[55]
35	Mn–Fe binary oxides	Toluene	443	100	[56]
36	Fe/TiO_2-pillared montmorillonite	Toluene	648	100	[57]

Table 13.2 Catalysts for VOC oxidation by photo and photothermal catalysis

Sl No	Catalyst	VOC	Conversion (%)	Experimental conditions	References
1	Fe-doped MCM-41	Trichloroethylene	90	365 nm	[58]
2	Fe/TiO_2	Acetaldehyde	90	White light	[59]
3	Ba-doped $BiFeO_3$	Benzene and toluene	81% (Benzene) and 91% (Toluene)	Visible light 50 min irradiation	[60]
4	Au/Fe_2O_3	Formaldehyde	30	Blue light	[61]
5	Iron oxide micropine dendrites	Toluene	55	150W Xe lamp, 200 min irradiation	[62]
6	Mesoporous $ZnFe_2O_4$	Benzene	60	60 W tungsten lamp, 30 min irradiation	[63]
7	Fe-doped TiO_2	Acetaldehyde	100	Visible light, 500 min irradiation	[64]
8	Graphene/ Fe^{3+}–TiO_2	Formaldehyde	58	–	[65]
9	N-doped graphene/ Fe_2O_3	Acetaldehyde	55	–	[66]
10	Mesoporous amorphous Mn–Fe oxide	Benzene	90% at 287	$\lambda > 420$ nm Vis-IR and $\lambda >$ 830 nm IR irradiation	[12]

Table 13.3 Catalysts for VOC oxidation by plasma catalysis

Sl No	Catalyst	VOC	Conversion (%)	Specific input energy (J/l)	References
1	Fe_2O_3/sepiolite	Toluene	90	550	[67]
2	Fe/cordierite	Diethyl ether	95	600	[68]
3	Fe-doped manganese oxide octahedral molecular sieves	Trichloroethylene	90	130	[69]
4	$LaFeO_3$	Ethyl acetate	85	600	[70]
5	Fe_x-Mn_y/Al_2O_3	Toluene	100	1500	[71]
6	ZrMnFe/Sepiolite	Toluene	95	950	[72]

increasing the number of molecules interacting with the active site. In addition, the acid–base properties of support help in more dispersion of noble metal over the catalyst. Despite being less active, TMOs are good alternatives to SNMCs due to low cost, reducibility and thermal stability, and most importantly resistance to poisoning which is most common with noble metal catalysts. The activity of a catalyst or the reaction rate of the oxidation mainly depends on physical and chemical properties as well as the morphologies of active metal and support.

13.3 CO Oxidation

CO is a gaseous air pollutant produced due to the incomplete combustion of fuels from automobiles, industrial processes and power generation. Indoor sources include leaking chimneys, unvented kerosene and gas space heaters and gas stoves. At very high concentrations in indoor or enclosed environments, CO causes dizziness, confusion, unconsciousness or even death. CO is a colorless and odorless gas and can irreversibly bind with haemoglobin causing depletion in the oxygen levels in cells, which ultimately leads to cell death. CO is aptly described as a "silent killer". Developing an efficient catalytic oxidation system for CO is highly desired, not only because it is poisonous but its industrial significance in the synthesis of methanol and other fuel and pure hydrogen in proton membrane exchange fuel cells [73].

The state-of-the-art catalysts for CO oxidation are noble metals but their use is limited because of high cost, low abundance and poisoning. High dissociation probability, low adsorption energy due to the half-filled d-bands and low cost have made TMOs as an attractive alternative [73]. SNMCs are also actively pursued as it shows increased exposure of active sites and decreases the consumption of expensive metal component. Bimetallics of noble metals with transition metals such as Mn, Fe, Co, Ni and Cu retain the superior catalytic property of the noble metals at a lower cost. Au is the most investigated noble metal catalyst due to the presence of Lewis acid sites, ease of size and shape [2]. In SNMCs, the nature of the support plays an important role since the reaction either takes place at the interface of the metal and the oxide support or as a spillover of reactive species from or into the oxide layer. Also, semiconductor metal oxides like TiO_2, Fe_2O_3 and NiO form more stable catalysts than insulating metal oxides such as Al_2O_3 and SiO_2. The Turnover Frequency (TOF) of Au catalysts changes significantly compared to Pt with the preparation method. The table given below indicates clearly that contact structure determines activity in supported Au catalysts [74] (Table 13.4).

In general, Strong Metal Support Interaction (SMSI) can be explained as the change in catalytic reactivity of reducible oxides supported by group VIII metals after the high-temperature reduction process. Au particles supported on reducible oxides such as TiO_2, Fe_2O_3 and CeO_2 possess improved oxidation activity compared to unsupported ones. SMSI induces both electronic and geometric effects on the catalyst and it can be strong or weak. Contact at the interface induces electronic redistributions leading to the formation of a new phase at the metal-support interface

Table 13.4 Comparison of the activity of Au and Pt-supported catalysts for CO oxidation [74]

Metal	Preparation method	Diameter of the particle (nm)	$T_{50\%}$ (K)	TOF at 300 K (s^{-1})
Pt	Deposition	1.3	334	2.7×10^{-3}
	Impregnation	1.4	339	3.8×10^{-3}
	Phase distortion	2.4	363	9.2×10^{-3}
Au	Deposition	3.1	282	3.4×10^{-2}
	Deposition	2.7	253	1.2×10^{-1}
	Impregnation	10	481	–
	Phase distortion	4.6	477	9.6×10^{-6}

[75]. As a geometric effect, metals supported on reducible oxides exhibit SMSI, which is the encapsulation of metal by a thin layer from the oxide support. It is shown that Pt supported on Fe_2O_3 (111) also exhibits SMSI via encapsulation due to the strong adhesion energies between Pt and iron oxide. Pt particles heated above 800 K in a vacuum exhibit structure that is like ultrathin FeO (111) film on Pt (111) single crystal. The catalyst showed higher activity compared to Pt (111) surface which is explained due to the formation of inverted catalysts or highly dispersed FeO_x nanoparticles on the Pt (111) surface [76] (Fig. 13.6).

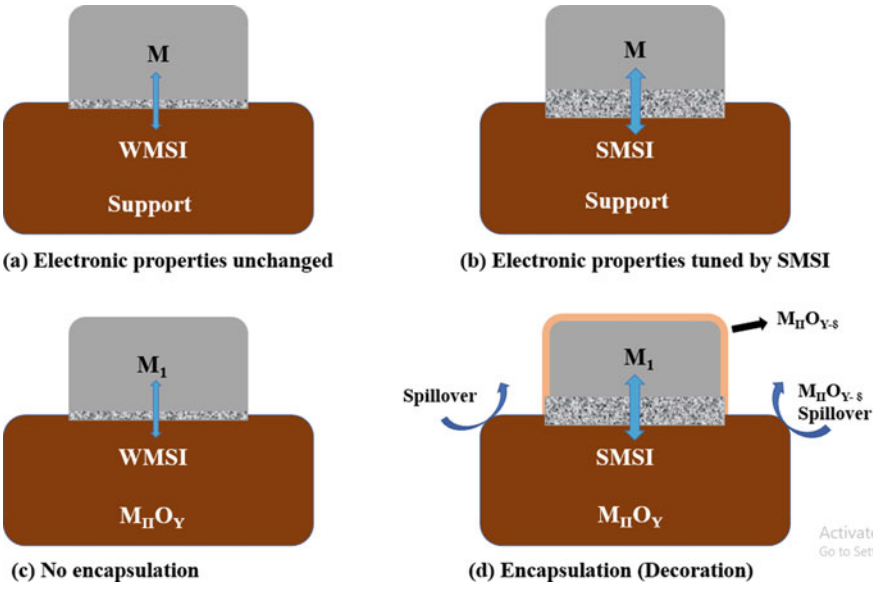

Fig. 13.6 Diagram showing electronic effects (**a**, **b**) and geometric effects (**c**, **d**) of SMSI Adapted from ref [75] with permission from Elsevier

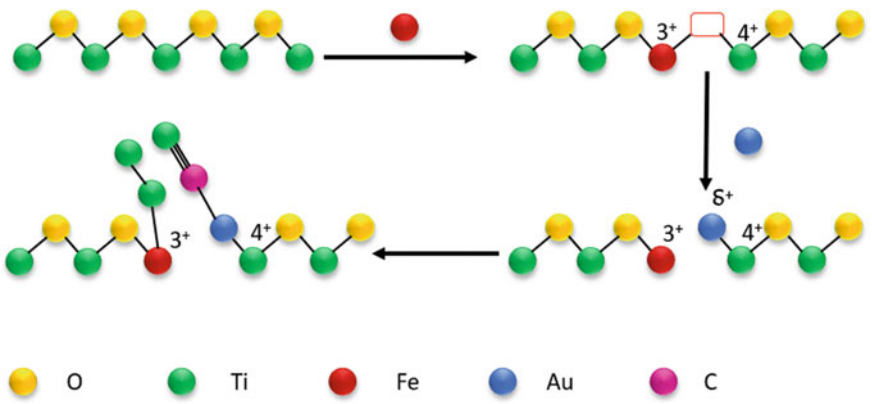

Fig. 13.7 Mechanism of CO oxidation over Fe-doped TiO_2 Adapted from ref [77] with permission from Wiley VCH GmbH

A significant number of studies on low-temperature CO oxidation catalysts are based on Au nanoparticles supported on iron oxide. Since the oxidation reaction occurs at the interface of Au nanoparticles and support, several factors like the size of the Au particle, the nature of support and the contact structure between support and Au were reported [74] to be controlling the catalytic activity. Cui et al. reported that increasing the pH value during synthesis is proportional to the catalytic activity due to stronger interaction between Au–OH–Fe or Au–Fe–O structure. They also found that calcination temperatures above 673 K eliminated surface hydroxyl groups which resulted in lower catalytic activity [2]. Oxidation of CO on iron oxides can occur in presence of oxygen and it is considered to proceed through dissociative adsorption of oxygen and removal of oxygen by CO through an Eley–Rideal mechanism [76]. Given below is a schematic representation of CO oxidation catalyzed by Au supported on Fe-doped TiO_2 which clearly indicates that Fe catalyzes the dissociation of oxygen molecules [77] (Fig. 13.7, Table 13.5).

Iron oxide-based catalysts tested for CO oxidation along with the temperature and conversion are given below as a table. Complete conversion of CO at lower temperatures is exhibited by catalysts with noble metals. Besides, the activity of the supported catalysts is in the order of Au > Pt > Pd. Particularly, among transition metal oxide catalysts, good activity was observed when iron was combined with Cu followed by Co. When iron oxide is used as the support, geometric and electronic effects of SMSI improve the catalytic activity.

Table 13.5 Comparison of activity of catalysts for CO oxidation

S. no	Catalyst	T (K)	Conversion (%)	References
1	$Ce_{1-x}Fe_xO_{2-\delta}$	673	100	[28]
2	Fe–Co mixed oxide	423	100	[78]
3	$LaFeO_3$	914	90	[79]
4	PtCu/ɣ-Fe_2O_3	298	100	[80]
5	Pt/exsolved FeOx/$LaFeO_3$	296	100	[81]
6	Au/Fe_2O_3	263	50	[82]
7	CuO/Fe_2O_3	373	100	[83]
8	10% CuO/α-Fe_2O_3 nanorods	373	100	[84]
9	Fe–Co mixed metal oxide	473	100	[85]
10	Pt/FeO_x	296	100	[86]
11	Pd/FeO_x	475	100	[87]
12	Fe_2O_3	573	100	[88]
13	CuO-doped $Fe_4Ti_{10}Sn_{10}$ composite oxides	423	100	[89]
14	Fe, Ce and Al pillared bentonite	573	100	[90]
15	Au/Fe_2O_3	398	100	[91]
16	Au/$FeTiO_2$–Fe	363	100	[92]

13.4 Selective Catalytic Reduction (SCR) of NO*x*

Nitrogen oxides (NO, NO_2, and their derivatives), in general, denoted as NO_x is a gaseous pollutant that can cause photochemical smog, acid rain and ozone depletion leading to global warming and eutrophication problems. Major sources are automobiles and other industries and there are regulations for power plants and engines regarding emissions. According to the United States Environmental Protection Agency, the NO_x emission of an engine should be within the limit of 0.02–0.10 g/bhp-hr. Amount of NO_x and VOCs is responsible for the presence of hydroxyl radicals hence the oxidizing ability of the stratosphere. In urban areas where a high concentration of NO_x is present, it controls radical production hence the oxidizing ability, and in rural areas with relatively low concentrations of NO_x VOCs control the radical production. The reaction of NO with VOCs which is responsible for the photochemical smog is shown below (Fig. 13.8).

Photochemical smog is brown in color and affects the throat, causes chest pain, the difficulty of breathing for humans, cracking of rubber and damages plant life too. Hence, reducing and mitigating NO_x is important.

SCR of NO by NH_3 is widely used for removing NO from the atmosphere. In SCR, NO_x is converted to dinitrogen and water in the presence of a catalyst as well as a reducing agent. Commonly used reducing agents are anhydrous or aqueous ammonia or urea solution which is added to the stream of gas which flows through the catalyst. Commercially used catalytic systems for SCR reactions are V_2O_5–MoO_3/TiO_2 and

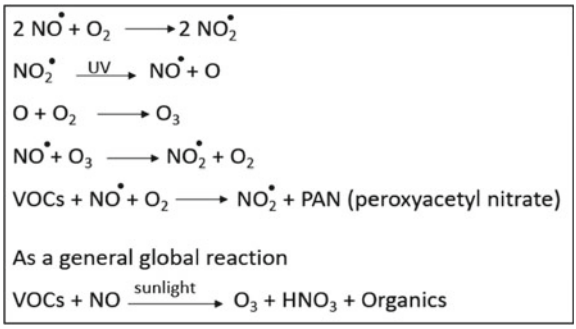

Fig. 13.8 Reaction of NO with VOCs generating photochemical smog [93]

V_2O_5–WO_3/TiO_2 [94, 95]. The commercial system has some drawbacks such as a reduction in the selectivity of N_2 in the temperature range of 573–673 K, the need to reheat the stack gas, sulfur poisoning and the toxicity of vanadium pentoxide [96–98]. TMOs are investigated the most due to the easy gain and loss of *d* electrons, low cost and stability [99]. A few Fe-based catalysts that showed good conversion in the low-temperature range were Fe–MnO_x and Fe_xTiO_y [100, 101]. Mn is explored extensively due to the variable oxidation states and redox stability hence the activity at the lowest temperature. But the drawback of Mn is with low selectivity of N_2 and sensitivity toward SO_2 in the gas flow [102–104]. Due to the environment-friendly nature and low cost, easy reducibility and mobility of active surface oxygen, iron oxides have also been explored nowadays either in combination with other transition metals or as support with other elements [100, 105]. The drawback associated with iron oxide is low surface acidity, low N_2 selectivity above 623 K and low resistance to SO_2 and H_2O.

Mechanism of SCR with NH_3

The possible mechanism for SCR of NO in presence of NH_3 catalyzed by $Mn_2O_3^-$ Doped Fe_2O_3 is shown in Fig. 13.9. Four types of species are indicated by DRIFTS spectra after the adsorption of NO on the catalyst, they are gaseous NO_2, bidentate nitrates, linear nitrites and monodentate nitrites. Adsorbed NH_4^+ ions combine with NO_2^- to form NH_4NO_2. Fe and Mn are involved in a redox cycle to continue the reaction, while NH_3 acts as the hydrogen source for the reduction. After each cycle, Fe^{3+} is regenerated by Mn^{4+}. Mn^{2+} is again oxidized by oxygen to continue the cycle of reaction.

Different catalytic systems involving iron as a dopant or support, the temperature of SCR and the percentage conversion are given in Table 13.6. Fe–Mn system is investigated the most and it shows the maximum activity at the lowest possible temperature. Activity at the lowest temperature is exhibited by porous MnO_x–FeO_x nanoneedles (Sl no 3) which can be due to the uniform distribution of the ions, availability of redox sites, porous structure and strong acidic sites. Various catalysts were tried for the NH_3-catalyzed SCR reaction. It has been observed that the modified catalyst exhibits improved activity over the commercial catalysts known and have good selectivity toward nitrogen.

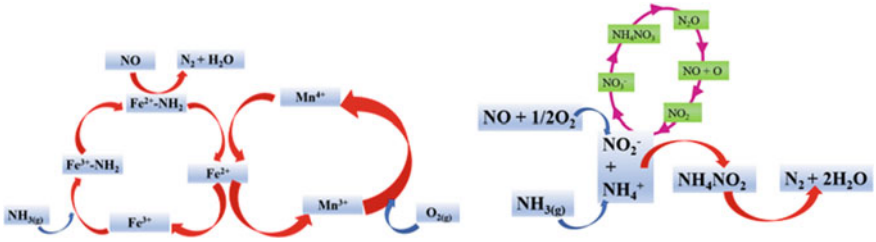

Fig. 13.9 Mechanism of SCR with NH_3 in presence of $Mn_2O_3^-$ doped Fe_2O_3 hexagonal microsheets. Adapted from ref [106, 107] with permission from Elsevier and American Chemical Society

Table 13.6 Comparison of activity of catalysts for SCR reaction

Sl No	Catalyst	T (K)	Conversion (%)	References
1	Mn_2O_3-doped Fe_2O_3 hexagonal microsheets	473	98	[106]
2	MnO_x supported on Fe–Ti spinel	448	100	[107]
3	Porous MnO_x–FeO_x nanoneedles	393	100	[108]
4	MnO_2-doped Fe_2O_3 hollow nanofibers	423	98	[109]
5	Fe–W mixed oxide	523	100	[105]
6	$MnFeO_x$ nanorods	473	98	[110]
7	Dy-doped $MnFeO_x$ nanowires	423	100	[111]
8	Co–Fe mixed oxide	443	100	[112]
9	$Fe_9Ti_1O_x$	523	80	[113]
10	WO_3–FeO_x	523	98	[114]
11	12-tungsto phosphoric acid/iron oxide	523	100	[115]
12	Mn–Fe oxides on Fe mesh	453	98	[116]
13	Fe-modified MnO_2	523	75	[117]
14	$MnFeO_x$/CNT	413	100	[118]
15	Mesoporous Mn–Fe Spinel	398	100	[119]

13.5 Fenton Reaction

The Fenton process was developed in 1894 by a French scientist Henry J Fenton who discovered that at pH 2–3, tartaric acid can be oxidized by the Fe^{2+}/H_2O_2 system. Fenton's process comes under the category of Advanced Oxidation Processes (AOP). The importance of this process is that toxic organic pollutants cannot be easily removed by conventional wastewater treatment processes and the abundant availability of resources such as iron and H_2O_2. Depending on the number of phases involved in the reaction, it can be classified into a homogenous Fenton process where only a single phase is involved and a heterogenous Fenton process where dual phases are present. The classical reaction is a homogenous Fenton process with Fe^{2+}

interacting with H_2O_2 in the solution state. In the presence of H_2O_2, which acts as an oxidizing agent, ferrous ions (Fe^{2+}) are converted to ferric ions (Fe^{3+}) (Eq. 13.1). This oxidation is the first step in Fenton's reaction. This results in the formation of a hydroxide ion (OH^-) and a hydroxyl radical (·HO) as byproducts. To continue the activation of H_2O_2, Fe^{2+} can be obtained via the reduction of Fe^{3+} by H_2O_2 (Eq. 13.2). The reduction of Fe^{3+} is very slow and generates hydroperoxyl radicals ($HO_2^{\cdot}$) which has a weaker oxidation ability than ·HO. Two different oxygen free radicals are formed when hydrogen peroxide molecules undergo disproportionation (Eq. 13.3). The produced hydroxide ions and protons combine to form water (Eq. 13.4).

$$Fe^{2+} + H_2O_2 \rightarrow Fe^{3+} + OH^- + \cdot HO \tag{13.1}$$

$$Fe^{3+} + H_2O_2 \rightarrow HO_2^{\cdot} + Fe^{2+} + H^+ \tag{13.2}$$

$$2H_2O_2 \rightarrow HO_2^{\cdot} + {}^{\cdot}HO + H_2O \tag{13.3}$$

$$Fe^{2+} + H_2O_2 + H^+ \rightarrow Fe^{3+} + {}^{\cdot}HO + H_2O \tag{13.4}$$

To improve the efficiency of the process, Fenton's process is often coupled with electro/UV/sono such as to increase the amount of ·HO and the regeneration of Fe^{2+} to Fe^{3+} [120]. Even then there are some disadvantages associated with the process. A continuous supply of H_2O_2 is required which makes the process economically non-viable and the formation of solid ferric sludge needs to be removed periodically along with the loss of iron ions. Overall, the process becomes expensive [121–123]. Increased production of reactive oxygen species was observed in hybrid systems where two of the modified Fenton process were combined like in Photo-Electro-Fenton (PEF). Even though an enhancement in activity is observed, compared with the real situation of huge amounts of wastewater reduced chemical consumption cannot be equated to electricity loss. Considering the example of the electro-Fenton process even though the process efficiency is higher, Fe is getting consumed at the anode. Recovery and reuse of iron sludge in this context may be addressed by using acid treatments and ion exchange. Ferrites thus prepared were again employed in the process.

Introducing iron in the heterogeneous solid phase has proved to be safe, efficient and cost-effective. Homogenous and heterogeneous Fenton processes differ in the fact that in heterogenous Fenton, ·HO production occurs on the surface of the catalyst, and also the reactant molecules get adsorbed on the active sites and after the reaction, they get desorbed and active sites are free for the next cycle [124, 125].

$$X - Fe^{2+} + H_2O_2 \rightarrow X - Fe^{3+} + \cdot OH + OH^- \tag{13.5}$$

$$Fe^{3+} + H_2O_2 \rightarrow X - Fe^{2+} + \cdot O_2H + H^+ \tag{13.6}$$

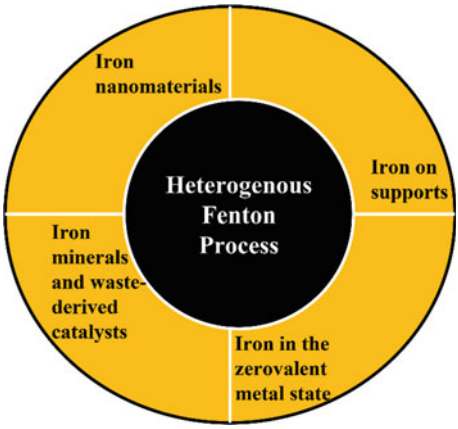

Fig. 13.10 Forms of iron catalysts employed for heterogenous Fenton process

Table 13.7 Iron-based heterogeneous catalysts used for the degradation of various pollutants

Sl No	Catalyst	Pollutant	Removal efficiency (%)	References
1	Magnetite	Reactive blue 19	87	[130]
2	Magnetite	Acid red 18	83	[131]
3	Haematite	Acid red 18	81.5	[131]
4	Iron molybdophosphate	Landfill lechate	82	[132]
5	Pd/Fe_3O_4	Humic acid	90	[133]
6	Chalcopyrite	Tetracycline	99	[134]
7	Pyrite	Levofloxacin	95	[135]

Reaction rate increases with higher surface area and porosity as usual with general catalysts are observed here too [126].

Advantages of heterogenous Fenton process [127–129] (Fig. 13.10, Table 13.7).

- Operating under a wide temperature range
- Zero formation of iron sludge hence reducing additional removal costs
- Easy handling and safe storage
- Easy recovery by sedimentation, filtration and magnetic separation

13.6 Conclusion

Mitigation of environmental pollutants by catalytic technology is one of the promising areas of research that can directly address the goals set by the UN and other international agreements. Particularly, the literature suggests that iron and iron oxide-based catalysts or supports have been extensively tested due to their intrinsic activity or promotional activity as support, high natural abundance, low cost and no

toxicity. The chapter discussed iron oxide applied in four environmentally important reactions such as VOC oxidation, CO oxidation, SCR reaction of NO_x, and Fenton reaction. After comparing the catalytic activity, it can be understood that Fe plays a significant part in improving the catalytic activity. Although the major challenges with respect to activity and selectivity remain to be addressed. It is however possible that economically viable large-scale catalytic processes are likely to contain iron in their composition.

Acknowledgements The authors thank IIT Palakkad for the infrastructure and support. The author S. Anaina 2nd year BS–MS student from IISER Berhampur worked as an intern for two months in the group of Dr. Dinesh Jagadeesan at IIT Palakkad.

References

1. Cornell RM, Schwertmann U (2003) The iron oxides: structure, properties, reactions, occurrences, and uses, vol 2. Wiley-vch, Weinheim
2. Tanaka S, Kaneti YV, Septiani NLW, Dou SX, Bando Y, Hossain SA, Kim J, Yamauchi Y (2019) A review on iron oxide-based nanoarchitectures for biomedical, energy storage, and environmental applications. Small Methods 1800512:1–44
3. Kankaria A, Nongkynrih B, Gupta SK (2014) Indoor air pollution in India: implications on health and its control. Indian J Commun Med Off Publ Indian Assoc Prevent Soc Med 39:203–207
4. Medford AJ, Vojvodic A, Hummelshøj JS, Voss J, Abild-Pedersen F, Studt F, Bligaard T, Nilsson A, Nørskov JK (2015) From the Sabatier principle to a predictive theory of transition-metal heterogeneous catalysis. J Catal 328:36–42
5. Rothenberg G (2008) Catalysis: concepts and green applications. Wiley-VCH, Weinheim
6. He C, Cheng J, Zhang X, Douthwaite M, Pattisson S, Hao Z (2019) Recent advances in the catalytic oxidation of volatile organic compounds: a review based on pollutant sorts and sources. Chem Rev 119:4471–4568
7. Zhang Z, Jiang Z, Shangguan W (2016) Low-temperature catalysis for VOCs removal in technology and application: a state-of-the-art review. Catal Today 264:270–278
8. Weon S, He F, Choi W (2019) Status and challenges in photocatalytic nanotechnology for cleaning air polluted with volatile organic compounds: visible light utilization and catalyst deactivation. Environ Sci Nano 6:3185–3214
9. Ollado L, Jansson I, Platero-Prats AE, Perez-Dieste V, Escudero C, Molins E, Doucastela LC et al (2017) Elucidating the photoredox nature of isolated iron active sites on MCM-41. ACS Catal 7:1646–1654
10. Ghoussoub M, Xia M, Duchesne PA, Segal D, Ozin G (2019) Principles of photothermal gas-phase heterogeneous CO_2 catalysis. Energy Environ Sci 12:1122–1142
11. Nair V, Muñoz-Batista MJ, Fernández-García M, Luque R, Colmenares JC (2019) Thermo-photocatalysis: environmental and energy applications. Chemsuschem 12:2098–2116
12. Chen C, Li Y, Yang Y, Zhang Q, Wu J, Xie X, Shi Z, Zhao X (2019) Unique mesoporous amorphous manganese iron oxide with excellent catalytic performance for benzene abatement under UV-vis-IR and IR irradiation. Environ Sci Nano 6:1233–1245

13. Li Y, Han S, Zhang L, Yu Y (2021) Manganese-based catalysts for indoor volatile organic compounds degradation with low energy consumption and high efficiency. In: Transactions of Tianjin University, pp 1–14
14. Meyyappan M (2009) A review of plasma enhanced chemical vapour deposition of carbon nanotubes. J Phys D Appl Phys 42:1–15
15. Gohier A, Minea TM, Djouadi AM, Granier A, Dubosc M (2006) Limits of the PECVD process for single wall carbon nanotubes growth. Chem Phys Lett 421:242–245
16. Gohier A, Minea TM, Djouadi AM, Granier A (2007) Impact of the etching gas on vertically oriented single wall and few walled carbon nanotubes by plasma enhanced chemical vapor deposition. J Appl Phys 101:1–8
17. Neyts EC, Ostrikov K, Sunkara MK, Bogaerts A (2015) Plasma catalysis: synergistic effects at the nanoscale. Chem Rev 115:13408–13446
18. Varanda LC, Morales MP, Jafelicci M, Serna CJ (2002) Monodispersed spindle-type goethite nanoparticles from Fe(III) solutions. J Mater Chem 12:3649–3653
19. Ge S, Shi X, Sun K, Li C, Uher C, Baker JR, Banaszak Holl MM, Orr BG (2009) Facile hydrothermal synthesis of iron oxide nanoparticles with tunable magnetic properties. J Phys Chem C 113:13593–13599
20. KhanFaisal I, Ghoshal AK (2000) Removal of volatile organic compounds from polluted air. J Loss Prevent Process Ind 13:527–545
21. Belessi VC, Ladavos AK, Armatas GS, Pomonis PJ (2001) Kinetics of methane oxidation over La–Sr–Ce–Fe–O mixed oxide solids. Phys Chem Chem Phys 3:3856–3862
22. Ma X, Suo X, Cao H, Guo J, Lv L, Sun H, Zheng M (2014) Deep oxidation of 1, 2-dichlorobenzene over Ti-doped iron oxide. Phys Chem Chem Phys 16:12731–12740
23. Wang G, Wang Y, Qin L, Zhao B, Guo L, Han J (2020) Efficient and stable degradation of chlorobenzene over a porous iron–manganese oxide supported ruthenium catalyst. Catal Sci Technol 10:7203–7216
24. Silva H, Hernandez-Fernandez P, Baden AK, Hellstern HL, Kovyakh A, Wisaeus E, Smitshuysen T et al (2019) Supercritical flow synthesis of PtPdFe alloyed nanoparticles with enhanced low-temperature activity and thermal stability for propene oxidation under lean exhaust gas conditions. Catal Sci Technol 9:6691–6699
25. Fan J, Niu X, Teng W, Zhang P, Zhang W, Zhao D (2020) Highly dispersed Fe–Ce mixed oxide catalysts confined in mesochannels toward low-temperature oxidation of formaldehyde. J Mater Chem A 8:17174–17184
26. Mathew T, Suzuki K, Ikuta Y, Takahashi N, Shinjoh H (2012) Mesoporous ferrihydrite with incorporated manganese for rapid removal of organic contaminants in air. Chem Commun 48:10987–10989
27. Sazama P, Moravkova J, Sklenak S, Vondrova A, Tabor E, Sadovska G, Pilar R (2020) Effect of the nuclearity and coordination of Cu and Fe sites in β zeolites on the oxidation of hydrocarbons. ACS Catal 10:3984–4002
28. Li D, Li K, Xu R, Zhu X, Wei Y, Tian D, Cheng X, Wang H (2019) Enhanced CH_4 and CO Oxidation over $Ce_{1-x}Fe_xO_{2-\delta}$ hybrid catalysts by tuning the lattice distortion and the state of surface iron species. ACS Appl Mater Interf 11:19227–19241
29. House MP, Carley AF, Echeverria-Valda R, Bowker M (2008) Effect of varying the cation ratio within iron molybdate catalysts for the selective oxidation of methanol. J Phys Chem C 112:4333–4341
30. Mao J, He D, Zhao Y, Zhang L, Luo Y (2022) Sulfur-resistance iron catalyst in sulfur-containing VOCs abatement modulated through H_2 reduction. Appl Surf Sci 584(152631):1–11
31. Xue T, Li R, Gao Y, Wang Q (2020) Iron mesh-supported vertically aligned Co–Fe layered double oxide as a novel monolithic catalyst for catalytic oxidation of toluene. Chem Eng J 384:1–35
32. Bonelli R, Albonetti S, Morandi V, Ortolani L, Riccobene PM, Scirè S, Zacchini S (2011) Design of nano-sized FeO_x and Au/FeO_x catalysts supported on CeO_2 for total oxidation of VOC. Appl Catal A Gen 395:10–18

33. Guo M, Li K, Zhang H, Min X, Liang J, Hu X, Guo W, Jia J, Sun T (2020) Promotional removal of oxygenated VOC over manganese-based multi oxides from spent lithium-ions manganate batteries: modification with Fe, Bi and Ce dopants. Sci Total Environ 740:1–43
34. Xia H, Chen Y, Wu J, Shao S, Chen G, Zhang H, Dai Q, Wang X (2021) Oxidative decomposition of chlorobenzene over iron titanate catalysts: the critical roles of oxygen vacancies and adsorption geometries. Appl Catal A Gen 617:1–9
35. Xia Y, Wang Z, Feng Y, Xie S, Liu Y, Dai H, Deng J (2020) In situ molten salt derived iron oxide supported platinum catalyst with high catalytic performance for o-xylene elimination. Catal Today 351:30–36
36. Das DP, Parida KM (2007) Fe(III) oxide pillared titanium phosphate (TiP): an effective catalyst for deep oxidation of VOCs. J Mol Catal A Chem 276:17–23
37. Sanchis R, Dejoz A, Vázquez I, Vilarrasa-García E, Jiménez-Jiménez J, Rodríguez-Castellón E, López Nieto JM, Solsona B (2019) Ferric sludge derived from the process of water purification as an efficient catalyst and/or support for the removal of volatile organic compounds. Chemosphere 219:286–295
38. Xue T, Li R, Zhang Z, Gao Y, Wang Q (2020) Preparation of MnO_2 decorated $Co_3Fe_1O_x$ powder/monolithic catalyst with improved catalytic activity for toluene oxidation. J Environ Sci 96:194–203
39. Tsoncheva T, Ivanova R, Henych J, Velinov N, Kormunda M, Dimitrov M, Paneva D, Slušná M, Mitov I, Štengl V (2016) Iron modified titanium–hafnium binary oxides as catalysts in total oxidation of ethyl acetate. Catal Commun 81:14–19
40. Li D, Li C, Suzuki K (2013) Catalytic oxidation of VOCs over Al-and Fe-pillared montmorillonite. Appl Clay Sci 77:56–60
41. Durán FG, Barbero BP, Cadús LE, Rojas C, Centeno MA, Odriozola JA (2009) Manganese and iron oxides as combustion catalysts of volatile organic compounds. Appl Catal B Environ 92:194–201
42. Nogueira FGE, Lopes JH, Silva AC, Lago RM, Fabris JD, Oliveira LCA (2011) Catalysts based on clay and iron oxide for oxidation of toluene. Appl Clay Sci 51:385–389
43. Yang K, Liu Y, Deng J, Zhao X, Yang J, Han Z, Hou Z, Dai H (2019) Three-dimensionally ordered mesoporous iron oxide-supported single-atom platinum: highly active catalysts for benzene combustion. Appl Catal B Environ 244:650–659
44. Minicò S, Scirè S, Crisafulli C, Maggiore R, Galvagno S (2000) Catalytic combustion of volatile organic compounds on gold/iron oxide catalysts. Appl Catal B Environ 28:245–251
45. Wang HC, Liang HS, Chang MB (2011) Chlorobenzene oxidation using ozone over iron oxide and manganese oxide catalysts. J Hazard Mater 186:1781–1787
46. Tsoncheva T, Ivanova R, Dimitrov M, Paneva D, Kovacheva D, Henych J, Vomáčka P et al (2016) Template-assisted hydrothermally synthesized iron-titanium binary oxides and their application as catalysts for ethyl acetate oxidation. Appl Catal A Gen 528:24–35
47. Wang Y, Wang G, Deng W, Han J, Qin L, Zhao B, Guo L, Xing F (2020) Study on the structure-activity relationship of Fe–Mn oxide catalysts for chlorobenzene catalytic combustion. Chem Eng J 395(125172):1–13
48. Xia Y, Dai H, Jiang H, Zhang L, Deng J, Liu Y (2011) Three-dimensionally ordered and wormhole-like mesoporous iron oxide catalysts highly active for the oxidation of acetone and methanol. J Hazard Mater 186:84–91
49. Morales MR, Barbero BP, Cadús LE (2007) Combustion of volatile organic compounds on manganese iron or nickel mixed oxide catalysts. Appl Catal B Environ 74:1–10
50. Hammiche-Bellal Y, Zouaoui-Mahzoul N, Lounas I, Benadda A, Benrabaa R, Auroux A, Meddour-Boukhobza L, Djadoun A (2017) Cobalt and cobalt–iron spinel oxides as bulk and silica supported catalysts in the ethanol combustion reaction. J Mol Catal A Chem 426:97–106
51. Li Z, Yan Q, Jiang Q, Gao Y, Xue T, Li R, Liu Y, Wang Q (2020) Oxygen vacancy mediated $Cu_yCo_{3-y}Fe_1O_x$ mixed oxide as highly active and stable toluene oxidation catalyst by multiple phase interfaces formation and metal doping effect. Appl Catal B Environ 269:1–13
52. Djinović P, Ristić A, Žumbar T, Dasireddy VDBC, Rangus M, Dražić M, Popova M, Likozar B, Logar MZ, Tušar NN (2020) Synergistic effect of CuO nanocrystals and Cu-oxo-Fe clusters

on silica support in promotion of total catalytic oxidation of toluene as a model volatile organic air pollutant. Appl Catal B Environ 268:1–30
53. Li C, Shen Y, Jia M, Sheng S, Adebajo MO, Zhu H (2008) Catalytic combustion of formaldehyde on gold/iron-oxide catalysts. Catal Commun 9:355–361
54. Sanchis R, Cecilia JA, Soriano MD, Vázquez MI, Dejoz A, Nieto JML, Rodríguez Castellón E, Solsona B (2018) Porous clays heterostructures as supports of iron oxide for environmental catalysis. Chem Eng J 334:1159–1168
55. Ma X, Wen J, Guo H, Ren G (2020) Facile template fabrication of Fe–Mn mixed oxides with hollow microsphere structure for efficient and stable catalytic oxidation of 1,2-dichlorobenzene. Chem Eng J 382:1–41
56. Chen J, Chen X, Xu W, Xu Z, Chen J, Jia H, Chen J (2017) Hydrolysis driving redox reaction to synthesize Mn–Fe binary oxides as highly active catalysts for the removal of toluene. Chem Eng J 330:281–293
57. Liang X, Qi F, Liu P, Wei G, Su X, Ma L, He H et al (2016) Performance of Ti-pillared montmorillonite supported Fe catalysts for toluene oxidation: the effect of Fe on catalytic activity. Appl Clay Sci 132:96–104
58. Collado L, Jansson I, Platero-Prats AE, Perez-Dieste V (2017) Carlos eof isolated iron active sites on MCM-41. ACS Catal 7:1646–1654
59. Saqlain S, Cha BJ, Kim SY, Ahn TK, Park C, Oh JM, Jeong EC, Seo HO, Kim YD (2020) Visible light-responsive Fe-loaded TiO_2 photocatalysts for total oxidation of acetaldehyde: fundamental studies towards large-scale production and applications. Appl Surf Sci 505:1–9
60. Soltani T, Lee BK (2017) Comparison of benzene and toluene photodegradation under visible light irradiation by Ba-doped $BiFeO_3$ magnetic nanoparticles with fast sonochemical synthesis. Photochem Photobiol Sci 16:86–95
61. Chen X, Zhu H-Y, Zhao J-C, Zheng Z-F, Gao X-P (2008) Visible-light-driven oxidation of organic contaminants in air with gold nanoparticle catalysts on oxide supports. Angew Chem 120:5433–5436
62. Wu H, Wang L (2014) Phase transformation-induced crystal plane effect of iron oxide micropine dendrites on gaseous toluene photocatalytic oxidation. Appl Surf Sci 288:398–404
63. Tabari T, Singh D, Jamali SS (2017) Enhanced photocatalytic activity of mesoporous $ZnFe_2O_4$ nanoparticles towards gaseous benzene under visible light irradiation. J Environ Chem Eng 5:931–939
64. Kim SY, Saqlain S, Cha BJ, Zhao S, Seo HO, Kim YD (2020) Annealing temperature-dependent effects of Fe-loading on the visible light-driven photocatalytic activity of rutile TiO_2 nanoparticles and their applicability for air purification. Catalysts 10:1–18
65. Low W, Boonamnuayvitaya V (2013) Enhancing the photocatalytic activity of TiO_2 co-doping of graphene—Fe^{3+} ions for formaldehyde removal. J Environ Manag 127:142–149
66. Wang H, Raziq F, Qu Y, Qin C, Wang J, Jing L (2015) Role of quaternary *N* in *N*-doped graphene—Fe_2O_3 nanocomposites as efficient photocatalysts for CO_2 reduction and acetaldehyde degradation. RSC Adv 5:85061–85064
67. Liu J, Liu X, Chen J, Li X, Zhong F (2021) Plasma-catalytic oxidation of toluene on Fe_2O_3/sepiolite catalyst in DDBD reactor. J Phys D Appl Phys 54(475201):1–13
68. Trinh QH, Mok YS (2015) Non-thermal plasma combined with cordierite-supported Mn and Fe based catalysts for the decomposition of diethylether. Catalysts 5:800–814
69. Sultana S, Ye Z, Veerapandian SKP, Löfberg A, De Geyter N, Morent R, Giraudon JM, Lamonier JF (2018) Synthesis and catalytic performances of K-OMS-2, Fe/K-OMS-2 and Fe-K-OMS-2 in post plasma-catalysis for dilute TCE abatement. Catal Today 307:20–28
70. Cai Y, Zhu X, Hu W, Zheng C, Yang Y, Chen M, Gao X (2019) Plasma-catalytic decomposition of ethyl acetate over $LaMO_3$ (M= Mn, Fe, and Co) perovskite catalysts. J Ind Eng Chem 70:447–452
71. Qin L, Zhao B, Chen W, Liu X, Han J (2022) Refluxing-coprecipitation to synthesize Fe_x–Mn_y/γ-Al_2O_3 catalyst for toluene removal in a nonthermal plasma-catalysis reactor. Mol Catal 517:1–14

72. Liu J, Liu X, Chen J, Li X, Ma T, Zhong F (2021) Investigation of ZrMnFe/sepiolite catalysts on toluene degradation in a one-stage plasma-catalysis system. Catalysts 11(828):1–12
73. Al Soubaihi RM, Saoud KM, Dutta J (2018) Critical review of low-temperature CO oxidation and hysteresis phenomenon on heterogeneous catalysts. Catalysts 8:1–19
74. Haruta M (2004) Gold as a novel catalyst in the 21st century: preparation, working mechanism and applications. Gold Bull 37:27–36
75. Pan C-J, Tsai MC, Su WN, Rick J, Akalework NG, Agegnehu AK, Cheng SY, Hwang BJ (2017) Tuning/exploiting strong metal-support interaction (SMSI) in heterogeneous catalysis. J Taiwan Instit Chem Eng 74:154–186
76. Sun YN, Qin ZH, Lewandowski M, Carrasco E, Sterrer M, Shaikhutdinov S, Freund HJ (2009) Monolayer iron oxide film on platinum promotes low temperature CO oxidation. J Catal 266:359–368
77. Carrettin S, Hao Y, Aguilar-Guerrero V, Gates BC, Trasobares S, Calvino JJ, Corma A (2007) Increasing the number of oxygen vacancies on TiO_2 by doping with iron increases the activity of supported gold for CO oxidation. Chem A Eur J 13:7771–7779
78. Biabani-Ravandi A, Rezaei M, Fattah Z (2013) Low-temperature CO oxidation over nanosized Fe–Co mixed oxide catalysts: effect of calcination temperature and operational conditions. Chem Eng Sci 94:237–244
79. Ciambelli P, Stefano Cimino S, De Rossi LL, Minelli G, Porta P, Russo G (2001) $AFeO_3$ (A= La, Nd, Sm) and $LaFe_{1-x}Mg_xO_3$ perovskites as methane combustion and CO oxidation catalysts: structural, redox and catalytic properties. Appl Catal B Environ 29:239–250
80. Yamamoto TA, Nakagawa T, Seino S, Nitani H (2010) Bimetallic nanoparticles of PtM (M= Au, Cu, Ni) supported on iron oxide: radiolytic synthesis and CO oxidation catalysis. Appl Catal A Gen 387:195–202
81. Zheng B, Gan T, Shi S, Wang J, Zhang W, Zhou X, Zou Y, Yan W, Liu G (2021) Exsolution of iron oxide on $LaFeO_3$ Perovskite: a robust heterostructured support for constructing self-adjustable Pt-based room-temperature CO oxidation catalysts. ACS Appl Mater Interf 13:27029–27040
82. Moreau F, Bond GC (2006) CO oxidation activity of gold catalysts supported on various oxides and their improvement by inclusion of an iron component. Catal Today 114:362–368
83. Cheng T, Fang Z, Hu Q, Han K, Yang X, Zhang Y (2007) Low-temperature CO oxidation over CuO/Fe_2O_3 catalysts. Catal Commun 8:1167–1171
84. Cao J, Wang Y, Ma T, Liu Y, Yuan Z (2011) Synthesis of porous hematite nanorods loaded with CuO nanocrystals as catalysts for CO oxidation. J Nat Gas Chem 20:669–676
85. Biabani-Ravandi A, Rezaei M, Fattah Z (2013) Study of Fe–Co mixed metal oxide nanoparticles in the catalytic low-temperature CO oxidation. Process Saf Environ Protect 91:489–494
86. Liu G, Walsh AG, Zhang P (2020) Synergism of iron and platinum species for low-temperature CO oxidation: from two-dimensional surface to nanoparticle and single-atom catalysts. J Phys Chem Lett 11:2219–2229
87. Kast P, Friedrich M, Teschner D, Girgsdies F, Lunkenbein T, D'Alnoncourt RN, Behrens M, Schlögl R (2015) CO oxidation as a test reaction for strong metal–support interaction in nanostructured Pd/FeO_x powder catalysts. Appl Catal A Gen 502:8–17
88. Li P, Miser DE, Rabiei S, Yadav RT, Hajaligol MR (2003) The removal of carbon monoxide by iron oxide nanoparticles. Appl Catal B Environ 43:151–162
89. Wu Y, Dong L, Li B (2018) Effect of iron on physicochemical properties: enhanced catalytic performance for novel Fe_2O_3 modified $CuO/Ti_{0.5}Sn_{0.5}O_2$ in low temperature CO oxidation. Mol Catal 456:65–74
90. Carriazo JG, Martinez LM, Odriozola JA, Moreno S, Molina R, Centeno MA (2007) Gold supported on Fe, Ce, and Al pillared bentonites for CO oxidation reaction. Appl Catal B Environ 72:157–165
91. Carabineiro SAC, Bogdanchikova N, Tavares PB, Figueiredo JL (2012) Nanostructured iron oxide catalysts with gold for the oxidation of carbon monoxide. RSC Adv 2:2957–2965

92. Hinojosa-Reyes M, Camposeco-Solis R, Zanella R, Rodríguez-González V, Ruiz F (2018) Gold nanoparticle: enhanced CO oxidation at low temperatures by using Fe-doped TiO_2 as support. Catal Lett 148:383–396
93. Falls A, Seinfeld J (1978) Continued development of a kinetic mechanism for photochemical smog. Environ Sci Technol 12:1398–1406
94. Wang J, Tian GL, Cui SP, Wang YL (2018) Different precipitant preparation of nickel-doped Mn/TiO_2 catalysts for low-temperature SCR of NO with NH_3. Mater Sci Forum 913:976–984
95. Dumesic JA, Topsøe N-Y, Topsøe H, Chen Y, Slabiak T (1996) Kinetics of selective catalytic reduction of nitric oxide by ammonia over vanadia/titania. J Catal 163:409–417
96. Busca G, Lietti L, Ramis G, Berti F (1998) Chemical and mechanistic aspects of the selective catalytic reduction of NO_x by ammonia over oxide catalysts: a review. Appl Catal B Environ 18:1–36
97. Tounsi H, Djemal S, Petitto C, Delahay G (2011) Copper loaded hydroxyapatite catalyst for selective catalytic reduction of nitric oxide with ammonia. Appl Catal B Environ 107:158–163
98. Dunn JP, Koppula PR, Stenger HG, Wachs IE (1998) Oxidation of sulfur dioxide to sulfur trioxide over supported vanadia catalysts. Appl Catal B Environ 19:103–117
99. Cai S, Zhang D, Zhang L, Huang L, Li H, Gao R, Shi L, Zhang J (2014) Comparative study of 3D ordered macroporous $Ce_{0.75}Zr_{0.2}M_{0.05}O_2$ (M = Fe, Cu, Mn, Co) for selective catalytic reduction of NO with NH_3. Catal Sci Technol 4:93–101
100. Chen Z, Wang F, Li H, Yang Q, Wang L, Li X (2012) Low-temperature selective catalytic reduction of NOx with NH_3 over Fe–Mn mixed-oxide catalysts containing $Fe_3Mn_3O_8$ phase. Ind Eng Chem Res 51:202–212
101. Liu F, He H, Zhang C, Feng Z, Zheng L, Xie Y, Hu T (2010) Selective catalytic reduction of NO with NH_3 over iron titanate catalyst: catalytic performance and characterization. Appl Catal B 96:408–420
102. Yu J, Guo F, Wang Y, Zhu J, Liu Y, Su F, Gao S, Xu G (2010) Sulfur poisoning resistant mesoporous Mn-base catalyst for low-temperature SCR of NO with NH_3. Appl Catal B 95:160–168
103. Cai S, Zhang D, Shi L, Xu J, Zhang L, Huang L, Li H, Zhang J (2014) Porous Ni–Mn oxide nanosheets in situ formed on nickel foam as 3D hierarchical monolith de-NO_x catalysts. Nanoscale 6:7346–7353
104. Zhang S, Zhang B, Liu B, Sun S (2017) A review of Mn-containing oxide catalysts for low temperature selective catalytic reduction of NO_x with NH_3: reaction mechanism and catalyst deactivation. RSC Adv 7:26226–26242
105. Li X, Li J, Peng Y, Zhang T, Liu S, Hao J (2015) Selective catalytic reduction of NO with NH_3 over novel iron–tungsten mixed oxide catalyst in a broad temperature range. Catal Sci Technol 5:4556–4564
106. Li Y, Wan Y, Li Y, Zhan S, Guan Q, Tian Y (2016) Low-temperature selective catalytic reduction of NO with NH_3 over Mn_2O_3-doped Fe_2O_3 hexagonal microsheets. ACS Appl Mater Interf 8:5224–5233
107. Yang S, Qi F, Xiong S, Dang H, Liao Y, Wong PK, Li J (2016) MnO_x supported on Fe–Ti spinel: a novel Mn based low temperature SCR catalyst with a high N_2 selectivity. Appl Catal B Environ 181:570–580
108. Ko S, Tang X, Gao F, Wang C, Liu H, Liu Y (2022) Selective catalytic reduction of NO_x with NH_3 on Mn, Co-BTC-derived catalysts: influence of thermal treatment temperature. J Solid State Chem 307:1–9
109. Zhan S, Qiu M, Yang S, Zhu D, Yu H, Li Y (2014) Facile preparation of MnO_2 doped Fe_2O_3 hollow nanofibers for low temperature SCR of NO with NH_3. J Mater Chem A 2:20486–20493
110. Li Y, Li Y, Wang P, Hu W, Zhang S, Shi Q, Zhan S (2017) Low-temperature selective catalytic reduction of NO_x with NH_3 over $MnFeO_x$ nanorods. Chem Eng J 330:213–222
111. Gao C, Xiao B, Shi JW, He C, Wang B, Ma D, Cheng Y, Niu C (2019) Comprehensive understanding the promoting effect of Dy-doping on $MnFeO_x$ nanowires for the low-temperature NH_3-SCR of NO_x: an experimental and theoretical study. J Catal 380:55–67

112. Shao C, Liu X, Meng D, Xu Q, Guo Y, Guo Y, Zhan W, Wang L, Lu G (2016) Catalytic performance of Co–Fe mixed oxide for NH_3-SCR reaction and the promotional role of cobalt. RSC Adv 6:66169–66179
113. Sun J, Lu Y, Zhang L, Ge C, Tang C, Wan H, Dong L (2017) Comparative study of different doped metal cations on the reduction, acidity, and activity of $Fe_9M_1O_x$ (M= Ti^{4+}, $Ce^{4+/3+}$, Al^{3+}) catalysts for NH_3-SCR reaction. Ind Eng Chem Res 56:12101–12110
114. Wang H, Ning P, Zhang Y, Ma Y, Wang J, Wang L, Zhang Q (2020) Highly efficient WO_3-FeO_x catalysts synthesized using a novel solvent-free method for NH_3-SCR. J Hazard Mater 388(121812):1–35
115. Wei Y, Chen Y, Wang R (2018) Rare earth salt of 12-tungstophosphoric acid supported on iron oxide as a catalyst for selective catalytic reduction of NO_x. Fuel Process Technol 178:262–270
116. Yao H, Cai S, Yang B, Han L, Wang P, Li H, Yan T, Shi L, Zhang D (2020) In situ decorated MOF-derived Mn–Fe oxides on Fe mesh as novel monolithic catalysts for NO_x reduction. New J Chem 44:2357–2366
117. Jia J, Ran R, Guo X, Wu X, Chen W, Weng D (2019) Enhanced low-temperature NO oxidation by iron-modified MnO_2 catalysts. Catal Commun 119:139–143
118. Zhang Y, Xu Z, Wang X, Lu X, Zheng Y (2015) Fabrication of Mn-FeO_x/CNTs catalysts for low-temperature NO reduction with NH_3. NANO 10:1–9
119. Wei L, Li X, Mu J, Wang X, Fan S, Yin Z, Tadé MO, Liu S (2020) Rationally tailored redox properties of a mesoporous Mn–Fe spinel nanostructure for boosting low-temperature selective catalytic reduction of NO_x with NH_3. ACS Sustainable Chem Eng 8:17727–17739
120. Ochando-Pulido JM, Pimentel-Moral S, Verardo V, Martinez-Ferez A (2017) A focus on advanced physicochemical processes for olive mill wastewater treatment. Separ Purif Technol 179:161–174
121. Karthikeyan S, Titus A, Gnanamani A, Mandal AB, Sekaran G (2011) Treatment of textile wastewater by homogeneous and heterogeneous Fenton oxidation processes. Desalination 281:438–445
122. Kishimoto N, Kitamura T, Kato M, Otsu H (2013) Reusability of iron sludge as an iron source for the electrochemical Fenton-type process using Fe^{2+}/HOCl system. Water Res 47:1919–1927
123. Babuponnusami A, Muthukumar K (2014) A review of Fenton and improvements to the Fenton process for wastewater treatment. J Environ Chem Eng 2:557–572
124. Garcia-Segura S, Bellotindos LM, Huang Y-H, Brillas E, Lu M-C (2016) Fluidized-bed Fenton process as alternative wastewater treatment technology: a review. J Taiwan Inst Chem Eng 67:211–225
125. Queiros S, Morais V, Rodrigues CSD, Maldonado-Hodar FJ, Madeira LM (2015) Heterogeneous Fenton's oxidation using Fe/ZSM-5 as catalyst in a continuous stirred tank reactor. Separ Purif Technol 141:235–245
126. Vorontsov AV (2019) Advancing Fenton and photo-Fenton water treatment through the catalyst design. J Hazard Mater 372:103–112
127. Poza-Nogueiras V, Rosales E, Pazos M, Sanroman MA (2018) Current advances and trends in electro-Fenton process using heterogeneous catalysts: a review. Chemosphere 201:399–416
128. Dulova N, Trapido M, Dulov A (2011) Catalytic degradation of picric acid by heterogeneous Fenton: based processes. Environ Technol 32:439–446
129. Casado J (2019) Towards industrial implementation of electro-Fenton and derived technologies for wastewater treatment: a review. J Environ Chem Eng 7:1–62
130. He Z, Gao C, Qian M, Shi Y, Chen J, Song S (2014) Electro-Fenton process catalyzed by Fe_3O_4 magnetic nanoparticles for degradation of C.I. reactive blue 19 in aqueous solution: operating conditions, influence, and mechanism. Ind Eng Chem Res 53:3435–3447
131. Ben Hafaiedh N, Fourcade F, Bellakhal N, Amrane A (2020) Iron oxide nanoparticles as heterogeneous electro-Fenton catalysts for the removal of AR18 azo dye. Environ Technol 41:2146–2153
132. Baiju A, Gandhimathi R, Ramesh ST, Nidheesh PV (2018) Combined heterogeneous electro-Fenton and biological process for the treatment of stabilized landfill leachate. J Environ Manag 210:328–337

133. Huang B, Qi C, Yang Z, Guo Q, Chen W, Zeng G, Lei C (2017) Pd/Fe_3O_4 nanocatalysts for highly effective and simultaneous removal of humic acids and Cr(VI) by electro-Fenton with H_2O_2 in situ electro-generated on the catalyst surface. J Catal 352:337–350
134. Barhoumi N, Olvera-Vargas H, Oturan N, Huguenot D, Gadri A, Ammar S, Brillas E, Oturan MA (2017) Kinetics of oxidative degradation/mineralization pathways of the antibiotic tetracycline by the novel heterogeneous electro-Fenton process with solid catalyst chalcopyrite. Appl Catal B Environ 209:637–647
135. Barhoumi N, Labiadh L, Oturan MA, Oturan N, Gadri A, Ammar S, Brillas E (2015) Electrochemical mineralization of the antibiotic levofloxacin by electro-Fenton-pyrite process. Chemosphere **141**:250–257

Chapter 14
Nonspherical Iron Oxide Particles: Synthesis and Applications in Interfacial Science and Engineering

Hemant Kumar, T. G. Anjali, and Madivala G. Basavaraj

Abstract The ability to synthesize highly stable monodisperse iron oxide particles of different sizes and shapes, in particular, hematite (α-Fe_2O_3), has enabled fundamental investigation of particle shape effects in colloids and interface science. In this chapter, an overview of wet chemical approaches for the synthesis of hematite particles of different shapes and their use in the fundamental study of interfacial behavior of particles is discussed.

Keywords Nonspherical colloids · Emulsions · Phase inversion · Adsorption · Detachment energy · Interfacial rheology

14.1 Introduction

Spherical particles are a class of symmetrical or isotropic three-dimensional objects in which any point on their surface is at the same distance from its center. This equal distance is the radius, which is the single characteristic dimension required to define the size of the spherical particle. On the other hand, not all points on the surface of a nonspherical or asymmetric particle are at same distance from the center [1–3]. The particles of irregular or arbitrary shape and particles of well-defined shapes, such as rods, ellipsoids, etc., are examples of nonspherical particles. The latter, that is, nonspherical particles of well-defined shapes have been an important class of particle systems that have enabled investigation of fundamental aspects related to particle shape effects in colloids and interface science [1, 2, 4].

H. Kumar · T. G. Anjali · M. G. Basavaraj (✉)
Polymer Engineering and Colloid Science (PECS) Laboratory, Department of Chemical Engineering, Indian Institute of Technology Madras, Chennai 600036, India
e-mail: basa@iitm.ac.in

H. Sahoo and J. K. Sahoo (eds.), *Iron Oxide-Based Nanocomposites and Nanoenzymes*, Nanostructure Science and Technology, https://doi.org/10.1007/978-3-031-44599-6_14

Colloidal and nanoscale particles can be synthesized via two broad class of methods, namely top-down and bottom-up techniques [5]. The top-down methods such as high-energy ball milling typically produce irregular particles, while the bottom-up strategies when carried out under controlled conditions can lead to the formation of regular shapes particles. In the bottom-up approach, particles are synthesized by assembling atoms or molecules via chemical reactions carried out under controlled conditions [6]. Some of the commonly used reaction schemes that have been successfully employed to prepare nonspherical colloids include metallic particles by reduction of metal salts [7], hydro-thermal reaction, forced hydrolysis [8, 9], modified Stober method [10], sol–gel methods [11], etc.

The iron oxide particles of different types that have been widely studied include-hematite (α-Fe_2O_3), maghemite (γ-Fe_2O_3), and magnetite (Fe_3O_4). This chapter deals with hematite (α-Fe_2O_3) particles which have found application in diverse areas such as paint technology, catalysis, and biomedical fields. In addition, hematite particles are widely used as model system for the investigation of fundamental aspects such as the effect of particle shape [2], surface charge [12], and external field [13] in colloids and interface science. This is primarily due to the fact that hematite particles (i) can be synthesized in various shapes, (ii) their surface charge can be tuned by changing pH of the dispersion medium, (iii) respond to external stimuli such as electric field and magnetic field [13]. The use of hematite particles to unearth the role of particle shape and charge effects on interfacial adsorption, emulsification, surface rheological properties of particle laden interfaces, and equilibrium configuration of particles is discussed.

14.2 Synthesis of Anisotropic Hematite Particles

The synthesis of anisotropic iron oxide particles of various shapes was pioneered by Eogan Matijevic in the late 1970s [14]. Several other follow-up studies on the synthesis of iron oxide particles of different shapes and sizes have been carried out later [15–18]. The procedure for large-scale production (few grams to few tens of grams) of nonspherical hematite particles via a gel–sol method was introduced in early 1990 [19]. The iron-based particles of different shape and size, such as hematite [14, 15], magnetite [20, 21], akaganeite (β-FeOOH) [18, 21] particles, iron(III) sulfate [22], and maghemite [23], have been synthesized in last few decades. The procedure for the synthesis of anisotropic hematite particles of different shape such as ellipsoids (spindles) [9, 24, 25], cubes [11, 25–27], double spheres [28], disks [29], plates [30, 31], dumbbells [28], nanorods [32], and sphero-cylinders [28] have been well documented. Another advantage of nonspherical hematite particles is their ability to respond to externally applied magnetic field [13]. These particles can be used as model colloids to study the magnetic field-assisted assembly, investigation of shape-directed self-assembly in the bulk and at interfaces, and for the design of complex and modular building blocks for photo-catalytic activity. While there are several methods available for the synthesis of hematite particles with uniform

shape and narrow size distribution, the two most commonly used methods are (i) forced hydrolysis method and (ii) gel–sol method. The shape and size of the hematite particles depend upon the concentration of the iron salt, reaction medium, aging time, reaction temperature, and the other reagents that act as catalyst and shape directing species. The synthesis of micron-sized hematite particles by force hydrolysis and sol–gel method has been reviewed recently [33].

Figure 14.1 shows the electron microscopy images of hematite particles of different shapes prepared by different reaction schemes. A brief description of the procedure for the synthesis of the hematite particles of few different shapes is presented below:

Nano-sized ellipsoids: The forced hydrolysis methods for the preparation of ellipsoids shown in Fig. 14.1g involves the use of iron(III) perchlorate, urea, and a small amount of phosphate ion [8]. The aspect ratio (AR, defined as the ratio of length of the major axis to the length of the minor axis) of resulting ellipsoids can be varied from $\sim$ 1 to $\sim$ 10 by increasing the concentration of phosphate ion. Typically, the reaction mixture consisting of different quantity of reagents is taken in an airtight Pyrex bottle and placed in a preheated hot air oven at 100 $\pm$ 1 °C for 24 h. After

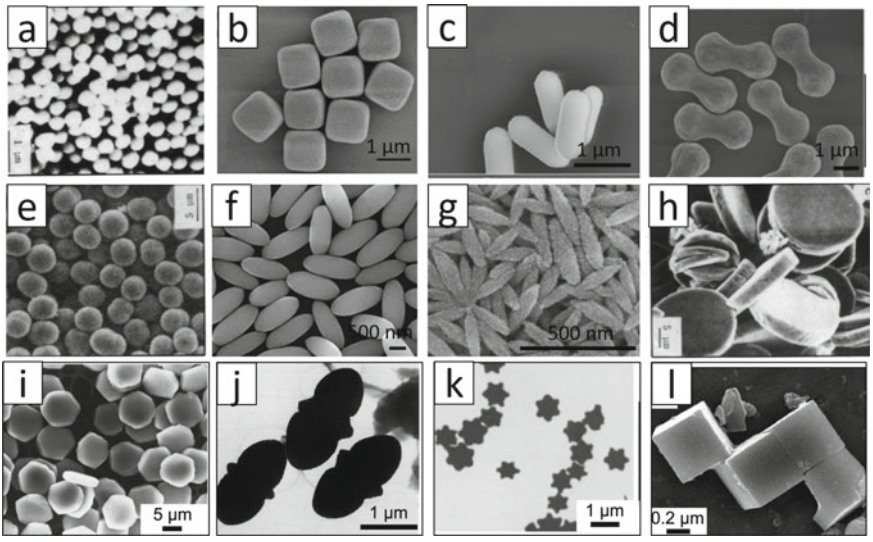

Fig. 14.1 Synthesis of different shape of α-Fe_2O_3 hematite iron oxide particles **a** sphere, reproduced with permission from the American Chemical Society [17]. **b** Cube **c** spherocylinder **d** peanut, reproduced with permission from Elsevier [34] **e** double sphere, reproduced with permission from the Chemical Society of Japan [35]. **f** Micro-ellipsoids, **g** nano-ellipsoids, reproduced with permission from the American Chemical Society [1]. **h** Disk, reproduced with permission from the American Chemical Society [17]. **i** Hexagonal platelets, reproduced with permission from Elsevier [31] **j** double ellipsoid reproduced with permission from Elsevier [36] **k** bipyramid reproduced with permission from Elsevier [16] **l** single crystal cubes, reproduced with permission from the American Chemical Society [37]

24 h, the reddish-brown reaction product is taken out of the oven, cooled to room temperature, and centrifuged at 6500 rpm for 45 min. The sediment consisting of hematite particles is washed multiple times with Milli-*Q* water until the supernatant is clear.

Micron sized ellipsoids: The micron-sized hematite α-Fe_2O_3 ellipsoids shown in Fig. 14.1f are synthesized by the forced hydrolysis of ferric chloride [9]. In this reaction scheme, $FeCl_3$ is used as an iron precursor. This is added to an equal volume of ethanol and water. Further, NaH_2PO_2 is introduced into the reaction mixture to control the aspect ratio of the ellipsoids. The Pyrex glassware with all the reagents is tightly stoppered and kept in a preheated oven maintained at 100 ± 1 °C for seven days. After 7 days, the reaction mixture is taken out and cooled at room temperature. The particles in the reaction product are observed to settle to the bottom of the Pyrex bottle. The supernatant at the top was carefully discarded, and the reddish-brown sediment at the bottom is washed with Milli-*Q* water several times to remove unreacted chemicals.

Cube, peanut, and spherocylinders: Hematite particles of the cube, peanut, and spherocylindrical shape shown in Fig. 14.1b–d of different sizes can be prepared by the gel–sol method developed by Sugimoto [11]. For the synthesis of hematite peanuts, firstly, $FeCl_3$ salt is dissolved in water, the solution is vigorous stirred, and then, NaOH solution is slowly added to the mixture followed by the addition of Na_2SO_4 solution. For the synthesis of spherocylindrical shape, a similar procedure is followed, except that the concentration of Na_2SO_4 used is smaller. For the synthesis of cube shape particles, no Na_2SO_4 solution is required. The condensed ferric hydroxide gel formed after the mixing step is aged at 100 °C for 8 days. The Pyrex bottle was removed from the oven and kept at room temperature to cool. The reaction product is transferred in centrifuging tubes to remove the unreacted chemicals and to recover hematite particles.

14.3 Effect of Surface Charge on Adsorption of Ellipsoids to Interfaces

The spontaneous adsorption of particles to the fluid–fluid interface without or with the intervention of external factors is crucial for the development of two- and three-dimensional functional materials [38]. The adsorption of particles to the interface created during the mixing of two or more immiscible fluids is of prime importance for the design of particle-stabilized Pickering emulsions or foams. Amphiphilic molecules such as surfactants or surface active microgel particles have the tendency to readily adsorb to fluid–fluid interface. On the other hand, the adsorption of colloidal particles to interfaces depends on several factors such as surface charge, size, three-phase contact angle, nature of the fluid–fluid interface, etc.

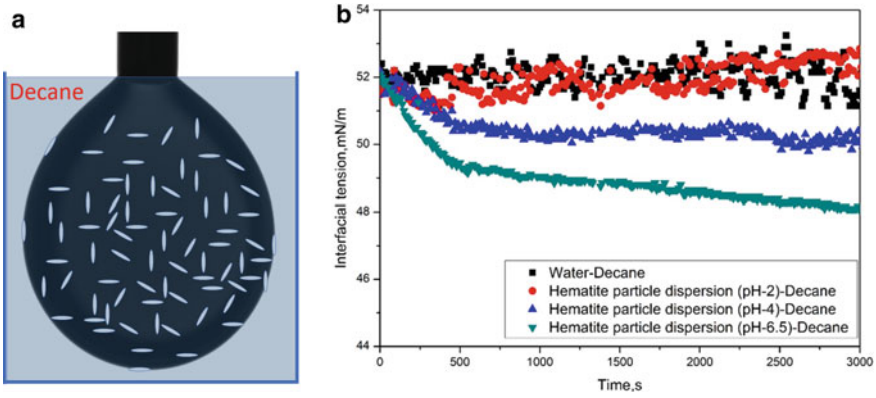

Fig. 14.2 **a** Schematic representation of the pendant drop technique used to measure the interfacial tension of decane-water interface by considering a pendant drop of aqueous dispersion of ellipsoids and decane **b** The temporal evolution of the interfacial tension. The figure in **b** is reproduced with permission from the Royal Society of Chemistry [39]

The adsorption of particles to a fluid–fluid interface can be studied by monitoring the temporal variation of surface tension. The reduction in the interfacial tension is an indication of adsorption of particles to interfaces. In this method, the shape profile of a particle laden pendant droplet which is described by the Young–Laplace equation combined with a numerical procedure is used to calculate surface tension. The aqueous hematite ellipsoids of 254 nm average major axis length and 55 nm average minor axis length which corresponds to an average aspect ratio, AR = 4.6 at pH = 2, 4 and 6.5 are considered. The zeta potential of the particles at these pH are + 36.4, + 50.0 and + 6.4 mV, respectively. A 25 μL volume pendant drop (also called handing drop) (0.3 wt% particle concentration) is created by taking these dispersions in a syringe to which a needle with a flat tip is attached and is brought in contact with an oil medium, decane, taken in a rectangular glass cuvette. This is shown schematically in Fig. 14.2a.

The entire system is maintained at a constant temperature throughout the experiment. The pendant drop image shown in Fig. 14.2a is recorded by using a high-speed CCD camera attached to a contact angle goniometer at 25 ± 2 °C temperature.

The temporal evolution of the surface tension of decane–water interface and for decane–aqueous ellipsoid dispersion interface is shown in Fig. 14.2b. The surface tension of decane–water is found to be 52 ± 0.5 mN m^{-1} and is nearly constant throughout. This is expected since neither water nor decane has any surface-active components. In the case of aqueous hematite dispersions at pH 2, the surface tension variation is like that for decane–water. However, for the case of hematite dispersions at pH 4 and 6.5, the surface tension is found to decrease with time pointing to the adsorption of hematite ellipsoid to the decane–water interface. For the dispersion of hematite ellipsoids at pH 4 and 6.5 in contact with decane, the surface tension decreased with time indicating that ellipsoidal particles adsorb to the decane–water

interface. It is to be noted that other conditions such as particle concentration, aspect ratio, and temperature are same in all the experiments and therefore, the difference in the adsorption behavior at different pH must be due to surface charge of particles. As the particles in an aqueous pendant drop (medium with high dielectric constant) approach the decane phase (medium with low dielectric constant) due to Brownian diffusion arising due to their thermal motion, the particles experience an energy barrier due to image charge effect. The strength of the energy barrier increases with increase in surface charge and therefore, highly charged ellipsoids in aqueous dispersions at pH 2 do not adsorb to the interface as reflected from the constant value of interfacial tension of decane–water interface. Since the particles in the aqueous dispersions at pH 6.5 are weakly charged, the height of the energy barrier is lower and hence the reduction in the surface tension at any time instance is highest, and therefore, the ellipsoids in the dispersion at pH 6.5 show higher tendency to adsorb to decane–water interface. It is also possible to influence the adsorption of particles to fluid–fluid interfaces by the addition of salt [39]. High-energy mixing such as that used in emulsification is yet another way to provide sufficient energy for the particles to cross the energy barrier and force the particles to adsorb at fluid–fluid interface.

14.4 Contact Angle and Orientation of Anisotropic Hematite Particles at Fluids Interfaces

When particles are used as interface stabilizers, the measurement of the three-phase contact angle becomes important as it dictates the type of emulsion and foam formed, which are commonly encountered in cosmetic, food, and pharmaceutical formulations. The emulsions and foams are also used extensively in ceramic processing, especially for the creation of novel functional porous materials. The accurate measurement of contact angle is critical for determining the interfacial attachment energy of particles as well as the nature of electrostatic and capillary interactions.

The three-phase contact angle measures the equilibrium position of particles adsorbed at the interface. Consider a spherical particle adsorbed at the interface of two fluids, f_1 and f_2. If the surface tension of particle–fluid 1 interface is γ_{pf1}, the surface tension of particle–fluid 2 interfaces is γ_{pf2}, and the fluid 1–fluid 2 interfacial tension is γ_{f1f2}, the cosine of the three-phase contact angle (θ) as defined by Young's Eq. (14.1) is:

$$\cos\theta = \frac{\gamma_{\mathrm{pf1}} - \gamma_{\mathrm{pf2}}}{\gamma_{f1f2}} \tag{14.1}$$

A schematic representation of a spherical particle which resides more in fluid 1 such that the contact angle θ is less than 90° is shown in Fig. 14.3a. The surface tension forces which act tangentially to the particle–fluid1, particle–fluid 2 and fluid 1–fluid 2 interface are marked. The three-phase contact angle θ is measured by drawing a tangent to the particle surface at the three-phase contact point. The angle inscribed

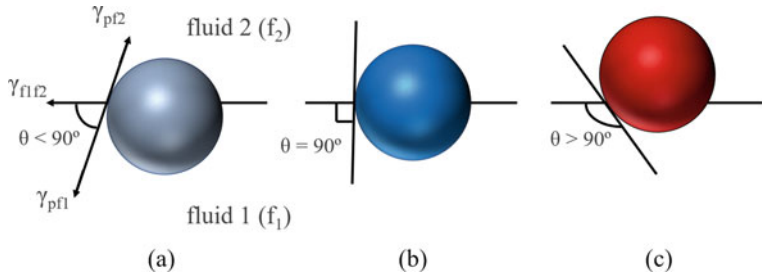

Fig. 14.3 A schematic of spherical colloids adsorbed at fluid 1–fluid 2 interface: **a** partially hydrophilic particle, **b** neutrally wetting particle, and **c** partially hydrophobic particle

between this tangent and the interface plane measured in the anticlockwise direction is the three-phase contact angle, θ. In most interfacial experiments, water is typically used as fluid 1 (also referred to as bottom phase or sub phase). Such particles with $0° < \theta < 90°$ shown in Fig. 14.3a are called partially hydrophilic particles. If $\theta = 90°$, the particles possess an equal affinity for both the fluids; such particles are said to be neutrally wetting, which is represented in Fig. 14.3b. Neutrally wetting particles share exactly half of their surface area with each fluid, that is, particle–fluid 1 contact area is equal to particle–fluid 2 contact area when $90° > \theta > 180°$, the particles are positioned at the interface with larger surface in contact with the upper phase (see Fig. 14.3c) and such particles are said to be partially hydrophobic.

Recently, a class of techniques called direct imaging methods that enable direct visualization of the equilibrium position of particles adsorbed at the interface has been developed [40–44]. These methods enable the measurement of the three-phase contact angle in an unambiguous way and also facilitate the visualization of interface deformation around interfacially bound particles [45]. The measurement of three phase contact angle of anisotropic particles, compared to spherical counterparts, is non-trivial and challenging due to shape induced interface deformation and multitude of orientations that nonspherical particles assume at the interface. Interferometry [42], gel trapping technique (GTT) [43], and the Freeze-fracture shadow-casting (FreSCa) cryo-SEM [43, 44] and methods that exploit hetero-aggregation [40, 41] are some of the direct methods used to measure the contact angle of spherical and non-spherical particles at fluid–fluid interfaces.

The three-phase contact angle of anisotropic iron oxide particles at air–water and decane–water interface has been measured using GTT method [34]. The representative SEM micrographs of peanut-shaped, sphero-cylindrical, and cuboidal hematite particles trapped at the PDMS surface shown in Fig. 14.4 are obtained following the gel trapping technique protocol. They represent the equilibrium position of hematite particles of different shapes adsorbed at the decane–water interface. From Fig. 14.4a, b, it is observed that peanut-shaped and spherocylindrical particles are adsorbed with their long axis parallel to the interface. The images show the fraction of surface area of the particles exposed to the water phase. The procedure used to measure the contact angle of peanut shaped particles is detailed in Fig. 14.4c, which shows the side view

of a peanut-shaped particle of lobe diameter, d. The projected contact line length, d_c, which corresponds to the length scale resulting due to intersection of the interface and the particle is also determined from the side view image. From Fig. 14.4c, it is clear that the particle resides more in the aqueous phase, that is, these particles are partially hydrophilic. For such particles, the three-phase contact angle is determined from the equation, $\sin\theta = \frac{d_c}{d}$ [43]. A similar procedure is used to determine the three-phase contact angle of spherocylindrical particles. The contact angle of hematite peanut shaped particles (length = 2.1 μm, lobe diameter = 0.9 μm, and aspect ratio, defined as the ratio of length to lobe diameter = ∼ 2.3) at air–water and decane–water interface is found to be 43 ± 3 and 50 ± 4, respectively. The contact angle for spherocylindrical particles (length = 1 μm, diameter = 0.62 μm, and aspect ratio = ∼2.3) at air–water and decane–water interface is 42 ± 2 and 48 ± 3, respectively. The details on the measurement of three phase contact angle of peanut and spherocylindrical particles of different sizes can be found in Anjali et al. [34].

Interestingly, the cuboidal particles as shown in Fig. 14.4d, f_1–f_3, and g_1–g_3 are found to adsorb to the fluid–fluid interface in three different orientations, namely, face-up, edge-up, and vertex-up. The top view and side view images corresponding to the three different orientations are shown in Fig. 14.4f_1–f_3 and g_1–g_3, respectively.

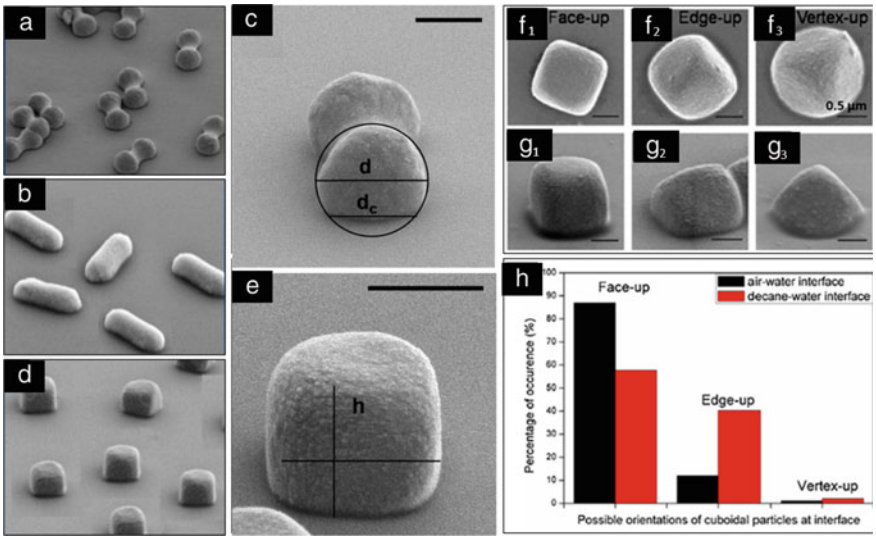

Fig. 14.4 The SEM images of the particles trapped in the PDMS surface obtained by the gel trapping technique (GTT): **a** peanut-shaped particles (AR = 2.2), **b** spherocylindrical particles (AR = 2.6), and **d** cuboidal particles (1200 nm). The scheme used to measure the wettability of dumbbell shaped and cuboidal particles is shown in (**c**) and (**e**) respectively. The top of cuboids in different orientations is shown respectively in $\mathbf{f_1}$, $\mathbf{f_2}$, and $\mathbf{f_3}$ with respective side view shown in $\mathbf{g_1}$, $\mathbf{g_2}$, $\mathbf{g_3}$ side view particles. The percentage occurrence of cuboids in different orientations at air–water and decane–water is shown in (**h**). The figures are reproduced with permission from Elsevier [34]

The frequency of occurrence of these orientations for the cuboids adsorbed at decane–water and air–water interfaces obtained by the analysis of orientation of more than 250 particles is shown in Fig. 14.4h. The face up orientation is found to be highly preferred and energetically more favorable.

The wettability of cuboidal shaped particles in the face-up configuration, wherein the two opposite faces of the cuboid is parallel to the interface, is calculated as the ratio of height of the cuboidal particles exposed to the water phase (h) that protruding from the PDMS to the length of the cuboid (a), which is depicted in Fig. 14.4e. The calculated value of h/a falls in the range of 0.73–0.84 for all the cuboidal particles of different sizes adsorbed at air–water and decane–water interfaces, which again confirms the partially hydrophilic nature of the hematite particles.

14.5 Detachment Energy of Anisotropic Particles from Fluid–fluid Interfaces

The surface free energy of detachment of a particle adsorbed to the interface is the difference in the surface energy of the fluid-particle-interface system and the surface energy of the fluid-particle system when it is removed from the interface and placed in one of the bulk fluids. The surface free energy of detachment also corresponds to the depth of the surface energy well in which the particles are trapped when they are adsorbed at the interface. The existence of surface energy well conceptualized by Pieranski, can also be calculated by the surface energy minimization approach [38]. Figure 14.5 shows the schematic of a spherical particle adsorbed at the water–air interface (P_{int}). The surface free energy of their detachment from the interface into the air (P_{air}) and from the interface into the water (P_{water}) are represented respectively by ΔG_{da} . and ΔG_{dw} with the subscripts representing detachment into air (da) and water (dw). When the interface is planar, that is, undeformed by the presence of particle, the detachment energy of a particle of any arbitrary shape from the interface into the air is given by Eq. 14.2 [46]:

$$\Delta G_{\text{da}} = \gamma_{\text{pfl}}\left(A_c + A_{\text{pw}}\cos\theta\right) \tag{14.2}$$

where γ_{aw} is the air–water interfacial tension, A_c is the area that the particle occupies when it is at the interface and A_{pw} is the area of the particle–water interface when it is adsorbed at the interface. For a spherical particles of radius r, A_c and A_{pw} are given respectively by $\pi(r\sin\theta)^2$ and $2\pi r^2(1+\cos\theta)$ [46]. Therefore, the expression for the energy of detachment of particles into the air takes the form:

$$\Delta G_{\text{da}} = \pi r^2 \gamma_{\text{aw}}(1+\cos\theta)^2 \tag{14.3}$$

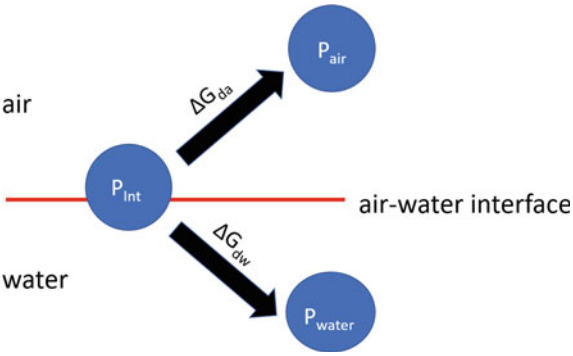

Fig. 14.5 A schematic of a spherical particle adsorbed to water–air interface (P_{int}) is shown to detachment from the interface such that it is present completely in the air (P_{air}) or water (P_{water})

The removal of a neutrally wetting ($\theta = 90°$) spherical colloidal particle of $r = 0.5$ μm from the air–water interface ($\gamma_{aw} = 72$ mN/m) requires an energy of the order of $10^7\ k_BT$ [38]. Therefore, colloidal scale particles are strongly adsorbed at the interface and therefore can be assumed to be irreversible. Equation 14.2 can be modified to account for particle shape effects. For a nonspherical particle of well-defined shape, for example, spherocylinder particles of long semi-axis (a) and short semi-axis (b), the detachment energy of the particle into the air is given by Eq. 14.4 [46].

$$\Delta G_{da} = \Delta G_{dw} + 4\pi r^2 \gamma_{aw} b^2 \cos\theta \left(\frac{b}{a}\right) \tag{14.4}$$

with the detachment energy into the water phase, ΔG_{dw} given Eq. 14.5:

$$\Delta G_{dw} = 4\pi b^2 \gamma_{aw} (1 - \cos\theta)^2 \left[1 + \frac{4\left(\left({}^{a}/_{b}\right) - 1\right)(\sin\theta - \theta\cos\theta)}{\pi(1 - \cos\theta)^2}\right] \tag{14.5}$$

The detachment energy of a cuboidal particles of side length (a) and the length exposed to the water phase (h) is given by Eq. 14.6:

$$\Delta G_{da} = \gamma_{aw}\left(a^2 + \left(a^2 + 4ah\right)\cos\theta\right) \tag{14.6}$$

The energy of detachment of spherocylindrical particles of different aspect ratio (a/b) and cuboidal particles adsorbed at air–water interface is listed in Tables 14.1 and 14.2, respectively. The data presented in Tables 14.1 and 14.2 are calculated from Eqs. (14.4) and (14.6) respectively. In all the cases, the energy of detachment is the order of $10^7\ k_BT$ indicating that these particles are irreversibly adsorbed to the interface.

Table 14.1 The surface free energy of detachment of spherocylindrical particles adsorbed at air–water interface into air, (r, is the radius of the sphere having the equal volume of each type of particles)

Particle type	Particle size, μm	Aspect ratio	r, μm	$\frac{\Delta G_{da}}{k_B T} \times 10^{-7}$
Spherocylinder	$a = 0.51; b = 0.31$	1.6	0.384	2.54
Spherocylinder	$a = 0.65; b = 0.25$	2.6	0.380	2.71
Spherocylinder (silica coated)	$a = 0.65; b = 0.28$	2.3	0.402	2.51

Table 14.2 The detachment energy of cuboidal shaped hematite particles from air–water interface into air

Side length (a), μm	Radius of the sphere having the equal volume of each type of particles (r), μm	$\frac{\Delta G_{da}}{k_B T} \times 10^{-7}$
0.5	0.31	1.824
0.8	0.5	4.56
1.2	0.745	10.4
1.5	0.931	16

14.6 Shape-Induced Interface Deformation

The shape of the interface in the immediate vicinity of particles are adsorbed to fluid–fluid interface depends on their size, shape, and wettability. The nature of interface deformation is an important factor that dictates the microstructure and properties of particle laden interfaces. The interface mediated interactions which are also referred to as capillary interactions come into existence when interface deformation around adjacent particles overlap. Therefore, there the investigation of three phase contact line and interface deformation around shape anisotropic particles and the resulting interfacial self-assembly has been a subject of considerable interest.

It is well known that the shape of the contact line for a spherical particle adsorbed to a fluid–fluid interface is a circle. However, for a nonspherical particle that is ellipsoidal in shape, the contact line is an undulated ellipse, that is it becomes non-planar. This results in certain regions of the interface being pulled up (elevation) or pulled down (depression) depending on the surface chemistry of the particles. This unique interface deformation solely due to particle shape anisotropy has been attributed to the fact that such particles when adsorbed to fluid–fluid interface, distort the interface in order to locally satisfy the Young's equation (Eq. 14.1) all along the three-phase contact line [42, 47, 48]. The elevation or the depression of three phase contact line around the particles are termed as capillary charges (poles)—the region that rises above the flat interface as a positive ("+") charge and that falls below as a negative ("−") charge. These capillary charges are analogous to the electric charges, with a difference that, the like capillary charges repel and the opposite ones attract

each other. In the limit of low Bond number (B_o), which is defined as the ratio of gravitational force to surface tension force, the magnitude of interface deformation "h" generated by an isolated colloidal particle adsorbed at a planar interface follows the 2D Laplace equation [48].

$$\nabla^2 h = 0 \tag{14.7}$$

A general solution to the above equation in terms of polar multipoles is of the form

$$h(r,\theta) = A_0 \ln r + A_1 \ln r^{-1} \cos(\theta + \alpha_1) + A_2 \ln r^{-2} \cos(2\theta + \alpha_2) + \cdots \tag{14.8}$$

where r and θ the polar coordinates in a particle centered reference frame. Each term in Eq. 14.4 corresponds to a specific type of interface deformation called the capillary multipole, namely monopole, dipole, quadrupole etc. Therefore, the capillary multipoles dictate the range and magnitude of capillary interaction between the interfacially trapped particles as well as their self-assembly [42, 48–50]. Thus, a clear understanding of the type of interface deformation around isolated particles is crucial in the prediction of directional interactions that they experience at the interface. Despite progress in the synthesis of particles of different shapes, the investigation on the particle shape induced interface deformations, from both numerical and experimental studies, is limited to particle of very few shapes [42, 48, 51–54].

The ellipsoids and rod-shaped particles adsorbed at fluid–fluid interfaces deform the interface to induce quadrapolar deformation, which results in the formation of unique assemblies of ellipsoids in tip–tip and side-side configurations [55]. The interfacial behavior of micron sized cuboidal hematite particles investigated by combining GTT, electron microscopy and optical surface profilometry revealed that the particle shape induced interface deformations are affected by the position of the particles with respect to the interface and by their orientation at the interface [51]. The direct visualization of the near field interface deformation around isolated cuboidal particles at the interface achieved through high resolution scanning electron microscopy (Fig. 14.6a–d) and a three-dimensional optical surface profiles (Fig. 14.6e–h) and two-dimensional height profiles (Fig. 14.6i–l) are observed to be in well agreement with the numerical predictions [52]. The nature the capillary multipoles that the hematite cuboids at fluid–fluid interface induce, as shown in the Fig. 14.4, can vary from monopolar to octupolar depending on their orientations at the interface [51, 52]. Particles in the face-up orientation exhibit either hexapolar or octupolar type deformation depending on their position with respect to the interface. The interface deformation is of hexapolar type, with depressions at three vertices and three elevations, when the particle position corresponds to the global energy minima. In the kinetically trapped, face-up orientation, the deformation is of octupolar nature with depression at the four vertices and elevations at the four sides. For the particles in the edge-up orientations, depending on position with respect to the interface, the deformations are of either quadrupolar or monopolar in nature. In the edge-up orientation, wherein the particles are trapped in a local energy minimum, the interface deformation is

quadrupolar, with elevations near the tilted sides and depressions near the other two sides. Cuboids in the other edge-up orientation which are trapped at the interface with their edges parallel to the interface induce a monopolar type deformation. Particles in the edge-up orientation in the kinetically trapped state deform the interface in a quadrupolar manner with elevations near the vertical sides and depressions near the slanting faces. The particle shape induced interface deformations around cuboidal particles adsorbed in the vertex-up orientation, which is a kinetically trapped state, is monopolar in nature similar to that induced by gravity, but with an opposite sign [48]. In summary, the nature of interface deformations around micron sized cuboids are affected by both the particle orientation and position with respect to the interface.

14.7 Surface Rheology of Hematite Ellipsoids

The response of particle laden interface to mechanical deformation is relevant for the design of emulsions, and other particle-stabilized high interface materials. In this context, pulsating drop analysis, Langmuir–Blodgett (LB) compression as well as shear and oscillatory surface rheology have been widely used to investigate the response of complex fluid interfaces loaded with one or more soft materials such as polymers, particles, surfactants, etc. The study of the response of interfacial systems to controlled deformation, known as interfacial rheology, can be broadly classified into two categories (i) surface shear and oscillatory rheology and (ii) dilatational surface rheology.

During surface shear rheology, a shear force is applied to the surface while the total surface area remains constant, which is represented schematically in Fig. 14.7a. The magnetic rod surface rheometer and conventional rheometers equipped with double wall ring, Du Noüy ring, or Bi-cone geometry can be used for surface rheological measurements. Similar to bulk rheology, which is used to probe deformation of materials in three dimensions, the surface rheology can also be carried out in rotational and oscillatory mode. In dilational surface rheology, the interfacial area is varied in a periodic manner by expansion or compression of the interface in a controlled way. The area change can facilitate interfacial adsorption or desorption of surface-active species to (or from) the interface from (or to) the bulk. A schematic representation of the dilatation of the interface leading to an increase or decrease interfacial area, typically achieved by oscillating the barriers of the LB trough with the help of a stepper motor or with the piezoelectric actuator in the case of pendant drops, is shown in Fig. 14.7b.

The response of a viscoelastic interface to the applied surface shear stress (σ^s) can be represents as:

$$\sigma^s = \gamma_0^s G^{s'} \sin \omega t + \gamma_0^s G^{s''} \cos \omega t \tag{14.9}$$

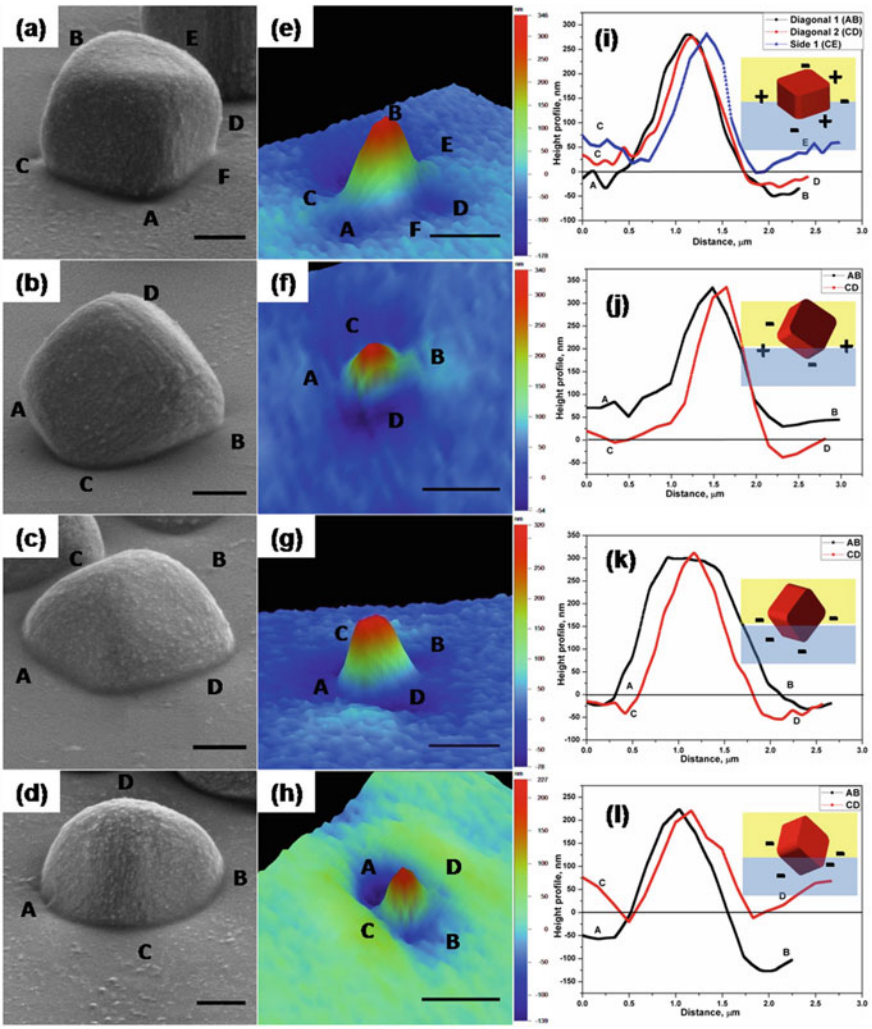

Fig. 14.6 The scanning electron microscopy images (**a**–**d**, scale bar: 0.5 μm), deformation of the interface around the particles recorded using surface profiler (**e**–**h**, scale bar: 5 μm), and the height profiles drawn along different lines **i**–**l** showing the nature of local deformation of the interface around hematite cuboids at decane–water interface. The length of the cuboids is 1500 nm. The images and height profiles are recorded from the PDMS samples in which the particles are trapped by the gel trapping technique. The interface deformation is identified to be hexapolar type in the face-up configuration (**a**, **e**, and **i**), quadrupolar in the tilted edge-up configuration (**b**, **f**, and **j**), and monopolar in the edge-up (**c**, **g**, and **k**) and vertex-up configuration (**d**, **h**, and **l**). The positive and negative sings in the insets **i**, **j** show the capillary charges associated with the interface deformation. The figures are reproduced with permission from American Chemical Society [51]

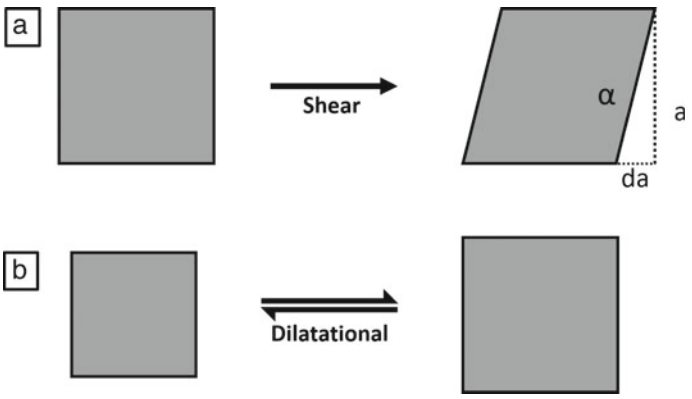

Fig. 14.7 A schematic representation of **a** surface shear and **b** surface dilatation to which an interface can be subjected

where γ_0^s is the surface shear strain. $G^{s'}$ storage modulus (elastic part), and $G^{s''}$ is the loss modulus (viscous part). Note that the superscript "*s*" is used to represent the surface. The interfacial rheology can be performed on soft materials adsorbed at either gas–liquid or liquid–liquid interface. The suitability of a particular method for the measurement of interfacial rheology depends on several parameters such as the concentration of interfacially adsorbed species, the nature of colloidal interactions, the type of fluids used to create the interface, etc. The study of the viscoelastic properties of interfacial monolayers involves the measurement of viscous surface modulus and elastic surface modulus. The interfaces are always surrounded by bulk phases, making the interpretation of the interfacial rheology measurements difficult and challenging. In general, it is desirable if the contribution of the surfaces dominate the effects that arising due to bulk flows created during interfacial rheology measurements. To this end, appropriate geometries have been designed to reduce the influence of bulk flow. Prior to initiating interface rheology measurements, the geometry used to deform the interface is carefully positioned at the interface, thereafter, complex materials are introduced at the interface using appropriate protocol. The total drag on the geometry is caused not only due to interface but also due to the presence of the sub-phase in the system. The Boussinesq (B_o) number, given by

$$B_0 = \frac{\text{Surface drag}}{\text{Sub phase drag}} = \frac{\eta_s}{\eta \times a} \tag{14.10}$$

which is a dimensionless parameter defined as a ratio of surface drag to subphase drag, is used to assess the influence of influence of bulk flow. In Eq. 14.10, η_s is the surface shear viscosity, η is the bulk viscosity of the sub-phase, and a is the characteristic length of the measuring geometry. The characteristic length should be as small as possible to get a higher Boussinesq number. If the value of $(B_0) \gg 1$, the interfacial stress dominates, and interfacial surface rheology data are more reliable.

In dilational surface rheology, the area of the interface is subjected to a periodic change either in the formation of sinusoidal, rectangular or triangular pulsation for a range of frequency using piezoelectric setup at a fixed amplitude resulting in expansion or compression of the interface. The response of the interface to the periodic change in area is expressed in the form of a frequency dependent quantity, dilational modulus (E),

$$E(\omega) = E'(\omega) + E''(\omega) = \frac{\mathrm{d}\gamma}{\mathrm{d}\ln A} = E'(\omega) + i\omega\eta \tag{14.11}$$

where the real part $E^{'}(\omega)$ = dilational elasticity and imaginary part $E^{''}(\omega) = i\omega\eta$ is the dilational viscosity.

Hematite ellipsoids have been used as model colloids to elucidate the effect of particle aspect ratio (AR, defined as the length of major axis to the length of minor axis) and surface coverage defined as the area occupied by the particles to the total area of the interface on the surface rheological properties shown respectively in Fig. 14.8a, b [2]. The surface storage and loss modulus of hematite ellipsoids of 2.8 and 4.6 aspect ratios obtained by strain amplitude sweep at a fixed frequency of 1 Hz is shown in Fig. 14.8a. The dispersions with same bulk concentrations are used to create the monolayer at oil–water interface at a surface coverage of about 0.7. A bi-cone geometry attached to a conventional stress rheometer is used to obtain these results as the monolayer is loaded with sufficient quantity of particle, that is, moderate-to-high particle surface coverage. The storage modulus increases with (i) increase in aspect ratio and (ii) increase in surface coverage of particles at the interface, as shown in Fig. 14.8a, b, respectively. The higher-storage modulus is argued to be due to particle-shaped induced capillary attraction between ellipsoids at the interface. The monolayer of higher aspect ratio ellipsoids (at a particular surface coverage) and higher surface coverage (at a particular aspect ratio) is found to have higher-storage modulus indicating that the interface is more elastic. At low strain, the surface storage modulus is found to remain constant. Thereafter, the surface storage modulus is observed to decrease monotonically as the applied strain is increased. The surface loss modulus is found to show a slight increment (bump) on the intermediate strain amplitude prior to continues to decrease at higher strain. This slight increment in surface loss modulus is an indication of breakup of the aggregated network of the ellipsoids formed at the fluid–fluid interface. The storage and loss modulus measured by frequency sweep tests are found to be independent of frequency, indicating that the monolayer of ellipsoids at fluid–fluid interface behave as two-dimensional colloidal gels [2].

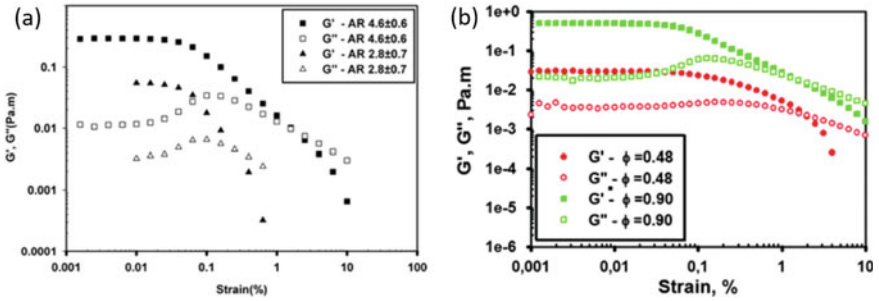

Fig. 14.8 The surface storage modulus and surface loss modulus of monolayers of hematite ellipsoids measured by strain sweep tests: **a** effect of aspect ratio investigated by spreading ellipsoids of AR = 2.8 and AR = 4.6 at decane–water interface at a surface coverage of 0.7 **b** effect of surface coverage studied by spreading ellipsoids of AR = 4.3 at 0.48 and 0.90 surface coverage. The figures are reproduced with permission from the Royal Society of Chemistry [2]

14.8 Emulsion Stabilization Using Anisotropic Iron Oxide Particles

The emulsions are a mixture of two immiscible liquids in which one phase exists as a droplet and the other as a continuous medium. Surface-active emulsifiers such as surfactants, polymers, polyelectrolytes, solid particles, biological material, or a combination of these adsorb at the interface and help the droplet to remain stable against coalescence [1, 51, 56, 57]. Emulsions stabilized by colloidal scale particles, known as Pickering emulsions, are known to be highly stable compared to emulsions stabilized by smaller molecules such as surfactants, polymers, or polyelectrolytes. The emulsions can be broadly classified as single, double, and multiple. There are two types of single emulsion, oil-in-water (o/w) and water-in-oil (w/o), which form depending on the wettability of the colloidal particles. The use of hydrophilic particles ($\theta < 90°$) for emulsification facilitates the formation of oil-in-water (o/w), and when the particles are hydrophobic ($\theta > 90°$), the resulting emulsions are of water-in-oil (w/o) type. The hematite nanoellipsoids [1, 2, 39, 58, 59], micro-ellipsoids [1], cube [58, 60], peanut [12, 58, 60], spherocylinder [58], have been shown to form highly stable o/w emulsions due to partially hydrophilic nature. The hematite particles of different shapes have been successfully used (i) to stabilize Pickering emulsions, (ii) demonstrate the influence of pH and salt on emulsification, (iii) pH induced destabilization of emulsions, and (iv) effect emulsion phase inversion.

14.8.1 Role of Aspect Ratio of Ellipsoids

The emulsification experiments carried out by manually mixing 1 wt% aqueous suspensions of hematite ellipsoids of different aspect ratios ranging from 1 to 6 and an

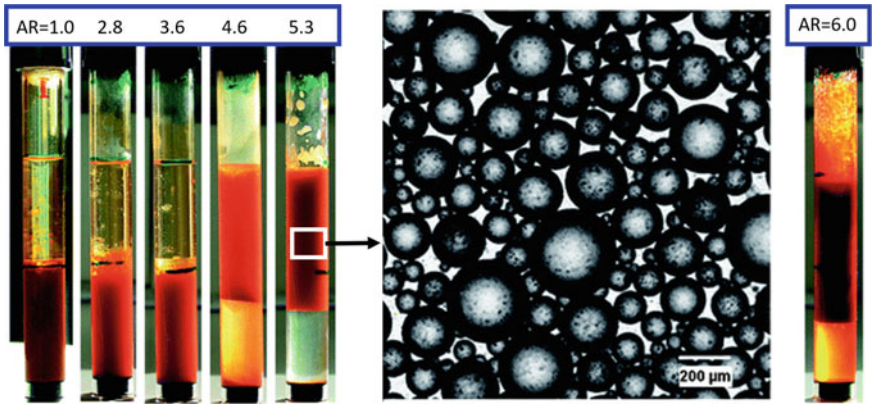

Fig. 14.9 The visual appearance of the vials after manual mixing of aqueous dispersions of hematite ellipsoids (1 wt% concentration) and decane, taken in equal volume. The aspect ratio (AR) of the particles in the aqueous dispersion is varied systematically. The approximate AR of the particles in the aqueous dispersion used (inscribed on the top of each vial) corresponds to 1.0, 2.8 ± 0.7, 3.6 ± 0.8, AR = 4.6 ± 0.9, 5.3 ± 0.8, and 6 ± 1. An optical microscopy of the oil-in-water emulsions stabilized by ellipsoids of AR = 5.3 ± 0.8 is also shown. The figure is reproduced with permission from the Royal Society of Chemistry [2]

equal volume of decane carried out for a duration of 1 min produced the results shown in Fig. 14.9. It is evident from the image of the vials that the dispersions of small aspect ratio ellipsoids and spheres and the oil phase completely phase-separate soon after the mixing process giving rise to an aqueous dispersion of hematite particles at the bottom and a clear oil phase at the top. However, with dispersions of higher aspect ratio ellipsoids, the mixing process resulted in the formation of clear water at the bottom of the vial and an emulsified oil that creams to the top. The microscopy image in Fig. 14.9 shows the microstructure of the emulsion when the aspect ratio of particles in the aqueous dispersion is 5.3. These results demonstrate the role of particle shape and the existence of a critical aspect ratio (4.6) beyond which Pickering emulsion can be formulated. These emulsions are found to be stabilized by a close packed monolayer of ellipsoids which prevent the coalescence of the drops and are found to exhibit exceptional stability. The formation as well as the stability of emulsions is attributed to shape induced capillary attraction that leads to interfaces with exceptional surface rheological properties [2].

14.8.2 Emulsions Stabilized by Cubes and Peanuts

The influence of average side length of the hematite cubes and particle concentration on the formation of Pickering emulsions is presented in Fig. 14.10a, b. The concentration of hematite cubes of average side length $d = 0.85$ is varied from 0.4 to 6.0 wt% and that of hematite cubes of average side length $d = 2.64$ is varied from 2.0

to 6.0 wt%. As visibly evident, the reddish-brown phase at the top consists of oil drops that cream to the top due to lower density. These oil-in-water emulsions are formed due to the adsorption of cubes on the surface of the drops generated during emulsification. It is evident from the image of the vials that very large millimeter sized drops are formed at low particle concentration and drops of smallest size are formed at the highest concentration. That is, the size of the emulsion drop is found to decrease with increase in particle concentration, irrespective of size of the cubes. The surface of the emulsion drops is found to be covered with monolayer of cubes with an average surface coverage up to 0.9. As shown in Fig. 14.10c, the volume of the emulsion phase as well as size and number of drops in the emulsions continue to remain the same even after the application of an external magnetic field of strength 1.33 T. However, the particles in the aqueous phase at the bottom, that is, those that did not adsorb to the oil–water interface during emulsification respond to the applied magnetic field and get attracted. Therefore, along with excellent storage stability, Pickering emulsions also exhibit excellent stability against applied magnetic field. However, the stability and surface coverage of particles on the drop surface can be tuned by the addition of a small quantity of acid or base as hematite particles respond to changes in pH [58].

The use of peanut shape iron oxide particles for emulsion stabilization [60] and the effect of pH and electrolyte concentration on their microstructure and stability has been elucidated [12]. It is shown that the surface charge of the particle, which can be modulated either by changing pH or the addition of electrolyte, is an important factor that dictate the formation and stability of emulsions.

14.8.3 Emulsion Phase Inversion

The conversion of an emulsion from one type to the other, for example, oil-in-water to water-in-oil or vice-versa is termed as emulsion phase inversion. The emulsion phase inversion is an effective strategy for the separation or removal of materials dispersed or dissolved in either oil or water. The manipulation of the wettability of the particles used to stabilize emulsions is a versatile strategy to achieve phase inversion of Pickering emulsions.

The phase inversion of emulsion stabilized by hematite ellipsoids has been demonstrated by in-situ modification of wettability of hematite particles by oleic acid [1]. The pristine hematite micro or nano size are hydrophilic and forms stable oil-in-water emulsion [1, 2, 12, 39, 58, 59, 61]. The reddish phase at the top of the vial (Fig. 14.11a) when observed under an optical microscope is found to consist of spherical drops which is shown in Fig. 14.11b. The surface of the emulsion is fully covered with ellipsoids, that is, the particles are closely packed and are mostly arranged in a side-to-side manner as shown in Fig. 14.11c. This close-packed monolayer of ellipsoids around the drop surface imparts higher stability to the Pickering emulsions. When

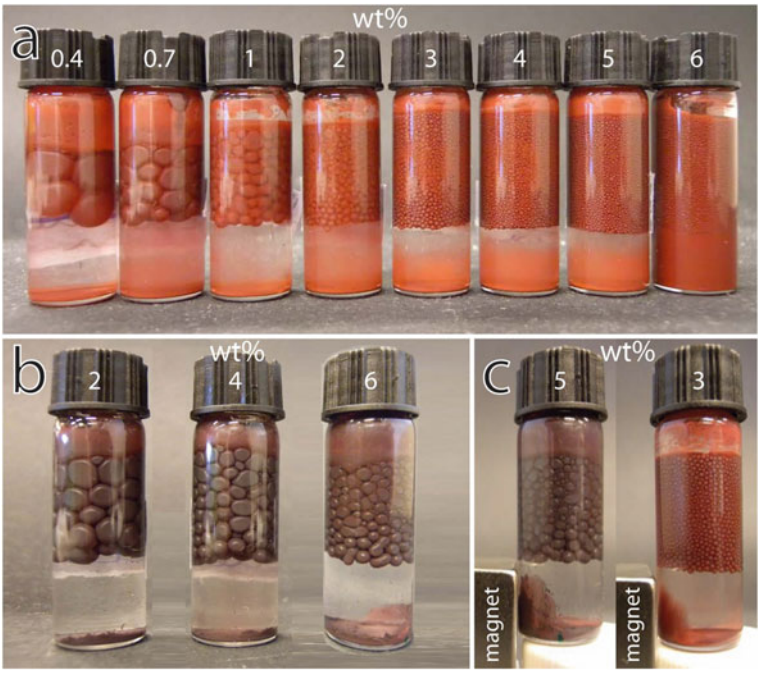

Fig. 14.10 Pickering emulsions stabilized by hematite cubes of average side length **a** $d = 0.85$ μm and **b** $d = 2.64$ μm prepared from equal volume mixture of aqueous dispersion and decane (2 ml each). The image of the vials in **a** and **b** demonstrate the effect of particle concentration. The effect of applied magnetic field to the Pickering emulsions is shown in the vials in **c** for cubes of $d = 2.64$ μm (left image) and $d = 0.85$ μm (right image). The concentration of particles in the aqueous dispersions used to prepare the emulsions is mentioned at the top of each vial. The figure is reproduced with permission from the American Chemical Society [60]

sufficient quantity of oleic acid is added to the oil-in-water emulsions stabilized by hematite particles and the contents of the vial is homogenized again, the emulsion is observed to change from oil-in-water to water-in-oil type. The drops are found to settle at the bottom as seen in vial in Fig. 14.11d as a consequence of higher density and large size. A drop test is used to identify that the emulsions are indeed of water-in-oil type. The oleic acid added to the emulsion phase adsorbed on the surface of the hematite particles during the re-homogenization step leading to the change in the wettability of the hematite particles changes from hydrophilic to hydrophobic. This is further confirmed by contact angle measurements. The contact angle of water drop on the substrate coated with unmodified ellipsoids immersed in decane is measured to be $\theta = 16 \pm 2$ °C. However, when 10 mM oleic acid is added, the contact angle of water drop on the substrate coated with oleic acid modified ellipsoids increased sharply to $\theta = 167 \pm 2$ °C. The side view of the water drops used to measure the contact angles are also shown in Fig. 14.11. Therefore, oleic acid can be used for

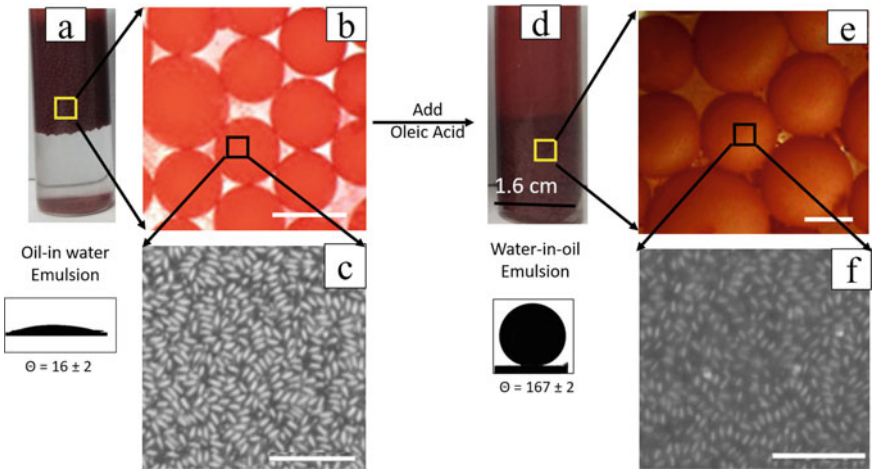

Fig. 14.11 The appearance (**a**), microstructure (**b**), and arrangement of particles on the surface of oil drops **c** in the oil-in-water emulsions stabilized by micro-ellipsoids. After the addition of 10 mM oleic acid and re-homogenisation, a phase inversion from oil-in-water to water-in-oil is observed. The appearance, microstructure, and arrangement of particles on the surface of water drops in the water-in-oil emulsions is shown respectively in (**d**, **e** and **f**). The side view of the water drops on a glass substrate coated with pristine micro-ellipsoids and oleic acid modified ellipsoids immersed in decane which are used to assess the wettability of particles are also presented. The scale bar in **b** and **e** is 1 mm and **c** and **f** is 10 μm. The figure is reproduced with permission from the American Chemical Society [1]

in-situ surface modification of hematite particles and effect emulsion phase inversion. The microscopy image of the drops and the arrangement of oleic acid modified ellipsoids on the surface of emulsion drops is shown respectively in Fig. 14.11e, f. Similar to the case of unmodified ellipsoid stabilized oil drops, the surface of water drops shown in Fig. 14.11f is completely covered with oleic acid-modified ellipsoids.

References

1. Kumar H, Dugyala VR, Basavaraj MG (2021) Phase inversion of ellipsoid stabilized emulsions. Langmuir 37(24):7295–7304
2. Madivala B, Vandebril S, Fransaer J, Vermant J (2009) Exploiting particle shape in solid stabilized emulsions. Soft Matter 5(8):1717–1727
3. Dugyala VR, Daware SV, Basavaraj MG (2013) Shape anisotropic colloids: synthesis, packing behavior, evaporation driven assembly, and their application in emulsion stabilization. Soft Matter 9(29):6711–6725
4. Dugyala VR, Basavaraj MG (2015) Self-assembly of nano-ellipsoids into ordered structures via vertical deposition. RSC Adv 5(74):60079–60084
5. Amendola V, Meneghetti M, Granozzi G, Agnoli S, Polizzi S, Riello P, Boscaini A, Anselmi C, Fracasso G, Colombatti M et al (2011) Top-down synthesis of multifunctional iron oxide nanoparticles for macrophage labelling and manipulation. J Mater Chem 21(11):3803–3813

6. Indiarto R, Indriana LPA, Andoyo R, Subroto E, Nurhadi B (2021) Bottom–up nanoparticle synthesis: a review of techniques, polyphenol-based core materials, and their properties. Eur Food Res Technol 14:1–24
7. Shavel A, Liz-Marzán LM (2009) Shape control of iron oxide nanoparticles. Phys Chem Chem Phys 11(19):3762–3766
8. Ocaña M, Morales M, Serna C (1999) Homogeneous precipitation of uniform α-Fe_2O_3 particles from iron salts solutions in the presence of urea. J Colloid Interf Sci 212(2):317–323
9. Ozaki M, Kratohvil S, Matijević E (1984) Formation of monodispersed spindle type hematite particles. J Colloid Interf Sci 102(1):146–151
10. Kuijk A, Van Blaaderen A, Imhof A (2011) Synthesis of monodisperse, rodlike silica colloids with tunable aspect ratio. J Am Chem Soc 133(8):2346–2349
11. Sugimoto T, Khan MM, Muramatsu A (1993) Preparation of monodisperse peanut-type α-Fe_2O_3 particles from condensed ferric hydroxide gel. Colloids Surf A Physicochem Eng Aspects 70(2):167–169
12. Anjali TG, Basavaraj MG (2018) Influence of pH and salt concentration on Pickering emulsions stabilized by colloidal peanuts. Langmuir 34(44):13312–13321
13. Lama H, Dugyala VR, Basavaraj MG, Satapathy DK (2016) Magnetic field-driven crack formation in an evaporated anisotropic colloidal assembly. Phys Rev E 94(1):012618
14. Matijević E (1976) Preparation and characterization of monodispersed metal hydrous oxide sols. Colloids and surfaces. Springer, New York, pp 24–35
15. Matijević E (1977) The role of chemical complexing in the formation and stability of colloidal dispersions. J Colloid Interf Sci 58(2):374–389
16. Matijević E, Scheiner P (1978) Ferric hydrous oxide sols: III. Preparation of uniform particles by hydrolysis of Fe(III)–chloride, –nitrate, and –perchlorate solutions. J Colloid Interf Sci 63(3):509–524
17. Matijevic E (1981) Monodispersed metal (hydrous) oxides-a fascinating field of colloid science. Accounts Chem Res 14(1):22–29
18. Matijevic E (1993) Preparation and properties of uniform size colloids. Chem Mater 5(4):412–426
19. Sugimoto T, Sakata K (1992) Preparation of monodisperse pseudo cubic α-Fe_2O_3 particles from condensed ferric hydroxide gel. J Colloid Interf Sci 152(2):587–590
20. Shavel A, Rodríguez-González B, Spasova M, Farle M, Liz-Marzán LM (2007) Synthesis and characterization of iron/iron oxide core/shell nanocubes. Adv Funct Mater 17(18):3870–3876
21. Sugimoto T, Matijević E (1980) Formation of uniform spherical magnetite particles by crystallization from ferrous hydroxide gels. J Colloid Interf Sci 74(1):227–243
22. Matijević E, Sapieszko RS, Melville JB (1975) Ferric hydrous oxide sols I. Monodispersed basic iron(III) sulfate particles. J Colloid Interf Sci 50(3):567–581
23. Ozaki M, Matijević E (1985) Preparation and magnetic properties of monodispersed spindle-type γ-Fe_2O_3 particles. J Colloid Interf Sci 107(1):199–203
24. Ishikawa T, Matijevic E (1988) Formation of monodispersed pure and coated spindle-type iron particles. Langmuir 4(1):26–31
25. Sugimoto T, Wang Y, Itoh H, Muramatsu A (1998) Systematic control of size, shape and internal structure of monodisperse α-Fe_2O_3 particles. Colloids Surf A Physicochem Eng Aspects 134(3):265–279
26. Hamada S, Matijević E (1982) Formation of monodispersed colloidal cubic hematite particles in ethanol + water solutions. J Chem Soc Faraday Trans I Phys Chem Conden Phases 78(7):2147–2156
27. Hamada S, Matijević E (1981) Ferric hydrous oxide sols. IV. Preparation of uniform cubic hematite particles by hydrolysis of ferric chloride in alcohol–water solutions. J Colloid Interf Sci 84(1):274–277
28. Sugimoto T (1989) Preparation and characterization of monodispersed colloidal particles. MRS Bull 14(12):23–28
29. Sapieszko RS, Matijević E (1980) Preparation of well-defined colloidal particles by thermal decomposition of metal chelates. I. Iron oxides. J Colloid Interf Sci 74(2):405–422

30. Ozaki M, Ookoshi N, Matijević E (1990) Preparation and magnetic properties of uniform hematite platelets. J Colloid Interf Sci 137(2):546–549
31. Sugimoto T, Wang Y (1998) Mechanism of the shape and structure control of monodispersed α-Fe_2O_3 particles by sulfate ions. J Colloid Interf Sci 207(1):137–149
32. Kloust H, Zierold R, Merkl J-P, Schmidtke C, Feld A, Poselt E, Kornowski A, Nielsch K, Weller H (2015) Synthesis of iron oxide nanorods using a template mediated approach. Chem Mater 27(14):4914–4917
33. Meijer J, Rossi L (2021) Preparation, properties, and applications of magnetic hematite microparticles. Soft Matter 17(9):2354–2368
34. Anjali TG, Basavaraj MG (2016) Contact angle and detachment energy of shape anisotropic particles at fluid–fluid interfaces. J Colloid Interf Sci 478:63–71
35. Hamada S, Niizeki S, Kudo Y (1986) The precipitation of monodispersed α-iron(III) oxide particles from iron(III) chloride–glycine system in aqueous and 2-propanol/water media. Bull Chem Soc Jpn 59(11):3443–3450
36. Bailey JK, Brinker CJ, Mecartney ML (1993) Growth mechanisms of iron oxide particles of differing morphologies from the forced hydrolysis of ferric chloride solutions. J Colloid Interf Sci 157(1):1–13
37. Jia B, Gao L (2008) Growth of well-defined cubic hematite single crystals: oriented aggregation and Ostwald ripening. Cryst Growth Des 8(4):1372–1376
38. Pieranski P (1980) Two-dimensional interfacial colloidal crystals. Phys Rev Lett 45(7):569
39. Dugyala VR, Anjali TG, Upendar S, Mani E, Basavaraj MG (2016) Nano ellipsoids at the fluid–fluid interface: effect of surface charge on adsorption, buckling and emulsification. Faraday Discuss 186:419–434
40. Sabapathy M, Md KZ, Kumar H, Ramamirtham S, Mani E, Basavaraj MG (2022) Exploiting heteroaggregation to quantify the contact angle of charged colloids at interfaces. Langmuir 38:7433–7441
41. Sabapathy M, Kollabattula V, Basavaraj MG, Mani E (2015) Visualization of the equilibrium position of colloidal particles at fluid–water interfaces by deposition of nanoparticles. Nanoscale 7(33):13868–13876
42. Loudet J-C, Yodh AG, Pouligny B (2006) Wetting and contact lines of micrometer-sized ellipsoids. Phys Rev Lett 97(1):018304
43. Paunov VN (2003) Novel method for determining the three-phase contact angle of colloid particles adsorbed at air–water and oil–water interfaces. Langmuir 19(19):7970–7976
44. Isa L, Samudrala N, Dufresne ER (2014) Adsorption of sub-micron amphiphilic dumbbells to fluid interfaces. Langmuir 30(18):5057–5063
45. Maestro A, Guzmán E, Ortega F, Rubio RG (2014) Contact angle of micro and nanoparticles at fluid interfaces. Curr Opin Colloid Interf Sci 19(4):355–367
46. Binks BP, Horozov TS (2006) Colloidal particles at liquid interfaces. Cambridge University Press, Cambridge
47. Lehle H, Noruzifar E, Oettel M (2008) Ellipsoidal particles at fluid interfaces. Eur Phys J E 26(1):151–160
48. Botto L, Lewandowski EP, Cavallaro M, Stebe KJ (2012) Capillary interactions between anisotropic particles. Soft Matter 8(39):9957–9971
49. Madivala B, Fransaer J, Vermant J (2009) Self-assembly and rheology of ellipsoidal particles at interfaces. Langmuir 25(5):2718–2728
50. Dasgupta S, Katava M, Faraj M, Auth T, Gompper G (2014) Capillary assembly of microscale ellipsoidal, cuboidal, and spherical particles at interfaces. Langmuir 30(40):11873–11882
51. Anjali TG, Basavaraj MG (2017) Shape-induced deformation, capillary bridging, and self-assembly of cuboids at the fluid–fluid interface. Langmuir 33(3):791–801
52. Soligno G, Dijkstra M, van Roij R (2018) Self-assembly of cubic colloidal particles at fluid–fluid interfaces by hexapolar capillary interactions. Soft Matter 14(1):42–60
53. Lewandowski EP, Cavallaro M, Botto L, Bernate JC, Garbin V, Stebe KJ (2010) Orientation and self-assembly of cylindrical particles by anisotropic capillary interactions. Langmuir 26(19):15142–15154

54. Soligno G, Dijkstra M, van Roij R (2016) Self-assembly of cubes into 2D hexagonal and honeycomb lattices by hexapolar capillary interactions. Phys Rev Lett 116(25):258001
55. Loudet J-C, Alsayed AM, Zhang J, Yodh AG (2005) Capillary interactions between anisotropic colloidal particles. Phys Rev Lett 94(1):018301
56. Binks BP (2002) Particles as surfactants-similarities and differences. Curr Opin Colloid Interf Sci 7(1–2):21–41
57. Kumar H, Basavaraj MG (2022) Plant latex as a versatile and sustainable emulsifier. Langmuir 38(43):13217–13225
58. Anjali TG, Basavaraj MG (2017) General destabilization mechanism of pH-responsive Pickering emulsions. Phys Chem Chem Phys 19(45):30790–30797
59. Kumar H, Upendar S, Mani E, Basavaraj GM (2022) Destabilization of Pickering emulsions by interfacial transport of mutually soluble solute. J Colloid Interf Sci 633:166–176
60. De Folter JW, Hutter EM, Castillo SI, Klop KE, Philipse AP, Kegel WK (2014) Particle shape anisotropy in Pickering emulsions: cubes and peanuts. Langmuir 30(4):955–964
61. Upendar S, Mani E, Basavaraj MG (2021) Pickering emulsions stabilized by sphere-spheroid mixtures. J Dispers Sci Technol 42(13):2022–2031

Chapter 15
Role of Magnetic Nanomaterials in Biotechnological Applications

Shibani Mohapatra, Soumyaranjan Senapati, Jyotirmayee Giri, Adarshi Bhattacharya, Manisha Dash, Tapan Kumar Bastia, Prasanta Rath, and Alok Kumar Panda

Abstract The advent of nanoscience is considered bringing out the next breakthrough in medicine and biotechnology. For the past few decades, many research groups throughout the world are involved in synthesizing novel nanomaterial for several biotechnological applications. In the current chapter, the different types of magnetic nanoparticles along with their properties are discussed. Consequently, the different physical and chemical methods adopted for the synthesis of magnetic nanoparticles have been discussed. The applications of magnetic nanoparticles in biotechnology have been discussed in breadth. Firstly, the role of magnetic nanoparticles in magnetic resonance and sentinel lymph node imaging has been discussed. Thereafter, magnetically triggered drug release and utilization of magnetic nanoparticles in cryopreservation has been elaborated. Finally, the role of MNPs in bacterial sequestration and in cancer diagnosis and therapy has been outlined.

Keywords Magnetic nanoparticles · Biotechnology · Cancer · Imaging · Biosensing · Proteins · DNA

15.1 Introduction

Since the ninth century or a very long time ago, when Mesopotamian artisans used nanoparticles to create a dazzling effect on the surface of pots, there has been a strong scientific interest in the study of nanoparticles (NPs), which are currently the subject of much The Greek word from which "nano" is derived means "dwarf" [1]. Small particles with a magnetic and Ferromagnetic (FM) structure are referred to

Shibani Mohapatra, Soumyaranjan Senapati: These authors contribute equally as first author

S. Mohapatra · S. Senapati · J. Giri · A. Bhattacharya · M. Dash · T. K. Bastia · P. Rath · A. K. Panda (✉)
Environmental Science Laboratory, School of Applied Sciences, Kalinga Institute of Industrial Technology, Deemed to be University, Bhubaneswar 751024, India
e-mail: alok.pandfch@kiit.ac.in

H. Sahoo and J. K. Sahoo (eds.), *Iron Oxide-Based Nanocomposites and Nanoenzymes*, Nanostructure Science and Technology, https://doi.org/10.1007/978-3-031-44599-6_15

as Magnetic Nanoparticles (MNPs) in popular usage [2]. According to the International Organization for Standardization (ISO), a nanoparticle is a "nano-object with all three exterior dimensions in the nanoscale," where the nanoscale is defined as lengths between 1 and 100 nm [3]. Due to their particular qualities, such as their huge surface areas and quantum size effects, nanoparticles are thought of as a different form of matter. Additionally, it represents a fascinating compound that is present in a variety of living things and has a wide range of bio applications. These innovative, easily manufactured nanoparticles have various biomedical uses among all the many types of nanoparticles. Magnetic fields can control magnetic nanoparticles that contain magnetic elements including chromium, iron, cobalt, gadolinium, manganese, and nickel as well as their chemical components such oxides, ferrites, and alloys. Magnetic nanoparticles' physical and chemical properties are strongly influenced by their crystalline structures, sizes, shapes, and chemical composition. In addition to the features that all nanomaterials share, such as a low Curie temperature, a high magnetic susceptibility, and superparamagnetic, magnetic nanoparticles have special magnetic properties [4]. The highest priority for nanoparticles is in medicine, pharmaceuticals, or diagnostics for medication delivery. MNP research has gained a lot of attention in recent years, both technologically and from a fundamental science perspective. Researchers from the fields of chemistry, physics, and biology have all demonstrated a similar interest in synthesizing, understanding, and advancing a variety of applications in the field of MNPs. Over the past 10 years, a lot of research has been conducted in this field due to the potential biological applications of nanosized magnetic particles, such as enhancing magnetic resonance imaging (MRI) quality, hyperthermic cancer cell therapy, site-specific medication delivery, and modifying cell membranes [5]. The right processes, including precipitation, co-precipitation, thermal breakdown, hydrothermal synthesis, microemulsion synthesis, and plant-mediated synthesis, have been created to manage the size and shape of iron oxide magnetic nanoparticles, which influence their importance. The goal of this chapter is to summarize the extensive progress in various biotechnological fields that have been made by different parameters and we can use in different fields, also. so that the reader can use the chapter as a reference if necessary.

15.1.1 History of Magnetic NPs

MNPs have long been a topic of discussion. The Nobel Prize winner Louis Neel's 1949 work on geomagnetism is credited with providing the first insights into the unconventional magnetic behavior of very small magnetic particles. At the time, the nanoparticles were called "fine grains," which indicates magnetic information storage, or other modern applications of such nanoparticles and no one thought about the nanotechnology applications and also anticipated the biomedical. Neel discovered in 1947 that Fe grains with a diameter of < 32 nm are single domain particles. The coercivity of these grains was very high. In 1949, L. Neel proposed foundational research on the magnetism of single-domain grains 2 years later [6], which provides

a quantitative explanation for several geomagnetism experiments' results. In contrast to the thermal remanence that igneous rocks (solidified lava) can develop in the Earth's magnetic field at room temperature, some researchers found that igneous rocks possessed a thermal remanence that was substantially stronger. Furthermore, they learned that rocks heated by the Earth's magnetic field become magnetized in the direction of the field. By tracing the magnetization of rocks, it is possible to infer that the Earth's magnetic field had reversed direction numerous times in the past. The research was also used to date ceramics using pottery ("Terres cuites" in Neel's article). Therefore, the original driving forces behind the research of MNPs were geological and cultural heritage dating, very dissimilar from current topics of interest, which are primarily in biomedicine [7], Neel discovered that under a certain single-domain radius, RSD (he determines RSD16nm for Fe), the single-domain magnetic structure is no longer stable and the magnetization reverses spontaneously in a period known as "relaxation time," giving rise to the "superparamagnetic" behavior. This relaxation period's equation as a function of applied field and temperature was given by Brown [8] investigated this further, and as a result, the Neel–Brown legislation is currently employed in modern MNP applications [9].

15.1.2 Different Types of MNPs

One type of nanoparticle (NP) known as a Magnetic Nanoparticle (MNP) exhibits certain reactions when a magnetic field is applied. It has a large explicit surface area, small molecular size, magnetic responsiveness, and superparamagnetic [10]. In general, MNPs can be selectively connected to functional molecules and permit transportation to a particular location under an external magnetic field [11]. Magnetic nanoparticles are made up of chemically bound nano-forms of magnetic elements like iron, gadolinium, cobalt, nickel, manganese, and chromium. For its nanoscale size, it is superparamagnetic, offering significant potential for a variety of uses. A particularly specific interaction known as magnetism undergoes significant alterations at the nanoscale level [12]. There are several types of magnetic nanoparticles, however, the most significant ones are listed below:

i. Oxides: Ferrite

The magnetic nanoparticles that have been studied the most up to this point are ferrite nanoparticles. Because they are superparamagnetic when ferrite nanoparticles are smaller than 128 nm, they don't have the capacity for self-aggregated [13]. Only when an external magnetic field is present do they exhibit magnetic behavior. The remanence equals zero when the external magnetic field is removed once more. Similar to non-magnetic oxide nanoparticles, ferrite nanoparticles frequently have surfactants, silicones, or derivatives of phosphoric acid added to their surfaces to promote their stability in solutions.

ii. Metallic with a shell

By using surfactants, polymers, precious metals, and moderate oxidation, magnetic nanoparticles' metallic cores can become passive. These Co core, Co O shell, and gold outer shell nanoparticles have recently been studied for their production and exchange bias effects. When exposed to oxygen, Co nanoparticles develop an antiferromagnetic Co O layer on their surface. Recently, graphene was utilized to make nanoparticles with a magnetic core made of either elementary iron or cobalt and a nonreactive shell. The following advantages over ferrite or elemental nanoparticles: A greater level of organic solvents as well as stability in basic and acidic solutions.

15.2 Properties of Magnetic Nanoparticles

Magnetic nanoparticles' physical and chemical properties are significantly influenced by the synthesis method and chemical composition. The particles typically have a size between 1 and 100 nm and may exhibit super par magnetism.

15.2.1 Surface Properties and Charge

Veiseh et al. hypothesized that proteins will absorb charged MNPs, removing them from circulation [14]. Strong negative MNPs in particular cause an increase in liver uptake, while positive MNPs also bind to non-specific cells. The basic principles of electrophoresis—the movement of dispersed colloids with a fluid—are established when an external electric field is applied, since these produces an electric potential distribution. For the synthesis and utilization of nanoparticles, Duran et al. provide examples, such as coating and medication loading.

15.2.2 Size Dependent

Magnetic nanoparticles exhibit a wide range of distinctive magnetic phenomena, as opposed to their bulk counterparts. Their variations in size, shape, and composition have an impact on fundamental magnetic properties, such as coactivity (Hc) and susceptibility. Each nanoparticle transforms into a single magnetic domain when its size falls below a crucial value (Dc), and when the temperature rises over the blocking temperature, it exhibits super paramagnetic activity (Tb). These specific nanoparticles respond swiftly to applied magnetic fields and behave like enormous paramagnetic atoms with hardly any remanence (residual magnetism) and coactivity (the field required to bring the magnetization to zero). Due to their properties, superparamagnetic nanoparticles are extremely sought-after for MR contrast agents.

15.2.3 Composition, Shape, and Size

We have covered the compositional aspect of MNPs in this paragraph. The three most common types of magnetic Nanoparticles (NPs) at the moment are metal, metal alloy, and metal oxide. The most common NPs are iron, cobalt, nickel, silver, gold [15], and silver. Ferrites ($CoFe_2O_4$ and $Mn0.6Zn0.4Fe_2O_4$) and iron oxides ($–Fe_2O_3$ and Fe_3O_4) make up the majority of metal oxide NPs, while other metal alloy NPs include FeCo, FePt, and other elements. Similar to MNPs, there are numerous varieties accessible today. Although the most typical ones are Fe oxides and still Fe with a somewhat consistent composition, numerous others can be used for certain applications. Currently, ferrites with rare earth (RE) metals and additional elements like Zn, Ni, Co, etc. are intended for biomedical applications. Pure metal particles are receiving a lot of attention because of the huge magnetism that pure FeCo alloy particles and Fe can achieve. For use in permanent magnets or storage media technologies, some materials, such as FePt, aspire to have a very significant magnetic uniaxial anisotropy. Normally, RE alloys like Sm–Co or Nd–Fe–B are used to make permanent magnets, but recent efforts to make magnets without RE have prompted the development of MNPs made of Co carbides and Fe with incredibly low iron and extremely high anisotropy [16].

Size: The method used to determine the particle size affects the parameter, which is not a fixed value. The following diameters or similar radii are at least distinguishable.

- Visual radius: The radius of the physical particle can be seen via transmission electron microscopy (TEM) and atomic force microscopy.
- Diffraction radius: The coherent diffracting portion of the particle has a radius of this size. Single crystal particles may have a chaotic surface layer that is visible in TEM but does not affect diffraction.

Magnetic radius: The particle's sensitivity to magnetic fields is dependent on the effective radius of its magnetic core. Because the surface atoms have fewer neighbors and hence experience less exchange and anisotropy interactions, the magnetic behavior changes even in well-ordered particles. This is important in the context of the superparamagnetic.

15.2.4 Particle Shape

It is impossible to find real spherical particles since crystals are crystalline and have preferred crystallographic planes at their surfaces. The precursor type and concentration can be modified, as well as the inclusion of contaminants while synthesizing in an organic medium. The formation of the particle is kinetically controlled at high precursor concentrations, changing the particle's shape to cubic or tetrahedral. Nanocapsules and iron oxide nanorods/nanorices with rod-like structures have potential applications in the field of biomedicine. Original methods can also be used to create octopuses, flowers, and other strange things [17].

15.3 Different Synthesis Methods

There are two primary ways to create MNPs, and they are as follows: physical methods and chemical approaches. The most popular techniques include wire explosion, ball milling/mechanical process, laser evaporation, and EEW.

15.3.1 Physical Methods

The physical procedures are employed by both top-down and bottom-up approaches. The bottom-up strategy can result in evenly distributed, fine nanoscaled minuscule particles as opposed to the top-down strategy. The prime example of a bottom-up method is laser evaporation [18]. By using a top-down approach, high-intensity ball milling is used to break down bulk materials into nanoparticle sizes. The mechanical crushing of NPs to obtain the desired form and size is difficult [19]. MNPs are also produced physically utilizing a variety of methods, such as the inert-gas condensation method and the wire explosion method.

15.3.1.1 Ball Milling or Mechanical Method

A top-down method of creating MNPs from bulk material is through ball milling. The mechanical grinding of particles with a coarse texture into particles with a fine texture is an easy and practical technique [20, 21]. This technique was initially created in 1970 [22]. Steel balls continuously colliding with solid materials impart kinetic energy to the solids, resulting in a powder that is nano- or micron-sized. The key variables influencing the creation of nano/micro size crystals are the ball to powder ratio, ball size, vibration speed, and milling time. The primary drawback of this procedure is product contamination [23].

15.3.1.2 Laser Evaporation of MNPs

A bottom-up method called laser evaporation creates nanoparticles by condensation from a liquid or gaseous phase. A quick method for producing MNPs is laser evaporation, which is also known as laser ablation. This method can also be used to create iron oxide MNPs. Choosing coarse-textured raw materials (in the m or mm size ranges) and evaporating them through the focus of a laser beam are required steps in this process. The quick condensing and gas phase nucleation of the material's vapors after cooling results in the formation of nanoparticles. This procedure is less expensive and more efficient than wet chemistry methods, which create hazardous waste and need expensive chemicals [24].

15.3.1.3 Wire Explosion Technique

The wire explosion approach, a novel physiochemical technology, allows for the safe and clean synthesis of MNPs. There is no need for any extra procedures, such as by-product retreatment or NP separation from solution, in this very effective one-step approach. This technique was previously used to make iron oxide MNPs to remove arsenic from water [25]. To create fewer polluted nano powders, it is environmentally friendly and uses little energy [26]. It is not possible to manufacture monodispersed NPs using this approach [27].

15.3.1.4 Electrical Explosion of Wires Method (EEW)

Creating metal nanoparticles with this technique is unusual. It was created by Professor Yuri Kotov [28, 29] and is based on the metal wire evaporating when subjected to a strong electric current pulse. The wire, which has a diameter of 0.1–0.5 mm, overheats to 104 K in a matter of milliseconds when exposed to a 5 kV voltage. Before cooling and solidifying into spherical metal nanoparticles, the metal rapidly evaporates, and the vapors disperse in the inert gas. As with an electrical fuse, the fundamental operating principle is the same (Fig. 15.1).

The following are the key characteristics and technological benefits of the EEW.

The metal wire can only be used if it is initially pure. It serves as a limiting factor in the production of precise spherical metal particles with high purity. Crucible, milling, ball, or jar, contamination is not a possibility. It is possible to synthesize carbides, metal oxides, nitrides, etc. by changing the gas environment (O_2, N_2, etc.). The wire diameter and applied pulse energy, length, gas pressure, and flow rate are simple-to-tune variables that affect particle size. The average particle sizes are in the 10–100 nm range.

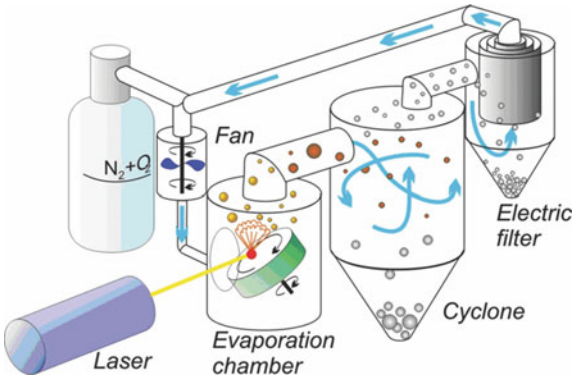

Fig. 15.1 Schematic representation fabrication of the iron oxide nanoparticles. Adapted with permission from AIP Publishing [30]

By synchronizing the supply and evaporation of the wire, a continuous pulsed system can be established in manufacturing. Because the high voltage is only applied briefly per microsecond, there is very little energy use. Since no waste is produced, the process is environmentally friendly.

Depending on the type of metal and the desired attributes of the finished product. The production rate of a single EEW device is considerable (100–500 g/h). The EEW's simple method for surface modification of nanoparticles—either during manufacture, as in the case of I.V., or afterward, when the particles are dropped into a reactive liquid—is arguably its most intriguing aspect [30]. The MNPs in EEW can be modified in situ using both simple liquids and solutions, and the process is adaptable. The active metal surface becomes inert due to saturated hydrocarbons (hexane).

15.3.2 Chemical Method of MNPs

The various bottom-up strategies used in chemical synthesis are diverse. Below is a detailed explanation of some popular techniques for creating MNPs. There are as follows: Coprecipitation method, Thermal decomposition, Hydrothermal, Microemulsion, MNPs coating, and functionalization.

15.3.2.1 Thermal Decomposition

In this procedure, monodispersed NPs are produced at high temperatures using organometallic precursors. This approach results in MNPs with good crystallinity, regulated size, and clearly defined shape. To create MNPs with the necessary size and form, the organometallic precursors are degraded in the presence of organic surfactants [31]. In the process of creating MNPs, stabilizing agents such as hexadecyl amine, fatty acids, and oleic acid are used. The stabilizing agents used in the breakdown process have the power to delay NP nucleation, which controls MNPS growth and helps produce the ideal size of < 30 nm and a spherical shape. This process purportedly resulted in the production of magnetically active iron composites and Fe_3O_4 nanocrystals [32]. Metal nanoparticles (NPs) are made by thermally dissolving the zero-valent metal precursor $Fe(CO)_5$, while high-quality iron oxide MNPs can also be made via oxidation. However, if precursors degrade in the presence of cationic metal centers, metal oxide nanoparticles can be produced instantly [31, 33]. This method has been recommended as one of the finest ways to make MNPs that are uniform and shape on a large scale [34]. The biomedical industry forbids the use of this process due to the risk of creating hazardous organic-soluble solvents [35]. When producing magnetic particles of lower sizes, coprecipitation is less efficient than thermal composition.

15.3.2.2 Coprecipitation

The most popular technique for creating MNPs with regulated size and magnetic characteristics is coprecipitation (Fig. 15.2). It is frequently used in biomedical applications and involves the use of less toxic materials and techniques. When we require a lot of nanocrystals, the coprecipitation method of making MNPs is very practical and simple. This process is frequently used to create NPs with regulated sizes and desirable magnetic characteristics.

To create MNPs, various metal ions are dissolved in a solvent. By employing ferric chloride, manganese ferrite ($MnFe_2O_4$) NPs were created ($FeCl_3$). During the coprecipitation process, several factors, including metal ions, pH, their concentrations, reaction temperature, salt type, and particle size and shape, can have an impact on the composition of MNPs. A quick and easy way to make uniformly dispersed NPs of tiny size is through the coprecipitation of MNPs. It can occasionally be difficult to regulate the shape of MNPs via coprecipitation, even though this method is chosen for its simplicity of application combined with sodium hydroxide (NaOH) salts and manganese (II) chloride ($MnCl_2$) as well as the metal ions or the precipitant.

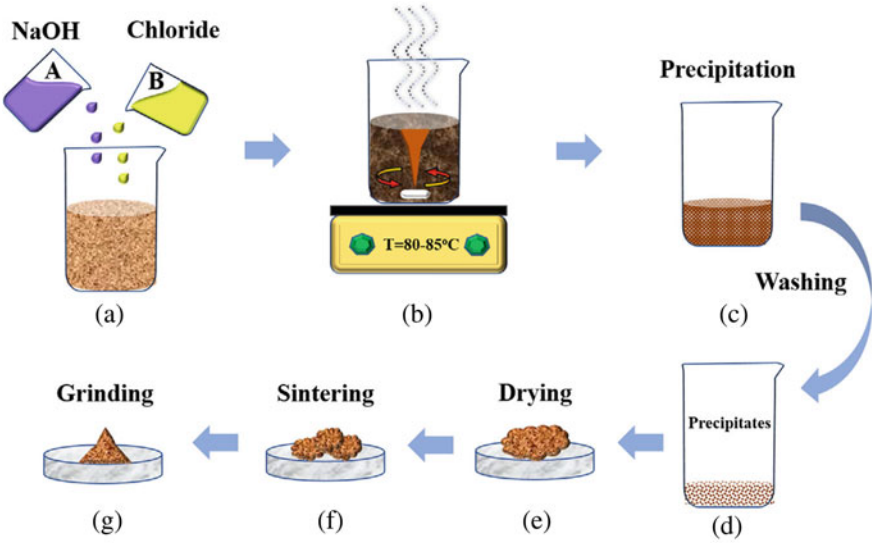

Fig. 15.2 Using the co-precipitation method, the above figure steps to synthesize ferrite nanoparticles: **a** solution of NaOH and chloride precursors, **b** stirring at 80–85 °C for 1 h, **c** precipitation, **d** precipitates after washing, **e** drying at 80 °C, **f** sintering at 1100 °C, and **g** ground final product. Adapted with permission from Wiley [36]

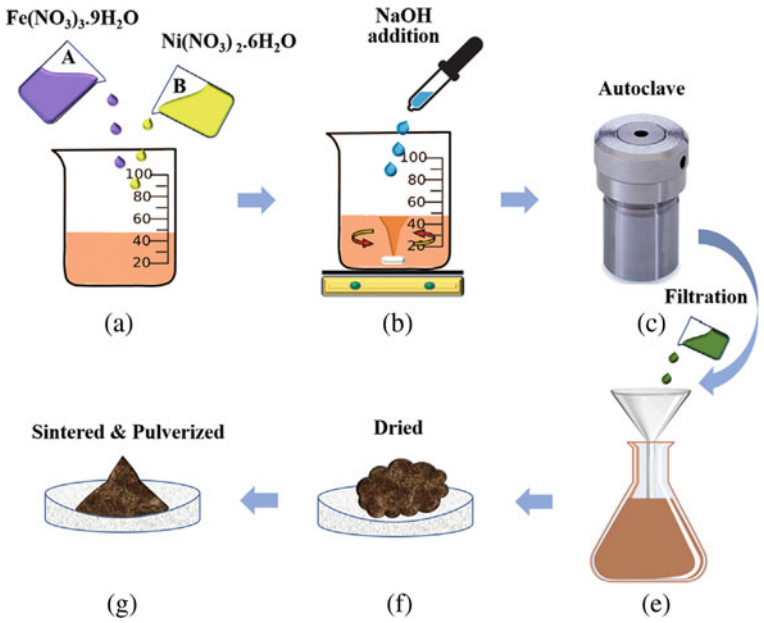

Fig. 15.3 Illustration of ($NiFe_2O_4/Fe_2O_3$) nanocomposite synthesis via hydrothermal method: **a** addition of $Fe(NO_3)_3{\cdot}9H_2O$ and $Ni(NO_3)_2{\cdot}6H_2O$ precursors, **b** magnetic stirring during the addition of NaOH(1 M) until to pH 12, **c** autoclave the mixture for 20 h at 180 °C, **d** filtration, **e** drying at 100 °C, and **f** annealed in the air for 2 h at 400–800 °C and pulverized to get the final product. Adapted with permission from Wiley [36]

15.3.2.3 Hydrothermal

Utilizing high pressure and temperature, this technique is utilized to create NPs in an aqueous solution (Fig. 15.3).

One of the successful solution reaction-based methods for producing MNPs at high pressure and temperature is hydrothermal synthesis, also known as solvothermal synthesis. MNPs are produced by the hydrothermal method via an oxidation and hydrolysis reaction [37]. You can make more NPs by contrasting this method with the microemulsion method. However, due to the high heat and pressure involved in this process, it must be carried out carefully and with specialized equipment. Comparatively, the hydrothermal process is preferred to others, such as sol–gel, since it results in NPs with the right size, shape, high crystallinity, and constant composition [38].

15.3.2.4 Microemulsion

To produce turbid systems of hydrophilic and lipophilic phases in surfactants, microemulsions and occasionally co-surfactants are utilized. This transparent,

isotropic system of water, oil, and amphiphile exists. This procedure involves mixing oil with a surfactant while stirring water magnetically at room temperature. Three types of emulsions exist microemulsions in which the ratios of the two components are roughly equal, oil in water (O/W), which is the aqueous phase with some oil droplets, water in oil (W/O), which is oil as the dominant phase with some water droplets. For instance, a surfactant coated with the droplets of water in an organic solvent in a microemulsion of the w/o type reduces the size of the MNPs [39, 40]. A w/o kind of microemulsion, which required using two microdroplets—one with a precipitating agent and another with a metal percussor which was used to make certain iron oxide MNPs [41]. MNPS was created using a silica coating and then changed with amino after this process, which was beneficial for separating tumor cells. By using microemulsion, small amounts of uniformly dispersed MNPs were produced.

15.3.2.5 MNPs Functionalization and Coating

MNPs are routinely coated with non-magnetic or magnetic materials to make them chemically stable and colloidal (ii) alter the magnetic properties of the MNPs; or (iii) give a different surface. One of the most popular types of coating materials is inorganic, such as silica (SiO_2), gold, or gadolinium. Another frequent option is non-polymer organic stabilizers such as oleic acid, stearic acid, phosphates, etc. Dextran, polyethylene glycol, polyvinyl alcohol, and others are common polymer stabilizers. In this case, the MNPs are fixed, which may not be appropriate for all applications. The MNPs are commonly covered in organic compounds during chemical synthesis. These organic coatings are very simple to create and may be applied on MNP surfaces physically or chemically to create a uniform single-particle covering with variable characteristics. Over the past few years, the surfaces of MNPs have been modified with biocompatible materials such as PEG, carbon, or gold for their prospective use in a range of applications, including the treatment of cancer [42]. It is quite simple to create these organic coatings, which can be applied physically or as already mentioned, by coating the MNPs with specific targeting ligands, therapeutic drugs, or contrast agents that can be employed to functionalize them. By doing so, it is possible to address some of the MNPs' most prevalent drawbacks, such as no specificity and a lack of biocompatibility, while simultaneously giving the MNPs new potential for multifunctional applications. In the context of biological applications, the functionalization of MNPs has drawn a lot of scientific attention. The functionalization of MNPs in biological applications has received a lot of scientific attention. For instance, chemotherapy drug molecules (such as doxorubicin) can be attached to the surface of MNPs, revolving them into magnetic drug carriers that can deliver a large dose of the drug to the tumor area and release the drug in a localized manner, reducing the toxicity of the drug to the rest of the body [43].

15.4 Characterization Methods of MNPS

To evaluate their physicochemical and magnetic properties, the MNPs are described using a variety of tools. Different physicochemical and magnetic properties can be demonstrated by varying the size of NPs. The following tools are used for characterization: Scanning Electron Microscopy (SEM), UV Spectrophotometer, Transmission Electron Microscopy (TEM), Mossbauer Spectroscopy (MS), Energy Dispersive X-ray Diffraction (EDXD), Atomic Force Microscopy (AFM), Fourier Transform Infrared (FT-IR) Spectroscopy [44]. We can utilize more and more of the instruments listed above to study the structure and magnetic characteristics of magnetic nanoparticles.

15.4.1 Surface and Size Morphology

Depending on modifications in size and form, MNPs' physicochemical properties can change. Surface area, size, and particle dispersion are calculated using the Brunauer–Emmet–Teller (BET) and Dynamic Light Scattering (DLS) methods. While it is possible to analyze the surface morphology of MNPs using techniques like SEM/FESEM, TEM/HRTEM, and AFM. We can quantify their diameter by using these tools to get pictures of them that give us a basic idea of their size and shape. Step height, surface roughness, and particle distribution location are used by the AFM technique. Using TEM, it is possible to learn about the size, composition, and morphology of NPs. SEM, on the other hand, offers details regarding the composition and surface topography of the materials. Size estimation is possible using field-emission SEM (FESEM), high-resolution TEM (HRTEM), and XRD methods. Using TEM, it is possible to identify NP aggregation state, crystallinity, lattice spacing, and electron phase shift [45, 46]. Use XRD to determine the crystallinity of NPs. The distribution and average size of the particles can be determined using methods including Mossbauer spectroscopy, DLS, and photon correlation spectroscopy.

15.4.2 Characterization of the Magnetic Properties

MNPs can be measured for magnetization and susceptibility. Magnetometers that use vibrating samples are ideal for this. SQUID magnetometry is needed when the sample quantity is extremely small. Hysteresis loops and other DC magnetization experiments provide values for spontaneous magnetization, remanence, and coercivity. The size distributions of the particles in SPM particles can be described by fits to the lognormal distribution of the Langevin function distributions [47]. The irreversibility temperatures and Zero-field Cooling-Field Cooling (ZFC–FC) curves of M(T) display blocking which offers additional insights into particle distribution

and interactions. The AC susceptibility, which scans the field's frequency and can track the blocking temperatures as a function of frequency throughout a broad range, is another characteristic of the Neel and Brown relaxation processes. 1 Hz to 1 MHz can be easily covered by common equipment.

Sometimes, it's challenging to distinguish between distinct magnetic phases with conventional techniques, and Mossbauer spectroscopy is a crucial tool for separating them. The method can also provide light on the superparamagnetic behavior since the collapse of the hyperfine field affects the blocking temperature. The interaction between absorber nuclei and gamma rays which is the origin of the Mossbauer effect has a comparable frequency of about 60 MHz, which is significantly faster than the much slower direct magnetization or susceptibility measurements described above. The heating efficiency of the MNPs is assessed using a physical metric called the Specific Absorption Rate (SAR). Thermal energy is shown as a unit. The MNPs release mass and time as magnetization switching processes take place in alternating magnetic fields. Serving as the SAR unit is W/g.

In the field of hyperthermia, the SAR parameter has been widely used to assess magnetic particle heating potential and to determine the upper and lower exposure limits for the frequency and field strength of the applied magnetic fields. The most important benefit of laboratory-made equipment is that it is designed and constructed with consideration of the requirements of the various experiments required by the research. Some equipment uses one of two measuring techniques: In some circumstances, a nonmagnetic, nonconducting thermometer records the temperature increase that occurs when the alternating field is applied. Other technologies get the SAR from the loop area via the high-frequency recording of the full hysteresis loop (100 kHz to 1 MHz).

15.5 Applications in Biotechnology

15.5.1 Magnetic Resonance Imaging

Over the past few decades, research in the fields of medicine and biology has been significantly influenced by nanoscience and nanotechnology. Nanoparticles have some unique qualities, such as a high surface-to-volume ratio, quantum properties, and the capability to transport other substances because of their small size. For many medical applications, these qualities make them appealing [48].

MRI or Magnetic Resonance Imaging is a technique that is frequently used for the diagnosis of cancer [49, 50]. Magnetic resonance imaging (MRI) creates images of tissues using the magnetic properties of protons rather than ionizing radiation [51]. This is a noninvasive imaging technique and this creates three-dimensional anatomical images which are useful for the early detection, diagnosis, and follow-up of diseases. Proton dipoles, typically derived from water molecules, are normally positioned within tissue and exhibit a magnetic response in MRIs at the moment

of investigation. There are some examples of Paramagnetic and super-paramagnetic materials like europium (Eu), gadolinium (Gd), manganese, and neodymium (Nd) as examples of paramagnetic materials and those containing iron oxide in the shape of magnetite (Fe_3O_4) and/or g-Fe_2O_3 are examples of super-paramagnetic materials. Iron oxide-based MNPs were used for molecular imaging as they induce a more effective contrast. A powerful and persistent external magnetic field aligns the magnetization of the protons and results in equilibrium magnetization along the z-axis (Mz). The injection of such an exogenous radio frequency (RF) pulse disrupts the equilibrium magnetization. This pulse provides energy to protons by spinning their magnetic moments off the *z*-axis, in phase, and at the flip angle. While emitting RF energy, the protons undergo various relaxation processes to return to their resting alignment. The distribution of signal intensity levels is represented by grayscale images created using the Fourier transform of the measured RF signals after a predetermined amount of time. Protons randomly orient themselves under normal circumstances, producing no overall magnetic moment. After the MRI machine creates the magnetic field, the protons position themselves either parallel or antiparallel to the primary magnetic field. This process, known as longitudinal magnetizable, produces a total magnetic vector (M) which reflects in the direction of the main magnetic field. Gradient coils inserted into the main magnets change the direction of the magnetic field, allowing MRI to image along the *x*, *z*, or *y* axes. Protons revolve around the primary magnetic field's long axis in-phase and out-of-phase at a pace that is directly proportional to the magnetic field's strength [52]. The net magnetizable vector then rotates 90° in the direction of the transverse plane as a result of radio frequency pulses used by doctors to excite protons into an energetic, in-phase condition. Protons finally return to their initial state of longitudinal out of phase and loosen up to their normal state via spin–lattice (T1) and spin–spin (T2) relaxation, respectively [53, 54]. Because of magnetic field inhomogeneities, protons de-phase significantly faster than T2, owing to T2 relaxation and these inhomogeneities [55]. Protons relax across the transverse plane to the longitudinal plane, causing changes in the net magnetic vector that are subsequently utilized to scan tissues.

To improve the accuracy of MRIs, contrast agents are used. Based on their capacity to influence T1 images and also known as T2/T2* relaxation times [56, 57]. T1 contrast agents change the water proton's longitudinal (T1) relaxation times to produce a strong signal and increase the clarity of cells and image intensity. Agents with T2/T2* affect the transverse (T2/T2*) relaxation times. Dark negative signal intensities are produced by water protons in images. Although SPN-based contrast agents are also known to impact T1, their main outcome on T2* relaxation allows for the finding of hypo-intense regions on the acquired image [58]. Because their ability to change T2 and T2* settling time is proportional to their ability to alter the local magnetic field, SPN-based contrast agents with high magnetic vulnerability and relaxivity are preferred.

SPNs have been used to identify and monitor individual cells, as well as to scan tissues and cell clusters [59]. A variety of non-specific SPN-based contrast agents are available for the application of general imaging [60]. These non-specific SPNs, however, are unable to aggregate successfully in limited microniches, including

tumor regions. Tumor-specific delivery of SPNs can boost their accumulation in cancer locations and improve MRI resolution by connecting tumor-specific targeting molecules to the SPN outer shell. Conjugating anti-fetoprotein and anti-glypican antibodies to the SPN shell, for example, can be utilized to target hepatocellular cancer precisely [62]. Future research into specialized contrast agents will improve the availability of MRI as a non-invasive and effective technology for imaging certain disorders. Non-specific SPN-based contrast agents, on the other hand, have unquestionably revolutionized tissue imaging and diagnosis.

15.5.2 Sentinel Lymph Node Imaging

Sentinel node imaging using lymphoscintigraphy reveals the lymph flow path from the cancer location as well as the lymph nodes that are most near the tumor. The term "sentinel lymph nodes" refers to these lymph nodes. The body's lymphatic system can better be visualized with the use of this nuclear medicine scan. In many ways, lymphatics are a complex network of tiny blood vessel-like structures, but instead of carrying blood, they carry a clear fluid called lymph. Numerous locations throughout the lymphatic pathways are home to lymph nodes. Lymphoscintigraphy depicts the lymphatics in numerous body regions and not only reveals their anatomical location and network structure but also their functionality.

Lymph nodes (glands) are small bean-shaped structures that function as nodes to filter lymphatic fluid, removing waste items such as viruses, germs, and cancer cells. The humoral immune system's antigen presentation and crucial processes in cell-to-cell contact also take place in lymph nodes. The first lymph node to collect drainage from particular tumor tissue is referred to as an SLN. There could be more than one SLN for a specific tumor in some circumstances. Since they are the location where the initial tumor has the most chance of spreading, SLNs are essential. Therefore, the malignancy seen in neighboring lymph nodes or SLNs (local lymph nodes) and/or additional accompanying organs determines the stage and degree of spread for oncologists. The spread of cancer informs the creation of a suitable course of treatment. No cancerous cells present SLNs show no evidence of spread; however, it could also imply that cancer has a minimal capacity to spread through a patient. Staging cancer and estimating the extent of In a patient, metastasis are crucial since they are significant. determinants of survival and recurrence. As a result, the presence of cancer in SLNs or surrounding lymph nodes (regional lymph nodes) and/or additionally linked organs aids oncologists in determining the stage and amount of cancer spread (metastasis) and informing the formulation of an effective treatment strategy. The absence of cancer cells in SLNs implies that no dissemination has occurred and may also indicate that cancer in the patient has a poor metastatic ability. The draining Lymph Node (dLN) nearest to the cancer is identified, followed by lymphadenectomy for biopsy to check for the presence of cancer cells. Torchia and colleagues achieved detection of SLNs in sedated pigs using interstitial and intradermal injections of ultra-tiny superparamagnetic iron oxide (USPIO) (0.25 mg

of ferumoxtran-10) in 2001 (Fig. 15.4). The ferumoxtran-10 (Combidex, Advanced Magnetics Incorporated, Cambridge, MA) first-generation USPIO nano-particle has a core diameter of 46 nm and hydrodynamic diameter of 20–40 nm, with only an iron oxide core coated with a layer of dextran. These particles have considerable T1 relaxation effects. Due to the dextran coating, ferumoxtran has a plasma half-life of even more than 24 h in humans. Ferumoxtran was discovered to elude the body's reticuloendothelial system due to its lengthy blood half-life. This makes it ideal for sentinel node mapping. In the study, MRI images were utilized to identify SLNs from 15 min to 48 h after injection. Hiraiwa et al. used a subcutaneous injection of commonly available thermoresponsive MNPs into the thoracic wall of rats to test them as MRI contrast agents. This study shed light on the viability of using commercially available MNPs for SLN mapping. The thermoresponsive polymer loadings of poly N-isopropyl acrylamide in the MNPs studied varied. Pouw et al. [62] used magnetic SLN mapping in ex vivo colorectal cancer tissue (12 patients) to demonstrate the feasibility of using a portable magnetic probe based on a vibrating samples magnetometer (Sentimag, Endomagnetics LTD., London, UK) to estimate the quantity of SPIONs in lymph nodes. With growing interest in noninvasive SLN imaging modalities, MNP-based systems are an appealing and practical option that has the potential to become the diagnostic tool of choice. Higher sensitivity for tracers, pictures with higher resolution, and no tissue penetration depth constraints provide clear advantages over traditional diagnostic procedures.

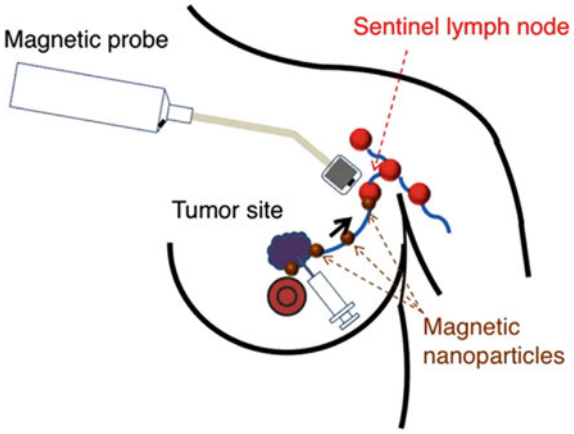

Fig. 15.4 Schematic depiction demonstrating the idea of magnetic detection of sentinel lymph nodes (SLNs) in breast cancer patients using a handheld magnetic probe and magnetic nanoparticles (MNPs). MNPs are injected into the body and collected in the SLNs via the axillary lymphatic system, where they are detected by a magnetometer. Adapted with permission from Elsevier [61]

15.5.3 Magnetic Fluid Hyperthermia

Magnetic hyperthermia is the phenomenon of MNPs creating heat in response to an external magnetic field that alternates. Thermal energy is lost to the environment during magnetizable cycles due to frictional losses caused by the dynamics of viscous suspensions, hysteresis losses in multi-domain MNPs, and Néel or Brown relaxation. The hysteresis loop shows that the temperature increase in multi-domain ferromagnetic or ferrimagnetic substances is primarily due to hysteresis losses. The amount of thermal energy lost to the environment is calculated by combining the hysteresis loop area [63]. Hysteresis losses are heavily influenced by the magnetic field's intensity when it is applied. The type and size of an MNP domain structure have a large influence on the hysteresis of the MNPs and, as a result, their hyperthermia properties [64]. Despite the lack of hysteresis (under normal conditions), superparamagnetic materials lead to magnetic hyperthermia via Néel and Brownian relaxation. In this case, the magnetization of SPNs could be slower than just the magnetization of the applied magnetic field, generating a hysteresis loop that confers hyperthermia features on superparamagnetic materials [65]. SPN magnetizable lags behind the real magnetizable of the applied magnetic field due to the instability and gradual decay of nanoparticle magnetizable in a fluid. Initially the nanoparticles align against or with the applied magnetic field when the same is applied. As previously mentioned, Brownian relaxation refers to the interval that exists between the reversal of the magnetic field and the magnetizable state. When applied to this situation, Brownian relaxation produces heat as a result of friction between MNPs and the medium around them, such as blood. Brownian relaxation is thought to be size and viscosity dependent because it takes longer for Brownian relaxation to occur as MNPs grow in size and the carrier fluid's viscosity rises [66]. The heating effect depends on the amount of energy delivered per second, so the Néel and Brownian relaxation times have a significant impact. Only after MNPs have relaxed and become susceptible to magnetization once more can clinicians re-magnetize them. Consequently, the frequency of the alternating magnetic field should correspond to the estimated relaxation times for an efficient to create an efficient heating effect. Magnesium hyperthermia is one of the many potentials uses for MNPs in the management of infectious and cancerous diseases [51]. Additionally, by employing a heat-labile coating and magnetic hyperthermia, cytotoxic chemicals may be released into cancer cells in a controlled manner (Fig. 15.5).

Using an external magnetic field, Hu et al. recently demonstrated the regulated two medications release (Paclitaxel and Dox) from heat-sensitive polyvinyl alcohol (PVA) coated SPIONs. Furthermore, because of the antibody's anticancer action and the cancer cells' selectivity, antibody conjugation with MNPs increased hyperthermia efficacy. Examples include MNPs with anti-FGFR1 aptamer tags for improved MNPs and magnetic hyperthermia coupled with antibodies for improved anti-cancer effects of cryptotanshinone [67].

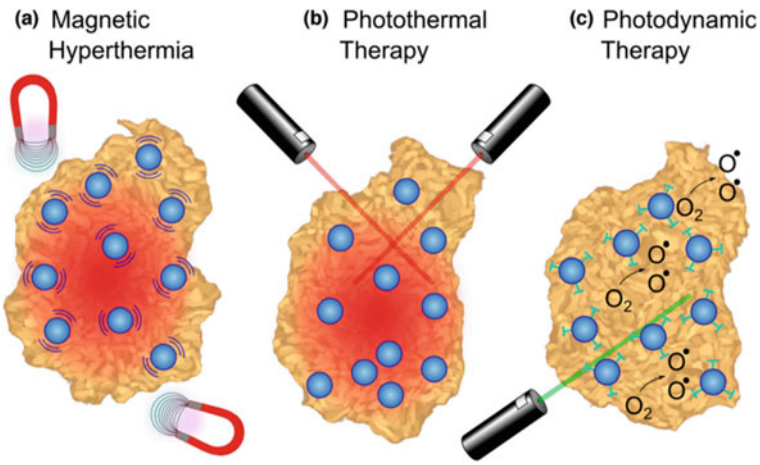

Fig. 15.5 Tumor ablation therapy using MNPs is gaining popularity, including **a** Photothermal treatment (cancer cell death by the heat generated from MNPs upon light), **b** hyperthermia is caused by magnets (necrotic tumor destruction by heat generated from MNPs upon alternating external magnetic field), and **c** photodynamic treatment (death of cancer cell using cytotoxic singlet oxygen species generated from MNPs conjugated with a photosensitizing agent. Adapted with permission from MDPI [67]

15.5.4 Magnetic Particle Imaging

Magnetic particle imaging (MPI) is a new biomedical imaging technology that enables the direct quantitative mapping of superparamagnetic iron oxide nanoparticle spatial distribution. Tomographic images with great temporal and spatial resolution can be created thanks to MPI's enhanced sensitivity and short picture capture times. MPI is projected to outperform currently available medical imaging modalities such as X-ray scans, Magnetic Resonance Imaging (MRI), Computed Tomography (CT), ultrasound, Positron Emission Tomography (PET), and Single Photon Emission Computed Tomography (SPECT).

Magnetic Particle Imaging (MPI) is a novel noninvasive tomographic method that directly detects superparamagnetic nanoparticle tracers. The approach has the potential to be applied to material science and diagnostic imaging. In medical research, it is now used to detect the three-dimensional placement and number of nanoparticles. Imaging uses zero ionizing radiation and can produce a signal at any depth inside the body. Scientists at the Royal Philips Research lab in Hamburg developed MPI in 2001. The first system was created and reported on in 2005. Since then, academics at other universities around the world have refined the technique. MPI hardware differs significantly from MRI hardware. By varying magnetic fields, MPI devices generate a signal from Superparamagnetic Iron Oxide (SPIO) nanoparticles. These fields are specifically designed to produce a single magnetic field-free zone. A signal is only created in this location. When this region is moved across a sample, an image

is produced. Because tissue has no natural SPIO, a signal has only been observed whenever the tracer is administered. This produces photos with no background. MPI is typically used in tandem with anatomical imaging modalities (such as CT or MRI) to provide information on the site of the tracer.

Magnetic particle imaging differs from magnetic resonance imaging (MRI) in the following ways: Even though the technology and imaging techniques appear to be comparable, the physics of magnetic particle imaging (MPI) differs from that of MRI. This can lead to some confusion, therefore it's critical to point out the distinctions. Magnetic field gradients, transmit and receiver coils, pulse sequences, relaxation effects, and the reciprocity concept will be familiar to MRI users. In contrast, MRI produces a signal from tissue, whereas MPI produces a signal only from Magnetic Nanoparticle (MNP) tracers. There is no background signal from anatomy in MPI. MPI is thus classified as a "molecular imaging" technique.

MPI has been proposed as a suitable platform for functioning brain imaging, which needs both extremely sensitive imaging and shorter scan times for appropriate temporal resolution. MPI is used to detect increases in Cerebral Blood Volume (CBV) produced by neuro activation. MPI-based functional neuroimaging has been demonstrated in rodents and offers a promising sensitivity advantage over other imaging techniques. In the long term, this could allow researchers to assess functional neuro activation on a single patient basis, integrating functional neuroimaging into clinical diagnostics.

15.5.5 Magnetically Triggered Drug Release

In recent years, a significant amount of research has concentrated on developing new ways of producing drug nanocarriers, such as dendrimers [68] nanoparticles [69–71], and nanogels [72]. Although the small size of these nanocarriers improves drug permeability and retention [73], these delivery systems are not selective and cannot control drug release correctly. Magnetic Nanoparticles (MNPs), also known as Superparamagnetic Iron Oxide Nanoparticles (SPIONs), have a unique advantage for hyperthermia and targeting when compared to other potential nanocarriers due to their intrinsic magnetic feature. When nanoparticles are subjected to a high-frequency magnetic field, they generate heat, which can be used for localized hyperthermia cancer therapy [74]. Drugs mixed with magnetic nanoparticles can be given to specific areas while avoiding adverse effects when modulated by an external magnetic field. These characteristics bode well for magnetic nanoparticle applications in biomedicine. As a result, considerable effort has been expended on the creation of controlled targeted delivery and release by hyperthermia in a local high-frequency alternating magnetic field (HAMF) [75–77].

Since nanoparticles aggregate in organs and tissues other than the designated target location, there is a great deal of interest in developing nanoparticle drug carriers that release their therapeutic payload in response to external stimuli [78]. Magnetism is one among many techniques for producing "triggered" releases; other famous

examples include light, ultrasound, and temperature. Magnetism can be beneficial since triggered pharmaceutical release can be combined with imaging techniques such as MRI or MPI, as well as other therapies such as MFH. Furthermore, tissue penetration depth does not limit magnetic triggering, and MNPs can be modified and functionalized in a variety of ways [79]. Because of their biocompatibility, liposomes have been a favored alternative for drug administration in general. Doxil, a liposomal version of the chemotherapy medication doxorubicin, is currently in clinical usage and decreases doxorubicin's cardiotoxicity. Several different liposomal nanomedicines have been explored in clinical trials; however, they do not improve overall survival when compared to delivering free medication. As a result, ways of triggering drug release in liposomes, such as the construction of magneto-liposomes, which may release medicine in response to an AMF, have been examined. The heat emitted by the MNPs in an AMF elevates the heat of the liposomal membrane above the transition point, allowing the drug to leak out of the liposome.

The magnetically driven release has also been achieved with polymeric nanoparticles and hydrogels. The mechanism of release is comparable to that of liposomes. MNPs in an AMF generate heat that is used to activate a polymer or hydrogel transition, allowing for higher drug release. Drug cargo may also be loaded onto the particle via thermally labile bonds that dissolve when an AMF is present. The fundamental challenge in using these carriers is minimizing passive, diffusion-driven release at body temperature to near zero while maintaining sufficient release in the AMF [80]. In this strategy, patients would be given nanoparticle drug carriers, which would subsequently be scanned using MPI to detect particle location and heated using an AMF to achieve localized drug release. Particles may be photographed without significant heating because the AMF strengths used for imaging with MPI are significantly lower than those required to activate heat and medication release. The future of magnetically triggered drug release is promising, given the multiple potential platforms for magnetically triggered release and the advancing MPI technology.

15.5.6 Nano Warming of Cryopreserved Tissue and Organs

A key obstacle in meeting the needs of transplant patients is the lack of methods for preserving vascularized organs and tissues. The window between organ/tissue procurement and transplantation could be extended beyond the current preservation time limit (3–24 h depending on the organ/tissue), allowing for thorough testing, careful matching of donors and recipients, and treatment preparation [82]. Cryopreservation through vitrification has the potential for a significant increase in tissue shelf-life. Using highly concentrated concentrations of cryoprotective chemicals, this method permits biologics to be stored at cryogenic temperatures (CPAs) [81]. CPAs enable the liquid to cool to a glassy state, which suppresses crystallization and counteracts the damaging effects of ice formation within the tissue.

Although vitrifying small tissues has been successful, it has been difficult to maintain the structural stability and functioning physiology of large multicellular tissues

and organs. The primary problem is connected with existing rewarming technologies, which include immersing complete organs in a temperature-controlled bath, resulting in thermomechanical strains generated by temperature gradients. One method to overcome this challenge is nano-rewarming, which uses CPA solutions containing SPIONs (magnetic CPA or mCPA), which release heat in reaction to an applied AMF. The study of nano-rewarming is extremely new. Etheridge et al. [82] suggested the fundamental idea of warming a vitrified solution with an AMF. Theoretical research on thermomechanical stresses during magnetic particle imaging-guided drug delivery followed this (MPI). The use of selection field gradients with superposed alternating magnetic fields (AMFs) can be used to photograph and/or heat magnetic nanoparticles (MNPs). By using this technique, doctors may be able to see where the MNP and medicine are located and then only activate the release of heat and the drug where they want it.

Wang et al. [83] used nano-rewarming to cryopreserve human umbilical cord mesenchymal stem cells. The scientists showed that mCPA improved vitrified cells' viability upon AMF rewarming. The particles used in the assays were made using the co-precipitation technique. Particle coating and particle persistence in the CPA solution are not mentioned by the authors. Without any coating, particles produced by the coprecipitation technique are very likely to aggregate and precipitate in fluids other than water. Highly negative particles cause quick nonspecific internalization, as shown in their uptake tests. While being in its early stages, nano-rewarming appears to hold great promise for organ banking. Nanoparticles produced by the coprecipitation method have been used in investigations thus far. The simplicity with which enormous amounts of nanoparticles can be created is a benefit of this type of synthesis. However, polydispersity and low repeatability of warming rates are the key drawbacks. Prior studies' physicochemical and magnetic characterization of mCPAs is restricted, making a rigorous evaluation of formulation improvements unfeasible [84].

15.5.7 Proteins and DNA Separation

Extraction, purification, and selective manipulation of peptides and proteins is a critical necessity in biotechnology and life sciences. Electrophoresis, ultrafiltration, precipitation, and chromatography are examples of traditional methods [85]. In terms of effectiveness and selectivity, affinity chromatography is frequently regarded as the method of choice among those available. However, liquid chromatography can only be used on pre-treated solutions. In homogenous matter, such as protein synthesis mixes, the particulate-free circumstances required for proper commercial column use are incompatible. Because it uses affordable materials and does not require laborious sample preparation, magnetic separation utilizing MNPs is an interesting alternative technique for the selective and trustworthy capture of certain proteins, DNA, and entire cells [86]. Magnetic separation works on a fairly simple premise. MNPs with an immobilized affinity tag, ion-exchange groups, or hydrophobic ligands are mixed

in with the required compounds. Any biological fluid or fermentation broth, including whole blood, plasma, urine, or crude cell lysates, may be utilized as samples. After a suitable incubation period during which the affinity species are permitted to tightly bind to the ligands attached to the MNPs, the complexes are isolated by magnetic decantation, and the impurities are removed. Finally, using the proper elution procedures, the target molecules are purified and removed from the MNPs. MNPs functionalized with ligands containing Ni^{2+}-chelating species, such as nitrilotriacetic acid (NTA), are currently used in the most extensively researched affinity tag-based method for magnetic separation of proteins. This method enables the preferential sequestration of (6 His)-tagged proteins with highly conserved folding down to picomolar concentrations.

New developments in the isolation of biomolecules using MNPs imply that this technique has the potential to be generic and adaptable. Similarly, if appropriate anchors and ligands are applied, various affinity tags that selectively engage with distinct biological targets might be anticipated. To create a tight and reversible capture ideal for Ab sorting, for instance, MNPs functionalized with specific peptides, such as protein A or G, with significant affinities for the Fc region of human IgG Abs can be utilized. For many reasons, MNP protein separation is superior to conventional affinity chromatography. The purification process is easy, rapid, affordable, and scalable [87]. Nano-sized sequestrants have a high surface-to-volume ratio; therefore, little material is needed for the separation procedure. Additionally, no specific tools like centrifuges, filters, or liquid chromatography systems are required for magnetic separation, and there is no need for sample concentration after elution. It is important to note that there are currently automated methods for protein separation or nucleic acids. To separate and concentrate DNA or RNA, selective oligonucleotides grafted onto MNPs can be utilized. These allow the capture of complementary strands [88].

15.5.8 Biosensing with Magnetic Nano Switches

A nano biosensor detects biological agents like antibodies, nucleic acids, infections, and metabolites. The basic idea is to attach bio-analytes of interest to bioreceptors, which then modify the physiochemical signal associated with the binding. Highly sensitive NP-based biosensors have been created as a result of the special electrical, magnetic, and optical properties of specific metal and metal oxide nanoparticles functionalized with affinity ligands, as well as agglomerative phenomena brought on by particular interactions at their surface. For the colorimetric and fluorescence-based detection of oligonucleotides, proteases, Abs, and other molecular species, gold nanoparticles and semiconductor nanoparticles (so-called quantum dots) have been utilized extensively [89]. The main disadvantage of optical biosensing assays is the requirement to reduce sample turbidity or background signals from biological extracts. By utilizing the unusual magnetic properties of MNPs, a new class of nanosensors has been produced. The Weissleder group made the initial suggestion for magnetic relaxation nano switches in a series of influential papers that showed

the effectiveness of this new nano biosensor for the precise and sensitive detection of a wide range of biological species, including DNA, and proteins, pathogens, and processes like enzymatic function. These magnetic relaxation switches were made up of 3–5 nm iron oxide MNPs coated with a 10 nm thick dextran layer that was crosslinked and functionalized with amino groups to covalently anchor the affinity ligands. In the presence of a specific molecule that is specifically recognized by the affinity ligands anchored on the MNPs, such nano switches can undergo reversible assembly, resulting in a change in transverse magnetic relativity ($R2 = 1/T2$) of water protons near the floating nano dipole.

The outer-sphere diffusion theory states that when MNP clusters are sufficiently small, such as within a few hundred nanometers, the assembly has the effect of lowering the average $T2$ value. $T2$ is increased relative to individual MNPs dispersed in the same fluid or matrix when big agglomerates (with sizes ranging from a few micrometers) develop. With magnetic relaxation nano-sensor assays designed to produce reversible nano assemblies upon MNP interaction with specific analytes in solution in either a forward (clustering) or reverse (de-clustering) configuration, both approaches are advantageous depending on the experimental requirements.

Recently, a multiplexed, quantitative, and quick analysis of unprocessed biological material using a chip-based diagnostic magnetic resonance (DMR) device was established. Assemblies of MNPs with higher magnetization promote molecular interaction amplification, which produces the signal. The device's potential has been demonstrated by simultaneously measuring the quantity and presence of proteins, recognizing bacteria, and researching them at the molecular level with extraordinary sensitivity [88].

15.5.9 Bacteria Detection and Sequestration with MNPs

Bacteria are one of the most common living organisms on the planet, having adapted to all available biological niches. As symbionts and parasites, bacteria have a biodiverse impact on the ecological system. They benefit their hosts and are economically significant in the food, agricultural, pharmaceutical, and petroleum industries, among others. They do, however, exhibit pathogenicity to humans and other living things. The presence of unwanted microbes in natural resources makes them difficult to utilize [90].

In complex biological mixtures, bacteria at low concentrations are typically challenging to identify using conventional analytical techniques. However, it is anticipated that nanotechnology would improve environmental monitoring and clinical diagnostics by enhancing sensitivity, selectivity, and analytical time-efficiency. To capture and identify ultralow-level bacteria, Gu et al. developed the MNP system. The D-Ala-D-Ala dipeptide, a crucial component of the microbial capsule, is strongly bound by polyvalent vancomycin, enabling the magnetic capture and enrichment of bacteria. The reported detection limit of this approach, which is comparable to the best polymerase chain reaction assays, was four colony-forming units (cfu) per mL.

Gram-negative bacteria like *E. coli* were also isolated and detected using FePt@Van MNPs. Bacteria might be found in blood samples thanks to the FePt@Van and fluorescent dye combo. By utilizing the interactions between bacteria and the carbohydrates on mammalian cell surfaces, El-Boubbou et al. developed silica-coated magnetic glyco-NPs that could identify *E. coli* strains in 5 min while also eliminating up to 88% of the bacteria from the sample. *Staphylococcus aureus* cells in a mixed cell population could be targeted and trapped with exceptional efficiency and selectivity by MNPs functionalized with a single-domain Ab [91]. The authors employed MNPs with high inherent susceptibility to selectively target infections. The detecting signal was amplified and measured using a miniaturized NMR device after the specimen was concentrated in a microfluidic chamber.

15.5.9.1 MNPs in Cancer Diagnosis

Recently, the development of more effective and economical nanosized contrast agents for CT and MRI for cancer than those already on the market has attracted a lot of attention. Superparamagnetic iron oxide particles (50–100 nm in size) are considered potential MR contrast agents by certain researchers because of their significantly higher magnetic susceptibility than traditional MR contrasts like gadolinium. Many of the commercially available contrast agents for MRI today are composed of superparamagnetic iron oxide (SPIO) nanoparticles covered with carboxydextrane. By synthesizing SPIO nanoparticles with the ability to disperse in chitosan, scientists have generated ferrofluid, which is used to improve MRI contrast agents. In the aforementioned experiment, such MRI image contrast values were comparable to Resovists'. Additionally, there have been advancements made in the diagnosis of colorectal cancer; iron-oxide or iron-cored nanoshells can now be utilized as contrast agents for MRI imaging, which, in addition to being non-invasive, could lead to the development of powerful and practical diagnostic tools.. Recently, magnetic micro/nanoparticles have been employed extensively as signal reporters to find malignant cells and identify other biomolecules. Due to their unique magnetic properties, nanoparticles play two key functions in bioassays: acting as a probe and carrying surface markers for a variety of covalent and non-covalent reactions with antibodies, nucleic acids, and other recognition molecules.

15.5.9.2 MNPs in Cancer Therapy

In recent years, the use of magnetic nanoparticles in cancer treatment has grown significantly. The best therapeutic potential, according to some authors, is found in applications that have three parts: a therapeutic load, a magnetic core, and a recognition layer. Now, a variety of techniques can be used to conjugate these particle suspensions with antibodies while still maintaining the colloidal stability and integrity of the particles. Many types of nanoparticles combined with the anti-Human Epidermal

Growth Factor Receptor 2 (HER2) monoclonal antibody have been created and investigated due to promising results in biological and preclinical applications for the treatment of breast cancer. Another possible method for treating breast cancer is hormone-conjugated nanoparticle therapy. For instance, some publications assert that LHRH- superparamagnetic iron oxide nanoparticles (SPIONs) can be used to target cancer cells in both primary breast tumors and lung metastases by assessing the sub-cellular distribution of SPIONs in tumors and organs using transmission electron microscopy. Overall, there are still a lot of difficulties to be solved before iron-based nanoparticles that target tumors may be successfully deployed in vivo. Functional group modifications of the drugs during conjugation with a nanoparticle, low drug loading efficiency, nanomaterials' failure to reach tumor tissue from the blood, drugs being transported to cancer cells' endosomes or lysosomes instead of their cytoplasm, and a decrease in targeting ability due to weak connections with a nanoparticle are a few examples. Given that many medical professionals think cancer treatment should be based on the quality of life both during and after treatment as well as prognostic factors and chemotherapy, tolerability, compliance, and quality of life may therefore become the most important factors in cancer therapy in the future. According to our analysis, magnetic nanoparticles provide a significant future potential for efficient cancer treatment. Thus, regional health agencies must support laboratories engaged in the development and production of nanoparticles with adequate financing and other resources. Chemotherapy and radiotherapy will undoubtedly continue to be indispensable tools in the fight against cancer, but as nanotechnology develops, it will open up new applications for these tried-and-true treatments.

15.6 Conclusions

Biotechnological and biological applications of MNPs span a wide spectrum of applications magnetic resonance imaging (MRI) to therapeutic agents in cancer treatment. The use of the MNPs for a particular application requires a specific method for synthesis, which results in synthesis of the MNPs having special properties. In addition, the development of an efficient MNPs system for delivering genes into targeted cells, which is a main strategy for understanding gene/protein functions and to improve therapeutics are the field which have a lot of scope to be explored.

References

1. Buzea C, Pacheco II, Robbie K (2007) Nanomaterials and nanoparticles: sources and toxicity. Biointerphases 2(4):MR17–MR71
2. Kang T et al (2017) Surface design of magnetic nanoparticles for stimuli-responsive cancer imaging and therapy. Biomaterials 136:98–114
3. Bruno I, Frey JG (2017) Connecting chemistry with global challenges through data standards. Chem Int 39(3):5–8

4. Wu K et al (2019) Magnetic nanoparticles in nanomedicine: a review of recent advances. Nanotechnology 30(50):502003
5. Berry CC, Curtis AS (2003) Functionalisation of magnetic nanoparticles for applications in biomedicine. J Phys D Appl Phys 36(13):R198
6. Barbara B (2019) Louis Néel: his multifaceted seminal work in magnetism. C R Phys 20(7–8):631–649
7. Rossi LM, Quach AD, Rosenzweig Z (2004) Glucose oxidase–magnetite nanoparticle bioconjugate for glucose sensing. Anal Bioanal Chem 380(4):606–613
8. Brown WF (1963) Thermal fluctuations of a single-domain particle. Phys Rev 130(5):1677
9. Alonso J et al (2018) Magnetic nanoparticles, synthesis, properties, and applications. Magnetic nanostructured materials. Elsevier, Amsterdam, pp 1–40
10. Alavijeh AA et al (2019) The potential of magnetic nanoparticles for diagnosis and treatment of cancer based on body magnetic field and organ-on-the-chip. Adv Pharm Bull 9(3):360
11. Ma Y et al (2018) Polyacrylic acid functionalized Co0. 85Se nanoparticles: an ultrasmall pH-responsive nanocarrier for synergistic photothermal-chemo treatment of cancer. ACS Biomater Sci Eng 4(2):547–557
12. Kronmüller H (2007) General micromagnetic theory. In: Handbook of magnetism and advanced magnetic materials
13. Dhalani J et al (2018) An approach to identify sterol entities from abrus precatorius's seeds by GC-MS
14. Duran E, Firehammer J, Gonzalez J (2008) Liberation psychology as the path toward healing cultural soul wounds. J Counsel Develop 86(3):288–295
15. Chithrani B, Ghazani AA, Chan WCW (2006) Determining the size and shape dependence of gold nanoparticle uptake into mammalian cells. Nano Lett 6:662–668
16. El Gendy AN et al (2015) Chemical composition and antimicrobial activity of essential oil of wild and cultivated Origanum syriacum plants grown in Sinai, Egypt. Ind Crops Prod 67:201–207
17. Roca A et al (2009) Progress in the preparation of magnetic nanoparticles for applications in biomedicine. J Phys D Appl Phys 42(22):224002
18. Biehl P et al (2018) Synthesis, characterization, and applications of magnetic nanoparticles featuring polyzwitterionic coatings. Polymers 10:91
19. DeCastro CL, Mitchell BS (2002) Nanoparticles from mechanical attrition. In: Synthesis, functionalization, and surface treatment of nanoparticles, p 5
20. 戸高義一 et al (2003) ショットピーニングによる鉄材料表面のナノ結晶化. 日本金属学会誌 67(12):690–696
21. El-Eskandarany MS (2013) Mechanical alloying: for fabrication of advanced engineering materials. Elsevier Science, Amsterdam
22. Koch E (1970) Ammonium nitrate explosives for civil applications handbook of combustion organic chemistry of explosives high energy materials nd [2] Benjamin JS Dispersion strengthened superalloys by mechanical alloying. Metall Trans 1:2943–2951
23. Ali A et al (2021) Review on recent progress in magnetic nanoparticles: synthesis, characterization, and diverse applications. Front Chem 9:629054
24. Amendola V, Meneghetti M (2009) Laser ablation synthesis in solution and size manipulation of noble metal nanoparticles. Phys Chem Chem Phys 11(20):3805–3821
25. Remsburg C et al (2019) Analysis of microRNA functions. Methods Cell Biol 151:323–334
26. Tang ZK, Magonov NS, Ozturk B (2003) Nanostructured artificial nacre. Nat Mater 2:413
27. Kawamura T et al (2016) Cardiomyocytes derived from MHC-homozygous induced pluripotent stem cells exhibit reduced allogeneic immunogenicity in MHC-matched non-human primates. Stem Cell Rep 6(3):312–320
28. Kotov YA (2003) Electric explosion of wires as a method for preparation of nanopowders. J Nano Part Res 5:539–550
29. Kurlyandskaya G, Bebenin N, V. Vas'Kovsky, (2011) Giant magnetic impedance of wires with a thin magnetic coating. Phys Metals Metallogr 111(2):133–154

30. Safronov A et al (2013) Spherical magnetic nanoparticles fabricated by laser target evaporation. AIP Adv 3(5):052135
31. Effenberger KA, Urabe VK, Jurica MS (2017) Modulating splicing with small molecular inhibitors of the spliceosome. Wiley Interdiscip Rev RNA 8(2):e1381
32. Ren J et al (2019) Single-cell transcriptomes and whole-brain projections of serotonin neurons in the mouse dorsal and median raphe nuclei. Elife 8:e49424
33. Frey MM et al (2009) Photolysis imprint in the nitrate stable isotope signal in snow and atmosphere of East Antarctica and implications for reactive nitrogen cycling. Atmosph Chem Phys 9(22):8681–8696
34. Kudr J et al (2017) Magnetic nanoparticles: from design and synthesis to real world applications. Nanomaterials 7(9):243
35. Faraji J, Metz GA, Sutherland RJ (2010) Characterization of spatial performance in male and female long-evans rats by means of the Morris water task and the ziggurat task. Brain Res Bull 81(1):164–172
36. Anik MI et al (2021) Recent progress of magnetic nanoparticles in biomedical applications: a review. Nano Select 2(6):1146–1186
37. Reddy LH et al (2012) Magnetic nanoparticles: design and characterization, toxicity and biocompatibility, pharmaceutical and biomedical applications. Chem Rev 112(11):5818–5878
38. Zahid A et al (2019) Pharmacological inhibitors of the NLRP3 inflammasome. Front Immunol 10:2538
39. Mosayebi J, Kiyasatfar M, Laurent S (2017) Synthesis, functionalization, and design of magnetic nanoparticles for theranostic applications. Adv Healthcare Mater 6(23):1700306
40. Lopez Perez J et al (1997) Advances in the preparation of magnetic nanoparticles by the microemulsion method. J Phys Chem B 101(41):8045–8047
41. Lakshmanan R et al (2013) Effect of magnetic iron oxide nanoparticles in surface water treatment: trace minerals and microbes. Bioresour Technol 129:612–615
42. Gupta AK, Gupta M (2005) Synthesis and surface engineering of iron oxide nanoparticles for biomedical applications. Biomaterials 26(18):3995–4021
43. Rui H et al (2010) Effects of heat treatment on internal browning and membrane fatty acid in loquat fruit in response to chilling stress. J Sci Food Agricult 90(9):1557–1561
44. GESAMP, IMO/FAO/UNESCO-IOC/UNIDO/WMO/IAEA/UN/UNEP/UNDP (2015) Joint group of experts on the scientific aspects of marine environmental protection. Rep Stud GESAMP 90:96
45. Gabbasov R et al (2015) Mössbauer, magnetization and X-ray diffraction characterization methods for iron oxide nanoparticles. J Magnet Magnet Mater 380:111–116
46. Chekli L et al (2016) Analytical characterisation of nanoscale zero-valent iron: a methodological review. Analyt Chim Acta 903:13–35
47. Chantrell R, O'Grady K (1994) Applied magnetism. Kluwer Academic, The Netherlands, p 113
48. Rümenapp C, Gleich B, Haase A (2012) Magnetic nanoparticles in magnetic resonance imaging and diagnostics. Pharmaceut Res 29(5):1165–1179
49. Moore CM et al (2013) Image-guided prostate biopsy using magnetic resonance imaging–derived targets: a systematic review. Eur Urol 63(1):125–140
50. Schoots IG et al (2015) Magnetic resonance imaging in active surveillance of prostate cancer: a systematic review. Eur Urol 67(4):627–636
51. Williams HM (2017) The application of magnetic nanoparticles in the treatment and monitoring of cancer and infectious diseases. Biosci Horizons Int J Stud Res 10:1285
52. Schick F et al (1991) Localized Larmor frequency-guided fat and water proton MRI of the spine: a method to emphasize pathological findings. Magnet Reson Imag 9(4):509–515
53. Houmard JA, Smith R, Jendrasiak GL (1995) Relationship between MRI relaxation time and muscle fiber composition. J Appl Physiol 78(3):807–809
54. Hsu J-J, Lowe IJ (2004) Spin-lattice relaxation and a fast T1-map acquisition method in MRI with transient-state magnetization. J Magnet Reson 169(2):270–278

55. Kamada K et al (1994) Localized proton spectroscopy of focal brain pathology in humans: significant effects of edema on spin–spin relaxation time. Magnet Reson Med 31(5):537–540
56. Kato H et al (2003) Lanthanoid endohedral metallofullerenols for MRI contrast agents. J Am Chem Soc 125(14):4391–4397
57. Xing G et al (2008) The strong MRI relaxivity of paramagnetic nanoparticles. J Phys Chem B 112(20):6288–6291
58. Qin J et al (2007) A high-performance magnetic resonance imaging T2 contrast agent. Adv Mater 19(14):1874–1878
59. Nitin N et al (2004) Functionalization and peptide-based delivery of magnetic nanoparticles as an intracellular MRI contrast agent. JBIC J Biol Inorgan Chem 9(6):706–712
60. Tan H et al (2010) Synthesis of PEOlated Fe_3O_4@ SiO_2 nanoparticles via bioinspired silification for magnetic resonance imaging. Adv Funct Mater 20(5):722–731
61. Savliwala S et al (2020) Chapter 13: magnetic nanoparticles. In: Chung EJ, Leon L, Rinaldi C (eds) Nanoparticles for biomedical applications. Elsevier, Amsterdam, pp 195–221
62. Pouw JJ et al (2012) Ex vivo magnetic sentinel lymph node detection in colorectal cancer with a SPIO tracer. Magnetic particle imaging. Springer, New York, pp 181–185
63. Carrey J, Mehdaoui B, Respaud M (2011) Magnetic memory effect of nanocomposites. J Appl Phys 109:083921
64. Hergt R, Dutz S, Röder M (2008) Effects of size distribution on hysteresis losses of magnetic nanoparticles for hyperthermia. J Phys Conden Matter 20(38):385214
65. Usov N, Grebenshchikov YB (2009) Hysteresis loops of an assembly of superparamagnetic nanoparticles with uniaxial anisotropy. J Appl Phys 106(2):023917
66. Kötitz R et al (1999) Investigation of Brownian and Néel relaxation in magnetic fluids. J Magnet Magnet Mater 201(1–3):102–104
67. Mukherjee S, Liang L, Veiseh O (2020) Recent advancements of magnetic nanomaterials in cancer therapy. Pharmaceutics 12(2):147
68. Yellepeddi VK, Ghandehari H (2016) Poly (amido amine) dendrimers in oral delivery. Tissue Barriers 4(2):e1173773
69. Beiranvand S, Eatemadi A, Karimi A (2016) New updates pertaining to drug delivery of local anesthetics in particular bupivacaine using lipid nanoparticles. Nanoscale Res Lett 11(1):1–10
70. DeMarino C et al (2017) Biodegradable nanoparticles for delivery of therapeutics in CNS infection. J Neuroimmune Pharmacol 12(1):31–50
71. Chen S et al (2016) Inorganic nanomaterials as carriers for drug delivery. J Biomed Nanotechnol 12(1):1–27
72. Soni G, Yadav K (2014) Nanogels as potential nanomedicine carrier for treatment of cancer: a mini review of the state of the art. Saudi Pharmaceut J 24:133–139
73. Davis ME, Chen Z, Shin DM (2008) Nanoparticle therapeutics: an emerging treatment modality for cancer. Nature 7:771
74. Brulé S et al (2011) Doxorubicin release triggered by alginate embedded magnetic nanoheaters: a combined therapy. Adv Mater 23(6):787–790
75. Liu T-Y et al (2008) Study on controlled drug permeation of magnetic-sensitive ferrogels: effect of Fe_3O_4 and PVA. J Control Release 126(3):228–236
76. Oliveira H et al (2013) Magnetic field triggered drug release from polymersomes for cancer therapeutics. J Control Release 169(3):165–170
77. Hua X et al (2017) Magnetically triggered drug release from nanoparticles and its applications in anti-tumor treatment. Drug Deliv 24(1):511–518
78. Brazel CS (2009) Magnetothermally-responsive nanomaterials: combining magnetic nanostructures and thermally-sensitive polymers for triggered drug release. Pharmaceut Res 26(3):644–656
79. Singh SK et al (2017) Drug delivery approaches for breast cancer. Int J Nanomed 12:6205
80. Kim D-H et al (2013) Stimuli-responsive magnetic nanomicelles as multifunctional heat and cargo delivery vehicles. Langmuir 29(24):7425–7432
81. Fahy G, Wowk B (2015) Chapter 2 principles of cryopreservation by vitrification. Methods Mol Biol 1257(978):1007

82. Etheridge ML et al (2014) RF heating of magnetic nanoparticles improves the thawing of cryopreserved biomaterials. Technology 2(03):229–242
83. Wang J et al (2016) Magnetic induction heating of superparamagnetic nanoparticles during rewarming augments the recovery of hUCM-MSCs cryopreserved by vitrification. Acta Biomater 33:264–274
84. Manuchehrabadi N et al (2017) Improved tissue cryopreservation using inductive heating of magnetic nanoparticles. Sci Transl Med 9(379):eaah4586
85. Smith AN et al (2000) Mutations in ATP6N1B, encoding a new kidney vacuolar proton pump 116-kD subunit, cause recessive distal renal tubular acidosis with preserved hearing. Nat Genet 26(1):71–75
86. Obata K et al (2002) Recent developments in laboratory automation using magnetic particles for genome analysis. Pharmacogenomics 3(5):697–708
87. García I et al (2011) Magnetic glyconanoparticles as a versatile platform for selective immunolabeling and imaging of cells. Bioconj Chem 22(2):264–273
88. Colombo M et al (2012) Biological applications of magnetic nanoparticles. Chem Soc Rev 41(11):4306–4334
89. Naresh V, Lee N (2021) A review on biosensors and recent development of nanostructured materials-enabled biosensors. Sensors 21(4):1109
90. Johne B, Jarp J, Haaheim L (1989) *Staphylococcus aureus* exopolysaccharide in vivo demonstrated by immunomagnetic separation and electron microscopy. J Clin Microbiol 27(7):1631–1635
91. Jesús M, Penadés S (2006) Glyconanoparticles: types, synthesis and applications in glycoscience, biomedicine and material science. Biochim Biophys Acta Gen Subjects 1760(4):636–651

Chapter 16
Conclusion

Jitendra Kumar Sahoo and Pooja Upadhyaya

In conclusion, efficient works on iron oxide have been aimed at different backgrounds, such as biomedical applications, photovoltaic applications, electronic applications, and the remediation of different water systems like sewage waste, industrial waste, ground waste, etc. For example, for the removal of different types of pollutants, including dyes, pesticides, toxic metal ions, pharmaceutical wastes, sewage wastes, etc., iron oxide is used as a chief element with different functionalities in the form of adsorbents, magnetic nanobeads, photocatalysts, heterogeneous catalysts, etc. Different types of contaminants are removed using various classes of modified iron oxide; for example, toxic dyes are removed using the magnetic behaviour of iron oxide, in which the toxic dyes are attracted towards the magnetic nanosystems and get separated from the water bodies. Similarly, water remediation of organic waste is based on photocatalysis, where iron oxide nanoparticles are used as photocatalysts, which helps in the degradation of organic waste in water bodies and leads to the purification of water. Zero-valent iron is used as an adsorbent for the decontamination of heavy metals and chlorinated hydrocarbons. The improvised magnetic iron oxide nanocomposites are used as an effective adsorbent for prohibiting the dyes, which have been surveyed universally due to their characteristics of getting easily separated, high reusability, high substance strength, and a limit of adsorption.

Due to its abundance, low cost, high surface area, magnetic property, and ease of preparation, iron oxide is largely used as an adsorbent as well as a heterogeneous catalyst for various environmental applications such as heavy metal removal, organic dye contaminants, biosensors, CO oxidation, VOC oxidation, SCR reaction, and Fenton reaction. In particular, in Chaps. 10 and 13, various methodologies like the solgel method, co-precipitation method, coagulation methods, etc., and the morphology of 0D, 1D, 2D, and 3D nanostructures are explained. The adsorptions as well as the catalytic mechanisms are described briefly through the incorporation

J. K. Sahoo (✉) · P. Upadhyaya
Department of Chemistry, GIET University, Gunupur, Rayagada, Odisha 765022, India
e-mail: kumarjitu8093@gmail.com

H. Sahoo and J. K. Sahoo (eds.), *Iron Oxide-Based Nanocomposites and Nanoenzymes*,
Nanostructure Science and Technology, https://doi.org/10.1007/978-3-031-44599-6_16

of several kinetic isotherm models like the Langmuir–Hinshelwood (L–H) mechanism, the Eley–Rideal (E–R) mechanism, and the Mars van Krevalan (MVK) mechanism. Again, all the above-mentioned environmental applications are also concisely explained with methodology, morphology, and schematics in these chapters.

Chapters 2, 4, and 12 address the decontamination of organic pollutants such as organic dyes, pesticides, pharmaceutical products, and organic wastes like phenols, benzene derivatives, etc. from industries, which contribute to the toxicity of the water resources. Out of the different forms of iron oxide, the modified Fe_2O_3 composites are largely used as an adsorbent for the removal of the above-mentioned organic pollutants, although the photovoltaic activity of different Fe_2O_3 functionalized composites has been used for the decontamination of various organic contaminants. The adsorption mechanisms, which involve electrostatic force, Vanderwall force, and surface diffusion, are briefly described. The photocatalytic mechanism, which involves oxidation and reduction due to the striking of the photon particles, is briefly described. There are different parameters that regulate the kinetics of these mechanisms, such as pH, temperature, contact time, adsorbent dose, etc. The optimum values of each parameter for all the composites are mentioned in the above chapters.

As the magnetic character of iron oxide enhances the separation of various magnetic contaminants in wastewater, Chap. 11 provides knowledge about the magnetic iron oxide nanoparticles, their preparation methods, morphology, and schematics that show the separation of contaminants from water. The magnetic behaviour makes it easier to separate the contaminants through a magnet and increases the percentage of reusability for the removal of various contaminants. The removal of heavy metals, pesticides, antibiotics, and dyes using these magnetic nanoparticles is concisely described in this chapter. For the removal of different types of contaminants, the adsorption process is largely used as it is cost-effective, has a large surface area, is easy to prepare, and has magnetic properties. But the large use of this adsorbent can also cause toxicity in the surrounding area. So the main challenge is to reuse the modified iron oxide adsorbent the maximum number of times. Chapter 9 describes the methods by which the adsorbent can be reused several times under various controlled parameters and circumstances. Regeneration and reusability of various iron oxide modified composites are mentioned, and the disposal process of the adsorbent is also concisely mentioned in this chapter.

Iron oxide has many functions and applications, of which the ability to form zerovalent ions is one of them. This ability of iron oxide to form nanozerovalent iron oxide (nZVI) ions can be used in wastewater management processes. The low reduction potential (0.44) of this nanozerovalent iron oxide ion enables the contaminants to get adsorbed on this nZVI, but other iron oxides have a higher reduction value, which makes the nZVI a more efficient and appropriate adsorbent for the removal of chlorinated hydrocarbons and heavy metals like arsenic (As). The preparation of the Nzvi mechanism of adsorption is mentioned in Chap. 11, along with the kinetics and the optimum values of different parameters for each modified composite. Similarly, the non-spherical form of iron oxide and its application for interfacial science and engineering are mentioned in Chap. 14.

Apart from the adsorption and catalytic behaviour and uses of iron oxide in super capacitors, it is also an active part of nanozymes, which helps to increase the rate of biological processes in humans or any living organism. Since natural enzymes are costly, difficult to control, difficult to store, and take more time to complete a reaction, it was seen in literature studies that the enzymatic behaviour of iron oxide-based grafted enzymes is more vigorous towards biological processes. The methods to prepare these nanozymes are concisely mentioned in Chaps. 3 and 6. Also, the various strategies and applications such as diagnosis of tumours and their therapy, enzyme cascades and substrate-based detection, anti-bacteria and biofilm elimination, iron-based nanozymes for cancer treatment, cardioprotection, and wound healing are well described. In Chap. 15, different composites of modified iron oxide nanoparticles are also mentioned, which are used in various biomedical applications and have a greater impact in the future. Some biomedical applications that are mentioned in this chapter are: magnetic resonance imaging, sentinel lymph node imaging, magnetic fluid hyperthermia, magnetic particle imaging, magnetically triggered drug release, protein and DNA separation, MNPs in cancer diagnosis, etc. The preoperational methods are also included in this chapter, which include physical and chemical methods. The physical methods consist of ball milling or mechanical methods; laser evaporation of MNPs; wire explosion technique; electrical explosion of wires method (EEW); and the chemical methods consist of thermal decomposition, co-precipitation, hydrothermal, and microemulsion. The methods of functionalization are also mentioned, which include several factors of MNPs like surface properties and charge, particle shape, composition, shape, and size.

This book also consists of some composites made up of iron oxide modified with graphene oxide, which are also easy to prepare, have a large surface area, require less cost, and, moreover, conduct electricity. Due to this, iron oxide-based composites can be used as super capacitors. Also, iron oxides are found in different polymorphic structures that exhibit magnetic characteristics, catalytic activities, biocompatibilities, and other multifunctional properties. Moreover, bismuth ferrite oxide is used for photovoltaic applications such as electronics, spintronic devices, optics, etc.

Future Perspective

Since iron oxide is one of the most abundant elements in the earth's crust, the use of iron oxide derivative products for decontamination can be a cost-effective process. As we have discussed, iron can be used in different forms and for different functions; iron oxide should be produced on a large scale rather than in a laboratory process. Despite having several applications for iron oxide magnetic nanocomposite, there are several challenges regarding the synthesis of nanocomposite, such as stability, toxicity, and bioavailability. Most of the preparation methods are either chemical or physical, which involve the consumption of a large amount of energy and sometimes produce toxic nanocomposites. Thus, eco-friendly methods should be developed, leading to sustainable development. As the computational study shows a change in the properties of iron oxides moving from laboratory scale to industrial scale, the research work should develop some conventional methods to produce these iron oxide nanocomposites at large scales. In the field of nanoenzymes, iron oxide nanocomposites are

still less active compared to natural enzymes, and few studies have been carried out on their selectivity. Therefore, to improve activity and selectivity by mimicking bioenzymes, we need to have a deeper understanding of the catalytic mechanism at the nanoscale.

By taking the reference of different functionalities of iron oxide, such as photocatalyst, nanoenzyme, heterogeneous catalyst, nanoparticles, etc., some different metal oxides can also be synthesized by using these methodologies, which could be used for water decontamination or remediation, which will lead to sustainable development along with a healthy lifestyle.

Index

H. Sahoo and J. K. Sahoo (eds.), *Iron Oxide-Based Nanocomposites and Nanoenzymes*, Nanostructure Science and Technology, https://doi.org/10.1007/978-3-031-44599-6